

Aircraft Studies of Atmospheric Chemistry over the North Atlantic

By

Gavin D. Edwards

A thesis submitted in partial fulfilment of the
requirements for the degree of

Doctor of Philosophy

University of Leicester

November 2000

UMI Number: U485335

All rights reserved

INFORMATION TO ALL USERS

The quality of this reproduction is dependent upon the quality of the copy submitted.

In the unlikely event that the author did not send a complete manuscript and there are missing pages, these will be noted. Also, if material had to be removed, a note will indicate the deletion.



UMI U485335

Published by ProQuest LLC 2013. Copyright in the Dissertation held by the Author.
Microform Edition © ProQuest LLC.

All rights reserved. This work is protected against
unauthorized copying under Title 17, United States Code.



ProQuest LLC
789 East Eisenhower Parkway
P.O. Box 1346
Ann Arbor, MI 48106-1346

The work described in this thesis was conducted at the Department of Chemistry at the University of Leicester, between October 1997 and November 2000. The work is that of the author, unless acknowledged in the text or references.

This work has not been submitted for any other degrees or at any other Universities

Signed: Gavin D. Edwards

Date: 1/2/2001

Acknowledgements

Much thanks has to go to the people who have helped me over the last three years. First of all to my supervisor Dr. Paul S. Monks, who's guidance, patience and help has been much appreciated, especially his wise decisions in sending me to Colorado and Washington D.C. during the course of my Ph.D. It seems a long time ago now when it was just Paul and I making up the whole of the atmospheric chemistry research group but you know what they say about "little acorns"...

A big thank you also goes to all the other members of the PSM group for their input and help with respect to my work and for the final proof reading of this thesis. They are some of the best people you could ever want to work with. Of course, no comments regarding Gavin S, Gavin P, Gary, Andrew and Mona would be complete without a mention of Coffee Time. I will miss our "serious" discussions on the power of butchers muslin, the new album by "Tepid Hamster" or the latest additions to the PSM-Group Book of Quotations. I look forward to reading it when it comes out in paperback.

I would like to thank other people who have been important to me over the last three years. First of all, Helen and Veryan, my housemates and good friends for putting up with me and my various ways and for teaching me some good lessons. The same goes for my other true friends, Nicola Farley and Chris Gowing whose dedication, motivation and inspiration for me is second to none.

I would like to acknowledge the EPSRC for their financial support during my Ph.D. and finally, to express my love and thanks to Mum and Dad for their never-ending love and support in whatever I do.

"We are all lunatics, but he who can analyse his delusions is called a philosopher"

-Ambrose Bierce

Aircraft Studies of Atmospheric Chemistry over the North Atlantic

Gavin D. Edwards

November 2000.

In this thesis, the broad topic of atmosphere chemistry over the Northern Atlantic is considered, especially using trace gas climatologies as indicators of the influence of continental outflow of anthropogenic pollutants on the composition and chemistry of this region. The data described were obtained during recent aircraft measurements campaigns conducted aboard the UK MRF C-130 Hercules platform, under the auspices of the UK-NERC ACSOE (Atmospheric Chemistry Studies in Oceanic Environment) and the EU MAXOX (MAXimum OXidation rates in the free troposphere) campaigns. Instruments mounted on this aircraft platform provided *in situ* measurements of the concentrations of O_3 , NO_x , NO_y , H_2O_2 , CH_3OOH , CO and $HCHO$ in the free troposphere over the North Atlantic. This thesis describes, in part, the validation of measured modelled trace gas distributions *via* trace gas climatologies over the broad latitude range $20^\circ N$ to $60^\circ N$ by way of data bins ranging from 0-8 km. This climatological analysis provides an insight into the distribution of trace gas in this region, especially on a seasonal basis. Results suggest a number of photochemical tracers show pronounced seasonal variation over altitudes less than 8km. The exact nature of this seasonal variation is discussed, along with possible evidence of a wide spread photochemical source for a pronounced springtime ozone maximum in these environments.

The validation of aircraft measurements has been investigated *via* model analysis. Climatology data has been compared to the outputs of a chemistry transport model. This work shows that for some tracers the model is able to reproduce measured values with a high degree of accuracy, while for others the model shows underestimations of measured values. The development of a 0-D Flight Track Box Model (FTBM) is also described. The model has been used to investigate the oxidising capacity of the free troposphere *via* comparisons of modelled $[HO_2]$ and $[OH]$ to concentrations measured *in situ* during the 1997 SONEX (Subsonic aircraft Ozone and Nitrogen oxide EXperiment) aircraft campaign and, to data derived from the application of simple "steady state" algorithms. Results suggest that the FTBM is able to reproduce $[OH]$ and $[HO_2]$ within the stated accuracy of the measurements quoted for the SONEX experiment, where simple "steady-state" models seem to underestimate $[HO_x]$ owing to the complex chemistry of the mid and upper-troposphere.

Two fixed-bandwidth photoelectric radiometers for the *in situ* measurement of the photolysis of ozone into $O(^1D)$ have been developed. These radiometers were deployed on the C-130 platform during the ACSOE and MAXOX campaigns. A full characterisation of these radiometers is described, together with $j(O^1D)$ measurements. The factors that influenced this photolysis frequency during the ACSOE campaign are also discussed, together with comparisons to modelled data from a full radiative transfer treatment.

The performance of ground based instruments for the measurement of photolysis frequencies during field deployment at the 1998 International Photolysis Modelling and Measurement Intercomparison (IPMMI) in Boulder CO, USA is also described. The results of this experiment are summarised, with an emphasis on the performance of a new diode array spectroradiometer. The instrument was used to measure both actinic flux and $j(O^1D)$ and $j(NO_2)$ at IPMMI. The relative accuracy of these measurements is compared to photolysis frequencies derived using similar and differing experimental techniques. Data suggests the instrument performed adequately, but the problem of poor stray light rejection in the single monochromator used in the instrument has the potential to propagate significant errors in these data. A full error analysis together with instrument characterisation has been performed and is reported. The feasibility of using such instruments in the field for the measurement of atmospheric photolysis frequencies is also discussed.

Content

Abstract

Chapter 1: The Earth's Atmosphere

1.1)	Structure of the Atmosphere	1
1.2)	Composition of the Atmosphere	3
1.3)	Ozone in the Atmosphere	4
1.4)	Photochemistry	6
1.5)	<i>j</i>-(O¹D)	8
1.6)	Other Radical Chemistry	10
1.7)	Measurements and Modelling Atmospheric Chemistry	12
1.8)	This Thesis	14

Chapter 2: Seasonal Trace Gas Climatologies over the North Atlantic: Measurement

2.1)	Introduction	16
2.2)	Work Described in this Chapter	18
	2.2.1) The C-130 Hercules Aircraft	20
2.3)	The ACSOE Aircraft Campaign	22
2.4)	ACSOE Spring and Summer Trace gas Climatologies	27
	2.4.1) ACSOE O ₃ Climatologies	27
	6.9.2) ACSOE CO Climatologies	29
	6.9.3) ACSOE NO _x and NO _y Climatologies	32
	6.9.4) ACSOE Peroxide Climatologies	36
	6.9.5) ACSOE HCHO Climatologies	41
2.5)	Summary of ACSOE Campaign	43
2.6)	The MAXOX Aircraft Campaign	44
	2.6.1) Spring and Summer Climatology Comparison	46
	2.6.2) MAXOX O ₃ Climatologies	46
	2.6.3) MAXOX CO Climatologies	48
	2.6.4) MAXOX NO Climatologies	49
	2.6.5) MAXOX NO ₂ and NO _x Climatologies	50

2.6.6)	MAXOX NO _y Climatologies	52
2.6.7)	Climatologies of Other Trace Gases	54
2.7)	MAXOX-ACSOE Climatology Comparisons	54
2.7.1)	MAXOX-ACSOE Ozone Climatology Comparisons	55
2.7.2)	MAXOX-ACSOE Summer CO Climatology Comparisons	57
2.7.3)	MAXOX-ACSOE Summer HCHO Climatology Comparisons	57
2.7.4)	MAXOX-ACSOE Summer H ₂ O ₂ Climatology Comparisons	59
2.7.5)	MAXOX-ACSOE NO Climatology Comparisons	63
2.7.6)	MAXOX-ACSOE NO _y Climatology Comparisons	65
2.8)	Summary of Climatology data	67

Chapter 3: Seasonal Trace Gas Climatologies over the North Atlantic: Modelling

3.1)	Introduction	71
3.1.1)	Box Models	71
3.1.2)	Chemistry Transport Models	73
3.2)	Box Modelling of ACSOE Trace Gas Concentrations	74
3.2.1)	Box Modelling of [HO _x] data	75
3.2.2)	Box Model P(HO _x) and L(HO _x) pathways	81
3.3)	Ozone Tendencies During the ACSOE Campaign	83
3.3.1)	Control of Ozone During ACSOE Spring Flight Campaign	90
3.3.2)	Control of Ozone During ACSOE Summer Flight Campaign	94
3.4)	Summary of ACSOE Modelled Data	97
3.5)	Intercomparison of Data Measured During MAXOX to CTM Predictions	98
6.9.2)	Comparison of Measured and Modelled [O ₃] During MAXOX Spring	99
6.9.3)	Comparison of Measured and Modelled [O ₃] During MAXOX Summer	100
6.9.4)	Comparison of Measured and Modelled [CO] During MAXOX Spring	101
3.5.4)	Comparison of Measured and Modelled [CO] During MAXOX Summer	101
3.5.5)	Comparison of Measured and Modelled [NO] During MAXOX Spring	102
3.5.6)	Comparison of Measured and Modelled [NO] During MAXOX Summer	103
3.5.7)	Comparison of Measured and Modelled [NO _x] During MAXOX Spring	103
3.5.8)	Comparison of Measured and Modelled [NO _x] During MAXOX Summer	103

3.5.9)	Comparison of Measured and Modelled [NO _y] During MAXOX Spring	104
3.5.10)	Comparison of Measured and Modelled [NO _y] During MAXOX Summer	105
3.6)	MAXOX Ozone Tendencies	107
3.6.1)	MAXOX Flight A700, 2/8/99	107
3.6.2)	MAXOX Flight A701, 4/8/99	110
3.6.3)	MAXOX Flight A702, 5/8/99	112
3.6.4)	MAXOX Flight A703, 6/8/99	115
3.6.5)	MAXOX Flight A705, 9/8/99	117
3.7)	Overall Features of Ozone Tendencies	119
3.8)	Summary of MAXOX Ozone Tendencies and MAXOX-CTM Comparisons	122

Chapter 4: Flight Track and Steady State Modelling of [HO_x] from Aircraft Platforms

4.1)	Introduction	124
4.2)	The SONEX Campaign	128
4.3)	Steady-State HO_x Calculations During SONEX	130
4.4)	Steady-State HO_x during the ACSOE Campaign	139
4.5)	Modelling HO_x Along Aircraft Flight-Tracks	143
4.6)	FTBM vs. <i>in situ</i> SONEX data	145
4.7)	SONEX Modelling Conclusions	149
4.8)	ACSOE Flight Track Modelling	153
4.9)	Overall Summary	156

Chapter 5: Measurement of *In-Situ* Photolysis Frequencies from Aircraft Platforms

5.1)	Introduction	158
5.2)	Factors Influencing j-(O¹D)	161
5.2.1)	Change in Contributions to j -(O ¹ D) from Direct/Diffuse Flux	163
5.2.2)	Temperature Effects	164
5.3)	Characterisation of j-(O¹D) Aircraft Filter Radiometers	166
5.3.1)	Optics System	168
5.3.2)	Angular Response	168

5.3.3)	Bandpass Filter	169
5.3.4)	Photomultiplier Tube	171
5.3.5)	Calibration	173
5.4)	Performance of j-(O¹D) Radiometers During ACSOE	175
5.4.1)	ACSOE Flight A578	176
5.4.2)	ACSOE Flight A579	180
5.4.3)	ACSOE Flight A580	184
5.5)	Modelling Photolysis Frequencies During ACSOE	186
5.6)	Model and Measured j-(O¹D) Profiles	191
5.7)	Remaining Issues	193
5.8)	Overall Summary	194

Chapter 6: The International Photolysis Measurement and Modelling Intercomparison (IPMMI) Experiment

6.1)	Introduction	195
6.2)	j-O(¹D) Filter Radiometer	198
6.3)	Performance of j-(O¹D) filter radiometer at IPMMI	199
6.4)	j-(NO₂) Filter radiometer	202
6.5)	Performance of j-(NO₂) filter radiometer at IPMMI	205
6.6)	Diode Array Spectroradiometer	206
6.6.1)	Instrument Optics	206
6.6.2)	Spectroradiometer Wavelength Calibration Drift and Resolving Power	209
6.6.3)	Instrument Calibration	210
6.6.4)	Effect of Uncertainty in Molecular Parameters	211
6.6.5)	Absolute Sensitivity	212
6.7)	Importance of Stray Light and Dark current	213
6.7.1)	Stray Light Rejection Estimation and Incorporation	213
6.7.2)	Comparison to Model data	216
6.7.3)	Implications of Stray Light Rejection for Photolysis Frequencies	218
6.8)	Improved Stray Light Corrections	223
6.9)	Effect of Molecular Parameters	226
6.9.1)	Effect of Quantum Yield on j -(O ¹ D)	227
6.9.2)	Effect of Cross Section on j -(O ¹ D)	229

6.9.3) "Best" Molecular Data Recommendations During IPMMI	229
6.10) Conclusions	233
Chapter 7: Overall Conclusions	
7.1): Summary of this Thesis	235
References	237
Postgraduate Record of Achievement, 1997-2000	259

Prefix

The units and abbreviations used in this thesis are those commonly in use in atmosphere chemistry and are summarised as follows:

pptv: parts per trillion by volume

ppbv: parts per billion by volume

ppmv: parts per million by volume

pphv: parts per hundred by volume

$k_{(A+B)}$: kinetic rate constant for the reaction of species "A" with species "B"

$j-(X)$: the photodissociation rate constant of species "X"

$j-(O^1D)$: the photodissociation rate constant of ozone to yield the excited oxygen atom (O^1D)

[X]: concentration of species "X"

HO_x : the sum of the hydrogen oxide species OH and HO_2

NO_x : the sum of nitrogen oxide species NO and NO_2

NO_y : Total sum of all reactive nitrogen ($NO+NO_2+HONO+HO_2NO_2+NO_3+N_2O_5$
+PAN+ HNO_3 + organic nitrate+ nitrate aerosol)

Chapter One: The Earth's Atmosphere

<i>1.1)</i>	Structure of the Atmosphere	<i>2</i>
<i>1.2)</i>	Composition of the Atmosphere	<i>4</i>
<i>1.3)</i>	Ozone in the Atmosphere	<i>5</i>
<i>1.4)</i>	Photochemistry	<i>6</i>
<i>1.5)</i>	<i>j</i>-(O¹D)	<i>8</i>
<i>1.6)</i>	Other Radical Chemistry	<i>10</i>
<i>1.7)</i>	Measurements and Modelling Atmospheric Chemistry	<i>12</i>
<i>1.8)</i>	This Thesis	<i>14</i>

Chapter 1: The Earth's Atmosphere

The processes that occur in the atmosphere of the Earth have been one of the most closely studied areas in science over the last few decades, not only with respect to chemistry, but also from the point of view of physics and meteorology. The thin envelope of mainly oxygen and nitrogen that surround our planet is one of the contributing factors to the existence of life. The planet Earth's atmosphere has undergone large-scale evolution from the primordial gases that existed when the Earth formed from the solar nebula and may be continuing to do so. Recent advancements in atmospheric science such as sub parts per trillion detectors and sophisticated computer models have lead to increased understanding of the elementary kinetic, chemical and photochemical reactions that occur in the atmosphere at a time when the need for understanding has never been greater.

It is evident from recent discoveries that anthropogenic activity can seriously perturb the natural chemistry of atmosphere. A triatomic oxygen species called ozone exists in various concentrations throughout the atmosphere, but is found in greatest concentrations in the region of the atmosphere lies *ca.* 10-50 km above the Earth's surface. Here the "ozone layer" provides the surface of the Earth with a protective shield absorbing damaging UV radiation and preventing these wavelengths from reaching the surface. The identification of catastrophic stratospheric ozone loss over the Antarctic continent (Farman *et al.* [1985]) and its link to the large scale use of chlorofluorocarbons (Molina and Rowland, [1974]) proved that human activities can have potentially damaging effects on the natural equilibrium that exists between the atmosphere, the lithosphere, hydrosphere and biosphere. This has been combined with increasing problems such as the "photochemical smog", "global warming" and the increase in extreme weather caused by events such as the shift in Pacific Ocean currents known as El Niño. Increasingly, this area of science has become a matter of public as well as scientific debate. This thesis details work that attempts to increase our understanding of one of these areas of atmospheric science, photochemistry of ozone and related compounds in the region of the atmosphere known as the troposphere.

1.1: The Structure of the Atmosphere

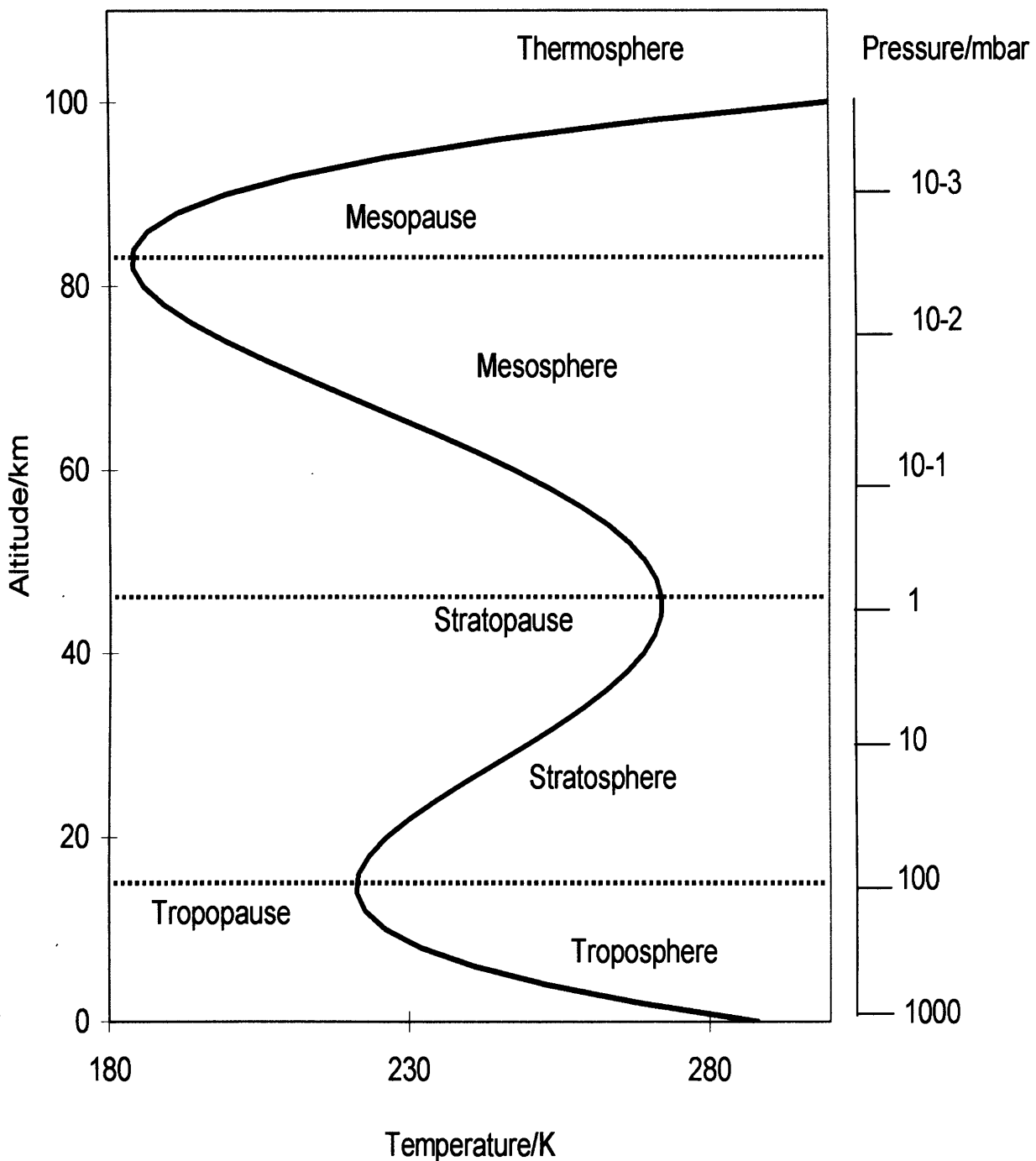
In order to understand fully the research described in this thesis, it is necessary to consider some background regarding the scale and the complex process that occur in the whole

atmosphere. Temperature variations in the atmosphere are very important in considering the physical and chemical processes that occur in the atmosphere. The profile of increasing and decreasing temperature is often used to subdivide the atmosphere into several distinct regions known as the troposphere, stratosphere, mesosphere, thermosphere and exosphere (see Figure 1.1). Moving from the Earth's surface temperature decreases at the rate of *ca.* -7°C for every kilometre of height gained (Finlayson-Pitts and Pitts, [1986]), where thermodynamic transformations occur without the exchange of heat between an air parcel and the surrounding atmosphere. This behaviour is characteristic of an adiabatic lapse rate and occurs for the first 10 km or so of the atmosphere. This is the region of the atmosphere known as the troposphere.

The troposphere itself can be subdivided into two separate regions. The first of these is the "planetary boundary layer". This occupies the first 0.5 - 2.5 km of the troposphere during the day, but owing to radiative cooling, may collapse to only a few hundred meters at night. The boundary layer is that part of the troposphere that is directly influenced by the planet beneath and responds to surface forcing such as heat exchange and evaporation (Stull [1988]). The marine boundary layer that exists over the oceans has additional cooling effects owing to the coupling of this region to the ocean below. The net effect in terms of air mass flow is that in the boundary layer the wind speed and shear forces are governed by horizontal pressure together with the Coriolis force. The net effect of the boundary layer is to localise the dynamic mixing of atmospheric gases with the layer acting almost as a pre-concentrator, especially for atmospheric trace gases. Above the planetary boundary layer is the region of the troposphere often called the *free* troposphere. In the free troposphere, atmospheric trace gases often have concentrations that are often much lower than for those found in the boundary layer with transport of these gases possible over a much greater range.

The free troposphere can therefore be considered a "geostrophic layer", a layer that is decoupled from the surface and has limited interaction with the planet beneath. After 10 or so kilometre's, there is breakdown in the adiabatic lapse rate and a temperature inversion at the so-called tropopause. Although the exact height at which the tropopause occurs varies according to latitude and season. Above this region, the temperature gradient shows an increase with respect to height. This is the region of the atmosphere characterised by warmer air sitting on top of cooler air resulting in a layered structure that lends its name to this atmospheric region, the stratosphere. The stratosphere contrasts the troposphere in that it receives limited heat energy from the planet below and energy is due to chemical reaction and solar energy.

Figure 1.1: Atmospheric Temperature and Pressure Profile



1.2: The Composition of the Atmosphere

The bulk composition of the atmosphere is around 78% nitrogen and 21% oxygen. The remaining 1% is made up of noble gases, and other species such as water vapour and CO₂. The general composition of the troposphere is similar to that of the bulk atmosphere. Although the troposphere appears to be unchanging, it is an active dynamic system with gaseous species continually being exchanged between the atmosphere, the oceans and land (Seinfeld and

Pandis, [1999]). The composition of the troposphere reflects this dynamic nature owing to the presence of trace gases in the atmosphere. These trace gases have both natural and anthropogenic origin. Since the troposphere is the region of the atmosphere closest to the Earth, it is the region of the atmosphere most strongly influenced by emission of trace gases both by the biosphere and *via* anthropogenic activities. Although the concentrations of these trace gases may be small, their presence has major effect on the chemical and radiative state of the troposphere. In fact, trace gases are seen to control chemistry in the troposphere since both N₂ and O₂ are essentially unreactive. The atmospheric residence time of these trace gases varies according to their own lifetime and also due to meteorological constraints since species released into the troposphere *via* surface sources are subject to transport in both the horizontal and vertical directions. A list of the more important chemically active trace gases is shown in Table 1. (Cox *et al.* [1981]).

Table 1.1: The Sources of Trace gases in the Troposphere

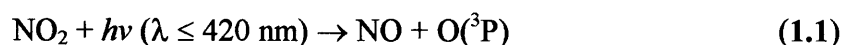
Trace gas	Natural Sources	Anthropogenic Sources
CO	Natural forest fires, oxidation of natural methane.	Incomplete combustion of hydrocarbons.
CO ₂	Forest fires, plant respiration	Combustion processes
CH ₄	Enteric fermentation in animals, termite mounds, organic matter decay	Paddy fields, agriculture, petroleum industry
Other volatile Organic compounds	Vegetation, biological sources, agriculture	Petroleum and related industries, combustion of fossil fuels
N ₂ O	Bacteria, oceanic sources	Combustion of fossil fuels
O ₃	Transport from stratosphere, photolysis of natural NO ₂	Photodissociation of man-made NO ₂
HCl	Ocean spray, volcanoes	Rockets motors, degradation of halocarbons

1.3 Ozone in the Atmosphere

One of the most important of all atmospheric trace gases is ozone. It is found throughout the atmosphere in various concentrations. The ozone molecule was first identified as early as 1840 (Schonbien, [1840]). Its existence in the atmosphere was confirmed by chemical means in 1858

(Houzeau, [1858]) and spectroscopically in 1881 (Hartley, [1881]). Around ninety percent of the ozone that is found in the Earth's atmosphere is found in the stratosphere, in the "ozone layer", around 15 - 30 km above the surface of the Earth. Here ozone exists in concentrations of several parts per million and effectively acts as a biological shield for the planet, absorbing UV radiation in the UV-B wavelength region that is damaging to DNA and potentially toxic to biological systems. Consequently, these wavelengths are unable to penetrate to the Earth's surface. In fact, all wavelengths below around 290 nm are absorbed by gases above the troposphere and do not reach the Earth's surface, hence the so-called "atmospheric cut-off" exists at *ca.* $\lambda = 290$ nm with respect to radiation in the troposphere.

Ozone is also found throughout the troposphere, usually in concentrations of around 10-100 ppbv. Until the mid 1970's it was believed that tropospheric ozone was entirely stratospheric in origin. Tropospheric ozone was considered essentially inert, with stratospheric ozone being transported across the tropopause before ultimate destruction at the Earth's surface. (Junge [1962], Fabien, [1974]) Although stratospheric-tropospheric exchange is an important source of tropospheric ozone, especially in the upper troposphere, it only accounts for a small fraction of the O₃ measured in the whole troposphere. The work of several authors in the mid 1970's was instrumental in the realisation of the photochemical nature of tropospheric ozone (*e.g.* Levy, [1972], [1973], Crutzen, [1973], Chamedies and Walker, [1973]). Ozone is formed in the troposphere by one photochemical process only, involving the photolysis of NO₂. The work of Leighton (1961) was fundamental in the identification that NO₂ photolysis initiates the principal ozone-forming reaction in photochemical smog. These reaction schemes involving the photodissociation of NO₂ are now recognised as the major production process for all tropospheric ozone



The ground state oxygen atom produced in reaction 1.1 is able to react with an oxygen atom in the presence of a third body to form ozone *viz*



There has been recent evidence that levels of ozone in the troposphere are increasing. Examination of historical data records by Volz and Kley (1988) has shown that background concentrations of ozone have doubled over the last century. Through careful examination and

re-evaluation of the seasonal ozone cycles at Montsouris, Paris taken from 1876-1886 together with data taken from Arkona (1983) there is clear evidence of not only a massive increase in the concentration of tropospheric ozone, but also there is evidence for seasonal perturbation. Logan (1985) suggested a seasonal variation in the remote Northern Hemisphere troposphere with surface sites experiencing a broad maximum in ozone concentration during late spring/early summer. Many previous studies have observed similar results, with the literature over the last several years reporting a spring maximum in ozone concentration at various Northern Hemisphere surface sites. (Oltmans, [1981], Winkler, [1988], Oltmans and Levy, [1994], Harris *et al.* [1998], Yeinger *et al.* [1999]). The ozonesonde work of Oltmans *et al.* (1996) using measurements taken in the remote free troposphere also show peak ozone concentrations are observed in Northern Hemisphere spring. Aircraft results obtained by Penkett *et al.* (1998) also showed large ozone concentrations up to 7000m, which the authors assigned as being photochemical in origin and a contributory to the spring ozone maximum. A summary of this and other work on the origins Northern Hemisphere spring ozone maximum has recently been compiled by Monks (2000).

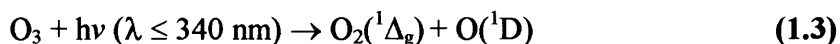
The seasonal cycle of tropospheric ozone has created a debate as to the exact nature of this strong maximum. So far, two possible explanations have been proposed. The first is that the peak ozone arises from stratospheric transport of ozone into the troposphere during this season (Logan, [1985]) while the second focuses on *in-situ* chemical production (Penkett and Brice, [1986]; Liu *et al.* [1987]). Recent evaluations including model studies of this phenomenon (*e.g.* Yeinger *et al.* [1999]) have suggested that both of these mechanisms have importance and thus, a combination of both stratospheric-tropospheric exchange and chemical production is likely to fully account for these observations.

1.4: Photochemistry

If an atmospheric gas molecule absorbs radiation of sufficient energy to break the chemical bonds within it then it can undergo photodissociation. It is the photolysis of atmospheric trace gases that is the major driving force for almost all tropospheric chemistry and in some respects, the region may be regarded as a giant photochemical reactor. Radiation capable of photolyzing such species is referred to as "actinic flux". This actinic flux may be direct or diffuse solar radiation that may be Rayleigh scattered, Mie scattered or even reflected light. However, not all extraterrestrial solar wavelengths encountered by the Earth's atmosphere can penetrate to the

troposphere. The existence of certain species in the regions above the troposphere has the effect of gas molecules within these layers absorbing light of certain wavelengths.

Photochemistry is of particular importance with respect to troposphere ozone. As described in section 1.3, the bulk of troposphere ozone is photochemical in nature. Ozone is formed in this region of the atmosphere *via* the photodissociation of the NO₂ molecule *via* reaction 1.1. Ozone itself is also photochemically labile. At the Earth's surface, actinic flux in the wavelength range between 290-340 nm can photodissociate O₃, the photodissociation forming an oxygen molecule and an oxygen atom. The oxygen atom is formed in one of two possible electronic states. The vast majority of ozone is photolysed to form ground state oxygen, O(³P). This reaction is essentially a null cycle as O(³P) can be recycled back to O₃ *via* reaction (1.2). However, a fraction of the photolysis proceeds in accordance with equation (1.3). Here the oxygen atom is formed in its first excited state, O(¹D).



Around 90% of all O(¹D) formed are collisionally quenched back to O(³P) by collision with atmospheric O₂ or N₂ molecules. Of the remaining O(¹D), owing to this excited state being highly energetic (around two electron volts above the ground state), this excited oxygen has sufficient energy to react with troposphere water vapour. O(¹D) atoms that are not collisionally quenched can react *via* equation (1.4) to form the OH radical



Atmospheric pressure and water vapour concentration control the amount of troposphere OH formed in reaction (1.4) but in the marine boundary layer about 10% of O(¹D) formed go onto generate OH. Since two OH radicals are formed in reaction (1.4) the total OH yield is around 0.2 molecules of OH per ozone molecule photolysed. The OH radical is important in understanding much of the chemistry of the troposphere. Despite its high reactivity, unlike most radicals formed in the troposphere, OH cannot be collisionally deactivated through reaction with background species such as oxygen and nitrogen. The hydroxyl radical does however react with atmospheric trace gases, in most cases as the first and rate-determining step. OH is an essential oxidising agent in the troposphere, controlling the removal and overall concentration of many atmospheric trace species. OH is therefore regarded as the primary tropospheric oxidant; a "cleanser" for the troposphere that is sufficiently powerful to

oxidatively remove atmospheric trace gases both natural and anthropogenic in origin. (Ehhalt [1987], [1991] [2000]).

1.5: j -(O^1D)

It is evident that the driving force for all OH chemistry must derive back to the photolysis of ozone described in equation (1.3). From elementary kinetics, it is possible to write a rate equation for this process. Reaction (1.3) is seen to be a photodissociation process hence, it is necessary to replace the kinetic rate constant " k " with a photochemical rate constant, " j ". The rate of photodissociation of ozone, being referred to as j -(O^1D). The evaluation of this reaction will be an integral part of this thesis (see Chapter 5 and Chapter 6). It has been shown [e.g. Madronich *et al.* (1987), Hofzumahaus (1992a and 1992b), Volz-Thomas *et al.* (1994), Müller *et al.* (1995); Shetter *et al.* (1996); Kraus *et al.* (2000)] that for a trace gas molecule that is photochemically labile, in order to calculate its photolysis frequency the experimentally measured cross sections $\{\sigma(\lambda, T)\}$ and quantum yield $\{\phi(\lambda, T)\}$, in addition to the measured actinic flux $\{F(\lambda)\}$ must be evaluated. Hence, for a molecule photolysed between wavelengths λ_1 and λ_2 it can be shown that

$$j = \int_{\lambda_1}^{\lambda_2} \sigma(\lambda, T) * \phi(\lambda, T) * F(\lambda) \, d\lambda \quad (1.5)$$

A typical plot of actinic flux, quantum yield, cross section and the variance of j -(O^1D) with wavelength is shown in Figure 1.2. The importance of accurate molecular parameters in the overall evaluation of photolysis frequencies has been of ongoing concern in the literature over the last decade. Although the cross section of ozone has been well quantified (Brock and Watson [1980], Molina and Molina [1986]), recently it has been shown that understanding of the quantum yield for O^1D is far from complete. Until quite recently, it was assumed that the quantum yield of O^1D tended to zero at wavelengths greater than *ca.* 310nm (DeMore *et al.* 1994). This observation was called into question by several authors who reported observations of a "tail" in the O^1D quantum yield that stretched out to 325nm and beyond (Michelson *et al.* [1994], Ball *et al.* [1997], Talukdar *et al.* [1998], Bauer *et al.* [2000]). These more recent recommendations assume that quantum yield below $\lambda=325$ nm is produced owing to excited ozone with O^1D at $\lambda>325$ nm being formed owing to spin forbidden routes.

Figure 1.2: Change in Molecular Parameter and Actinic Flux with Wavelength

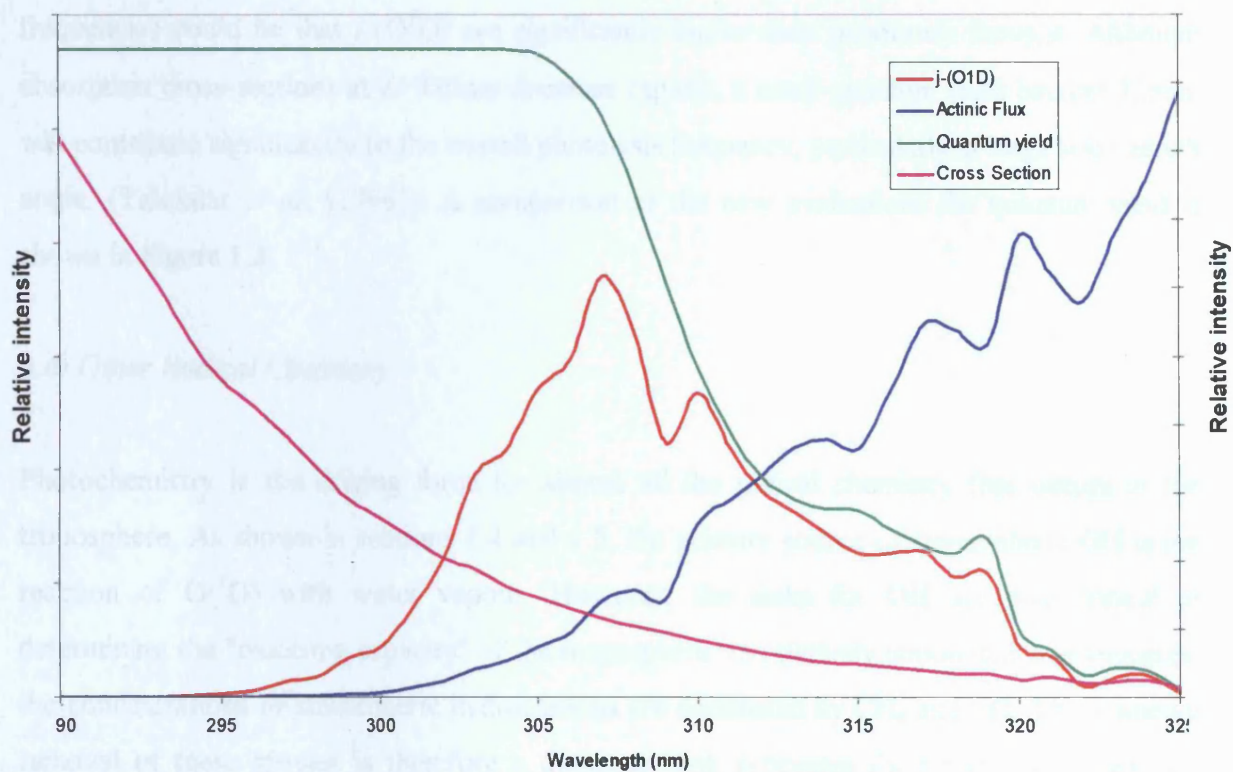
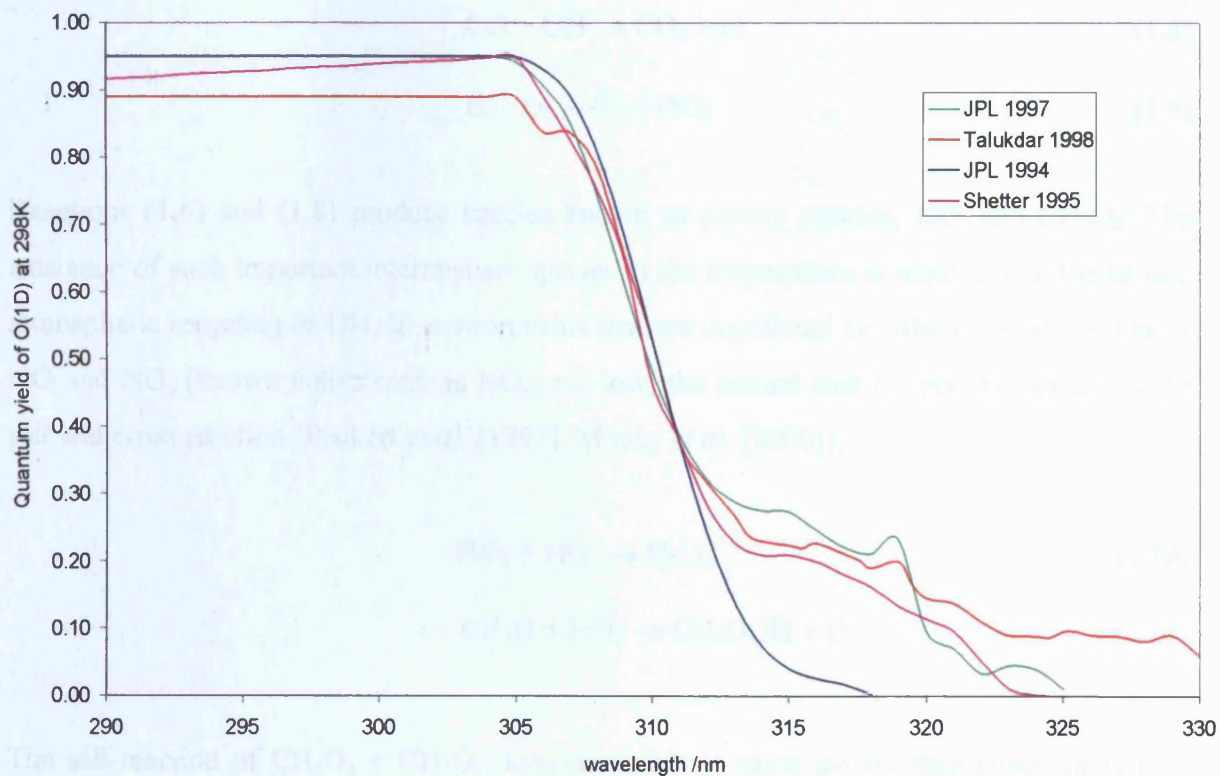


Figure 1.3: Re-evaluation of Resent O(1D) Quantum Yield Data with respect to Wavelength



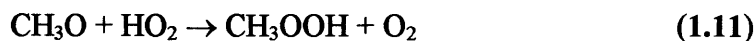
Current recommendations suggest that the threshold for production of O(¹D) may extend to *ca.* 375nm and beyond (Bauer *et al.* [2000]). Consequences for the evaluation of photolysis frequencies could be that *j*-(O¹D) are significantly higher than previously thought. Although absorption cross-sections at $\lambda > 320\text{nm}$ decrease rapidly, a small quantum yield beyond 325nm will contribute significantly to the overall photolysis frequency, particularly at large solar zenith angle. (Talukdar *et al.* [1998]). A comparison of the new evaluations for quantum yield is shown in Figure 1.3.

1.6: Other Radical Chemistry

Photochemistry is the driving force for almost all the radical chemistry that occurs in the troposphere. As shown in sections 1.4 and 1.5, the primary source of tropospheric OH is the reaction of O(¹D) with water vapour. However, the sinks for OH are also critical in determining the "oxidising capacity" of the troposphere. In relatively unpolluted environments, the concentrations of atmospheric hydrocarbons are dominated by CH₄ and CO. The oxidative removal of these species is therefore a dominant sink processes for tropospheric hydroxyl radicals



Reactions (1.6) and (1.8) produce species known as peroxy radicals, HO₂ and CH₃O₂. The existence of such important intermediate species in the troposphere is important in the natural atmospheric recycling of OH. In environments that are unpolluted *i.e.* where concentrations of NO and NO₂ (known collectively as NO_x) are low, the natural sink for peroxy radicals is the self and cross reaction (Penkett *et al.* [1997], Monks *et al.* [2000]);



The self-reaction of CH₃O₂ + CH₃O₂ does occur but is much slower than cross-reaction of CH₃O₂ + HO₂, the difference in rate being around an order of magnitude. (Carpenter *et al.*

[1997]). However, in polluted environments that show considerable levels of NO_x , the reaction between peroxy radicals and NO_x is important. Such reactions do not necessarily lead to the removal of OH however. In the presence of significant concentrations of NO_x , compensation for the loss of OH can occur, with HO_2 and other peroxy radicals formed from reaction of OH with CH_4 and CO are able to regenerate OH *via* reaction with NO;

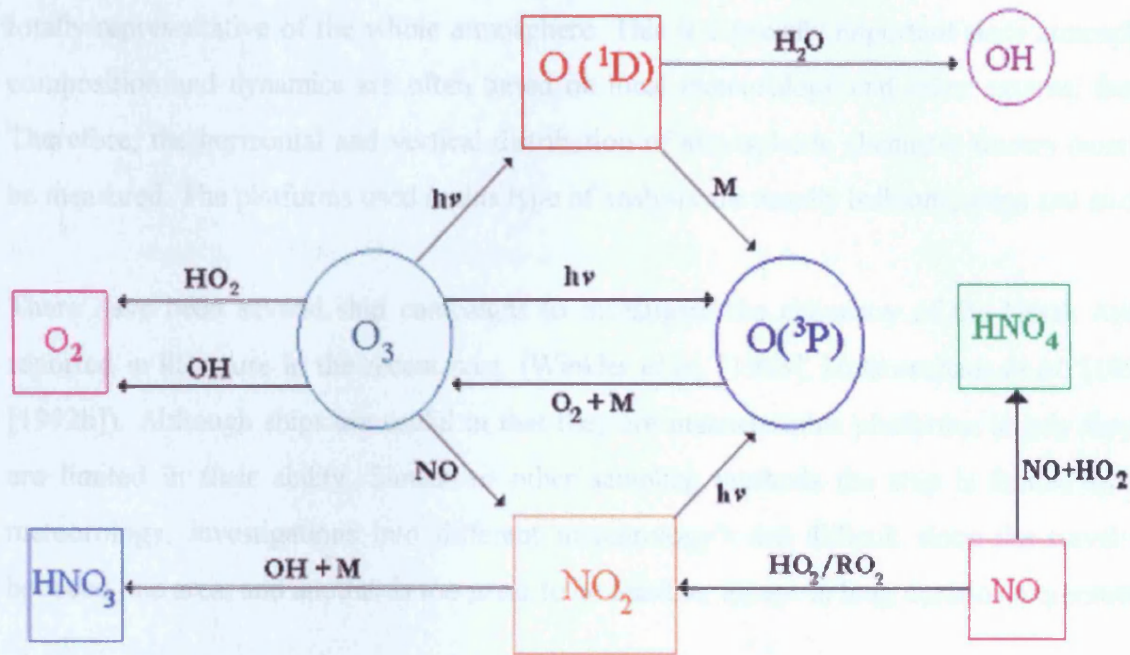


Net ozone production can then occur from the photolysis of the NO_2 produced *via* reaction (1.1) while photolysis of this ozone can then lead to reformation of OH *via* equation (1.4). From the above reactions, it is clear that the production or loss of ozone is dependent on competition between reaction (1.12) and (1.14), together with reaction (1.15).



Thus, it is often the concentration of NO_x that is the determining factor in assessing the concentration of OH in the troposphere (Crutzen, [1973], Penkett *et al.* [1997], Carpenter *et al.* [1997], Crawford *et al.* [1997]). These relationships with respect to the North Atlantic free troposphere will be explored in detail in Chapters 2, 3 and 4. It is clear that ozone photochemistry described in this thesis is an integral part of the chemistry of the troposphere and photochemical changes in troposphere [O_3] are linked to many other areas of atmospheric chemistry. Summaries of the most important processes that are linked to ozone photochemistry are shown in Figure 1.4.

Figure 1.4: Key Ozone Reactions in the Troposphere



1.7: Measurements and Modelling of Atmospheric Chemistry

In-situ measurements on the concentration of tropospheric trace gases have always played a crucial role in the understanding of atmospheric chemistry owing to the need for validation of atmospheric models of the process described in this chapter by accurate measurement. The most widely used measurement platform in atmospheric chemistry is the field site. These provide fixed areas in which measurements are taken and the site can be specifically chosen in order to investigate a specific region of the atmosphere, *e.g.* the research station at Cape Grim, Tasmania to investigate the unpolluted remote marine boundary layer (Ayres *et al.* [1992], Penkett *et al.* [1997], Monks *et al.* [2000]), or the atmospheric station at the summit of the Jungfraujoch to measure in the free troposphere (Schuepbach *et al.* [1999], Zanis *et al.* [1999], Carpenter *et al.* [2000]). The great advantage of the field site is that often there is permanently mounted equipment at the site and hence the station is capable of simultaneous measurement 365 days of the year.

Surface measurements and theoretical models are important in identification of species and the characterisation of the chemical reactions they undergo, but these techniques may not be totally representative of the whole atmosphere. This is especially important since atmospheric composition and dynamics are often based on local meteorology and other external factors. Therefore, the horizontal and vertical distribution of atmospheric chemistry tracers must also be measured. The platforms used in this type of analysis are usually balloons, ships and aircraft.

There have been several ship campaigns to investigate the chemistry of the North Atlantic reported in literature in the recent past. (Winkler *et al.* [1988], Hofzumahaus *et al.* [1992a], [1992b]). Although ships are useful in that they are manoeuvrable platforms, largely they too are limited in their ability. Similar to other sampling methods the ship is limited to local meteorology, investigations into different meteorology's are difficult since the travel time between one area, and another is too great to be feasible, except in long duration experiments.

Balloons and kites, when tethered, are very useful and cheap method of monitoring atmospheric chemistry since they can be fitted with monitoring devices and released providing not only local data, but also obtaining vertical profiles as the balloon increases in altitude. (Knapp *et al.* [1998], Dearellano *et al.* [1994]). They also have the advantage of ground-based control and can make long duration measurements over day and night. There are limits to their effectiveness however. When released, balloons are free to move in only the vertical plane with horizontal movement dictated by winds. In addition, balloons have a low payload capacity and are battery operated hence, may be limited in the equipment they can carry. Therefore, despite their ability in making additional measure in the vertical, the effectiveness of balloon-based platforms is restricted to similar limitations as ground based monitoring.

The net result is that investigating atmospheric chemistry over different latitudes on a rapid timescale is only possible using aircraft. The fact that aircraft have sufficiently large cruise speeds to allow travel over a vast range of potential distances means that an aircraft is not restricted to one location and can provide data over a vast range of geography, chemistry and meteorology during the same flight. The use of aircraft to study atmospheric chemistry is now a very well established technique (Saunders *et al.* [1992], Bregman *et al.* [1995], Jacob *et al.* [1996], Davis *et al.* [1996], Marengo *et al.* [1998], Thompson *et al.* [1999], Law *et al.* [2000]).

1.8: This Thesis

The majority of the data described in this thesis was obtained during aircraft campaigns flown by the Meteorological Research Flight (MRF) Lockheed C-130 Hercules, as described by Nicholls (1978). The aircraft is shown in Figure 1.5. The C-130 is large four-engine former transport aircraft known as "Snoopy" that has been modified extensively from the military version. The aircraft is now devoted exclusively to meteorological research and is owned and operated by MRF with the aid of a RAF crew. This aircraft platform was used to measure the distribution and concentration of atmosphere trace gases in the free troposphere over Northern Europe and the North Atlantic. The measurements obtained *via* this aircraft platform were taken during detachment to the Azores (39° N, 27° W) during the ACSOE campaign is discussed in Chapter 2 and 3, where this data is compared to data recorded in a second aircraft campaign, the MAXOX program flown during 1999 and a chemistry transport model. Comparisons of *in-situ* measurements and modelled data will show that there is considerable variation in the seasonal tracer climatology and between data taken in the polluted/unpolluted environments in the Northern Hemisphere free troposphere.

Figure 1.5: The Meteorological Research Flight C-130 Hercules Aircraft



Chapter 4 describes attempts to quantify the measurements of the free troposphere during these aircraft campaigns through additional model studies. Specifically, a flight track box model has been developed, the output of which is compared to steady state modelled $[\text{HO}_x]$ data and to values measured *in-situ* $[\text{HO}_x]$ during the SONEX aircraft campaign. Chapter 5 concentrates on the *in-situ* measurement of photolysis frequencies from aircraft platforms. It deals with the performance of two recently developed fixed bandwidth photoelectric radiometers that have been used to measure the photolysis frequency $j(\text{O}^1\text{D})$. These radiometers have been used to collect data of ozone photolysis in both the ACSOE and MAXOX aircraft campaigns. A full description of the instruments as well as an extensive characterisation is described in Chapter 5, along with the comparison of *in-situ* $j(\text{O}^1\text{D})$ data to values provided by radiative transfer models. Finally, Chapter 6 moves away from the use of aircraft in that it describes the International Photolysis Measurement and Modelling Intercomparison (IPMMI) experiment. This was an international intercomparison of techniques in order to ascertain the ability to measure atmospheric photolysis frequencies and actinic flux from several techniques, and details the performance of a new diode array spectroradiometer instrument.

Chapter Two: Aircraft Climatologies over the North Atlantic : Measurement

2.1)	Introduction	16
2.2)	Work Described in this Chapter	18
2.3)	The ACSOE Aircraft Campaign	22
2.4)	ACSOE Spring and Summer Trace gas Climatologies	27
2.5)	Summary of ACSOE Campaign	43
2.6)	The MAXOX Aircraft Campaign	44
2.7)	MAXOX-ACSOE Climatology Comparisons	54
2.8)	Summary of Climatology data	67

Chapter 2: Seasonal Trace Gas Climatologies over the North Atlantic: Measurement

2.1 Introduction

There are still large uncertainties in the budget of free tropospheric trace gases over the world's oceans and in particular, the North Atlantic. The importance of ozone and its precursors in the chemistry of the oceanic free troposphere is now well established (Crutzen, [1973], Logan *et al.* [1981], Liu *et al.* [1987]). Ozone photolysis in the presence of water vapour is the primary production channel for the formation of the hydroxyl radical, OH, which initiates the oxidative removal of trace gases in the troposphere (Levy, [1972], [1973], Ehhalt, [2000]). However, the transport of anthropogenic pollutants from continental outflow and its effect on the natural cycles of the marine environment is still an issue of continuing concern. These problems have been compounded by the large spatial variability of tropospheric trace gases and the net result is that understanding of the climatological distribution of these species is far from complete.

Much work has been carried out in the recent past to quantitatively assess the impact of human activities on the free troposphere, for example, through *in-situ* measurement and large scale (climatological) modelling. The Pacific Exploratory Missions (PEM) undertaken by the NASA DC-8 as part of the NASA sponsored Global Tropospheric Experiment has greatly enhanced our understanding of the free troposphere, particularly over the Pacific. Aircraft missions during PEM-West A sampled air masses in the western Pacific area when meteorological conditions indicated a flow of air towards the Asian continent. Hoell *et al.* (1996) showed that there was minimal anthropogenic influence in these air masses. This was followed by a second series of PEM-West B flights where continental outflow air, together with air of tropical origins, was sampled (Merrill *et al.* [1996], Crawford *et al.* [1997]).

During PEM-West A and B, seasonal variations were identified in the concentration of tropospheric trace gases. Talbot *et al.* (1997) noted that there was enhanced [H₂O₂] and [CH₃OOH] during the summer campaign (PEM West-A) in comparison to the winter campaign (PEM West B), which was attributed to the suppression of winter photochemistry. The latitude distributions of these peroxides were remarkably similar in the two campaigns. Similarly, a reduced photochemical environment in winter caused the concentration of methane and other hydrocarbons to be higher in PEM-West B as noted by Blake and co-workers (1996). Crawford *et al.* (1997) showed that the tendency for ozone production over the Pacific

was separated into two distinct photochemical regions, 20°-30° N and 30°-50° N. Despite their remote location, both regions seemed to show a regime of net ozone production, which was attributed to an elevated concentration of ozone precursors transported to the Pacific *via* continental outflow. However, Akimoto *et al.* (1996) recorded surface concentrations of both CO and O₃ that were significantly higher than concurrent measurements from the DC-8. Akimoto and co-workers (1996) therefore suggested that measurements made during the PEM-West missions and subsequent data were not truly representative of the continental outflow of anthropogenically produced trace gases, since at no time was the DC-8 clearly in a region of pure continental outflow. The net ozone production observed by Crawford *et al.* (1997) may therefore indicate that even the remote Pacific is subject to large-scale ozone production.

Measurements over the North Atlantic have also been reported, in particular, from the 1993 Northern Atlantic Regional Experiment (NARE) (Parrish *et al.* [1993]). Data have been obtained from ozonesonde measurements and *via* aircraft missions giving information on both concentration and the horizontal and vertical distribution of ozone and its precursors. Peterson *et al.* (1998) reported on the concentrations of nitrogen species from a surface site in the Azores. These authors observed [NO_x] and [NO_y] < 100 pptv at this location. This compares to the measurements and model studies of Schultz *et al.* (1998), where 400-500 pptv of NO_y was observed, along with 50 pptv of NO_x, for a free troposphere surface site in Tenerife. Parrish *et al.* (1998) reported on the seasonal variation in ozone concentration from several Northern Atlantic surface sites. The data suggested a strong seasonal variation, with a pronounced spring ozone maximum being observed in these surface site data. Correlations between O₃ and CO were also reported. These were similar to the data recorded in 1993 from surface locations discussed by Parrish *et al.* (1993). Penkett *et al.* (1998) observed ozone concentrations and levels of peroxide during expeditions into the North Atlantic during spring and summer as part of the first NARE experiment. The authors reported observations of strong "layers" in which peroxide and ozone correlation were positively correlated during summer in the lower free troposphere. Spring data suggested large production of tropospheric ozone up to altitudes of 7 km, which was believed to show influences of the springtime ozone maximum in the Northern Hemisphere.

Singh *et al.* (1999) have recently obtained data on the distribution of nitrogen tracers measured during the SONEX mission in the upper troposphere of the North Atlantic. A more detailed description of SONEX is found in Chapter 4. The variability of [NO] was shown to be so great

as to make the quantitative analysis of sources of nitrogen species in the region difficult. Singh *et al.* (1999) therefore highlighted the need for accurate modelling of $[\text{NO}_x]$ in the troposphere.

Peroxide data have also been collected by Perros (1993) during the TROPOZ II experiment. Over 43,000 H_2O_2 measurements were collected over a latitude range of 60°N to 60°S , from a ship. The author indicated that the distribution of peroxide on the global scale suggested minimal control by anthropogenic emissions. These conclusions have been supported by organic and hydrogen peroxide measurements made by O'Sullivan *et al.* (1999). The authors reported that the latitudinal distribution of peroxides over the Pacific indicated photochemical control of $[\text{H}_2\text{O}_2]$. Jacob *et al.* (1996) have also obtained trace gas concentration data over the South Atlantic basin during the TRACE-A aircraft mission. Using model data in conjunction with *in-situ* measurements, Jacob *et al.* (1996) suggested a close balance between production and loss of O_3 in the free troposphere up to a ceiling of 12 km. These observations suggested purely photochemical ozone production, loss, and a negligible contribution of stratospheric-tropospheric exchange. This seems to contrast the work of Oltmans *et al.* (1996), where the authors showed that using ozonesondes launched from surface sites including the Azores, there was strong day-to-day variability in the ozone profiles in both spring and summer. Also observed in the data were layers of ozone that were attributed directly to stratospheric-tropospheric exchange in the mid and upper troposphere over the North Atlantic.

2.2: Work Described in this Chapter

The work described in this chapter attempts to quantify the spatial distribution and the seasonal and regional climatologies of atmospheric trace gases measured during a series of aircraft missions designed to investigate the chemistry of the North Atlantic free troposphere. The ACSOE (Atmospheric Chemistry Studies in the Oceanic Environment) campaign is a UK thematic research programme funded by NERC (The Natural Environmental Research Council). The principal aims were to investigate the chemistry of the oceanic troposphere with data from surface sites and aircraft sorties. The aircraft portion of the wider ACSOE program aimed to bring about a clearer understanding of natural processes in the remote free troposphere, specifically how these processes are influenced by the continental outflow of anthropogenic pollutants. This chapter deals with one portion of ACSOE, specifically aircraft investigations into the chemistry of the marine free troposphere over the North Atlantic. The platform used in this investigation was the C-130 Hercules operated by the UK Meteorological Office is described in detail in section 2.2.1. Data obtained from this aircraft platform were

taken during the aircrafts detachment to the Azores (39° N, 27° W) islands in the mid-North Atlantic. Data collected during two detachments are described. The first was during April 1997, the second in September 1997. These data provided an opportunity to study the seasonal climatology of trace gases in the "background" free troposphere of the Northern Atlantic, away from significant anthropogenic source regions.

In contrast to the ACSOE campaign, the 1999 MAXOX project (described in detail by Hov *et al.* [2000]) was an aircraft campaign based in the UK. The main objective of the MAXimum OXidation rates in the free troposphere (MAXOX) project used the C-130 aircraft platform to investigate the annual cycle of ozone in the troposphere and the influence of anthropogenic pollution on a continental and hemispheric scale. The overall aim of MAXOX was to investigate if there is a chemical element in the formation of a spring ozone maximum observed in background air over Europe and the North Atlantic. It was an additional aim to observe the role of ozone destruction in the free troposphere in summer outside polluted layers, which are often found throughout the troposphere over the oceans, *e.g.* the remote Pacific. The concentration contrasts in ozone precursors and intermediate species, including free radicals, between the atmospheric boundary layer and the free troposphere was likely to be more marked when measured over the European continent, as compared to the oceanic environment investigated in ACSOE. It was a major objective of MAXOX to quantify these parameters, especially an assessment of the strength of the exchange of pollution between the atmospheric boundary layer and the free troposphere during spring and the early summer period. Specifically, measurements of NO_x and VOC budgets in the boundary layer and the free troposphere were made in order to show that a concentration exists for oxides of nitrogen where the oxidation rates of precursors have maxima, as indicated by theoretical calculations. This has close links to the tendency of the troposphere to produce or destroy ozone. MAXOX aimed to quantify if there is a shift from net photochemical production of ozone to net photochemical destruction for a certain concentrations of NO.

The work described in this chapter considers these two aircraft campaigns both individually with respect to the seasonal distribution of trace gases, and from comparisons of the two individual datasets as a whole. Owing to the nature of the two aircraft campaigns, these data provide an opportunity to compare and contrast the seasonal climatologies of trace gases in the background free troposphere over the Northern Atlantic Ocean to that of the semi-polluted free troposphere measured during the spring and summer MAXOX campaigns. Each aircraft

flight series will be considered individually with respect to a seasonal climatology analysis before a full inter-campaign comparison of the overall trends.

2.2.1 The C-130 Aircraft

This chapter describes measurements made from the MRF C-130 Hercules as described by Nicholls (1978) and outlined in brief in Chapter One. The C-130 is large four-engine former RAF transport aircraft operated by the MRF with the aid of an RAF crew. It has a maximum range of 5,000 km and has a home base situated at Boscombe Down, Wiltshire. The aircraft can be instrumented in a number of different configurations, which were customised for the various campaigns. A large number of instruments can be housed inside the aircraft, taking air from a number of air inlets. Alternatively, instruments may be fitted directly to the exterior of the aircraft. The aircraft was equipped to measure several trace gases species *in-situ* during ACSOE and MAXOX, many of which were the same as deployed during the OCTA program described by Bethan *et al.* (1998) and the TACIA missions described by Hov *et al.* (1998).

The instrumentation deployed aboard the C-130 during the ACSOE and MAXOX campaigns measured O₃, CO, NO, NO_y, HCHO, *j*-(NO₂), *j*-(O¹D) and both organic and hydrogen peroxide. More information on the detection methods used aboard the aircraft is found in Table 2.1. In brief, a modified commercial UV Photometry Ozone Analyser (TECO 49) measured ozone aboard the aircraft. (Hov *et al.* [1998], [2000]). The instrument differed from the commercial only in that separate pressure and temperature sensors were used along with an increased sampling rate. Estimated range of detection is quoted as 0-2000 ppbv with a detection limit of 2 ppbv and a precision of 2%. The deployment of a four-channel chemiluminescence analyser similar to that described by Fahey *et al.* (1989) enabled the *in-situ* measurement of both NO and NO_y. Odd nitrogen was measured by the chemiluminescence detector following the conversion of NO_y to NO *via* a gold tube at 300°C in 0.1% CO. This NO was then checked against gas flow titration of NO using HNO₃ from a permeation tube. NO taken from the air manifold was measured directly *via* chemiluminescence. The estimated precision in the NO_{xy} instrument is given as *ca.* 1 pptv. The CO instrument is a resonance fluorescent detector as described by Gerbig *et al.* (1999), with an estimated detection limit of 3 ppbv in a one second sample and a precision of 2 ppbv.

The peroxide detector is described in detail by Penkett *et al.* (1998). The measurement technique is based on a reaction where a peroxidase enzyme catalyses the conversion of

Table 2.1: Instrumentation Deployed Aboard the MRF C-130 (Table adapted from Hov *et al.* [2000])

Species	Technique	Detection Limit	Accuracy
CO *	Resonance Fluorescence	3 ppbv	30%
HCHO	Fluorimetric detection	0.25 ppbv	23%
NO	Chemiluminescent reaction with ozone	10 pptv	21%
NO ₂ *	Photolysis to form NO, followed by chemiluminescence	20 pptv	26%
NO _y	Thermal decomposition to NO, followed by chemiluminescence	20 pptv	21%
H ₂ O ₂	Fluorimetric detection	40 pptv	10%
ROOH	Fluorimetric detection	40 pptv	10%
Ozone	UV detection	2 ppbv	2%
Water Vapour	Dew point conversion	±0.1°C change	3%
<i>j</i> -(O ¹ D)	Photoelectric Radiometer	1 x 10 ⁻⁷ s ⁻¹	30%
<i>j</i> -(NO ₂)	Photoelectric Radiometry	1 x 10 ⁻⁵ s ⁻¹	15%

* indicated instrument not deployed/malfunctioned

inorganic and organic peroxide to form a fluorescent dimer. Difference in solubility determines the inorganic/organic peroxide partitioning by the addition of a second stripping coil. Formaldehyde was measured by a continuous fluorimetric method *via* the reaction of HCHO with sampled in air drawn into the aircraft by a PTFE inlet. HCHO in ambient air is reacted with an ammonium etholate/pentadione/methanoic acid solution to form 3,5-diacetyl-1,4-dihydrolutidine, which is excited at $\lambda=410\text{nm}$. The fluorescence decay of 3,5-diacetyl-1,4-dihydrolutidine at $\lambda=520\text{nm}$ provides the method of detection. The full specifications of the instrument are described by Hov *et al.* (2000).

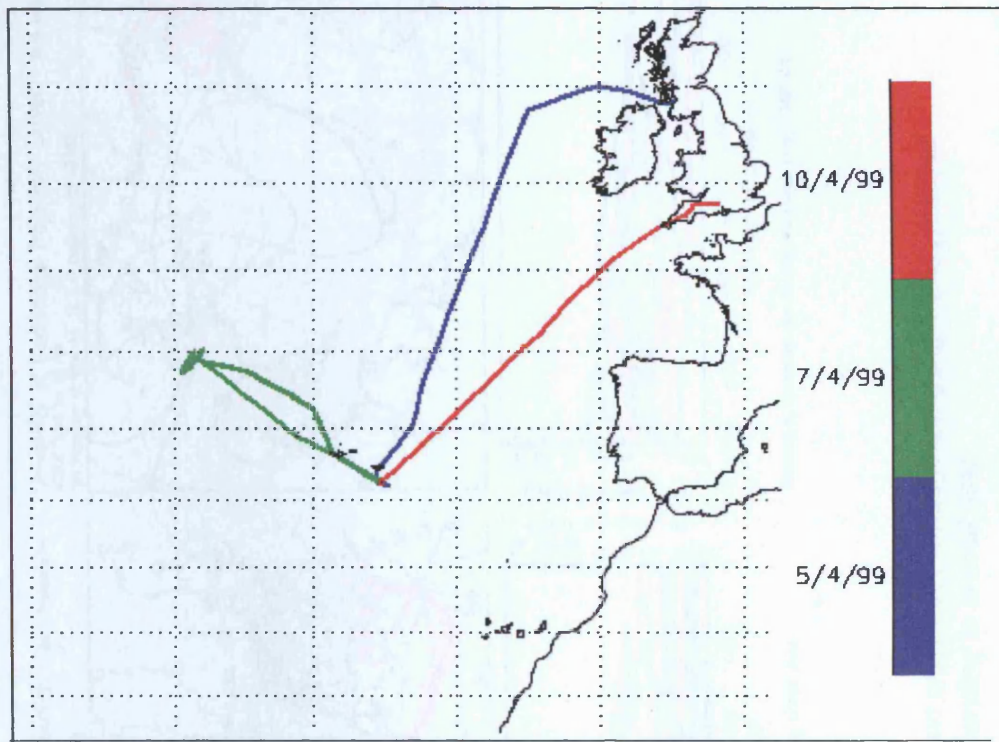
Data for all instruments were recorded using the aircraft's on board logging system (DRS) and downloaded into an on-board computer (HORACE). Measured data were recorded along with aircraft latitude, longitude and altitude on a one-second time-scale. The values were manually sorted into thirteen altitude bins beginning with data recorded when the aircraft was at altitudes equal to, or less than 0.5 km. Subsequent bins then were constructed sequentially until a ceiling of 6.5 km or 8 km, where applicable, was reached. Separation of bins was 500 m in all cases. Once each associated data point had been placed in its corresponding altitude bin, the data were sorted by latitude. The latitude bins used ranged from 20° N to 60° N with a separation of 1°. The final sorting then yielded an average concentration for each tracer at each latitude along with a total number of data points associated with each average.

2.3: The Atmospheric Chemistry Studies in the Oceanic Environment (ACSOE) Aircraft Campaign

As outlined in section 2.2, the ACSOE series of aircraft missions took place over two separate legs. The spring portion of the ACSOE campaign was a series of aircraft missions flown in early April 1997 with the aim of investigating the budget of tropospheric oxidants in marine air at mid-latitudes in the Northern Hemisphere. The spring flight series comprised three flights, a transit flight from the UK to the Azores on 5/4/97 (A533), a flight in the marine free troposphere NW of the Azores on 7/4/97 (A534) and finally a transit flight back to the UK on 10/4/97 (A536). A composite of the aircraft flight tracks for the spring flights series is shown in Figure 2.1.

During the spring series of flights, trajectories were available to the ACSOE community *via* the World Wide Web. The University of Cambridge Trajectory server utilises meteorological data from the European Centre for Medium range Weather Forecasts (ECMWF) in order to indicate the origin of air masses. Trajectories were calculated using the University of Reading's Offline Trajectory Code and the T106 L50 ECMWF (*ca.* 1° x 1° with 50 levels in the vertical component) wind fields. The trajectories are 3D, using the vertical grid component of the wind and are calculated at 5-minute time interval along the aircraft flight path. Trajectories for the April flight series indicated that the C-130 encountered several different air masses in this spring campaign, a composite of these trajectories is shown in Figure 2.2.

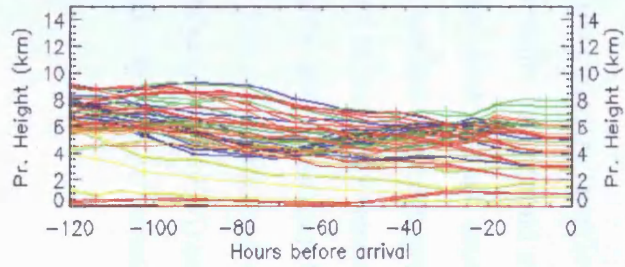
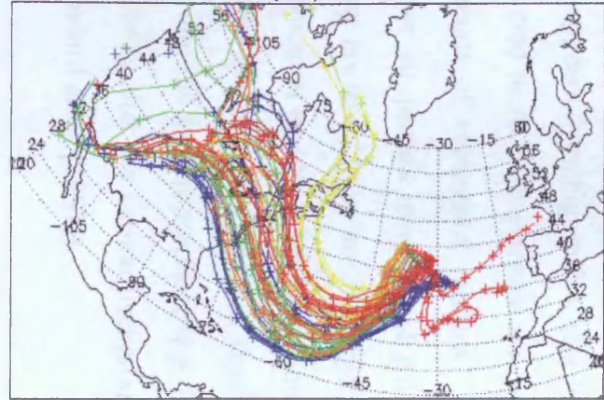
Figure 2.1: Composite of Aircraft Flight Tracks During Spring Portion of ACSOE Campaign



From inspection of the trajectories (Figure 2.2), the spring flights seem to have sampled mainly clean air that appears to have been over the ocean for several days at low-and mid-tropospheric altitudes. This is contrasted by air masses that showed significant continental outflow. Indeed, almost all air masses sampled on the 7/4/97 flight originated over the mid western United States before transport to the North Atlantic. Similarly, during the two transit flights there is evidence that air masses encountered by the C-130 had circulated near the European continent before the aircraft sampled them. The net result is that the ACSOE spring flight series that aimed to sample predominantly marine air, may have in fact, sampled a mixture of continental outflow and "background" free tropospheric air.

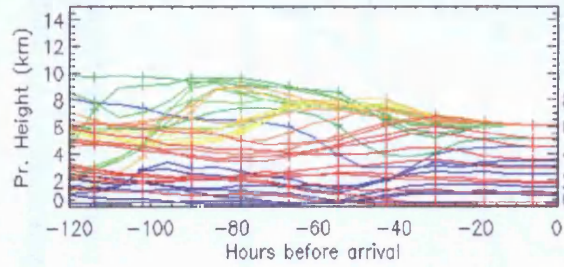
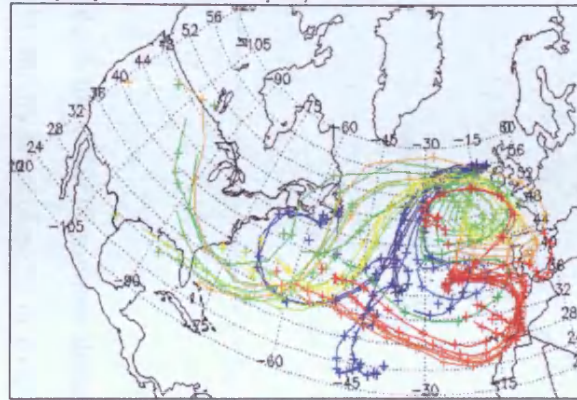
The second leg of the ACSOE aircraft campaign was a series of several flights in late summer of 1997. Eight flights were flown during this portion of the ACSOE campaign, including two transit flights from/to the UK. A composite of the aircraft flight tracks during this summer leg of the campaign is shown in Figure 2.3. The September campaign was also strongly influenced by air masses that have origins other than the remote free troposphere. From the composite of trajectories shown in Figure 2.4 it appears that, to some degree, the North Atlantic during September 1997 was under the influence of continental outflow.

University of Cambridge Trajectory Server. Back trajectories
 ACSOE flight on 7 Apr
 1st trajectory at time 11' 12 Last trajectory at 16'59Z



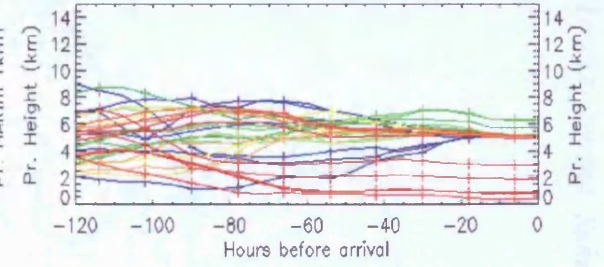
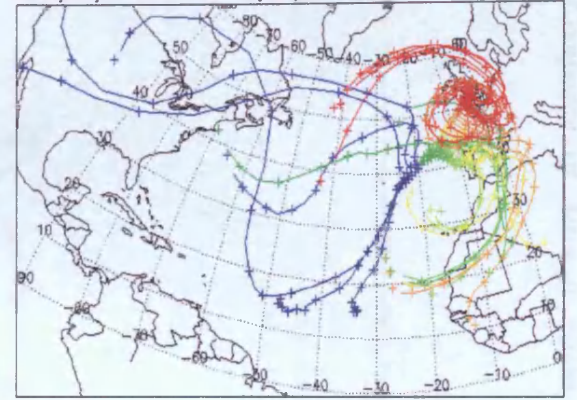
Prepared by Cambridge and Reading Universities using ECMWF data

University of Cambridge Trajectory Server. Back trajectories
 ACSOE flight on 5 Apr
 1st trajectory at time 11' 0Z Last trajectory at 11' 1Z



Prepared by Cambridge and Reading Universities using ECMWF data

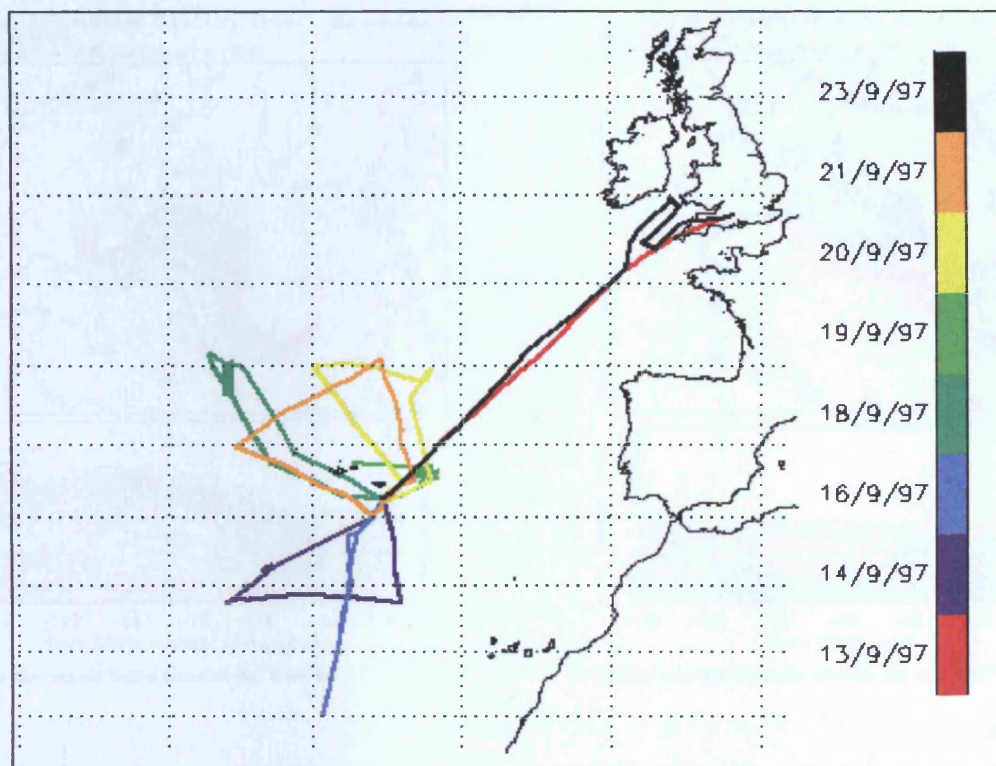
University of Cambridge Trajectory Server. Back trajectories
 ACSOE flight on 10 Apr
 1st trajectory at time 11' 12 Last trajectory at 15'18Z



Prepared by Cambridge and Reading Universities using ECMWF data

Figure 2.2: Trajectories For Spring Portion of ACSOE Aircraft Campaign. (Trajectories are coloured according to arrival time)

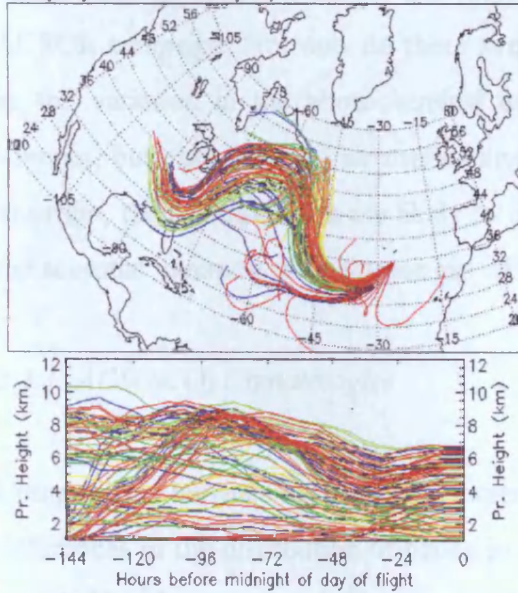
Figure 2.3: Composite of Aircraft Flight Tracks During Summer Portion of ACSOE Campaign



Almost all flights in the ACSOE summer detachment appear to have sampled air that has been lifted from the boundary layer close to or over the USA before transport of these air-parcels to the remote environment close to the Azores. There is however a strong vertical gradient in the trajectories. It appears from Figure 2.4, that in the boundary layer/lower free troposphere, the air masses sampled in ACSOE summer are essentially background marine air, which was free from the influence of continental outflow. This contrasts air sampled at higher altitudes, specifically those air parcels investigated with vertical altitudes greater than around 4 km. These air masses are likely to be heavily subjected to human influence owing to uplift by fronts or similar (convective) events. It has been shown by several authors that fronts associated with any low-pressure system can transport significant concentrations of trace gases from the boundary layer into the free troposphere (*e.g.* Bethan *et al.* [1998]) and episodes of continental outflow significantly alter the natural background chemistry of remote environments (Davis *et al.* [1996], Crawford *et al.* [1997])

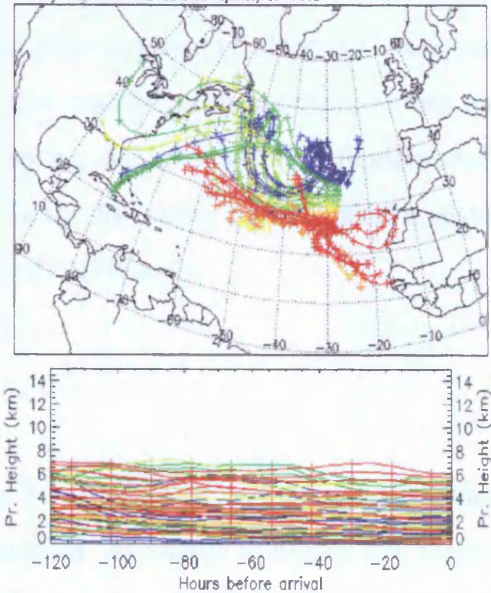
Figure 2.4: Trajectories for Summer Portion of ACSOE Flight Campaign. (Trajectories are coloured according to arrival time).

University of Cambridge Trajectory Server. Back trajectories
 ACSOE flight on 14 Sep
 1st trajectory at time 16:02 Last trajectory at 19:59Z



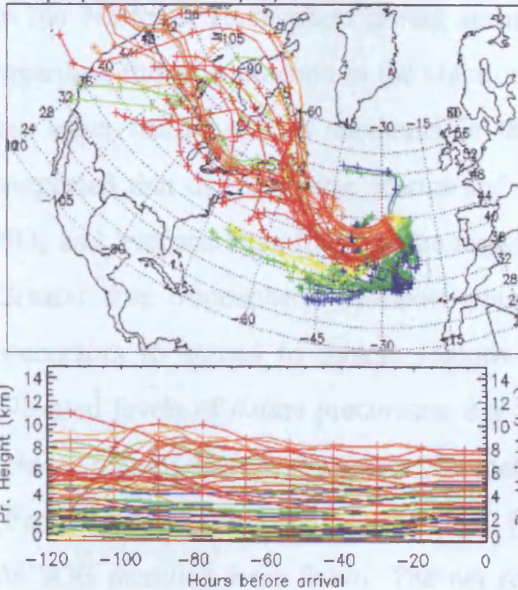
Prepared by Cambridge and Reading Universities using ECMWF data

University of Cambridge Trajectory Server. Back trajectories
 ACSOE flight on 16 Sep
 1st trajectory at time 12:32 Last trajectory at 16:59Z



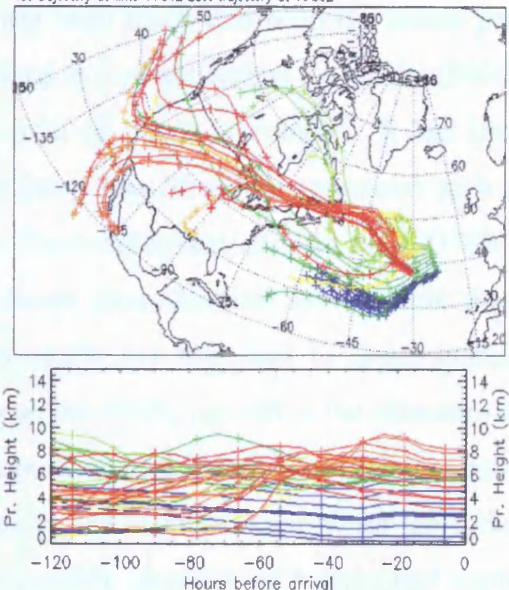
Prepared by Cambridge and Reading Universities using ECMWF data

University of Cambridge Trajectory Server. Back trajectories
 ACSOE flight on 20 Sep
 1st trajectory at time 11:32 Last trajectory at 16:59Z



Prepared by Cambridge and Reading Universities using ECMWF data

University of Cambridge Trajectory Server. Back trajectories
 ACSOE flight on 21 Sep
 1st trajectory at time 11:51Z Last trajectory at 16:59Z



Prepared by Cambridge and Reading Universities using ECMWF data

2.4: ACSOE Spring and Summer Trace gas Climatologies

From inspection of the trajectories, a meteorological picture of the North Atlantic free troposphere during the ACSOE campaign can be developed. It is clear that there are several differences between the spring and summer seasons investigated during the course of the ACSOE campaign. Not only do these aircraft missions differ in terms of obvious factors such as the variation in the photochemical environment that can be expected from spring and summer, but also since the air-masses investigated in spring and summer differ fundamentally in origin, their composition are likely to be different. In the following climatological analysis, the seasonal variation of each trace gas will be considered individually.

2.4.1: ACSOE O₃ Climatologies

Comparisons between spring and summer ozone data for the ACSOE campaign shows clear differences in the distribution of ozone in these two seasons. As shown in Figure 2.5, there is *ca.* 15-25 ppbv more ozone measured in the spring flights compared to those flown in summer (up to a ceiling of *ca.* 3.5 km). The large gradient in the data up to this altitude during summer is similar to the data of Oltmans *et al.* (1996), where a significantly steeper gradient was observed in the ozone altitude profile in August ozonesonde data when compared with data recorded in May. This seems to suggest that these observations may indicate that there is a widespread ozone maximum in the remote marine boundary layer and lower free troposphere in the Northern Hemisphere during spring. There has been much debate in the recent past regarding this phenomenon in the literature. As outlined in a recent review by Monks (2000), the exact nature of this maximum in the annual cycle of ozone is complex. It has been suggested that during spring, storms and convective fronts may lift ozone precursors such as NO_x and hydrocarbons from source regions into the free troposphere (Bethan *et al.* [1998]). Greater free tropospheric transport potential and lower photochemical losses allow these precursors to spread to remote regions that are normally not subjected to direct impact. Elevated levels of ozone precursors, *e.g.* the NO_x reservoir PAN, can affect the chemistry of remote regions such as the Azores by thermal decomposition well into the late spring months. (Penkett and Brice [1986], Beine *et al.* [1997]) This period includes April, when the spring ACSOE missions were flown. The net result is the possible elevation of background ozone levels to those observed by the C-130 during the spring campaign.

Figure 2.5: Averaged Ozone Concentration During ACSOE Spring and Summer showing 1σ Standard Deviation Bars.

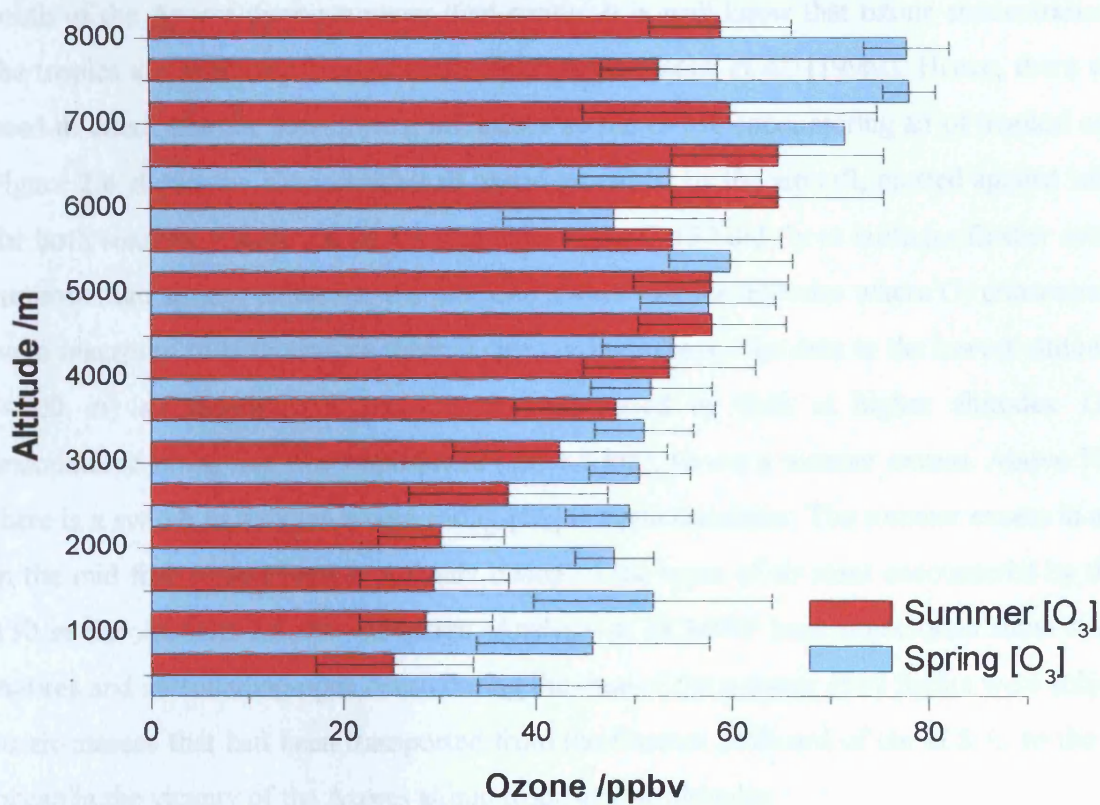
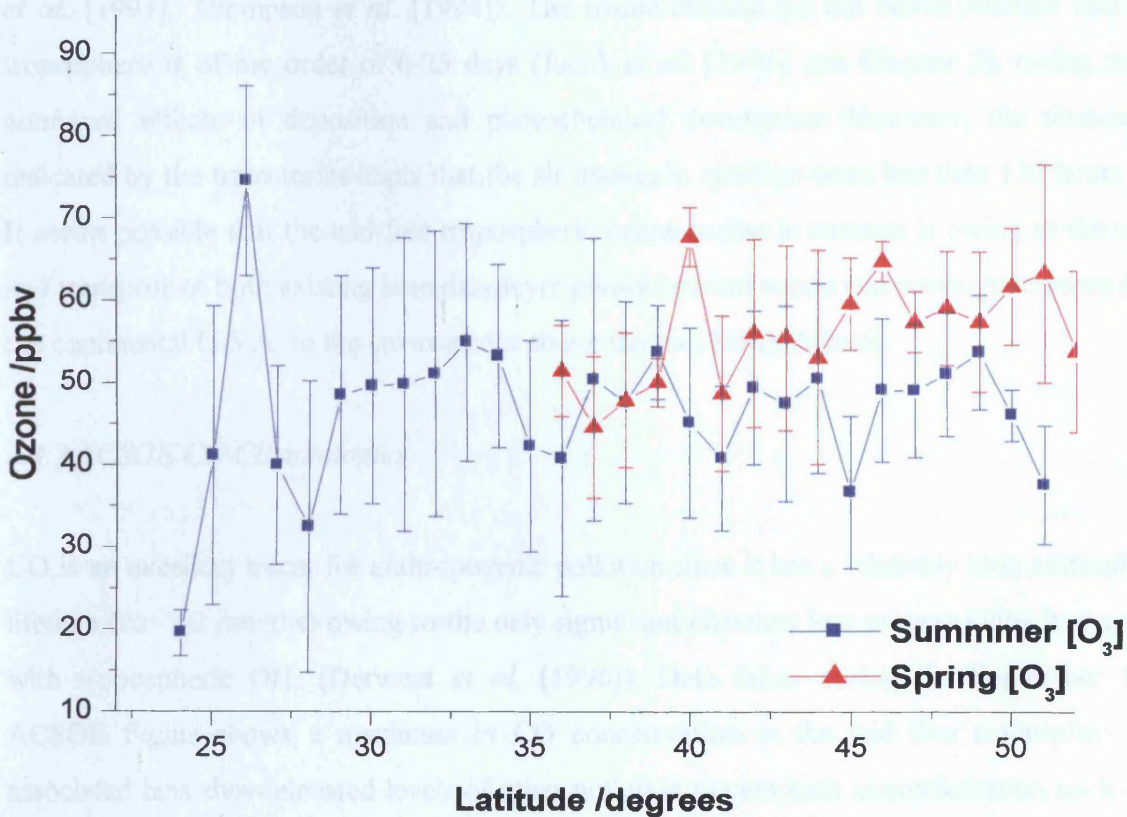


Figure 2.6 Latitudinal Variation in Averaged ACSOE Ozone Concentrations with 1σ Standard Deviation Bars (for each data point).



These observations are supported by an analysis of the latitudes over which the campaign was flown. It was evident from the aircraft flight logs that the C-130 flew more missions to the south of the Azores during summer than spring. It is well known that ozone concentrations in the tropics are different to more northerly latitudes (Jacob *et al.* [1996]). Hence, there was a need to check that the results were not biased by the C-130 encountering air of tropical origin. Figure 2.6 shows the concentration of ozone measured by the aircraft, plotted against latitude for both seasons. Figure 2.6 shows that indeed, the C-130 did fly to latitudes further south in summer than spring. However, the plot also shows that for latitudes where O_3 concentrations were measured in both seasons there is clear spring excess. The data in the lowest altitude bin (<500 m) as shown in Figure 2.5, are contrasted by data at higher altitudes. Ozone encountered in the mid free troposphere (*ca.* 4-7 km), shows a summer excess. Above 500 m, there is a switch to a region where spring $[O_3]$ is again dominant. The summer excess in ozone in the mid free troposphere is probably owing to the types of air mass encountered by the C-130 in the ACSOE summer campaign. Analysis of ECMWF back trajectories show that the Azores and surrounding open ocean during the time of the summer 1997 flights were subjected to air-masses that had been transported from the Eastern Seaboard of the U.S.A. to the open ocean in the vicinity of the Azores at mid tropospheric altitudes.

Significant amounts of tropospheric ozone are thought to be transported into the North Atlantic *via* continental outflow from Europe and North America (Parrish *et al.* [1993], Jacob *et al.* [1993], Thompson *et al.* [1994]). The ozone lifetime for the North Atlantic mid free troposphere is of the order of 6-25 days (Jacob *et al.* [1996], see Chapter 3), owing to the combined effects of deposition and photochemical destruction. However, the time-scales indicated by the trajectories imply that the air masses in question were less than 120 hours old. It seems possible that the mid-free tropospheric ozone excess in summer is owing to the uplift and transport of both existing boundary layer photochemical ozone and ozone precursors from the continental U.S.A. to the environment above the mid North Atlantic.

2.4.2 ACSOE CO Climatologies

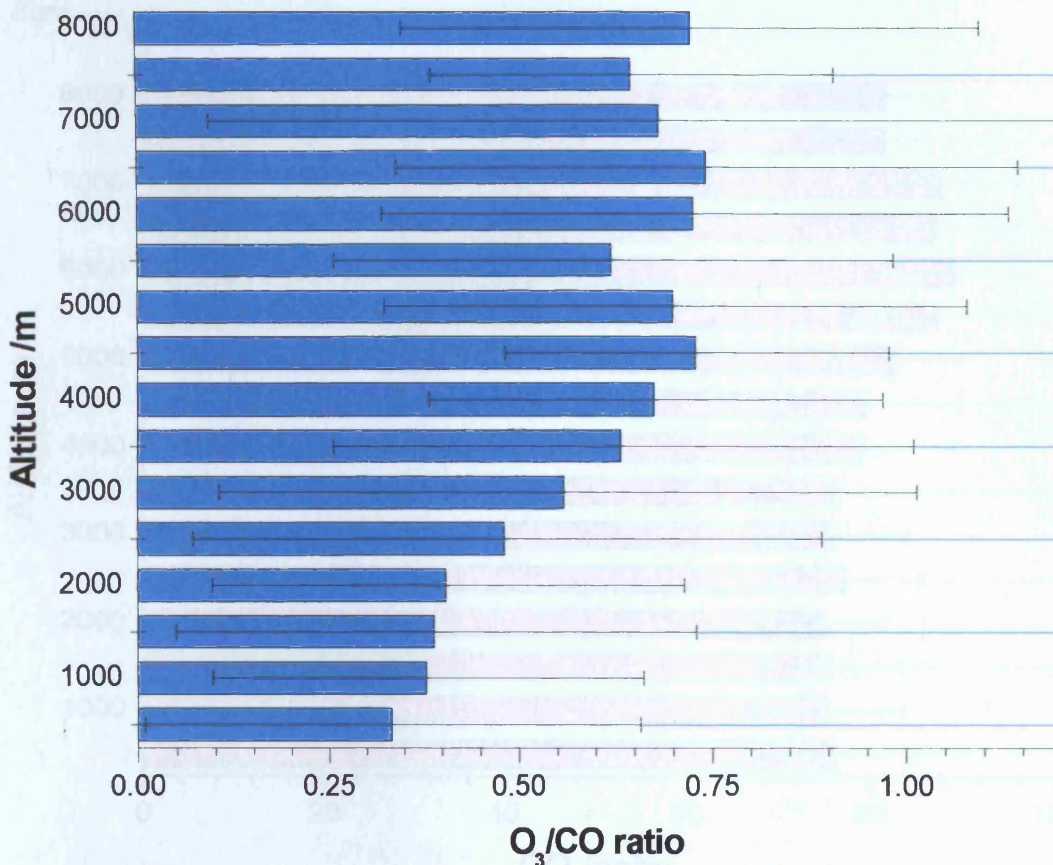
CO is an excellent tracer for anthropogenic pollution since it has a relatively long atmospheric lifetime (*ca.* 1-2 months) owing to the only significant chemical loss process being its reaction with tropospheric OH. (Derwent *et al.* [1996]). Data taken during the September 1997 ACSOE flights shows a maximum in CO concentration in the mid free troposphere and associated bins show elevated levels of other pollution tracers such as condensation nuclei and

black carbon soot. The maximum ceiling of the C-130 during ACSOE was around 8 km. As stated previously, for these altitude bins there is an excess of spring ozone. This spring ozone maximum may be due to stratospheric-tropospheric exchange (STE). It is well documented that the tropopause in spring lies at an altitude that is less than summer. For the Azores, ozonesondes indicate that the tropopause lies between 12-14 km for spring (Oltmans *et al.* [1996]). Hence, during spring injection of stratospheric air in the troposphere could account for the elevated ozone levels measured in these data bins, while in summer altitudes of 8 or 9 km are insufficient to be significantly affected by STE. A good indicator for air of stratospheric origin is air that is high in [O₃] but low in [CO] owing to the absence of natural stratospheric sources of CO.

A plots of the O₃/CO ratio with altitude during the summer is shown in Figure 2.7. The plot shows a clear altitude dependency in this ratio. Close to the ocean surface, where summer concentrations of ozone are relatively low, the ratio is of the order of 0.3. This is similar to the surface O₃/CO ratio of 0.3-0.4 reported over much of the Northern Atlantic, both from sea level surface sites and those in the lower troposphere (Anderson *et al.* [1993], Parrish *et al.* [1998]). This ratio increases with altitude to *ca.* 4500 m. Above this altitude, the ratio shows little altitude variation up to a ceiling of 8500 m. For these mid free troposphere bins, the ratio is *ca.* 0.6-0.75. At these altitudes, the concentration of ozone is three times higher than at the surface, while [CO] only increases by 10 ppbv. This relative change in the magnitude of the numerator and denominator in the O₃/CO ratio explains the increase in the ratio and gives an indication that the air masses at these altitudes are still tropospheric in origin. For air of a purely stratospheric origin brought into the troposphere by a tropospheric fold or similar troposphere subsidence (Schuepbach *et al.* [1998]), the relative change in the magnitude of [CO] vs. [O₃] would be expected to show an increase in [O₃] but a corresponding decrease in [CO] (Harris *et al.* [1998]). Since both CO and ozone increase with altitude, air masses measured during ACSOE summer are likely to be almost purely tropospheric in origin.

As stated previously, a direct comparison of the seasonal CO data for the individual legs of the ACSOE campaign is impossible owing to the absence of a CO instrument during the spring missions. Summer CO concentrations do however offer a guide as to the distribution of this trace gas over the North Atlantic, as CO is a relatively good tracer for anthropogenic influences. The oxidation of CO can lead to both production and destruction of ozone depending on the levels of precursors such as hydrocarbons and NO_x. (Crutzen [1974]). This has added importance since despite long term measurements made in the 1980's suggesting that

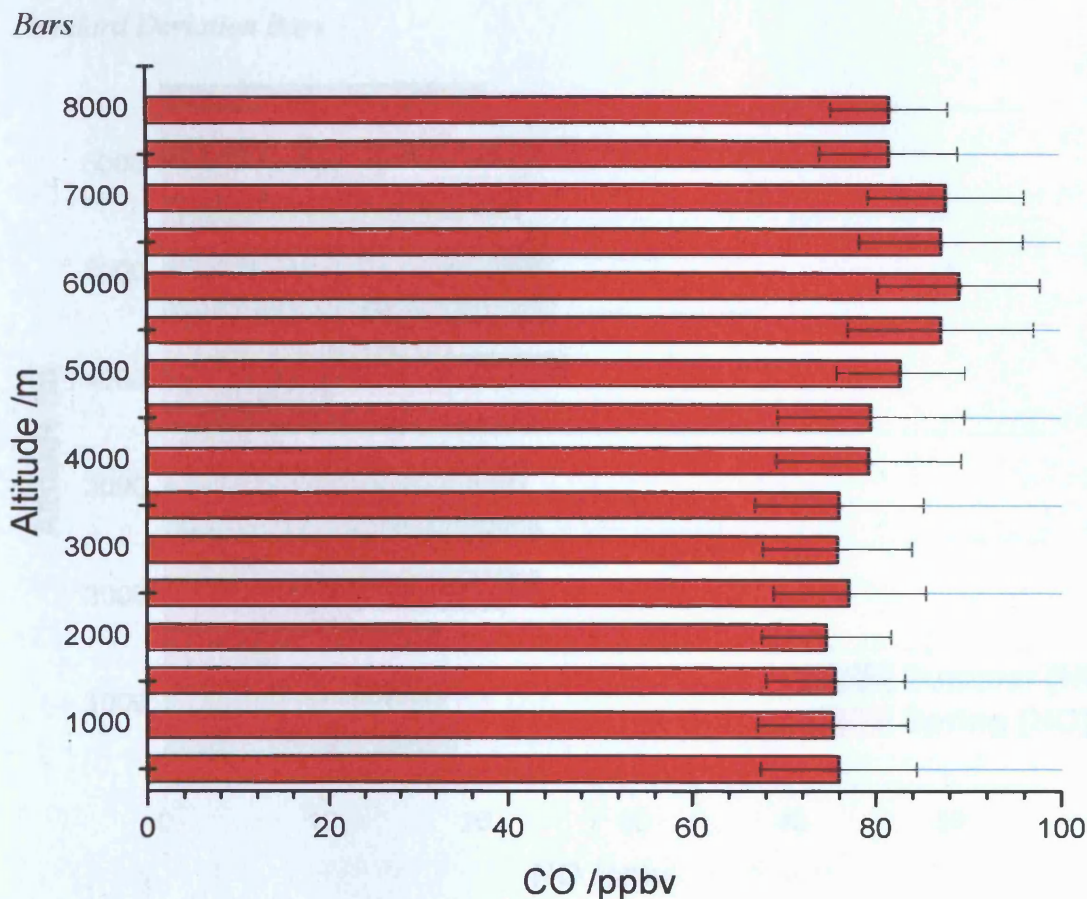
Figure 2.7: Averaged ACSOE Summer O_3/CO Ratio showing 1σ Standard Deviation Bars



tropospheric CO is increasing, there is recent evidence for a decrease in the net CO concentration at surface sites in the U.S. and mid Atlantic free troposphere. (Hallock-Waters *et al.* [1999]).

Over the latitudes investigated by the C-130 during summer, [CO] is found to have a concentration of between 75 and 90 ppbv, as shown in Figure 2.8. Also of note is that there is a generally similar [CO] with respect to altitude, up to 5 km. Peak concentration in CO was observed in the mid free troposphere bins, which was concurrent with the summer ozone excess at these altitudes. Trajectories suggest that both these peaks are probably due to air that has been transported to the Azores and surrounding ocean by convective uplift of air from the polluted boundary layer of the eastern continental US. Above this peak is a general decrease in CO concentration to around 80 ppbv. This is still higher than was detected in the marine boundary layer and lowest of the free troposphere bins.

Figure 2.8: Averaged CO Data for ACSOE Summer Flights showing 1 σ Standard Deviation

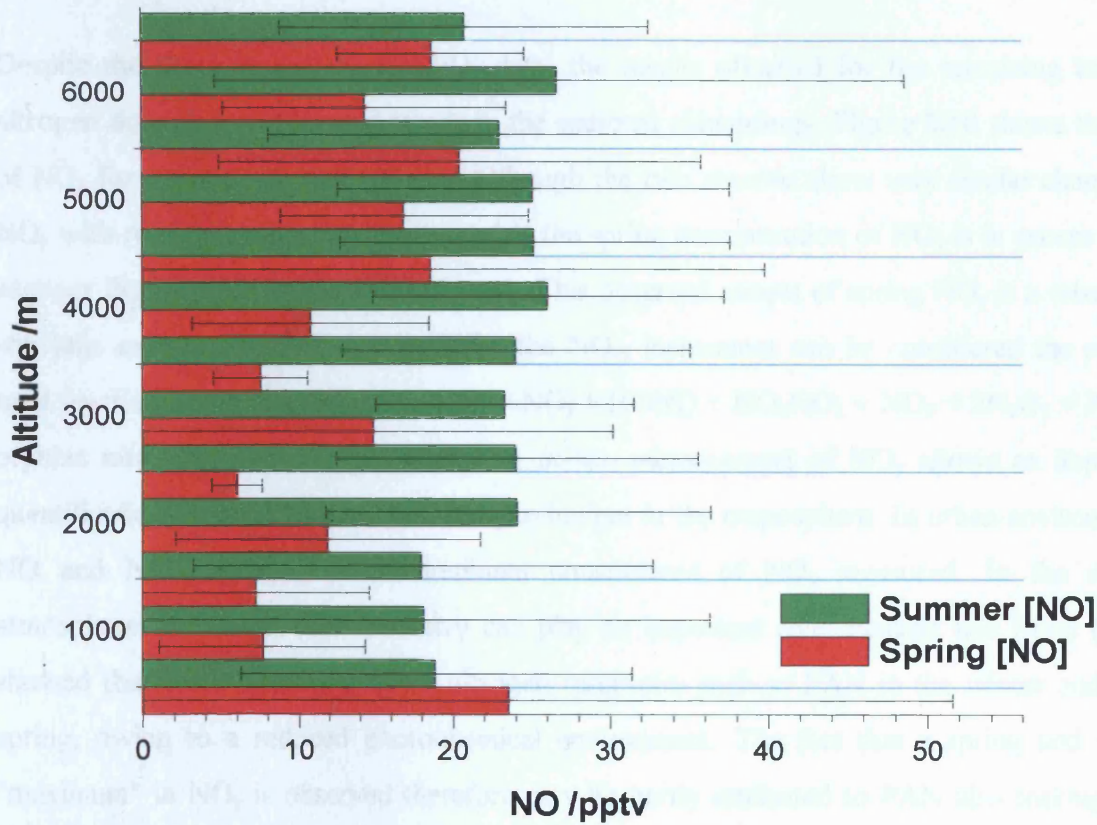


2.4.3 ACSOE NO_x and NO_y Climatologies

The averaged distribution of $[\text{NO}]$ over the Atlantic as measured by the C-130 during spring and summer is shown in Figure 2.9. From this plot, there is no obvious trend in the distribution of $[\text{NO}]$ in either season with respect to altitude. Summer concentrations are found to be in general greater than spring with little altitude variation. For the spring flights, the greatest concentration of NO is found near the surface, ($[\text{NO}]$ ca. 22 pptv). Above this altitude, the concentrations of NO fall but increase once again in the mid-free troposphere above 4 km. For all data bins, the average concentration is <25 pptv.

It is difficult to draw any conclusions as to the nature of total NO climatologies owing to the variability in the data. This was compounded by other problems experienced by the NO_{xy} instrument, specifically the failure of the NO_2 detector during ACSOE. Hence, there was no measured $[\text{NO}_2]$ during the campaign. (S.A. Penkett, *private communication*). The NO_2 conversion efficiency was also used to produce NO_y mixing ratios; *i.e.* NO_2 was used as substitute for all reactive nitrogen oxides. Following results from an intercomparison flight with the NOAA P3 aircraft in the middle of the ACSOE Azores, campaign in September 1997,

Figure 2.9: Averaged NO Concentration During ACSOE Spring and Summer showing 1 σ Standard Deviation Bars.



it appears that the NO_{xy} instrument's NO_y inlet was not able to sample/transmit nitric acid. The NO_y mixing ratios reported by this instrument is more likely to be a measure of $(\text{NO}_{y\text{total}} - \text{HNO}_3)$. For the purposes of this work, the $(\text{NO}_{y\text{total}} - \text{HNO}_3)$ data is still described as NO_y .

Owing to the absence of measured NO_2 , the data described here were calculated from photostationary state relationships between ozone, NO and the photolysis frequency $j\text{-(NO}_2)$ (Leighton 1961). It can be shown that in photostationary state,

$$\text{NO}_2 = \left(\frac{k_{(\text{NO}+\text{O}_3)}[\text{NO}][\text{O}_3]}{j\text{-(NO}_2)} \right) \quad (2.1)$$

Using *in-situ* data for NO, ozone and $j\text{-(NO}_2)$, corresponding concentrations of NO_2 can be obtained by solving equation (2.1) along the aircraft flight track and binning the data in the usual way. Derived NO_2 is therefore dependent on the assumption that air masses encountered during ACSOE were under photostationary state conditions. This approach can lead to over

and underestimation of NO_2 (Carpenter *et al.* [1998]), but did provide an indicator of probable $[\text{NO}_2]$.

Despite the shortcomings of the NO_y data, the results obtained for the remaining reactive nitrogen does show interesting trends in the seasonal climatology. Figure 2.10 shows the plot of NO_y for both spring and summer. Although the two seasons show very similar changes in NO_y with respect to altitude, it is clear that the spring concentration of NO_y is in excess of the summer flights by an average of 145 pptv. This observed excess of spring NO_y is a result that warrants explanation. NO_y measured by the NO_{xy} instrument can be considered the sum of total reactive odd nitrogen species ($\text{NO} + \text{NO}_2 + \text{HONO} + \text{HO}_2\text{NO}_2 + \text{NO}_3 + 2\text{N}_2\text{O}_5 + \text{PAN} + \text{organic nitrate} + \text{nitrate aerosol}$). Hence, *in-situ* measurement of NO_y allows an important quantification of the total oxidised nitrogen budget in the troposphere. In urban environments NO and NO_2 are usually the dominant constituents of NO_y measured. In the remote atmosphere however, PAN chemistry can play an important role. Penkett and Brice (1986) showed that there is a build up of nitrogen reservoirs such as PAN in the winter and early spring, owing to a reduced photochemical environment. The fact that a spring and winter "maximum" in NO_y is observed therefore may be partly attributed to PAN also making up a large portion of the NO_y detected. Using photostationary state NO_2 to estimate total NO_x , the NO_x/NO_y ratio for the two seasons showed that the lowest NO_x/NO_y ratios were observed in the spring free troposphere where ratios at 3-6.5 km were consistently around 0.1-0.2. The plots of the NO_x/NO_y data are shown in Figure 2.11. These data suggests that a significant portion of the detected NO_y is species other than NO and NO_2 . This contrasts the summer where the NO_x/NO_y ratio is closer to 0.5. These data compare to NO_x/NO_y ratios calculated by Liang *et al.* (1998) where ratios of 0.2 in summer and 0.6 in winter were calculated in the continental US boundary layer, which may indicate that the NO_x component of the total oxidised nitrogen is higher during summer.

Figure 2.10: Averaged NO_y Concentration During ACSOE Spring and Summer showing 1σ Standard Deviation Bars.

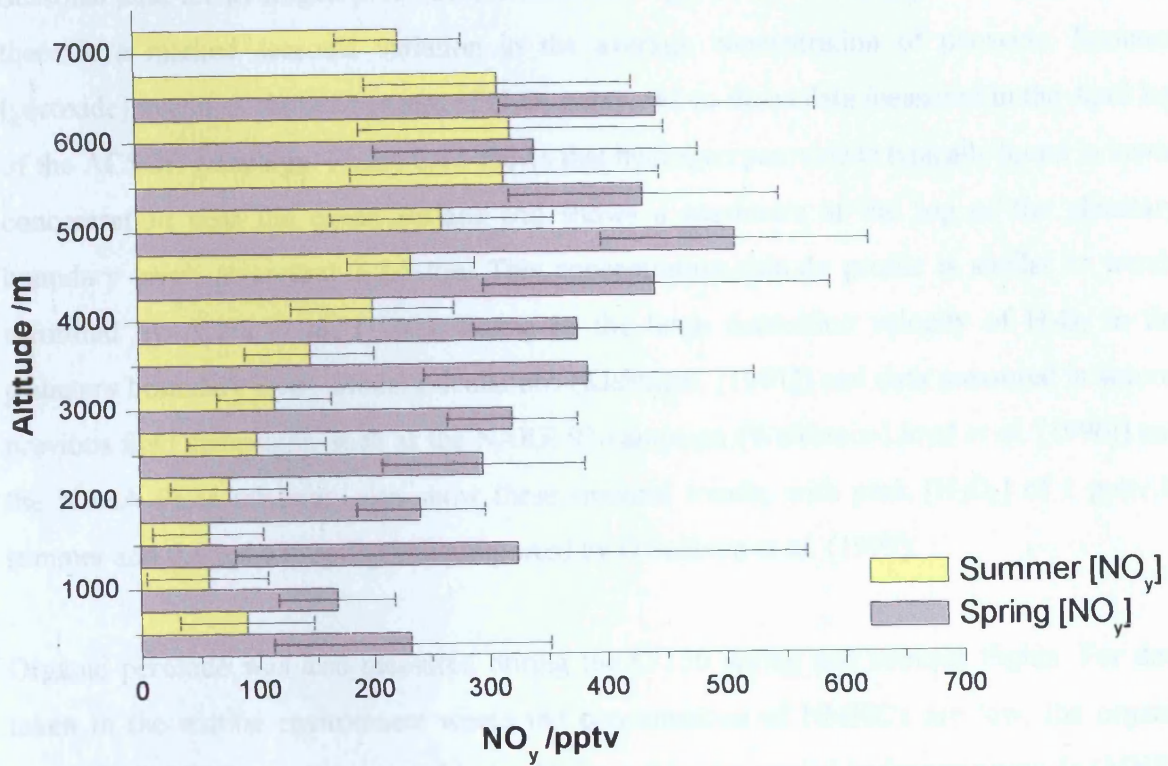
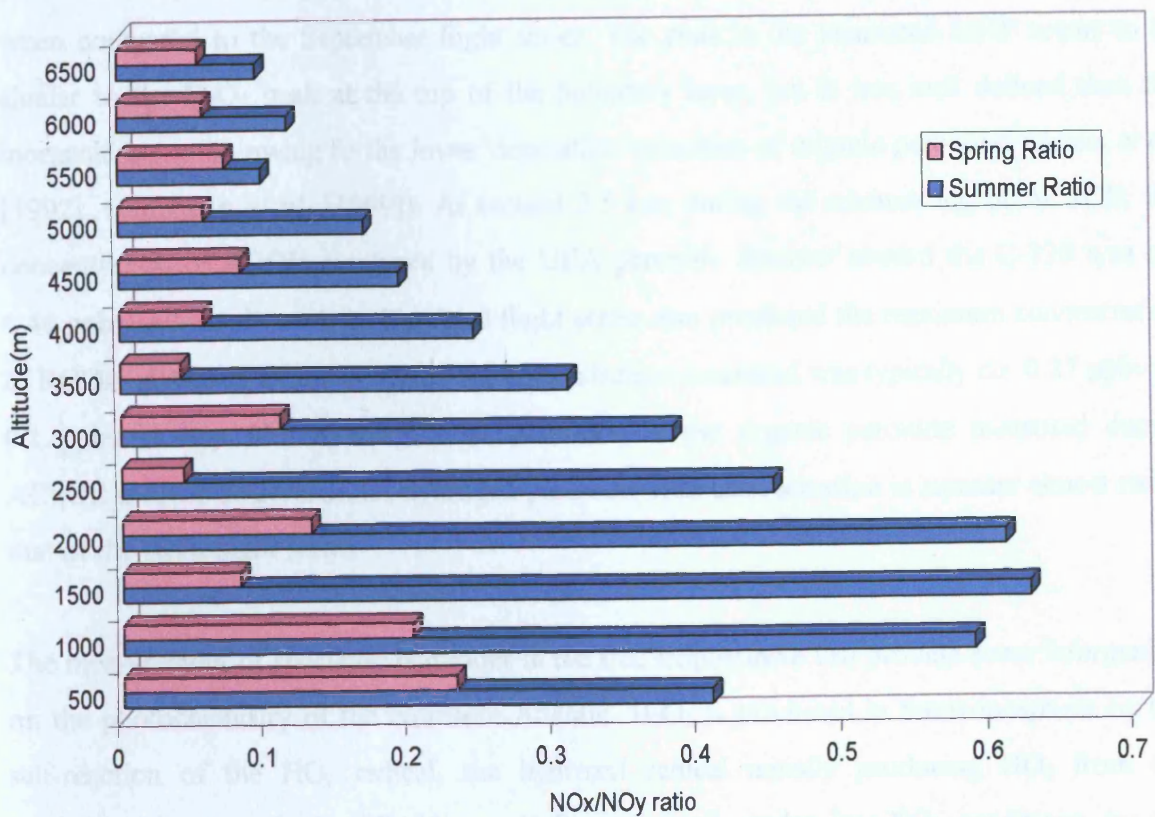


Figure 2.11: Spring and Summer Averaged NO_x/NO_y Data During ACSOE



2.4.4: ACSOE Peroxide Climatologies

Seasonal data for hydrogen peroxide are shown in Figure 2.12. As with several other tracers, there is a marked seasonal variation in the average concentration of peroxide. Summer [peroxide] averages show an excess of H_2O_2 compared to those data measured in the April leg of the ACSOE campaign. Figure 2.12 shows that hydrogen peroxide is typically found in lower concentration near the ocean surface and shows a maximum at the top of the planetary boundary layer, at around 1-2.5 km. This concentration-altitude profile is similar to trends identified by Ayers *et al.* (1992), owing to the large deposition velocity of H_2O_2 in the planetary boundary layer. Model calculations (Kleinman, [1991]) and data measured in several previous field campaigns, such as the NARE 93 campaign (Weinstein-Lloyd *et al.* [1996]) and the NASA PEM missions, also show these seasonal trends, with peak [H_2O_2] of 1 ppbv in summer and 0.8 ppbv in spring being reported by O'Sullivan *et al.* (1999).

Organic peroxide was also measured during the C-130 spring and summer flights. For data taken in the marine environment where the concentration of NMHC's are low, the organic peroxide (ROOH) may be assumed to be dominated by the methyl hydrogen peroxide (MHP), CH_3OOH component (O' Sullivan *et al.* [1999]). Figure 2.13 shows, as with the inorganic peroxide component, [ROOH] detected in spring were observed at lower net concentrations when compared to the September flight series. The peak in the measured MHP seems to be similar to the H_2O_2 peak at the top of the boundary layer, but is less well defined than the inorganic peroxide owing to the lower deposition velocities of organic peroxides (Ayers *et al.* [1992], O'Sullivan *et al.* [1999]). At around 2.5 km, during the summer leg of ACSOE, the concentration of ROOH measured by the UEA peroxide detector aboard the C-130 was *ca.* 0.40 ppbv (± 0.2 ppbv at 1σ). The April flight series also produced the maximum concentration of ROOH at similar altitudes, where the concentration measured was typically *ca.* 0.27 ppbv (± 0.1 ppbv at 1σ). Hence, the seasonal variation in the organic peroxide measured during ACSOE is much larger than for hydrogen peroxide, with concentration in summer almost twice that of the April flight series.

The measurement of speciated peroxides in the free troposphere can provide some information on the photochemistry of the Northern Atlantic. H_2O_2 is produced in the troposphere by the self-reaction of the HO_2 radical, the hydroxyl radical initially producing HO_2 from the oxidation of tropospheric CO. Hence, H_2O_2 is formed, under low- NO_x conditions, by the reaction sequence (2.2)-(2.5)

Figure 2.12: Averaged H_2O_2 Concentration During ACSOE Spring and Summer showing 1σ Standard Deviation Bars.

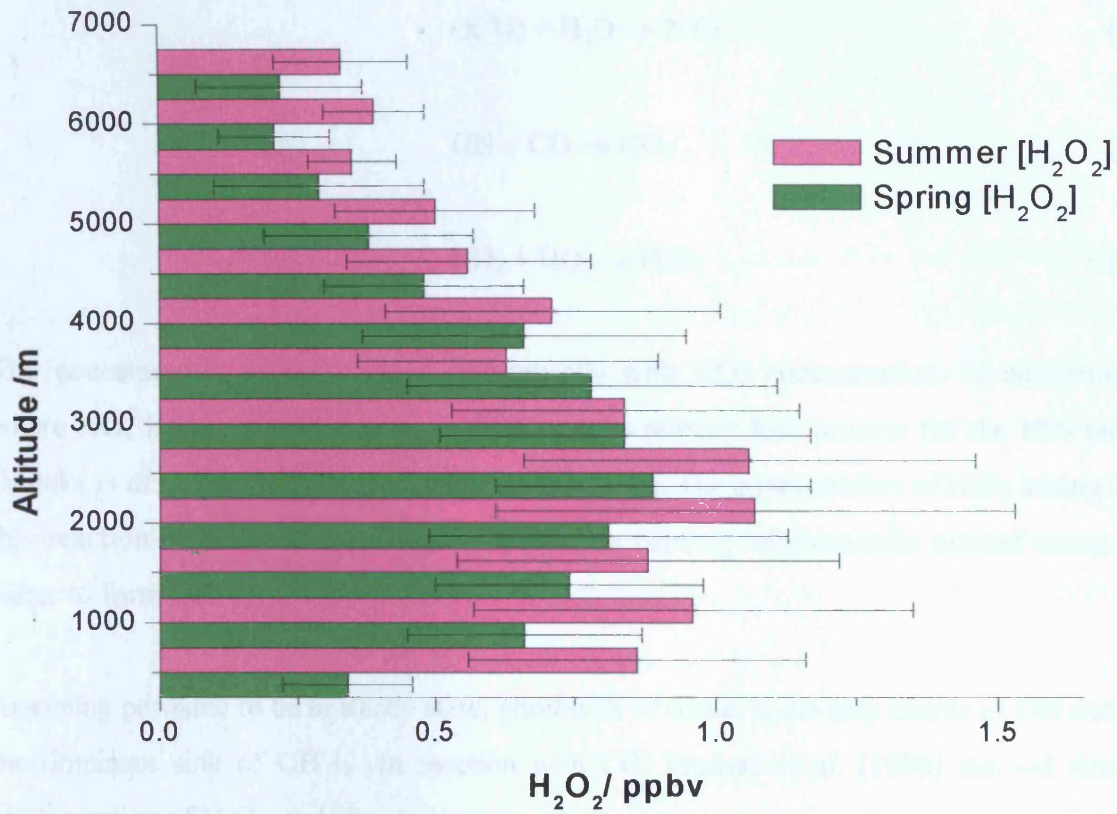
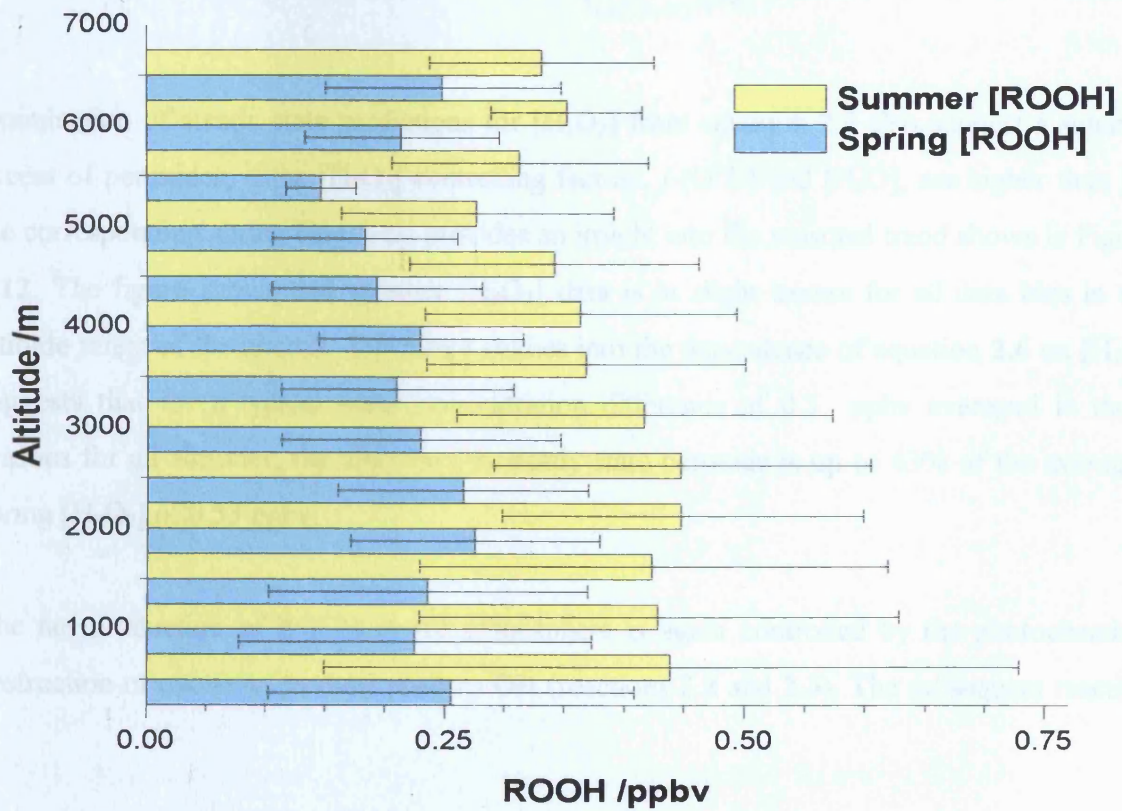


Figure 2.13: Averaged ROOH Concentration During ACSOE Spring and Summer showing 1σ Standard Deviation Bars.





The concentration of H_2O_2 varies quadratically with HO_2 concentration. In environments where NO_x is low, the self-reaction of HO_2 is the primary loss process for the HO_2 radical (Monks *et al.* [1998], [2000], Carpenter *et al.* [1997]). The concentration of H_2O_2 arising from this reaction directly reflects the rate of reaction between electronically excited ozone and water to form OH.

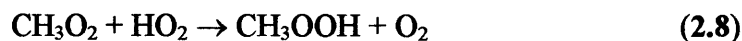
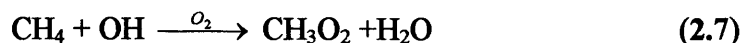
Assuming peroxide to be in steady state, photolysis of ozone is the only source of OH and that the dominant sink of OH is *via* reaction with CO, Penkett *et al.* [1998] showed that the concentration of H_2O_2 could be equated as

$$[\text{H}_2\text{O}_2] = \frac{(j(\text{O}^1\text{D})k_{(\text{O}^1\text{D})+\text{H}_2\text{O}} \cdot [\text{O}_3] \cdot [\text{H}_2\text{O}])}{k_{((\text{O}^1\text{D})+\text{M})} \cdot [\text{M}]} \quad (2.6)$$

Examination of steady state predictions for $[\text{H}_2\text{O}_2]$ from equation 2.6 also suggest a summer excess of peroxides, if the $[\text{H}_2\text{O}_2]$ controlling factors, j -(O^1D) and $[\text{H}_2\text{O}]$, are higher than for the corresponding spring data. This provides an insight into the seasonal trend shown in Figure 2.12. The figure shows that summer $[\text{H}_2\text{O}_2]$ data is in slight excess for all data bins in the altitude range of the aircraft. Sensitivity studies into the dependence of equation 2.6 on $[\text{H}_2\text{O}]$ suggests that for a typical water concentration difference of 0.3 ppbv averaged in these seasons for all altitudes, the difference in steady state peroxide is up to 43% of the averaged spring $[\text{H}_2\text{O}_2]$ of 0.53 ppbv.

The net production of ROOH in the troposphere is again controlled by the photochemical destruction of ozone to produce primary OH (reactions 2.2 and 2.3). The subsequent reaction

of methane or higher hydrocarbons with HO_x can then form organic peroxides as shown by reaction (2.7) and (2.8):



As with hydrogen peroxide, the concentration of peroxy radicals RO₂ and HO₂ control the ultimate formation of ROOH. Using the model data described in Chapter 3, model [HO₂] and [RO₂] were shown to be higher for the April flight series than the corresponding September flight campaign. It would seem a contradiction therefore to measure less organic peroxide in April since production of ROOH *via* reaction 2.7 would be in large excess during April compared to September. This is a slightly puzzling result. As with all trace gases concentrations the photochemical balance between production and destruction for these trace compounds must be taken into account.

Model data as described in Chapter 3 suggests that the balance of [CH₃O₂] in spring and summer is biased towards the April flights. Figure 3.6 shows that spring [CH₃O₂] is 2-3 pptv higher than summer in the lower free troposphere. [OH] however showed a small summer excess (Figure 3.1). Owing to the formation of methyl hydrogen peroxide being coupled to the concentration of [HO₂] and [CH₃O₂], it would seem that simple photochemical arguments alone cannot account for the strong summer ROOH excess observed in the ACSOE dataset. Model data suggests that production of ROOH would be higher in spring, while loss reactions (*e.g.* reaction of ROOH with OH) should also be greater during the April portion of ACSOE. Therefore, is the summer excess in these species a result of secondary factors such as transport or heterogeneous chemistry?

Peroxides do have sufficient lifetimes (*ca.* 5 days, Derwent *et al.* [1996]) to allow long-range transport. Transport of air masses containing elevated levels of peroxide were observed by Weinstein-Lloyd *et al.* (1996) during the 1993 NARE campaign. The authors reported that measurements of speciated peroxide from an aircraft platform flying off the coast of the USA, and found concentrations of H₂O₂ were enhanced in episodes of continental outflow of aged, low NO_x air-masses. Similarly, O'Sullivan *et al.* (1999) reported the influence of long-range pollution plumes on the chemistry of the remote Pacific. From the trajectory data obtained for ACSOE in spring and summer there do appear to be several episodes of distinct continental

outflow, particularly during the summer series of aircraft missions. Here, air masses of U.S. origin have been transported to the remote marine free troposphere close to the Azores. Therefore, is the influence of these episodes of continental outflow causing a perturbation of the background photochemistry with the net result being the transport of large amounts of peroxide into the free troposphere?

This is a difficult question to answer since there are several pieces of conflicting evidence. Continental outflow is usually associated with high levels of ozone and its precursors rather than elevated peroxides. However, the summer data for ACSOE suggests that these species are not present in large concentrations compared to the spring, with data showing lower concentrations of ozone in summer, except at high altitudes where the influence of continental outflow and/or stratospheric-tropospheric exchange was cited as an explanation for the levels of ozone measured by the aircraft (section 2.4.1). These "plumes" seem to be low in $[\text{NO}_x]$ and $[\text{O}_3]$ but high in [peroxides] and peroxide precursors (CO , CH_4 and NMHC's). Data on these concentrations are not available since only CO was measured and even with these data, the absence of seasonal comparisons makes the discussion of seasonal climatology difficult.

If transport of peroxides is the explanation for the levels measured in summer of 1997 then clearly additional processing has occurred in these air masses. The speciation of ROOH and H_2O_2 is such that the organic peroxide excess in summer is almost twice that of spring, while H_2O_2 concentrations are only fractionally higher. The ratio of $\text{ROOH}/\text{H}_2\text{O}_2$ has been identified as a good indicator of heterogeneous removal of inorganic peroxides due to the preferential removal of H_2O_2 owing to its high solubility when compared to ROOH . (Cohan *et al.* [1999], O'Sullivan *et al.* [1999]). Assuming the transport argument to hold true for ACSOE summer measurements, then there must have been large-scale heterogeneous removal of H_2O_2 transported in to the oceanic environment in order to account of the relatively small increase in summer H_2O_2 combined with a large increase in ROOH . This may not be surprising owing to the formation of a large tropical storm during September 1997. The U.S. National Hurricane Centre later upgraded it to a class three hurricane name "Erika". Hurricane Erika was encountered by the C-130 as part of the ACSOE summer campaign. Over the course of its life, this hurricane passed into the North Atlantic and by mid September the feature passed close to the Azores. On September 15th and 16th, the aircraft flew into air masses that had been processed and/or influenced by the passage of this hurricane. The huge amount of cloud normally associated with tropical storms increased the likelihood of increased wet deposition of soluble species *e.g.* hydrogen peroxide. The influence of Hurricane Erika on the

H₂O₂/ROOH ratio may go some way to explain why the inorganic peroxide excess measured during ACSOE summer is so small *c.f.* [ROOH] for the same season.

Although the use of transport arguments with respect to concentration of detected peroxides and their precursors from continental sources may explain some of the features observed in the summer Azores campaign, clearly the exact nature of the elevated peroxide concentration is still under question. Only with a firmer quantitative analysis from detailed model studies of [CH₃OOH] and [H₂O₂] are these questions likely to be fully answered.

2.4.4 ACSOE HCHO Climatologies

Measuring the concentrations of HCHO during spring and summer was a major aim of the ACSOE project since data from ship campaigns indicate little variation in HCHO concentration with respect to latitude (Lowe and Schmidt, [1983]). These data were, however, collected in the same season. A comparison of spring and summer HCHO data measured *via* the C-130 platform is plotted in Figure 2.14. This figure shows generally good overall agreement in the shape of the concentration profiles with respect to altitude. The net concentrations measured from the C-130 also appear to be very similar in magnitude, with [HCHO] ranging from 0.5 to over 1 ppbv being observed. In almost all of the altitude bins, spring [HCHO] measurements are shown to be higher than for corresponding altitudes during the summer leg. The ACSOE spring flight on 7/4/97 may have some bias in this however. This flight indicated a pollution plume in which [HCHO] in excess of 3 ppbv were measured. In order to ascertain any potential bias these plume data were removed from the data average. Removal of these spikes did effect the overall spring concentration profile for the 1km bin, but the overall trend is unaffected and spring remains the dominant season by *ca.* 0.15 ppbv.

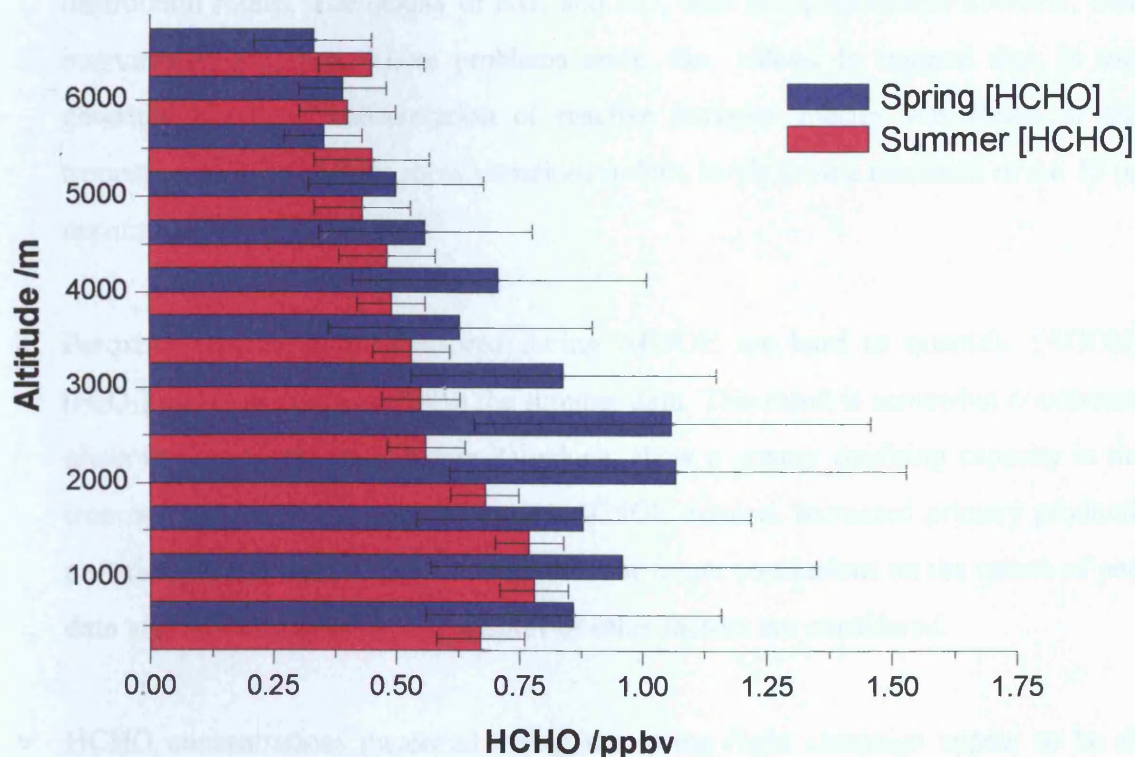
The slight spring excess of HCHO is potentially a feature of the reactions that control HCHO levels in the troposphere. HCHO is produced by the reactions of peroxy radicals and destroyed *via* reaction with OH or through photochemical destruction *viz*





The net excess observed during the spring ACSOE flight series may be directly linked with the photochemical environment. During April, model data (Chapter 3) suggests that there are generally higher levels of OH in the free troposphere over the Azores, than for the corresponding September missions. In terms of the budget of HCHO, owing to its solubility, the question of heterogeneous as well as photochemical losses must be considered. If, like the peroxides discussed previously, there was larger cloud uptake of soluble species during the summer leg owing to the proximity of Hurricane Erika, these factors may also contribute to the lower [HCHO] observed during the summer campaign. Overall, when assessing the true summer budget of HCHO, the data would suggest that a winter build up of HCHO hydrocarbon precursors and enhanced spring HO_x levels coupled with enhancement of heterogeneous summer chemistry probably need to be considered.

Figure 2.14: Averaged HCHO Concentration During ACSOE Spring and Summer showing 1 σ Standard Deviation Bars.



2.5: Summary of ACSOE Campaign

The data bin approach adopted in this work has illustrated that the climatologies of trace gases measured during April and September over the North Atlantic are very different. Considering the comparison of ACSOE spring data with similar flights in summer then the following can be concluded.

- Ozone concentrations over the unpolluted North Atlantic Ocean suggest a maximum concentration in late April up to an altitude of *ca.* 3 km. This seems to agree with reports in the literature from surface sites of a Northern Hemisphere spring ozone maximum. Higher altitude bins show elevation in $[O_3]$ that may be linked to transport of ozone and its precursors from continental U.S., or similar increases owing to stratospheric-tropospheric exchange through subsidence events.
- Spring data shows that $[NO_y]$ ranges from 150-500 pptv, as compared to 100-400 pptv in summer. NO_x/NO_y ratios suggest that there are major influences of other reactive nitrogen reservoirs, possibly PAN during the spring flights which are not present during summer owing to recycling of NO_y back to NO_x *via* thermal decomposition, or other NO_y destruction routes. The quality of NO_x and NO_y data are questionable however, owing to instrumental problems. These problems aside, the values do suggest that, in summer, generally a greater concentration of reactive nitrogen species was found in the free troposphere. Both seasons show variations in NO_x levels from a minimum of *ca.* 15 pptv to maximum of *ca.* 50 pptv.
- Peroxide concentrations measured during ACSOE are hard to quantify. $[ROOH]$ and $[H_2O_2]$ are found to be higher in the summer data. This result is somewhat counterintuitive given the model results (Chapter 3), which, show a greater oxidising capacity in the free troposphere during April for the spring ACSOE mission. Increased primary production of peroxides is therefore likely in this season, but firmer conclusions on the nature of peroxide data are difficult, especially if transport or other factors are considered.
- HCHO concentrations measured during the spring flight campaign appear to be slightly higher than those of the summer leg, with peak concentrations *ca.* 0.5-1.2 ppbv. The April data suggesting an excess of HCHO in this season may be attributed to a winter build up of precursors to HCHO production

2.6: Maximum Oxidation Rates in the Free Troposphere (MAXOX) Campaign

As described in section 2.2, the 1999 MAXOX campaign was an aircraft mission that investigated the "maximum oxidation" rates of the free troposphere over the UK and European mainland. The MAXOX campaign was broken up into two separate legs. The first series of aircraft missions were flown out of the UK during April of 1999, while the summer portion were flown in July and August of 1999 out of both the UK and Germany. The aircraft flight tracks for both the spring and summer legs of the MAXOX campaign are shown in Figure 2.15 and 2.16. *In-situ* data taken during the C-130 missions were compared in a similar way as the ACSOE values, in order to quantify the effect of the seasonal change on the concentration and distribution of tracers over the semi-polluted environment of the UK mainland and European continent. A summary of the flight objectives for MAXOX is shown in Table 2.2

Figure: 2.15: Composite of Aircraft Flight Tracks During the MAXOX Spring Campaign

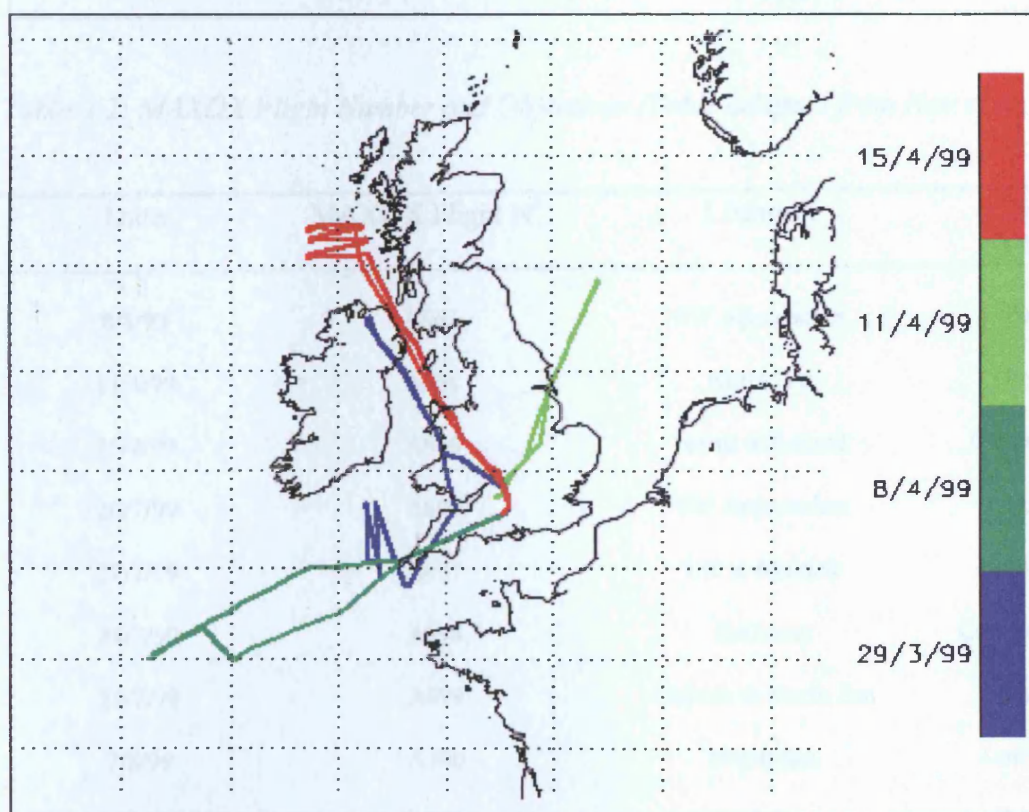


Figure 2.16: Composite of Aircraft Flight Tracks During the MAXOX Summer Campaign

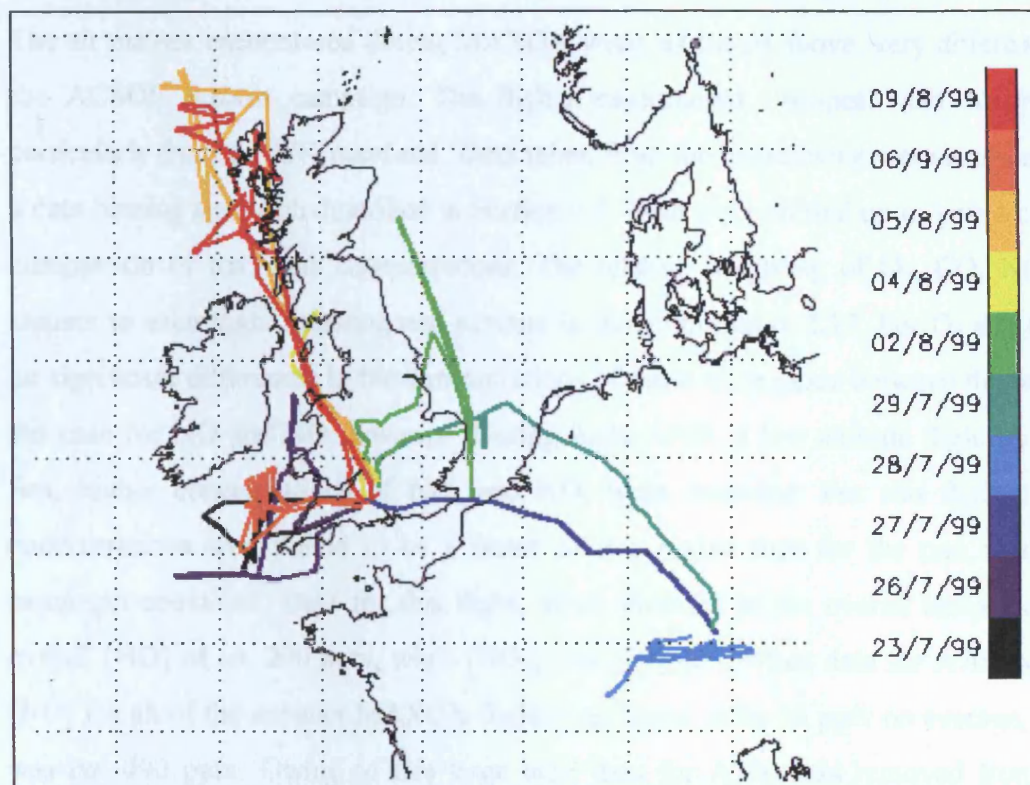


Table 2.2: MAXOX Flight Number and Objectives (Table adapted from Hov et al. [2000])

Date	MAXOX Flight N°.	Location	Sampling Objectives
8/4/99	A662	SW Approaches	Polluted Air
11/4/99	A664	North Sea	Polluted Air
15/4/99	A666	North of Ireland	Clean and polluted
26/7/99	A696	SW Approaches	Polluted Air
27/7/99	A697	UK to Munich	High Altitude Air
28/7/99	A698	Germany	Continental Pollution
29/7/99	A699	Munich to North Sea	High Altitude Air
2/8/99	A700	North Sea	Low Altitude Air
4/8/99	A701	Irish Sea	Deep Profiling
5/8/99	A702	Western Isles	Clean and polluted
6/8/99	A703	SW Approaches	High Altitude Air
9/8/99	A704	Western Isles	Deep Profiling

2.6.1: Spring and Summer Climatology comparison

The air masses encountered during MAXOX were, as stated above, very different to those of the ACSOE Azores campaign. The flights encountered European and Atlantic air only, particularly from the UK mainland. Data taken from the instruments were analysed initially by a data binning approach described in Section 2.2. Data were plotted up to give a climatological comparison of trace gas concentrations. The relative weighting of O₃, CO, NO, NO_y with respect to each flight in spring and summer is shown in Figure 2.17. For O₃ and CO there are no significant differences in the concentrations of these trace gases between flights. This is not the case for NO and NO_y however. During flight A700, a low altitude flight over the North Sea, higher concentrations of NO_x and NO_y were recorded. For this flight the NO/NO_y concentrations were found to be a factor of two higher than for the rest of the MAXOX campaign combined. Data for this flight, when included in the overall climatology, gave an overall [NO] of *ca.* 200 pptv, while [NO_y] was 533 pptv. When data for A700 was removed, [NO] for all of the summer MAXOX flights was found to be 66 pptv on average, while [NO_y] was *ca.* 490 pptv. Owing to this large bias, data for A700 was removed from the overall climatology analysis for both [NO] and [NO_y]. A summary of all [NO] data is described in Section 2.7.3 and Table 2.2.

2.6.2: MAXOX Ozone Climatologies

A plot of ozone data for the MAXOX spring leg, together with that for the MAXOX summer leg is shown in Figure 2.18. From Figure 2.18, it can be seen data for the two seasons are different in terms of the absolute concentration of ozone measured by the aircraft. Despite poor absolute correlation ($R^2=0.3$ for a plot of [O₃]_{summer} vs. [O₃]_{spring} {not shown}), the seasonal difference is relatively small, only around 5-10 ppbv for most altitudes. Concentrations in both seasons show an even distribution with respect to altitude and, in general, both seasons show that [O₃] increases with respect to altitude. Summer concentrations of ozone are in excess of that measured during spring for all of the data bins used in the analysis. Most summer data lies in a concentration band of around 40-60 ppbv. This is in contrast to spring, where the concentrations were typically from around 40-50 ppbv. The fact that the spring data show levels of ozone consistently below that of summer is interesting from the point of view of the Northern Hemisphere spring ozone maximum. One of the major goals of the MAXOX program was to investigate the causes of this phenomenon was indeed the result of photochemistry as has been postulated by several authors (*e.g.* Liu *et al.* [1987],

Figure 2.17: Average Trace Gas Concentration for each flight during MAXOX Summer Campaign

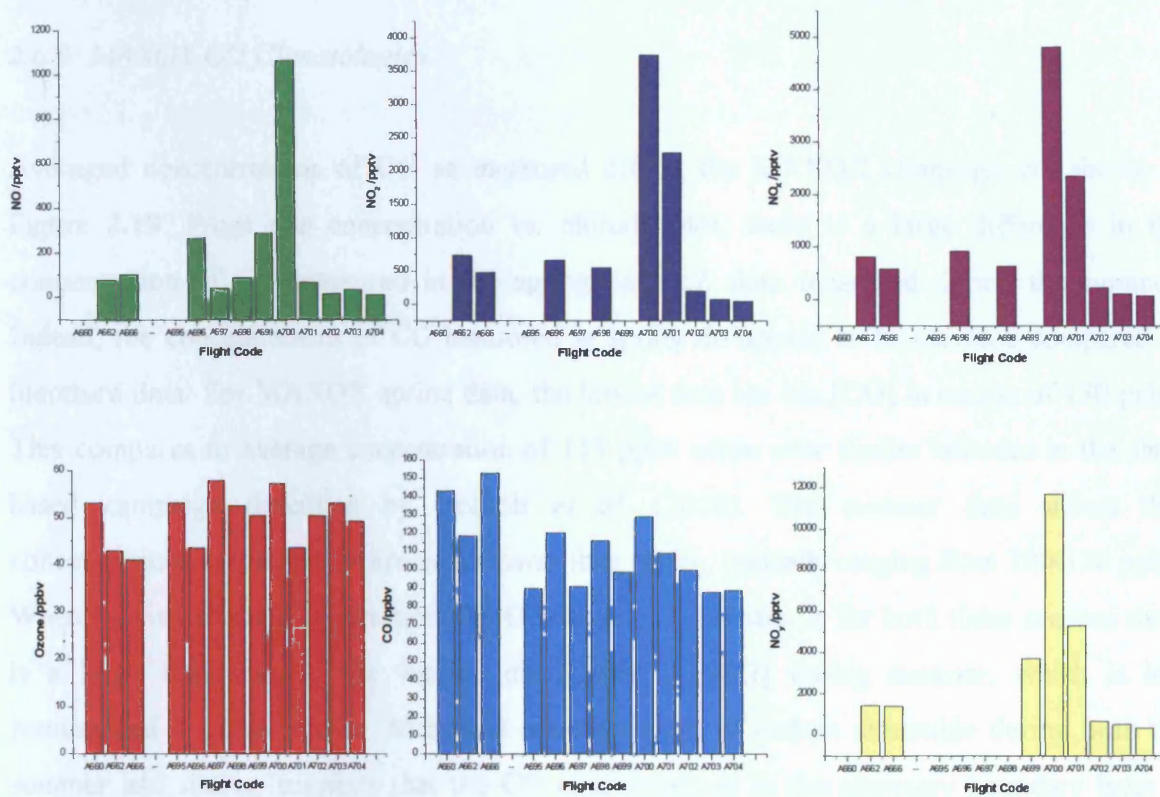
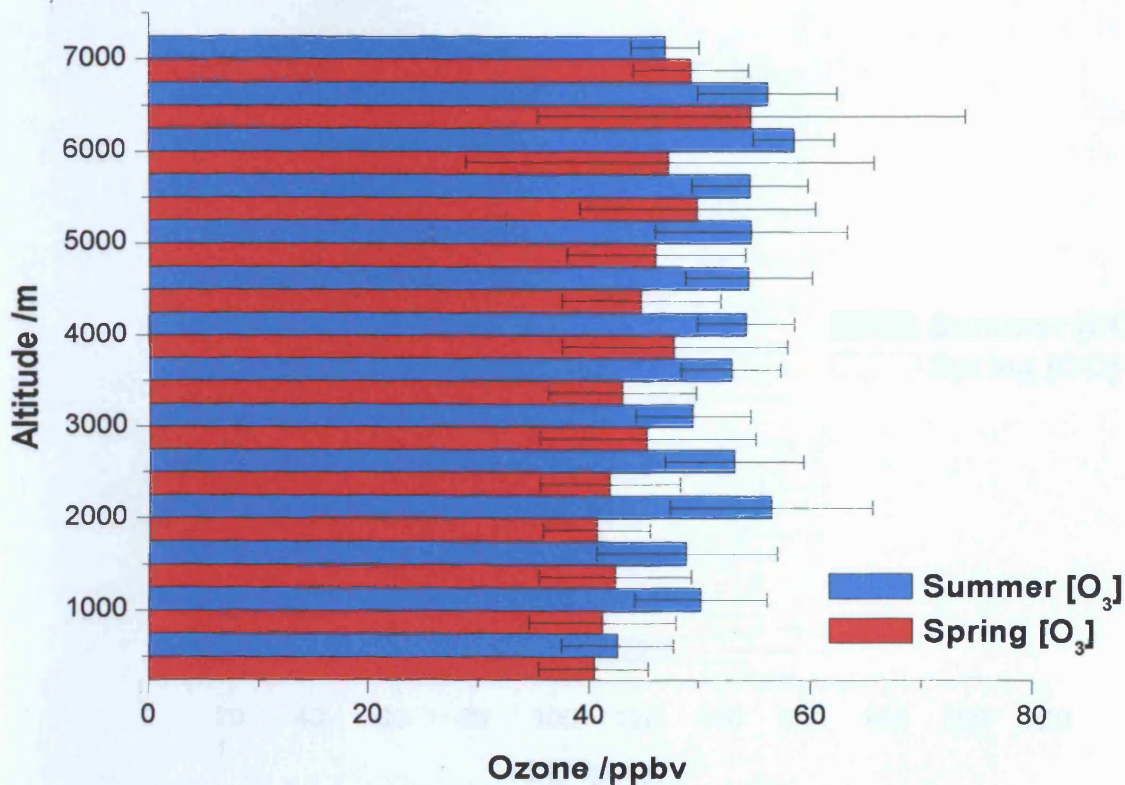


Figure 2.18: Averaged Ozone Concentration During MAXOX Spring and Summer showing 1 σ Standard Deviation Bars.

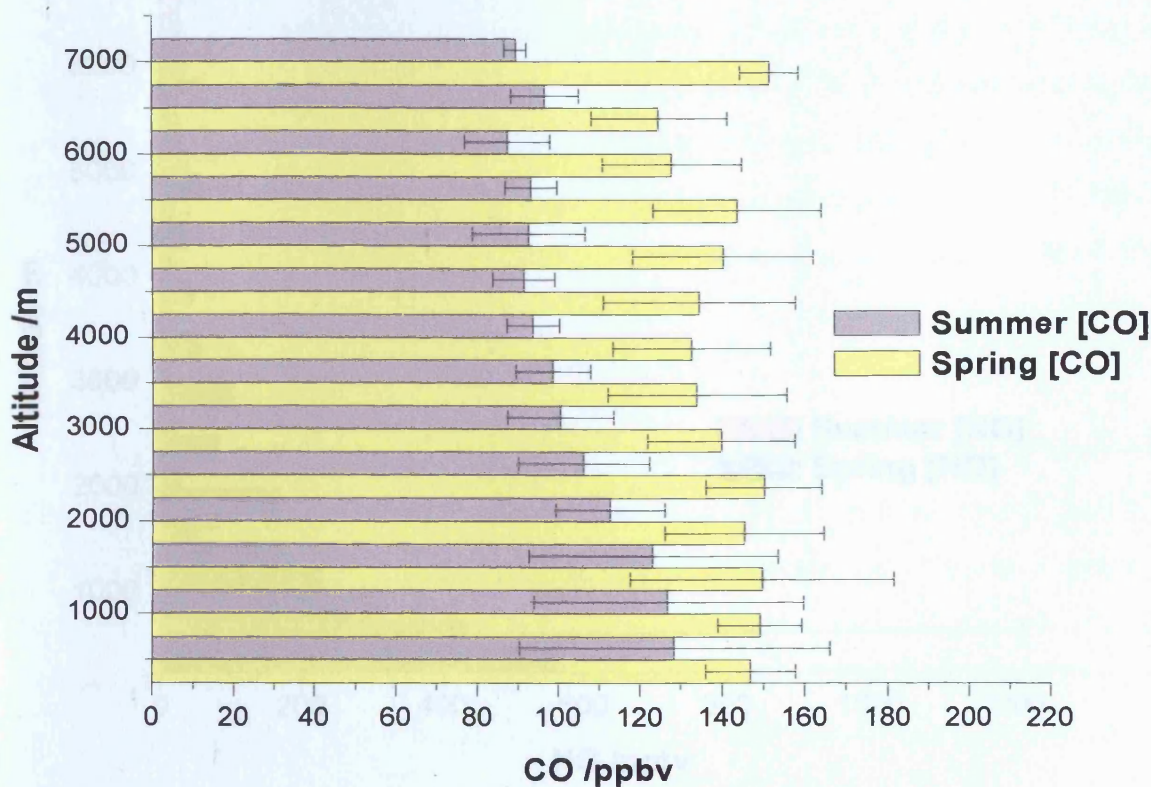


Monks, [2000]). The fact that summer, *not* spring, shows the dominant concentration of ozone is therefore a little surprising and is a feature that will to be investigated further in Section 2.7.

2.6.3: MAXOX CO Climatologies

Averaged concentrations of CO as measured during the MAXOX campaign are shown in Figure 2.19. From this concentration vs. altitude plot, there is a large difference in the concentration of CO measured in the spring data *c.f.* data measured during the summer. Indeed, the concentrations of CO measured in spring do appear to be elevated compared to literature data. For MAXOX spring data, the lowest data bin has [CO] in excess of 130 ppbv. This compares to average concentration of 115 ppbv taken over similar latitudes in the ship-based campaign described by Notholt *et al.* (2000). The summer data shows that concentrations in this season are much lower than spring, typically ranging from 100-130 ppbv. When looking at the concentration of CO with respect to altitude for both these seasons there is a large difference in the vertical distribution in [CO] during summer, which is less pronounced in summer data. Measured concentrations of carbon monoxide during both the summer and spring, suggests that the CO concentrations in the planetary boundary layer is higher than in the free troposphere.

Figure 2.19: Averaged CO Concentration During MAXOX Spring and Summer showing 1σ Standard Deviation Bars.



As [CO] is an excellent tracer for pollution owing to its large anthropogenic source and relatively long atmospheric lifetime, this data suggests that the boundary layer investigated during MAXOX was probably heavily polluted, particularly in the spring flight series. Above this polluted boundary layer, [CO] in spring is more evenly distributed. In the mid-free troposphere above *ca.* 4 km, the data shows almost no vertical variation.

2.6.4: MAXOX NO Climatologies

The [NO] vs. altitude profiles for spring and summer MAXOX flights shows that the concentration was different with respect to two seasons. Figure 2.20 shows a large-scale vertical structure in the trace gas profiles. However, from Figure 2.17 and the discussion in section 2.6.1, [NO], [NO₂] and [NO_y] data measured in MAXOX was shown to have some flight-to-flight bias. Specifically, data from one flight, A700 (2/8/99) was found to contain [NO_x] and [NO_y] that were significantly higher than other MAXOX flights. The flight track information suggests that during this mission, a low altitude run over the North Sea was flown to investigate surface air masses that were heavily polluted with anthropogenic nitrogen compounds. From Table 2.3 the average [NO] for flight A700 was 1065 pptv.

Figure 2.20: Averaged NO Concentration During MAXOX Spring and Summer showing 1σ Standard Deviation Bars.

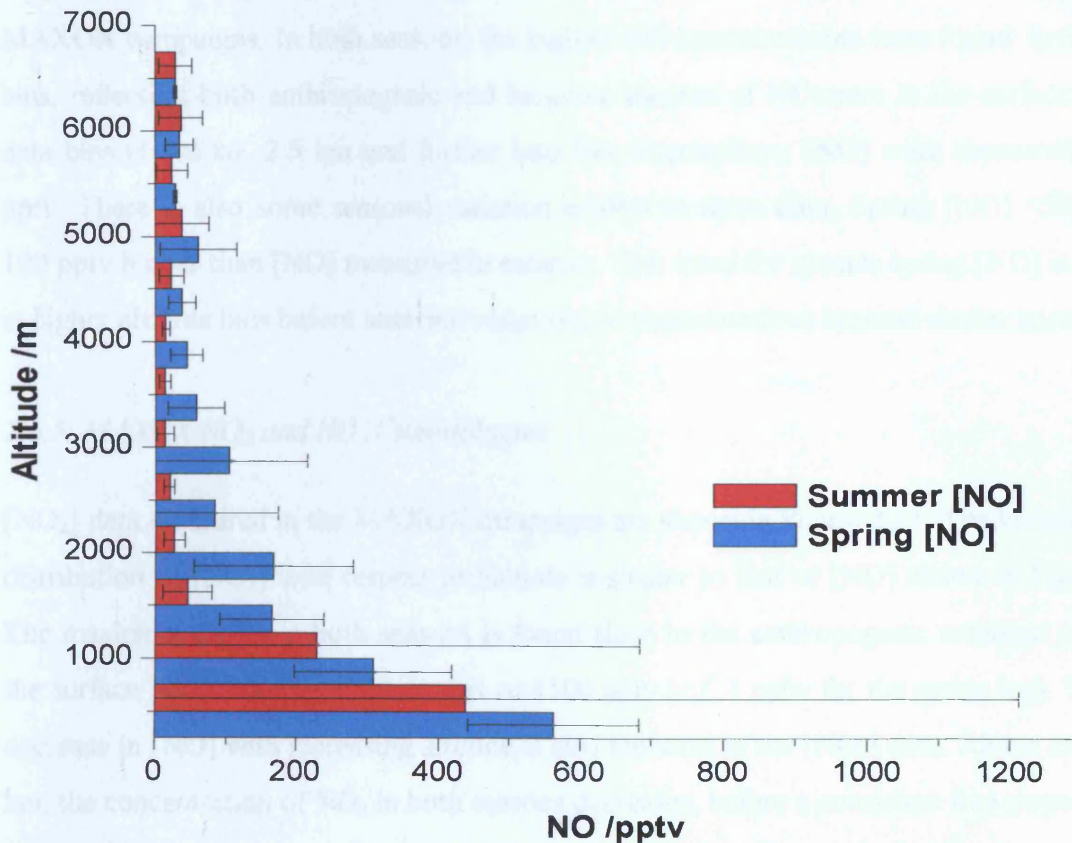


Table 2.3: Average [NO] for MAXOX Summer Flights with 1 σ Standard Deviation

MAXOX Flight Number	[NO] /pptv	Standard Deviation /1 σ
A695	N/A*	N/A*
A696	267.2	369.4
A697	41.9	128.3
A698	87.7	91.1
A699	288.5	864.7
A700	1065.8	2872.6
A701	68.9	216.8
A702	19.6	14.2
A703	35.2	57.6
A704	13.4	10.6

*No data owing to instrument failure

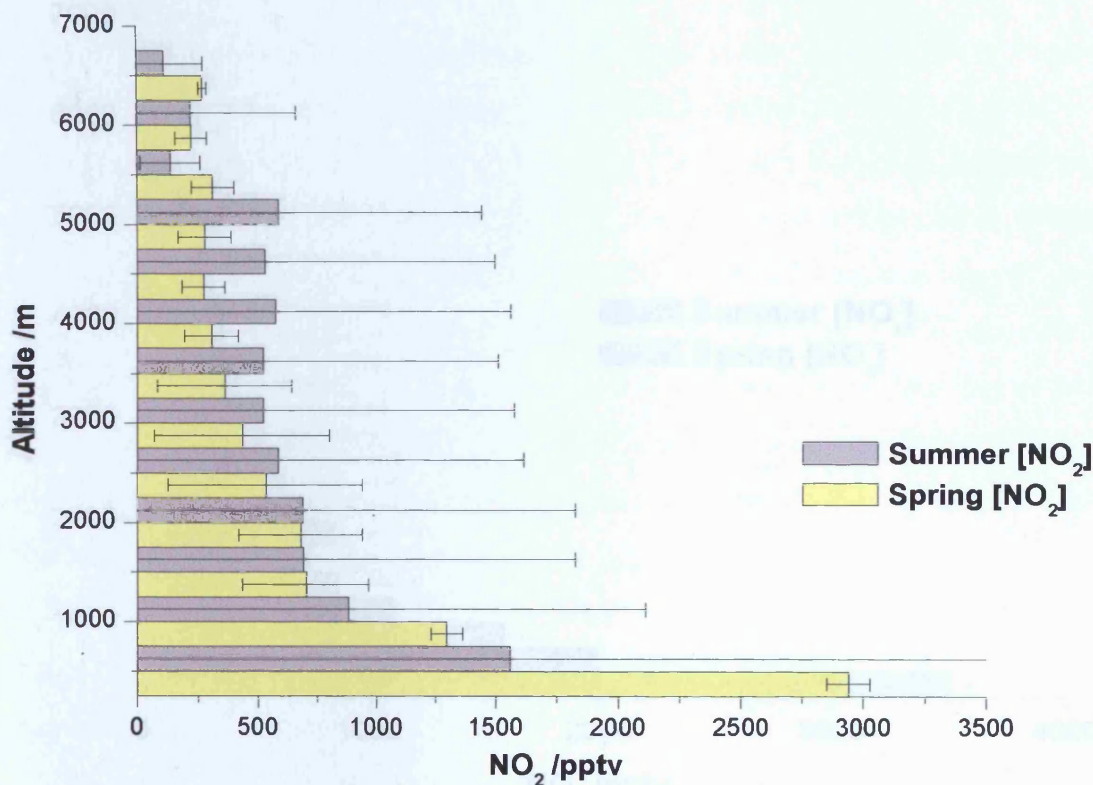
As a result, it was decided to remove these data from the spring summer climatology in order to ascertain a more "unbiased" picture of the description of [NO] in MAXOX.

In general, the largest concentrations of NO were found close to the surface during both MAXOX campaigns. In both seasons, the highest NO concentrations were found in the 500 m bins, reflecting both anthropogenic and biogenic sources of NO were at the surface. For the data bins above *ca.* 2.5 km and further into free troposphere, [NO] were measured at <200 pptv. There is also some seasonal variation evident in these data. Spring [NO] <500m were 100 pptv higher than [NO] measured in summer. This trend for greater spring [NO] is repeated in higher altitude bins before seasonal variations in concentrations become similar at *ca.* 5 km.

2.6.5: MAXOX NO₂ and NO_x Climatologies

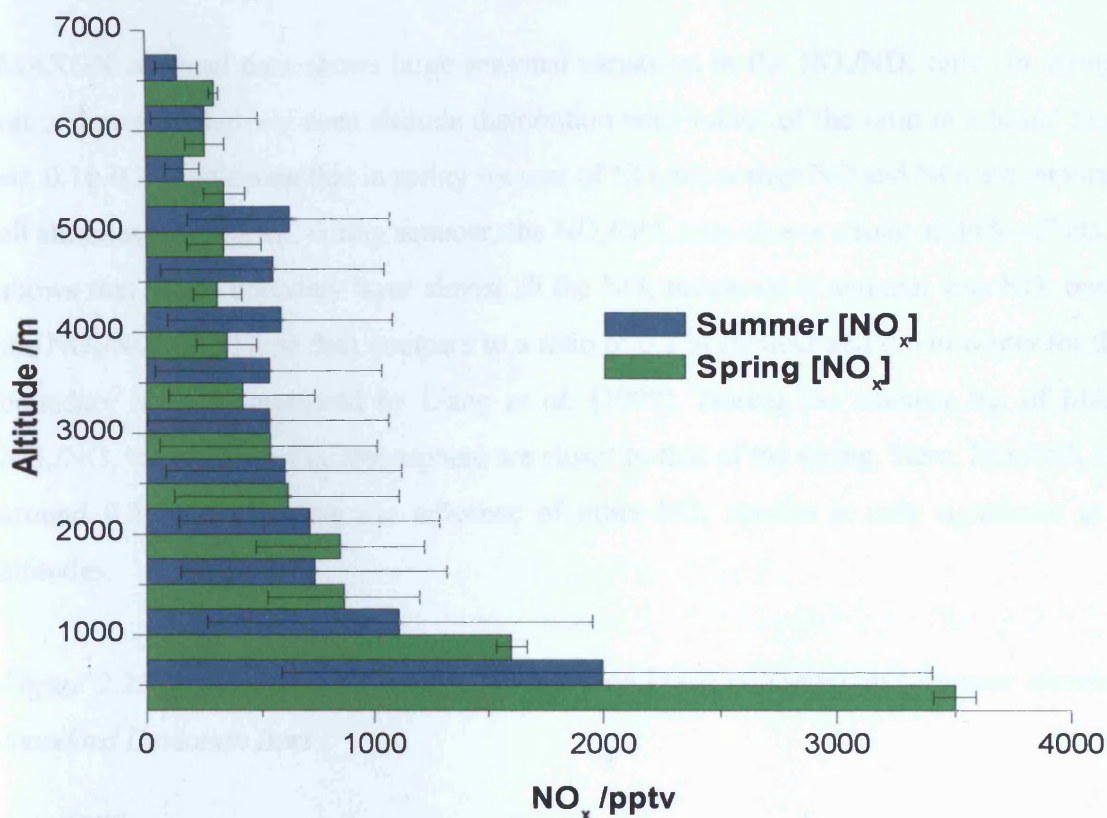
[NO₂] data measured in the MAXOX campaigns are shown in Figure 2.21. The variation in the distribution of [NO₂] with respect to altitude is similar to that of [NO] shown in Figure 2.20. The maximum [NO₂] in both seasons is found close to the anthropogenic emission sources at the surface. [NO₂] during summer was *ca.* 1500 pptv (*c.f.* 3 ppbv for the spring leg). The rapid decrease in [NO] with increasing altitude is also repeated in the [NO₂] data. Above around 0.5 km, the concentration of NO₂ in both seasons decreases, before a consistent free troposphere

Figure 2.21: Averaged NO_2 Concentration During MAXOX Spring and Summer showing 1σ Standard Deviation Bars.



$[\text{NO}_2]$ profile is observed at altitudes greater than 2 km. For the mid-free troposphere, $[\text{NO}_2]$ during the spring campaign is around 300 pptv compared to 500 pptv for the summer flights. These trends are repeated in the data for NO_x , during both spring and summer. The total sum of NO and NO_2 plotted against altitude is shown in Figure 2.22. The figure shows that $[\text{NO}_x]$ are dominated by $[\text{NO}_2]$ with the concentration/altitude profile showing the same features as that for NO in both spring and summer data. With respect to seasonal trend, Figure 2.22 shows that concentrations of NO_x measured during the summer campaign are slightly greater than those measured during spring, when averaged over all altitudes. The lowest bin (<500 m) contains the highest NO_x concentrations in both seasons. However, the seasonal trend is reversed. For these data, spring $[\text{NO}_x]$ is *ca.* 3.5 ppbv, compared to *ca.* 2 ppbv the same altitudes during summer. Above the boundary layer, $[\text{NO}_x]$ for both datasets falls off with respect to altitude. In the free troposphere, $[\text{NO}_x]$ in both seasons remains between 200-400 pptv.

Figure 2.22: Averaged NO_x Concentration During MAXOX Spring and Summer showing 1σ Standard Deviation Bars.



2.6.6: MAXOX NO_y Climatologies

Figure 2.23 shows the variation of $[\text{NO}_y]$ with altitude, as measured during the MAXOX spring campaign. During the spring flights, the concentration of measured NO_y decreases with respect to increasing altitude, up to around 2.5 km. Above this altitude, $[\text{NO}_y]$ varies consistently around the 500-700 pptv mark. Data measured in the summer portion of the MAXOX campaign indicates different altitude dependences. $[\text{NO}_y]$ at the surface is of similar magnitude to all altitudes with no data bin showing a pronounced maximum in $[\text{NO}_y]$. The general trend is that, for data measured in summer, the concentration of NO_y increases with increasing altitude. In all cases, the free tropospheric summer concentration of NO_y is greater than for spring $[\text{NO}_y]$, usually by a factor of around two.

Binned NO_x/NO_y values for the two seasons also prove interesting. The ratio of $\text{NO}+\text{NO}_2$ divided by the total oxidised nitrogen budget reflects the chemical processing that has occurred in air masses after the initial introduction of NO_x (Seinfeld and Pandis, [1998]). Since in polluted environments there is generally a large anthropogenic source of NO_x and, owing to

the large timescale needed to convert NO_x into NO_y , such regions have NO_x/NO_y ratios close to unity. A plot of the seasonal variation in this ratio is shown in Figure 2.24.

MAXOX seasonal data shows large seasonal variations in the NO_x/NO_y ratio. In spring, the ratio shows a relatively even altitude distribution with values of the ratio in a broad range of *ca.* 0.10-0.20, indicating that in spring sources of NO_y other than NO and NO_2 are important at all altitudes. In contrast, during summer, the NO_x/NO_y ratio shows strong altitude effects. Data shows that in the boundary layer almost all the NO_y measured in summer was NO_x owing to the $\text{NO}_x/\text{NO}_y \sim 1$. These data compare to a ratio of 0.2 in summer and 0.6 in winter for the US boundary layer as measured by Liang *et al.* [1998]. During the summer leg of MAXOX NO_x/NO_y values in the free troposphere are closer to that of the spring. Here, NO_x/NO_y ratio is around 0.2-0.4, suggesting the influence of other NO_y species is only significant at these altitudes.

Figure 2.23: Averaged NO_y Concentration During MAXOX Spring and Summer showing 1σ Standard Deviation Bars

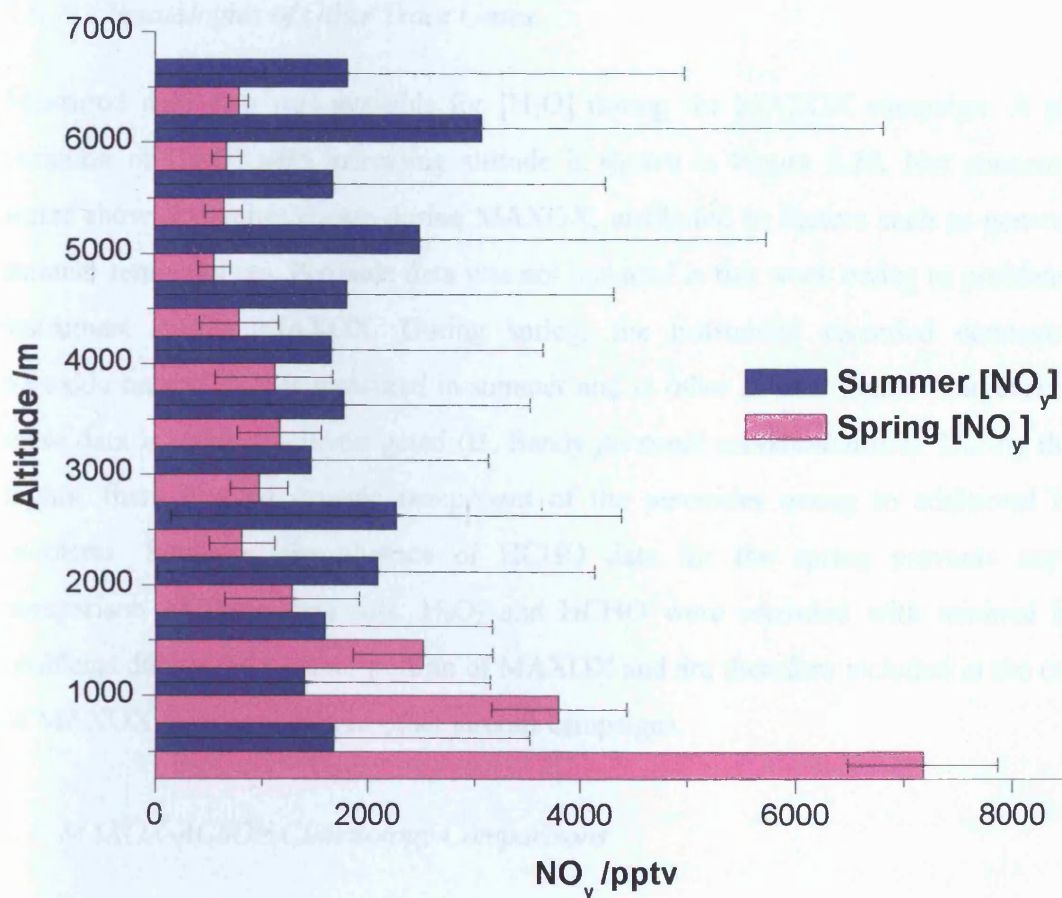
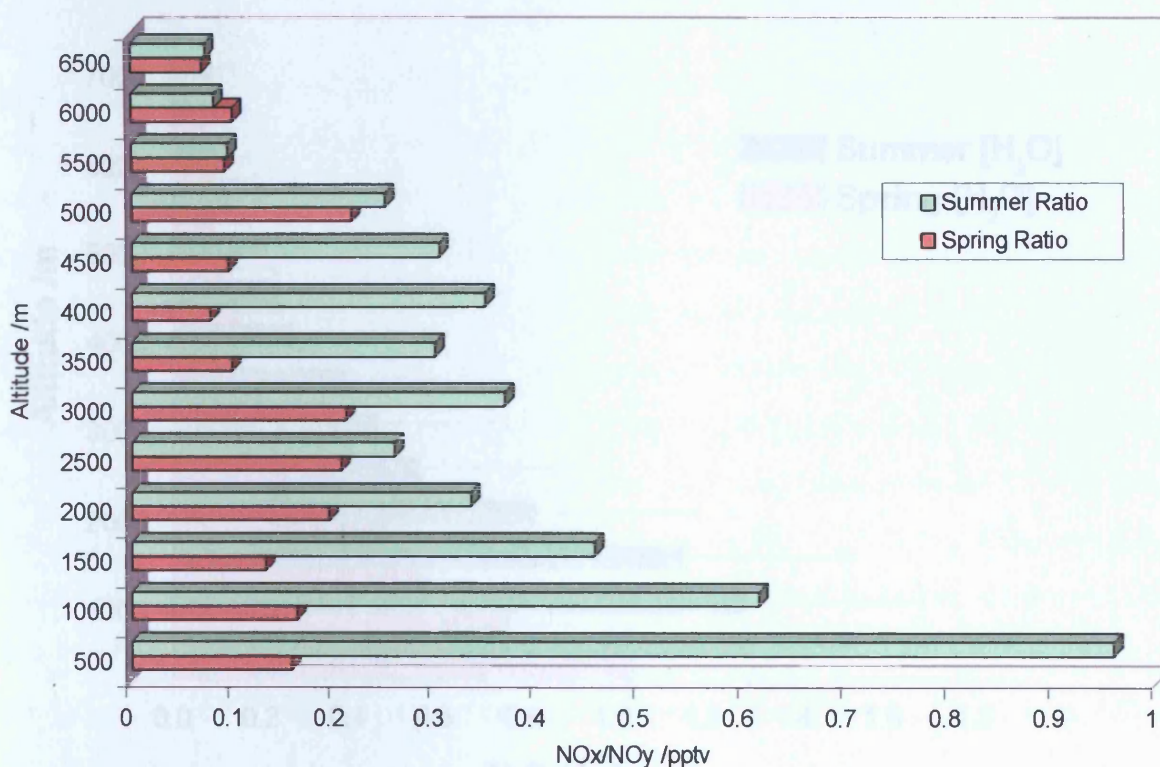


Figure 2.24: Averaged NO_x/NO_y Ratios During Spring and Summer MAXOX Campaign



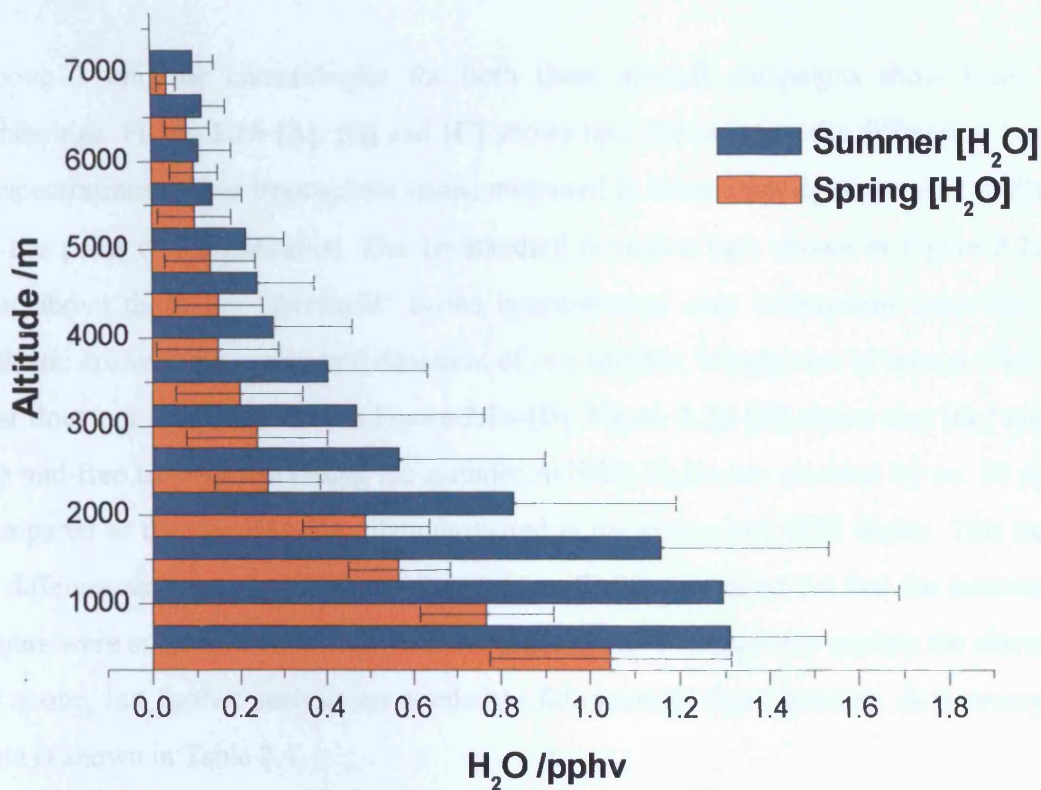
2.6.7: Climatologies of Other Trace Gases.

Measured data also was available for $[\text{H}_2\text{O}]$ during the MAXOX campaign. A plot of the variation of $[\text{H}_2\text{O}]$ with increasing altitude is shown in Figure 2.25. Net concentrations of water show a summer excess during MAXOX, attributed to factors such as generally higher summer temperatures. Peroxide data was not included in this work owing to problems with the instrument during MAXOX. During spring, the instrument recorded concentrations of peroxide only 10% that measured in summer and in other aircraft flights. The exact nature of these data is still being investigated (B. Bandy *personal communication*). During the summer flights, there was no organic component of the peroxides owing to additional instrument problems. Similarly, the absence of HCHO data for the spring prevents any seasonal comparison of these data sets. H_2O_2 and HCHO were recorded with minimal instrument problems during the summer portion of MAXOX and are therefore included in the comparison of MAXOX measured data to other aircraft campaigns.

2.7: MAXOX-ACSOE Climatology Comparisons

The fact that ACSOE and MAXOX campaigns were aircraft missions in two different environments provides an opportunity to compare the climatologies of both campaigns in an

Figure 2.25: Averaged H_2O Concentration During MAXOX Spring and Summer showing 1σ Standard Deviation Bars



effort to evaluate the distribution of tracers in the "background" atmosphere of the remote free troposphere with those in the semi-polluted atmosphere over UK/European mainland.

2.7.1: MAXOX-ACSOE Ozone Climatology Comparisons

Figure 2.26 shows a comparison of MAXOX Spring/Summer with ACSOE Spring/Summer ozone data. Considering the data shown in Figure 2.26-[A], concentrations of ozone measured during the MAXOX spring campaign compare well to those values measured during the spring leg of ACSOE. Similarly, from Figure 2.26-[B], difference between ACSOE summer and MAXOX summer are also clear. $[O_3]$ found in MAXOX summer data around 25-30 ppbv higher than for the same season during ACSOE. From Section 2.4.1, it was identified that the seasonal distribution of ozone concentration in ACSOE was suggestive of an isolated spring ozone maximum in the remote Northern Atlantic region. Assuming this to be correct, the seasonal comparison also allows speculation on the nature of the MAXOX data. From Figure 2.26-[A] and [C], owing to the similarities between $[O_3]$ ACSOE spring and MAXOX spring and summer it can be generalised that the below 3 km, ACSOE data shows a isolated spring

ozone maximum, while the MAXOX data shows a much broader "maximum" which encompasses both spring and summer.

Above 3 km, the climatologies for both these aircraft campaigns show many seasonal similarities. Figure 2.26-[A], [B] and [C] shows that above 3 km, the differences between the concentrations of free troposphere ozone measured in these campaigns are very similar, almost to the point of insignificance. The 1σ standard deviation bars shown in Figure 2.26 suggest that above the 3 km "threshold" ozone concentration over widespread areas the Northern Atlantic are within one standard deviation of one another, irrespective of season. The only data that does not show this trend is Figure 2.26-[D]. Figure 2.26-[D] shows that $[O_3]$ measured in the mid-free troposphere during the summer ACSOE flights are elevated by *ca.* 10 ppbv when compared to the corresponding data measured in the spring MAXOX flights. This may be due to different air masses composition. It was identified from section 2.4 that the summer ACSOE flights were subject to continental outflow from the U.S. which may explain the elevated levels of ozone, but further analysis are needed to full quantify these features. A summary of these data is shown in Table 2.4.

Figure 2.26: Spring and Summer Average Ozone Concentration During MAXOX and ACSOE with 1σ Standard Deviation Bars.

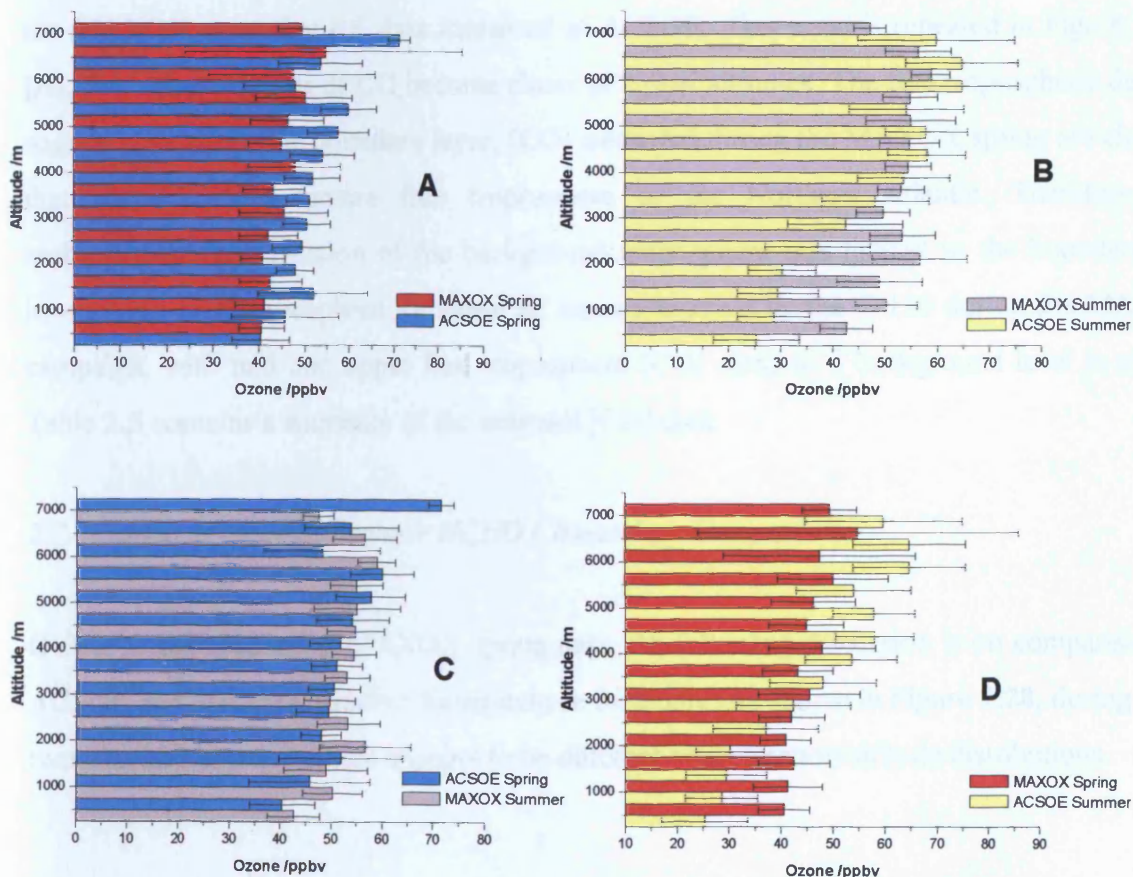


Table 2.4: Comparison of [O₃] measured during MAXOX and ACSOE Spring and Summer Campaigns

Campaign	Max O ₃ Stdev /1σ		Min O ₃ Stdev /1σ		Average O ₃ Stdev /1σ	
	/ ppbv		/ ppbv		ppbv	
ACSOE Spring	78.1	2.7	40.4	6.4	55.6	7.0
ACSOE Summer	64.6	10.8	25.3	8.3	47.8	9.1
MAXOX Spring	50.0	10.7	40.5	5.0	45.5	9.8
MAXOX Summer	58.7	3.6	42.7	5.1	52.5	5.8

2.7.2: MAXOX-ACSOE Summer CO Climatology Comparisons

Since there were no CO measurements made during the ACSOE spring campaign, the comparison is limited to summer only. Figure 2.27-[A] and [B] is a plot of the MAXOX and ACSOE summer values. The results do seem to support the belief that the MAXOX campaign was flown in a far more polluted environment than ACSOE. From Figure 2.27-[B], during the same season (summer), concentration of CO are consistently around a factor of two higher in the MAXOX campaign *c.f.* data measured in ACSOE. This trend is repeated in Figure 2.27-[A], but concentrations of CO become closer at higher altitudes. The free tropospheric data do suggest that above the boundary layer, [CO] measured during the MAXOX spring are close to that found in the remote free troposphere of the Northern Atlantic. Therefore, the anthropogenic perturbation of the background troposphere was limited to the boundary and lower most free troposphere for those air masses sampled by the C-130 during the MAXOX campaign, with mid and upper free troposphere [CO] close to a background level in spring. Table 2.5 contains a summary of the seasonal [CO] data.

2.7.3: MAXOX-ACSOE Summer HCHO Climatology Comparisons

Owing to the absence of MAXOX spring data, the following discussion is on comparisons of ACSOE and MAXOX summer formaldehyde data only. As shown in Figure 2.28, during these two aircraft campaigns there appears to be different concentration/altitude distributions.

Figure 2.27: Spring and Summer Average CO Concentration During MAXOX and ACSOE with 1σ Standard Deviation Bars.

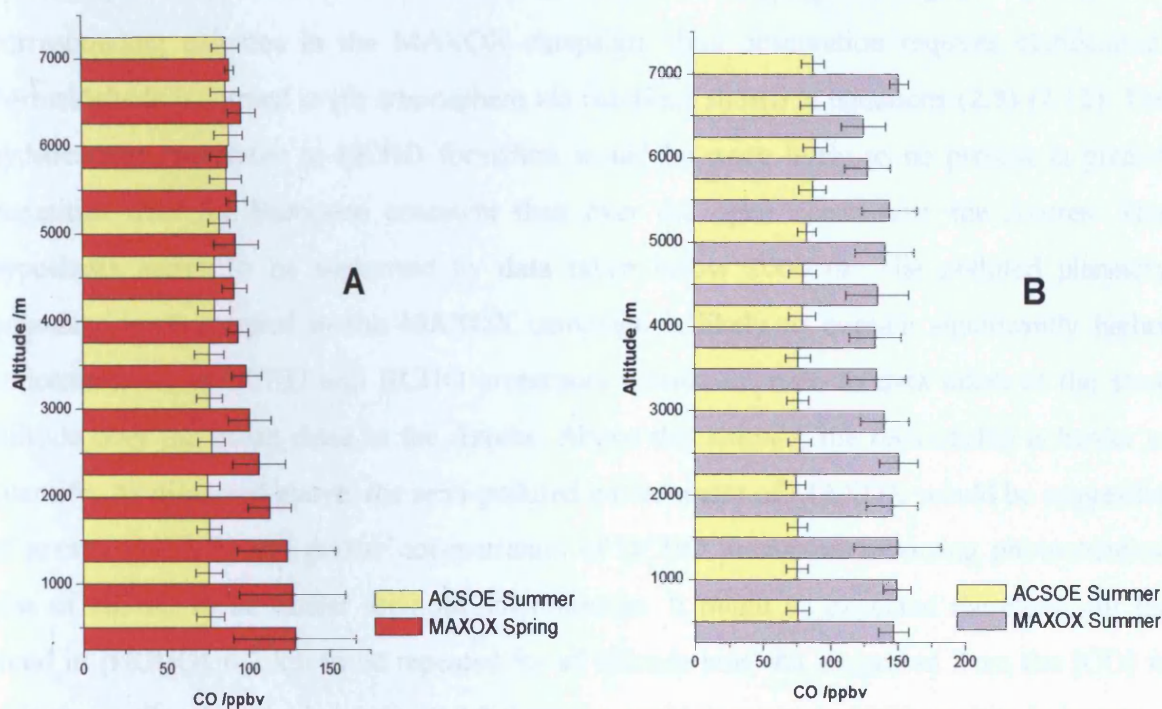


Table 2.5: Comparison of [CO] measured during MAXOX and ACSOE Spring and Summer Campaigns

Campaign	Max CO		Stdev / 1σ		Min CO		Stdev / 1σ		Average CO		Stdev / 1σ	
	/ ppbv		/ ppbv		/ ppbv		/ ppbv		/ ppbv		/ ppbv	
ACSOE Spring	N/A*	N/A*	N/A*	N/A*	N/A*	N/A*	N/A*	N/A*	N/A*	N/A*	N/A*	N/A*
ACSOE Summer	87.6	8.5	75.3	8.1	80.3	8.4						
MAXOX Spring	149.7	7.1	125.0	16.4	140.9	16.6						
MAXOX Summer	128.3	37.7	90.0	10.6	103.2	14.9						

N/A* Data not available owing to absence of instrument

Considering data measured during the MAXOX campaign, HCHO is shown to have higher concentrations at altitudes <2000 m. Above this altitude, the concentration of HCHO falls

away quite rapidly as altitude increases. In comparison, the decrease in [HCHO] with altitude is far less pronounced for the ACSOE data set. The net result is that above 2000 m, the average [HCHO] measured in the summer ACSOE campaign is higher than for the corresponding altitudes in the MAXOX campaign. This observation requires clarification. Formaldehyde is formed in the troposphere *via* reactions shown in equations (2.9)-(2.12). The hydrocarbon precursors to HCHO formation would be more likely to be present in greater quantities over the European continent than over the open ocean near the Azores. This hypothesis seems to be supported by data taken below 2000 m. The polluted planetary boundary layer sampled in the MAXOX campaign is likely to contain significantly higher concentrations of HCHO and HCHO precursors when compared to data taken at the same altitude over the ocean close to the Azores. Above this altitude, the relationship is harder to quantify. As discussed above, the semi-polluted environment of MAXOX would be suggestive of greater [HCHO] and greater concentration of HCHO precursors assuming photochemical loss of HCHO to be similar for both environments. It might be expected therefore, for the trend in [HCHO] < 2 km to be repeated for all altitude bins. As suggested from the [CO] vs altitude profiles describe in section 2.7.2 there is a rapid decrease in [CO] as altitude increases in the MAXOX dataset. Using [CO] as a tracer for pollution, it might be expected that the precursors to HCHO formation show similar trends. The net result is that, away from the boundary layer concentration of HCHO precursors are similar, if not lower than the "background" concentrations measured in ACSOE. However, without more detailed information on the relative distributions of these species however, it is difficult to support these arguments. The distribution of HCHO for both aircraft campaigns is summarised in Table 2.6.

2.7.4: MAXOX-ACSOE Summer H₂O₂ Climatology Comparisons

The comparison between [H₂O₂] data recorded during the summer MAXOX campaign and those data measured in the summer flights during the ACSOE detachment is shown in Figure 2.29. This concentration vs. altitude plot suggests a similar absolute concentration of hydrogen peroxide, and a similar altitude distribution of H₂O₂ in both aircraft campaigns. Both aircraft missions seem to show the peak peroxide concentration occurring the top of the planetary boundary layer at around 2-2.5 km. Concentrations in both series of flights indicated that peak [H₂O₂] was *ca.* 1 ppbv. These data seem to agree with previous studies (*e.g.* Kleinman [1991], Ayers *et al.* [1992], O'Sullivan *et al.* [1999]) regarding the relationship between concentration and altitude for hydrogen peroxide.

Figure 2.28: Summer Only Average HCHO Concentration During MAXOX and ACSOE with 1σ Standard Deviation Bars.

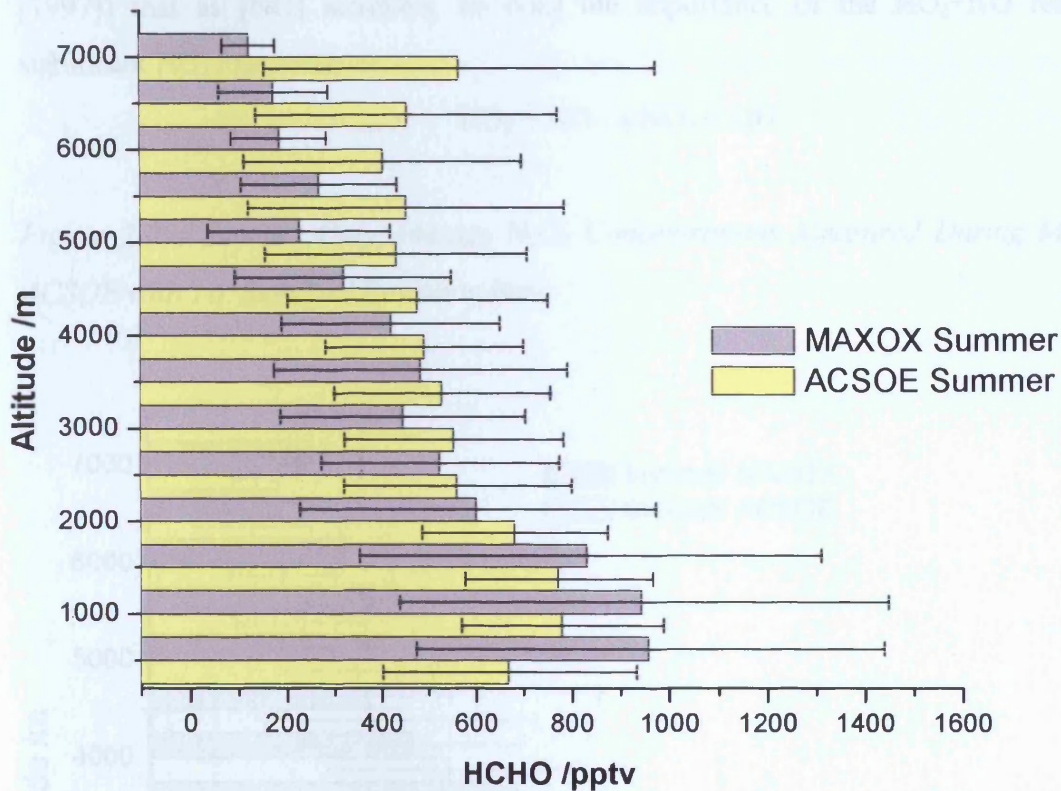


Table 2.6: Comparison of [HCHO] measured during MAXOX and ACSOE Spring and Summer Campaigns

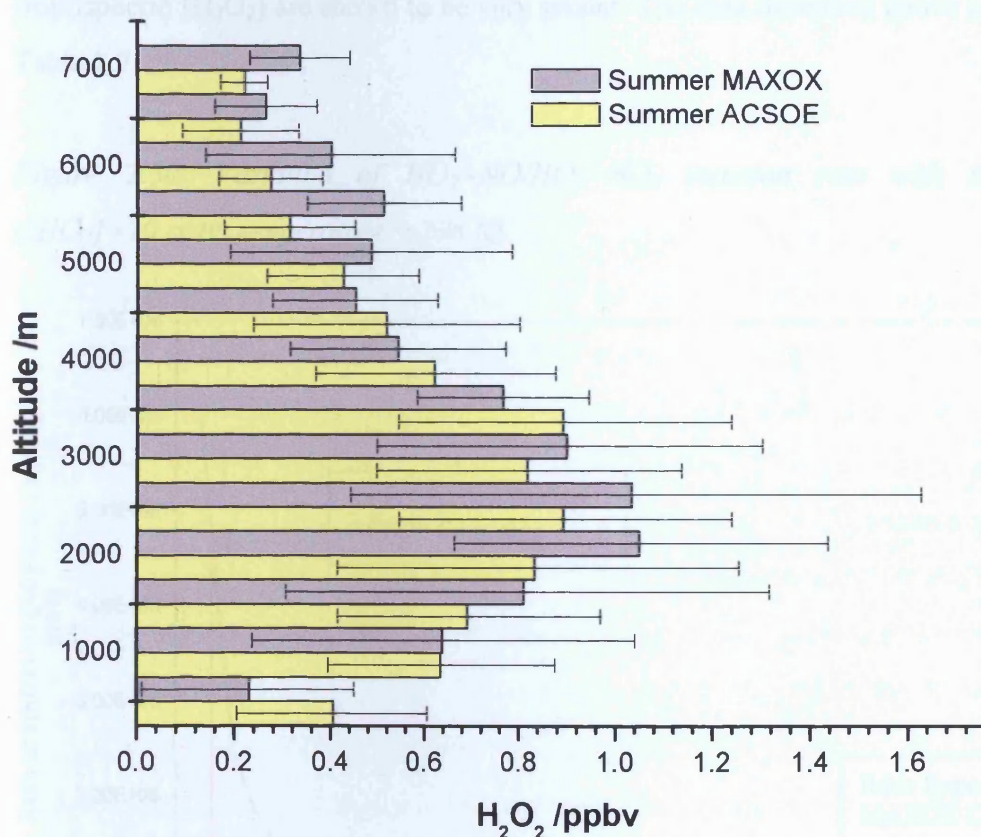
Campaign	Max HCHO		Min HCHO		Average HCHO	
	Stdev	1σ	Stdev	1σ	Stdev	1σ
	/ ppbv		/ ppbv		/ ppbv	
ACSOE Spring	1.3	1.2	0.3	0.2	0.7	0.5
ACSOE Summer	0.8	0.2	0.4	0.3	0.5	0.2
MAXOX Spring	N/A*	N/A*	N/A*	N/A*	N/A*	N/A*
MAXOX Summer	1.0	0.5	0.1	0.05	0.5	0.3

N/A* Data not available owing to absence/malfunction of instrument

It was expected that the concentration of H_2O_2 , as measured in the MAXOX series of flights, would be lower than for corresponding altitudes during the ACSOE summer campaign owing to the elevated $[\text{NO}]$ measured in MAXOX summer. It has shown (*e.g.* Carpenter *et al.* [1997]) that as $[\text{NO}]$ increases, so does the importance of the $\text{HO}_2 + \text{NO}$ reaction as a significant HO_2 loss route *viz*



Figure 2.29: Summer Only Average H_2O_2 Concentrations Measured During MAXOX and ACSOE with 1σ Standard Deviation Bars.



Thus, in air masses containing elevated NO , reaction (2.13) is the dominant HO_2 sink and not the self-reaction between HO_2 and HO_2 to form hydrogen peroxide (reaction [2.5]). As shown in Figure 2.30, for a constant temperature (298K) and $[\text{HO}_2]$ (10 pptv), the ratio of $k_{(\text{HO}_2 + \text{HO}_2)}[\text{HO}_2] / k_{(\text{HO}_2 + \text{NO})}[\text{HO}_2][\text{NO}]$ varies as $[\text{NO}]$ increases. This "competition" for HO_2 by NO suggests that reaction (2.13), is particularly important where there was elevated $[\text{NO}]$ measured in the MAXOX campaign, specifically below around 2 km. As indicated in Figure 2.30, the ratio of $k_{(\text{HO}_2 + \text{HO}_2)} / k_{(\text{HO}_2 + \text{NO})}$ during the MAXOX campaign would be around four times lower than for the ACSOE campaign, assuming the same concentration of initial HO_2 .

Although H_2O_2 has a large deposition velocity in the planetary boundary layer (Ayers *et al.* 1992), net peroxide production at these altitudes during MAXOX would be expected to be lower than for the "background" atmosphere sampled in the ACSOE missions, where the concentration of NO was lower. From Figure 2.29, the only significant difference in $[\text{H}_2\text{O}_2]$ between the aircraft campaigns is for data measured below 500 m which may be due to the competition between reactions (2.13) and (2.5). In the European free troposphere sampled during the MAXOX campaign, concentrations of NO were found to be only slightly above background free troposphere (see section 2.7.3). Production of H_2O_2 above 2 km is therefore likely to be unhindered by NO chemistry. This seems to be reflected in the concentration of free tropospheric H_2O_2 measured during the MAXOX and ACSOE missions, where free tropospheric $[\text{H}_2\text{O}_2]$ are shown to be very similar. The data described above are summarised in Table 2.7.

Figure 2.30: Variation of $\text{HO}_2+\text{NO}/\text{HO}_2+\text{HO}_2$ reaction rate with increasing $[\text{NO}]$ ($[\text{HO}_2]=10$ pptv, temperature = 298 K)

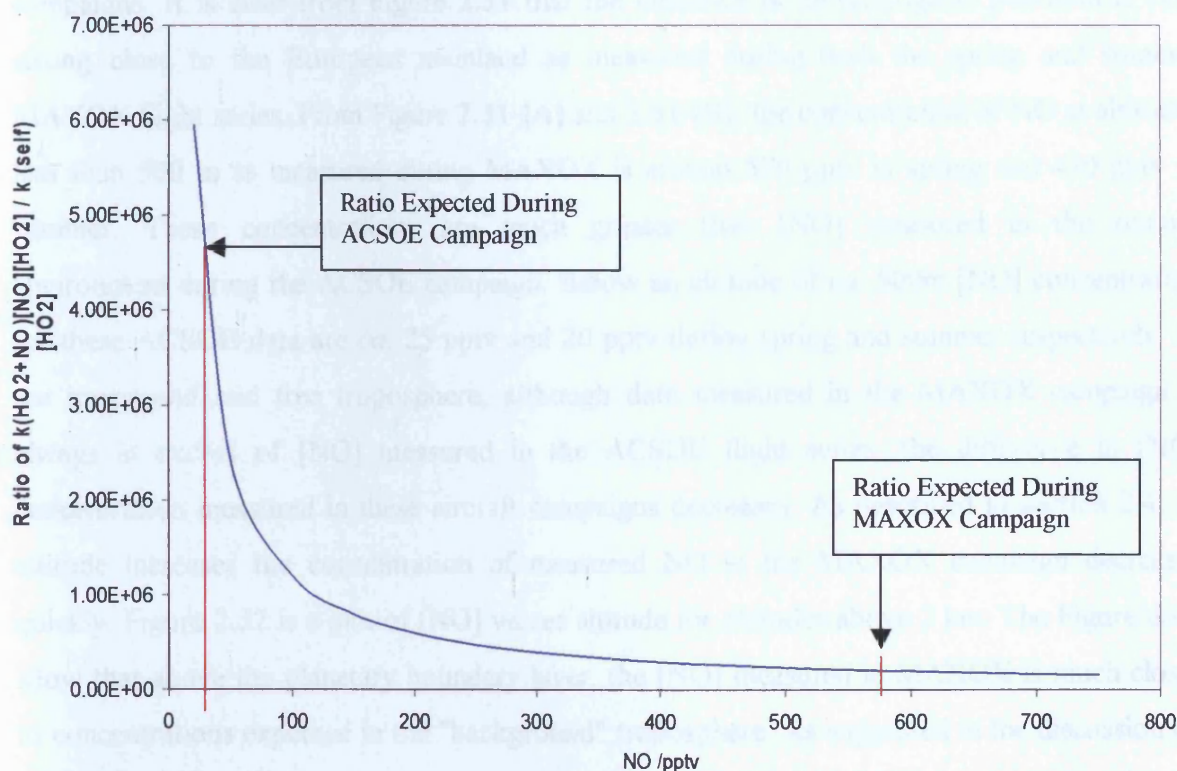


Table 2.7: Comparison of [H₂O₂] measured during MAXOX and ACSOE Spring and Summer Campaigns

Campaign	Max H ₂ O ₂ / ppbv	Stdev /1σ	Min H ₂ O ₂ / ppbv	Stdev /1σ	Average H ₂ O ₂ / ppbv	Stdev /1σ
ACSOE Spring	0.7	0.4	0.2	0.1	0.5	0.3
ACSOE Summer	0.9	0.3	0.2	0.1	0.6	0.2
MAXOX Spring	N/A*	N/A*	N/A*	N/A*	N/A*	N/A*
MAXOX Summer	1.1	0.3	0.4	0.4	0.7	0.2

* not available owing to instrument failure

2.7.4: MAXOX-ACSOE NO Climatology Comparisons

Figure 2.31 shows a comparison of [NO] measured in the MAXOX and ACSOE aircraft campaigns. It is clear from Figure 2.31 that the influence of anthropogenic pollution is very strong close to the European mainland as measured during both the spring and summer MAXOX flight series. From Figure 2.31-[A] and 2.31-[B], the concentration of NO at altitudes less than 500 m as measured during MAXOX is around 570 pptv in spring and 420 pptv in summer. These concentrations are much greater than [NO] measured in the remote environment during the ACSOE campaign. Below an altitude of *ca.* 500m [NO] concentration for these ACSOE data are *ca.* 25 pptv and 20 pptv during spring and summer respectively. In the lower and mid free troposphere, although data measured in the MAXOX campaign is always in excess of [NO] measured in the ACSOE flight series, the difference in [NO] concentration measured in these aircraft campaigns decreases. As described in section 2.4, as altitude increases the concentration of measured NO in the MAXOX campaign decreases quickly. Figure 2.32 is a plot of [NO] verses altitude for altitudes above 2 km. The Figure does show that above the planetary boundary layer, the [NO] measured in MAXOX is much closer to concentrations expected in the "background" troposphere. As suggested in the discussion on other anthropogenic pollution tracers such as CO (section 2.7.2) [NO] shows similar altitude trends. It maybe, therefore, that above the heavily polluted boundary layer, the mid free troposphere, as measured during the spring and summer MAXOX, campaign was less perturbed by anthropogenic pollutants. However, a more complex and detailed analysis is needed to support this hypothesis. Table 2.8 contains a summary of the [NO] data.

Figure 2.31: Spring and Summer Average NO Concentrations Measured During MAXOX and ACSOE with 1σ Standard Deviation Bars.

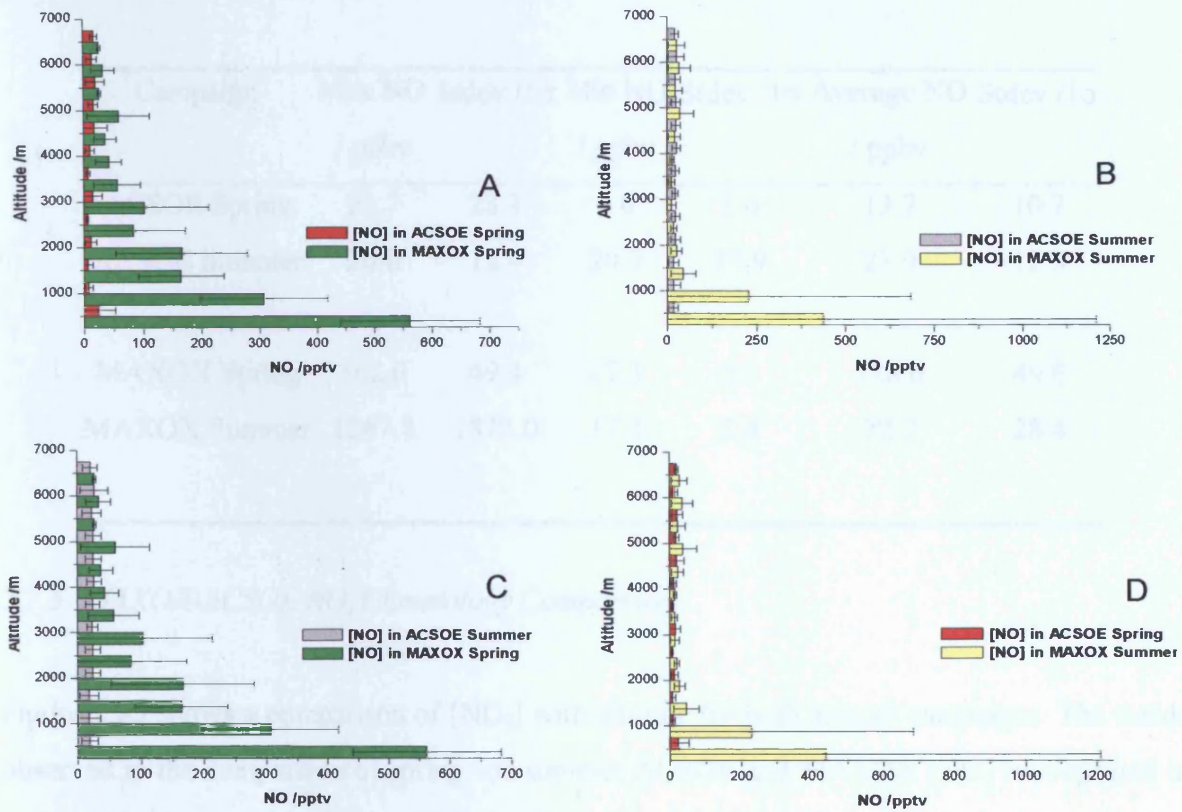


Figure 2.32: Spring and Summer Average Free Tropospheric NO Concentrations Measured During MAXOX and ACSOE with 1σ Standard Deviation Bars.

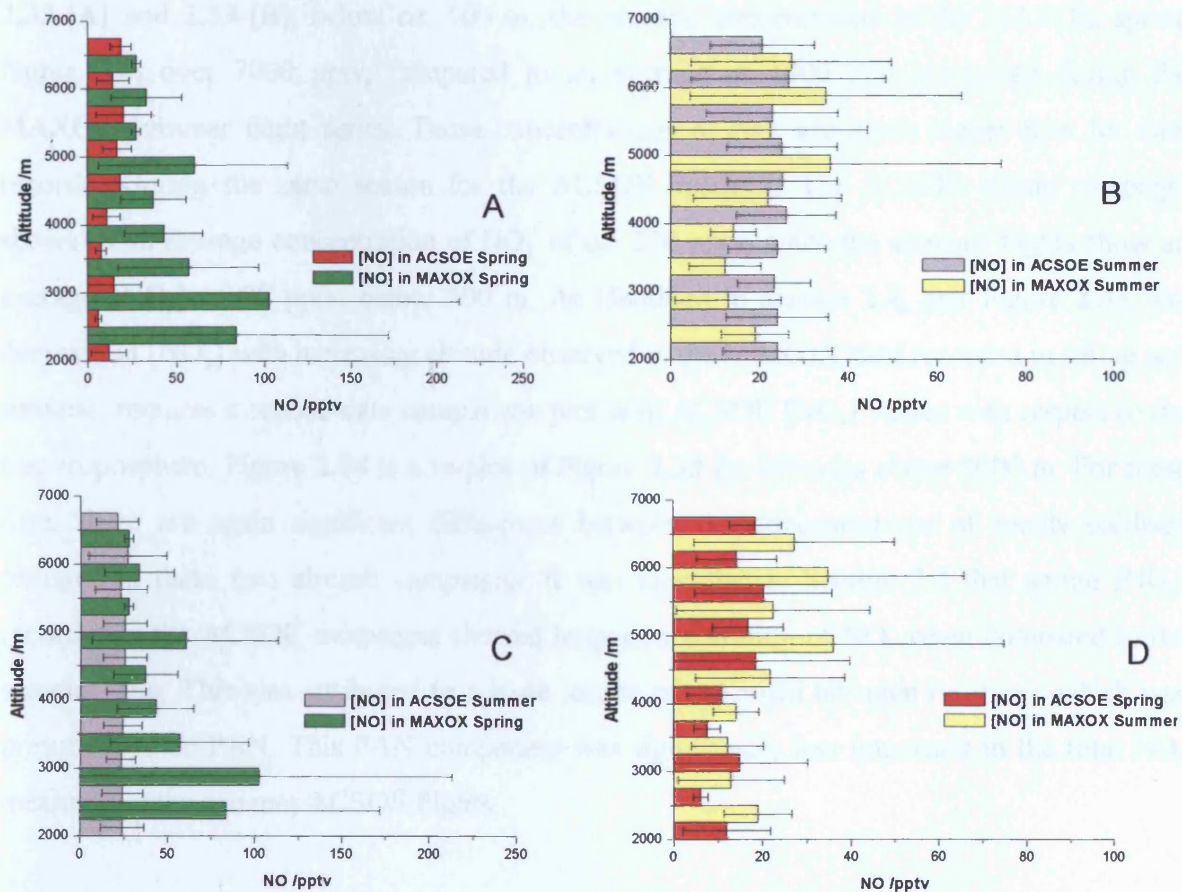


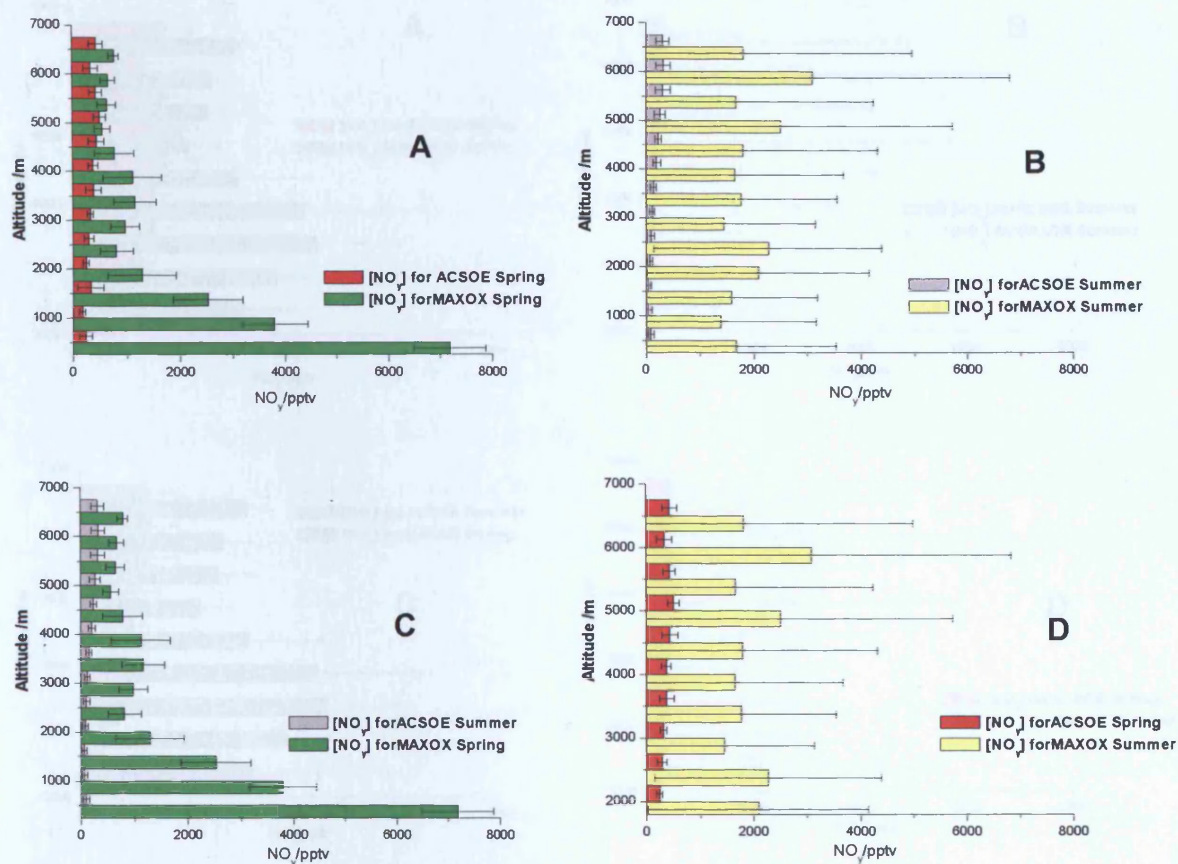
Table 2.8: Comparison of [NO] measured during MAXOX and ACSOE Spring and Summer Campaigns

Campaign	Max NO		Min NO		Average NO	
	Stdev /1σ	Stdev /1σ				
	/ ppbv		/ ppbv		/ ppbv	
ACSOE Spring	23.7	28.1	6.0	1.6	13.7	10.7
ACSOE Summer	26.0	12.4	20.7	17.9	23.0	12.3
MAXOX Spring	562.0	49.4	27.3	2.3	128.6	49.6
MAXOX Summer	1267.8	1872.0	17.4	2.4	72.7	28.4

2.7.5: MAXOX-ACSOE NO_y Climatology Comparisons

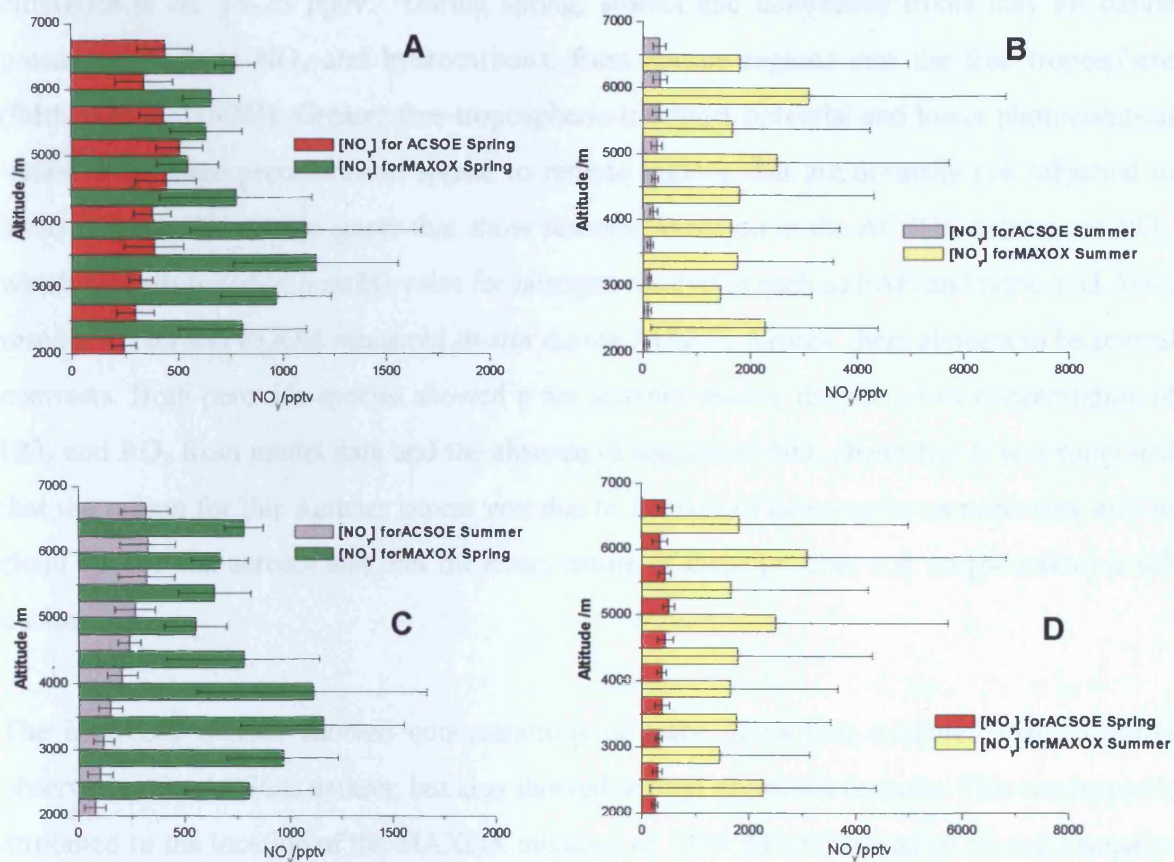
Figure 2.33 shows a comparison of [NO_y] with altitude for both aircraft campaigns. The trends observed in the comparison of spring and summer ACSOE and MAXOX [NO] are repeated in terms of [NO_y], specifically there is a large excess of [NO_y] measured in both the spring and summer MAXOX flight series, when compared to the "background" atmosphere investigated during the spring and summer ACSOE campaign. Considering data for [NO_y] shown in Figure 2.33-[A] and 2.33-[B], below *ca.* 500 m, the average concentration in the MAXOX spring flights was over 7000 pptv, compared to an average of 1800 pptv measured during the MAXOX summer flight series. These concentrations of NO_y are much higher than for data recorded during the same season for the ACSOE missions. The ACSOE spring campaign shows as an average concentration of NO_y of *ca.* 220 pptv, while the summer flights show an average [NO_y] of 90 pptv, below 500 m. As identified in section 2.4, and Figure 2.33, the decrease in [NO_y] with increasing altitude observed in the MAXOX data recorded in spring and summer, requires a second data comparison plot with ACSOE [NO_y] values with respect to the free troposphere. Figure 2.34 is a re-plot of Figure 2.33 for altitudes above 2000 m. For these data, there are again significant differences between the concentrations of totally oxidised nitrogen in these two aircraft campaigns. It was identified in Section 2.4 that spring [NO_y] recorded in the ACSOE campaigns showed large concentration of NO_y when compared to the summer data. This was attributed to a large source of unknown nitrogen reservoir, which was presumed to be PAN. This PAN component was significantly less important in the total NO_y measured in the summer ACSOE flights.

Figure 2.33: Spring and Summer Average NO_y Concentrations Measured During MAXOX and ACSOE with 1σ Standard Deviation Bars.



In comparison, in the free troposphere over the European continent there is a large excess of $[\text{NO}_y]$ which seems to remain even in the summer data. From Figure 2.33-[A], $[\text{NO}_y]$ as measured in MAXOX spring, is generally of similar magnitude to those data recorded in the ACSOE spring flights. Figure 2.33-[B], shows that during the MAXOX summer series of aircraft missions there is an order of magnitude difference in the total free tropospheric $[\text{NO}_y]$, with the MAXOX data suggesting $[\text{NO}_y]$ of around 2 ppbv, *c.f.* 200-300 pptv for summer $[\text{NO}_y]$ measured during ACSOE. It therefore seems that the opposite trend in $[\text{NO}_y]$ concentration is observed for the MAXOX data set when compared to seasonal data measured in the ACSOE campaign. This opposite seasonal trend for MAXOX values is also shown in Figure 2.33-[C] and 2.33-[D]. This poses the question, what is the exact composition of NO_y for both seasons in both these aircraft campaigns? The MAXOX flight series was flown in the semi-polluted environment of the European continent, presumably containing higher concentrations of compounds such as PAN and nitric acid.

Figure 2.34: Spring and Summer Average Free Tropospheric NO_y Concentrations Measured During MAXOX and ACSOE with 1σ Standard Deviation Bars.



This may be combined with additional air processing of the air masses sampled during the MAXOX flight series, where NO_x has been converted into NO_y . However, without speciation of the total NO_y or more detailed studies of the difference between the air masses sampled, firm conclusions on these apparently different seasonal climatologies data is difficult to attain.

2.8: Summary of Climatology data

Trace gas climatologies have been compiled from the ACSOE (Azores) and MAXOX (UK/Europe) aircraft based campaigns. These data have been separated into individual data bins with respect to altitude and trace gas concentration and averaged over the latitude ranges investigated by the MRF C-130 aircraft. The ACSOE Azores aircraft campaign of 1997 provided data on the remote marine free troposphere over the North Atlantic. In this dataset, several important trace gas climatologies have been identified. From $[\text{O}_3]$ measured in ACSOE, the altitude distribution for ozone showed a maximum in the spring data up to an altitude of *ca.* 3 km. Many previous studies have observed similar results over the last several years reporting a spring maximum in ozone concentration at various Northern Hemisphere surface

sites. (e.g. Monks, 2000). The data shown in this analysis indicates that there is an excess of ozone found in the spring aircraft bins up to an altitude of around 4000 m where the seasonal difference is *ca.* 15-25 ppbv. During spring, storms and convective fronts may lift ozone precursors such as NO_x and hydrocarbons, from source regions into the free troposphere (Bethan *et al.* [1998]). Greater free tropospheric transport potential and lower photochemical losses allow these precursors to spread to remote regions that are normally not subjected to direct impact. Other trace gases that show seasonal variation in the ACSOE dataset are NO_y, which was attributed to possible roles for nitrogen reservoirs such as PAN and nitric acid. With respect to NO and ROOH measured *in-situ* during ACSOE Azores, there appears to be several contrasts. Both peroxide species showed a net summer excess, despite a low concentration of HO₂ and RO₂ from model data and the absence of significant NO_x chemistry. It was suggested that the reason for this summer excess was due to the role of heterogeneous processes such as cloud uptake and aerosol loss, but the exact nature of these process, *e.g.* on [peroxide] is still unclear.

The MAXOX dataset showed concentrations of trace gases that exhibited many features observed in the ACSOE dataset, but also showed several additional features. This can be partly attributed to the location of the MAXOX missions of 1999. MAXOX was an aircraft campaign over the European continent and surrounding free troposphere. Data on trace gas concentrations sampled below *ca.* 2 km show that the planetary boundary layer in MAXOX was heavily polluted. Concentrations of tracers normally associated with large scale human influence such as NO and CO were recorded at levels indicative of heavy pollution over a wide range of latitudes encountered in the MAXOX campaign. However, this contrasts with data recorded at altitudes >2 km. Above the planetary boundary layer, MAXOX climatology data suggests that the concentration of these gases in the European free troposphere are close to those measured in the remote North Atlantic. For altitude bins above 2 km, tracers such as CO, NO_x, NO_y and ozone are similar or only slightly elevated above levels measured in the ACSOE campaign, a dataset that was considered representative of a clean, unperturbed environment.

A comparison of trace gas climatologies for both these aircraft campaigns show that, for the European free troposphere, there is no evidence of an isolated spring only ozone maximum. The seasonal variation in [O₃] in MAXOX was small, a maximum of 18 ppbv difference between MAXOX spring and MAXOX summer. This compares to the 53 ppbv difference observed in the ACSOE dataset. From the MAXOX data there seems to be a much broader spring and summer ozone maximum over the European continent, which contrasts the isolated

spring only ozone maximum found in the Azores. Other seasonal trend analyses suggest the North Atlantic, as investigated by the MAXOX and ACSOE aircraft campaigns shows some similar trends with respect to trace gas concentration, but also differences. Although there are large spatial distributions of these trace gas averages and only two seasons have been investigated, a summary of these seasonal trends is shown in Table 2.9.

Table 2.9: Seasonal Trends in MAXOX c.f. ACSOE Trace Gas Climatology Data.

Tracer	MAXOX Campaign	ACSOE Campaign
Ozone	Broad Spring/Summer Maximum	Spring Maximum
CO	Spring "Maximum"	N/A
NO	Spring "Maximum"	Summer "Maximum"
NO ₂	Spring "Maximum"	Summer "Maximum"*
NO _x	Spring "Maximum"	Summer "Maximum"*
NO _y	Summer "Maximum"	Spring "Maximum"†
H ₂ O ₂	N/A	Summer "Maximum"
ROOH	N/A	Summer "Maximum"
HCHO	N/A	Spring "Maximum"
H ₂ O	Summer "Maximum"	Summer "Maximum"

*NO₂ data derived from photostationary state assumptions (see section 2.4.3)

N/A =Data not available for spring and/or summer

†Assigned as NO_y, but is (NO_y - HNO₃) due to instrument problems (described in section 2.4.3)

Overall, there are clear statistical limitations to the construction of trace gas climatologies using aircraft data, but nonetheless the use of this analysis to give a broad overview of the concentration of species over large latitude ranges has provided useful a picture of the aircraft data investigated here. In particular, climatology analysis gives an insight into the free tropospheric trace gas distribution over the North Atlantic on a seasonal basis in both the remote (ACSOE) and semi polluted environment (MAXOX). Data analysis has shown that a

number of photochemical trace gases, particularly ozone, show a pronounced seasonal variation at altitudes <8 km. The combination of tracers and their altitude distributions are suggestive of a photochemical origin for this spring ozone maximum (Monks 2000). Further measurements are required in combination with detailed model analysis to place this and other MAXOX /ACSOE suppositions on a firmer basis.

Chapter Three: Aircraft Climatologies over the North Atlantic : Modelling

3.1)	Introduction	72
3.2)	Box Modelling of ACSOE Trace Gas Concentrations	75
3.3)	Ozone Tendencies During the ACSOE Campaign	85
3.4)	Summary of ACSOE Modelled Data	98
3.5)	Intercomparison of Data Measured During MAXOX to CTM Predictions	100
3.6)	MAXOX Ozone Tendencies	108
3.7)	Overall Features of Ozone Tendencies	120
3.8)	Summary	123

Chapter 3: Seasonal Trace Gas Climatologies over the North Atlantic: Modelling

3.1 Introduction

Atmospheric models that simulate the complex chemistry and dynamics of the troposphere have been used successfully in the past to predict both local and global tropospheric chemistry under a range of conditions and locations. Significant progress has been made in the computation speed of microcomputers, such that even the most complex models can now be run from desktop PCs. In Chapter 2 it was shown for many trace gases, climatological analysis yields some interesting conclusions, while for others it was more difficult to ascertain the chemistry occurring over the North Atlantic. As a result, model analysis of these data has been attempted in order to clarify the remaining issues. The modelling described in this chapter is broken down into two phases. The first phase is the application of a box model to ascertain the HO_x budget and photochemical environment associated with the data bins created for ACSOE Azores aircraft data. The second phase of the model analysis concerns the application of a chemistry transport model to the MAXOX dataset. This model dataset was obtained from the Norwegian Institute for Air Research (NILU) model and made freely available to the MAXOX community. These data have been used to investigate ozone photochemistry during the second portion of the MAXOX program, which comprised aircraft missions flown in summer of 1999.

3.1.1: Box Models

The first model used in this chapter is the box model that considers the atmosphere to be a reaction chamber or box into which trace gases species are emitted and undergo chemical and photochemical transformation (*e.g.* Schere and Demerjian [1978]). These are usually static models that allow no complex air mixing to take place, such as flux to and from the boundary layer/free troposphere, or surface deposition. Despite the relatively simple approach and limitations of spatial resolution, box models have been used successfully in the literature, especially when they are constrained to measured trace gas concentrations. For example, Zanis (1999) used a box model to investigate ozone photochemistry in the free troposphere at the Jungfraujoch in the Swiss Alps during the Free Troposphere Experiment (FREETEX) 96 and FREETEX 98. Data suggested a net ozone production rate during spring of 0.3 ppbv h⁻¹ was predicted, which compared well to the calculated ozone production rate of 0.13 ppbv h⁻¹

based on measured data alone. Zanis (1999) suggested that these data were representative of a net ozone production in spring in the lower free troposphere over much of the European continent. Carpenter *et al.* [2000] used a similar box model data to calculate the net ozone production rates and ozone production efficiencies at the Jungfraujoch. The authors report a net ozone production in the lower free troposphere of *ca.* 2 ppbv per day with a typical yield of 20-30 ozone molecules produced per NO_x molecule oxidised.

A closed box model with a gas-phase photochemical reaction mechanism was employed to simulate several scenarios based upon aircraft observations by Klem *et al.* (2000) to ascertain the ozone forming potential of VOCs and NO_x for plumes observed from several cities and a power plant in eastern Germany. Ozone production was found to be limited by the initial VOC concentrations for all of the simulated plumes, with higher O₃ concentrations produced with reduced initial NO_x.

Carshaw *et al.* (1999a , 1999b) have used a box model to investigate controlling factors in the HO_x budget during the wider ACSOE program, specifically at the recent Eastern Atlantic Summer Experiment 1996, (EASE96) at Mace Head, Ireland. In general, the observationally constrained box model was able to reproduce measured [HO_x] with good accuracy over a wide range of conditions, although modelled [HO₂] did appear to be overestimated when compared to measured data. Conversely, [HO_x] predictions were seen to underestimate measured [HO_x] during the Schauinsland Ozone Precursor Experiment (SLOPE 96) (Volz-Thomas *et al.* [2000]). During the experiment, polluted air masses, rich in NO_x and VOCs, were modelled using data obtained *via* measurements at two ground-based sites and from a small aircraft. Measured [OH] was almost a factor of two larger than predictions suggested using a chemical box model constrained by the measured trace gas concentrations and photolysis rates.

Crawford *et al.* (1996) used a photochemical box model to investigate ozone photochemistry in the remote Pacific. The authors suggested that in this remote region a net ozone production prevailed in the planetary boundary layer and lower free troposphere and up to *ca.* 4 km. Net increase in the total ozone column in this environment was 1-3%, per day suggesting the influence of continental outflow at these latitudes. Similar models have been used by Davis *et al.* (1993), (1996), based on aircraft observations to investigate the background photochemistry of the remote Pacific. A close balance between production and destruction of ozone was predicted in this region, with strong altitude dependence on the factors controlling P/L(O₃). Negative ozone tendency (*i.e.* net ozone loss) was found to be the generally

predicted at low altitudes, switching to positive ozone tendency (*i.e.* net ozone production) above 6 km. Davis *et al.* (1993), (1998), attributed this effect to altitude variations in [H₂O], which was found to be the most important factor in the control of modelled [HO_x].

3.1.2: Chemistry Transport Models

A more complex class of models are those that consider air parcels containing initial concentrations of trace gases, which are allowed to move along a given trajectory. These so-called "Lagrangian" models are effectively extension of a box model into a series of adjacent interconnected boxes (Wayne *et al.* [1973], Finlayson-Pitts and Pitts, [1999]). These Lagrangian models are the basis for more complex systems, known as Eulerian models (Ames *et al.* [1978]), which have been used to evaluate chemistry and transport on a global scale. Chemistry transport models (CTM's), have been developed over the last fifteen years or so (*e.g.* Levy, [1985]), and consider factors ignored by simpler systems, notably as the effect of local, regional and global air mixing and circulations, and are able therefore to provide data on trace gas concentrations on a global as well as a regional scale. Most CTMs utilise horizontal and vertical grids in order to parameterise local-scale chemistry but the most detailed of these models often have difficulty in reproducing all factors that affect tropospheric chemistry, such as convective storm systems. However, CTMs have provided insights into factors that effect large-scale chemistry of the background troposphere. For example, the MATCH model developed by Crutzen *et al.* (1999) has provided information on the photochemical control of ozone in the remote troposphere. MATCH predicted similar, if slightly larger, continental outflow of pollutants into the Northern Atlantic when compared to the concentration of trace gases measured by Parrish *et al.* (1993) during the first NARE experiment.

In remote areas, the MATCH model predicted regions of widespread ozone destruction that contrasted with the net ozone production observed near the continents. The model also suggested major production of tropospheric HO_x from sources such as formaldehyde photolysis in addition to production involving the reaction of O(¹D) with water. Similar results were obtained using the CTM model developed at the University of Bergen (Flatøy *et al.* [1995]), where ozone production rates as high as 1.5 ppbv h⁻¹ were observed for model scenarios constrained using 3 ppbv of NO_x and 20 ppbv of NMHC's.

In a comparison, the outputs of five models were compared with two years worth of *in-situ* aircraft data provided by the MOZAIC program, Law *et al.* (2000) found variable agreement

to instrumental problems as described in Chapter Two. $[\text{NO}_2]$ used in the model was therefore calculated from the steady state assumptions as described in Chapter Two.

Photolysis frequencies were calculated *in-situ* by the box model. These values were parameterised by the use of the exponential

$$j = A \exp.(B \sec \theta) \quad (3.1)$$

where θ is the solar zenith angle. Parameters A and B were set to the predicted values by the two-stream isotropic scatter radiative transfer model of Hough (1988). Data for the spring were optimised for 10/4/97, while summer data were optimised for 18/9/97. Data for pressure, concentration of air molecules, and temperature were set to the U.S. standard atmosphere (USSA [1976]). Methane concentrations were set to the 1750 ppbv during both seasons, a value typical of $[\text{CH}_4]$ for the Northern Hemisphere (Wayne, [1991]). The models were each run for 10 days in order to reach steady state before the output data were analysed.

3.2.1: Box Modelling of $[\text{HO}_x]$

The model runs from the box models provided 15-minute average calculated values for $[\text{OH}]$, $[\text{HO}_2]$ and $[\text{CH}_3\text{O}_2]$. These were then summed in order to obtain the total integrated HO_x and RO_2 from 6am to 6pm. The model results are shown in Figures 3.1-3.3. From Figure 3.1, $[\text{OH}]$ is *ca.* 5×10^6 molecules cm^{-3} in the lowest bin. Concentration falls off quickly as altitude increases, and $[\text{OH}]$ at 6.5km is only *ca.* 1.2×10^6 molecules cm^{-3} . Seasonal variation is also observed in the total $[\text{OH}]$ field. Modelled spring $[\text{OH}]$ is higher at the surface, but for the lower free troposphere bins, the summer has excess modelled $[\text{OH}]$ of up to *ca.* 1.5×10^6 molecules cm^{-3} . Total $[\text{HO}_2]$ was found to be far in excess of $[\text{OH}]$ and total $[\text{HO}_x]$ is dominated by $[\text{HO}_2]$. This seems to support data obtained by other workers (*e.g.* Faloon *et al.* [2000]) who reported in the clean, low NO_x environment of the Northern Pacific, the OH/HO_2 ratio is heavily biased to the HO_2 side of this "interconversion ratio". The interconversion ratio as described by Faloon *et al.* [2000] was in the range of 0.04, compared to 0.01 for the ACSOE Azores data described here, when averaged over all altitudes. $[\text{HO}_2]$ showed net spring excess, and consequently the total sum of OH and HO_2 showed similar spring excess.

Figure 3.1 Modelled [OH] During Spring and Summer for the ACSOE Campaign. (Data are a diurnal averages from 6am-6pm GMT)

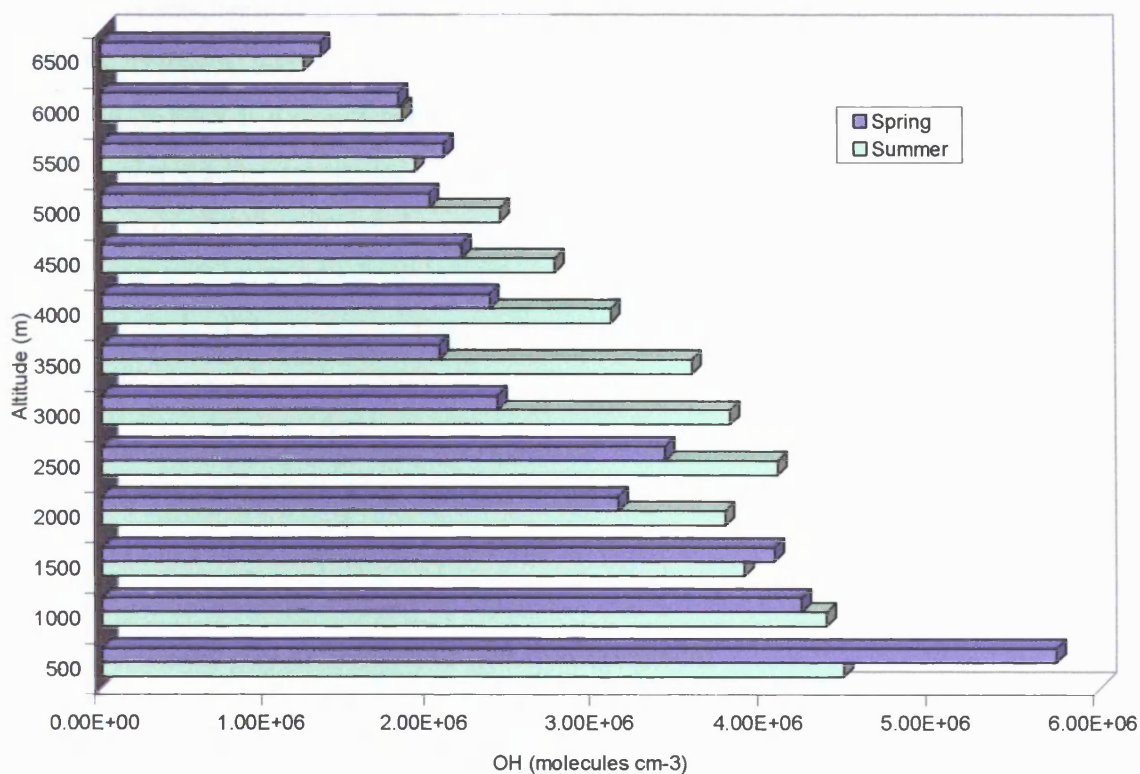
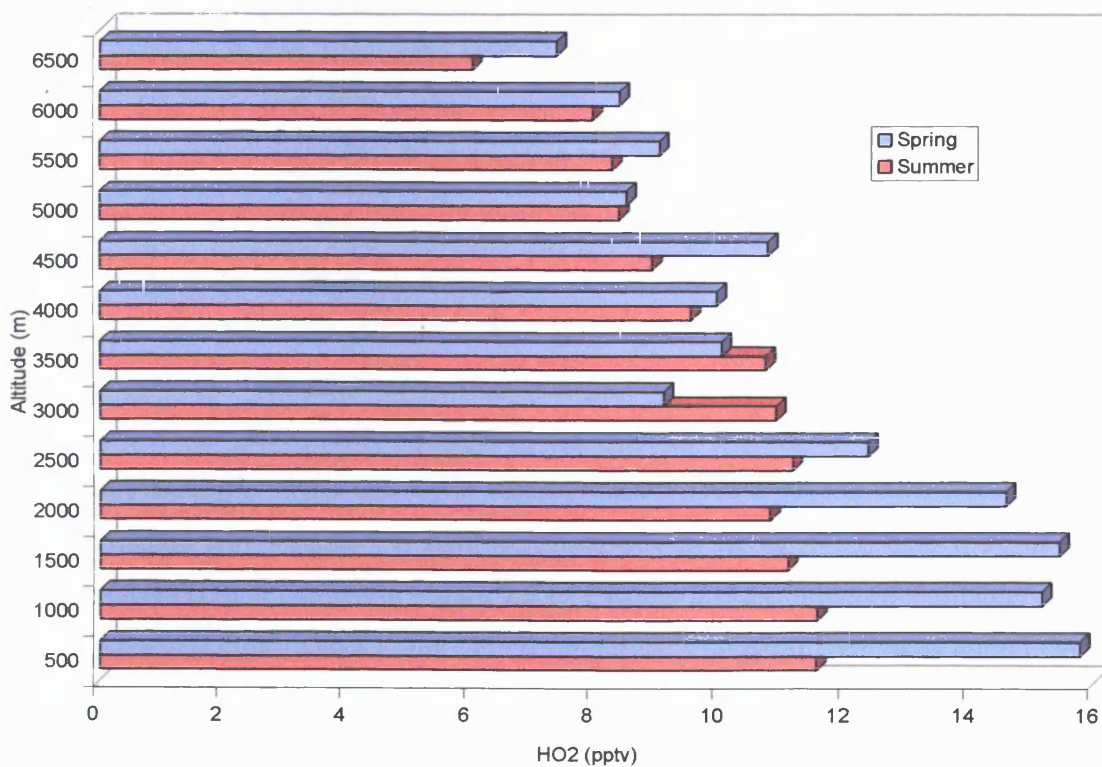


Figure 3.2: Modelled [HO₂] During Spring and Summer for the ACSOE Campaign. (Data are diurnal averages from 6am-6pm GMT)



between model prediction and *in-situ* measurements of [O₃]. Each model was able to reproduce the seasonal trends in ozone for many locations, but many underestimated [O₃] for Northern Hemisphere tropospheric sites. Model studies into ozone photochemistry have been made by Derwent and Davis (1999), who showed that over many regions of Europe, formation of PAN is a significant loss process in the destruction of NO_x. Other model results have re-enforced the importance of the non-linear dependence of ozone formation on [NO_x]. Derwent *et al.* (1999) calculated ozone production efficiencies (E_n), at various simulations of [NO_x], with E_n = 4-20 being observed for most [NO_x] scenarios. The authors suggested that for the majority of the European troposphere, P(O₃) is NO_x-limited. The same conclusion was reported by Brasseur *et al.* (1996), who showed that there has been a 4% increase in summer ozone concentrations in the upper troposphere owing to direct injection of NO_x and other precursors from aircraft in the commercial flight lanes in the UT/LS region of the atmosphere, (at 8-12 km in altitude), since the early 1990s.

3.2: Box Modelling of ACSOE Trace Gas Concentrations

In order to validate the data provided by *in-situ* measurements obtained during the ACSOE missions, modelling of the photochemical environment was necessary. A photochemical box model was written using FACSIMILE, a computer program used for numerical analysis and modelling chemical kinetics and transport. Details of FACSIMILE model construction and the FACSIMILE data "language" was described by Curtis and Sweetenham (1987). This box model was a modified version of the model described by Zanis (1999) that was used to model the lower free troposphere from the measurements taken at the ground-based site of the Jungfraujoch (JFJ) at an elevation of 3,580 m. The original model comprised 136 kinetic and photochemical reactions and was optimised for Jungfraujoch conditions. The JFJ model was used as a working template for this work and suitably modified such that a separate box model was developed for each of the aircraft data bins. For each of these bins, the concentrations of trace gases used to constrain the model were set to the spring/summer measured average. Data used to constrain the model included O₃, NO, H₂O, HCHO, H₂O₂, ROOH, C₂H₆, C₂H₄, C₃H₈ and C₃H₆ measurements. Measured CO data were used for the summer flights, but since no CO data were available in spring, [CO] data were interpolated using the CO/O₃ ratio (shown in Figure 2.7 of Chapter 2). As shown by Parrish *et al.* (1993), (1998) there was little change in the CO/O₃ ratio over a range of conditions during the NARE I and NARE II experiments. It was assumed in this work that the ratio between CO and ozone was the same in both seasons and hence, CO mixing ratios were interpolated for each altitude bin and used to constrain the spring model runs. *In-situ* NO₂ data was also unavailable owing

Figure 3.3: Modelled $[HO_x]$ During Spring and Summer for the ACSOE Campaign. (Data are diurnal averages from 6am-6pm GMT)

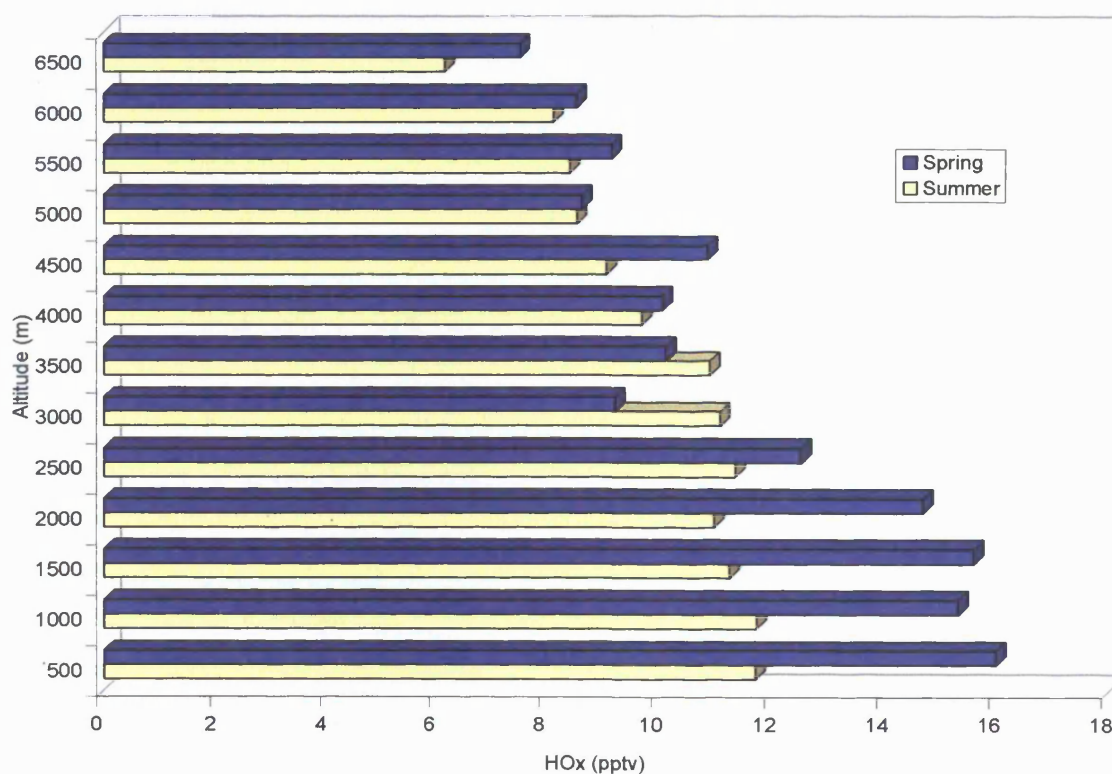


Figure 3.2 shows that the typical concentration of HO_2 modelled during the ACSOE campaign was of the order of 6-16 pptv. Again, there is strong altitude dependence in the $[HO_2]$, as well as some seasonal variation. Spring concentrations of HO_2 in the boundary layer, were far higher than during summer for the corresponding altitude. For those data bins <2km in spring, concentrations of HO_2 were around 4-5 pptv higher than in summer for similar altitudes. Contrasting this, free tropospheric $[HO_2]$ showed far less seasonal variation with spring excesses being of the order of 1-2 pptv.

It has been observed by several authors (e.g. Jaeglé *et al.* [1997], Wennberg *et al.* [1998], Collins *et al.* [1999]) that in the lower free troposphere, the production of HO_x is essentially controlled by the reaction of $O(^1D)$ with water vapour. Total $[HO_x]$ is often found to have strong water dependence (Davis *et al.* [1996]). Examination of the HO_x -water relationship for the ACSOE dataset showed similar correlations, with variations in $[H_2O]$ tracking the fall off in $[HO_x]$ as altitude increases.

Figure 3.4: Correlations Between $[HO_x]$ From Box Model and $[H_2O]$ during ACSOE Spring Campaign

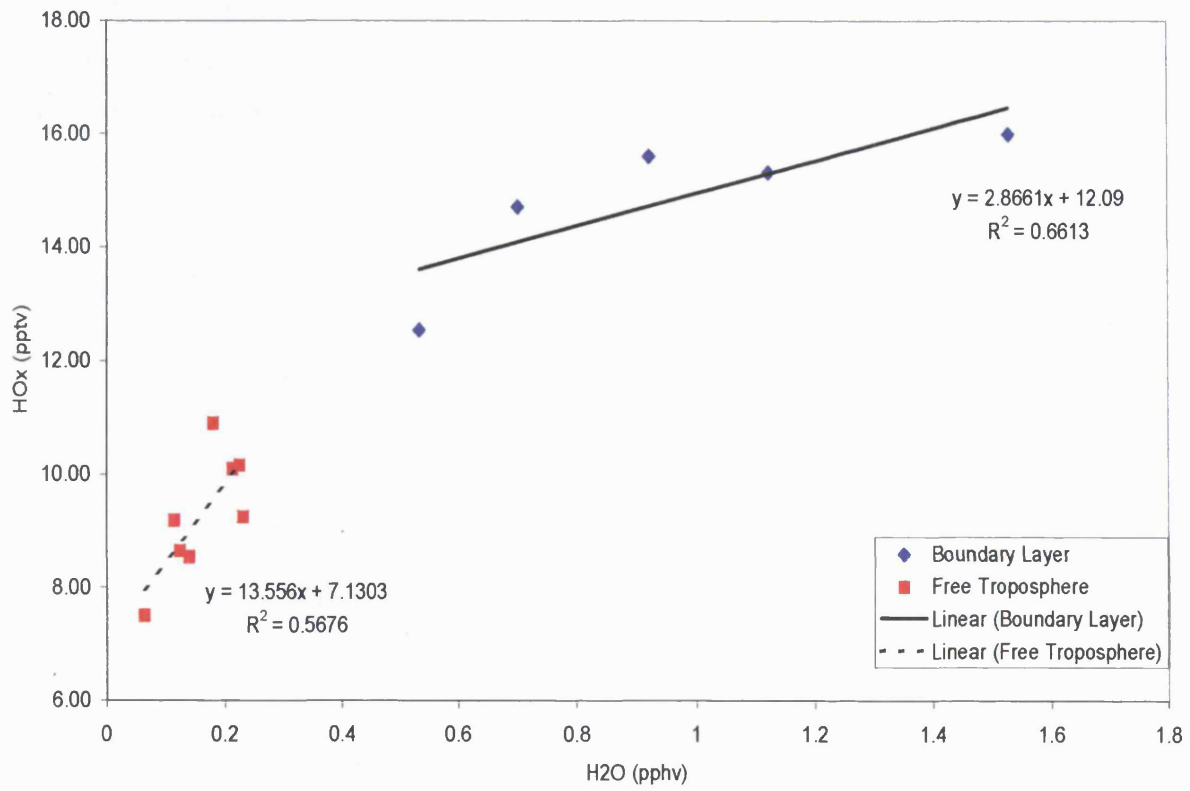
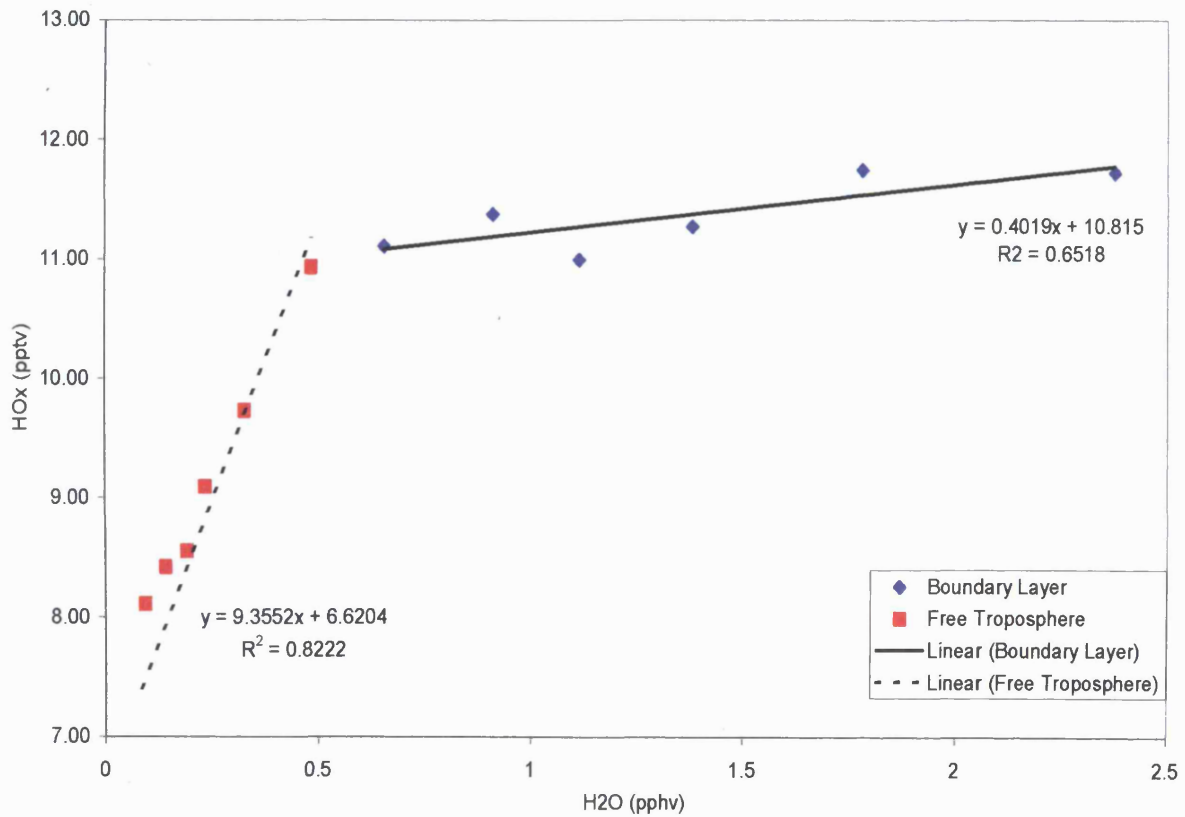


Figure 3.5: Correlations Between $[HO_x]$ From Box Model and $[H_2O]$ during ACSOE Summer Campaign



Figures 3.4 and 3.5 show that during both the spring and summer, there are two regimes of H₂O/HO_x correlation. In the free troposphere, the linear dependence of [HO_x] on [H₂O] is strong, with an R² value of *ca.* 0.82 in summer, *ca.* 0.55 in spring, owing to the relative decrease of [H₂O] with altitude in the free troposphere and planetary boundary layer. Considering the data for spring, from Figure 3.6, above 3 km the gradient of the line plotting the correlation between [H₂O] and altitude is steep, reflecting that there is a rapid fall off in [H₂O] as altitude increases. This contrasts the boundary layer below 3 km. At these lower altitudes, the fall off in [H₂O] less pronounced. Figure 3.4 and 3.5 suggest that when H₂O is abundant (concentrations > *ca.* 0.5 ppbv), the overall sensitivity of HO_x production to absolute water concentration is small, *i.e.* large variations in [H₂O] do not control the level of HO₂+OH. This contrasts directly with the regime of [H₂O] < 0.5 ppbv, where [HO_x] is very sensitive to [H₂O]. The non-zero intercept of the plot shown in Figures 3.4 and 3.5 suggests that although there is strong sensitivity of [HO_x] to water concentration, there is still significant production of HO_x where [H₂O] tends to zero. These HO_x production pathways are likely to be acetone and formaldehyde photolysis, as described in Chapter 4.

Figure 3.6: Altitude Dependence of [H₂O] during ACSOE Spring Campaign

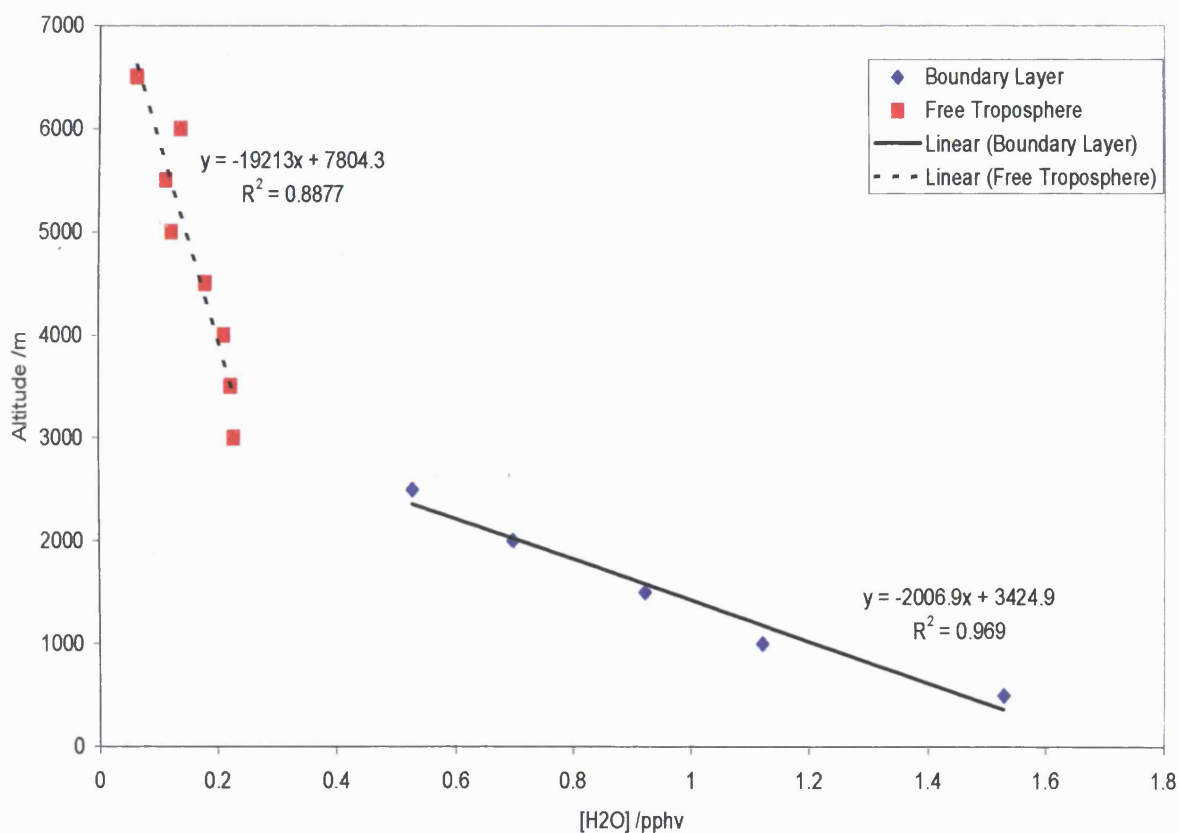
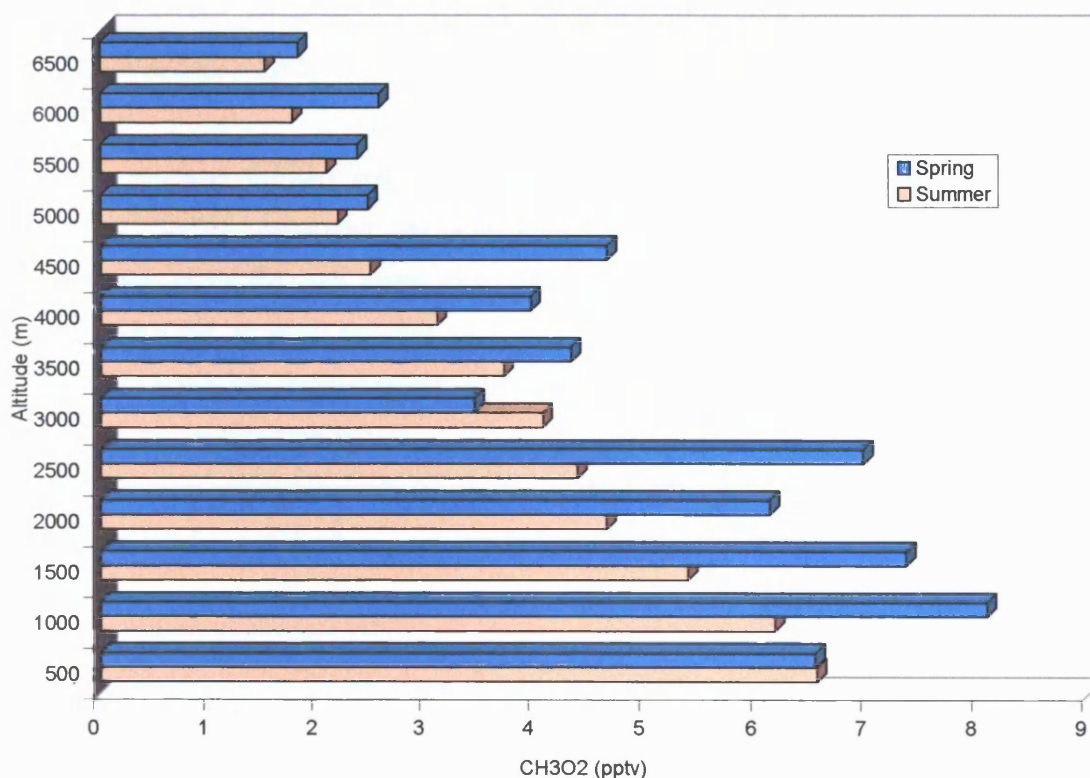


Figure 3.7: Modelled $[CH_3O_2]$ During Spring and Summer for the ACSOE Campaign. (Data are diurnal averages from 6am-6pm GMT)



CH_3O_2 model outputs for spring and summer are shown in Figure 3.7. The plot illustrates the difference in the seasonal concentration of peroxy radicals. In general, the levels of the methyl peroxy radical were around 6-8 pptv at low altitude, before falling off to a minimum of 1-2 pptv at 6.5 km. As with HO_x , the greatest concentrations of CH_3O_2 were found in spring, with concentrations consistently 1-2 pptv higher than summer values throughout the altitudes investigated by the use of the box model.

From these results, a picture of the photochemical environment over the North Atlantic can be formed. The results described in Chapter 2 showing the likelihood of enhanced photochemical activity in April, relative to September, are supported by the box model outputs, which showed that concentrations of HO_x and RO_2 were consistently higher in April than for the same regions during September. However, the partitioning of HO_x means that the OH component of $[HO_x]$ is higher in summer. This may be related to the CO data used to constrain the model. As stated above, $[CO]$ during spring were interpolated from the CO/O_3 ratio. Taking the 500m bin as a typical example, $[CO]$ for this altitude bin during spring was around 121 ppbv, compared to a measured concentration of 75 ppbv during summer. The net result of there being much more CO in spring than summer is that despite the fact that photochemical production of OH being higher in spring, OH radicals react rapidly with the

spring excess of CO in order to form HO₂. Thus, the "free" OH in summer is actually greater than that predicted in spring.

3.2.2: Box Model P(HO_x) and L(HO_x) pathways

The key steps in P(HO_x) and L(HO_x) pathways for the binned HO_x data have also been analysed. The key production step in the formation of HO_x as indicated by the model output is the reaction of O(¹D) with water vapour. For the spring flight the total flux of P(HO_x) was found to be *ca.* 57 pptv per day with the contribution of *j*-(O¹D) followed by reaction of excited oxygen with water vapour making up *ca.* 76% of the total, when averaged over all altitudes. The role of [HO_x] sources such as *j*-(HCHO) is relatively minor in the box model results. In all the data, the role of both formaldehyde and peroxide photolysis does increase with increasing altitude however. This is a reflection of the importance of secondary production routes where [H₂O] is low and thus, the primary production channel of O(¹D) + H₂O is suppressed (Singh *et al.* [1995], Jaeglé *et al.* [1997], [2000]). The pathway strengths of these P(HO_x) routes in spring and summer are shown in Figures 3.8 and 3.9.

The loss routes of modelled HO_x during the two legs of the ACSOE campaign are dominated by the loss of HO₂ through its self-reaction and cross-reaction with CH₃O₂. Figure 3.10 shows that during the spring, HO_x loss is dominated by the HO₂ self-reaction with *ca.* 60% of HO_x lost *via* this pathway. Although the HO₂ self-reaction is the dominant pathway for all model scenarios, the relative importance of other loss routes increases as altitude increases, as the relative concentrations of NO_x, CH₃O₂ and HO₂ vary. This trend is repeated in the data for summer, as shown in Figure 3.11.

Figure 3.8: Modelled $[HO_x]$ Production Pathways During ACSOE Spring Campaign

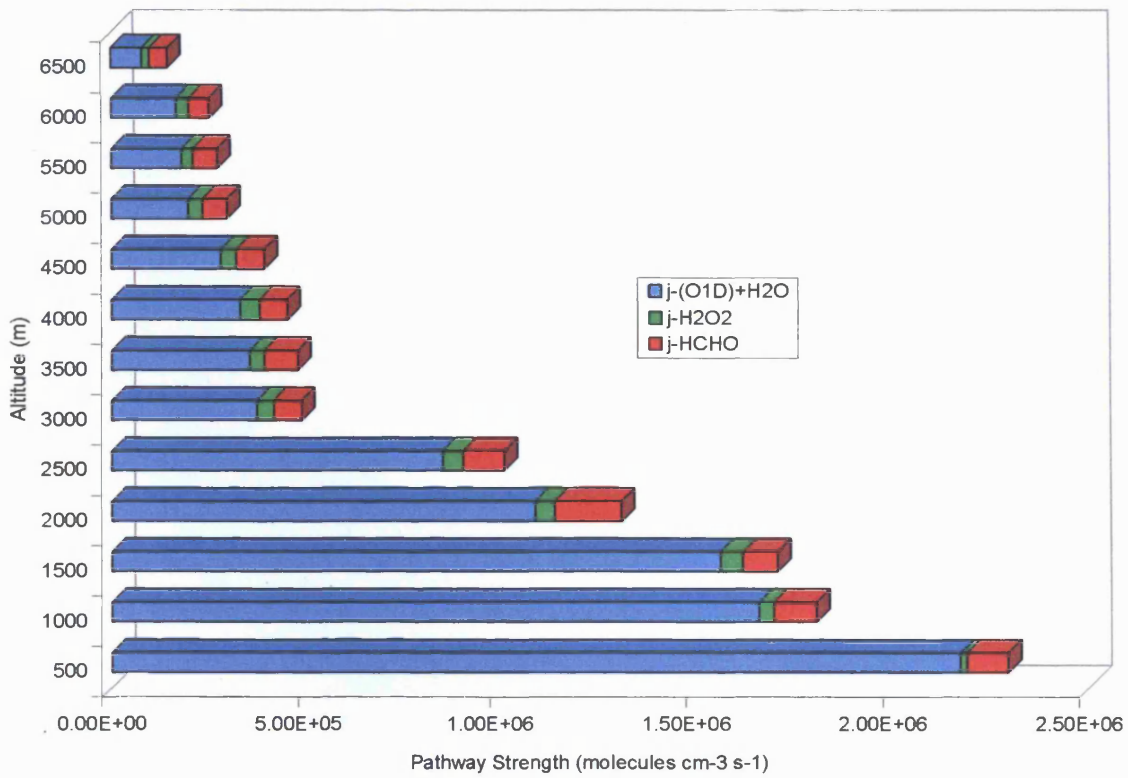


Figure 3.9: Modelled $[HO_x]$ Production Pathways During ACSOE Summer Campaign

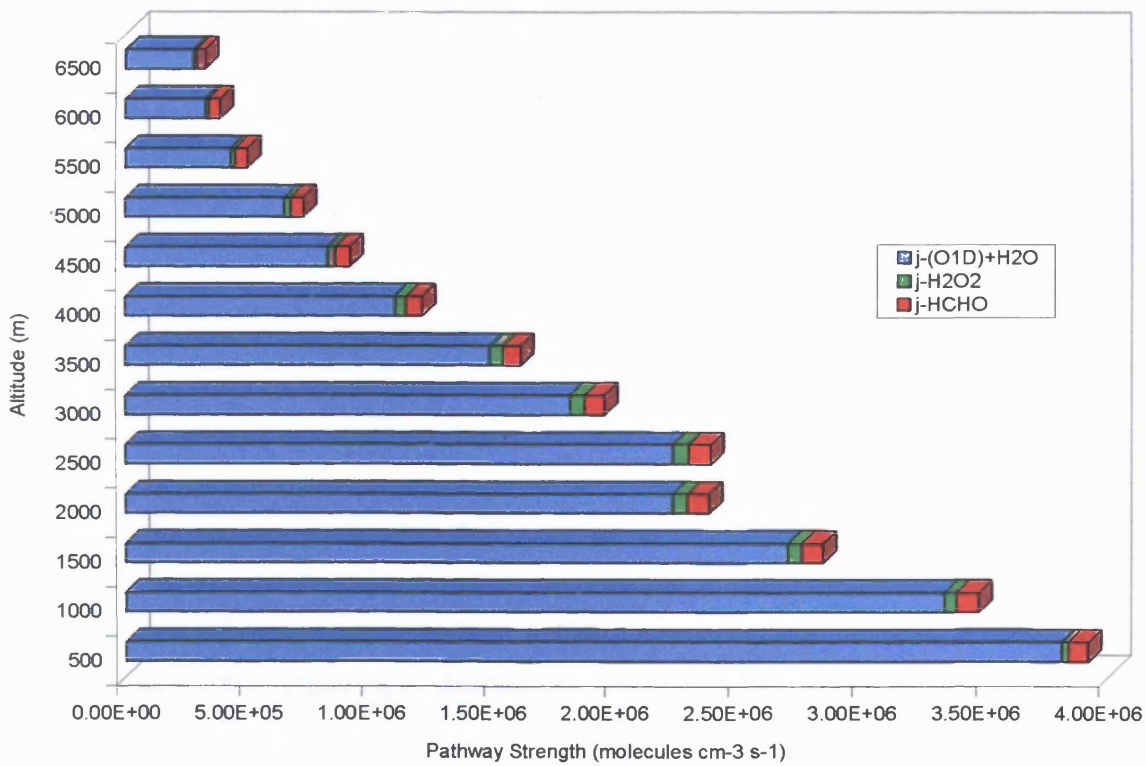


Figure 3.10: Modelled HO_x Loss Pathways for ACSOE Spring Campaign

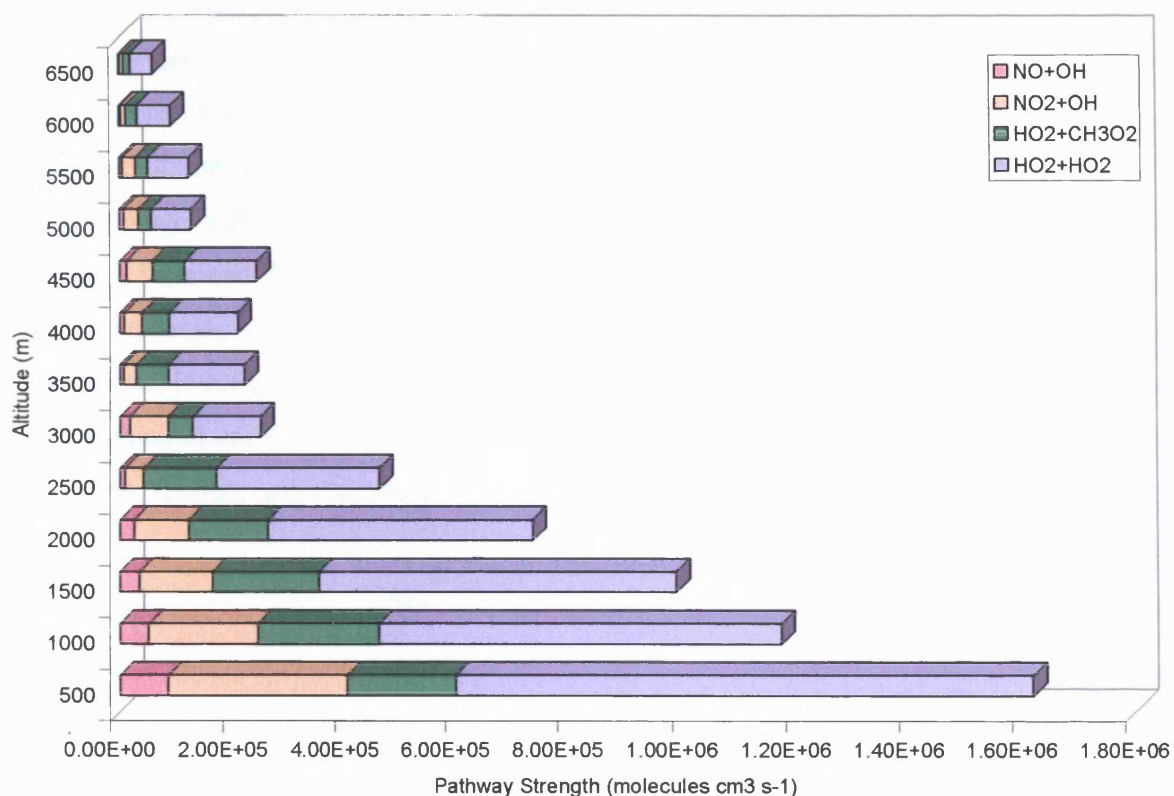
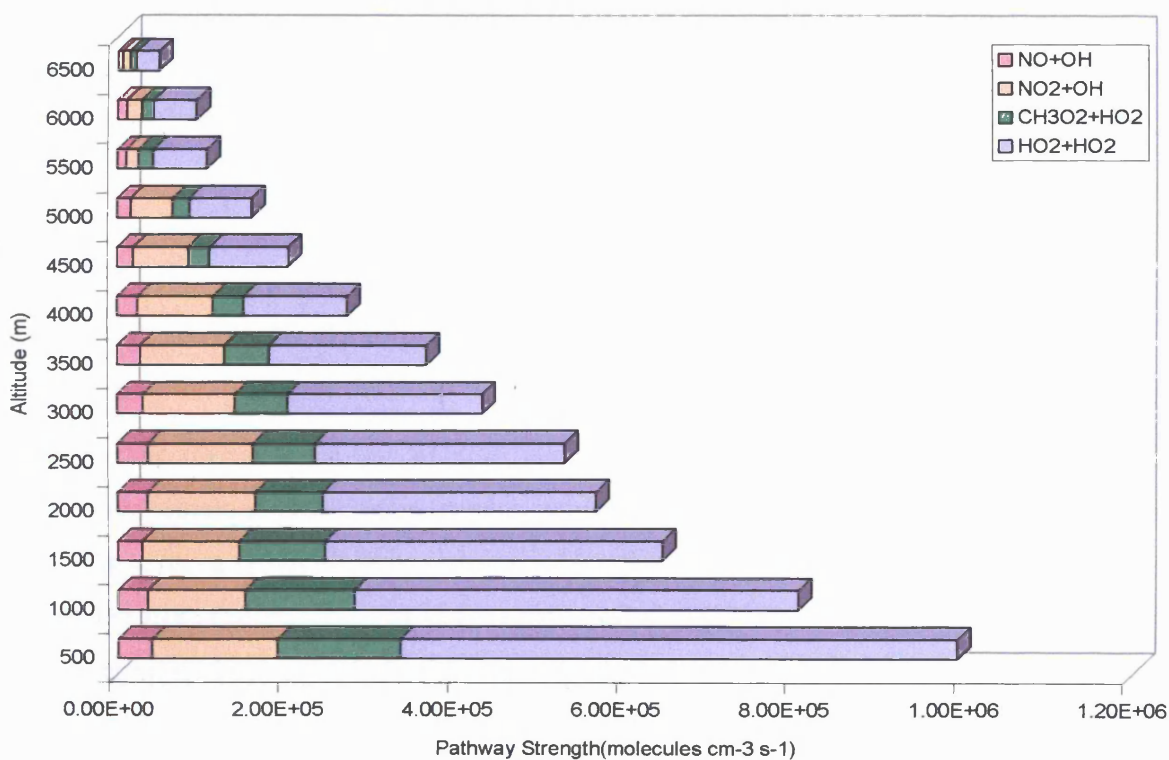


Figure 3.11: Modelled HO_x Loss Pathways for ACSOE Summer Campaign



3.3: Ozone Tendencies During the ACSOE Campaign

Modelled values of the concentrations of HO_x and CH₃O₂ during the ACSOE Azores campaign also enable the calculation of ozone production and loss rates. The ability and the efficiency of the atmosphere to produce and destroy ozone is important in assessing the anthropogenic influence on the oceanic free troposphere (Seinfeld and Pandis, [1998] Finlayson Pitts and Pitts, [1986], [1999]). There is still conflicting evidence as the nature of ozone tendencies in the remote environment with some authors suggesting ozone production (Davis *et al.* [1996], Crawford *et al.* [1997]) and some observing a net ozone loss (Jacob *et al.* [1996], Penkett *et al.* [1998]) in remote environments. Brasseur *et al.* (1998) showed that for a low-NO_x regime, ozone production is given by:

$$P(O_3) = \{k_{(HO+NO)}[HO_2] + k_{(RO_2+NO)}[RO_2]\} * [NO] \quad (3.2)$$

While ozone destruction is given by

$$L(O_3) = j - O(^1D).F.[O_3] + \{k_{(O_3+OH)}[OH] + k_{(O_3+HO_2)}[HO_2]\} * [O_3] \quad (3.3)$$

where, F is the fraction of O(¹D) atoms formed that react to produce OH. From Penkett *et al.* (1997), F is given by

$$F = \frac{k_{(H_2O+O(^1D))}[H_2O]}{k_{(M+O(^1D))}[M] + k_{(H_2O+O(^1D))}[H_2O]} \quad (3.4)$$

and $k_{(M+O(^1D))}$ is the rate of collisional quenching of O(¹D) to O(³P)

For the data taken during the ACSOE campaign, all of the variables in equation (3.2) and (3.3) were obtained from either model or measured parameters. The net ozone tendency, $\tau(O_3)$, is given as $P(O_3)-L(O_3)$, *i.e.* the subtraction of equation (3.3) from (3.2). $\tau(O_3)$ was calculated from the necessary model outputs and subsequently worked up in order to calculate the daily production and loss rate. A plot of the 24-hour mean ozone tendency is shown in Figure 3.12.

Figure 3.12: Ozone Tendencies for ACSOE Spring and Summer Data (24 hour Calculated Average)

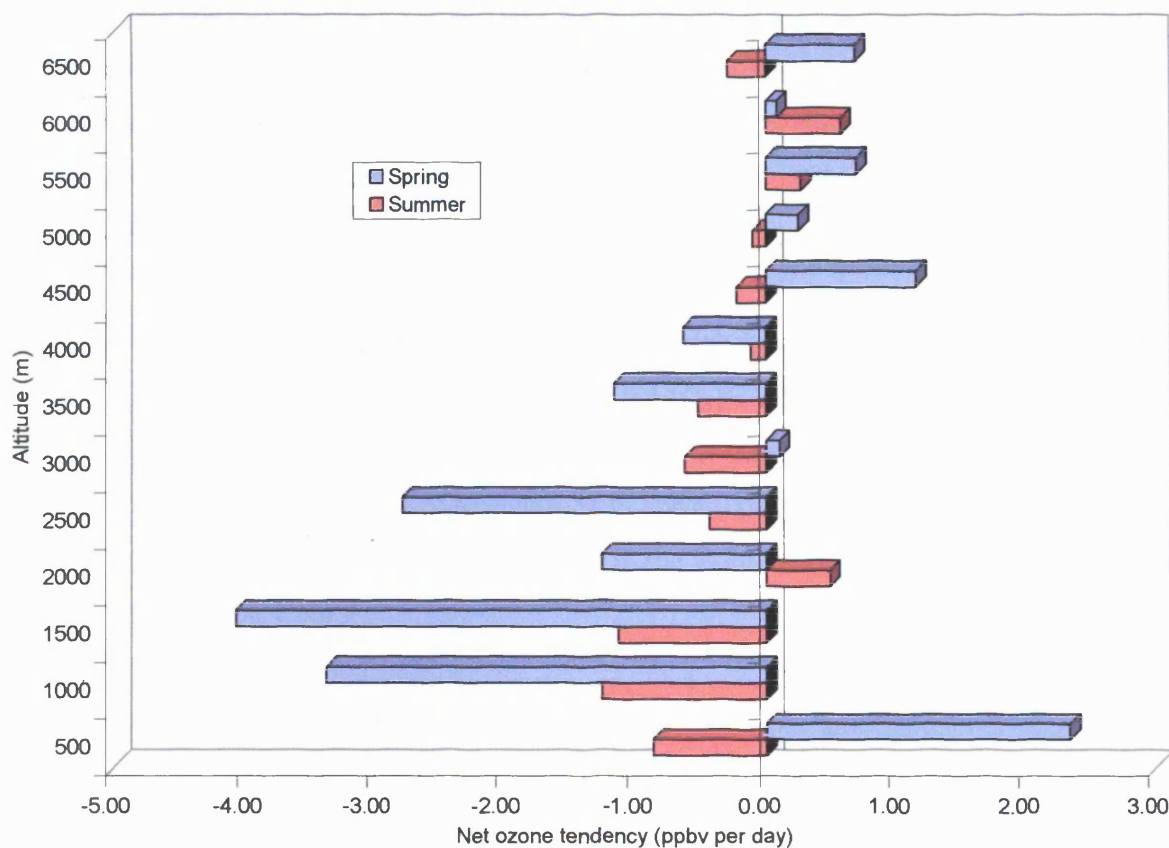


Figure 3.12 shows that using the relationships described by Brasseur *et al.* (1998), the combination of measured and modelled data predict a general ozone loss over the North Atlantic, as encountered by the C-130 during the ACSOE Azores campaign, of between -0.1 and -4.0 ppbv per day. These results may be compared to a general ozone production of +3-+9 ppbv per day suggested by Zanis (1999) as typical of the European continent. However, some altitudes show a net production of ozone. Specifically, the spring data bins for 500m, 3000m and all altitude bins >4500m show a net production of ozone of up to 2 ppbv per day. For the September flights, similar trends were observed in the 2000m, 5500m and 6000m bins, where $\tau(\text{O}_3)$ is shown to be up to +0.5 ppbv per day. Altitude dependence in net ozone tendency was also reported by Davis *et al.* (1996), but clearer "split" was observed in the data by altitude for PEM-West than that suggested here. For values calculated over the remote Pacific, below 6 km, the autumn showed a $L(\text{O}_3)$ of up to 4.3 ppbv per day, while values calculated above 6 km, showed $P(\text{O}_3)$ of 1.8 ppbv per day.

The reason for a net ozone production in some bins while others, in the same season, show a net ozone loss requires investigation. For the free troposphere, production and loss of ozone is dictated by the concentration of NO_x and peroxy radicals. With respect to peroxy radicals, it

was shown in section 3.2, that both $[\text{HO}_2]$ and $[\text{CH}_3\text{O}_2]$ decrease systematically with altitude, since they are chemically coupled to $[\text{H}_2\text{O}]$. From the binned $[\text{NO}]$ data described in Chapter 2, $[\text{NO}]$ appeared to show a more random altitude dependence (see Chapter 2, Figure 2.9). It is therefore the NO_x dependence that is the key to the production/loss of ozone. The literature has shown (*e.g.* Davis *et al.* [1996], Crawford *et al.* [1997], Brasseur *et al.* [1998]) that the production/loss of ozone in remote regions, relatively free from human influence, is often under NO_x control.

There is a critical concentration of NO, $\text{NO}_{\text{critical}}$, which is defined as the point at which O_3 formation and destruction are equal, *i.e.* $\text{P}(\text{O}_3) = \text{L}(\text{O}_3)$. A comparison of $\text{NO}_{\text{critical}}$ with NO thus provides an indication of the sensitivity of ozone tendency to small changes in $[\text{NO}]$. For the data obtained during the ACSOE missions in spring and summer, a plot of $\tau(\text{O}_3)$ against NO can provide an estimate of $\text{NO}_{\text{critical}}$ as this is the value of NO where a trend line crosses the y axis in a $y=mx+c$ plot.

The relationship between NO and $\tau(\text{O}_3)$ for the averaged April and September data is shown in Figures 3.13 and 3.14. From these plots, it is clear that the tendency for production of ozone is NO_x dependent. Straight-line plots of $\tau(\text{O}_3)$ against measured $[\text{NO}]$ shows high levels of correlation in both seasons. From Figure 3.13, spring data has the strongest NO_x dependence, where $R^2 = 0.84$. The $\text{NO}_{\text{critical}}$ level for spring is of the order of 15 pptv (± 1.6 pptv at 1σ) of NO. The summer data also show $\tau(\text{O}_3)$ is dependent on the level of NO, with $R^2 = 0.6$. Summer value of $\text{NO}_{\text{critical}}$ is slightly higher than for spring at 24 pptv (± 1.3 pptv at 1σ). This compares to the critical NO values of 6-17 pptv calculated by Davis *et al.* (1996) and the 4-18 pptv to yield net ozone production over the remote Pacific calculated by Crawford *et al.* (1997). The gradients of the plots shown in Figure 3.12 and 3.13 indicate the sensitivity of τO_3 to $[\text{NO}]$, *i.e.* the steeper the gradient of a linear fit, the smaller the change in $\tau(\text{O}_3)$ for a given $[\text{NO}_x]$. From Figure 3.13, the gradient of the spring data line is 2.8, while from Figure 3.14, the gradient during the summer is 4.1. The shallower slope observed in spring data suggests that the ozone tendency is more sensitive to changes in background $[\text{NO}_x]$ during the spring series of aircraft flights than during the summer leg of the ACSOE campaign.

Figure 3.13: Correlation between $\tau(O_3)$ and NO for ACSOE Spring data

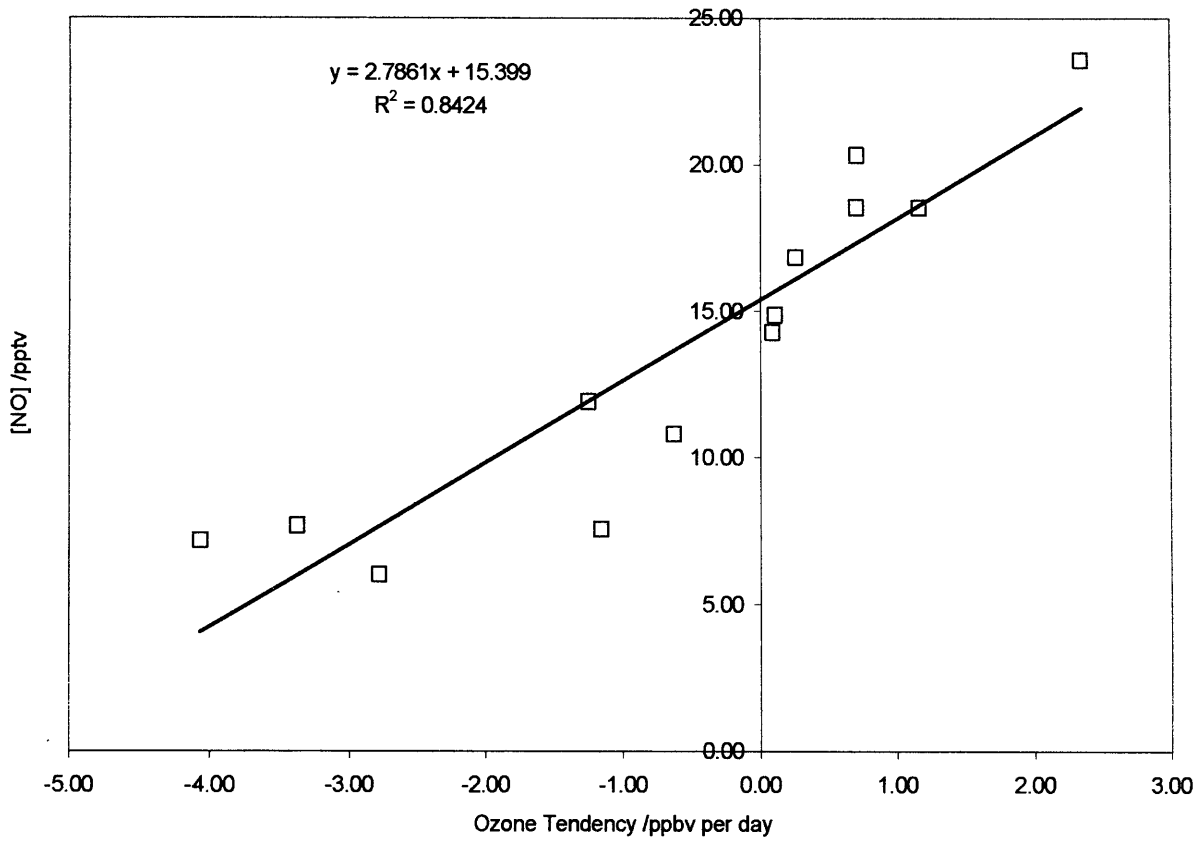


Figure 3.14: Correlation between $\tau(O_3)$ and NO for ACSOE Summer data

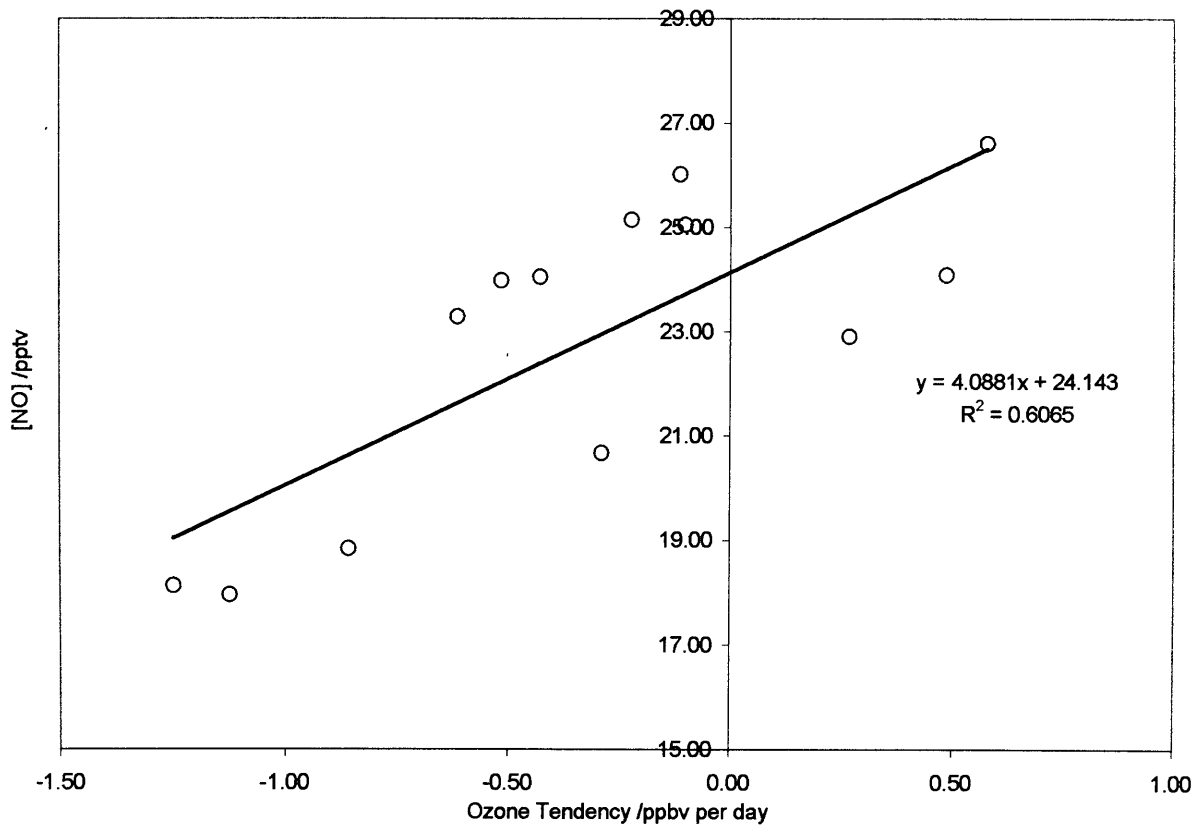


Table 3.1: Spring Box Model Sensitivities with Respect to Trace Gas Concentration (when averaged over all altitudes).

	Midday [HO _x] (pptv)	% Change from Base Model	Midday HO ₂ + RO ₂ (pptv)	% Change from Base Model	τ (O ₃) (ppbv per day)	% Change from Base Model
Base model	13.92	-	19.45	-	-0.82	-
1.1 x <i>j</i> -(O ¹ D)	14.51	+4.1	20.30	+4.2	-1.04	+21.1
0.9 x <i>j</i> -(O ¹ D)	13.30	-4.4	18.57	-3.6	-0.61	-26.0
2 x [NO]	14.23	+2.1	18.52	+4.8	-1.28	+36.0
0.5 x [NO]	13.56	-2.5	20.26	-4.0	-0.49	-40.2
2 x [CO]	15.05	+7.5	18.68	+4.0	-0.72	+19.1
0.5 x [CO]	12.81	-8.0	20.43	-4.8	-0.89	-7.9
2 x [O ₃]	18.72	+25.6	26.67	+27.1	-0.70	+14.6
0.5 x [O ₃]	10.36	-25.6	14.19	-27.0	-1.08	-24.1
1.1 x [CH ₄]	13.84	+0.5	19.83	+2.0	-0.70	+14.6
0.9 x [CH ₄]	14.01	-0.6	19.07	-2.0	-0.95	-13.7

The general sensitivity of [HO_x] and [CH₃O₂] produced by the model to variations in the measured data and hence, the sensitivity of τ(O₃) was investigated. During this analysis, the effect on the overall predicted [HO_x] and [HO₂+RO₂] at midday was considered through variation in the concentrations of initial trace gases used to constrain the model. Concentrations of ozone, CO, NO, were varied by a factor of two, while *j*-(O¹D) and [CH₄] data were varied by 10%. These changes in the model parameters and their effects on the model predictions for spring and summer are shown in Tables 3.1 and 3.2. Using trace gas measurements taken in both portions of the ACSOE campaign, the results suggest that the model is most sensitive to the concentration of ozone and CO used to initially constrain the model. This is important, as [CO] for spring data was interpolated from the CO/O₃ ratio owing to the absence of *in-situ* data measured during the ACSOE spring leg. A factor of two change in [CO] was found to cause an 8% variation in [HO_x]. Modelled [CH₃O₂] was found to be more sensitive to [CO]. This is attributed the relative importance of the reaction between OH and CO/CH₄. A 100% increase in [CO] causes a decrease in the modelled [CH₃O₂] of up to 34%. Similarly, increasing the [CO] in the model causes a decrease in the concentration of

Table 3.2: Summer Box Model Sensitivities with Respect to Trace Gas Concentration (when averaged overall altitudes).

	Midday [HO _x] (pptv)	% Change from Base Model	Midday HO ₂ + RO ₂ (pptv)	% Change from Base Model	τ (O ₃) (ppbv per day)	% Change from Base Model
Base Model	13.39	-	18.85	-	-1.03	-
1.1 x j- (O ¹ D)	13.95	+4.0	19.69	+4.3	-1.45	+29.0
0.9 x j- (O ¹ D)	12.80	-4.4	17.95	-4.8	-0.62	-39.8
2 x [NO]	13.59	+1.5	17.64	+6.4	-1.81	+43.1
0.5 x [NO]	13.02	-2.8	19.96	-5.6	-0.41	-60.1
2 x [CO]	14.44	+7.2	18.17	+3.6	-0.88	+14.6
0.5 x [CO]	12.45	-7.0	19.63	-0.4	-1.11	-7.2
2 x [O ₃]	18.09	+26.0	26.02	+27.6	0.19	+18.4
0.5 x [O ₃]	10.02	-25.1	13.78	-27.0	-2.08	-48.1
1.1 x [CH ₄]	13.33	+0.5	19.73	+4.5	-0.83	+19.4
0.9 x [CH ₄]	13.45	-0.5	18.45	-21.2	-1.23	-12.2

CH₃O₂ by up to 34%. Hence, where [CO] is higher than the normal "background" level used in the model, the most important OH loss route is the reaction of OH and CO described in equation (3.6) and P(CH₃O₂) is reduced.



Conversely, where [CO] is 50% lower than the normal "background" concentration of CO used to constrain the model, reaction (3.6) is no longer the dominant loss route for OH. The most important loss route for OH therefore becomes the formation of CH₃O₂, viz



The maximum change in ozone tendency for the spring portion of the ACSOE campaign when introducing the variations in the concentration of CO used to constrain the model was

$\pm 12\%$. These trends were repeated in the analysis of the sensitivities with respect to trace gases measured during the summer leg of the ACSOE campaign. Upon changing $[\text{CO}]$ by $\pm 50\%$, $[\text{HO}_x]$ during summer were found to change by 7%. Similarly, $[\text{RO}_2]$ was found to change 32% and $\tau(\text{O}_3)$ changed by 8% when compared to the predictions of the original box model. Changing $[\text{O}_3]$ used to constrain the model caused similar effects. For the model constrained to spring, trace gas concentrations, a 50% change in $[\text{O}_3]$ caused a change in $[\text{HO}_x]$ of 26%, while $[\text{CH}_3\text{O}_2]$ was changed by 30%. Net ozone tendency was found to vary by 15% upon increasing or decreasing the initial $[\text{O}_3]$ by 50%. For the summer box model data, variations in model data were found to be 26% for $[\text{HO}_x]$, 33% for $[\text{RO}_2]$ and 51% in $\tau(\text{O}_3)$ respectively when increasing or decreasing the initial ozone concentration by 50%.

3.3.1: Control of Ozone During ACSOE Spring Flight Campaign

Davis *et al.* (1996) have suggested that water is the major chemical-controlling factor in the latitudinal trend of O_3 loss in remote environments such as the Pacific Ocean. As described in Section 3.2, the control of $[\text{HO}_x]$ is linked to the concentration of water. The correlation of water to ozone loss for the data measured during the ACSOE campaign, suggests that the level of ozone destruction is closely linked to $[\text{H}_2\text{O}]$ for the North Atlantic free troposphere. Figure 3.15 shows that the correlation between $L(\text{O}_3)$ and H_2O is relatively high in the April series of aircraft missions, with $R^2 = 0.8$. Analysis of the relative importance of ozone destruction pathways for April suggests that destruction of ozone in spring is dominated by photolysis to $\text{O}(^1\text{D})$ and subsequent reaction with water vapour to form OH. Figure 3.16 shows that these reactions account for between 37% and 51% of total ozone destruction flux of 1.19 ppbv per day, when averaged over all altitudes. Recycling of HO_2 to OH *via* the reaction of ozone with HO_2 makes up between 45% and of 32% of $L(\text{O}_3)$ during spring, with the $\text{O}_3 + \text{OH}$ reaction making up the remaining 12% to 18%. These values are in agreement with model results described by Wang *et al.* (2000) where a net $P(\text{O}_3)$ of *ca.* 1 ppbv per day and $L(\text{O}_3)$ of 2.4 ppbv per day were calculated for air masses encountered in the Pacific.

Figure 3.15: Modelled $L(O_3)$ and its Correlation to $[H_2O]$ During ACSOE Spring Data

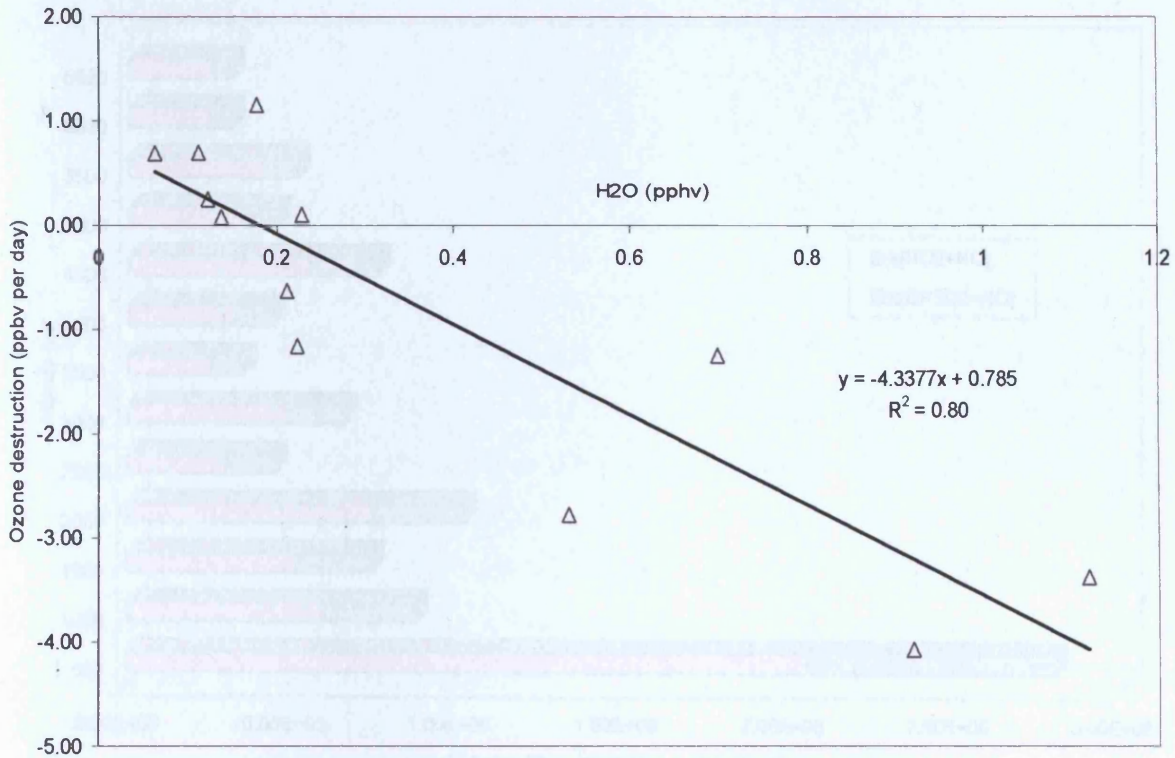


Figure 3.16: Relative Importance of $L(O_3)$ Pathways During ACSOE Spring Data

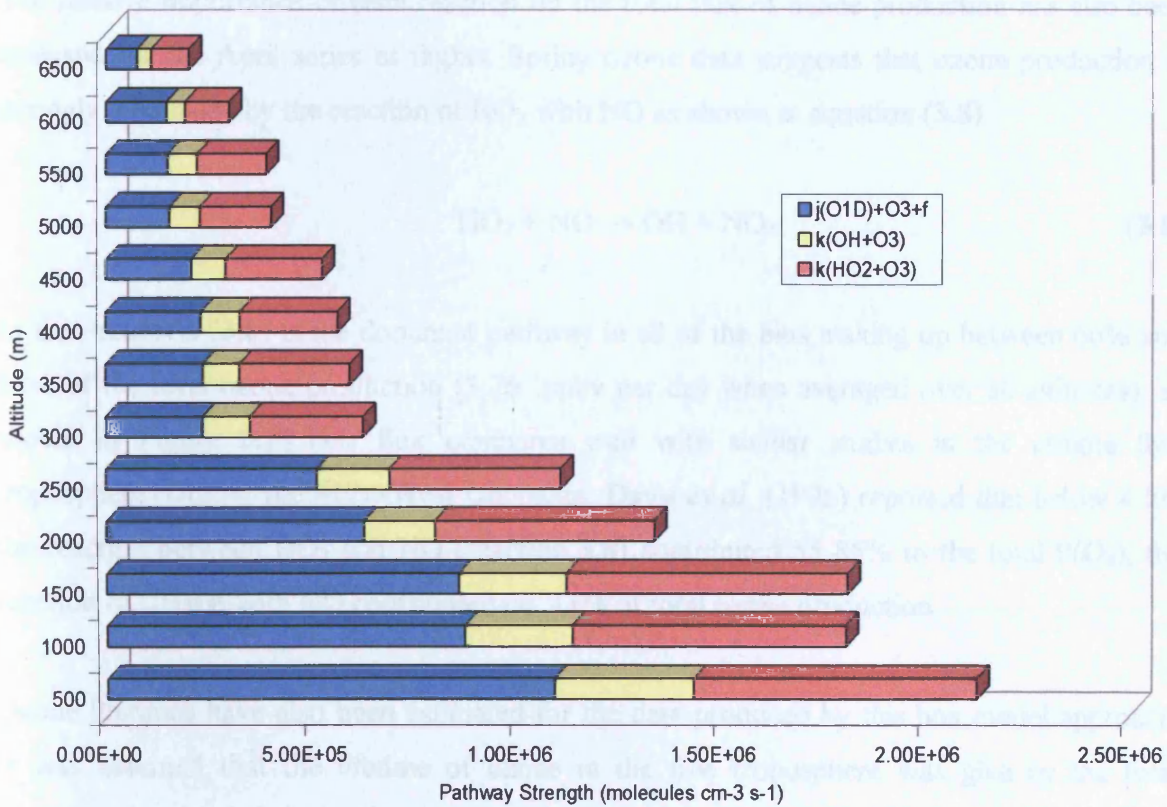
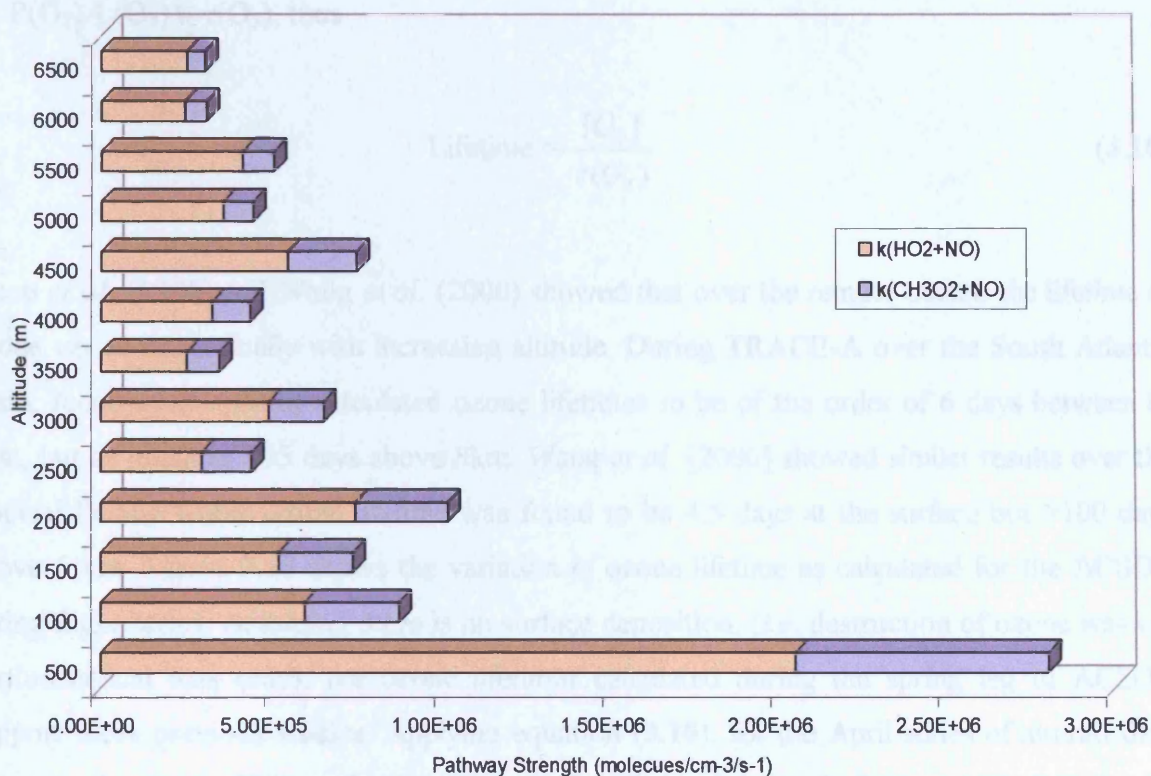


Figure 3.17: Relative importance of P(O₃) Pathways in ACSOE Spring



The relative importance of each reaction on the total flux of ozone production has also been analysed for the April series of flights. Spring ozone data suggests that ozone production is strongly influenced by the reaction of HO₂ with NO as shown in equation (3.8)



In fact, reaction (3.8) is the dominant pathway in all of the bins making up between 66% and 82% of the total ozone production (3.76 ppbv per day when averaged over all altitudes), as shown in Figure 3.17. This flux compares well with similar studies in the remote free troposphere. During the PEM-West campaign, Davis *et al.* (1996) reported that below 4 km the reaction between HO₂ and NO (reaction 3.8) contributed 55-85% to the total P(O₃), the reaction of CH₃O₂ with NO contributed *ca.* 11% of total ozone production.

Ozone lifetimes have also been estimated for the data produced by this box model approach. It was assumed that the lifetime of ozone in the free troposphere was give by the total concentration of O₃, divided by the difference between the rate of ozone production and the rate of ozone destruction, *i.e.*

$$\text{Lifetime} = \frac{[O_3]}{\{P(O_3) - L(O_3)\}} \quad (3.9)$$

as, $P(O_3) - L(O_3) \equiv \tau(O_3)$, thus

$$\text{Lifetime} = \frac{[O_3]}{\tau(O_3)} \quad (3.10)$$

Jacob *et al.* (1996) and Wang *et al.* (2000) showed that over the remote oceans the lifetime of ozone varies dramatically with increasing altitude. During TRACE-A over the South Atlantic basin, Jacob *et al.* (1996) calculated ozone lifetimes to be of the order of 6 days between 0-4km, but as much as 105 days above 8km. Wang *et al.* [2000] showed similar results over the tropical Pacific where ozone lifetime was found to be 4.5 days at the surface but >100 days above 5 km. Figure 3.18 shows the variation in ozone lifetime as calculated for the ACSOE spring flight series. Assuming there is no surface deposition, (*i.e.* destruction of ozone was *via* photochemical loss only), the ozone lifetimes calculated during the spring leg of ACSOE support these previous studies. Applying equation (3.10), for the April series of aircraft data suggests the mean lifetime for ozone over the North Atlantic is between 12 days in the boundary layer and over 80 days in the mid free troposphere.

Figure 3.18: Calculated Average Ozone Lifetimes with respect to Altitude for ACSOE Spring Campaign

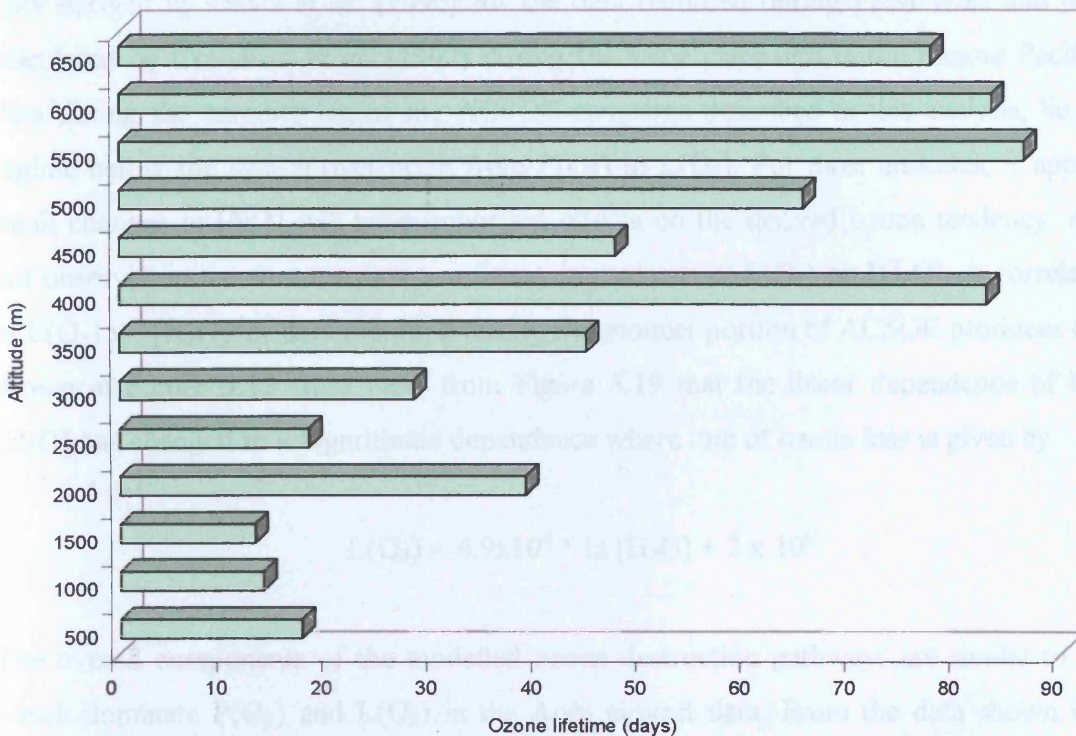
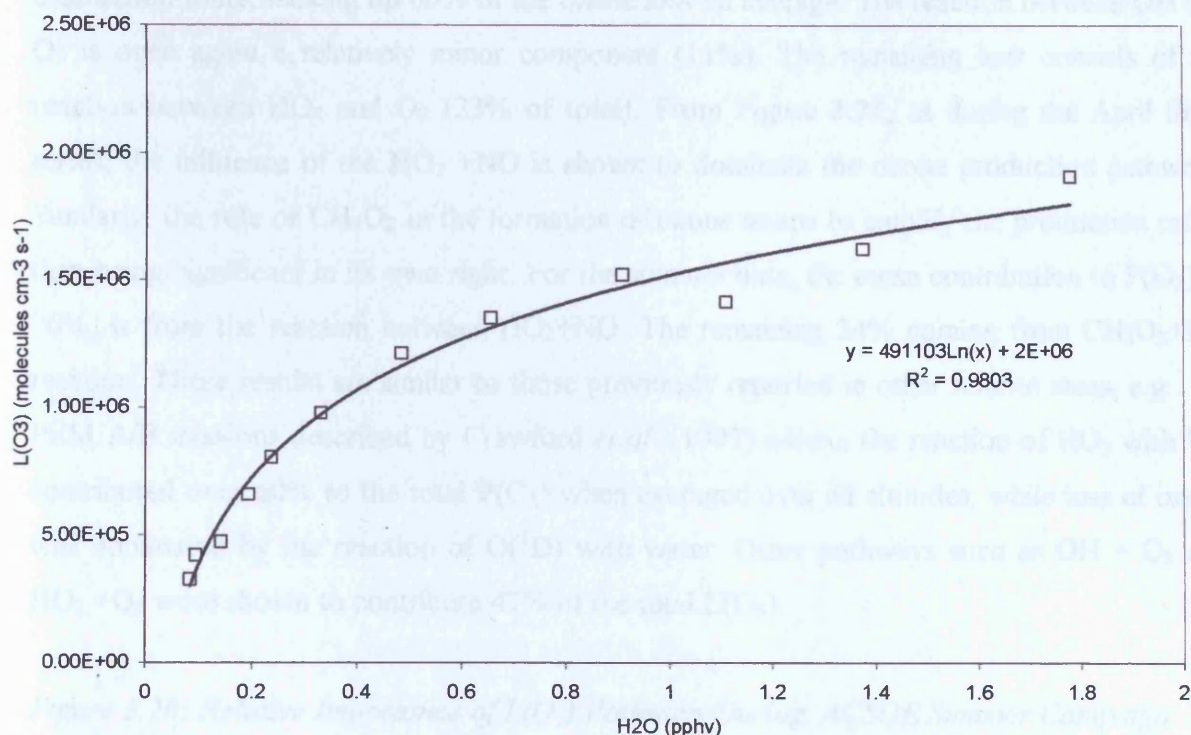


Figure 3.19: Correlation between $L(O_3)$ and $[H_2O]$ During ACSOE Summer Campaign



3.3.2: Control of Ozone During ACSOE Summer Flight Campaign

The plot of NO versus $\tau(O_3)$ for summer was shown in Figure 3.13. The data suggests a correlation between summer NO levels and $\tau(O_3)$ that is less pronounced than during the April flights. The correlation between $\tau(O_3)$ and [NO] was 0.61. Calculated NO_{critical} data were observed to be higher in the summer, the level being *ca.* 25 pptv. This value compares to 6-17 pptv derived by Davis *et al.* (1996) for the data recorded during PEM-West and 4-18 pptv calculated by Crawford *et al.* (1997) during the same campaign in the remote Pacific. Most data during the summer leg of the ACSOE campaign described in this analysis, lie in a NO regime below the switch over point from P(O₃) to L(O₃). For most altitudes, it appears that small changes in [NO] will have important effects on the derived ozone tendency. A feature not observed in the summer data is a linear dependence of L(O₃) on [H₂O]. A correlation plot of L(O₃) vs. [H₂O] for data recorded during the summer portion of ACSOE produces the curve shown in Figure 3.19. It is clear from Figure 3.19 that the linear dependence of L(O₃) on [H₂O] has changed to a logarithmic dependence where rate of ozone loss is given by

$$L(O_3) = 4.9 \times 10^6 * \ln [H_2O] + 2 \times 10^6 \quad (3.11)$$

The overall components of the modelled ozone destruction pathways are similar to that which dominate P(O₃) and L(O₃) in the April aircraft data. From the data shown in Figure

3.20, photolysis of ozone followed by reaction of $O(^1D)$ with water is the most important destruction route, making up 66% of the ozone loss on average. The reaction between OH and O_3 is once again a relatively minor component (11%). The remaining loss consists of the reaction between HO_2 and O_3 (23% of total). From Figure 3.21, as during the April flight series, the influence of the $HO_2 + NO$ is shown to dominate the ozone production pathways. Similarly, the role of CH_3O_2 in the formation of ozone seems to amplify the production rather than being significant in its own right. For the summer data, the mean contribution to $P(O_3)$ of 76%, is from the reaction between $HO_2 + NO$. The remaining 24% coming from $CH_3O_2 + NO$ reaction. These results are similar to those previously reported in other remote areas, e.g. the PEM A/B missions described by Crawford *et al.* (1997) where, the reaction of HO_2 with NO contributed over 60% to the total $P(O_3)$ when averaged over all altitudes, while loss of ozone was dominated by the reaction of $O(^1D)$ with water. Other pathways such as $OH + O_3$ and $HO_2 + O_3$ were shown to contribute 47% of the total $L(O_3)$.

Figure 3.20: Relative Importance of $L(O_3)$ Pathways During ACSOE Summer Campaign

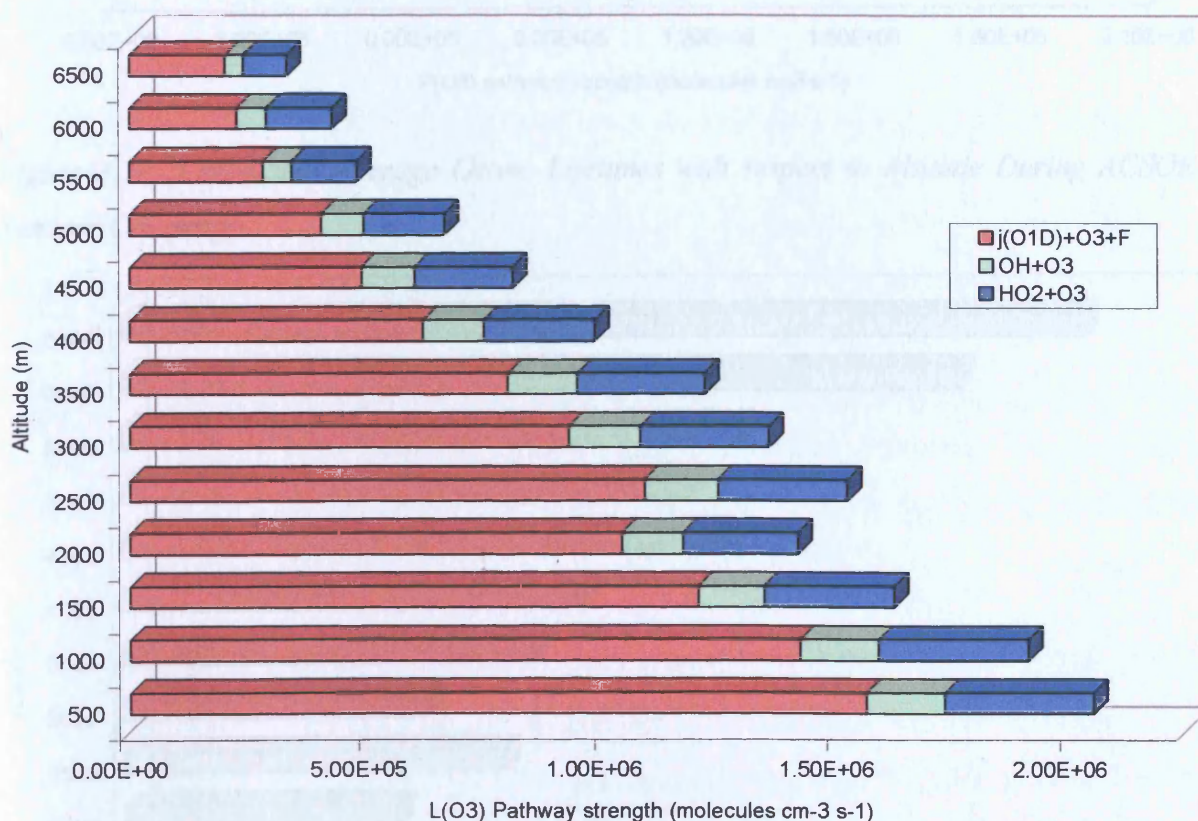


Figure 3.21: Relative importance of P(O₃) Pathways During ACSOE Summer Campaign

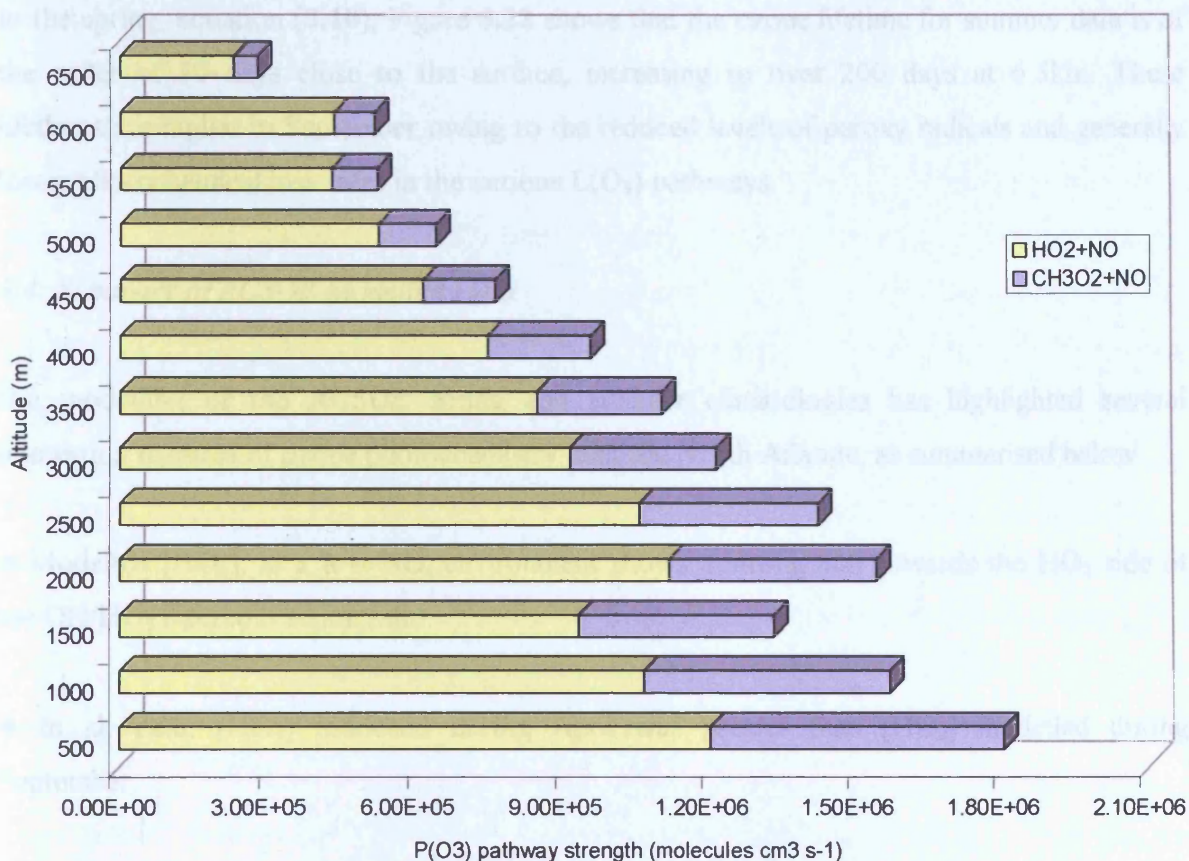
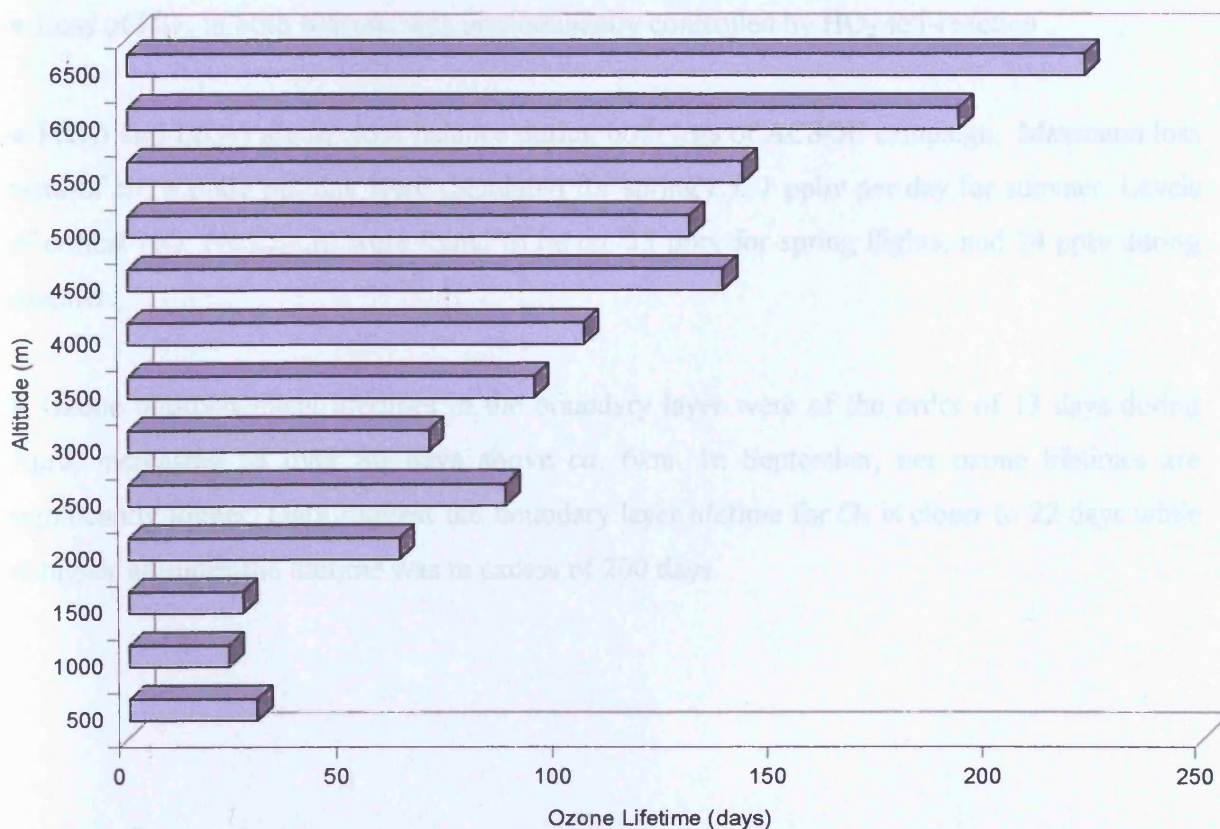


Figure 3.22: Calculated Average Ozone Lifetimes with respect to Altitude During ACSOE Summer Campaign



Ozone lifetimes have also been calculated for these summer data. Using similar calculations to the spring, equation (3.10), Figure 3.22 shows that the ozone lifetime for summer data is of the order of 30 days close to the surface, increasing to over 200 days at 6.5km. These lifetimes are higher in September owing to the reduced levels of peroxy radicals and generally lower photochemical loss rates in the various $L(O_3)$ pathways.

3.4: Summary of ACSOE Modelled Data

Bin modelling of the ACSOE spring and summer climatologies has highlighted several interesting features of ozone photochemistry over the North Atlantic, as summarised below

- Modelled $[HO_x]$, in a low- NO_x environment shows a strong bias towards the HO_2 side of the OH/HO_2 interconversion ratio.
- In all data, $[HO_x]$ modelled during April was greater than $[HO_x]$ modelled during September.
- Production of HO_x in both seasons was controlled by the reaction of $O(^1D)$ atoms with water over essentially all altitudes.
- Loss of HO_x in both seasons was predominantly controlled by HO_2 self-reaction
- $P(O_3)$ and $L(O_3)$ are in close balance during both legs of ACSOE campaign. Maximum loss rates of *ca.* 4 ppbv per day were calculated for spring *c.f.* 1 ppbv per day for summer. Levels of critical NO , ($NO_{critical}$), were found to be *ca.* 15 pptv for spring flights, and 24 pptv during summer.
- Ozone photochemical lifetimes in the boundary layer were of the order of 13 days during April, increasing to over 80 days above *ca.* 6km. In September, net ozone lifetimes are significantly longer. Data suggest the boundary layer lifetime for O_3 is closer to 22 days while at higher altitudes the lifetime was in excess of 200 days.

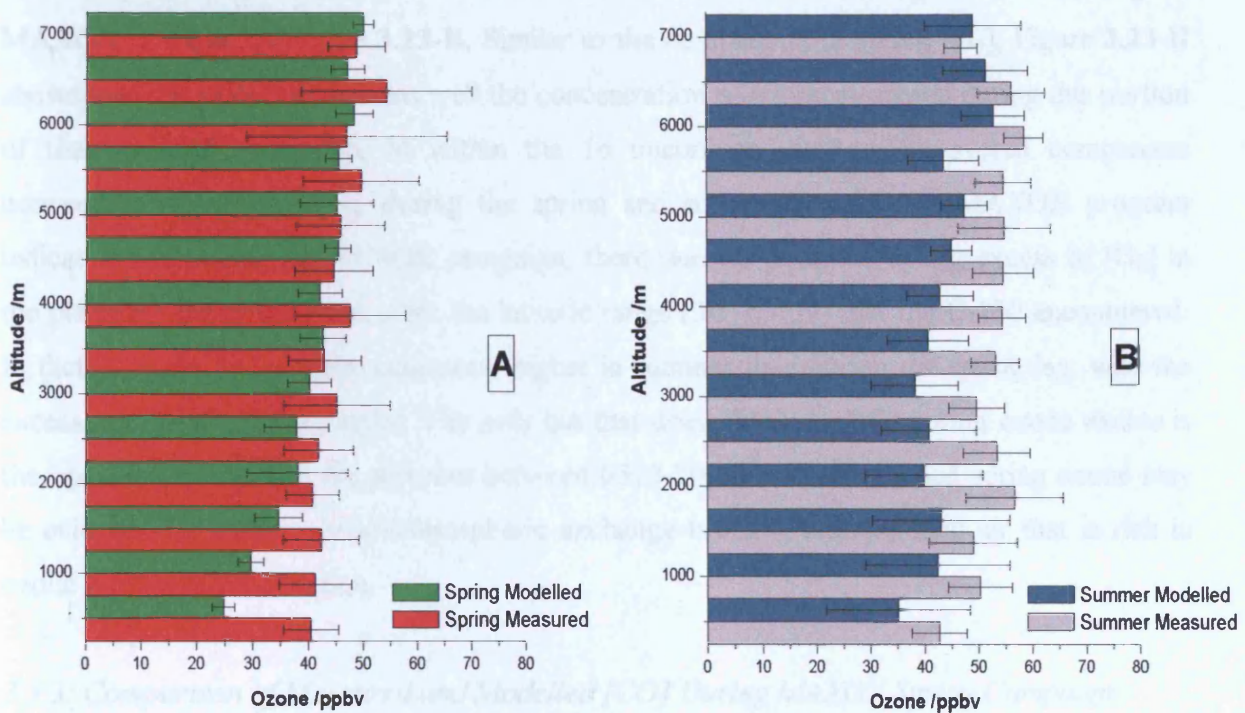
3.5: Intercomparison of Data Measured During MAXOX to CTM Predictions

The data collected during the MAXOX aircraft campaign, described in Chapter Two, have also been investigated *via* a chemistry transport model/measurement comparison. For this data set, MAXOX trace gas concentrations measured *in-situ* from the C-130 platform have been compared to outputs from the Chemistry Transport Model (CTM), developed by the University of Bergen. This model, may be accessed *via* the World-Wide-Web and uses meteorological data provided by the Norwegian Meteorological Institute (NWP). The model incorporates a second model, known as NORLEM, as described by Nordeng (1984) and Grønås *et al.* (1995). The Bergen CTM itself uses integrations on a stereographic map projection. The model user can easily change the horizontal domain, grid resolution, position and number of vertical layers and model height. The model grid resolutions normally used are between 25 and 150 km at 60° N with 10-30 equally spaced vertical layers extending up to pressure heights of between *ca.* 100 and 30 hPa. The meteorological fields from the NWP forecasts are stored with one-hour resolution. The CTM forecasts then start at 06:00 or 18:00 (universal time), the input consisting of a chain of independent 6 hour long forecast segments. The transport part of the CTM has been described by Flatøy *et al.* (1995), (2000) and the chemistry part by Flatøy and Hov (1996).

Dr. F. Flatøy supplied data from the Bergen model (CTM) analysis runs to the MAXOX data community. Concentrations of trace gases were provided from the model runs that were calculated by the model along the aircraft flight track during each mission in the MAXOX campaign, with necessary changes in latitude and height accounted for. Using these modelled data along the flight tracks, trace gas concentrations could be separated *via* the usual data bin approach in order to compare the model climatologies to those measured *in-situ*. Each measured trace gas climatology was compared to its model equivalent separately.

Figure 3.23: CTM Modelled and Measured Spring and Summer [O₃] Data During MAXOX.

The Bars are 1 σ Standard Deviations.



3.5.1: Comparison of Measured and Modelled [O₃] During MAXOX Spring Campaign

Figure 3.23-A shows that the agreement between the modelled and measured ozone data during the April series of MAXOX missions was relatively good. In almost all altitude bins the modelled ozone concentration lies within one standard deviation of the measured value. The only potential area of concern are the lowest altitude bins. Within the boundary layer, the CTM underestimates the measured concentration, with the difference being *ca.* 15 ppbv. This disagreement was too large to be accounted for by measurement/model uncertainties. It is quite likely therefore that the CTM needs further refinement in this area specifically with respect to the surface ozone precursor source/sink ratio.

3.5.2: Comparison of Measured and Modelled [O₃] During MAXOX Summer Campaign

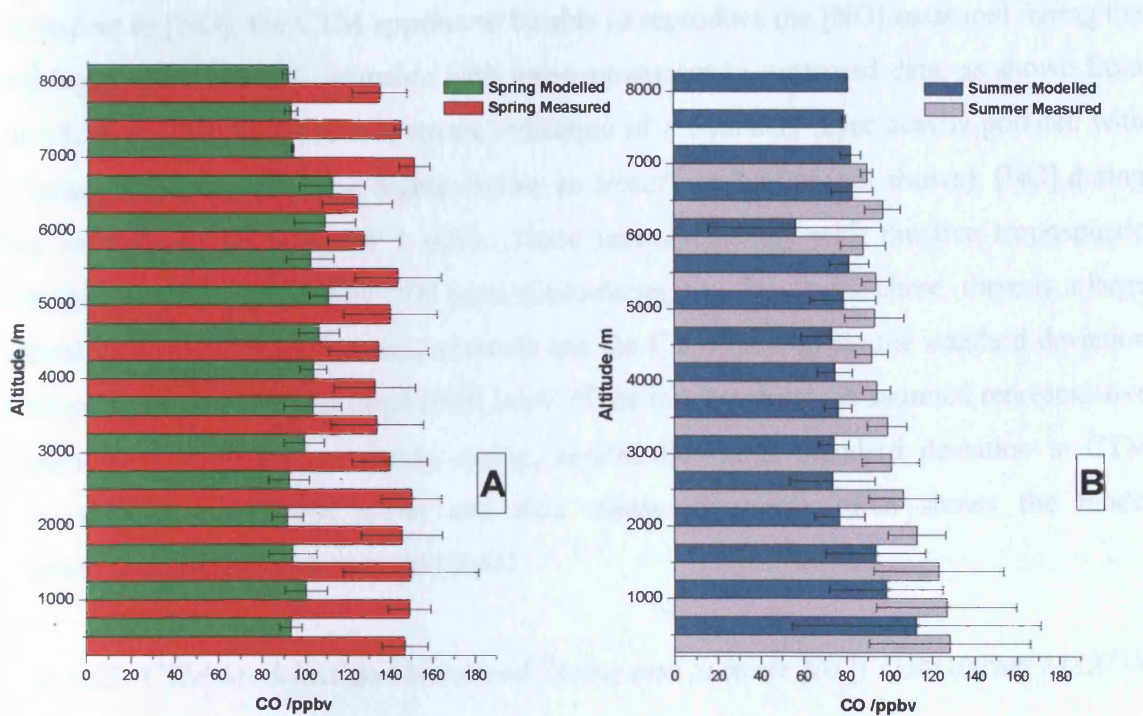
The comparison of measured and CTM ozone concentrations during the summer leg of MAXOX is shown in Figure 3.23-B. Similar to the comparison of spring [O₃], Figure 3.23-B shows that the model reproduces well the concentration of ozone measured during this portion of the MAXOX campaign, to within the 1 σ uncertainty limits. The overall comparison between the measured data during the spring and summer legs of the MAXOX program indicates that, unlike the ACSOE campaign, there was no observed spring excess of [O₃] in the planetary boundary layer, over the latitude range (30°-60° N) that the C-130 encountered. In fact, concentrations were constantly higher in summer than during the spring leg, with the excess ranging from 2-15 ppbv. The only bin that does show a slight spring ozone excess is the uppermost, the data for altitudes between 6500-7000m. This increased spring ozone may be evidence for stratospheric-tropospheric exchange bringing stratospheric air that is rich in ozone into the UT/LS region.

3.5.3: Comparison of Measured and Modelled [CO] During MAXOX Spring Campaign

The [CO] measured *in-situ*, together with [CO] predicted by the CTM, during the spring portion of the MAXOX campaign is shown in Figure 3.24-A. The data shown in Figure 3.24-A suggests that the model has problems accurately predicting the measurements for MAXOX conditions. In all of the data bins <3 km, the agreement is poor between the CTM and *in-situ* data, with almost all the model data lying outside the 1 σ standard deviation bars. The measurements indicate that there is a constantly large excess of CO, up to 50 or 60 ppbv for altitudes <3 km compared to the predictions of the model. The general concentration/height profile of the model data is similar to the measured values. The CTM indicates that there is little variation in [CO] with increasing altitude. For all data [CO] are consistently around 90-100 ppbv. The measured data have a mean concentration of 130-140 ppbv over all altitudes. This concentration of CO is at the upper reaches of the tropospheric background level (Parrish *et al.* [1998], Hallcock-Waters *et al.* [1999]). The tropospheric CO budget is dominated by anthropogenic sources (Finlayson-Pitts and Pitts [2000]) thus, [CO] measured in MAXOX are likely to be driven by local sources rather than by general chemistry. Local anthropogenic sources of CO not considered in the model could significantly effect [CO] measured during the spring portion of the MAXOX program and bias of the modelled [CO] may result.

Figure 3.24: CTM Modelled and Measured Spring and Summer [CO] Data during MAXOX.

The Bars are 1σ Standard Deviations.



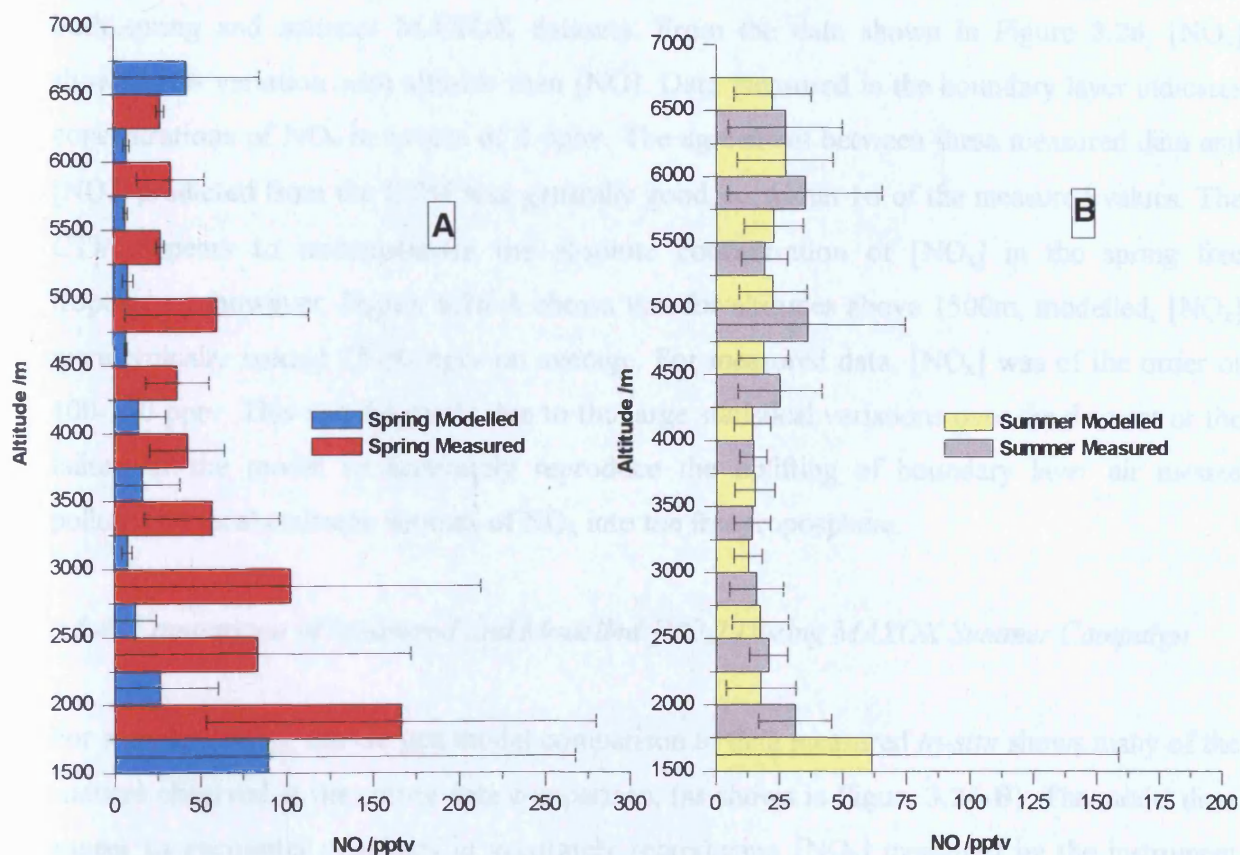
3.5.4: Comparison of Measured and Modelled [CO] During MAXOX Summer Campaign

Figure 3.24-B shows that for the summer portion of MAXOX, there is far better general agreement between [CO] predicted by the CTM and [CO] measured *in-situ* from the C-130 than during the spring leg. Only in the mid free troposphere are any significant differences observed between modelled and measure [CO] (beyond the 1σ standard deviation). Typically, measured [CO] concentrations are shown to be around 100 ppbv in the free troposphere as suggested from the CTM, with consistently higher CO concentrations measured *in-situ*. Assuming the measured [CO] to be accurate, the CTM reproduces the large excess in [CO] that was observed in the measured data when the C-130 was below 500m in altitude. Hence, the CTM models the polluted boundary layer quite well during the summer leg of MAXOX up to an altitude of 2000m.

3.5.5: Comparison of Measured and Modelled [NO] During MAXOX Spring Campaign

With respect to [NO], the CTM appears to be able to reproduce the [NO] measured during the spring leg of the MAXOX campaign with some agreement to measured data, as shown from Figure 3.32-A. Overall, there is a strong indication of a boundary layer heavily polluted with NO during the MAXOX spring flights. Below an altitude of 2000m (not shown), [NO] during spring were found to be up to 1 ppbv. These contrast greatly with the free tropospheric concentrations that are less than 100 pptv. Considering the free troposphere, there is a large statistical variation both in the measurements and the CTM data, given the standard deviation that often larger than the measured [NO] itself. If the measured data is assumed representative of typical NO concentration during spring, despite this large standard deviation in CTM values, agreement between CTM and data measured *in-situ* often shows the model consistently underestimated measured [NO].

Figure 3.25: CTM Modelled and Measured Spring and Summer [NO] Data during MAXOX. The Bars are 1 σ Standard Deviations.



3.5.6: Comparison of Measured and Modelled [NO] During MAXOX Summer Campaign

During the summer leg of the MAXOX program, measured concentration of NO in the planetary boundary layer were found to be even greater than during spring, and this showed a greater contrast to the free troposphere. Measured [NO] for altitudes 0-500 and 500-1000m were in excess of 1500 pptv. [NO] provided by the model agrees well when compared to measured [NO] during this season, as shown by Figure 3.25-B. The variability of modelled [NO] is smaller than for the corresponding 1σ standard deviations values modelled during spring. Figure 3.25-B shows that the model reproduces measured [NO] with a better degree of agreement over the free troposphere altitude range, with all values lying within the 1σ standard deviation.

3.5.7: Comparison of Measured and Modelled [NO_x] During MAXOX Spring Campaign

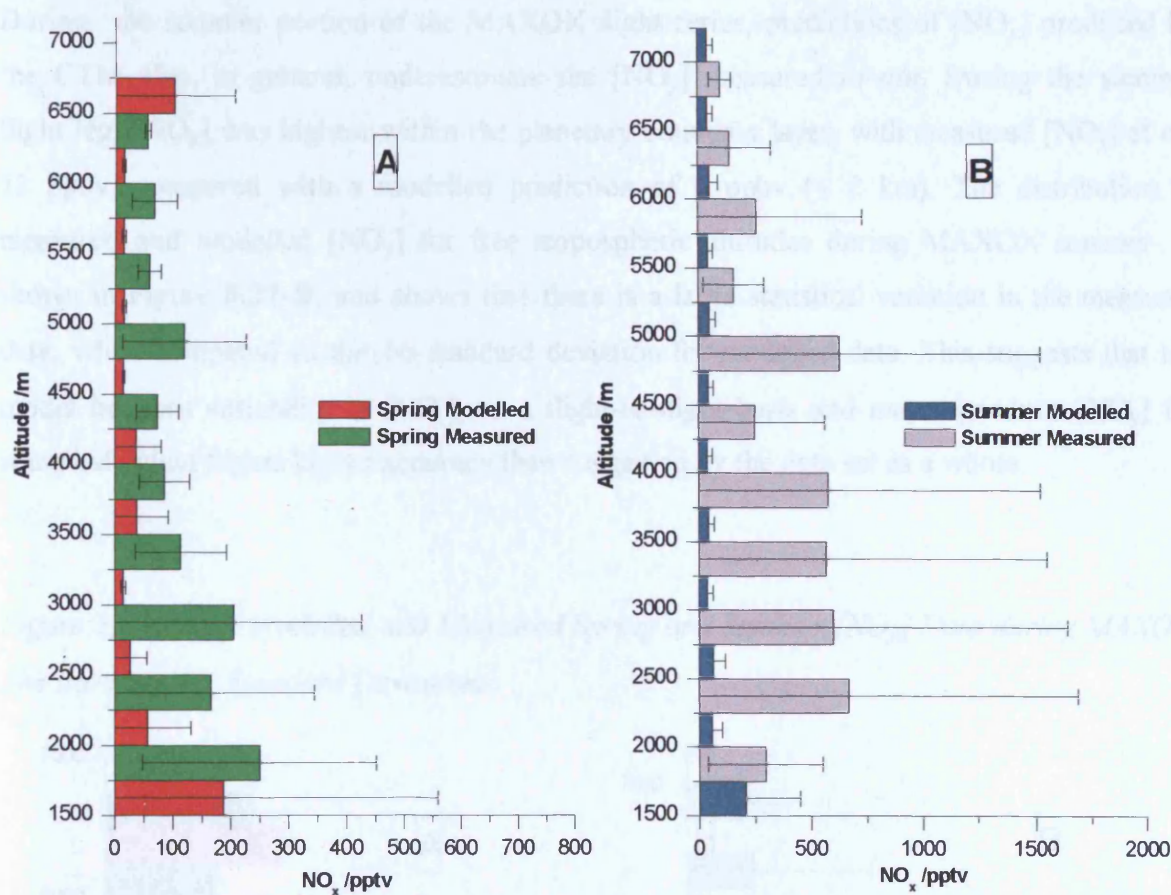
During MAXOX, the instrument problems associated with measurement of NO₂ in ACSOE were corrected and *in-situ* measurements of the sum of NO and NO₂, *i.e.* total [NO_x] were available. Climatology data for [NO_x] was compared to the prediction of the Bergen CTM for both spring and summer MAXOX datasets. From the data shown in Figure 3.26, [NO_x] showed less variation with altitude than [NO]. Data measured in the boundary layer indicates concentrations of NO_x in excess of 2 ppbv. The agreement between these measured data and [NO_x] predicted from the CTM was generally good, to within 1σ of the measured values. The CTM appears to underestimate the absolute concentration of [NO_x] in the spring free troposphere however. Figure 3.26-A shows that for altitudes above 1500m, modelled, [NO_x] were typically around 25-50 pptv on average. For measured data, [NO_x] was of the order of 100-150 pptv. This may be partly due to the large statistical variations over the data set or the failure of the model to accurately reproduce the uplifting of boundary layer air masses polluted by local emission sources of NO_x into the free troposphere.

3.5.8: Comparison of Measured and Modelled [NO_x] During MAXOX Summer Campaign

For summer [NO_x], the Bergen model comparison to data measured *in-situ* shows many of the features observed in the spring data comparison, (as shown in Figure 3.26-B). The model does appear to encounter problems in accurately reproducing [NO_x] measured by the instrument aboard the aircraft. Summer [NO_x] measured by the NOxy instrument is consistently higher than predicted. Measured concentrations of NO_x at free troposphere altitudes are shown in Figure 3.26-B to be 300-600 pptv, compared to the model prediction of 60-100 pptv. Boundary layer concentrations of NO + NO₂ (not shown) are in better agreement (> 4 ppbv).

Figure 3.26: CTM Modelled and Measured Spring and Summer [NO_x] Data during MAXOX.

The Bars are 1σ Standard Deviations.



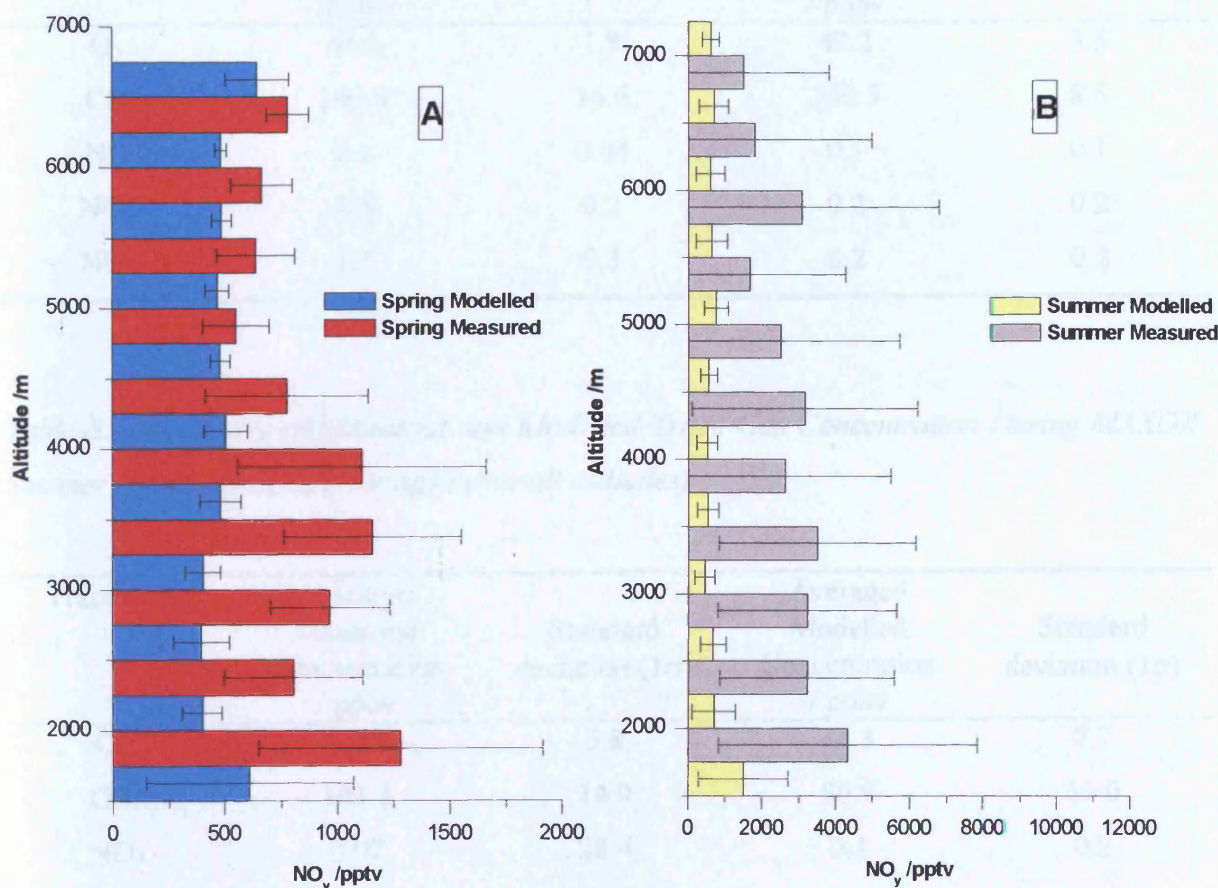
3.5.9: Comparison of Measured and Modelled [NO_y] During MAXOX Spring Campaign

The comparison of modelled and measured [NO_y] data during the April series of MAXOX flights shows similar features to those observed with respect to [NO_x]. The model also seems to have difficulty in reproducing the absolute concentration of total oxidised nitrogen measured in spring, even in the free troposphere as shown in Figure 3.27-A. A similar model underestimation of [NO_y] was observed in the boundary layer (not shown). Measured [NO_y] value during MAXOX spring leg were highest near the surface, where concentrations in excess of 7 ppbv were detected whereas modelled concentrations were 3.5 ppbv during spring. For altitudes >2.5 km, measured [NO_y] was in the range 500-1000 pptv. The CTM predictions for the free troposphere agreed reasonably well with the measured values (generally within a 1σ standard deviation), however there are several altitudes where the CTM shows an underestimation. For these measured values, [NO_y] was in the range of 100-200 pptv on average, while the model prediction was < 100 pptv.

3.5.10 Comparison of Measured and Modelled [NO_y] During MAXOX Summer Campaign

During the summer portion of the MAXOX flight series, predictions of [NO_y] produced by the CTM also, in general, underestimate the [NO_y] measured *in-situ*. During the summer flight leg, [NO_y] was highest within the planetary boundary layer, with measured [NO_y] at ca. 12 ppbv, compared with a modelled prediction of 6 ppbv (< 2 km). The distribution of measured and modelled [NO_y] for free tropospheric altitudes during MAXOX summer is shown in Figure 3.27-B, and shows that there is a large statistical variation in the measured data, when compared to the 1σ standard deviation for modelled data. This suggests that the model has less variability in [NO_y] on a flight-to-flight basis and may reproduce [NO_y] for some individual flights higher accuracy than suggested by the data set as a whole.

Figure 3.27: CTM Modelled and Measured Spring and Summer [NO_y] Data during MAXOX. The Bars are 1σ Standard Deviations.



A summary of the model/measured comparisons for [NO_y] and other trace gases measured during the MAXOX campaign are given in Tables 3.3 and 3.4. From Table 3.3 the comparison of measured and modelled data during spring suggests that when averaged over all altitudes the CTM is able to reproduce measured concentration of ozone and NO with a high degree of accuracy, while modelled values of [CO], [NO_x] and [NO_y] are underestimated. Similar comparisons of modelled and measured data during summer are shown in Table 3.4. During the July and August MAXOX flights the CTM was able to accurately predict [O₃], [NO] and [CO] with a high degree of accuracy, with modelled [NO_x] and [NO_y] showing an underestimation of measured concentrations.

Table 3.3: Summary of Measured and Modelled Trace Gas Concentration During MAXOX Spring Campaign (Data averaged over all altitudes)

Trace Gas	Averaged Measured Concentration /ppbv	Standard deviation (1σ)	Averaged Modelled Concentration / ppbv	Standard deviation (1σ)
O ₃	45.5	1.8	42.2	3.5
CO	140.9	16.6	100.5	8.6
NO	0.1	0.04	0.1	0.1
NO _x	0.8	0.2	0.2	0.2
NO _y	1.7	0.3	0.2	0.2

Table 3.4: Summary of Measured and Modelled Trace Gas Concentration During MAXOX Summer Campaign (Data averaged over all altitudes)

Trace Gas	Averaged Measured Concentration / ppbv	Standard deviation (1σ)	Averaged Modelled Concentration / ppbv	Standard deviation (1σ)
O ₃	52.5	5.8	44.3	7.7
CO	103.3	14.9	80.9	16.0
NO	0.07	28.4	0.1	0.2
NO _x	0.5	0.4	0.3	0.5
NO _y	1.6	0.9	1.1	0.9

3.6: MAXOX Ozone Tendencies

Although comparison between model calculations of trace gas concentrations and measurements made *in-situ* has identified areas of potential concern in the performance of the CTM, it was assumed that the output of the CTM was able to predict concentration of trace gases measured *in-situ* with sufficient accuracy to use a combination of modelled and measured data to calculate flight track ozone tendencies during the MAXOX campaign. The reactions that control P(O₃) and L(O₃) were described in section 3.3. The majority of concentrations of trace gases that control ozone production/loss were measured *in-situ* during MAXOX, hence, equations 3.2 and 3.3 could be solved *via* substitution. Only [OH] and [HO₂] were not measured during the MAXOX campaign. For these parameters, CTM output data were used. In order for the correct time format to be used, all measured data was converted to the same time format as the model, specifically 100-second averages, with linearly interpolated values if necessary. The parameter denoted as *F*, (see equation (3.4), was calculated on a one-second time frame and similarly averaged up to 100 seconds. Typically values of the *F* parameter indicated that the conversion of O(¹D) → OH had an efficiency of 5-10% during MAXOX. Since modelled [HO_x] data was only available for August (F. Flatøy, *private communication*), ozone tendencies for these flights only have been calculated. Each flight will be dealt with individually. The trajectories data used in this analysis are those available to the MAXOX data community *via* a database provided by the University of Cambridge, UK (CAS). (Cambridge Trajectory Server located at (www.atm.ch.cam.ac.uk/~steve/trajectories/)). In total, five MAXOX August flights have been considered in this chapter. A summary of the location and goals of these flights are given in Table 3.5.

3.6.1: MAXOX Flight A700, 2/8/99

Flight A700 was a low-level flight that sampled air masses close to the surface of the North Sea. Trajectories indicated that there were two major air masses encountered in flight A700. The first appeared to have travelled close to the surface over the European continent (Germany and Holland) before being sampled by the aircraft relatively early in the flight, including the low altitude run. This surface air was likely to be heavily polluted, owing to its origin and proximity to large-scale anthropogenic trace gas sources. The second air mass sampled had an oceanic origin, having travelled for many hours in the mid free troposphere. This air mass travelled across the Atlantic, across the Bay of Biscay and up over Normandy and the south of

Table 3.5: MAXOX August Flights Location, Aims and Trends

Flight code	Date	Location	Objective
A700	2/8/99	North Sea	Low Altitude Sampling
A701	4/8/99	Irish Sea	Deep Profiling
A702	5/8/99	Western Isles	Clean and polluted air sampling
A703	6/8/99	Bristol Channel	High altitude Sampling
A704	9/8/99	Western Isles	Deep Profiling

the UK. The trajectory data from the CAS server for this flight is plotted in Figure 3.28. Calculated flight track ozone tendencies for this flight are shown in Figure 3.29.

The data in Figure 3.29 shows that for the low altitude portion of the flight there was large-scale ozone production, especially in the middle of the sortie when the C-130 skimmed the surface at altitude of *ca.* 50 feet. Pollution tracers during this flight were very high, *e.g.* [CO] was in excess of 250 ppbv whilst [NO_x] for this low altitude period were similarly elevated, in excess of >10 ppbv. Overall, for this MAXOX flight, the net ozone tendency is positive, *i.e.* there is net production of ozone for all altitudes. Ignoring the low altitude, high NO_x portion of the flight, averaging the data for a 24 hour period indicates a net ozone production of 1.3 ppbv per day when averaged over the whole flight. NO_{critical} data for this flight was also worked up as described in Chapter 2. The level of "critical" NO, where L(O₃) switches to P(O₃) was calculated to be 16.8 pptv, when averaged for the entire flight. This compares to a mean concentration of NO that was 31 pptv for flight A700.

Figure 3.28: Trajectories for MAXOX Flight A700, 2/8/99.

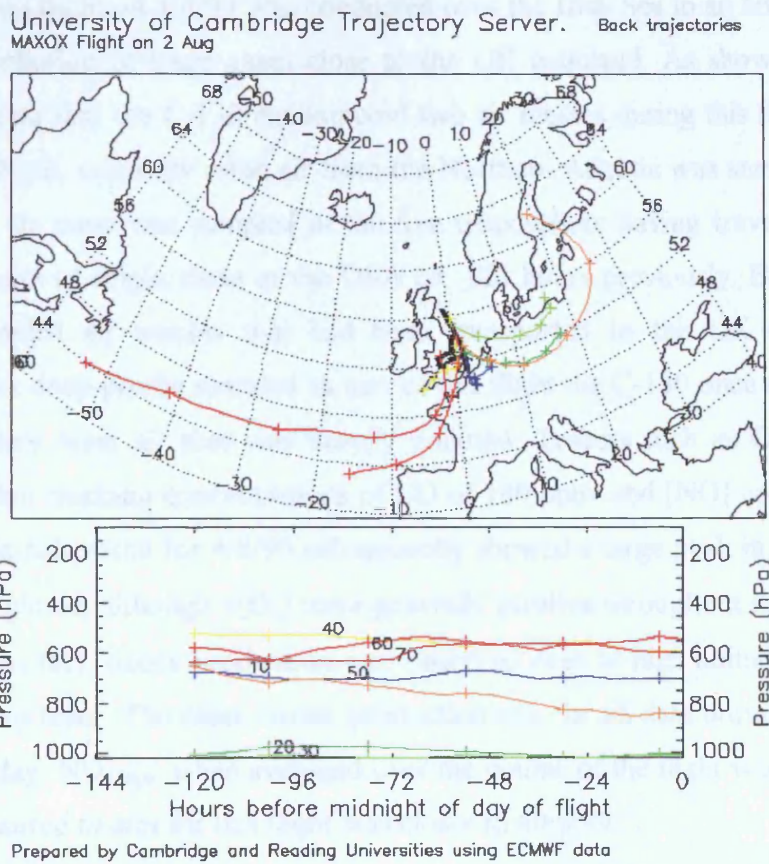
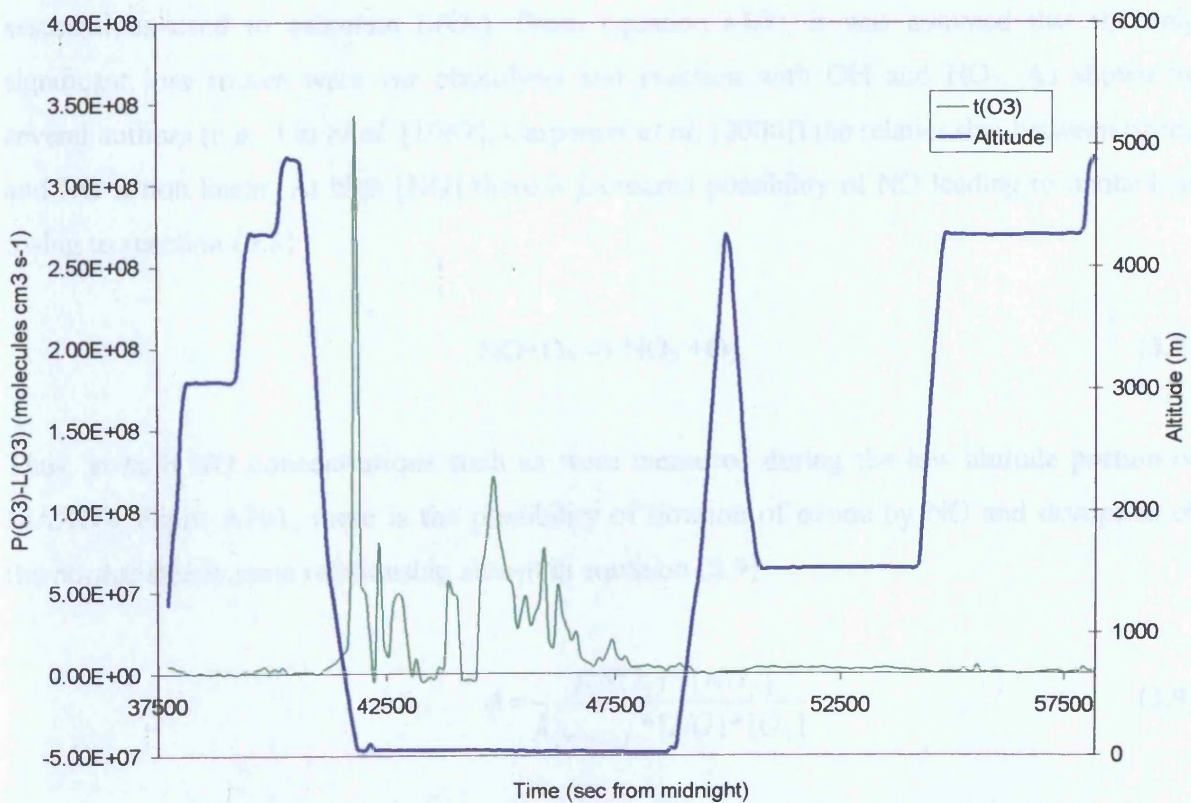


Figure 3.29: Ozone Tendency for MAXOX Flight A700, 2/8/99



3.6.2 MAXOX Flight A701, 4/8/99

The deep profiling flight on 4/8/99 was conducted over the Irish Sea in an attempt to ascertain the altitude distribution of trace gases close to the UK mainland. As shown in Figure 3.30, trajectories indicate that the C-130 encountered two air masses during this flight. For the vast majority of the flight, relatively clean air from the Northern Atlantic was sampled. Figure 3.30 shows that this air mass was sampled in the free troposphere having travelled off the open ocean, with a point of origin close to the USA *ca.* 120 hours previously. Below *ca.* 800 hPa the aircraft sampled air masses that had been transported to the UK from France and Germany. For the deep profile sampled as part of this flight the C-130 once again encountered planetary boundary layer air that was heavily polluted. Tracers such as CO and NO_x were high below 1.5 km reaching concentrations of CO of 180 ppbv and [NO] up to 350 pptv. The ozone tendencies calculated for 4/8/99 subsequently showed a large peak in ozone production in this pollution plume, although $\tau(\text{O}_3)$ were generally positive throughout the flight, as shown in Figure 3.31. In fact, ozone production was observed even at high altitudes away from the polluted boundary layer. The mean ozone production rate for all data during flight A701 was 11.4 ppbv per day. NO_{critical} when averaged over the course of the flight was *ca.* 15 pptv. The mean [NO] measured *in-situ* for this flight was closer to 40 pptv.

The large net ozone production calculated for this requires further quantification. The high value of P(O₃) (12 ppbv per day) is probably erroneous, owing to the breakdown of assumptions used to calculate L(O₃). From equation (3.3), it was assumed that the only significant loss routes were *via* photolysis and reaction with OH and HO₂. As shown by several authors (*e.g.*, Liu *et al.* [1987], Carpenter *et al.* [2000]) the relationship between ozone and NO is non linear. At high [NO] there is increased possibility of NO leading to ozone loss owing to reaction (3.8)

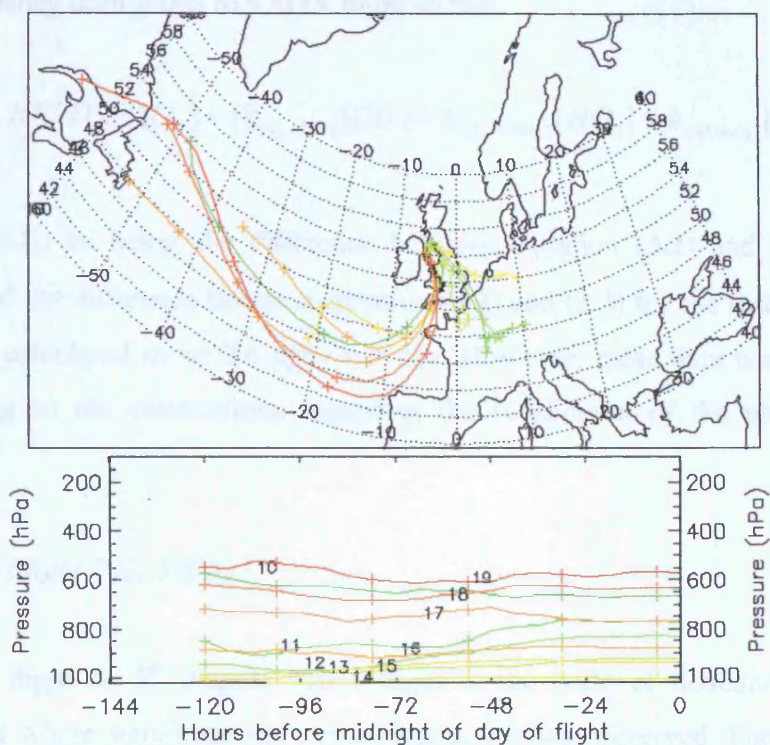


Thus, at high NO concentrations such as were measured during the low altitude portion of MAXOX Flight A701, there is the possibility of titration of ozone by NO and disruption of the normal steady state relationship shown in equation (3.9)

$$\phi = \frac{j(\text{NO}_2) * [\text{NO}_2]}{k_{(\text{NO} + \text{O}_3)} * [\text{NO}] * [\text{O}_3]} \quad (3.9)$$

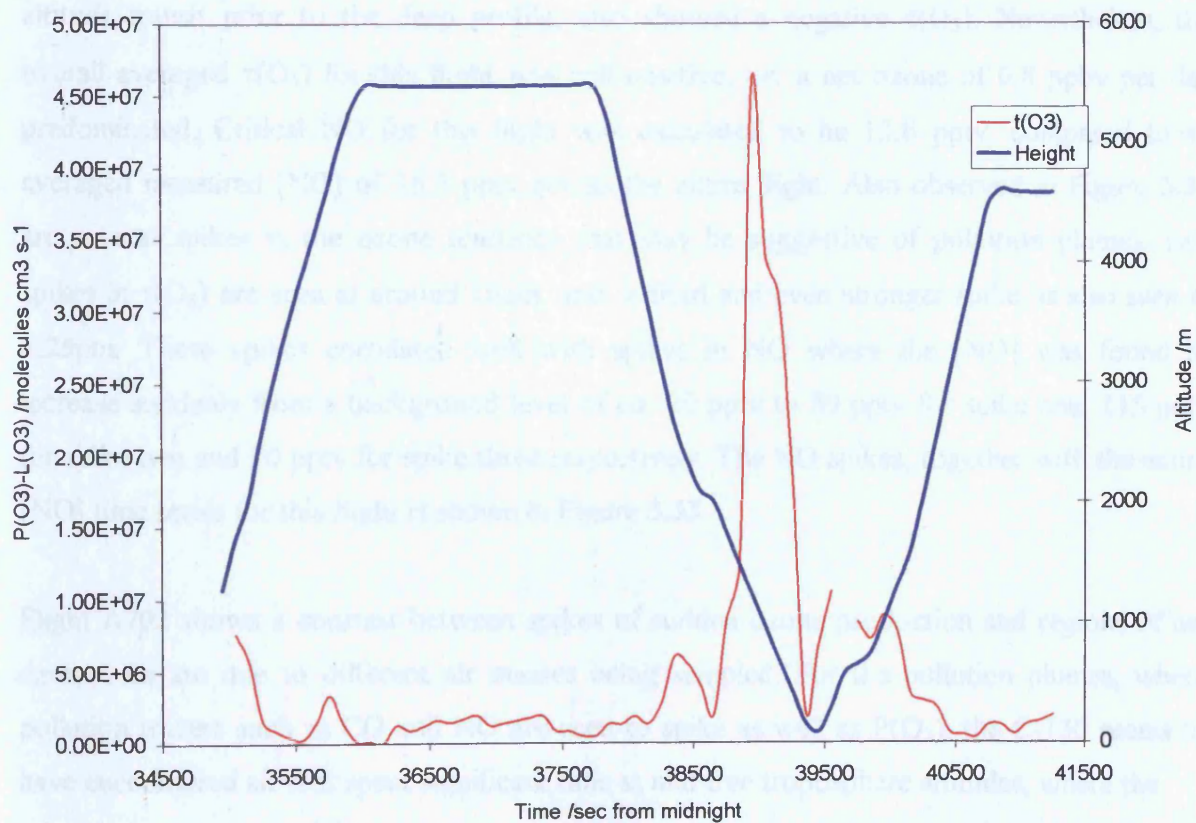
Figure 3.30: Trajectories for MAXOX Flight A701, 4/8/99

University of Cambridge Trajectory Server. Back trajectories
MAXOX Flight on 4 Aug



Prepared by Cambridge and Reading Universities using ECMWF data

Figure 3.31: Ozone Tendency for MAXOX Flight A701, 4/8/99



Assuming that this is the case, *i.e.* NO₂ produced by in reaction 3.8 does not go on and lead to subsequent ozone production, the additional NO+O₃ term in equation (3.3) does affect the net ozone tendency during this MAXOX flight so that

$$L(O_3) = jO(^1D).F.[O_3] + \{k_{(O_3+OH)}[OH] + k_{(O_3+HO_2)}[HO_2] + k_{(NO+O_3)}[NO]\} * [O_3] \quad (3.10)$$

Considering $\tau(O_3)$ as being the difference between equation (3.2) and (3.10) for the low altitude run and the difference between equation (3.2) and (3.3) for the rest of the flight, $\tau(O_3)$ for A701 was calculated to be 0.6 ppbv per day. However, these data need to be considered carefully owing to the assumptions regarding the breakdown of the photostationary state described.

3.6.3: MAXOX Flight 702, 5/8/99

The MAXOX flight on 5th August was a flight to the north of Scotland and was the first MAXOX flight where significant net ozone destruction was observed. Figure 3.32 shows the plot of $\tau(O_3)$ with respect to time for this flight. The flight track of the aircraft suggests that where C-130 began a deep profile at around 12:30pm the air masses encountered showed a large-scale photochemical loss of ozone, although portions of the flight such as the high altitude transit prior to the deep profile, also showed a negative $\tau(O_3)$. Nevertheless, the overall averaged $\tau(O_3)$ for this flight was still positive, *i.e.* a net ozone of 0.8 ppbv per day predominated. Critical NO for this flight was calculated to be 13.6 pptv, compared to an averaged measured [NO] of 16.5 pptv across the entire flight. Also observed in Figure 3.32 are several spikes in the ozone tendency that may be suggestive of pollution plumes, two spikes in $\tau(O_3)$ are seen at around 10am, and a third and even stronger spike, is also seen at 3:25pm. These spikes correlated well with spikes in NO where the [NO] was found to increase suddenly from a background level of *ca.* 20 pptv to 80 pptv for spike one, 115 pptv for spike two and 70 pptv for spike three respectively. The NO spikes, together with the entire [NO] time series for this flight is shown in Figure 3.33.

Flight A702 shows a contrast between spikes of sudden ozone production and regions of net ozone loss are due to different air masses being sampled. For the pollution plumes, where pollution tracers such as CO and NO are seen to spike as well as P(O₃), the C-130 seems to have encountered air that spent significant time at mid free troposphere altitudes, where the

Figure 3.32: Ozone Tendency for MAXOX Flight A702, 5/8/99

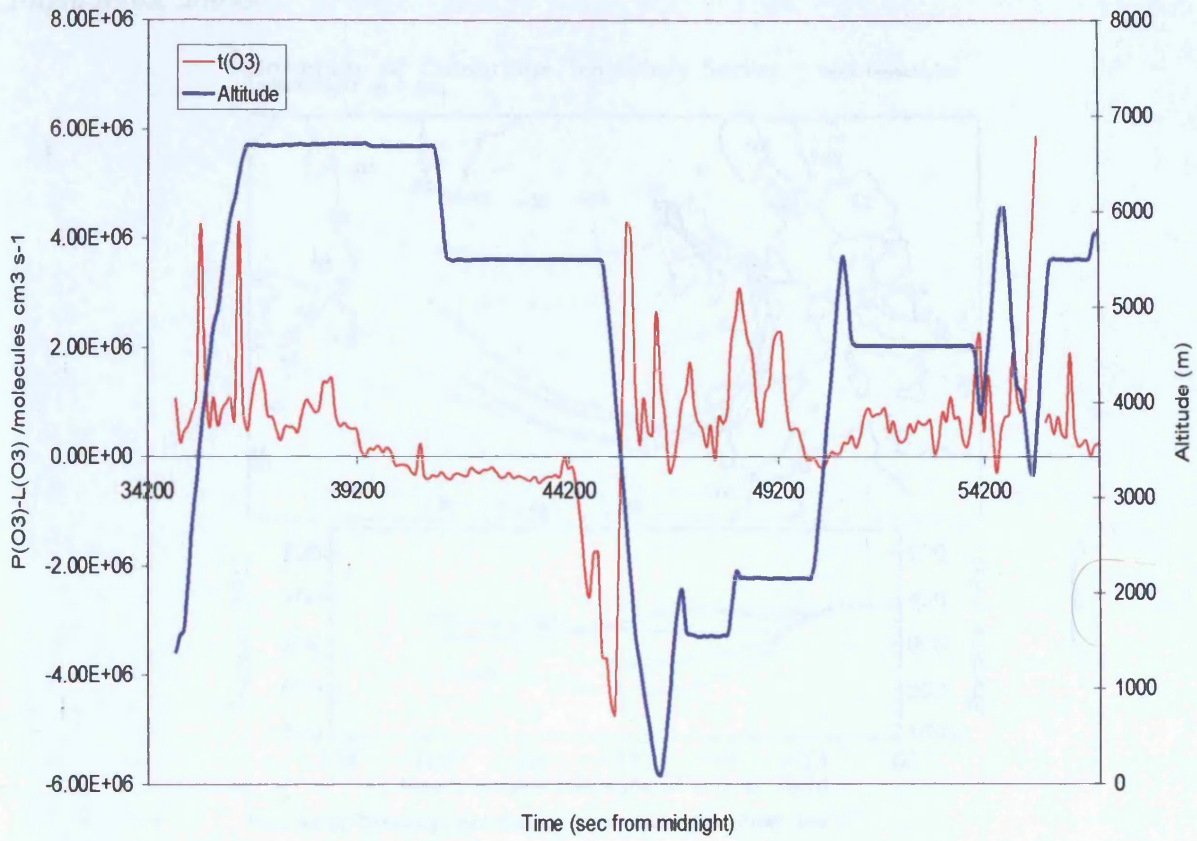


Figure 3.33: [NO] vs. time for MAXOX Flight A702, 5/8/99, Showing Pollution Plumes

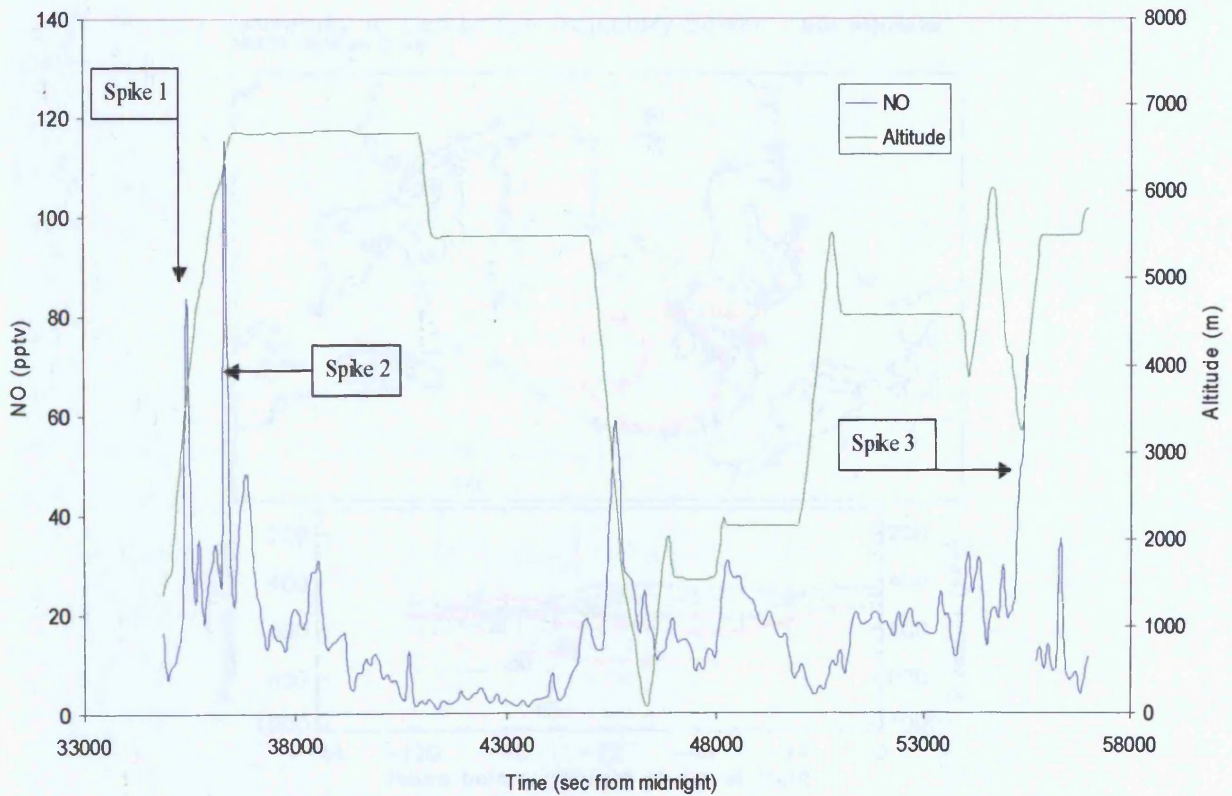


Figure 3.34: Back Trajectories of Air masses Associated with Plumes 1 and 2 for MAXOX Flight A702, 5/8/99.

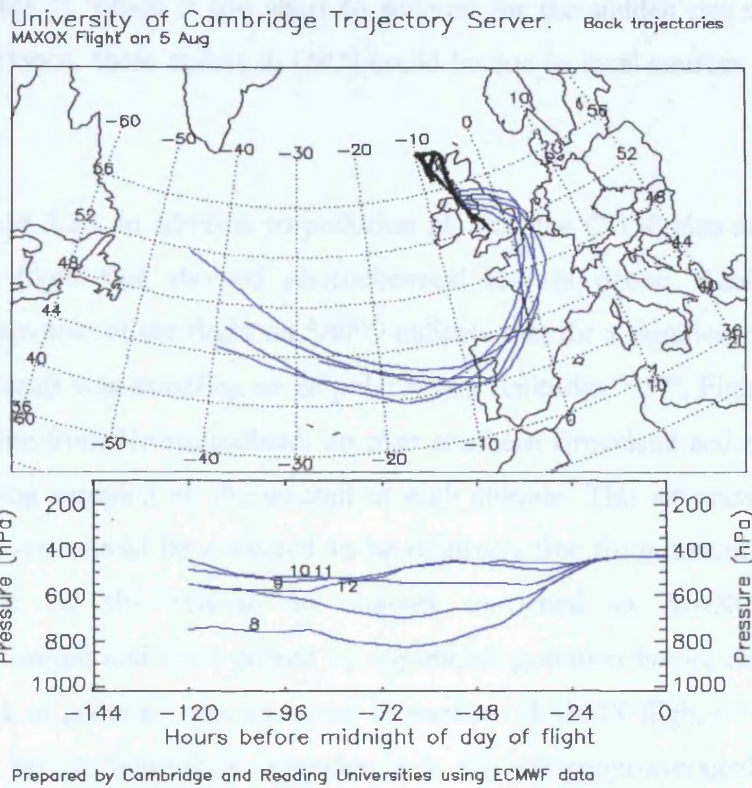
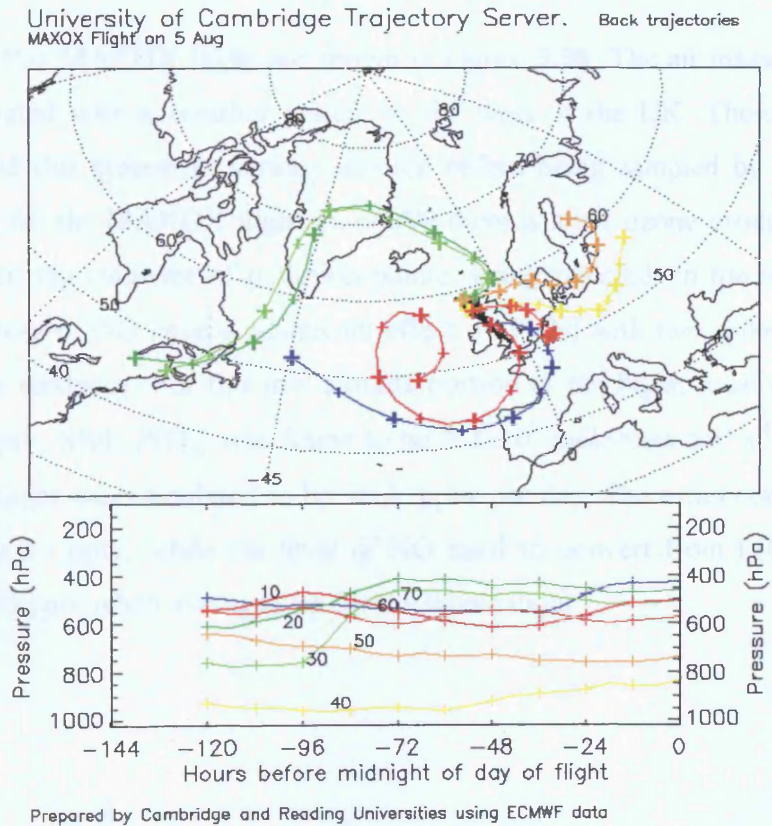


Figure 3.35: Overall Trajectories for MAXOX Flight A702, 5/8/99.



trajectories show no contact with the boundary layer for at least 72 hours (see Figure 3.34). The lifetime of NO in the troposphere is of the order of 1 day (Jacob *et al.* [1996], Finlayson-Pitts and Pitts [2000]), which is too short to account for the sudden rise in [NO] and thus, P(O₃) observed. Hence, these spikes in [NO] could be due to local sources, rather than long-range transport.

As shown in Figure 3.32, in addition to pollution plumes, the C-130 also sampled air masses in this MAXOX flight that showed photochemical loss of ozone. Analysis of the back trajectories for the whole of the flight on 5/8/99 indicate that for a significant portion of the O₃ loss period the aircraft was sampling air of polar origin (latitudes > 57°, Figure 3.35). This air seems to have come from Newfoundland, up over southern Greenland and down northeast of Iceland before being sampled by the aircraft at high altitude. This air mass has had minimal contact with land and would be expected to be relatively free from human influence. This is not representative of the typical air masses measured in MAXOX that are of European/Atlantic origin and have picked up significant pollution before detection by the C-130. The influence of polar air was also seen in another MAXOX flight (9/8/99) and may be the reason for a strong latitudinal dependence in the campaign-averaged $\tau(\text{O}_3)$, which is discussed in section 3.7.

3.6.4: MAXOX Flight A703, 6/8/99

Trajectories for this MAXOX flight are shown in Figure 3.36. The air masses sampled in this flight are associated with a weather system to the west of the UK. These air masses have circulated around this system at various altitude before being sampled by the C-130. Figure 3.37 shows that for the MAXOX flight on 6/8/99 there is a net ozone production throughout this flight with strong evidence of pollution plumes being sampled. In the early stages of the flight, local sources of NO have a significant effect on P(O₃) with two spikes observed in the calculated ozone tendency. For this low altitude portion of the flight, local sources NO often exceeded 200 pptv, while P(O₃) was found to be $> 1 \times 10^7$ molecules cm³ s⁻¹. The mean $\tau(\text{O}_3)$ over the whole flight was calculated to be +0.3 ppbv per day. The mean concentration of NO was found to be 34 pptv, while the level of NO need to convert from L(O₃) to P(O₃) *i.e.*, NO_{critical} was 8.66 pptv when averaged up for the whole flight.

Figure 3.36: Overall Trajectories for MAXOX Flight A703, 6/8/99.

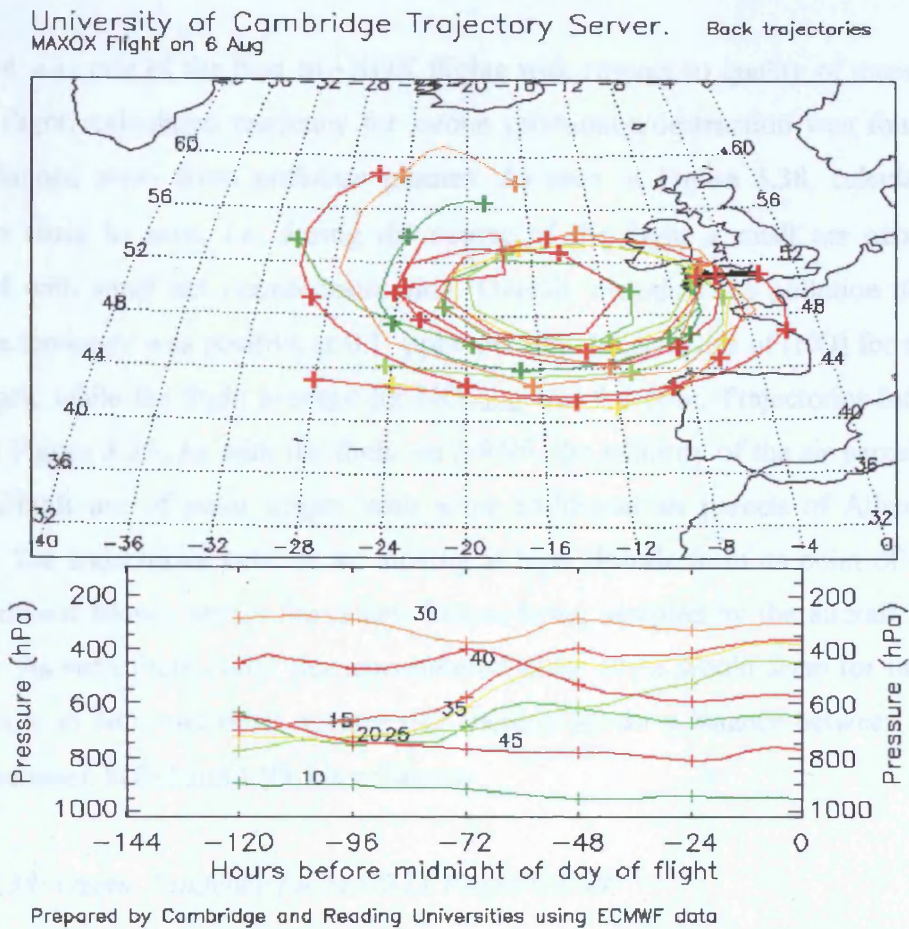
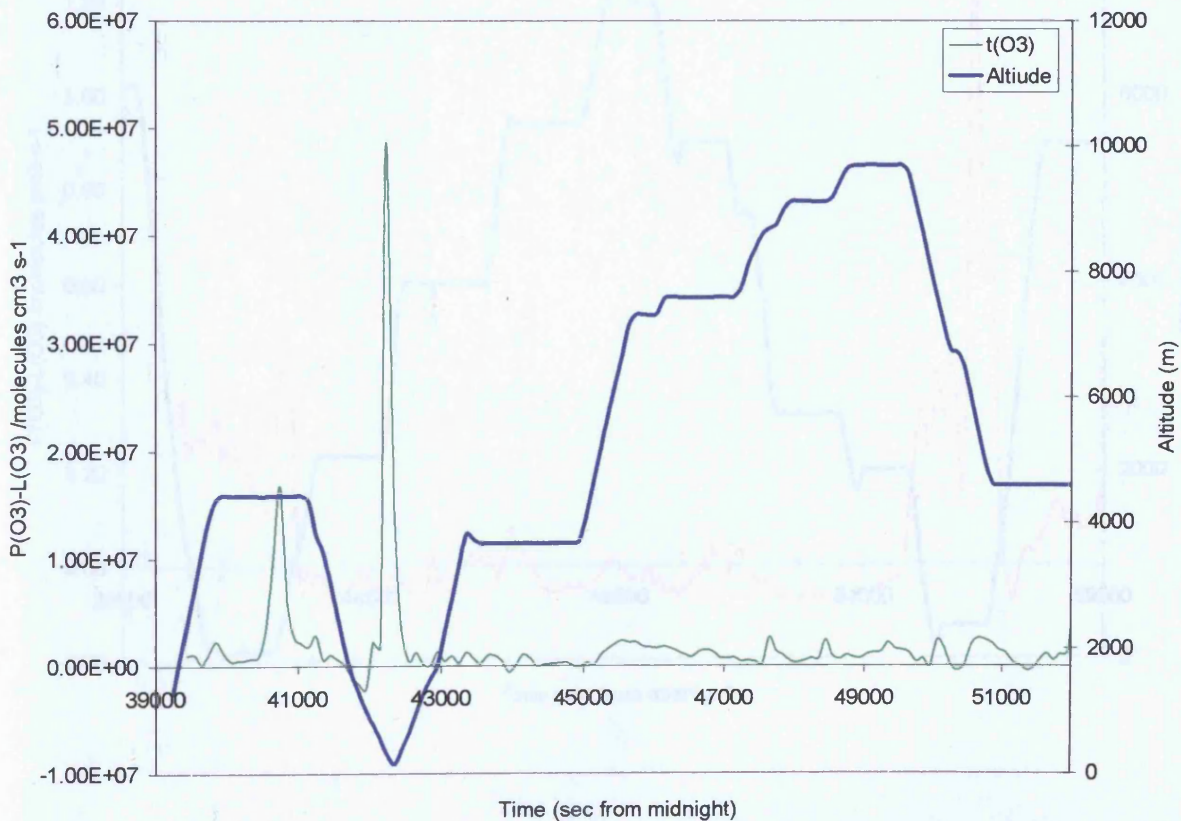


Figure 3.37: Ozone Tendency for MAXOX Flight 6/8/99



3.6.5: MAXOX Flight A704, 9/8/99

This flight was one of the best MAXOX flights with respect to quality of measurement data. For this flight, calculated tendency for ozone production/destruction was found to be very finely balanced away from pollution plumes. As seen in Figure 3.38, calculated values of $\tau(\text{O}_3)$ are close to zero, *i.e.* during the course of the flight a small net ozone production alternated with small net ozone destruction. Overall, including the pollution plume sampled, net ozone tendency was positive at 0.1 ppbv per day. Mean levels of $[\text{NO}]$ for this flight were *ca.* 12 pptv, while the flight average for $\text{NO}_{\text{critical}}$ was 9.4 pptv. Trajectories for this flight are shown in Figure 3.39. As with the flight on 5/8/99, the majority of the air parcels encountered by the aircraft are of polar origin, with some additional air parcels of Atlantic origin also sampled. The trajectories indicate air moving at high altitude from its point of origin close to Prince Edward Island, across the ocean, before being sampled by the aircraft to the west of Scotland. As with flight A701 that encountered polar air, it would seem for these air parcels that are low in NO_x and other species that there is almost a balance between photochemical balance between $\text{P}(\text{O}_3)$ and $\text{L}(\text{O}_3)$ is achieved.

Figure 3.38: Ozone Tendency for MAXOX Flight 9/8/99

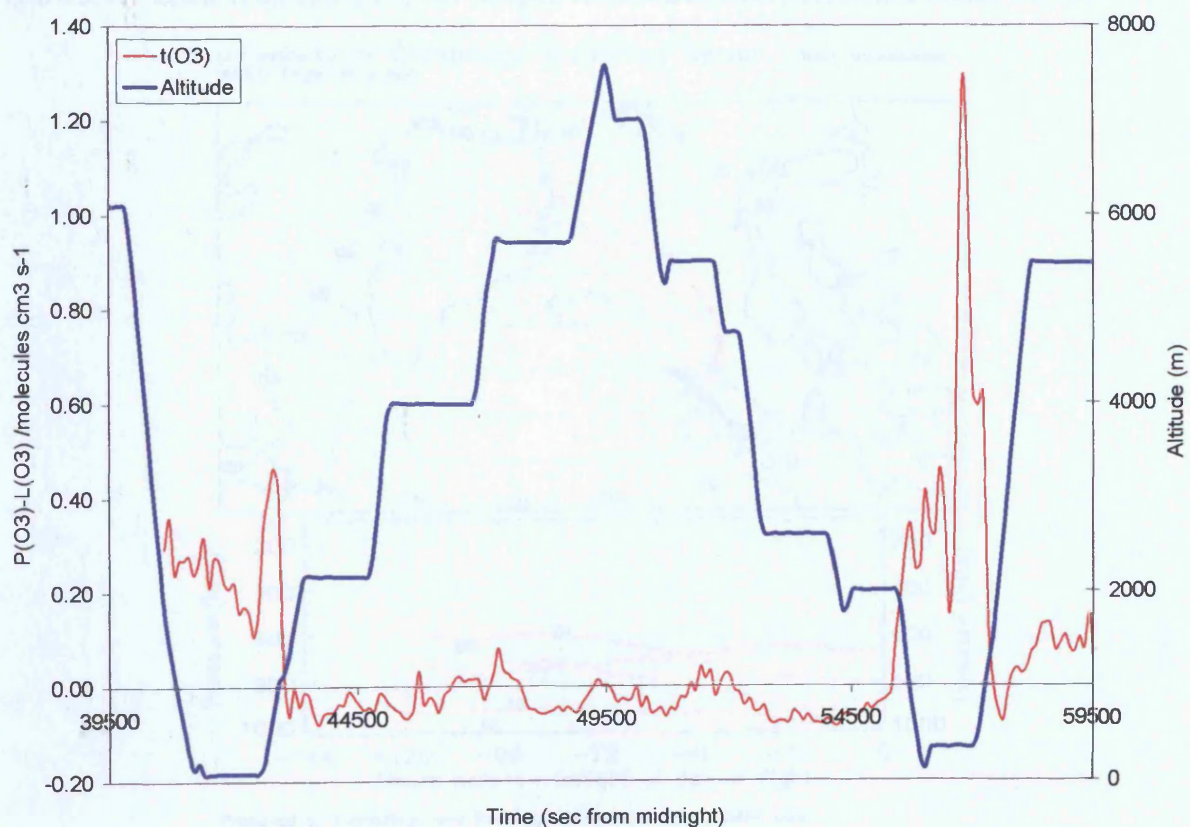
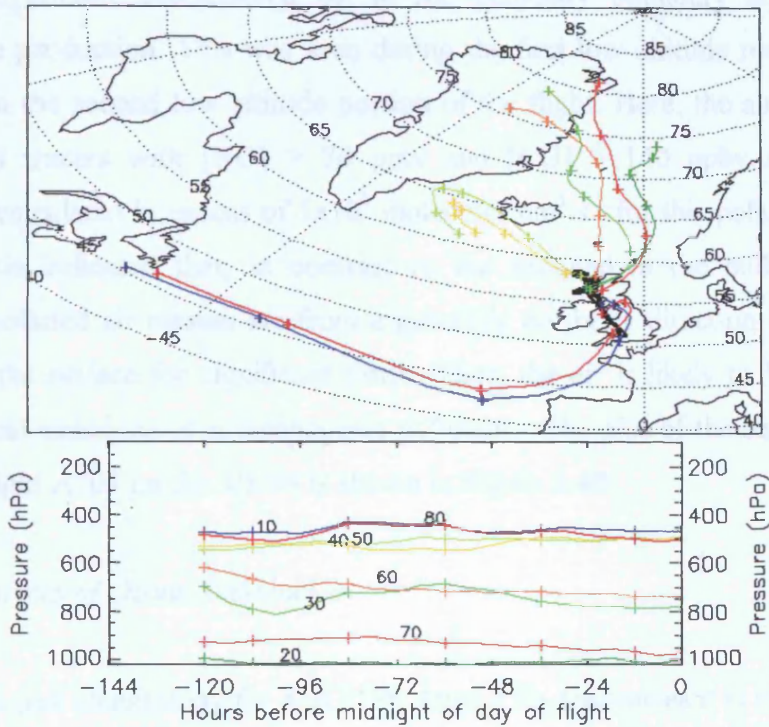


Figure 3.39: Trajectories for MAXOX Flight 9/8/99

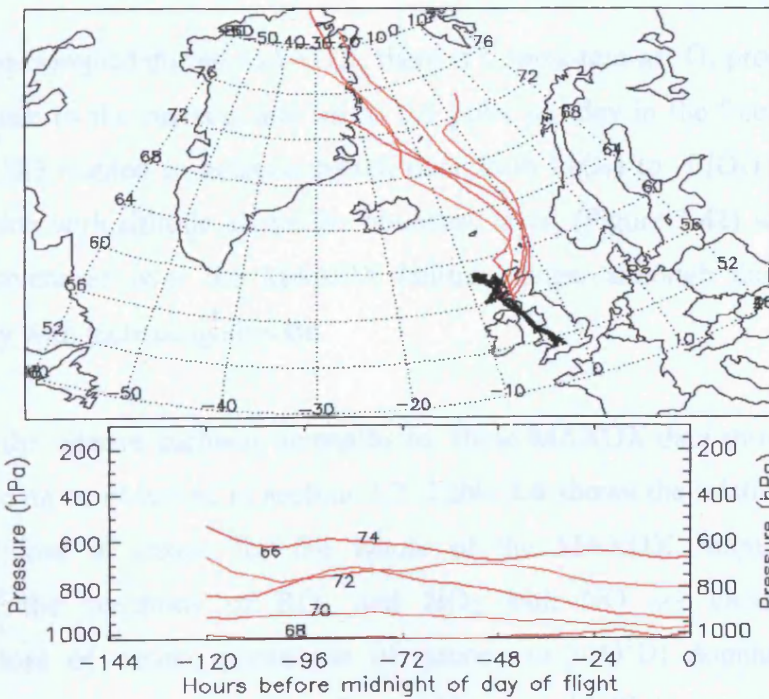
University of Cambridge Trajectory Server. Back trajectories
MAXOX Flight on 9 Aug



Prepared by Cambridge and Reading Universities using ECMWF data

Figure 3.40: Back Trajectories of Air masses Associated with Pollution Plumes 9/8/99.

University of Cambridge Trajectory Server. Back trajectories
MAXOX Flight on 9 Aug



Prepared by Cambridge and Reading Universities using ECMWF data

As with several other MAXOX flights, the overall average ozone tendency was influenced by the fact that the aircraft sampled significant pollution plumes during the flight. As shown in Figure 3.38 the aircraft encountered air in the planetary boundary layer that showed significant ozone production. This was seen during the first low altitude run, and to an even greater extent, in the second low altitude portion of the flight. Here, the air was found to be rich in pollution tracers with $[\text{NO}] > 70$ pptv and $[\text{CO}] > 140$ ppbv detected. Ozone production was calculated in excess of 1×10^7 molecules $\text{cm}^3 \text{s}^{-1}$ for this pollution plume. Back trajectory analysis indicated that, in contrast to the sampled in the middle of the flight, although these polluted air masses are from a generally northerly direction they had travelled close to the earth's surface for significant times. Thus, the air is likely to have been heavily influenced by local emissions of anthropogenic pollutants. The plot of the back trajectories for this portion of flight A703 on the 9/8/99 is shown in Figure 3.40.

3.7: Overall Features of Ozone Tendencies

Plotting up an overall climatology for MAXOX August O_3 tendencies it is clear that there is a net production of ozone at all altitudes investigated for this flight campaign. Since the August series of missions many air masses over a range of latitudes were sampled, data were summarised by binning $\tau(\text{O}_3)$ by altitude. Data were separated into a total of 16 data bins with a 500m separation in each case, as shown in Figure 3.41.

For the air masses sampled during MAXOX, there is a consistent net O_3 production of up to 2 ppbv per day close to the surface, and up to 0.5 ppbv per day in the free troposphere. The critical level of NO needed to achieve switch over from L(O_3) to P(O_3) was calculated to have little variation with altitude above the boundary layer, (Figure 3.42) with a value of 10-15 pptv when averaged over the MAXOX latitude range, although the level of $\text{NO}_{\text{critical}}$ decreases slightly with increasing altitude.

Examination of the relative pathway strengths for these MAXOX data showed similar trends in the P/L (O_3) data as observed in section 3.2. Table 3.6 shows the relative contributions to production and loss of ozone for the whole of the MAXOX August campaign. The contribution of the reactions of RO_2 and HO_2 with NO are closely matched. For photochemical loss of ozone, photolysis of ozone *via* $j\text{-(O}^1\text{D)}$ dominates during these MAXOX flights with a net contribution of over 60% to total L(O_3), compared to around 23% and 12% owing to reaction of O_3 with HO_2 and OH respectively.

Figure 3.41: Binned Ozone Tendency Data for MAXOX August Flights Series.

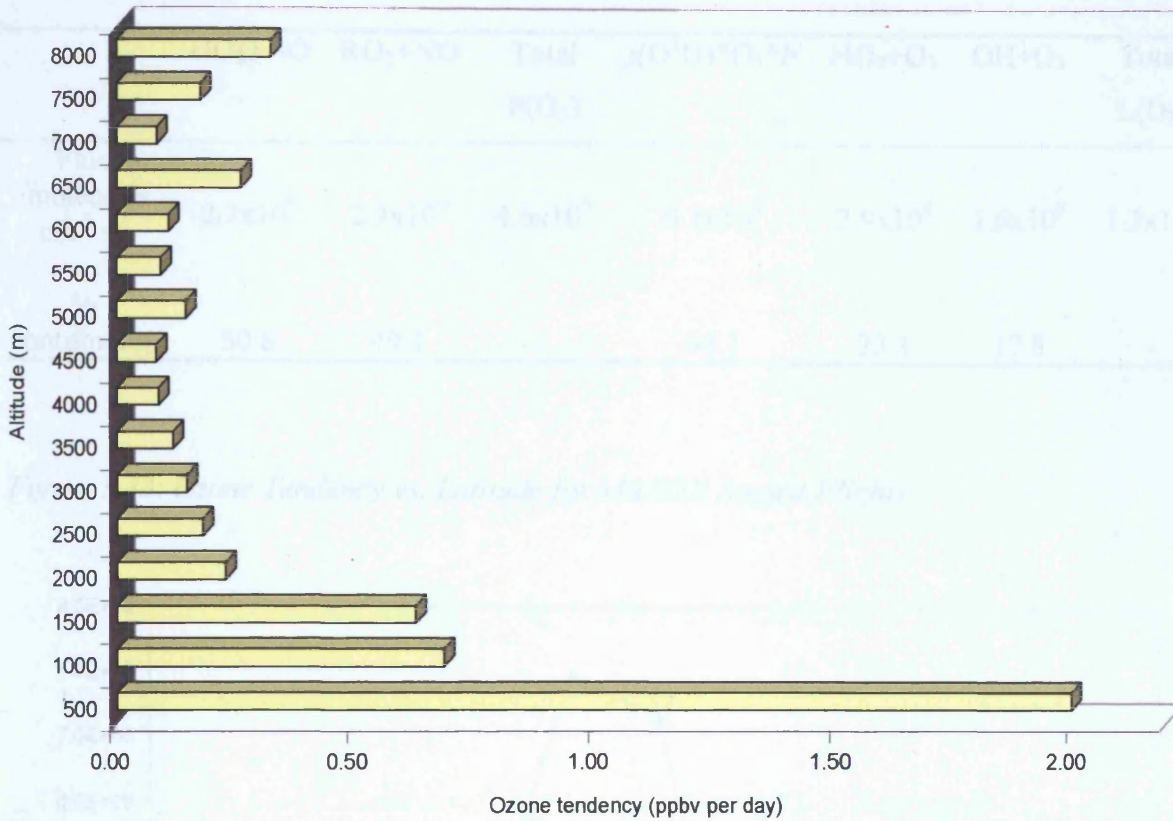


Figure 3.42: Binned $NO_{critical}$ data for Free Troposphere During MAXOX August Flights Series

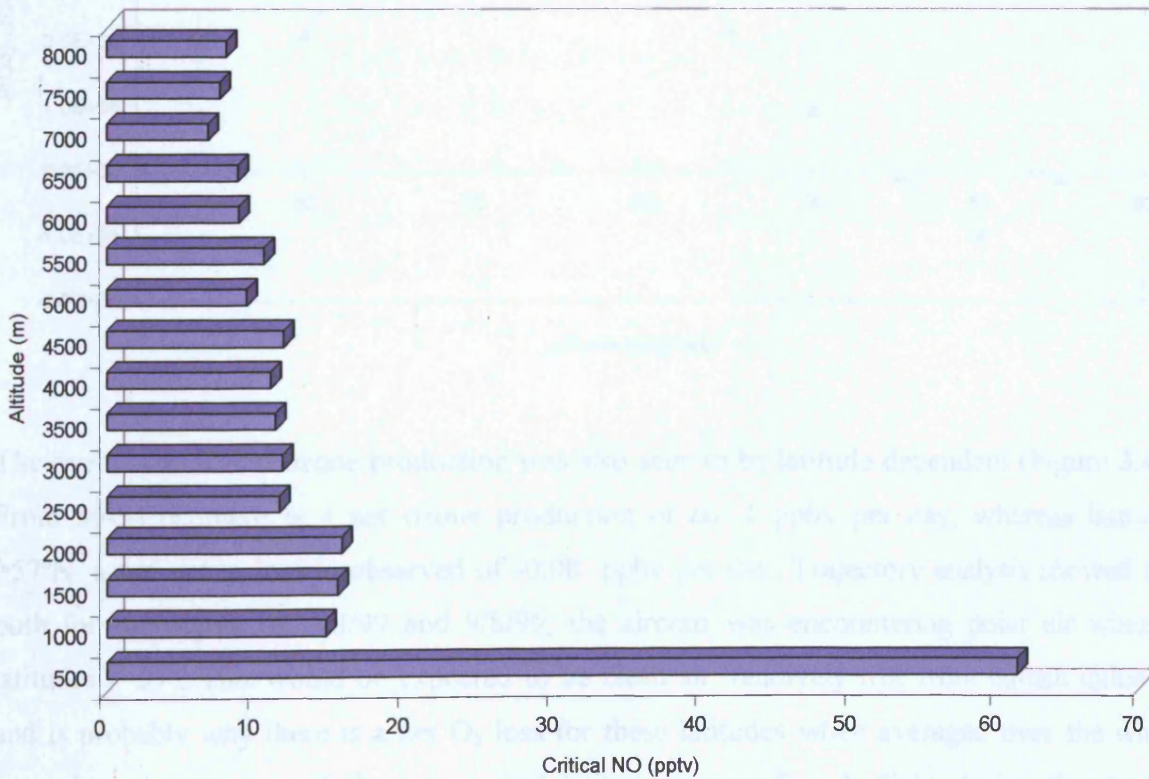
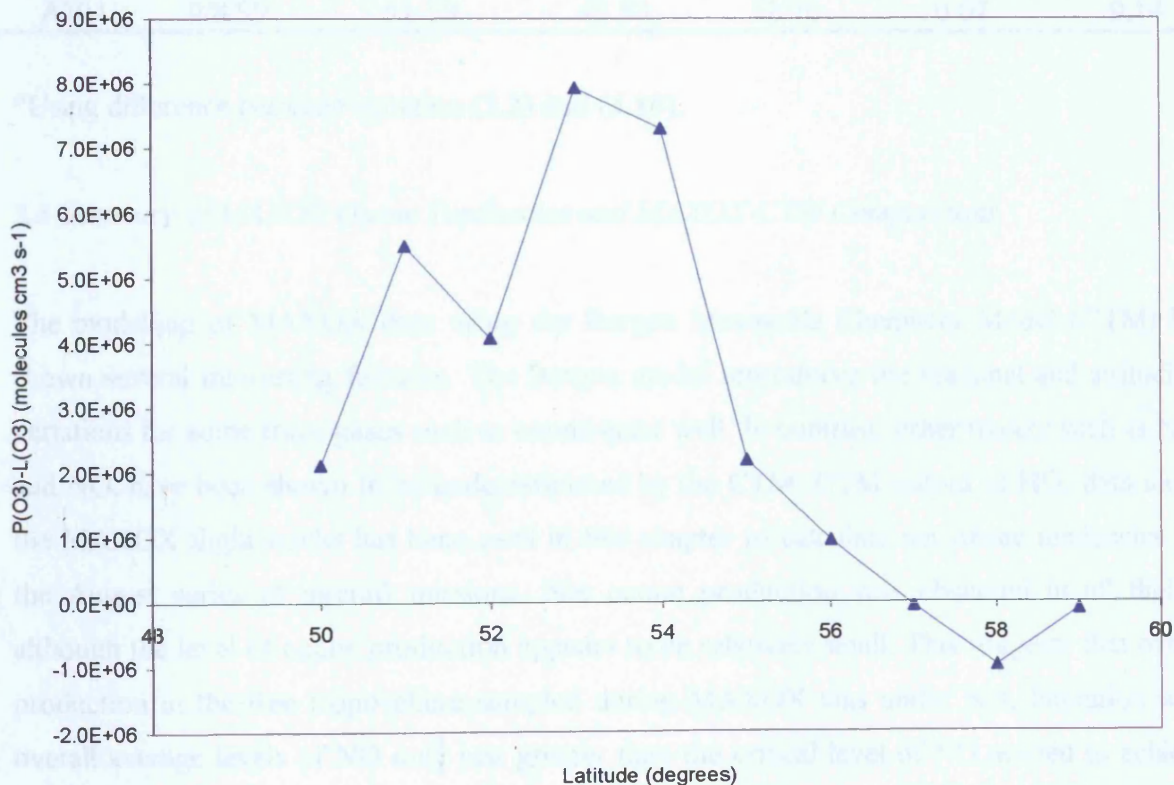


Table 3.6: Relative Pathway Strengths in Production and Loss of Ozone.

	HO ₂ +NO	RO ₂ +NO	Total P(O ₃)	<i>j</i> (O ¹ D)*O ₃ *F	HO ₂ +O ₃	OH+O ₃	Total L(O ₃)
Flux /molecules cm ⁻³ s ⁻¹	2.3x10 ⁹	2.3x10 ⁹	4.6x10 ⁹	8.1x10 ⁸	2.9x10 ⁸	1.6x10 ⁸	1.3x10 ⁹
% contribution	50.8	49.1	-	64.1	23.1	12.8	-

Figure 3.43: Ozone Tendency vs. Latitude for MAXOX August Flights



The overall calculated ozone production was also seen to be latitude dependent (Figure 3.43). From 50-54°N, there is a net ozone production of *ca.* 1 ppbv per day, whereas latitudes >57°N, a net ozone loss is observed of -0.08 ppbv per day. Trajectory analysis showed that both for the flights on 5/8/99 and 9/8/99, the aircraft was encountering polar air when at latitudes > 57°. This would be expected to be clean air, relatively free from human influence and is probably why there is a net O₃ loss for these latitudes when averaged over the whole campaign. A summary of the tracer, and latitude range of each flight during the August MAXOX flights is shown in Table 3.7.

Table 3.7: Summary of Latitude, Trace Gas Concentration, $\tau(O_3)$ and $NO_{critical}$ for MAXOX August Flights

Flight code	Date	Latitude Range / °N	O ₃ /ppbv	NO /pptv	$\tau(O_3)$ /ppbv per day	$NO_{critical}$ /pptv
A700	2/8/99	51-56	57.20	948.84	1.25	16.75
A701	4/8/99	52-55	48.80	49.40	0.57*	13.67
A702	5/8/99	52-59	50.70	16.53	0.81	13.63
A703	6/8/99	50-52	53.40	34.34	0.27	8.66
A704	9/8/99	51-59	48.83	12.70	0.07	9.14

*Using difference between equation (3.2) and (3.10)

3.8 Summary of MAXOX Ozone Tendencies and MAXOX-CTM Comparisons

The modelling of MAXOX data using the Bergen Mesoscale Chemistry Model (CTM) has shown several interesting features. The Bergen model reproduces the seasonal and altitudinal variations for some trace gases such as ozone quite well. In contrast, other tracers such as NO_x and NO_y have been shown to be underestimated by the CTM. CTM output of HO_x data along the MAXOX flight tracks has been used in this chapter to calculate net ozone tendencies for the August series of aircraft missions. Net ozone production was observed in all flights, although the level of ozone production appears to be relatively small. This suggests that ozone production in the free troposphere sampled during MAXOX was under NO_x limitation with overall average levels of NO only just greater than the critical level of NO needed to achieve net ozone production.

Binning of the ozone tendencies has shown that the overall trend in $\tau(O_3)$ has strong altitude dependence, with the planetary boundary layer showing a large-scale ozone production. This reflects the high concentrations of CO, NO_x and other tracers for anthropogenic pollution that were sampled at altitudes <2 km during the course of the campaign. It was noted in Chapter 2 that the free troposphere during the MAXOX campaign had a much lower human influence and this is supported by ozone tendency and $NO_{critical}$ data bin averages presented in this Chapter. For the free troposphere in the August MAXOX flights, there appears to be a much

smaller rate of ozone production when compared to the boundary layer, reflecting that these data are much closer to $\text{NO}_{\text{critical}}$. Also of note was the latitude dependence of the ozone tendency, owing to the types of air mass being sampled. For data taken at latitudes $>57^\circ\text{N}$ a net loss of ozone was calculated, where air parcels sampled had a polar origin and were likely to be "background" air masses, low in NO_x and thus showing a net ozone loss. In contrast, for the majority of MAXOX data, back trajectories suggested data were recorded in air masses that had been heavily influenced by the European continent, where a net ozone production was observed.

Chapter Four: Flight Track and Steady State Modelling [HO_x] From Aircraft Platforms

4.1)	Introduction	125
4.2)	The SONEX Campaign	130
4.3)	Steady-State HO_x Calculations During SONEX	131
4.4)	Steady-State HO_x during the ACSOE Campaign	140
4.5)	Modelling HO_x Along Aircraft Flight-Tracks	145
4.6)	FTBM vs. <i>in situ</i> SONEX data	147
4.7)	SONEX Modelling Conclusions	150
4.8)	ACSOE Flight Track Modelling	155
4.9)	Overall Summary	157

Chapter 4: Steady-State and Flight Track Modelling of [HO_x] from Aircraft Platforms

4.1 Introduction

The role that hydroxyl and hydroperoxy radicals OH and HO₂, (known collectively as HO_x), play in the chemistry of the troposphere was suggested almost thirty years ago. (Levy, [1972], Crutzen, [1974]). In general, the self-cleansing mechanisms that occur in the sunlit troposphere are principally controlled by the action of the hydroxyl radical. OH is a sufficiently powerful oxidising agent to remove almost all natural and anthropogenic trace gases from the troposphere and therefore significantly governs their atmospheric lifetime. The HO₂ radical has been shown to be a key intermediate in the production of ozone (*e.g.* Logan, [1981]) owing to the rapid reaction of NO with HO₂ to form NO₂, which, in turn, can be photolysed to form tropospheric ozone. HO_x radicals, although present at free troposphere concentrations of a few parts per trillion, are vital in the understanding tropospheric chemistry. As detailed in Chapters 1 and 2, the primary step in tropospheric OH production is the photodissociation of ozone into the excited oxygen species O(¹D) followed by the subsequent reaction with water vapour *viz.*

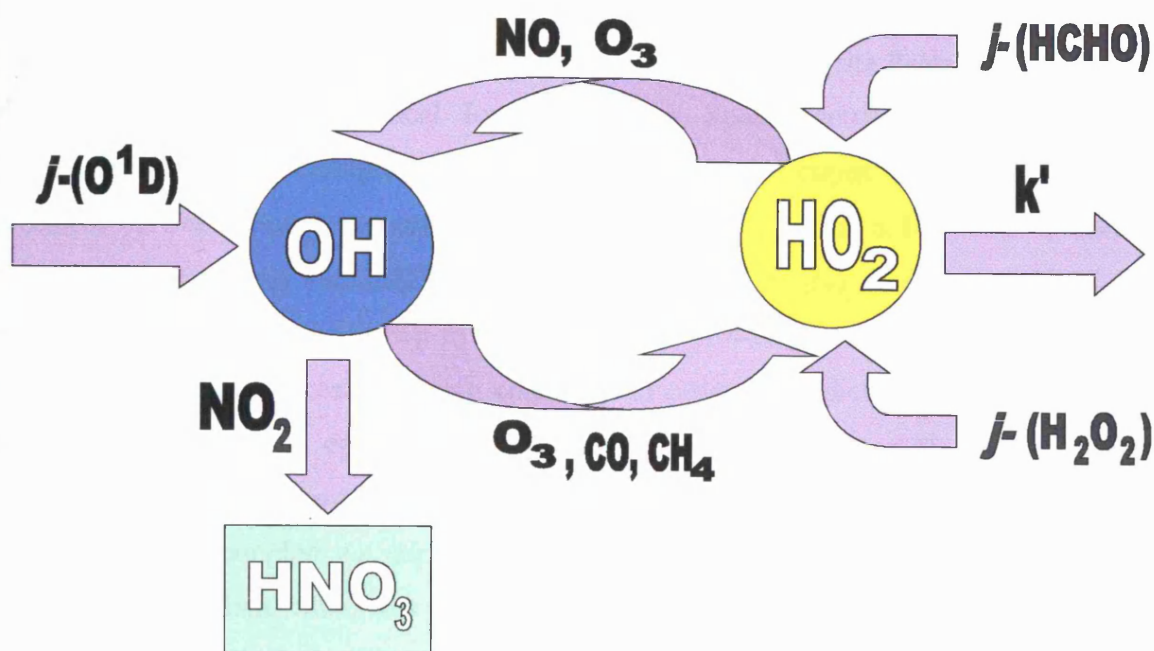


Similarly, HO₂ production is, in the main, controlled by the oxidative removal of CO by tropospheric OH.



It is clear that [HO_x] in the troposphere is intrinsically linked to photochemistry. Also, (*e.g.* Zanis [1999]), there is potential for the interconversion of HO_x. The partitioning of HO_x is controlled *via* the reaction of ozone, NO and hydrocarbons as shown schematically below

Figure 4.1, Sources, Sinks and Interconversion of Tropospheric HO_x (From Zanis [1999]).



Although the primary source of HO_x is production *via* reactions (4.2), there has been an ongoing debate in the literature as to the role of other sources of HO_x , particularly in the upper troposphere. It is now acknowledged that secondary HO_x produced by acetone and formaldehyde photolysis, combined with the convective uplift of methylhydroperoxide is of potential importance in the $[HO_x]$ budget of the upper troposphere. This is most prevalent in the UT/LS region where total water vapour concentration is low. Indeed, it has been postulated that these "secondary" HO_x sources are even more important than the reaction of $O(^1D)$ with water in the dry upper troposphere. (Singh *et al.* [1995], Jaeglé *et al.* [1997] [1998], [2000], Brune *et al.* [1998]). It is therefore clear that owing to the large number of sources and the complexity of the interaction there are still large degrees of uncertainty in our understanding of the total HO_x budget in the free troposphere.

There have been several major campaigns that have been undertaken to increase understanding of the reactions that control the total budget of tropospheric HO_x over the last decade. These include both ground based and aircraft measurements. Only in recent years, have direct measurements of OH and HO_2 been possible. The application of differential absorption spectroscopy (DOAS) in the 1980's gave the first experimental proof that OH radicals could be detected in the atmosphere. DOAS measurements also provided insights into

the diurnal nature of OH and its variations under different atmosphere conditions and trace gas concentration. (Hübler *et al.* [1984], Perner *et al.* [1987], Platt *et al.* [1988]).

In 1991, Eisele *et al.* (1994) measured OH from the summit of Fritz Peak in Colorado, USA using the Selected Ion Chemical Ionization Mass Spectrometry, (SICIMS), technique. Comparisons of this technique to simple box model predictions for OH showed good agreement between model/measured OH with errors being within a 1σ standard deviation. The same group during MLOPEX-2 at Mauna Loa, Hawaii also employed SICIMS where free troposphere OH_{max} was shown to be on the order of $4\text{-}6 \times 10^6$ molecule cm^{-3} . (Eisele *et al.* [1996]). Steady-state expressions were employed in order to predict radical concentrations in both clean and polluted episodes. In clean "downslope" air the authors reported good agreement between measured OH predictions. However, in episodes of pollution where "upslope" air was sampled, *i.e.* air transported from the boundary layer, measured [OH] was found to be only half what was predicted. The SICIMS technique was also used at the Tropospheric OH Photochemistry Experiment (TOHPE) at Idaho Hill, Colorado in 1993. (Mount and Williams [1997], Eisele *et al.* [1997]) where ratios of HO_2/OH ratios were obtained and were shown to agree well with calculated values in a low NO_x environment (<100 pptv). However, the net concentration of [OH] measured at TOHPE was shown to be far less than predicted *via* models. Indeed, the model seemed to show that for the conditions encountered during TOHPE, model overestimations of OH were as great as 51% (McKeen *et al.* [1997]).

The laser induced fluorescence detection of HO_2 and OH known as FAGE (Fluorescent Assay by Gas Expansion) pioneered by Hard *et al.* (1984) has been used to make *in-situ* measurements of HO_x . The application of FAGE technique has now been used extensively to measure HO_x on the ground and *via* aircraft platforms. Mather *et al.* (1997) compared the LIF detection of HO_x with SICIMS during TOPHE and saw excellent agreement between these two techniques and observed the NO_x dependency of the HO_x interconversion ratio. Similar results comparing FAGE with differential absorption spectroscopy were obtained by Plas-Dülmer (1998), from a rural site in Germany and during the POPCORN experiment. Similar work on HO_x chemistry comparing models and measurements of HO_x *via* FAGE and the peroxy radical amplification (PERCA) technique (Cantrell and Steadman [1984], Monks *et al.* [1996], [2000]) has recently been completed by Carslaw *et al.* (1999a, 1999b) during the recent Eastern Atlantic Summer Experiment 1996, (EASE96) at Mace Head, Ireland. Here, the authors show in general, there is a good level of agreement in radical concentrations from

an observationally constrained box model and data obtained from FAGE and PERCA techniques.

One of the first measurements of tropospheric OH from an aircraft platform was during the ACE 1 experiment (Maudlin *et al.* [1997]). Aircraft deployment of the SICIMS technique was undertaken and the authors measured lower tropospheric OH concentrations of the order of $8\text{--}15 \times 10^6$ molecules cm^{-3} . However, there appeared to be large variations in [OH], particularly in and above cloud fields. The application of FAGE technology on aircraft platforms gave the first measurements of HO_x in the upper troposphere during the 1995-96 STRAT campaign (Jaeglé *et al.* [1997]) The authors also showed the importance of acetone photolysis as a major HO_x production route. These results were confirmed during the SUCCESS aircraft missions described by Brune *et al.* (1998).

In the first part of this chapter, steady-state HO_x calculations have been used in order to ascertain the HO_x budget in the North Atlantic free troposphere using data from two aircraft campaigns. The first of these is the SONEX missions where steady-state calculations are compared to HO_x data measured *in-situ* by laser-induced fluorescence in order to test the accuracy of such relationships in predicting [HO_x]. The second aircraft campaign is the ACSOE missions to the Azores in the summer of 1997 as described in detail in Chapter 2 and 3. The use of steady-state calculations to predict HO_x along an aircraft flight track will be investigated in order estimate [HO_x] as measured by aircraft platforms. One of the limitations of the steady-state method is that often potentially important radical sources and sinks are overlooked. To increase the validation of this study, modelling of [HO_x] for aircraft missions in SONEX has been attempted. This is dealt with in the second part of the chapter. It shows that the application of a flight track box model, constrained to *in-situ* data, reproduces concentration and fine structure of HO_x data very well when compared to *in-situ* measurements made during SONEX. Using the box model approach, predictions of the HO_x budget have also been made with respect to the photochemical environment around the Azores as investigated during the summer ACSOE Azores series of aircraft missions.

4.2: The SONEX Campaign

The Subsonic Assessment of Ozone and NO_x Experiment (SONEX) was an aircraft campaign conducted over the North Atlantic in the autumn of 1997. The overall goal and accomplishments of SONEX are detailed elsewhere (Singh *et al* [1999], Thompson *et al.* [2000]). In brief, the major aims of SONEX were to investigate the North Atlantic flight corridor *via* the NASA DC-8 aircraft fitted with instruments to measure trace gas concentrations and photolysis frequencies. The rapid increase in the amount of air traffic in the North Atlantic flight corridor has been a growing area of concern for atmospheric scientists. There is mounting evidence that commercial sub-sonic aircraft, flying at altitudes of between eight and twelve kilometres, are perturbing the natural chemistry of the UT/LS region (Brasseur *et al* [1998]). Aircraft engines directly inject large amounts of NO_x into this region of the upper troposphere. At the UT/LS boundary the lifetime of NO_x is long and removal is slow which has, in turn, the potential to lead to significant ozone production. It has been suggested that aircraft emissions may have resulted in a net increase of 3-10 ppbv in upper tropospheric ozone for the North Atlantic (Brasseur *et al.* [1998]).

During SONEX, *in-situ* measurement of speciated HO_x was obtained *via* the FAGE instrument operated by Penn State University. The instrument, the Airborne Tropospheric Hydrogen Oxide Sensor (ATHOS), is an *in-situ* LIF detection system that utilises FAGE technology. The instrument has been run during several aircraft campaigns with large degrees of success (*e.g.* Brune *et al.* [1998], [1999], Jaeglé *et al.* [1998],[1999], Tan *et al.* [1998]). A full description of the instrument during its SONEX deployment is found in Faloon *et al.* (2000). The instrument works by probing atmospheric air drawn into a sample chamber *via* a supersonic jet expansion with a dye laser set at $\lambda=308\text{nm}$. The net effect is to electronically excite OH radicals within the air sample. Fluorescent decay ($A^2\Sigma \rightarrow X^2\Pi$, $v'=0 \rightarrow v''=0$) of the excited OH is then detected *via* a photon counting photomultiplier tube. In order to detect HO₂ additional reactions are carried out on the sample gas drawn into the chamber. Specifically, known concentrations of NO are injected into the air sample to rapidly oxidise NO into NO₂ and thus reduce HO₂ radicals within the air sample into OH. A second detection of this "secondary" OH *via* LIF is then obtained in order to quantify the total HO_x in the sample. HO₂ is subsequently calculated from subtraction of "primary" OH from the total HO_x detected. Estimates indicate that the absolute accuracy of this detector is *ca.* 40% while detection limits are better than 0.03 pptv. (Faloon *et al.* [2000])

The driving force for OH formation in much of the troposphere, is *via* ozone photolysis as shown in equations (4.1) and (4.2). During SONEX, photolysis frequencies were measured using the scanning double monochromator spectroradiometer operated by the National Center for Atmospheric Research. This instrument is the same that was run by the NCAR group at the IPMMI experiment (see Chapter 6) and is described fully by Shetter and Müller (1999). Spectra from 280 - 700 nm were scanned every 15 seconds in order to measure atmospheric photon flux across this wavelength region. From the relations described in Chapter 6, it is possible to calculate photolysis frequencies of molecules such as ozone from using *in-situ* actinic flux measurements, together with respective molecular data *i.e.* molecular absorption cross section and quantum yields. Using such methods photolysis frequencies $j\text{-}(O^1D)$, $j\text{-}(NO_2)$, $j\text{-}(\text{acetone})$ and $j\text{-}(\text{HCHO})$ were obtained for all SONEX flights.

Ozone data during the SONEX missions were obtained *via* the NASA Langley instrument described by Gregory *et al.* (1996) and provided *in-situ* detection of ozone *via* chemiluminescence. The detection limit was 1 ppbv and the estimated accuracy was *ca.* 5%. NO_x data was also obtained during SONEX *via* chemiluminescence. Again, the detector used was the same that provided data during the NASA PEM campaigns as described by Kondo *et al.* (1997). The precision of the 10 second NO measurements at a height of 10km was estimated from photon count fluctuations to be 6 pptv for NO at 2σ . The estimated accuracy was quoted at 10% (Koike *et al.* [2000]). The University of Rhode Island provided data on speciated peroxide and formaldehyde. Detection of hydrogen peroxide and MHP was *via* HPLC detection as described by O'Sullivan *et al.* (1999) and Cohan *et al.* (1999). Detection limits were found to be *ca.* 20 pptv, \pm 30%. Finally, hydrocarbon data on concentrations of CO and $[CH_4]$ in addition to $[H_2O]$ during SONEX were provided by tuneable diode laser spectroscopy. This TDL detector was deployed on the DC-8 in the same configuration as the PEM-Tropics campaign (Vay *et al.* [1998], [2000]). Detection limits for hydrocarbon species were found to be 1 ppbv (\pm 2%) and 1ppm (\pm 5%) for H_2O respectively.

4.3: Steady-State HO_x Calculations During SONEX

It is possible estimate the concentration of OH in a low NO_x and VOC environment such as the free troposphere from steady state analysis. Assuming production of OH is controlled by ozone photolysis, and the main OH losses proceed through reactions with CO and CH₄, the net concentration of OH is essentially under steady state. As shown by Penkett *et al.* (1997) and Zanis (1999), assuming net HO_x interconversion by ozone is the same for HO₂ as it is for OH, the net concentration of OH can be equated as;

$$[OH] = \frac{2 \cdot (j(O^1D)) \cdot F \cdot [O_3]}{k_{(M+O^1D)} \cdot (k_{(CH_4+OH)}[CH_4] + k_{(CO+OH)}[CO])} \quad (4.4)$$

$k_{(M+O^1D)}$ is the rate of collisional quenching of O(¹D) to O(³P) *via* reaction (4.5)



"F " is the fraction of excited oxygen that goes on to form tropospheric OH. Making the assumption that the reaction of O(¹D) with water is small in comparison to the amount quenched, it was shown by Penkett *et al.* (1997) that this fraction is given by

$$F = \frac{k_{(H_2O+O^1D)}[H_2O]}{k_{(M+O^1D)}[M]} \quad (4.6)$$

Similarly, the total sum of peroxy radicals HO₂ and RO₂ under steady-state is given by;

$$[HO_2] + [RO_2] = \sqrt{\frac{F \cdot j(O^1D) \cdot [O_3]}{k'}} \quad (4.7)$$

Where, k' is a composite rate coefficient made up from the individual loss process of peroxy radicals in the clean, low NO_x environment. Under such conditions the self and cross-reactions are the dominant sinks for HO₂ and RO₂ *via* reactions (4.8) and (4.9);



The experimental value for k' can be derived by scatter plots of $[\text{HO}_2] + [\text{RO}_2]$ vs. $j \cdot (\text{O}^1\text{D})$ (Penkett *et al.* [1997], Monks *et al.* [1998]). However, for the purposes of these calculations k' can be calculated from the kinetic rate coefficients of reaction (4.8) and (4.9) *viz.*

$$k' = \alpha^2 k(2\text{HO}_2 \rightarrow \text{H}_2\text{O}_2) + \alpha(1-\alpha) \cdot k(\text{CH}_3\text{O}_2 + \text{HO}_2 \rightarrow \text{CH}_3\text{O}_2\text{H} + \text{O}_2) \quad (4.10)$$

Where α is found to be the ratio of the concentration of HO_2 divided by the total concentration of all peroxy radical species. As stated above, sources and sinks of OH and HO_2 not only governs partitioning of HO_x , but also HO_x interconversion. Zanis (1999) and Faloon *et al.* (2000) showed that the interconversion ratio of HO_x is given by the reactions described in Figure 4.1, and therefore by

$$\frac{[\text{HO}_2]}{[\text{OH}]} = \frac{k_{(\text{CO}+\text{OH})}[\text{CO}] + k_{(\text{CH}_4+\text{OH})}[\text{CH}_4] + k_{(\text{O}_3+\text{OH})}[\text{O}_3]}{k_{(\text{O}_3+\text{HO}_2)}[\text{O}_3] + k_{(\text{NO}+\text{HO}_2)}[\text{NO}] + (2 \cdot \sqrt{j(\text{O}^1\text{D})} \cdot [\text{O}_3] \cdot F \cdot k')} \quad (4.11)$$

The simple steady-state relationship equation (4.11) was shown by Zanis (1999) to provide an estimation of the interconversion ratio in the free troposphere environment of the Jungfraujoch in Switzerland (*ca.* 3,580m above sea level). From such relationships the evaluation of net HO_2 and thus, the total HO_x budget in such locations, can be calculated from the product of equations (4.11) and (4.4).

Using the relationship shown in equation (4.4), is possible to calculate HO_x for SONEX flights by constraining $j \cdot (\text{O}^1\text{D})$ and trace gases concentrations with *in-situ* measurements made from the DC-8. Rate constants for the reactions in equations (4.4) and (4.11) were taken from DeMore *et al.* (1997). The steady-state predictions for OH were calculated along the individual flight tracks for six SONEX flights and plotted against the measured OH data obtained by the FAGE instrument in order to ascertain a measure of the accuracy of the steady-state prediction. A composite of the steady-state/measured HO_x data for each of the SONEX flights is shown in Figures 4.2 and 4.3.

Figure 4.2: $[OH]$ Prediction from Steady-State Relationships with measured $[OH]$ Data

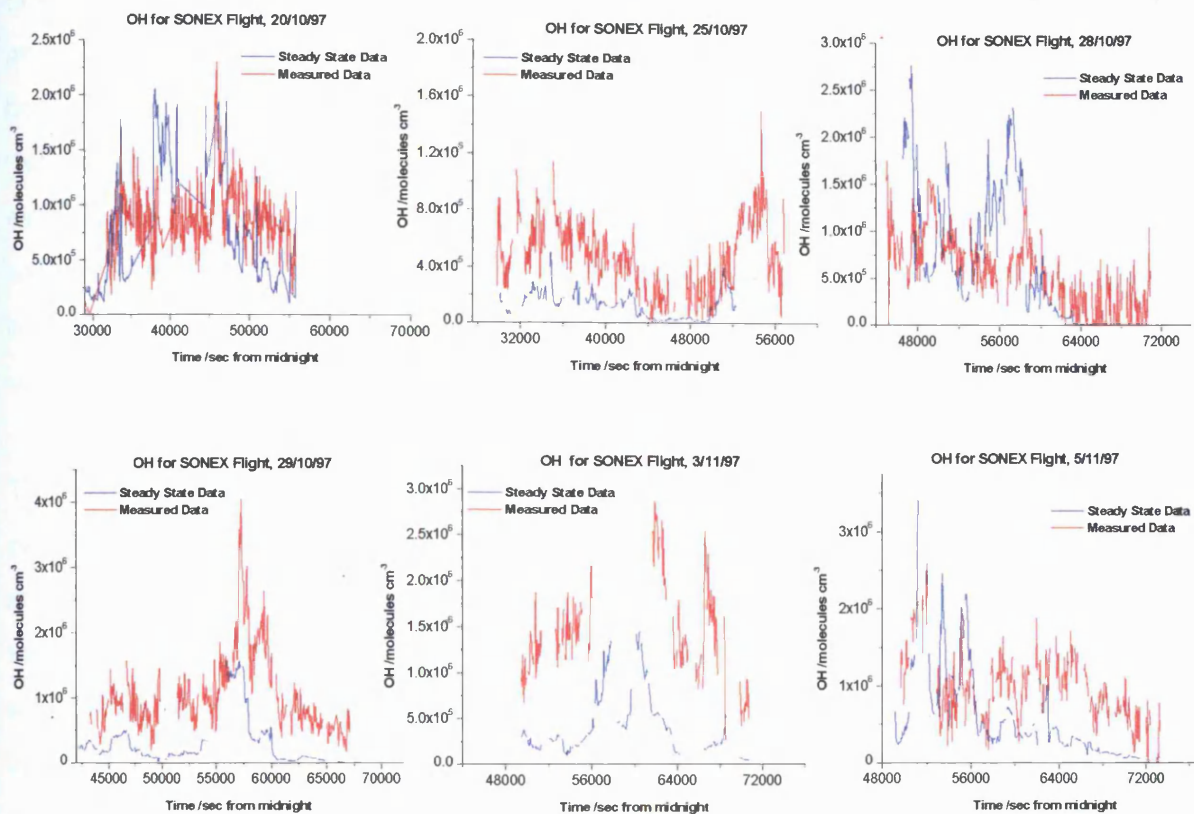
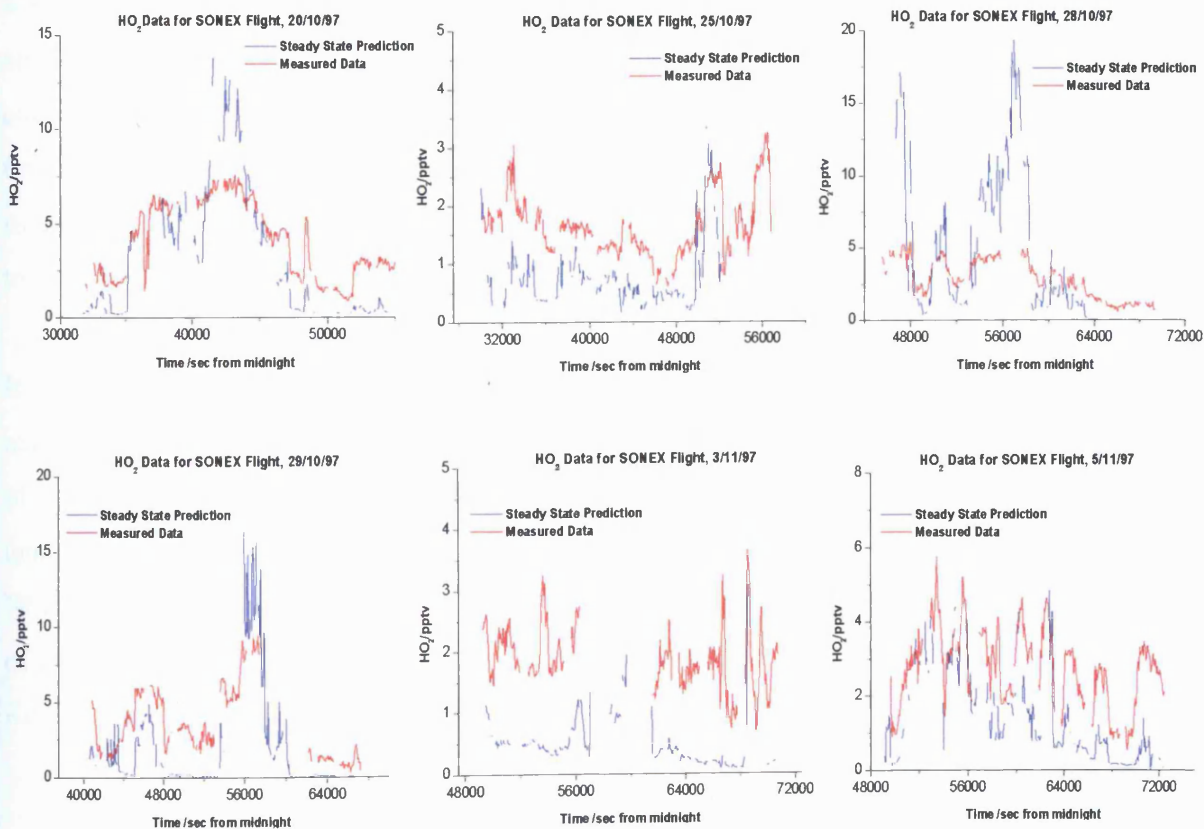


Figure 4.3: $[HO_2]$ Prediction from Steady-State Relationships with measured $[OH]$ Data



A general inspection of the data shown in Figures 4.2 and 4.3, the analyses made by Zanis (1999) seems to predict [OH] from aircraft data to a reasonable degree of accuracy. In general, agreements between the steady state predicted and measured [OH] are reasonable in both magnitude and structure. However, there is both underestimation and overestimation of the concentration of OH compared to that measured. This is shown not only between individual flights, but during individual flights as well. Correlation plots between steady state and measured [OH] are shown in Figure 4.4. Correlation coefficients for these data range between 0.21 and 0.71. Similarly, the correlations for HO₂ are shown in Figure 4.5, where the correlation coefficients range between 0.37-0.79.

The underlying reason for the large underestimations of the OH budget by steady-state calculation needs consideration. It is important in such analysis to consider both production and loss of HO_x in order to ascertain if the steady-state predictions are truly representative of these steps. Considering HO_x production, from Figure 4.1, steady-state OH production is solely from the reaction of (O¹D) atoms with water. The result is often a strong correlation between structure in the steady-state calculated OH/time plot to changes in water concentration for all SONEX flights. Large variations in water concentration produce [OH] that may be in excess of that measured *in-situ*, or more usually, underestimates the measured value. Plots of [OH] against [H₂O] for these measured and predicted data are shown in Figure 4.6. [OH] measured directly by the ATHOS instrument on the DC-8 during SONEX showed almost no correlation between the two parameters (Faloona *et al.* [2000]). Water vapour concentrations decrease rapidly with respect to altitude (*e.g.* USSA, [1976]). In areas of the free troposphere where the concentration of H₂O is low, the primary production channel for steady-state OH is likely to be suppressed, creating potential for a net underestimation of the total [OH].

It is clear that either other secondary sources of OH not included in equation (4.1) play a major role in the upper troposphere, or secondary sinks such as reaction with other NMHC's of the interconversion of OH into HO₂ *via* NO reaction are similarly important. It seems unlikely that there would be major influences of additional OH sinks since concentration of NMHC's were shown to be low enough for the conditions of SONEX that the dominant sinks of OH were oxidation of methane and CO as shown by equation (4.1) (Simpson *et al.* [2000], Koike *et al.* [2000]).

Figure 4.4: Correlations Between Steady-State Predictions and Measured OH Concentration During SONEX

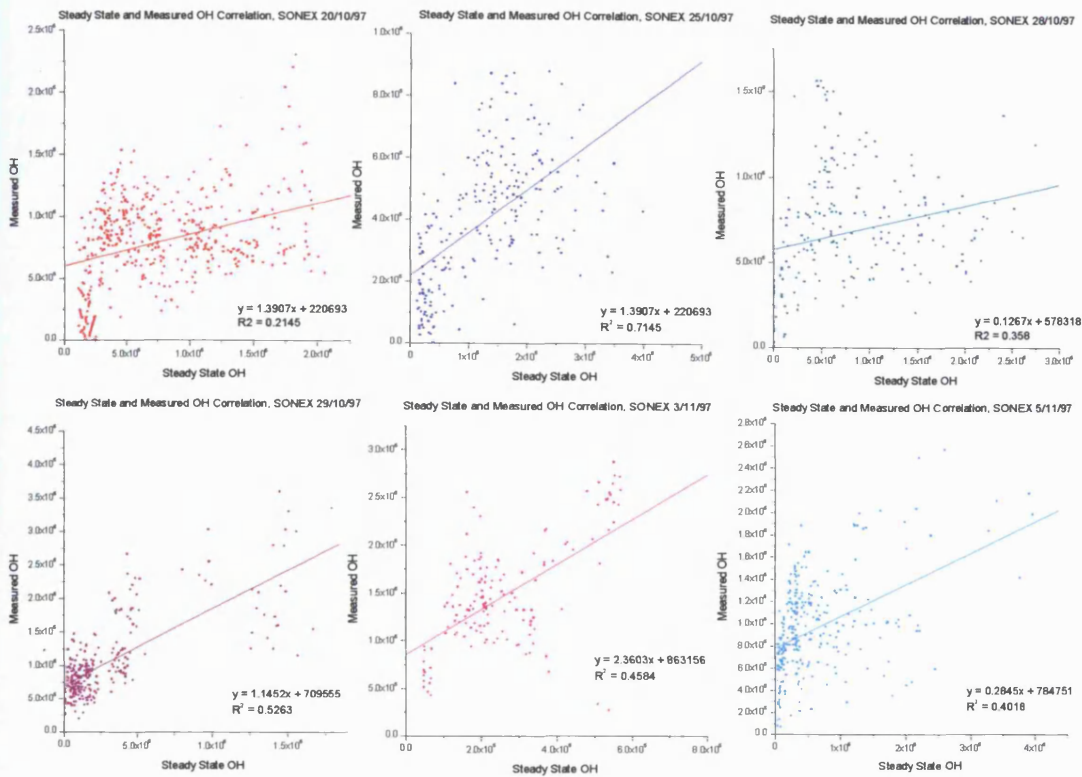


Figure 4.5: Correlations Between Steady-State Predictions and Measured HO₂ Concentration During SONEX

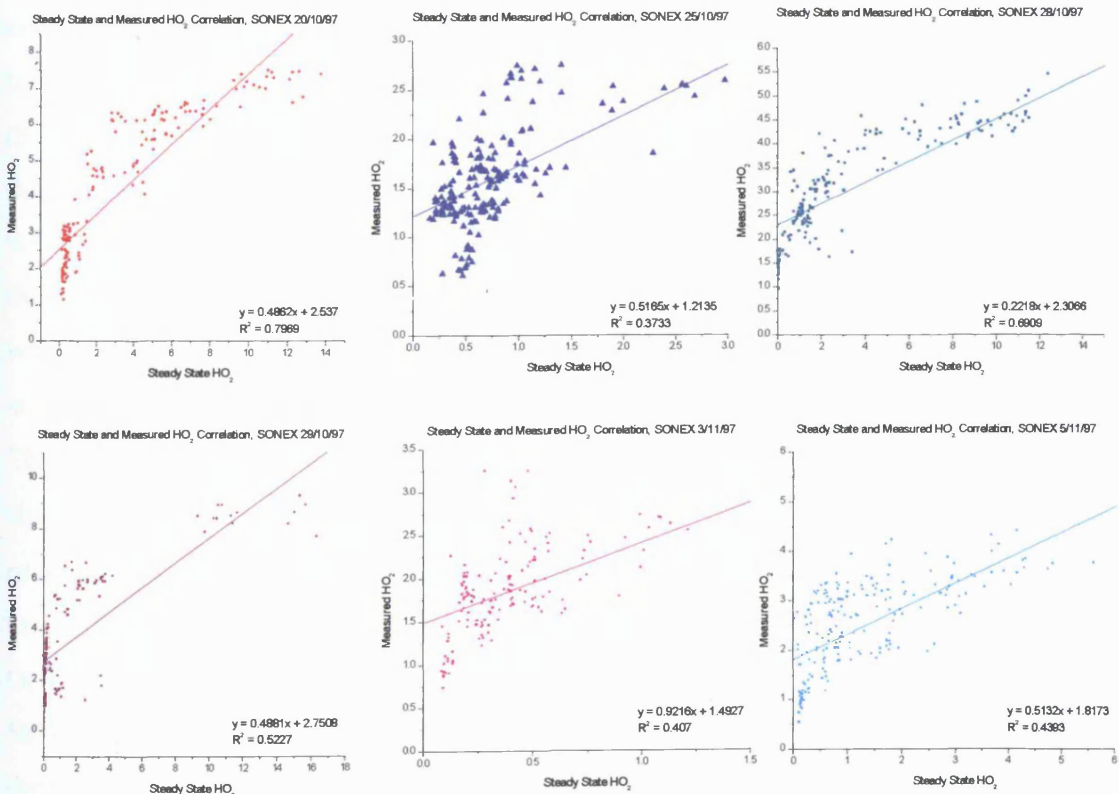
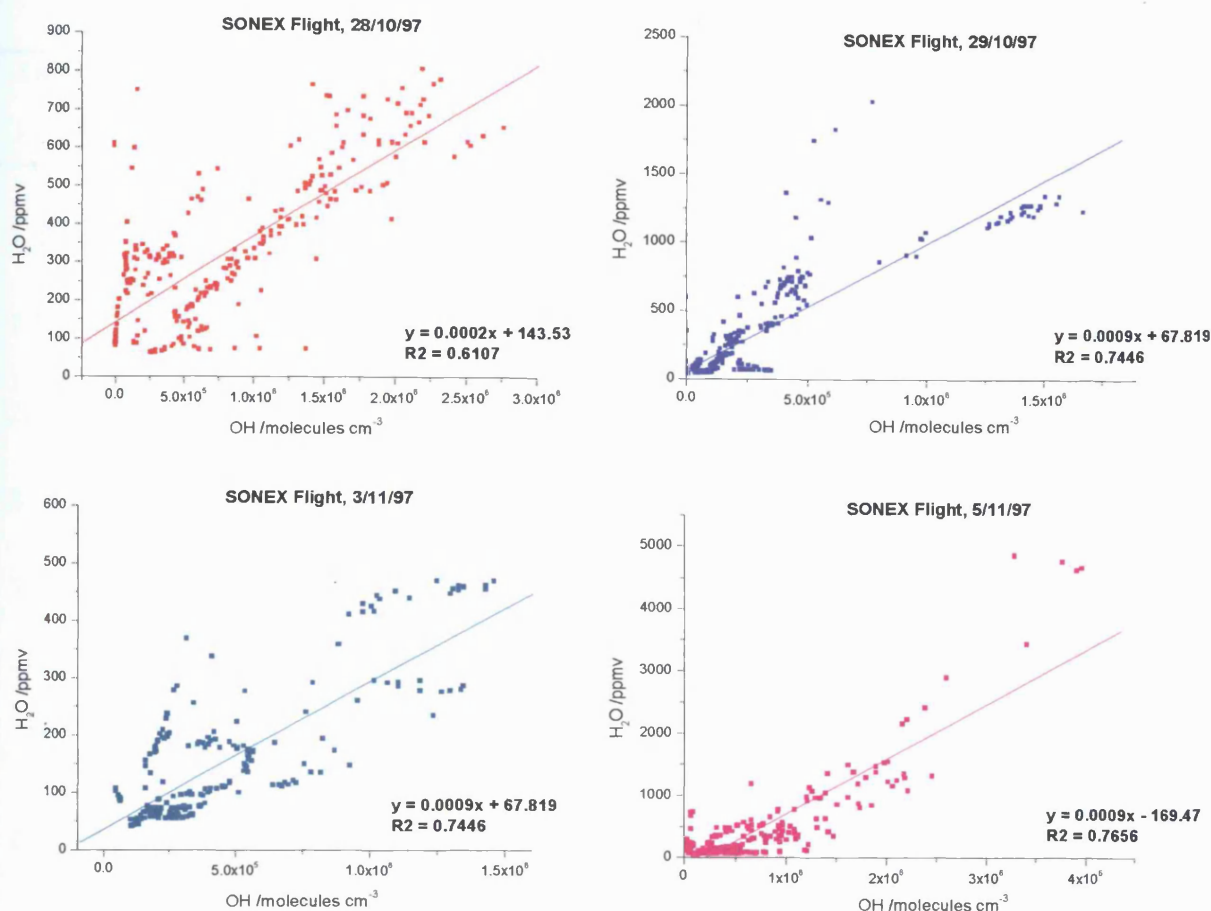


Figure 4.6: H_2O and OH Correlations for Steady-state OH



The concentrations of species measured *in-situ* during SONEX were used together with rate constants recommended by DeMore *et al.* (1997) to ascertain the most important of these production and destruction routes for HO_x during SONEX. It was assumed for this analysis that the production of OH is controlled by three reactions, the reaction of O(¹D) with water, the reaction of HO₂ with ozone and the reaction of HO₂ with NO. All other production routes were considered negligible. Considering the relative importance of these production routes, the analysis shows that the major source of OH during SONEX was not the reaction of O(¹D) with water as assumed in steady-state, but the recycling of HO₂ *via* the reaction of NO_x. This is not surprising given that [NO] in SONEX were often high, >10³ pptv for several flights. The underestimation of OH by steady-state is therefore probably strongly linked to the absence of HO₂→OH recycling in equation (4.4). A breakdown of these production/destruction routes for the measured SONEX HO_x shows that for the six flights investigated here only *ca.* 33% of the total OH budget comes directly from the reaction of O(¹D)+H₂O. This compares to *ca.* 9% from the reaction of HO₂ with ozone. The remaining 58% of measured OH is shown to be recycled from HO₂ by the reaction of NO. The total OH production rate for each separate flight is shown in Table 4.1.

Table 4.1: Contribution of OH Production Routes during SONEX (molecules $\text{cm}^{-3} \text{s}^{-1}$)

O(¹ D) + H ₂ O	% of total	HO ₂ +O ₃	% of total	HO ₂ + NO	% of total	Flight
3.37 x 10 ⁴	17%	2.21 x 10 ⁴	11%	1.45 x 10 ⁵	72%	20/10/97
1.56 x 10 ⁵	64%	2.18 x 10 ⁴	9%	6.74 x 10 ⁴	27%	25/10/97
2.29 x 10 ⁴	14%	3.07 x 10 ⁴	18%	1.14 x 10 ⁵	68%	28/10/97
8.63 x 10 ⁴	27%	4.73 x 10 ⁴	15%	1.83 x 10 ⁵	58%	29/10/97
7.05 x 10 ⁴	22%	1.62 x 10 ⁴	5%	2.41 x 10 ⁵	73%	3/11/97
2.76 x 10 ⁵	39%	3.97 x 10 ⁴	6%	3.88 x 10 ⁵	55%	5/11/97
1.08 x 10⁵	33%	2.91 x 10⁴	9%	1.90 x 10⁵	58%	SONEX steady- state average

The same form of analysis was repeated to investigate the relative importance of OH loss routes in SONEX. Data shows that the steady-state loss routes are well accounted for by steady-state equation (4.4). Considering reactions that remove OH in the air masses investigated in SONEX shows that overall, around 66% of OH is lost through the reaction of CO with the hydroxyl radical. The exact breakdowns of the loss routes for OH in SONEX are shown in Table 4.2. As shown in Figure (4.3) for most of the flights in SONEX there is also underestimation of the HO₂ budget from steady-state calculated data given by equation (4.11). The steady-state assumption in this equation is that all HO₂ derives from the interconversion ratio, *i.e.* from the reaction of species that convert OH into HO₂. It would seem that this assumption also has difficulty accounting for the [HO₂] measured during SONEX given the data in Figure 4.3. From Table 4.2, the major production step for P(HO₂) is the reaction of OH with CO and the reaction of O₃ with OH, both of which are accounted for by steady-state.

Table 4.2: Contribution of OH Loss Routes during SONEX (molecules cm³ s⁻¹)

HCHO	H ₂ O ₂	NO ₂	NO	CH ₄	CO	O ₃	Flight
+OH	+OH	+OH	+OH	+OH	+OH	+OH	
5.03x 10 ³	1.45x10 ³	8.61x10 ³	5.58x10 ³	1.91x10 ⁴	1.65x10 ⁵	1.45x10 ⁴	20/10/97
3.63x10 ³	3.95x10 ²	5.06x10 ³	3.0x10 ³	7.60x10 ³	7.95x10 ⁴	1.16x10 ⁴	25/10/97
9.33x10 ³	1.70x10 ³	1.15x10 ⁴	3.90x10 ³	1.72x10 ⁴	1.65x10 ⁵	1.34x10 ⁴	28/10/97
2.36x10 ⁴	2.41x10 ³	2.80x10 ⁴	2.10x10 ⁴	2.80x10 ⁴	2.45x10 ⁵	3.0x10 ⁴	29/10/97
8.58x10 ³	1.15x10 ³	2.2x10 ⁴	1.75x10 ⁴	1.93x10 ⁴	2.71x10 ⁵	1.80x10 ⁴	3/11/97
2.83x10 ⁴	1.56x10 ³	1.16x10 ⁵	2.35x10 ⁴	3.53x10 ⁴	3.10x10 ⁵	2.65x10 ⁴	5/11/97
1.31x10⁴	1.44x10³	3.19x10⁴	1.24x10⁴	2.10x10⁴	2.06x10⁵	1.90x10⁴	Average

However, these reactions alone seem to underestimate the total concentration of measured HO₂. This is not surprising with the mounting evidence for HO₂ sources other than OH interconversion being important in the HO₂ budget in the upper troposphere. Trace gases such as acetone, peroxide and formaldehyde have been identified as important HO₂ precursors (Singh *et al.* [1995], Jaeglé *et al.* [1997], Folkins *et al.* [1998], Brune *et al.* [1998]) and can generate large [HO₂] in dry air-masses.

It would seem that the relationships derived by Penkett *et al.* (1997) for the remote marine boundary layer, where water vapour is high, do have limitations in their applicability in the free troposphere. In contrast, Zanis (1999) used the relationship give in equation (4.4) successfully at the Jungfraujoch during FREETEX 96. Using the steady-state prediction of OH, the relationship seems to be applicable in the lower to mid free troposphere where H₂O is abundant enough (*ca.* 2 g kg⁻¹, Zanis [1999]) to make the reaction of excited oxygen atoms with water vapour the dominant source of HO_x. In areas of the UT/LS region, H₂O is often less than 100ppm. This level appears to be the "cut-off" for HO_x production in such dry areas as described by Singh *et al.* (1995). If [H₂O] falls below *ca.* 100 ppmv, the dominant source of HO_x production switches from O(¹D) + H₂O to other sources such as acetone and formaldehyde photolysis. The fact that the SONEX missions were flown at altitudes often in excess of 10km implies that dry air masses were encountered with regularity (Vey *et al.*

[2000]). In such areas HO_x production from secondary sources is likely to be dominate and thus, the relationship shown in equation (4.4) cannot account for the measured OH.

This conclusion also explains the observation that HO₂ data derived from the HO₂/OH interconversion ratio often overestimates HO₂. As shown by similar analysis made by Faloona *et al.*, (2000) the fact that the vast majority of the calculated and observed HO₂/OH ratios were greater than 10, the assumption that all HO_x lies in the HO₂ partition can be made. Thus, the relative HO₂ can be calculated *viz.*

$$R_{HO_x} = \frac{k_{(CO+OH)}[CO] + k_{(CH_4+OH)}[CH_4] + k_{(O_3+OH)}[O_3]}{k_{(NO+HO_2)}[NO] + k_{(O_3+HO_2)}[O_3]} \quad (4.12)$$

If the calculated R_{HO_x} is correct, multiplication of (4.12) by (4.4) will yield the HO₂ component of total HO_x. If, however the initial concentrations of OH predicted from steady-state are underestimated owing to the absence of secondary sources, then the HO₂ budget estimated from the HO_x interconversion ratio will be overestimated. This seems to be supported by the analysis of SONEX HO_x made by Faloona *et al.* (2000). In this similar study to the steady-state analysis described here, the authors showed that using the assumption that total HO_x is dominated by HO₂, equation (4.12) could be used to predict the concentration of R_{HO_x} within the 40% accuracy stated for measurements of HO_x.

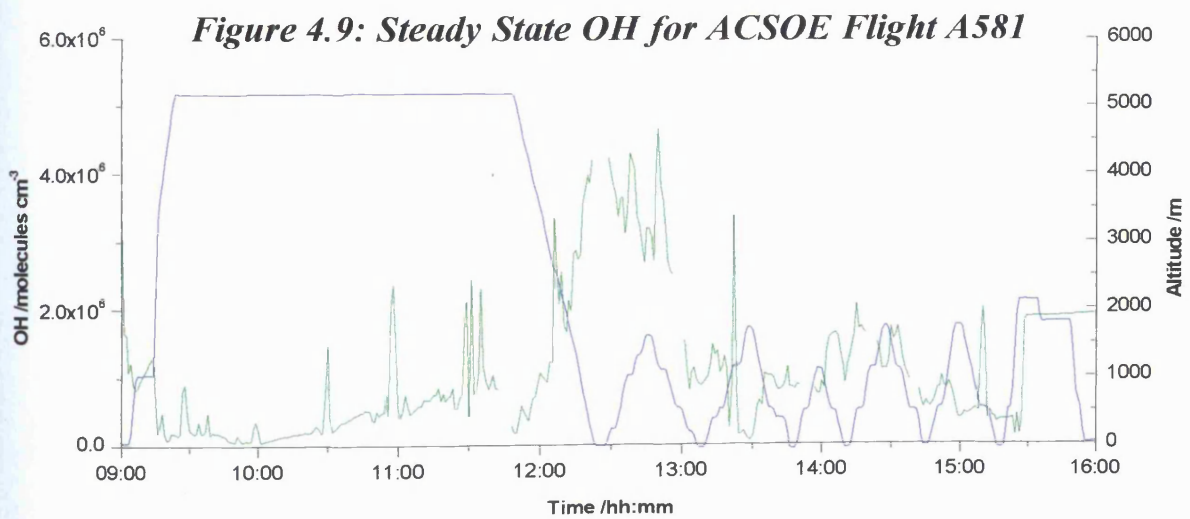
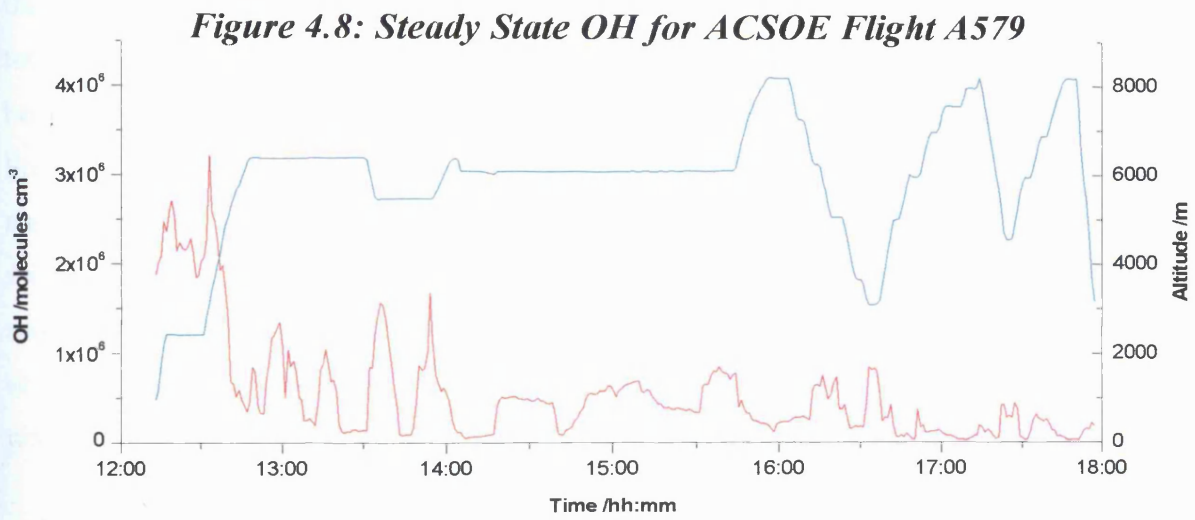
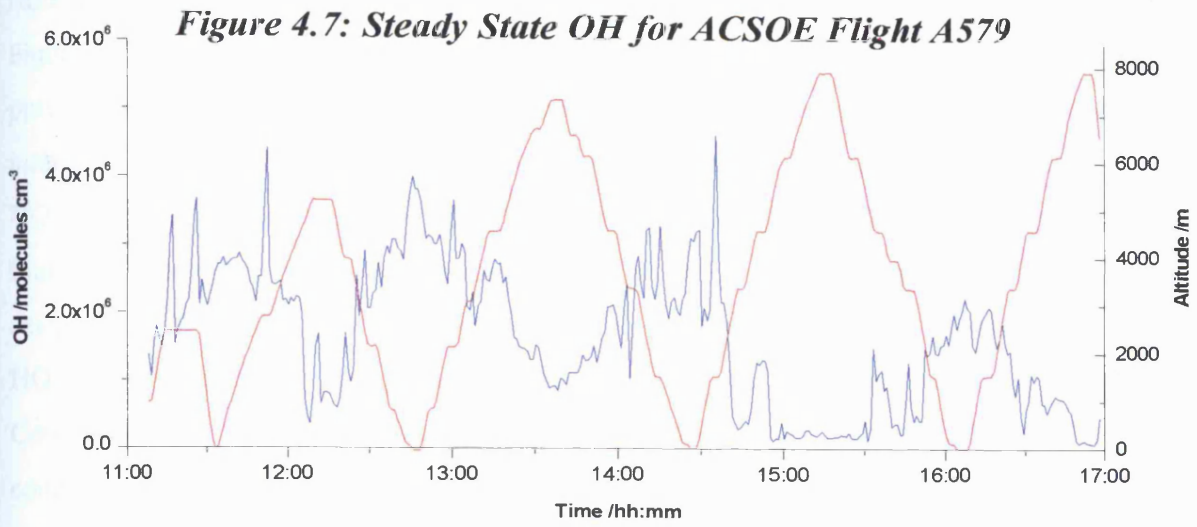
The application of simple steady-state approach to analyse aircraft data from the SONEX dataset has shown to have advantages and disadvantages in predicting both concentration and partitioning of HO_x species measured in during aircraft campaigns in the UT/LS region. However, the real interest in the application of steady-state was for data taken during the ACSOE campaign in the marine free troposphere as described in Chapters 2 and 3. It was therefore hoped that since the steady-state analysis described above seemed to be applicable for the lower and mid free troposphere then these relationships could be used to predict HO_x concentrations for individual ACSOE flights in summer 1997. Since in the ACSOE missions the C-130 flew at altitudes much lower than SONEX then the problem of secondary HO_x sources could be assumed to be small since [H₂O] was found to be significantly higher than the 100ppm "cut-off" in primary HO_x production suggested by Singh *et al.* (1995) and verified in the work described above. As stated elsewhere (Chapter 2), there were no *in-situ* measurements of HO_x made during the ACSOE aircraft campaign. All information on the

oxidising capacity of the free troposphere explored during ACSOE has been derived from model studies. If steady-state analysis could be used to successfully predict the HO_x budget along the flight tracks of individual flights then important information as to the budget and partitioning of HO_x could be obtained on a flight to flight basis.

4.4: Steady-State HO_x during the ACSOE Campaign

In this section, steady-state calculations are applied to the ACSOE Azores missions, during September 1997. Individual flights with the ACSOE code numbers A579 (20/9/97) A580 (21/9/97) and A581 (23/9/97) have been investigated. A summary of these flights and the goals of each are found in Chapter 5 (Table 5.1). *In-situ* data on concentration of O₃, CO, NO and H₂O was calculated on a one-second time based and then worked up into 1 minute HO_x averages. Since there was no *in-situ* data on the concentration of methane, a constant value of 1750 ppbv was assumed for all three-flights based on typical values measured in the background atmosphere of the Northern Hemisphere (Wayne [1991]). Concentration of air molecules was calculated along the flight track from *in-situ* measurements of pressure and deduced true temperature. Kinetic data was taken from the recommendations of DeMore *et al.* (1997). A composite of speciated HO_x is shown in Figure 4.7-4.10 as 1-minute averages.

From the 1-minute data averages shown in the Figures 4.7-4.10, during ACSOE summer [OH] values range from 1×10^5 molecules cm⁻³ to in excess of 4×10^6 . Also of note is the strong altitude dependence of the steady-state [OH]. Considering the data for A579 the aircraft altitude track indicates the motion of the C-130 as almost saw tooth like. This is where the aircraft flew vertical profiles in order to obtain a cross section of the air mass. The overall profile produces values of [OH] within the expected range of around 10^6 molecules cm⁻³ accepted as a typical OH concentration for most atmospheric conditions (Ehhalt, [1987]). However, the profiles do illustrate that the concentration of OH drops dramatically with increasing height. This is the result of falling in water vapour concentration as height increases. Owing to the primary production of OH being [H₂O] dependent it is consistent that [OH] must decrease with altitude. Also, clearly shown is the dependence of [OH] on time of day. Examinations of all flights show that at flight times greater than around 17:00 the total [OH] at altitudes similar to those measured previously is far less. This is a consequence of reduced production *via* ozone photolysis. Since *j*-(O¹D) is directly related to solar zenith angle, primary production of OH also includes some diurnal variation.



Steady-state estimates of $[\text{HO}_2]$ were also derived for these three flights during ACSOE summer *via* the HO_2/OH interconversion ratio. Data for A579, A580 and A581 is shown in Figures 4.10-4.12. As shown in these figures, $[\text{HO}_2]$ during ACSOE appears to be around 10 pptv. These values are however, dependent on altitude, solar zenith angle and on $[\text{NO}_x]$. The interconversion of OH into HO_2 is strongly affected by the concentration of the background NO and hence the interconversion ratio (ICR) should show similar NO dependence as was found by Brune *et al.* (1998) during the SUCCESS aircraft campaign. Specifically, the calculated ICR should have an inverse NO_x dependence since at low conditions of NO the HO_x partitioning should lie towards the HO_2 side of the system as illustrated in Figure 4.1. Conversely, the rapid reaction of HO_2 with NO forces the system to the OH side under conditions of high NO. During the ACSOE summer missions, NO values were observed to vary typically between 1 pptv and 2 ppbv. Plotting the ICR for all three flights against NO has the effect of describing the OH/ HO_2 partitioning for the flights described here. A plot of the total ICR verses total NO for these flights are shown Figure 4.13. The close relationship between HO_x and NO_x also explain the isolated peaks in the OH and HO_2 data shown above. Spikes in the data provided by the UEA NO_{xy} (see Chapter 2 for instrument description) that may be erroneous (S. Bauguitte, *personal communication*) do have the effect of causing some spikes in the data plots (*e.g.* the three spikes in OH for A579 between 11am and 12pm). These spikes were short lived and therefore can probably be attributed to instrument noise. However, since these data were not flagged as erroneous, the decision was taken to include them in data work-up.

Figure 4.10: Steady State HO_2 for ACSOE Flight A579

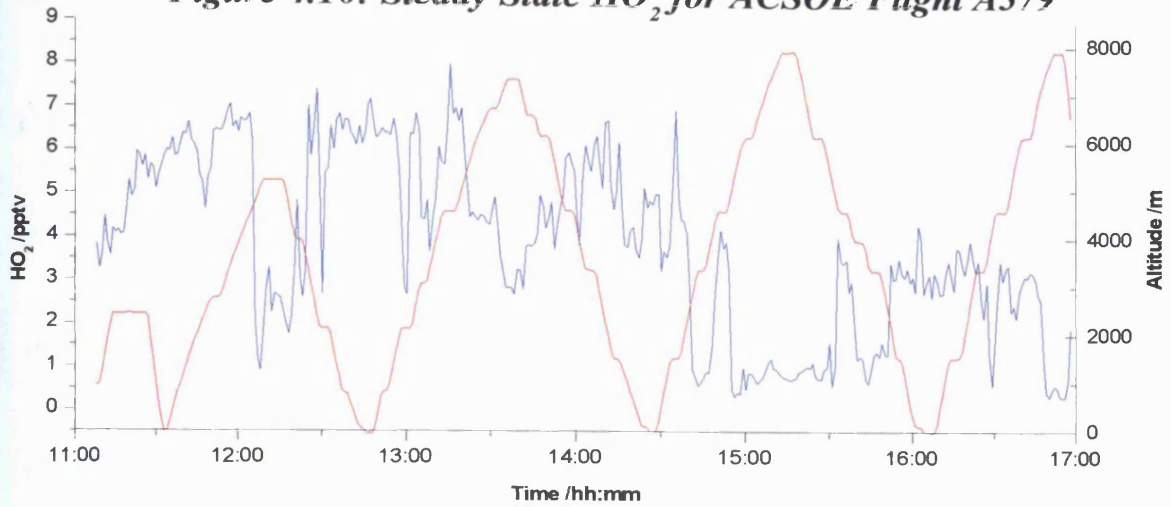


Figure 4.11: Steady State HO_2 for ACSOE Flight A579

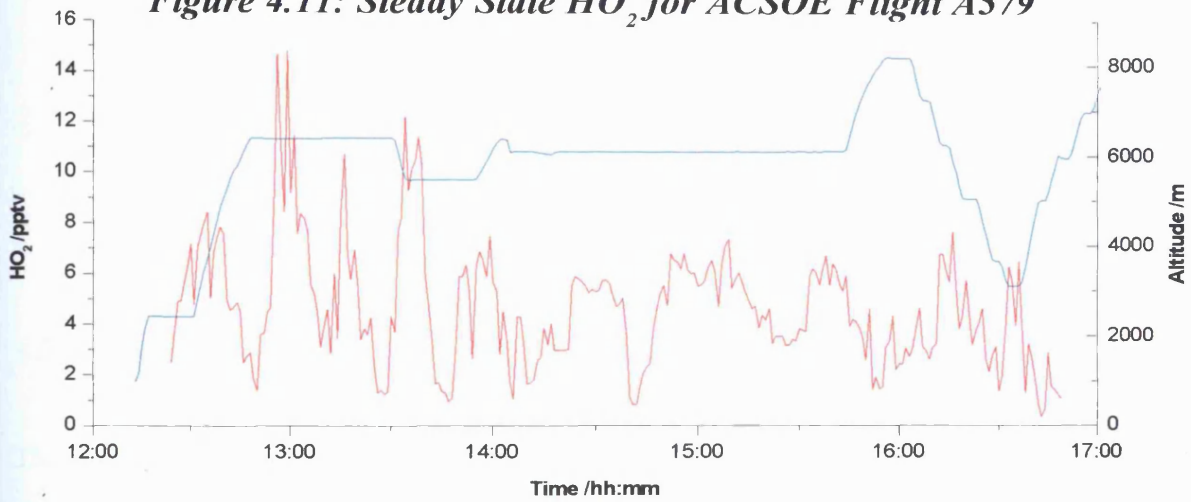


Figure 4.12: Steady State HO_2 for ACSOE Flight A581

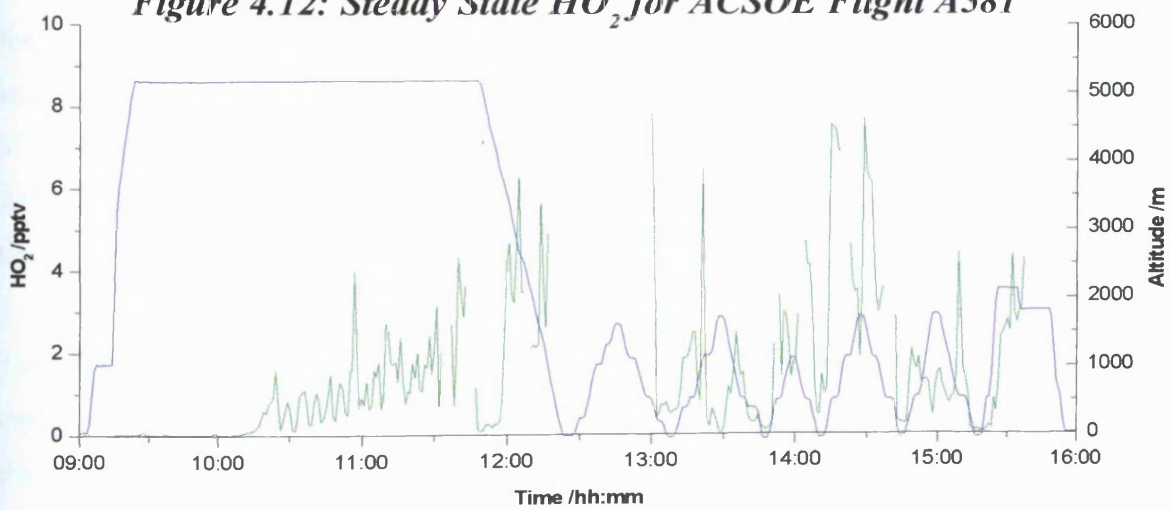
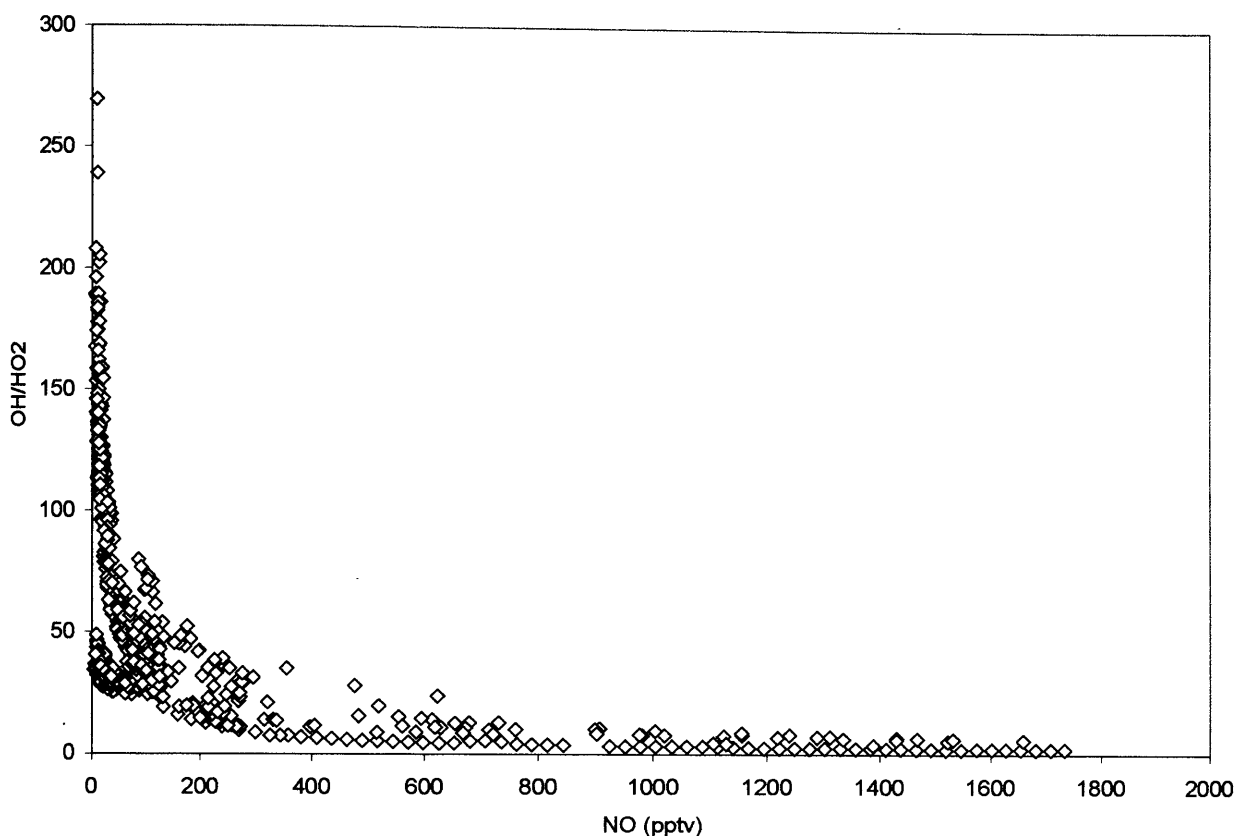


Figure 4.13: NO dependency of ICR during ACSOE Summer Flights



4.5 Modelling HO_x Along Aircraft Flight-Tracks

The main aim of the work described in this Chapter was to ascertain the applicability of steady-state algorithms in the prediction of $[HO_x]$ from aircraft. However, unlike the SONEX campaign, no *in-situ* measurement of OH and HO_2 was available during ACSOE. Hence, there was no way to investigate the steady-state predictions made above for this aircraft campaign. In order to investigate the applicability of the steady-state relationships described in section 4.3, box modelling of $[HO_x]$ along the aircraft flight tracks was undertaken. ACSOE flights A579, A580 and A581 were investigated using a newly developed flight track box model (FTBM).

The FTBM was written in FACSIMILE, a computer program used for numerical analysis and modelling chemical kinetics and transport. Details of FACSIMILE model construction and the FACSIMILE “language” are described by Curtis and Sweetenham (1987). A box model written using FACSIMILE was also used to predict the totally integrated $[HO_x]$ fields for aircraft altitude bins as described in Chapter 3. Similar FACSIMILE box model predictions of $[HO_2]$ and $[RO_2]$ have been compared to *in-situ* measurements of $[HO_2]$ and $[RO_2]$ during

ground base campaigns both in the boundary layer and free troposphere (Ayers *et al.* [1997], Zanis [1999], Monks *et al.* [2000]).

For the FTBM, data was constrained to available *in-situ* measurements. Typically, five minute averages of *in-situ* data for ozone, CO, NO, H₂O, HCHO, H₂O₂, and ROOH were used. Data for pressure, concentration of air molecules and temperature were also constrained to *in-situ* values. NO₂ data was derived from the photostationary state approximations as previously described in Chapter 2. Methane concentrations were not measured during the ACSOE campaign, therefore data on [CH₄] was set to 1750 ppbv.

Owing to the absence of several key photolysis frequency measurements, all photolysis rate coefficients were calculated by the FTBM. These values were parameterised by

$$j = A \exp(B \sec \theta) \quad (4.13)$$

The parameters A and B were set to the theoretical values calculated from a 2-stream isotropic scatter radiative transfer model (Hough [1988]). θ is the solar zenith angle, while Sec is the secant of the solar zenith angle at any given latitude, where

$$\sec = \frac{1}{\{\cos(\text{LHA})\cos(\text{lat}) * \cos(\text{dec}) + \sin(\text{lat}) * \sin(\text{dec})\}} \quad (4.14)$$

LHA is the local hour angle and dec is the solar declination angle, given by

$$dec = -0.4 * \cos\left(2\pi * \left[\frac{DOY + 10}{365}\right]\right) \quad (4.15)$$

where DOY is the day of year.

Photolysis frequencies for nine photochemical reactions were calculated. The increase in the solar declination angle with increasing altitude is not accounted for in equation (4.15). In order to account for this, data for DEC was obtained with respect to altitude from the US Navel Observatory Astronomical Applications Department *via* the World-Wide-Web (<http://aa.usno.navy.mil/AA/>). A full list of the kinetic parameters included in the model is shown in Table 4.3.

Table 4.3: Kinetic and Photochemical Data Used in FTBM. Temperature is absolute temperature, M is concentration of air molecules and J is a photolysis frequency. Rate constant data are taken from DeMore et al. (1997).

Reaction Number	Equation	Rate Expression
1	$O+OH \rightarrow H + O_2$	$2.2 \times 10^{-11} \exp(120/T)$
2	$O+HO_2 \rightarrow OH + O_2$	$3.0 \times 10^{-11} \exp(200/T)$
3	$O(^3P)+O_3 \rightarrow 2O_2$	$8.0 \times 10^{-12} \exp(2060/T)$
4	$O(^1D)+M \rightarrow O(^3P)+M$	$1.8 \times 10^{-11} [N_2] \exp(1100/T) + 3.2 \times 10^{-11} [O_2] \exp(70/T)$
5	$O(^1D)+H_2O \rightarrow 2OH$	2.2×10^{-10}
6	$OH+HO_2 \rightarrow HO_2+OH$	$4.8 \times 10^{-11} \exp(250/T)$
7	$OH+H_2O_2 \rightarrow HO_2 + H_2O$	$2.9 \times 10^{-12} \exp(160/T)$
8	$O_3+OH \rightarrow O_2+HO_2$	$1.6 \times 10^{-12} \exp(940/T)$
9	$OH+H_2 \rightarrow H + H_2O$	$5.5 \times 10^{-12} \exp(-2000/T)$
10	$HO_2+HO_2 \rightarrow H_2O_2$	$(2.3 \times 10^{-13} \exp(600/T) + (1.7 \times 10^{-33} [M] \exp(1000/T)) * (1 + 1.4 \times 10^{21} [H_2O] \exp(2200/T)))$
11	$O_3+HO_2 \rightarrow OH + 2O_2$	$1.1 \times 10^{-14} \exp(500/T)$
12	$O(^3P) + NO_2 \rightarrow NO + O_2$	$6.5 \times 10^{-12} \exp(120/T)$
13	$NO+O_3 \rightarrow NO_2+O_2$	$2.0 \times 10^{-12} \exp(1440/T)$
14	$O_3+NO_2 \rightarrow NO_3+O_2$	$1.2 \times 10^{-13} \exp(2450/T)$
15	$NO+NO_3 \rightarrow 2NO_2$	$1.5 \times 10^{-11} \exp(170/T)$
16	$NO + HO_2 \rightarrow NO_2 + OH$	$3.5 \times 10^{-12} \exp(250/T)$
17	$NO_2+NO_3 \rightarrow NO + NO_2 + O_2$	$4.5 \times 10^{-14} \exp(1260/T)$
18	$NO_3+HO_2 \rightarrow NO_2 + OH + O_2$	3.5×10^{-12}
19	$NO_3+NO_3 \rightarrow 2NO_2 + O_2$	$8.5 \times 10^{-13} \exp(2450/T)$
20	$N_2O_5 + H_2O \rightarrow 2HNO_3$	1.3×10^{-21}
21	$NO_3 + OH \rightarrow HO_2 + NO_2$	2.2×10^{-11}
22	$OH+HO_2NO_2 \rightarrow NO_2 + HO_2 + OH$	$1.3 \times 10^{-12} \exp(380/T)$
23	$OH + HONO \rightarrow NO_2 + H_2O$	$1.8 \times 10^{-11} \exp(390/T)$
24	$OH + HNO_3 \rightarrow NO_3 + H_2O$	$7.2 \times 10^{-15} \exp(785/T) + (1.9 \times 10^{33} \exp(725/T) [M]) / (1 + (1.9 \times 10^{33} \exp(725/T) [M]) / 4.1 \times 10^{16} \exp(1440/T))$
25	$OH + HCHO \rightarrow HCO + H_2O$	1.1×10^{-11}
26	$HCO+O_2 \rightarrow HO_2 +CO$	$3.5 \times 10^{-12} \exp(140/T)$
27	$OH + CH_4 \rightarrow CH_3 + HO_2$	$2.45 \times 10^{-12} \exp(1775/T)$
28	$OH + CH_3OH \rightarrow HO_2 + HCHO$	$6.7 \times 10^{-12} \exp(600/T)$
29	$CH_3O_2 + CH_3O_2 \rightarrow CH_3O + CH_3O + O_2$	$0.3 * 2.5 \times 10^{-13} \exp(190/T)$
30	$HO_2 + CH_3O_2 \rightarrow CH_3OOH + O_2$	$3.8 \times 10^{-13} \exp(800/T)$
31	$OH + CH_3OOH \rightarrow CH_3O_2 + H_2O$	$0.7 * 3.8 \times 10^{-12} \exp(200/T)$
32	$OH + CH_3OOH \rightarrow CH_2OOH + H_2O$	$0.3 * 3.8 \times 10^{-12} \exp(200/T)$
33	$CH_3O_2 + CH_3O_2 \rightarrow CH_3O_2 + HCHO + H_2O$	$0.6 * 2.5 \times 10^{-13} \exp(190/T)$
34	$CH_3O_2 + CH_3O_2 \rightarrow CH_3O_2CH_3 + O_2$	$0.1 * 2.5 \times 10^{-13} \exp(190/T)$
35	$CH_3O + O_2 \rightarrow HCHO + HO_2$	$3.9 \times 10^{-14} \exp(900/T)$

36	$\text{CH}_3\text{O}_2 + \text{NO} \rightarrow \text{CH}_3\text{O} + \text{NO}_2$	$3.0 \times 10^{-12} * \exp(280/T)$
37	$\text{NO}_3 + \text{HCHO} + \text{O}_2 \rightarrow \text{HNO}_3 + \text{CO} + \text{HO}_2$	5.8×10^{-16}
38	$\text{O}_3 + h\nu \rightarrow \text{O}({}^3\text{P}) + \text{O}_2$	J 0
39	$\text{O}_3 + h\nu \rightarrow \text{O}({}^1\text{D}) + \text{O}_2$	J 1
40	$\text{H}_2\text{O}_2 + h\nu \rightarrow 2\text{HO}_2$	J 2
41	$\text{CH}_3\text{OOH} + h\nu \rightarrow \text{CH}_3\text{O}_2 + \text{HO}_2$	J 3
42	$\text{HNO}_3 + h\nu \rightarrow \text{OH} + \text{NO}_2$	J 4
43	$\text{HONO} + h\nu \rightarrow \text{OH} + \text{NO}$	J 5
44	$\text{HCHO} + h\nu \rightarrow \text{H}_2 + \text{CO}$	J 6
45	$\text{HCHO} + h\nu + \text{O}_2 \rightarrow \text{HO}_2 + \text{CO}_2$	J 7
46	$\text{NO}_3 + h\nu \rightarrow \text{NO}_2 + \text{O}({}^3\text{P})$	J 8
47	$\text{NO}_2 + h\nu \rightarrow \text{NO} + \text{O}_2$	J 9
48	$\text{HO}_2\text{NO}_2 + h\nu \rightarrow \text{HO}_2 + \text{NO}_2$	J 10
49	$\text{CH}_3\text{COCH}_3 + h\nu \rightarrow \text{CH}_3\text{CO} + \text{CH}_3$	J 11

4.6 FTBM vs. *in-situ* SONEX data

As described in section 4.2, measurements of HO_x were made *in-situ* during SONEX using the ATHOS instrument. Correlations between the FTBM prediction and the data obtained by laser induced fluorescence can be used to test the validity of the model output not only in terms of concentration of OH and HO_2 , but also in the fine structure observed as the aircraft moves horizontally and vertically in the atmosphere. In total four SONEX flights were tested using the flight track model. The plots of model data for OH, together with the *in-situ* data obtained from the FAGE instrument are shown in Figure 4.14. From Figure 4.14, the flight track box model is consistently within the stated uncertainty of the measurement of *ca.* 40% for measured OH and reproduces the structure of the time series with reasonable accuracy.

Correlation plots between FTBM and measured OH are shown in Figure 4.15. Correlation coefficients indicate that the typical agreement is on the order of 0.7-0.8 for three of the SONEX flights investigated. The SONEX flight on 5/11/97 has a correlation coefficient of *ca.* 0.4 owing to the model data for this flight showing large underestimations of the measured [OH]. Specifically, there is rapid decay in model [OH] prediction at around 60 000 – 70 000 seconds from midnight. This suggests that the decay is strongly coupled to increases in solar zenith angle at times greater than *ca.* 8pm (70 000 seconds after midnight). Obviously, at such time the primary OH production route from ozone photolysis tends to zero and therefore the model prediction of [OH] falls off rapidly. As described by Jaeglé *et al.* (2000), during SONEX HO_x concentrations were shown to vary at times where solar zenith angle was $>80^\circ$.

Figure 4.14: FTBM vs. Measured [OH] Data for Selected SONEX Flights

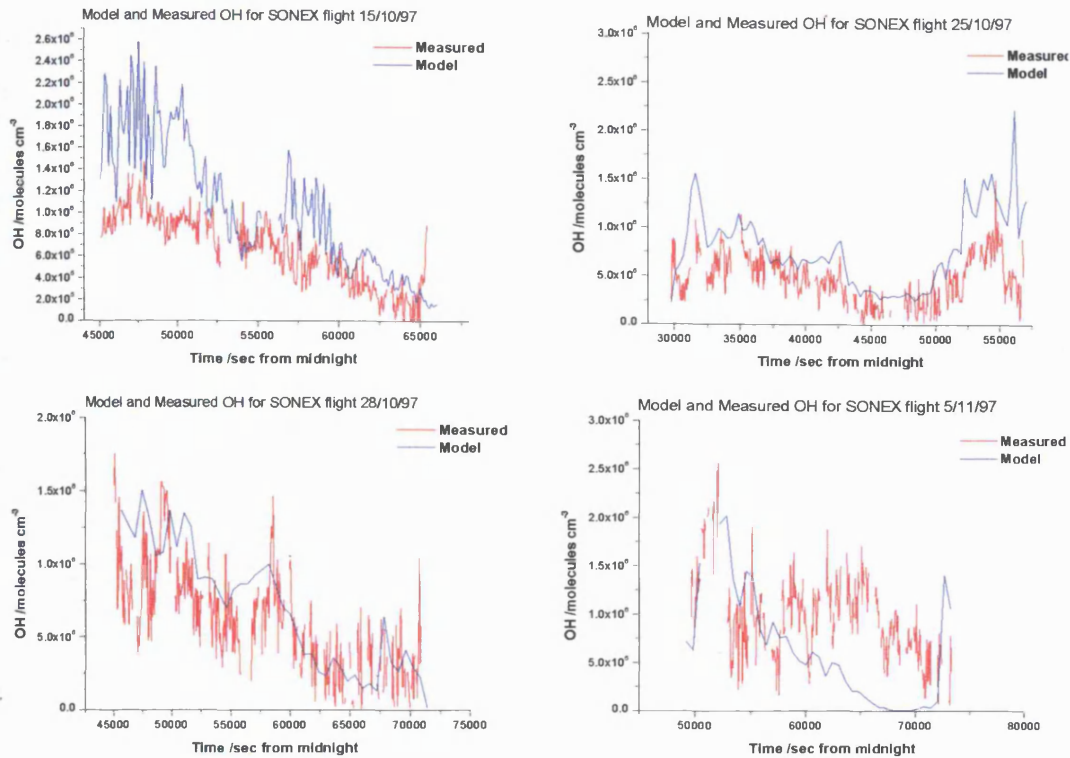
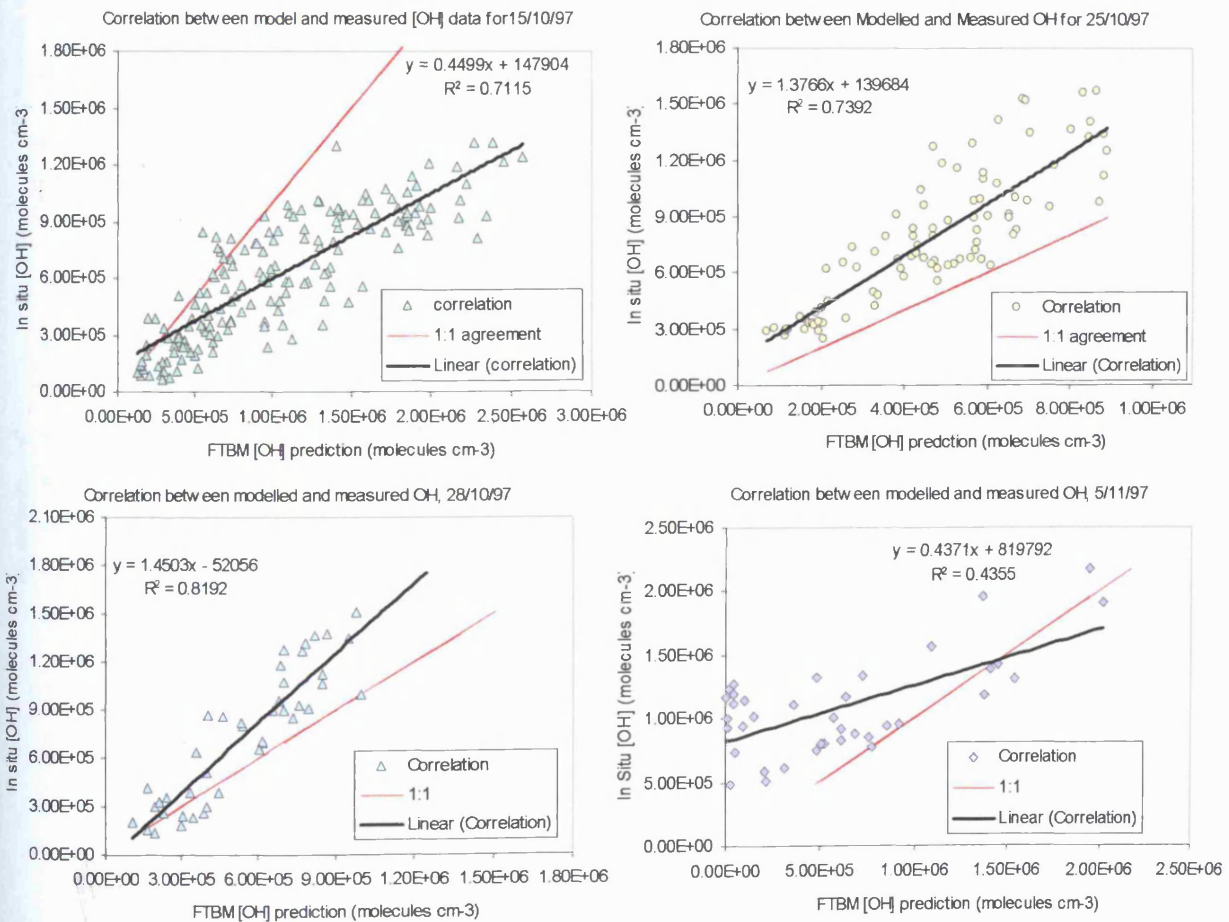


Figure 4.15: Correlation between FTBM and Measured [OH] For Selected SONEX Flights



At these times, steady-state and model predictions of [OH] could not account of the measured concentration through primary production alone. Hence, it was concluded by Jaeglé and co-workers that secondary sources such as HNO_4 were playing major roles in P-(OH). $[\text{HO}_2]$ data from the flight track box model is plotted together with that measured by the ATHOS instrument in Figure 4.16. The FTBM and measured data shown in Figure 4.16 show there is a general level of agreement in terms the structure of the time series plot but, in all cases, there is an over estimation of the total $[\text{HO}_2]$ in the FTBM. However, there is a large inter-flight variability. Specifically, the structure in HO_2 as measured during the 15/10/97 flight seems to be reproduced by the flight track model but concentrations of HO_2 are overestimated. The measured/modelled correlation plots for HO_2 are shown in Figure 4.17. Correlation coefficients are *ca.* 0.6-0.7 for 28/10/97 and 5/11/97, while flight 15/10/97 and 25/10/97 where $r^2 = 0.559$ and 0.172 respectively, owing to large overestimation of the measured $[\text{HO}_2]$ as compared to the FTBM.

Figure 4.16: Modelled and Measured HO_2 data for SONEX Using FTBM

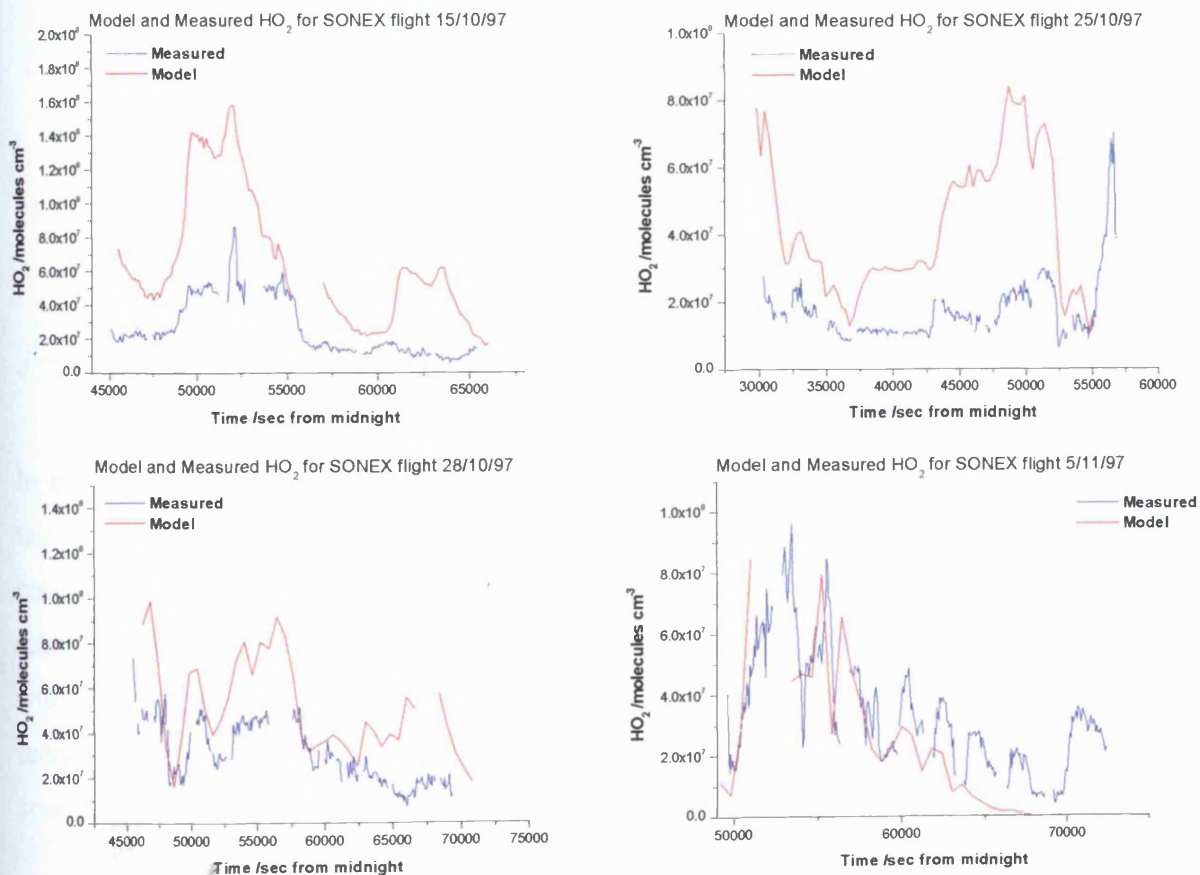
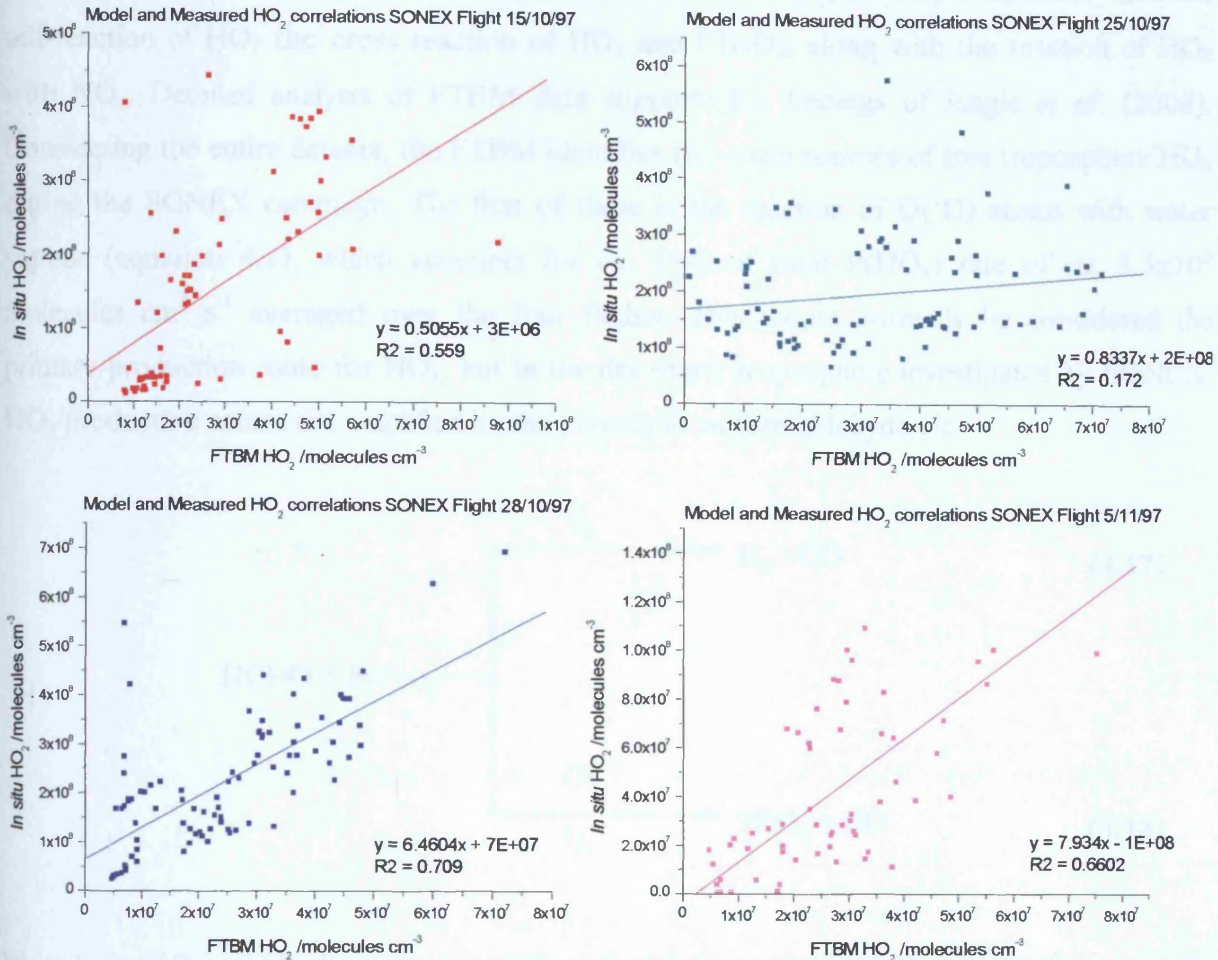


Figure 4.17: Modelled and Measured HO₂ Correlations during SONEX

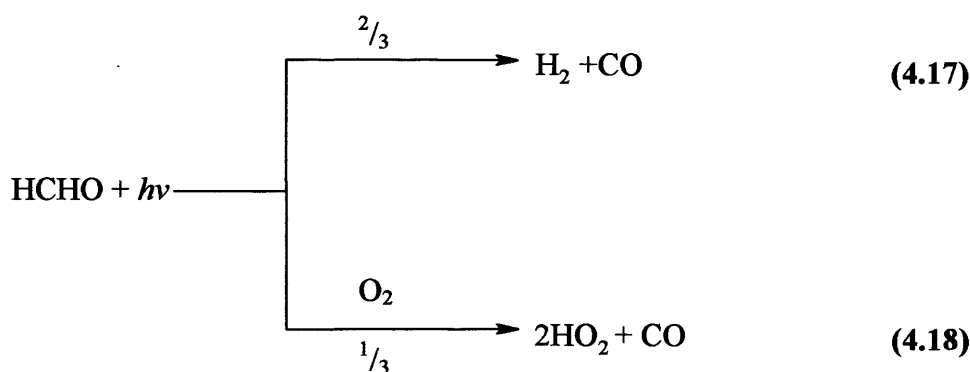


4.7: SONEX Modelling Conclusions

In summary, the model outputs from the newly developed flight track box model have been tested against *in-situ* [HO_x] data for SONEX flight series. In general, the model seems to reproduce [HO_x] of the UT/LS region to some degree of accuracy. Model data for OH show relatively good agreement to measured [OH], with FTBM predicted data comfortably lying within the quoted error of $\pm 40\%$ for the *in-situ* data. To a lesser extent the FTBM HO₂ data seems to show agreement to the measured [HO₂], but model data overestimates the absolute concentration.

In order to investigate the controlling processes, a detailed analysis into the production and loss routes of model HO_x was undertaken. The aim of this analysis was to identify the key production and loss routes absent from the steady-state relationships and to therefore increase understanding of why steady-state relationships seem to underestimate measured [HO_x].

Jaeglé *et al.* (2000) identified the key production processes for the HO_x measured in SONEX as the reaction O(¹D) + H₂O and the photolysis of formaldehyde. Key HO_x sinks were the self-reaction of HO₂ the cross reaction of HO₂ and CH₃O₂, along with the reaction of HO₂ with NO_x. Detailed analysis of FTBM data supports the findings of Jaeglé *et al.* (2000). Considering the entire dataset, the FTBM identifies two main sources of free troposphere HO_x during the SONEX campaign. The first of these is the reaction of O(¹D) atoms with water vapour (equation 4.2), which accounts for *ca.* 59% of total P(HO_x) rate of *ca.* 3.5x10⁵ molecules cm³ s⁻¹ averaged over the four flights. This would normally be considered the primary production route for HO_x, but in the dry upper troposphere investigated by SONEX, HO_x production routes are amplified by the photolysis of formaldehyde *viz.*



Photolysis of formaldehyde to produce HO₂ radicals *via* reaction (4.18) accounts for over 39% of the total HO_x production as predicted by the model. Other sources included in the analysis were reactions such as photolysis of hydrogen peroxide and nitric acid, but these were small in comparison (≤ 2%). A full breakdown of the relative pathway strengths in total P(HO_x) for the model constrained to SONEX *in-situ* data is shown in Table 4.4.

In terms of the most important HO_x loss routes, the FTBM seems to reproduce the results of Jaeglé *et al.* (2000). The flux data shown in Table 4.5 suggests that the model has four major loss routes. These are the self-reaction of HO₂, the cross-reaction of HO₂ with CH₃O₂ along with the reaction of OH with NO_x as described above. In the dry, relatively NO_x rich atmosphere of SONEX the NO_x chemistry is the dominant loss route, with *ca.* 54% of HO_x lost through reaction of OH with NO₂ to form nitric acid *viz.*



Table 4.4: Contributions to $P(\text{HO}_x)$ from SONEX Flight Track Models ($\text{molecules cm}^{-3} \text{ s}^{-1}$)

SONEX Flight	Total Flux	(O ¹ D)+ H ₂ O	% of total	$j\text{-(H}_2\text{O}_2)$	% of total	$j\text{-(HNO}_3)$	% of total	$j\text{-(HCHO)}$	% of total
15/10/97	8.0×10^4	6.69×10^4	83%	1.36×10^3	2%	2.74×10^3	3%	8.57×10^3	12%
25/10/97	2.80×10^5	1.56×10^5	55%	7.79×10^3	3%	6.48×10^1	2%	1.11×10^5	40%
28/10/97	1.14×10^5	4.24×10^4	37%	6.96×10^3	6%	5.32×10^3	5%	5.94×10^4	52%
5/11/97	8.51×10^5	5.64×10^5	66%	4.47×10^3	<1%	1.06×10^4	1%	2.85×10^5	32%
Average	3.5×10^5	2.07×10^5	59%	2.57×10^3	<1%	4.68×10^3	2%	1.36×10^5	39%

Table 4.5: Contributions to $L(\text{HO}_x)$ from SONEX Flight Track Models ($\text{molecules cm}^{-3} \text{ s}^{-1}$)

SONEX Flight	Average Flux	NO+OH → HONO	% of total	MeO ₂ +HO ₂ → MeOOH	% of total	2HO ₂ → H ₂ O ₂	% of total	NO ₂ +OH → HNO ₃	% of total
15/10/97	5.5×10^5	1.17×10^4	2%	3.31×10^4	6%	1.55×10^5	28%	3.48×10^5	64%
25/10/97	2.9×10^4	5.31×10^3	19%	3.57×10^3	12%	1.13×10^4	39%	8.97×10^3	30%
28/10/97	3.80×10^5	1.49×10^4	4%	3.31×10^4	8%	2.89×10^5	76%	4.33×10^4	12%
5/11/97	7.74×10^5	1.20×10^4	2%	1.64×10^4	2%	1.18×10^5	15%	6.28×10^5	81%
Average	3.81×10^5	1.10×10^4	3%	2.20×10^4	5%	1.43×10^5	38%	2.05×10^5	54%

The other dominant sink for HO_x in the model constrained to SONEX data is the self-reaction of HO₂, which accounts for over 37% of the total HO_x loss. A summary of the pathway strengths in the loss routes for model HO_x are shown in Table 4.5.

These modelled data and analyses increase the understanding of why steady-state relationships such as those described by Penkett *et al.* (1997) have problems predicting *in-situ* HO_x concentration as measured during SONEX. From equation (4.4), it is assumed in steady-state that the only production source for HO_x is the reaction of ozone to form O(¹D) and the subsequent reaction of this excited oxygen to form OH. All HO₂ concentrations are derived from this production step, with HO₂ formed by the recycling of OH. From the analysis of HO_x production and loss it is obvious that important P(HO_x) and L(HO_x) pathways are not accounted for in the relationships shown in equations (4.4) and (4.11). As shown from the model data and the results of Jaeglé *et al.* (2000) for the SONEX mission the primary production of HO_x is *via* routes such as formaldehyde photolysis in addition to the reaction of O(¹D) with water vapour. The absence of HCHO photolysis is likely to explain much of the underestimation of steady-state HO_x during SONEX.

Despite having identified these features, there are still areas where the model fails to reproduce the concentration of HO_x measured during SONEX. From Figure 4.17, it is apparent that FTBM [HO₂] for two of the SONEX flights overestimated measured [HO₂] by significant amounts. Considering the sources and sinks of HO₂, it was identified previously that the key P(HO₂) pathways are the recycling of OH → HO₂ *via* the action of NO₂, CO and ozone, combined with direct formation of HO₂ through photolysis of HCHO and H₂O₂. Considering these sources, it seems unlikely that there would be an overestimation of P(HO₂) that would be as non-systematic. If, for example, the model was overestimating production of HO₂ due to the photolysis of HCHO or H₂O₂ owing to the overestimation of *j*-values then it might be expected that all flights would overestimate HO₂ by similar amounts. Similarly, if the sinks for HO₂ were underestimating L(HO₂) owing to incorrect rate constants then the error would be more systematic, assuming the system is linear. The fact that the overestimation is non-systematic probably means that the overestimation is due to factors associated with each individual flight.

The flight track box model constructed in this analysis is obviously a simplified version of all the reactions that could occur in the real atmosphere. As identified by Jaeglé *et al.* (2000) the loss routes for HO₂ in SONEX were numerous. In the flight track box model the role of heterogeneous chemistry and the loss of HO₂ through reaction with higher organic peroxy

radicals (>2 carbon atoms), the species broadly described as RO₂ are ignored. If in flights such as 25/10/97 the role of RO₂ + HO₂, heterogeneous removal or other unknown reaction sinks were significant, the model would overestimate HO₂, maybe even by the large amounts observed in Figure 4.17. A summary of the comparisons between FTMB and the Harvard model described by Jacob *et al.* (1996) to observed [HO₂] and [OH] for these SONEX flights is shown in Table 4.6. Despite the potential shortcomings, the application of the flight track box model to SONEX data gives a level of confidence about the general applicability of such a model to aircraft data. Having shown that the FTBM is valid in predicting [HO_x], similar flight track models were developed in order to investigate HO_x budget for the ACSOE campaign.

Table 4.6: Comparisons of FTBM and Harvard Model correlations to in-situ [HO₂] and [OH] data for selected SONEX flights

Date	FTBM Correlation for [HO ₂]	Harvard Model Correlation for [HO ₂]*	FTBM Correlation for [OH]	Harvard Model Correlation for [OH]*
15/10/97	R ² = 0.6	R ² = 0.9	R ² = 0.7	R ² = 0.8
25/10/97	R ² = 0.2	R ² = 0.9	R ² = 0.7	R ² = 0.8
28/10/97	R ² = 0.7	R ² = 0.9	R ² = 0.8	R ² = 0.8
5/11/97	R ² = 0.7	R ² = 0.8	R ² = 0.4	R ² = 0.7

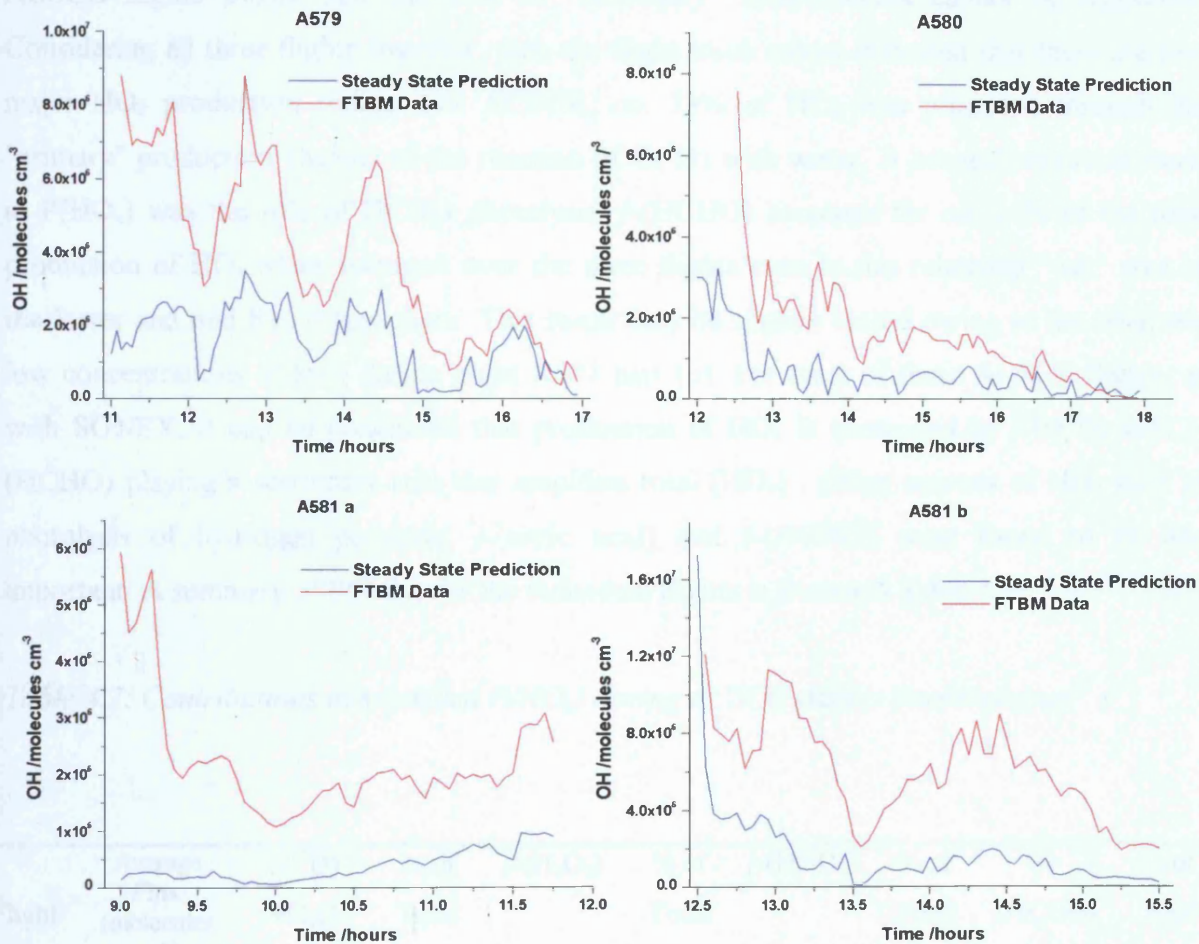
* Data taken from Faloona *et al.* (2000)

4.8: ACSOE Flight Track Modelling

As stated previously in section 4.5, three ACSOE flights were investigated with respect to steady-state predictions of [HO_x]. The same three flights A579, A580 and A581 were examined in terms of the flight track box model prediction of [HO_x]. For flight, A581 it was decided to break up the flight into two separate legs owing to the different photochemical environments encountered during this flight. The first part of A581 was the high altitude transit back to the UK in the mid free troposphere, where anthropogenic influences on background chemistry were observed to be low. This was in contrast to the second component, a series of saw tooth profiles in the UK boundary layer, which was heavily perturbed by anthropogenic pollutants. The model was constrained in a similar way to the SONEX missions, specifically with concentrations of ozone, CO, NO, H₂O, HCHO, H₂O₂,

and ROOH. Data for pressure, concentration of air molecules, and temperature was either constrained to *in-situ* values or calculated from *in-situ* values. Methane concentrations were again set at constant 1750 ppbv. With respect to NO₂ data then the photostationary state assumptions described in Chapter 2 allowed the calculation of [NO₂]. Model output was in 5-minute averages. These model data were then compared to [OH] predictions derived from steady-state assumptions as described in section 4.5. A comparison of these data is shown in Figure 4.18.

Figure 4.18: ACSOE Steady-State [OH] Predictions with FTBM Model [OH]



From Figure 4.18 FTBM data and steady-state predictions show many of the same general trends in [HO_x]. It is obvious from Figure 4.18 that the steady-state model calculation of the total HO_x budget is significantly lower than the FTBM output. From the SONEX data comparisons, it has been shown that the FTBM is a good representation of [HO_x]. Comparing the FTBM data to steady-state prediction, total HO_x is underestimated by 44% using the relationships described in equation (4.4) and (4.11). The individual budgets of OH and HO₂ appear to be under predicted by *ca.* 30% and 26% respectively by steady-state predictions *c.f.* FTBM data.

The underlying reason for the underestimation of steady-state model $[HO_x]$ was investigated by comparison of the sources and sinks for HO_x in the flight track box model. From section 4.5, it was believed that the primary production of HO_x in the environment of ACSOE would be through the reaction of $O(^1D)$ with water vapour since the oceanic free troposphere close to the Azores had concentrations of H_2O that were far more abundant than SONEX. The average water concentration of the flights considered in these analyses was 5029 ppmv, *c.f.* 2370 ppmv for SONEX. Consistently therefore, $[H_2O]$ was above the 100ppmv threshold identified by Singh *et al.* (1995) as the upper troposphere cut-off, where $O(^1D) + H_2O$ is no longer the primary HO_x production pathway. However, analysis of the model outputs for these three ACSOE flights shows that the role of "secondary" HO_x sources cannot be neglected. Considering all three flights together, then the flight track model indicated that there are two major HO_2 production routes. For ACSOE, *ca.* 73% of HO_x was produced through the "primary" production channel of the reaction of $O(^1D)$ with water. A second important route in $P(HO_x)$ was the role of HCHO photolysis. j -(HCHO) accounts for *ca.* 24% of the total production of HO_x when averaged over the three flights even in this relatively "wet" area of the lower and mid free troposphere. This result may be slightly biased owing to the relatively low concentrations of H_2O during flight A581 part (b). For most of these ACSOE flights, as with SONEX, it can be concluded that production of HO_x is controlled by j -(O^1D) with j -(HCHO) playing a secondary role that amplifies total $[HO_x]$. Other sources of HO_2 such as photolysis of hydrogen peroxide, j -(nitric acid) and j -(HONO) were found to be less important. A summary of $P(HO_x)$ for the individual flights is shown in Table 4.7.

Table 4.7: Contributions to Modelled $P(HO_x)$ during ACSOE Azores ($molecules\ cm^{-3}\ s^{-1}$)

Flight	Average Flux (molecules cm^{-3})	(O^1D) + H_2O	% of Total	j -(H_2O_2)	% of Total	j -(HNO_3)	% of Total	j - (HCHO)	% of Total
A579	2.53×10^6	1.15×10^6	45%	8.22×10^3	<1%	4.48×10^4	2%	1.33×10^6	53%
A580	1.44×10^6	2.69×10^5	19%	4.66×10^3	<1%	4.97×10^4	3%	1.12×10^6	78%
A581a	2.30×10^6	4.95×10^5	22%	1.65×10^4	<1%	3.48×10^4	2%	1.75×10^6	76%
A581b	4.30×10^6	1.94×10^6	45%	8.43×10^4	2%	5.02×10^4	1%	2.23×10^6	52%
Average	2.63×10^6	9.64×10^5	37%	2.84×10^4	1%	4.48×10^4	2%	1.59×10^6	60%

Considering the loss routes for HO_x in the summer series of ACSOE missions then again the FTBM shows a range of sinks. In the low NO_x environment of the remote free troposphere, it was assumed that the dominant sink for HO_x would be the self and cross reactions of peroxy radicals. The quantitative analysis described here shows that although these loss routes are important, they are not the dominant loss routes. These analyses suggest the role of NO_x chemistry cannot be neglected in ACSOE Azores data. For all three flights shown, the sum of L(HO_x) shows that only 8% of the HO_x budget is lost through the reaction of HO₂ with HO₂. This compared to *ca.* 73% owing to the formation of nitric acid from the reaction of OH with NO₂. Other loss routes identified in the model were the reaction of CH₃O₂ with HO₂ and the reaction of OH with NO. However, these were much smaller than the self-reaction of HO₂ or formation of HNO₃. The full breakdown of L(HO_x) pathways is shown in Table 4.8.

Table 4.8: Contributions to Modelled L(HO_x) during ACSOE Azores (molecules cm⁻³ s⁻¹)

Flight	Average		% of total	CH ₃ O ₂ + HO ₂	% of total	HO ₂ + HO ₂		NO ₂ + OH	
	Flux	NO+OH				% of total	% of total		
A579	3.45x10 ⁷	7.05x10 ⁶	21%	3.00x10 ³	<1%	3.45x10 ²	<1%	2.75x10 ⁷	79%
A580	3.15x10 ⁶	1.47x10 ⁵	5%	1.56x10 ⁵	5%	2.57x10 ⁶	81%	2.79x10 ⁵	9%
A581(a)	3.24x10 ⁴	4.14x10 ³	13%	5.94x10 ²	2%	2.58x10 ³	8%	2.51x10 ⁴	77%
A581(b)	1.46x10 ⁶	1.58x10 ⁵	11%	7.74x10 ⁴	5%	3.87x10 ⁵	27%	8.39x10 ⁵	57%
TOTAL	9.79x10 ⁶	1.84x10 ⁶	19%	5.92x10 ⁴	<1%	7.40x10 ⁵	8%	7.16x10 ⁶	73%

4.9: Overall Summary

In this Chapter, attempts to model the free tropospheric HO_x budget *via* steady-state model calculations and flight track box models have been made. This had been attempted for two separate and independent aircraft campaigns, SONEX and ACSOE, which investigated the North Atlantic free troposphere during summer and autumn 1997. Using steady-state relationships derived by Penkett *et al.* (1997) and modified for free troposphere application by Zanis (1999) it has been shown that these predictions have only limited ability in predicting HO_x over the range of conditions calculated. For the SONEX campaign steady-state derived HO_x was shown to be consistently lower than that measured *in-situ* by a laser induced fluorescence technique.

Attempts to model the chemistry of this region through the development of a new flight track have been more successful. Using a simple box model, $[\text{HO}_x]$ data has been modelled and has been shown to have adequate agreement to data measured during the SONEX campaign *via* the FAGE technique. This model seems to reproduce both the structure and concentration observed *in-situ* and has accuracy greater than the 40% quoted as the experimental uncertainty in the FAGE measurements of HO_2 and OH. The results obtained in this analysis do give some confidence that simple flight track box models can reproduce the chemistry of the free troposphere. Therefore, this model could be used to investigate the HO_x budget where no *in-situ* measurements were made. This was exactly the circumstance during the ACSOE campaign, and this flight track model has been applied to provide HO_x predictions for three of the ACSOE summer flights.

Through comparisons, ACSOE model outputs have shown that, steady-state derived relationships are consistently lower than the model prediction. This has been attributed to the absence of formaldehyde photolysis as a HO_x production route in the steady-state model. This "secondary" source has been shown to be as important, if not more important in the production of HO_x than the reaction of $\text{O}(^1\text{D})$ with water vapour. The absence or underestimation of this key production step combined with additional HO_x sinks owing to the important role of NO_x , makes the use of the steady-state relationships in their present form unworkable as useful tools in order to predict the fast photochemistry that occurs in the North Atlantic free troposphere. It seems therefore that although these steady-state relationships were shown to have good model correlation at static sites such as the Jungfraujoch (FREETEX) or the remote marine boundary layer site at Cape Grim (SOAPEX), their wider applicability in aircraft analysis requires further quantification.

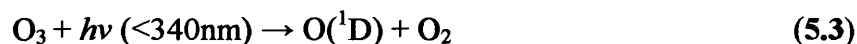
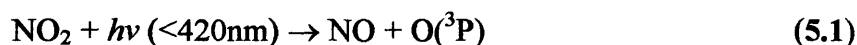
Chapter Five: Measurement of *In-Situ* Photolysis Frequencies From Aircraft Platforms

5.1)	Introduction	158
5.2)	Factors Influencing j-(O¹D)	161
5.3)	Characterisation of j-(O¹D) Aircraft Filter Radiometers	165
5.4)	Performance of j-(O¹D) Radiometers During ACSOE	175
5.5)	Modelling Photolysis Frequencies During ACSOE	186
5.6)	Model and Measured j-(O¹D) Profiles	192
5.7)	Remaining Issues	193
5.8)	Overall Summary	194

Chapter 5: Measurement of *In-Situ* Photolysis Frequencies from Aircraft Platforms

5.1 Introduction

The photodissociation of trace gas species in the troposphere is the driving force for much of the radical chemistry that occurs in the Earth's atmosphere. For example, ozone photolysis in the presence of water vapor is the primary production channel for the formation of the hydroxyl radical, OH, which initiates much of the oxidative removal of trace gases in the troposphere. Photochemical ozone production in the troposphere is also facilitated by photochemistry; hence the reaction scheme for the oxidative removal of hydrocarbons is under photochemical control;



In order to model accurately the total HO_x and NO_x budgets within the troposphere, validation of atmospheric photolysis frequencies by field measurement is often necessary. It has been shown by several authors (*e.g.* Madronich *et al.* [1987], Shetter and Müller *et al.* [1999]) that photochemical processes are directly proportional to actinic flux rather than pure irradiance. The actinic flux is defined as the flux density that is capable of producing photodissociation in photo actively labile molecules, while irradiance is the density of energy flux without consideration of the direction. For such a molecule, A, the photodissociation of A is characterised by the photolysis frequency *j*, where

$$j = \frac{1}{[A]} * \frac{d[A]}{dt} \quad (5.6)$$

The photolysis frequency, j , is dependent on local actinic flux, the absorption cross-section, σ and quantum yield, ϕ , for molecule A. These molecular parameters themselves are seen to be functions of both temperature and wavelength. Hence, a photolysis frequency can be evaluated as the integral of the product of solar actinic flux F , absorption cross-section and quantum yield with respect to wavelength;

$$j = \int_{\lambda_1}^{\lambda_2} \sigma(\lambda, T) * \phi(\lambda, T) * F(\lambda) \, d\lambda \quad (5.7)$$

In equation (5.7), the solar actinic flux is the net radiation available to photodissociate a molecule over a solid angle of $4\pi\text{sr}$. In order to evaluate photolysis frequencies, the actinic flux from all directions must be accurately quantified. In equation (5.7), λ_1 and λ_2 are the wavelength limits of photolysis. Below ca. 290nm, the so-called atmospheric "cut-off," no solar actinic flux is able to reach the ground owing to the total absorption of radiation by stratospheric ozone. For ground based instruments, the limit λ_1 is typically set to 290nm, with λ_2 being the upper limit of photolysis for the species A. λ_2 is typically 420nm for $j\text{-(NO}_2\text{)}$ and 340nm for $j\text{-(O}^1\text{D)}$ respectively.

Measurements of actinic flux and subsequent photolysis frequencies have been recorded in the literature over the last two decades using a variety of techniques. The first of these is the chemical actinometer. This technique has been used to measure $j\text{-(NO}_2\text{)}$ and $j\text{-(O}^1\text{D)}$ by several authors (*e.g.* Bahe, [1979], Dickerson *et al.* [1982], Blackburn *et al.* [1992], Shetter *et al.* [1996]). The technique relies on the direct exposure of O₃ or NO₂ to actinic flux by way of a $2\pi\text{sr}$ tube or dome arrangement. For a $j\text{-(NO}_2\text{)}$ chemical actinometer, detection is usually *via* chemiluminescence reaction of NO following photochemistry inside the reaction vessel. For $j\text{-(O}^1\text{D)}$, changes in conductivity of methanol have been used to detect artefacts of the photodissociation of ozone as described by Shetter *et al.* (1996). Chemical actinometers therefore do not require the use of molecular parameters in the evaluation of j values but do need accurate calibrations and are limited to one molecular species per instrument. The relatively long time responses and sheer bulk of such instruments often means that they are often not practical instruments for deployment in all platforms where measurement of photolysis frequencies is necessary (*e.g. via* aircraft platforms).

The development of a fixed bandwidth photoelectric radiometer by Junkermann *et al.* (1989) has led to the deployment of many such instruments for the measurement of photolysis rate

coefficients. The use of so-called fixed bandwidth radiometers as usable field instruments for both ground based and aircraft campaigns has been described by several authors (Hofzumahaus *et al.* [1992], Müller *et al.* [1992], Volz-Thomas *et al.* [1996]). These are compact devices based on the original concept by Junkermann and co-workers consisting of 2π sr quartz dome/diffusers to collect actinic flux. Photons are then passed through a bandpass filter set to transmit photons of the desired wavelength between limits λ_1 and λ_2 (see equation 5.1). A photomultiplier tube or similar device then detects photons. The variation of actinic flux with time is then recorded as a function of the measured PMT voltage. The time response is usually of the order of 1 second. Although filter radiometers are usually more practical and versatile than chemical actinometers, they still rely on absolute calibrations made against chemical actinometers to evaluate the j value. The main limitation of filter radiometers is that the bandpass filter each radiometer contains limits each device to a specific bandwidth of λ_1 to λ_2 . Therefore, these species-specific devices are limited to the evaluation of only one photolysis frequency per instrument.

The desire for accurate evaluation of actinic flux and photolysis frequencies by instruments with rapid time responses, together with the flexibility to measure several j values simultaneously has led to the development of spectroradiometry. These instruments determine actinic flux by scanning the spectral region between limits λ_1 and λ_2 and use the solution of integral shown in equation (5.7) to estimate photolysis frequency *via* the product of actinic flux and relevant molecular parameters. The advantage of these instruments is that several photolysis frequencies can be calculated simultaneously on a timescale limited to the scanning speed of the instrument only. Such instruments have been successfully used by Müller *et al.* (1995), McElroy and co-workers (1995) and by Shetter and Müller (1999).

In this chapter, factors that influence photolysis frequencies such as j -(O¹D) are explored, along with results of the direct measurement of j -(O¹D) from aircraft. It will be shown that the influence of altitude, temperatures and variations in molecular data are important in the determination of the overall photolysis frequency. Having considered these factors, detailed characterisations of the aircraft filter radiometers are described, along with a full error assessment and comparison of the measured data to models. It will be shown that these newly developed aircraft radiometers can measure j -(O¹D) accurately and can also provide important insight in the photochemical control of ozone in the North Atlantic free troposphere.

5.2: Factors Influencing j -(O¹D)

Photolysis frequencies such as j -(O¹D) are influenced by many physical parameters. Several authors (*e.g.* Hofzumahaus *et al.* [1992] Swartz *et al.* [1999]) have shown that factors such as albedo, total ozone column, solar zenith angle, temperature, season, latitude, clouds, aerosols and altitude all affect the measured photolysis frequency. Some of these factors such as solar zenith angle and altitude affect the net upwelling and downwelling actinic flux, while others, *e.g.* temperature, can affect the molecular absorption characteristics of the molecule undergoing photodissociation. In this chapter the photolysis frequency j -(O¹D), as measured *via* an aircraft platform has been investigated. This is particularly important since aircraft can sample many different latitudes as well as many different altitudes over the course of a single flight. A characterisation of the parameters that effect actinic flux, absorption cross-section and quantum yield is necessary in order to ascertain the net effect on photolysis frequencies as measured from these aircraft platforms.

5.2.1: Change in Contributions to j -(O¹D) from Direct/Diffuse Flux

The first and perhaps most relevant, with respect to aircraft measurement of photolysis rates, is the change in j -(O¹D) with increasing altitude. The effect of increasing height has several important features to consider with respect to j values. The first and most important is the difference in the relative importance of upwelling and downwelling radiation. Madronich (1987) showed that the calculation of total actinic flux that incidents an atmospheric trace gas molecule must include the combination of direct and diffuse radiation and scattering of light in the atmosphere and at the surface, *i.e.*

$$\text{Flux}_{\text{total}} = (\text{Flux}_{\text{direct}}) + (\text{Flux}_{\text{downwelling}}) + (\text{Flux}_{\text{upwelling}}) \quad (5.8)$$

As altitude increase, the relative importance of these parameters on the total flux changes. Specifically, as altitude increases the upwelling component of radiation becomes more important. Figure 5.1 shows the net contribution of direct and diffuse radiation to j -(O¹D) with respect to wavelength at the surface. These data were obtained from the TUV version 4 model described in section 5.4 (data optimised for 20/9/97 at 39°N, 44°W).

Figure 5.1: Contributions to $j(O^1D)$ from actinic flux with respect to wavelength at the surface

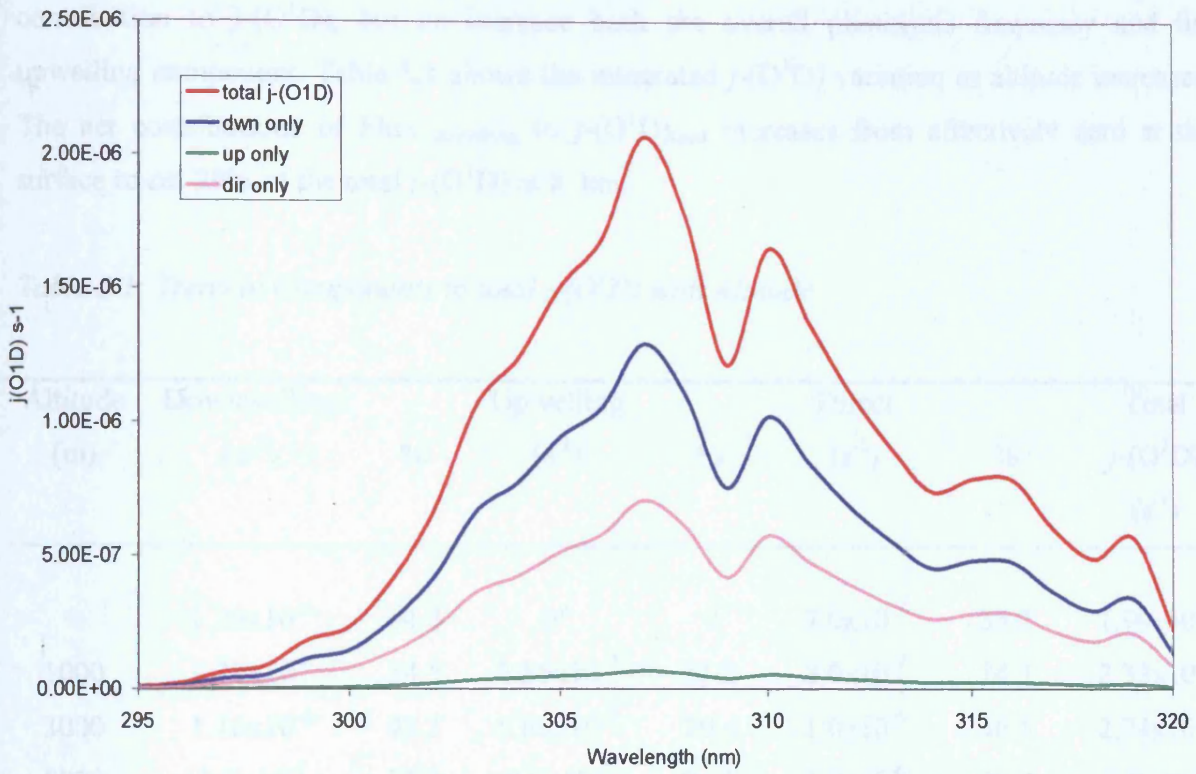


Figure 5.2: Contributions to $j(O^1D)$ from actinic flux with respect to wavelength at 8 km.

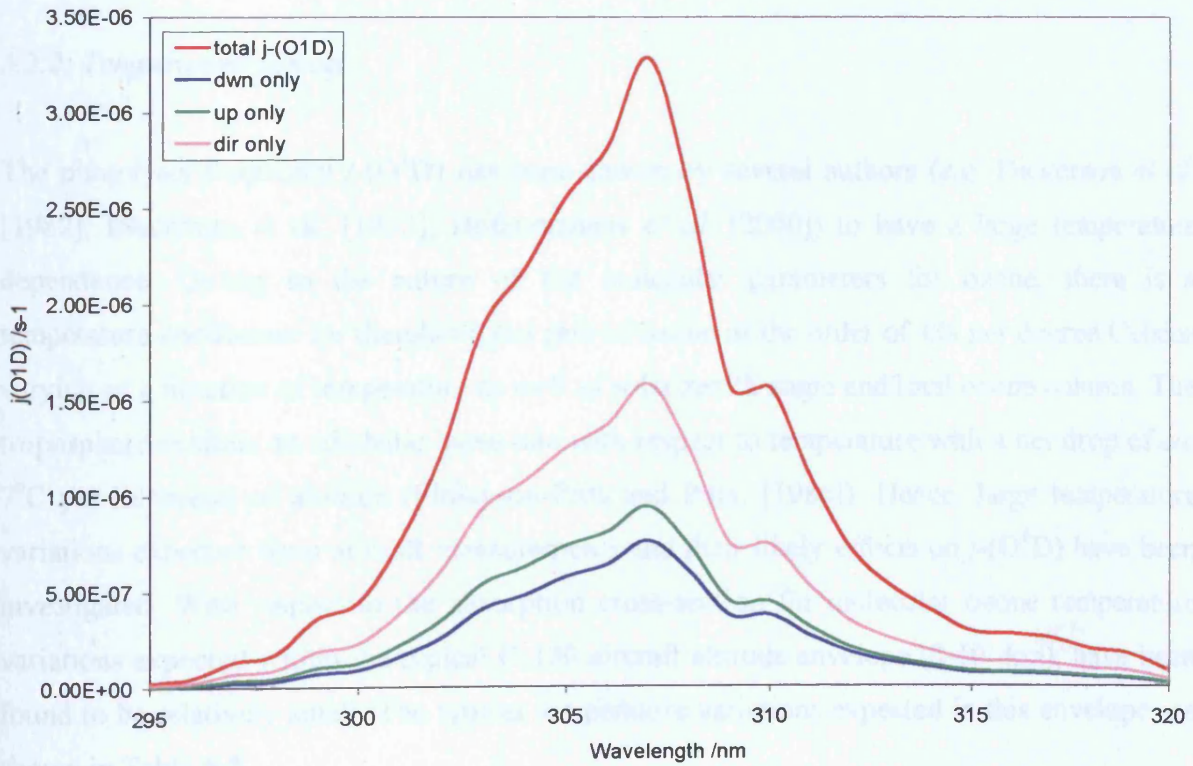


Figure 5.2 shows the variation in $j-(O^1D)$ with respect to wavelength for Flux_{total} at 8 km. Comparison of Figure 5.1 to 5.2 show that the increase in upwelling radiation as altitude increases is considerable. As altitude increases, there is a net decrease in the downwelling contribution to $j-(O^1D)$, but an increase both the overall photolysis frequency and the upwelling component. Table 5.1 shows the integrated $j-(O^1D)$ variation as altitude increases. The net contributions of Flux_{upwelling} to $j-(O^1D)$ _{total} increases from effectively zero at the surface to ca. 29% of the total $j-(O^1D)$ at 8 km.

Table 5.1: Trend in Components to total $j-(O^1D)$ with Altitude

Altitude (m)	Downwelling		Upwelling		Direct		Total $j-(O^1D)$ (s ⁻¹)
	(s ⁻¹)	%	(s ⁻¹)	%	(s ⁻¹)	%	
0	1.29x10 ⁻⁶	64.8	0*	0	7.0x10 ⁻⁷	35.2	1.99x10 ⁻⁶
1000	1.27x10 ⁻⁶	54.5	2.56x10 ⁻⁷	11.2	8.0x10 ⁻⁷	34.3	2.33x10 ⁻⁶
3000	1.18x10 ⁻⁶	43.1	5.60x10 ⁻⁷	20.4	1.0x10 ⁻⁶	36.5	2.74x10 ⁻⁶
5000	1.0x10 ⁻⁶	33.3	8.0x10 ⁻⁷	26.7	1.2x10 ⁻⁶	40.0	3.0x10 ⁻⁶
8000	7.61x10 ⁻⁷	24.8	9.0x10 ⁻⁷	29.4	1.4x10 ⁻⁶	45.8	3.06x10 ⁻⁶

* Only significant for high albedo surfaces e.g. snow.

5.2.2: Temperature Effects

The photolysis frequency $j-(O^1D)$ has been shown by several authors (e.g. Dickerson *et al.* [1982], Blackburn *et al.* [1992], Hofzumahaus *et al.* [2000]) to have a large temperature dependence. Owing to the nature of the molecular parameters for ozone, there is a temperature coefficient for the photolysis rate of ozone of the order of 1% per degree Celsius varying as a function of temperature as well as solar zenith angle and total ozone column. The troposphere exhibits an adiabatic lapse rate with respect to temperature with a net drop of ca. 7°C per kilometre of altitude (Finlayson-Pitts and Pitts, [1986]). Hence, large temperature variations expected from aircraft measurements and their likely effects on $j-(O^1D)$ have been investigated. With respect to the absorption cross-section for molecular ozone temperature variations expected within the typical C-130 aircraft altitude envelope (0-10 km), have been found to be relatively small. The typical temperature variations expected in this envelope are shown in Table 5.2.

Table 5.2: Temperature Variations with Respect to Altitude for C-130 Altitude Envelope

Altitude (m)	Temperature (K)
0	288.15
1000	281.65
2000	275.15
3000	268.66
4000	262.16
5000	255.68
6000	249.19
7000	242.70
8000	236.22
9000	229.73

(Temperatures from USSA, 1976.)

Figure 5.3: Variation in Ozone Absorption Cross-Section with Temperature (Molina and Molina [1986]).

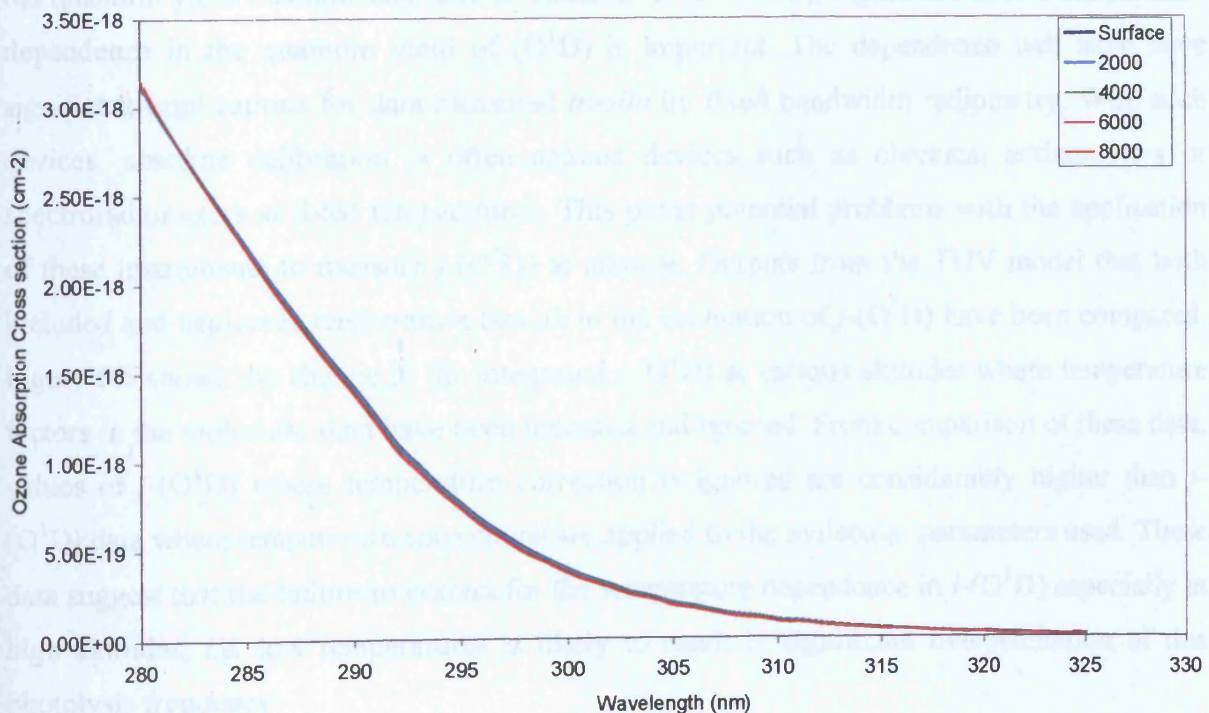
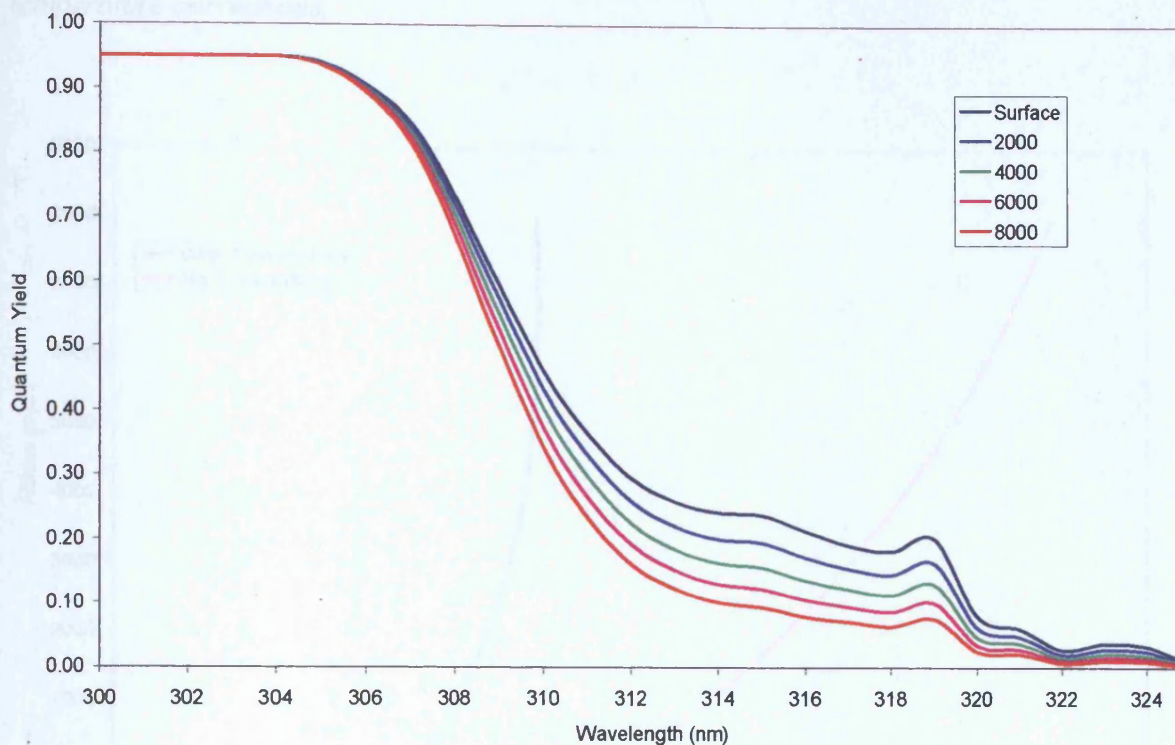
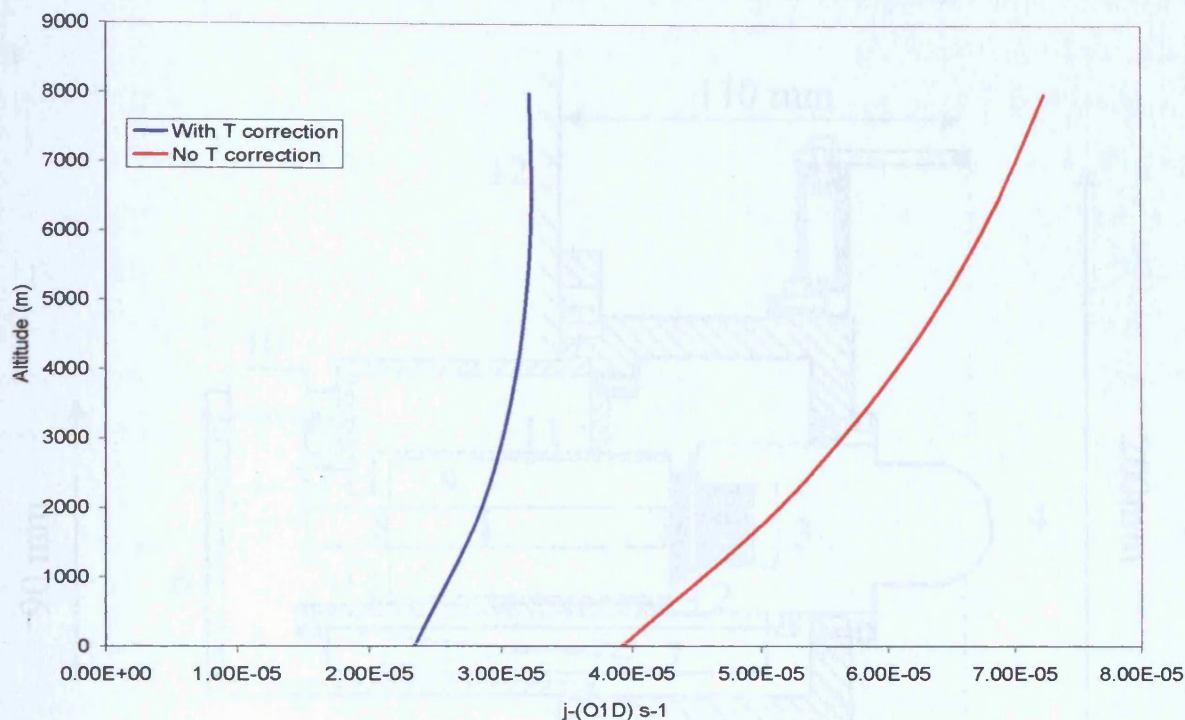


Figure 5.4: Variation in $O(^1D)$ Quantum Yield with Temperature (Talukdar *et al.* [1998])



Using the ozone absorption cross-section recommendations of Molina and Molina (1986), combined with temperature data from Table 5.2, Figure 5.3 shows that for the temperature ranges expected from 0-8 km, no significant variation in $\sigma(O_3)$ is observed. Conversely using the quantum yield recommendations of Talukdar *et al.* (1998), Figure 5.4 shows temperature dependence in the quantum yield of (O^1D) is important. The dependence will have significant implications for data measured *in-situ* by fixed bandwidth radiometry. With such devices, absolute calibration is often against devices such as chemical actinometers or spectroradiometers at fixed temperatures. This poses potential problems with the application of these instruments to measure $j(O^1D)$ at altitude. Outputs from the TUV model that both included and neglected temperature factors in the evaluation of $j(O^1D)$ have been compared. Figure 5.5 shows the change in the integrated $j(O^1D)$ at various altitudes where temperature factors in the molecular data have been included and ignored. From comparison of these data, values of $j(O^1D)$ where temperature correction is ignored are considerably higher than $j(O^1D)$ data where temperature corrections are applied to the molecular parameters used. These data suggest that the failure to correct for the temperature dependence in $j(O^1D)$ especially at high altitudes, *i.e.* low temperatures is likely to result in significant overestimation of this photolysis frequency.

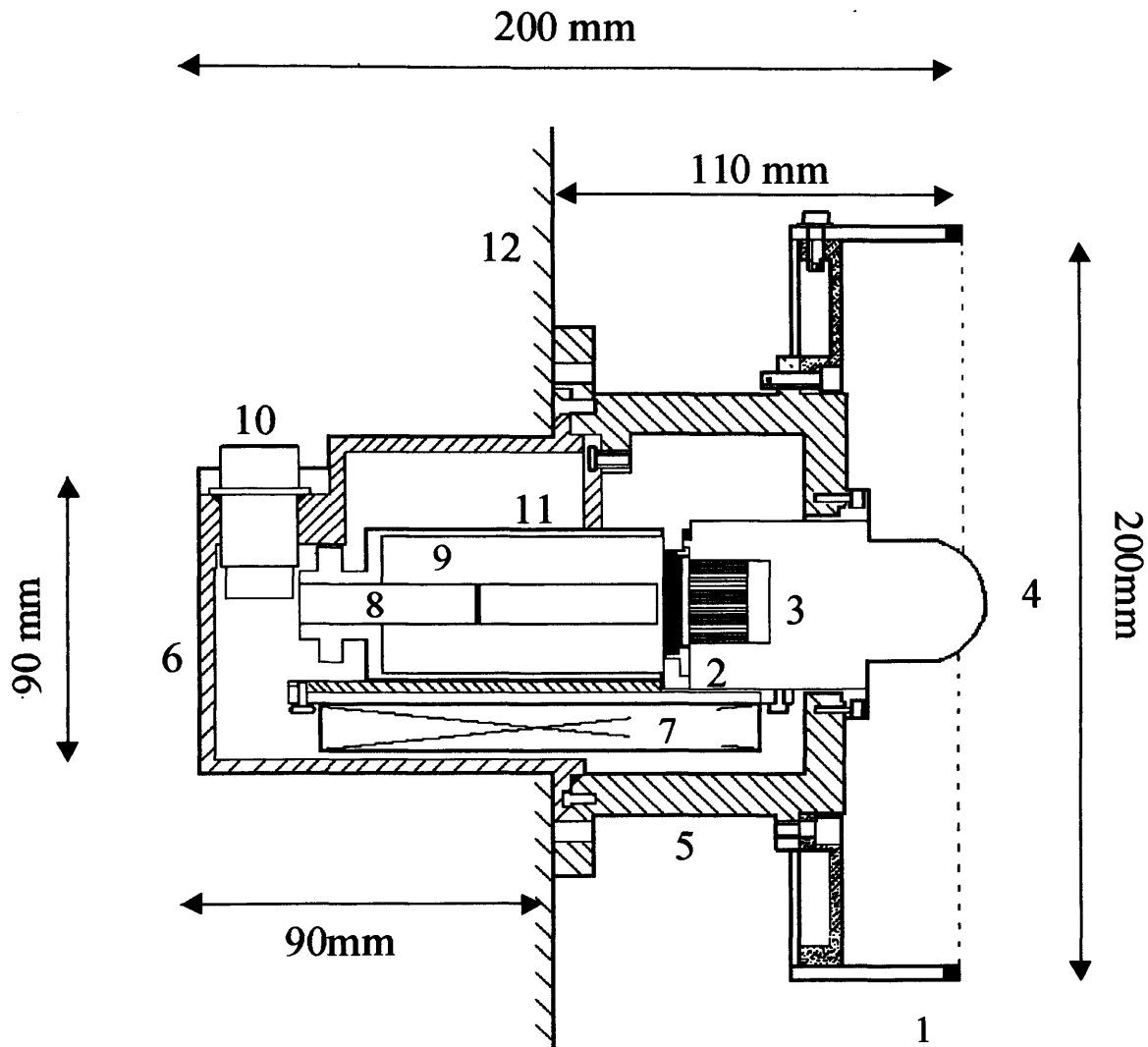
Figure 5.5: Change in Spectral Function of $j-(O^1D)$ with Altitude, with and without temperature corrections.



5.3: Characterisation of University of Leicester $j-(O^1D)$ Aircraft Filter Radiometers

The construction of the filter radiometers, as described in this chapter, began during the summer of 1997, using a modified design based on the photoelectric device described by Junkermann and co-workers (1989). In order to account for the photodissociation of a tropospheric ozone molecule, the full $4\pi sr$ spherical response must be accounted for. As shown in section 5.2, actinic flux contributing to $j-(O^1D)$ at any altitude need not be only direct flux. Rayleigh or Mie scattered light, as well as reflected and diffuse light contributes to the overall frequency. In order to account for this, two identical radiometers were deployed aboard the C-130 for the aircraft missions. The upper (zenith facing) radiometer was situated between the aircraft wings whilst an identical one (nadir facing) was below the aircraft nose. A schematic of the radiometers used aboard the C-130 is shown in Figure 5.6.

Figure 5.6: Schematic Representation of a Fixed Bandwidth Aircraft Radiometer



- | |
|--------------------------|
| 1. Artificial Horizon |
| 2. Filter |
| 3. Collimator |
| 4. Quartz Dome |
| 5. Top Body |
| 6. Lower Body |
| 7. PMT Supply |
| 8. PMT Assembly |
| 9. Heater Insulation |
| 10. Electrical Connector |
| 11. Central Holder |
| 12. Aircraft Skin |

5.3.1 Optics System

Atmospheric actinic flux was collected by way of a series of polished quartz domes, (supplied by R. Schmitt, MetCon, Glashütten, Germany), mounted atop each radiometer and capable of detecting light over a solid angle of 2π steradians. These are similar to 2π sr quartz dome/diffuser systems described elsewhere (e.g. Volz-Thomas *et al.* [1996], Hofzumahaus *et al.* [1999]) As described by Volz-Thomas *et al.* (1996), the original designs of Junkermann and co-workers are not applicable to aircraft platforms. During aircraft operation there is the possibility for the quartz grains used in the original design to rearrange due to shock or vibration and hence for the optical properties of the optical heads to alter. To allow aircraft *in-situ* measurement, the optical heads have been redesigned in accordance with the recommendations of Volz-Thomas *et al.* (1996).

The basic principle of operation involves the use of solid diffuser made up of several separate domes of sand blasted quartz. Photons incident on the outer dome pass through to the subsequent inner domes. As they pass through, photons undergo multiple refractions and reflections at the inner and outer surfaces. Thus, photons entering the optics are detected across the entire 2π sr angle. The outer dome has a height of *ca.* 3.5cm and width of *ca.* 3cm. As with ground-based instruments, it was necessary to limit the field of view of the instrument to 2π sr by use of a shadow ring. This consisted of a solid metal disk *ca.* 0.5cm thick and 20cm in diameter. At the extremity of this disk was positioned a movable vertical extension that could be raised or lowered as necessary to obtain a better 2π sr response. The external optics of the radiometer was sealed off from the internal components by use of a rubber "O" ring.

5.3.2 Angular Response

For an instrument of ideal sensitivity, all photons detected across the 2π sr solid angle would have the same probability of detection by the instrument, and such an instrument would have perfect rejection characteristics *i.e.* no photons would be detected at polar angles $>90^\circ$. The dome used for the detection of photons by the instrument was optimised to be as close to these ideal criteria as possible. However, perfect isotropic detection and perfect angular rejection is not achievable in a working instrument. Estimations of the potential anisotropy in the 2π sr optics, together with the overall angular rejection the instrument was therefore obtained. In order to test these parameters, the radiometer response was analysed with a 200W tungsten halogen lamp (*Oriel*) in a "light-box" as described in Chapter 6. The two instruments (upper

and lower facing radiometers) differed only slightly in their angular responses. For the upper, zenith-facing instrument, the anisotropy over 2π was shown to be $\pm 2.4\%$ or less for angles $\leq 80^\circ$. Between 90° and 100° , the sensitivity of the instrument was observed to decrease by *ca.* 60%, before rapidly falling to zero at angles between 100° and 110° . For the lower nadir facing radiometer, the response was found to be *ca.* 2.7% for angles $\leq 80^\circ$. For angles of rotation between 90° and 100° , the sensitivity of the instrument was observed to decrease by *ca.* 53%. The response tended to zero at angles between 105° and 110° . The experiment was repeated for several instrument geometries. All curves showed the same relative profile indicating that there was no significant geometric dependence in the angular response. Typical angular response characteristics for the two aircraft radiometers are shown in Figures 5.7 and 5.8.

5.3.3: Bandpass Filter

The bandpass filter used in the aircraft radiometers only transmits light within a defined spectral "window", ranging over several nanometres. In order to optimise the transmittance of wavelengths that contribute directly to $j\text{-(O}^1\text{D)}$ it was necessary to choose a filter that matched as closely as possible to the $j\text{-(O}^1\text{D)}$ action spectrum as shown in Figure 1.2 in Chapter 1. The filter used in both the zenith and nadir facing radiometers was a type B-P 35-7921 filter supplied by *Ealing*. This was a metal-dielectric-metal (MDM) filter with the manufacturer quoting a centre of maximum transmittance 15% at 300nm and a bandwidth of 10nm at full-width, half maximum (FWHM). In order to test these specifications the filters used in the aircraft radiometer construction were tested at the University of Leicester in a UV-Visible spectrometer (*Schmadzu*). The filter was used as the working cell in the two-cell system, the reference cell being background air. The resultant curve for the transmittance of the filter matched the manufacturers specifications well, as shown in Figure 5.9. The bandpass filter had a measured peak transmittance of *ca.* 14% at 299.9nm. The filter was observed to begin transmittance at *ca.* 281nm and the transmittance fell to zero at *ca.* 313nm. The bandpass itself was found *ca.* 10.1nm at FWHM.

Figure 5.7 Upper, Zenith Facing Filter Radiometer Angular Response Curve

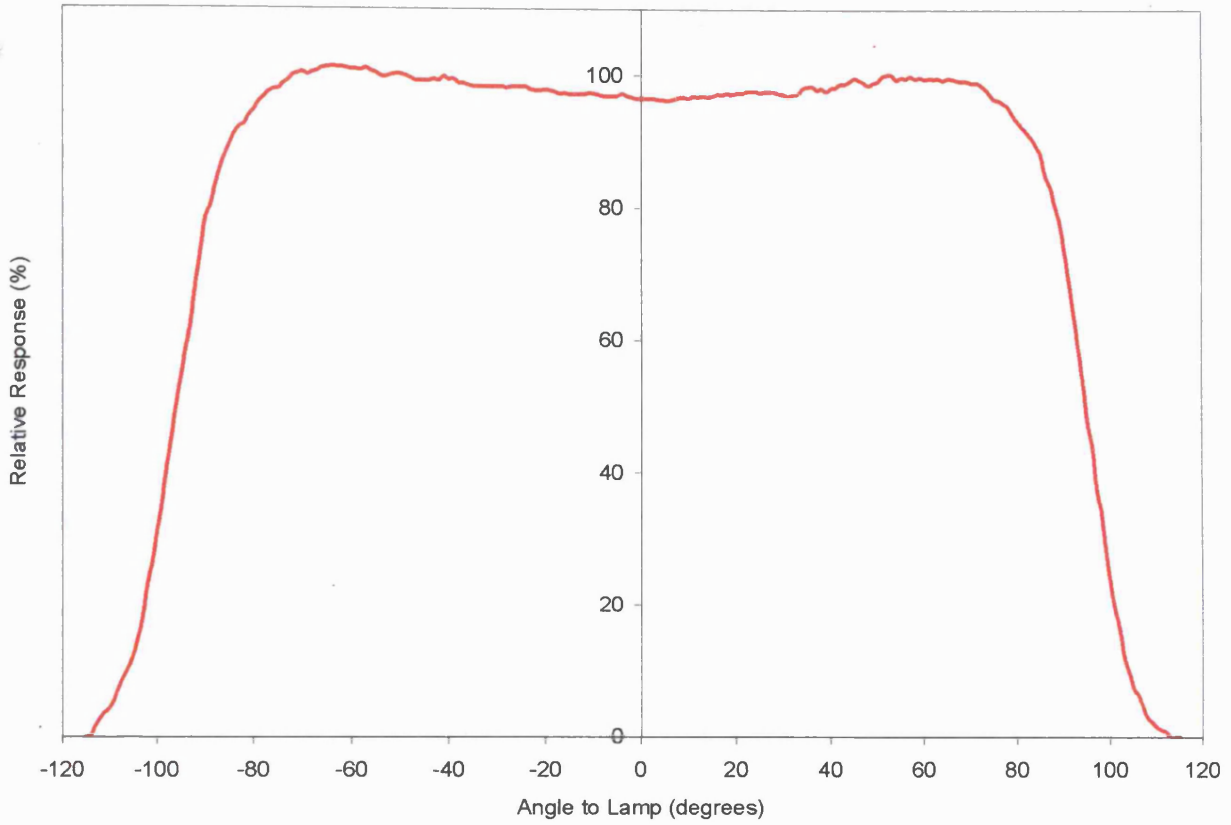


Figure 5.8 Lower, Nadir Facing Filter Radiometer Angular Response Curve

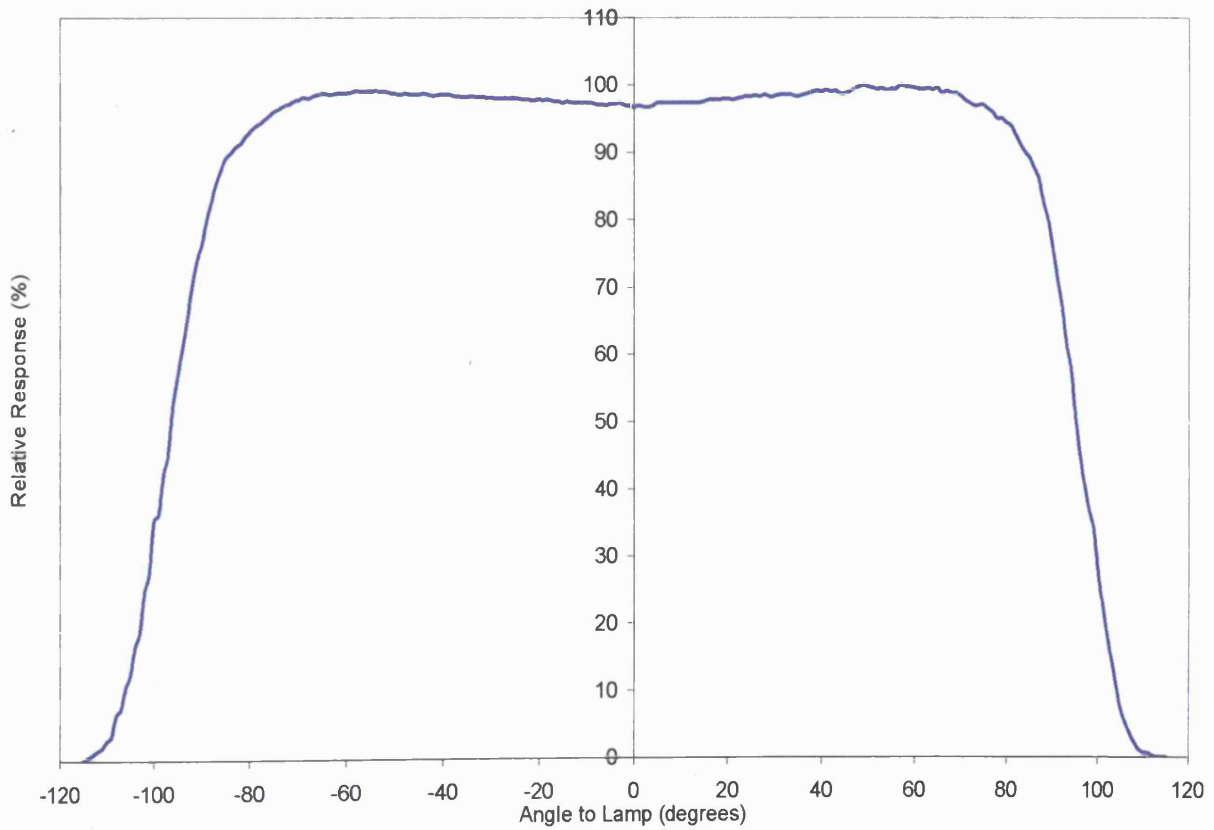
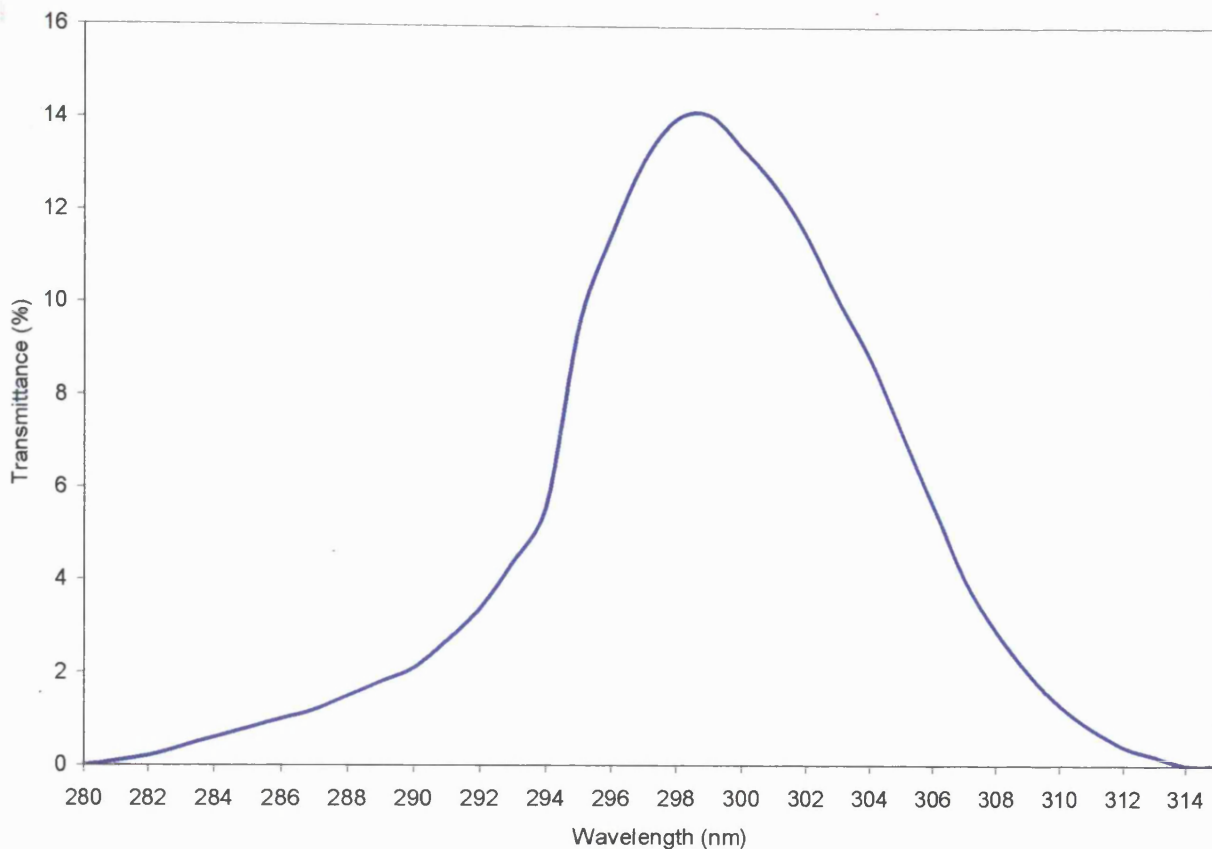


Figure 5.9 Transmittance of Aircraft Filter Radiometer Bandpass Filters

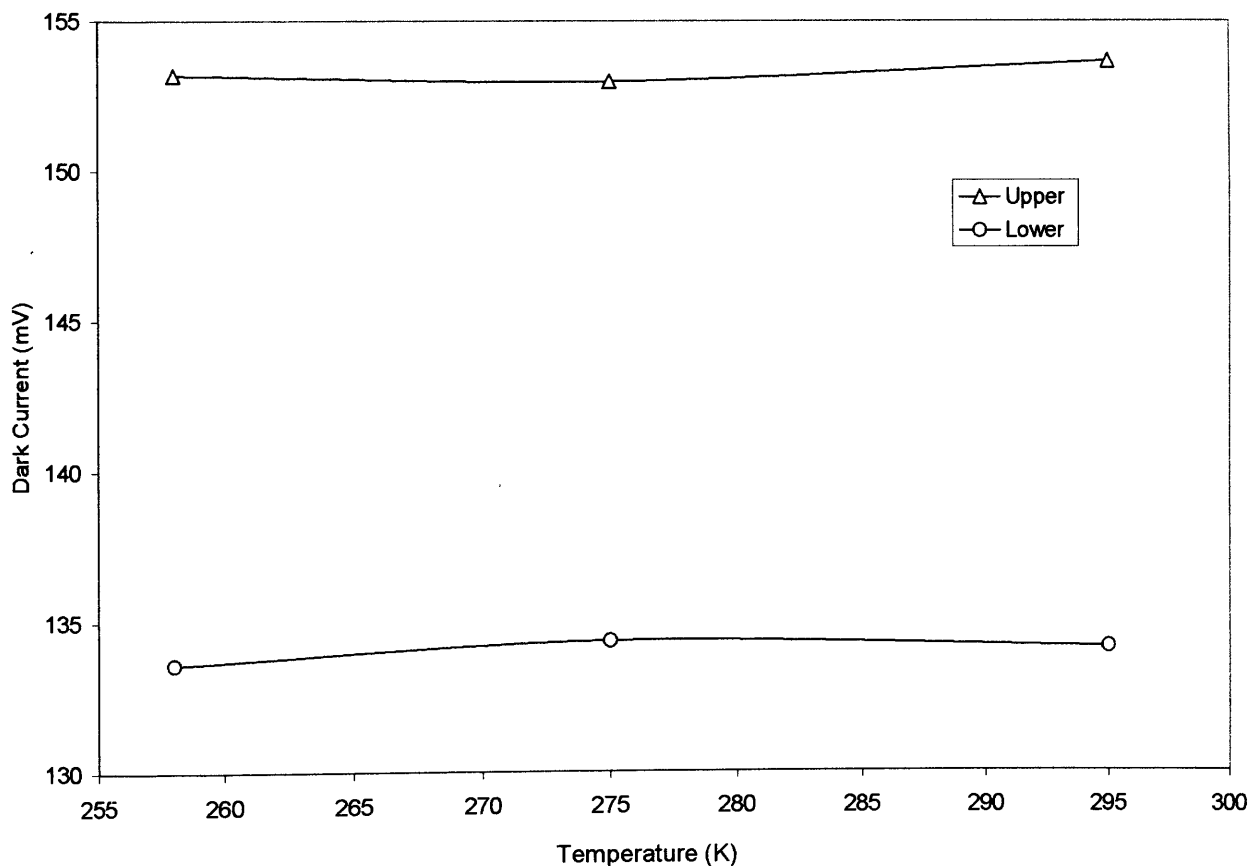


5.3.4 Photomultiplier Tube

Detection of photons passing through the bandpass filter was via a R1893 solar blind photomultiplier tube (PMT) (*Hamamatsu*). This photomultiplier is 10mm in diameter and has a broad transmittance of 160-320nm with peak transmittance at *ca.* 210nm. The amplification was *ca.* 3.0×10^5 at 1000V. Owing to the thermionic emissions of electrons from the PMT, there is often a residual current offset observed with these devices. Specifically, this manifests itself as a small current that exists even when the photomultiplier is exposed to no light. Hence, this dark current offset provides a potential source of error in the evaluation of photolysis frequencies when using devices such as photoelectric radiometers. The optical train in each radiometer was temperature stabilised to *ca.* 298K in order to minimise temperature dependence of thermionic emission, and hence, dark current. In order to gauge the effect of the so-called "dark current" from both the nadir and zenith facing radiometers, these devices were evaluated *via* a number of experiments.

The dark response of the two devices was estimated by connecting the radiometers to suitable power supplies and monitoring their responses whilst the 2π sr heads were covered in a blackout shroud. The data responses over time were then collected *via* a 21X micrologger (*Campbell Scientific Instruments*) and a laptop PC. For the course of these experiments, that dark current was observed to be *ca.* 154mV for the upper radiometer and *ca.* 134mV for the lower device. Since the externally mounted radiometers experience a wide range of temperature variation while aboard the C-130, any potential temperature dependence of the dark response also needed to be estimated. The experiment was therefore repeated for a wide range of temperatures, including placing the radiometers in the Chemistry Departments "cold room" at 275K in addition to a refrigerator packed with dry ice at *ca.* 258K. The typical dark current was seen to be fairly constant for both instruments over these ranges of temperatures indicating that there is no significant temperature dependence of the dark current and that the temperature stability of the radiometers when mounted aboard the C-130 is likely to be equally as good. A plot of the variation of dark current with temperature is shown in Figure 5.10.

Figure 5.10: Variation of Radiometer Dark Current with Temperature



5.3.5 Calibration

Since the two radiometers record the photolysis of ozone as a voltage (mV) the conversion of this voltage to absolute units (s^{-1}) was necessary. The radiometers were cross-calibrated against a reference ground based j -(O¹D) radiometer. This reference radiometer itself had been calibrated previously against a chemical actinometer (see Chapter 6). This meant placing the three radiometers in the same light, the assumption since if the radiometers are exposed to the same conditions, they should record the same photolysis frequency. In order to do this it was necessary to place the aircraft radiometers next to the calibrated filter radiometer on the roof of the University of Leicester's Chemistry Department on a day that was expected to be as cloud free as possible in order to minimise cloud interference.

From these cross calibration experiments it was possible to plot signal voltage from the two aircraft devices against the j -(O¹D) output of the reference filter radiometer. Third order polynomials were fitted to the resultant curves and from these, algorithms derived for the aircraft radiometers that allowed the calculation of j -(O¹D) in absolute units for any given solar zenith angle at the surface. A plot of the variation in j -(O¹D) for the duration of this experiment is shown in Figure 5.11, while the correlation between upper and lower aircraft radiometers and the reference radiometer is shown in Figure 5.12 and 5.13 respectively. As is shown in these figures, the regression of j -(O¹D) measured by the aircraft radiometers show a high degree of correlation to the reference device over the course of the roof-based experiment. This gave some confidence that these aircraft radiometers could measure free tropospheric photolysis frequencies with a reasonable degree of accuracy when mounted on the C-130 aircraft platform.

Figure 5.11: Variation in $j-(O^1D)$ for Aircraft and Reference Radiometers

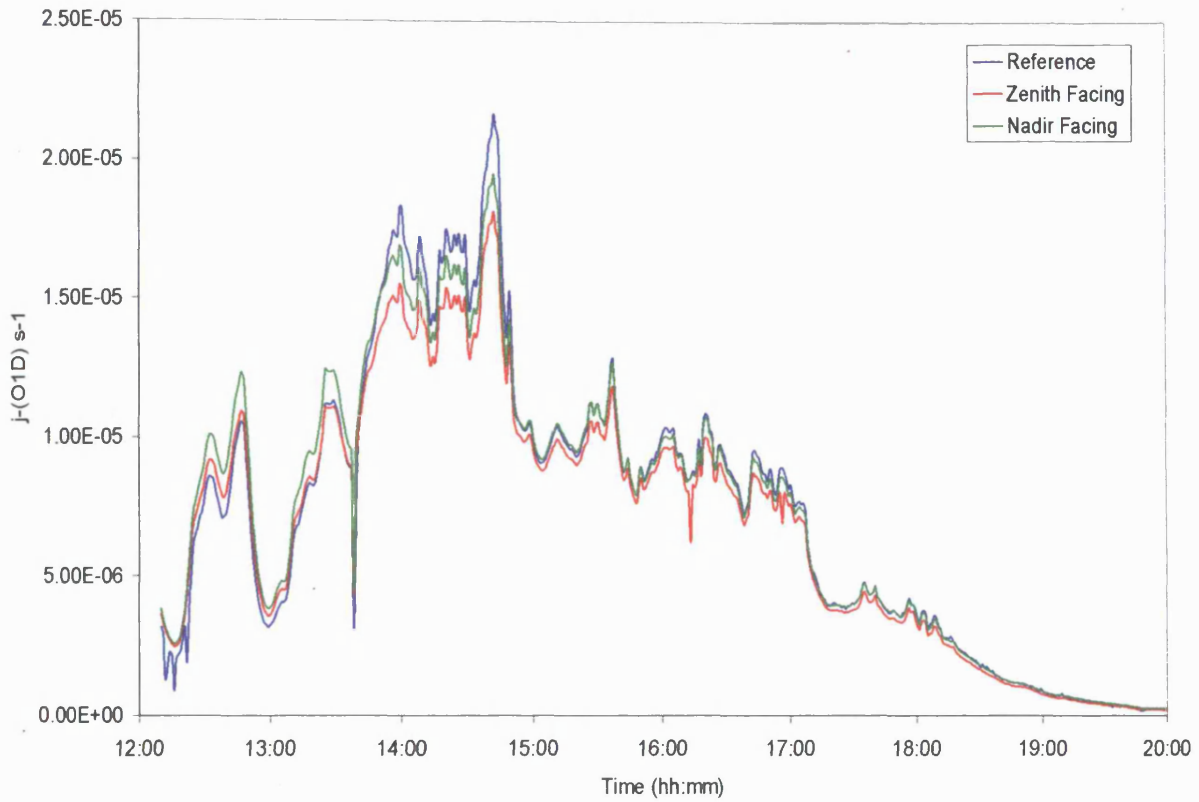


Figure 5.12: $j-(O^1D)$ Correlation for Upper Aircraft and Reference Radiometers

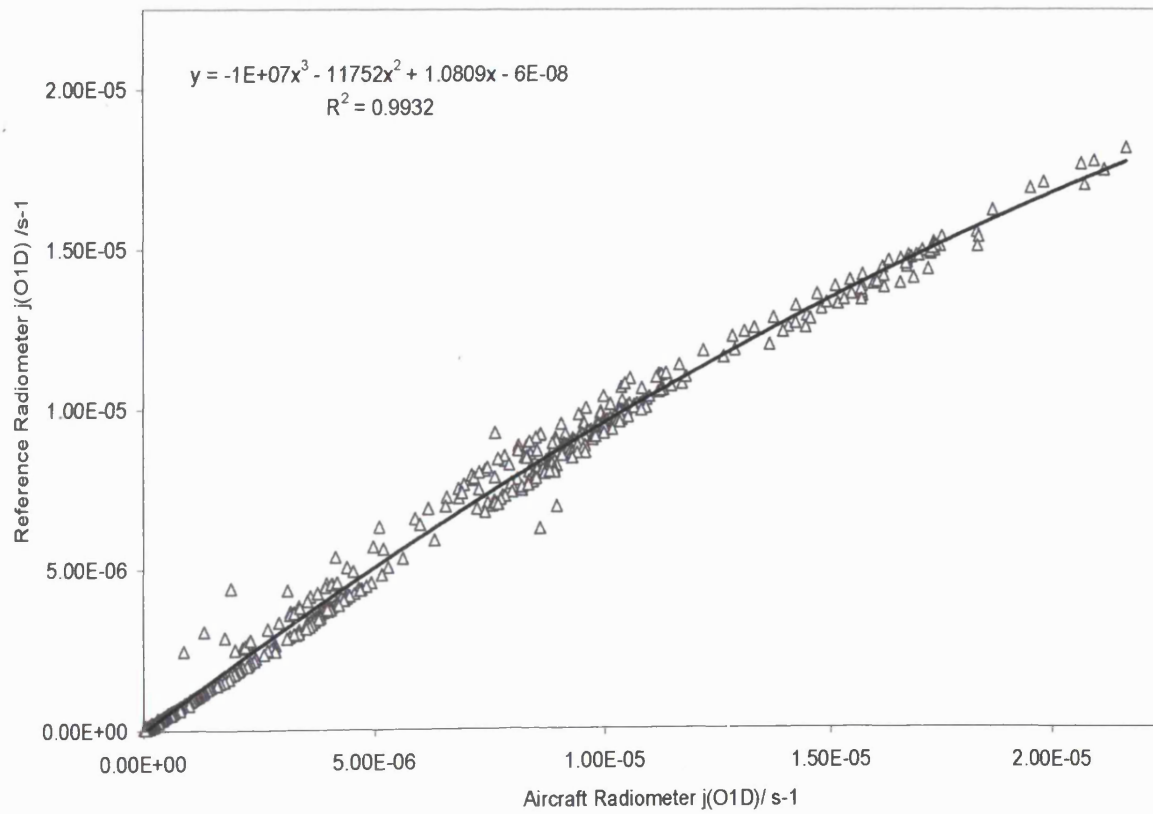
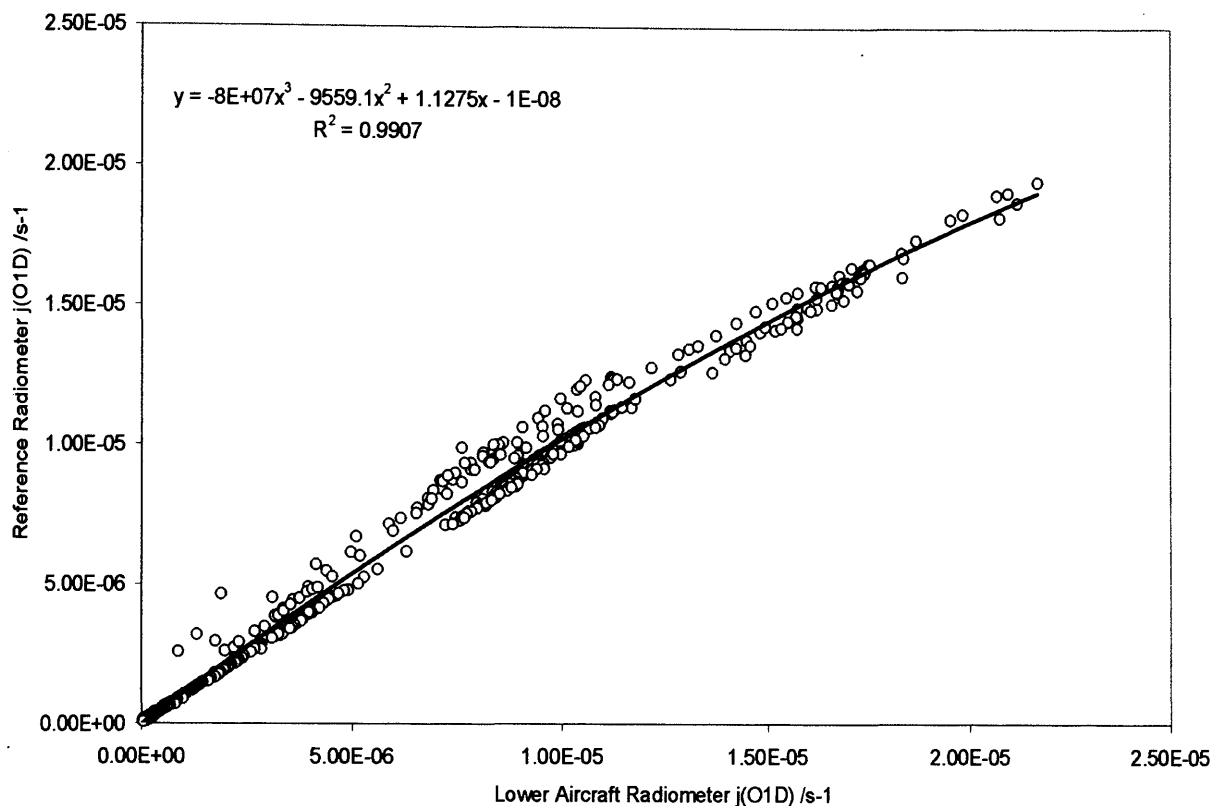


Figure 5.13: j -(O^1D) Correlation for Lower Aircraft and Reference Radiometers



5.4: Performance of j -(O^1D) Radiometers During ACSOE

The ACSOE Azores missions of September 1997 were the first aircraft campaign to fly with the aircraft radiometers aboard the MRF C-130. Details of the ACSOE campaign can be found elsewhere (Chapters 2 and 3). For this aircraft campaign, the radiometers provided data for four flights, A578 (19/9/97), A579 (20/9/97), A580(21/9/97) and A581(23/9/97). The radiometers were also flown on two other missions. These were a night flight, A574 (13/9/97), where the C-130 made its transit to the Azores and flight A575 on 14/9/97. For this flight, there were problems with the upper, zenith facing radiometer owing to saturation of the radiometer PMT. Hence, there was no useful *in-situ* data obtained for this flight. A summary of these flights and their goals is shown in Table 5.3.

Table 5.3: ACSOE Azores Mission Objectives

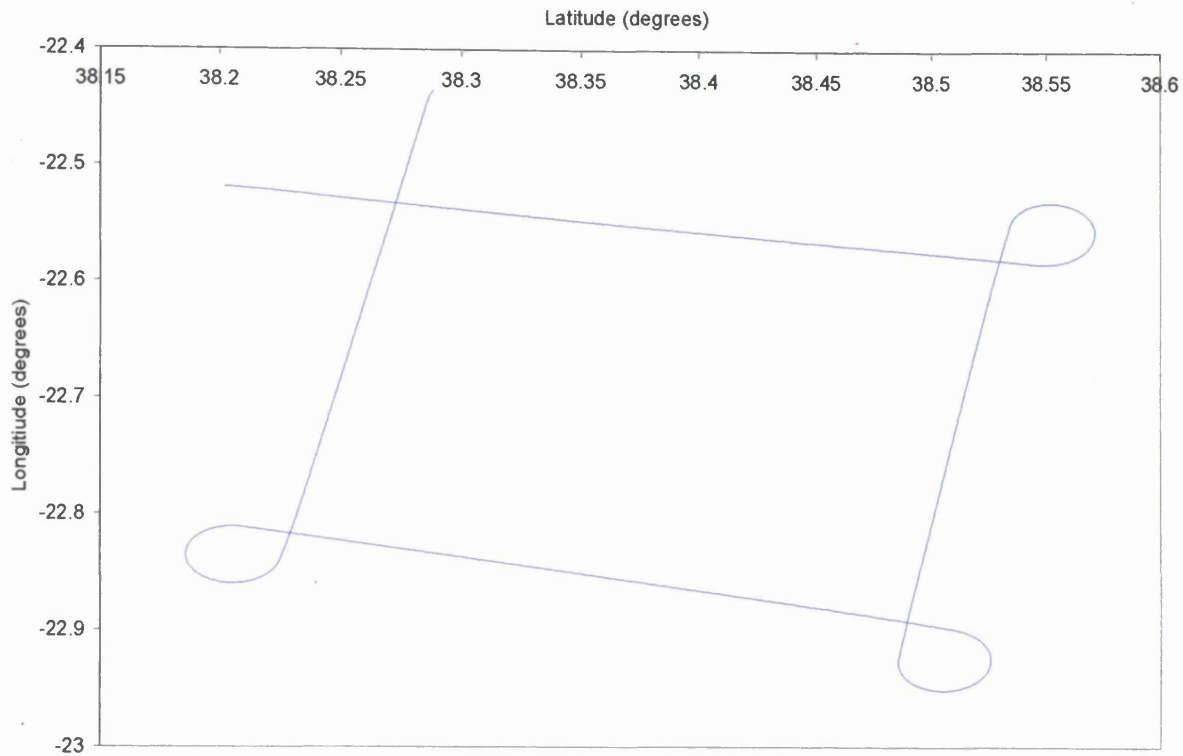
Date	Flight Code	Objective	Latitude (min/max)
19/9/97	A578	Radiometer test Flight	36.90°N-39.0°N
20/9/97	A579	Frontal Crossing Flight	35.60°N -44.10°N
21/9/97	A580	NOAA P3 comparison	35.90°N-44.36°N
23/9/97	A581	Transit flight to UK	36.96°N-51.90°N

5.4.1: ACSOE Flight A578

The first flight on which the j -(O¹D) radiometers were mounted aboard the aircraft was for flight A578 (see Table 5.3). This was a test flight to ascertain if the two radiometers were functioning correctly whilst mounted on the aircraft platform. In order to check this the aircraft made several manoeuvres designed to check operation and to find several important calibration parameters. The first was the "box pattern". During this manoeuvre, the aircraft flew at a constant height in a rectangular path that covered several kilometres. By performing such a flight track, it was possible to check the levelling factor of the aircraft and the direct flux monitored by the upper radiometer compared to the diffuse light seen by the lower (*Foot et al.* [1986]). The box pattern portion of flight A578 is shown in Figure 5.14.

The sum of the effective 4π sr angular response of the two radiometers under atmospheric conditions was also tested. ACSOE flight A578 was designed to do this. This is possible by flying circular patterns around the sun. Owing to the aircraft inclination during a turn, the radiometers axis must rotate around the zenith with the aircraft's roll angle. The net result was that the sun described a circle around the detector with the effective solar zenith angle seen by the radiometers varying between $(\theta_S - \theta_R)$ and $(\theta_S + \theta_R)$, where θ_S is the solar zenith angle and θ_R is the aircraft roll angle, (*Volz-Thomas et al.* [1996], *Shetter and Müller* [1999]).

Figure 5.14: Box Pattern Portion of Flight A578



The circular orbit around the sun also serves to analyse the contribution of direct flux to the lower radiometer signal during the flight, and therefore the effective deviation in the 4π response. It was assumed the lower radiometer only observed diffuse and scattered light, with its view restricted to 2π steradians by the concentric light shield attached. This hypothesis was tested by flying such circular orbits at varying degrees of roll and at different times of the day. These measurements allow observations of the effective zenith angle as the aircraft rotated about the angle $(\theta_S - \theta_R)$ and $(\theta_S + \theta_R)$ and investigate if the change in the effective zenith angle is sufficient to expose the lower radiometer to direct light. As the aircraft entered such a manoeuvre, there was an observed anticorrelated variation in the outputs of the two detectors that varied with a period of 360° , owing to the aircraft's inclination towards the horizon. Each radiometer no longer "sees" its original 2π sr hemisphere. The roll has the effect of forcing each radiometer 2π sr head to encroach into the 2π sr hemisphere normally seen only by the opposite detector. This "cross talk" obviously varies with aircraft roll angle but is a potential area for error in the 4π sr evaluation of $j-(O^1D)$. Hence, detailed analysis of A578 data was undertaken in order to evaluate this cross talk function.

For optimised conditions, the ratio of the signal from the zenith radiometer, U_{zenith} when divided by the signal from the nadir radiometer, U_{nadir} , should be unity, *i.e.* the decrease in the upper radiometer signal is compensated by a subsequent increase in the lower signal. Since

the radiometers are not placed directly over one another, the change in the response of one is not perfectly matched by the other. This can lead to a cross talk error. Hence, there is a parameter, y , that needs to be added to the signal of one hemisphere in order to reach perfect response at some roll angle, θ . A plot of the aircraft roll angle against y will result in an equation that describes the dependence of y on θ and hence a correction factor x that needs to be added/subtracted from the radiometer signal in order to achieve perfect response, *i.e.*

$$\frac{U_{zenith}}{U_{nadir}} = \text{Cross Talk Ratio} + \text{Cross Talk Correction, } y \quad (5.9)$$

where

$$U_{zenith} = y * U_{nadir} \quad (5.10)$$

and

$$U_{nadir} = \frac{U_{zenith}}{y} \quad (5.11)$$

During flight A578, the aircraft performed rolls of 15, 40, 42 and 60 degrees to the horizontal. A plot of the correction necessary to produce a perfect response against the roll angle of the aircraft gives an equation of correction of the form

$$y = 0.0124 * \theta + 0.002 \quad (5.12)$$

with a correlation of *ca.* 0.96. The plot of y verses θ for A578 is shown in Figure 5.15. The cross talk correction factor for any subsequent roll angle may be calculated. It was found the cross talk error for the majority of ACSOE flights that the aircraft roll angles were such that only minimum cross talk errors occurred. Throughout the summer campaign, the maximum cross talk error was on the order of *ca.* 6%. These uncertainties are coupled to other possible sources of error in the determination of j -(O¹D), the magnitudes of which are shown in Table 5.4. These include errors arising from the molecular parameters as shown by Hofzumahaus *et al.* (1999). Error propagation owing to the error in calibration is assumed to be small for the radiometers.

Figure 5.15: Plot of Cross Talk Correction (with 1σ Standard Deviation Error) and Aircraft Roll Angle

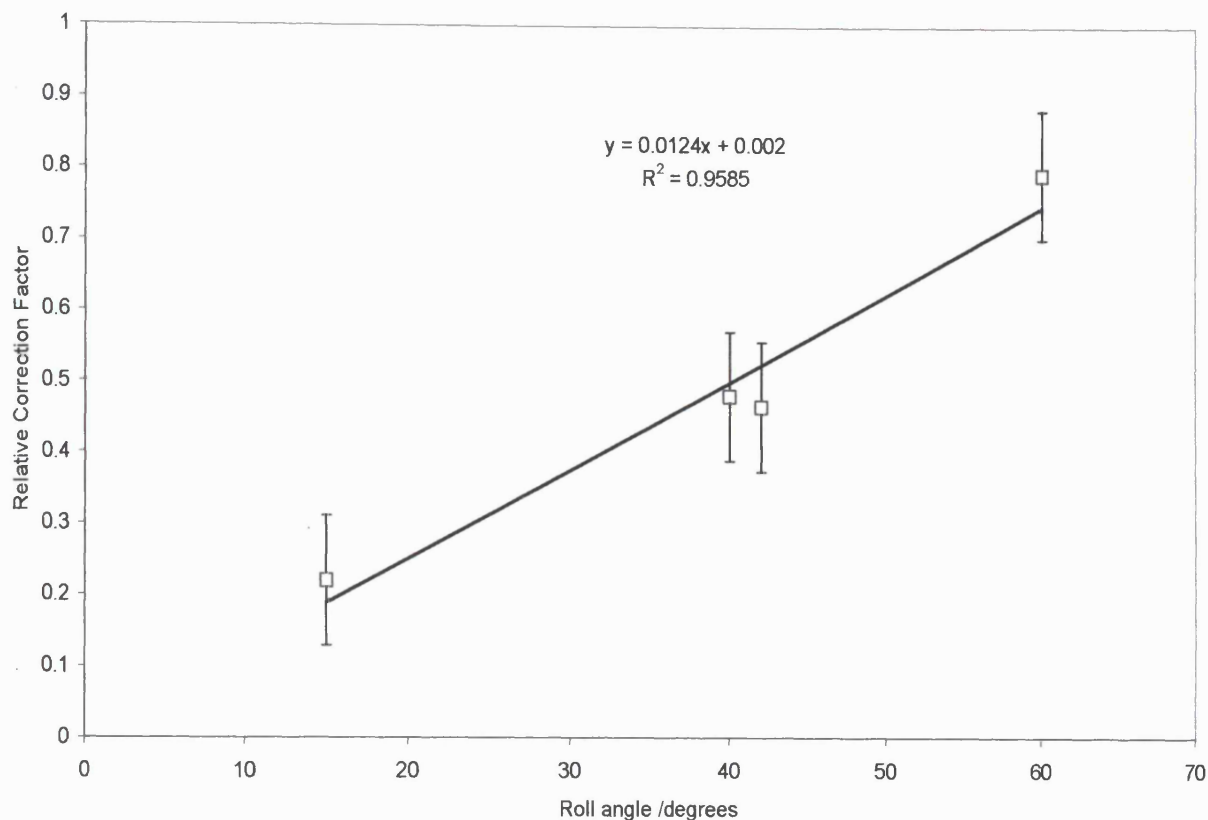


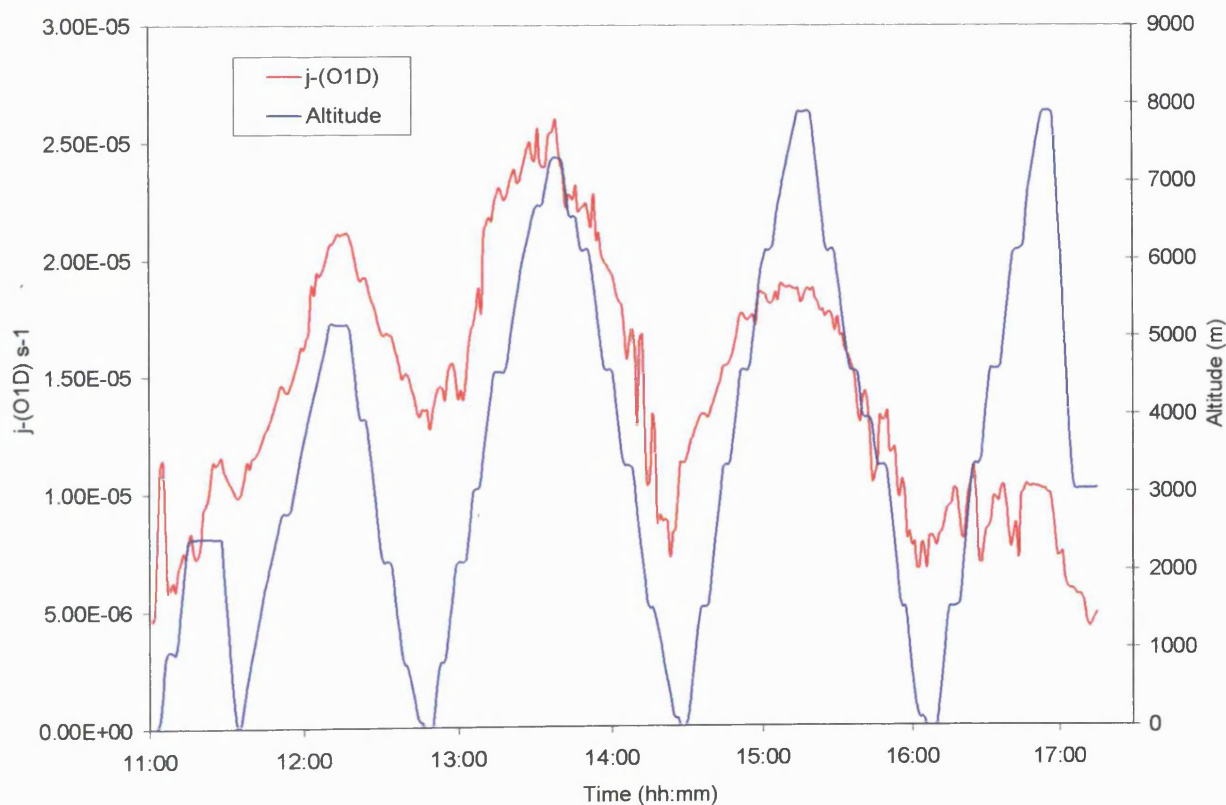
Table 5.4: Characterisation of Aircraft j -(O¹D) Radiometers

Error	Estimated Magnitude
Accuracy	ca. 30%
Precision	ca. 5%
Detection Limit	ca. $1 \times 10^{-7} \text{ s}^{-1}$
Time Response	1 second
Error in absorption cross-section	3%
Error in quantum yield	10%
Total Error in integrated j -(O ¹ D)	ca. 12% (from Hofzumahaus <i>et al.</i> [1999])
Angular Response Error	ca. 3%
“Cross Talk” Error	$\leq 6\%$
Dark Current Temperature Variation Error	Negligible

5.4.2: ACSOE Flight A579

The ACSOE mission on 20/9/97 was a flight that was designed to investigate the distribution of tracers in the free troposphere. Trajectory analysis suggested that for this flight, air parcels of US origin had been transported in to the North Atlantic by a frontal system to the ocean to the north of the Azores. The flight plan was to fly an almost triangular pattern from 38°N 22°W to 44°N 30° W, and back to 39° N 24° W in the hope to intersect the air masses transported from North America. Cross-sections were taken in these air parcels by flying a series of deep, stepped saw tooth profiles that were executed out on either side of a cold front. A band of convective cloud marked the cold front. The frontal zone itself was poorly defined, but several interesting layers were observed with distinct physical and chemical parameters associated with them. *In-situ* photolysis frequencies were measured for this flight *via* fixed bandwidth radiometry. The j -(O¹D) data in 1 minute averages for this flight, together with the aircrafts altitude as function of time is shown in Figure 5.16.

Figure 5.16: *In-situ* j -(O¹D) and Altitude Data for ACSOE Flight A579



As shown in Figure 5.16, the *in-situ* j -(O¹D) plot tracks the altitude profile as would be expected, *i.e.* j -(O¹D) is seen to increase with altitude and decrease over the course of the flight. This is directly correlated to the increase in solar zenith angle as time increases. During this flight, the aircraft also performed a series of profiles. This is where the aircraft moves such as it takes a cross-section of the atmosphere with minimum horizontal movement. During A579, there are several deep profiles and hence, these were a good opportunity to test the performance of the radiometers in assessing the change in *in-situ* j -(O¹D) with respect to altitude more precisely.

Figure 5.17 shows a composite of the vertical j -(O¹D) profiles as measured during the saw tooth portion of ACSOE flight A579. There are several features of note. The first is that all the profiles suggest that j -(O¹D) increases with respect to height as predicted from radiative transfer models (Ruggaber *et al.* [1994], Blindauer *et al.* [1996], Mattijssen *et al.* [1998] Liao *et al.* [1999]). However, often this general increase is marked by periods in which the photolysis frequency is seen to rapidly change over a relatively small change in altitude. These profiles are most likely cloud affected. A good example of this in the composite Figure 5.17 is the contrast between profiles 1 and 2. In profile 2, there is an essentially linear increase in the measured photolysis frequency from the surface to *ca.* 5 km. In profile 1 however, at around 4000m, the aircraft passed through cirrus or similar small cloud during the ascent. The net result is that multiple scattering caused by water droplets inside the clouds causes a rapid change in the measured photolysis rate over a short timescale. This manifests itself in the feature observed in profile one at height of *ca.* 4 km and several other short lived features observed in other profiles during A579.

Clouds play an important role in the evaluation of photolysis frequencies (Madronich, [1987], Tsay and Stamnes, [1992], van Weele *et al.* [1995], Crawford *et al.* [1999], Cess *et al.* [1999]). For clouds of sufficiently large optical depth, photolysis frequency usually increases dramatically as compared to cloud free conditions. Model predictions indicate an increase in photolysis frequency would be observed above and at the top of the cloud, while at the bottom of the cloud and below it, " j " values are predicted to be lower than for the corresponding clear sky value. Ruggaber *et al.* (1994) showed that the exact effect on photolysis frequencies from cloud is difficult to quantify. The more optically thick the cloud, the higher the maximum values of photolysis and the closer it is shifted to the cloud top. On the other hand, cloud of sufficient optical depth shift photolysis frequencies to lower values below the cloud. However, the dependence of photolysis frequency on the liquid water content of clouds is not linear.

Figure 5.17: Composite of $j-(O^1D)$ Profiles for ACSOE Flight A579

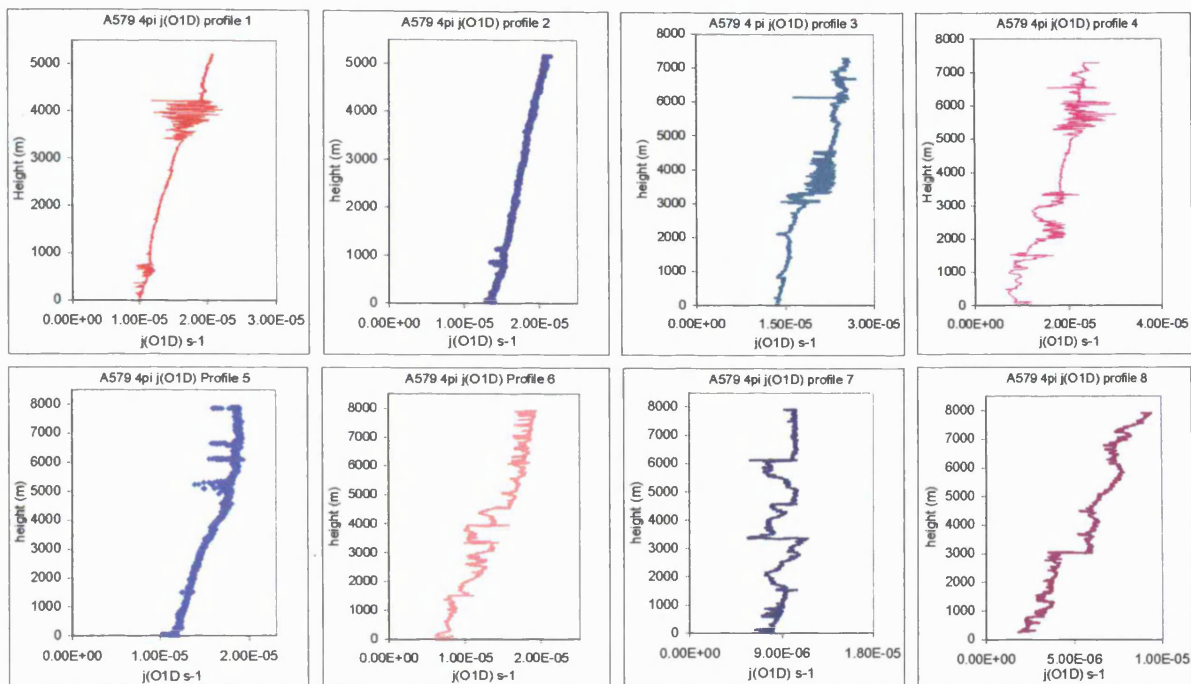
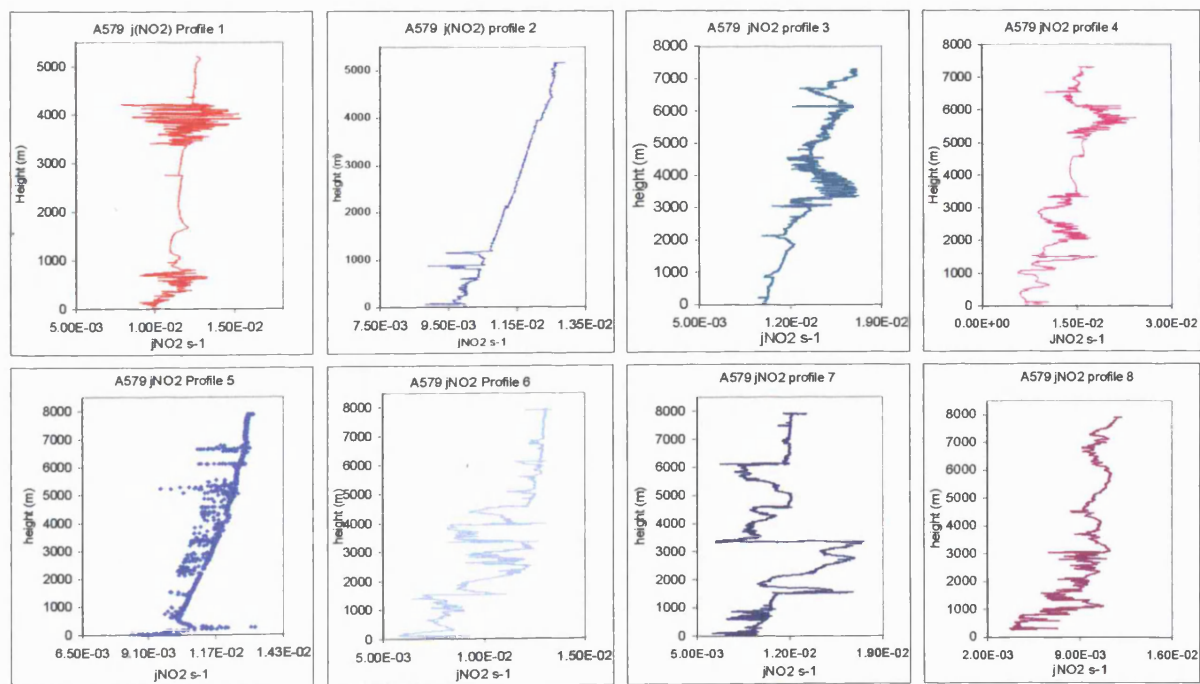


Figure 5.18: Composite of $j-(NO_2)$ Profiles for ACSOE Flight A579



These observations are reflected in the data taken during flight A579, along with other aircraft missions in the ACSOE campaign. The effect is clearly seen in profiles 7 and 8 in Figure 5.17. Profile 7 has two distinct areas where cloud effects are observed. The first is at *ca.* 3.5

km where there is a sharp and clear decrease in the measured $j\text{-(O}^1\text{D)}$ of 45% even though the altitude of the aircraft is almost constant. A second, similar feature is observed at *ca.* 6 km. It was noted in the mission log that at these times, the aircraft was passing through a thick layer of marine stratocumulus clouds. At these times, the corresponding change in $j\text{-(O}^1\text{D)}$ is closely matched by changes in the $4\pi sr j\text{-(NO}_2\text{)}$ data obtained *in-situ* and shown in Figure 5.18. As shown by Crawford *et al.* (1999), there should be a close correlation in the effect clouds have on both of these photolysis frequencies. However, differences are also likely, owing to the difference in the direct-to-diffuse ratio and differences in scattering for UV-A *i.e.* $j\text{-(NO}_2\text{)}$ and UV-B, *i.e.* $j\text{-(O}^1\text{D)}$.

Analysis of A579 profile 7 with respect to $j\text{-(NO}_2\text{)}$ shows similar observations to those observed in Figure 5.17. The profile shows a rapidly changing photolysis frequency at *ca.* 3.5 km. It does seem likely that for profile 7, the aircraft climbed through a thick cloud layer, and at the bottom of the layer, there was a 45% reduction in the measured $j\text{-(O}^1\text{D)}$. However, as suggested by Crawford *et al.* (1999) there should be differences in the magnitude of the changes with respect to $j\text{-(O}^1\text{D)}$ and $j\text{-(NO}_2\text{)}$. Since UV-B wavelengths are more easily scattered by features such as cloud and aerosol the net effect is there is often a more diffuse component to the actinic flux than for corresponding $j\text{-(NO}_2\text{)}$. It might be expected therefore that $j\text{-(NO}_2\text{)}$ experience different fluctuations with respect to clouds than $j\text{-(O}^1\text{D)}$. Indeed, this does seem to be the case for profile 7 since the effect of this cloud deck was to lower the measured $j\text{-(NO}_2\text{)}$ by 60%, *c.f.* 45% reduction in $j\text{-(O}^1\text{D)}$. After passing through the bottom of this cloud deck, the aircraft then proceeded to climb through the layer where photolysis values remained similar before increasing by 43% with respect to $j\text{-(O}^1\text{D)}$ and 46% for $j\text{-(NO}_2\text{)}$ at the top of, and just above the cloud deck.

Similarly, in profile 8 there is a cloud feature observed at 3 km where the aircraft either has entered, or is flying just above, a deck of stratocumulus cloud, as noted within the mission log. A good correlation is observed between measured $j\text{-(O}^1\text{D)}$ and $j\text{-(NO}_2\text{)}$ photolysis frequencies for this profile. For this feature, the net effect of the cloud deck is to increase in $j\text{-(O}^1\text{D)}$ by *ca.* 54%. However, for this feature the increase in $j\text{-(NO}_2\text{)}$ is only 20%. Thus, this seems to support the observations of Crawford *et al.* (1999) and various model calculations of that the relative effect of clouds on individual photolysis frequencies is dependent on several factors such as cloud type, optical depth, solar zenith angle, albedo and aerosol loading.

5.4.3 ACSOE Flight A580

The aircraft mission on the 21/9/98 was primarily an intercomparison flight between the C-130 and the DLR Falcon aircraft. The mission was designed so that the two aircraft could meet each other at a specific location and make side-by-side atmospheric chemistry measurements. The results from the separate sampling and analysis could then be recorded and compared to see the agreement between the two. The aircraft were together for a total of 59 minutes during which both flew a stepped profile, including a twenty minute horizontal run. It was indicated from the Bergen Mesoscale Chemistry Transport Model (Flatøy *et al.* [2000], Chapter 3) that the air being investigated by the aircraft should be fairly cloud free and that pollution from the US that had been uplifted and transported into the upper free troposphere might be intercepted. Again, *in-situ* measurements of $j\text{-}(O^1D)$ were made on this flight, the data for which is shown in Figure 5.19 as one-minute data averages.

As shown in Figure 5.19, flight A580 consisted of a long duration, high altitude leg followed by a series of shallow profiles near the end of the flight. In terms of the $j\text{-}(O^1D)$ data produced for this flight, the structure of the data-time series is far less pronounced than flight A579. However, cloud features are also evident from Figure 5.19. There are three spikes in the $4\pi j\text{-}(O^1D)$ data observed *ca.* 13:00. Also observed at this time were three concurrent peaks in the *in-situ* water vapour concentration measurement. This is supportive of the aircraft encountering a cloud field with a relatively large albedo. While flying over this cloud field there was a large concurrent pick-up in the signal of the nadir facing radiometers with respect to $j\text{-}(O^1D)$ and $j\text{-}(NO_2)$, while the zenith facing devices saw no appreciable change. The relative increase in the signals generated by the nadir instruments also indicate that the optical properties of the cloud allowed wavelength dependent reflection of radiation. The relative increase in the measured $j\text{-}(NO_2)$ was observed to be *ca.* 79%, much larger than the corresponding increase in $j\text{-}(O^1D)$. The percentage increase in the nadir facing $j\text{-}(O^1D)$ radiometer was closer to 40%. A plot of the change in the ratio of the $j\text{-}(O^1D)$ and $j\text{-}(NO_2)$ for the zenith (U_{zenith}) and nadir (U_{nadir}) facing radiometers is shown in Figure 5.20.

Figure 5.19: In-situ $j\text{-(O}^1\text{D)}$ Data Obtained During ACSOE Flight A580

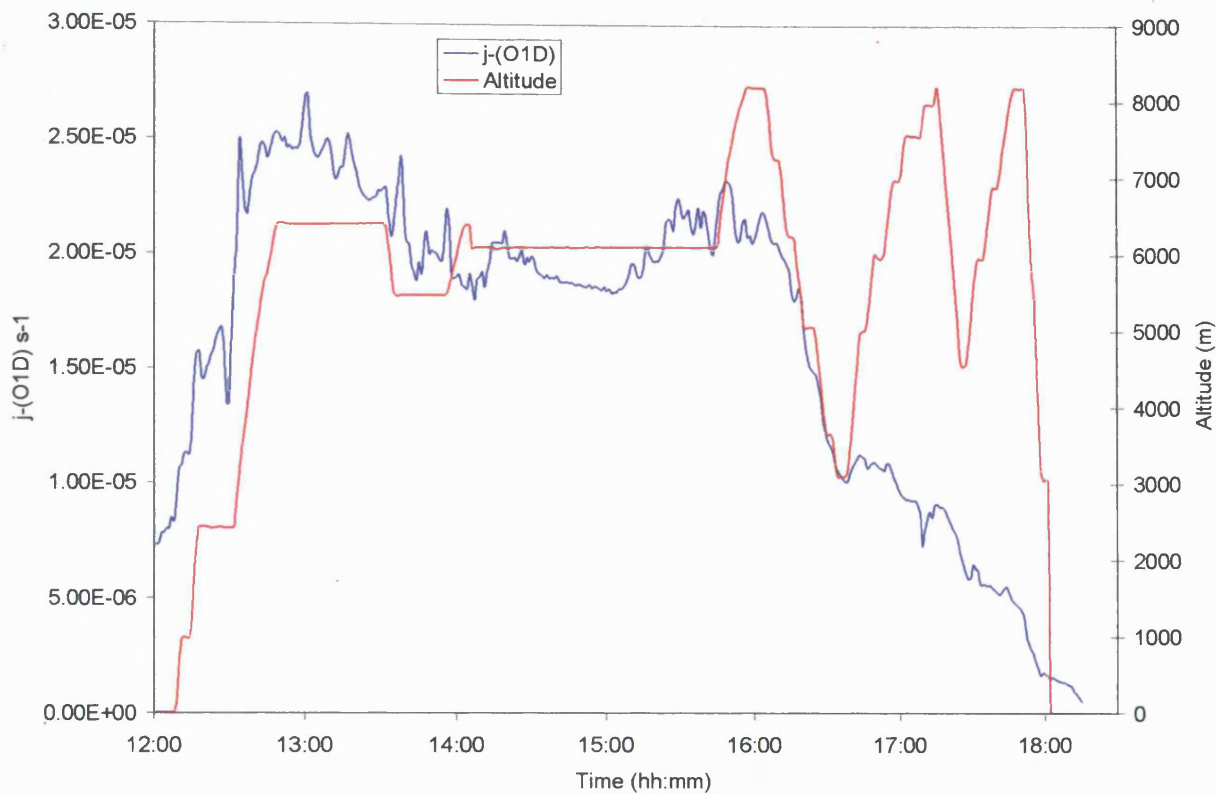
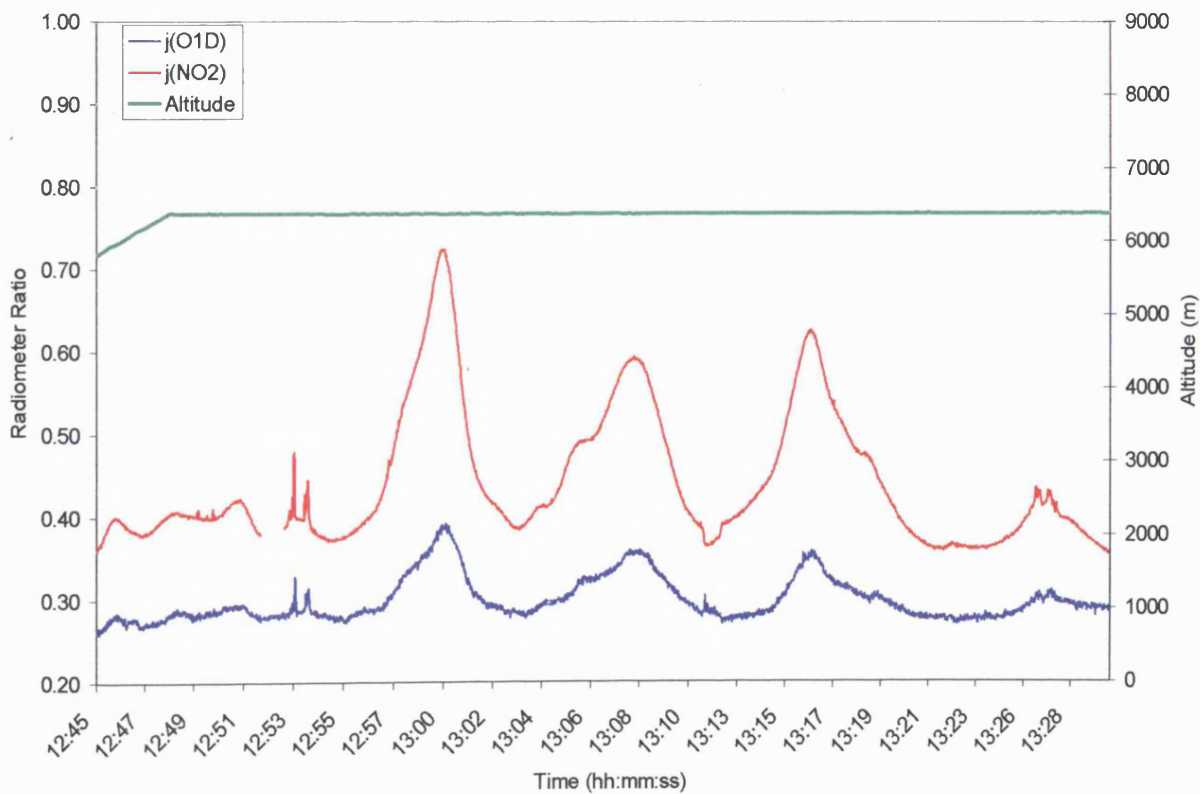


Figure 5.20: Effects on Clouds on Ratio of Signals $\left(\frac{U_{nadir}}{U_{Zenith}}\right)$ for $j\text{-(O}^1\text{D)}$ and $j\text{-(NO}_2)$ Aircraft Radiometers



5.5: Modelling Photolysis Frequencies During ACSOE

In-situ j -(O¹D) data obtained for the ACSOE Azores flight series was also compared to model data. Two models were used for the investigation. The first was the Tropospheric Ultraviolet-Visible (TUV), version 4.0, written and developed by Madronich and co-workers at the National Center for Atmospheric Research. (Madronich [1997], Madronich and Flocke [1998]). The radiative transfer code utilised by this model is based on the DIScrete Ordinate (DISORT) model developed by Stamnes *et al.* (1988). With respect to the radiative transfer scheme, the model was optimised with a pseudo-spherical n -stream discrete ordinate. This is similar to the plane-parallel n -stream discrete ordinate described by Stamnes *et al.* (1988), but with full pseudo-spherical calculation. (Zeng *et al.* [1996]). For the model outputs described here, the discrete ordinate was set to a total of eight weighted streams.

The TUV model is available through the Word-Wide-Web where, the user is able to download the necessary radiative transfer code. The model consists of a radiative transfer code and user interface. The model requires user input with respect to latitude, longitude, time and ozone column (DU). The TUV code was altered in such a way as to read-in data on latitude, longitude and height from a separate file in order to allow the model to solve the radiative transfer equations. The data output was in the form of photolysis frequencies along the aircraft flight track providing a time-series comparison with *in-situ* j -(O¹D) data.

Secondly, the *in-situ* j -(O¹D) profiles obtained by the C-130 were investigated *via* model comparison. This was done using the standard version of TUV, together with the simpler two-stream radiative transfer model based upon the original developments made by Hough (1988). In this model, calculations of photolysis frequencies assume that radiation consist of a direct beam along with a secondary source produced by scattered fluxes. The method assumes those direct or scattered photons either travel upwards or downwards at some angle, θ to the normal. For a direct beam that suffers no secondary scatter, the angle θ will be the solar zenith angle. Considering the total contribution of the two-stream assumption, direct solar radiation is the zeroth order downward flux and its corresponding reflectance is the zeroth order upward flux. Light that has been scattered by the n^{th} degree is the n^{th} order upward/downward flux. Hence, the total flux is the sum of these beams across n orders, *i.e.*

$$\text{Total Flux} = \sum_0^n F_n(\downarrow) + F_n(\uparrow) \quad (5.13)$$

Madronich (1987) and Zeng (1996), showed that for a two-stream model, the assumption that solar radiation is either upwelling or downwelling has drawbacks when compared to more complex radiative transfer solutions (*e.g.* multistream co-ordinates). In general, the agreement between these methods is good to a first approximation. Hence, it was decided to test both of the models relative ability to reproduce the photolysis frequencies measured *in-situ*.

The TUV radiative transfer model was utilised for all three of the summer flights during the ACSOE campaign, in order to evaluate the general agreement of the model and measured j -(O¹D) during the mission. All data assumed a cloud free atmosphere. Data for j -(O¹D) was run along the flight track using *in-situ* values of latitude, longitude and altitude. The model assumed clear sky conditions were maintained throughout and that aerosol effect was small (*i.e.* set to zero). A composite plot of the comparison between modelled data and measured photolysis frequencies are shown in Figure 5.21, while correlation plots between measured and modelled data are shown in Figure 5.22. From the data shown in Figures 5.21 and 5.22, there is a consistent overestimation in the modelled photolysis frequency when compared to the *in-situ* aircraft measurement. Specifically, there appears to be a generally constant offset in the model data at high zenith angles with the overestimation of the model being *ca.* $6 \times 10^{-6} \text{ s}^{-1}$ greater than the data measured *in-situ*. The offset does vary from flight to flight indicating that local meteorological effects are also important as expected.

The fact that the model output overestimates the measured data can be explained by considering a number of factors. First, the model assumed clear sky conditions were maintained throughout the flight, a condition that was obviously not the case for the ACSOE summer flights. As indicated in section 5.3, cloud factors were shown to have varying effects on measured photolysis rates and hence the combination of these cloud factors combined with aerosol loading would have the effect of altering photolysis frequencies from that predicted for a clear sky, low aerosol conditions. While this may go some way as to explain localised differences between model/measured j -values, it is unlikely that these effects alone would be sufficient to cause such a general overestimation of model j -(O¹D). In order to diagnose the possible cause of the overestimation, it is first necessary to gauge whether the model prediction of j -(O¹D) is too large or the *in-situ* measurement is too low.

Figure 5.21 Modelled and Measured j -(O¹D) for ACSOE Azores Flight Campaign

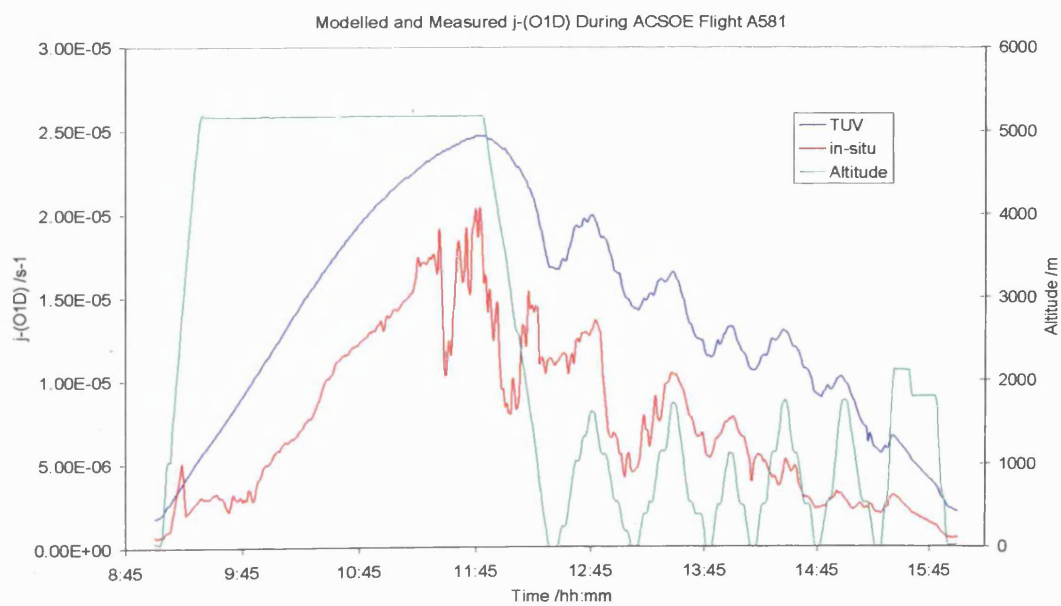
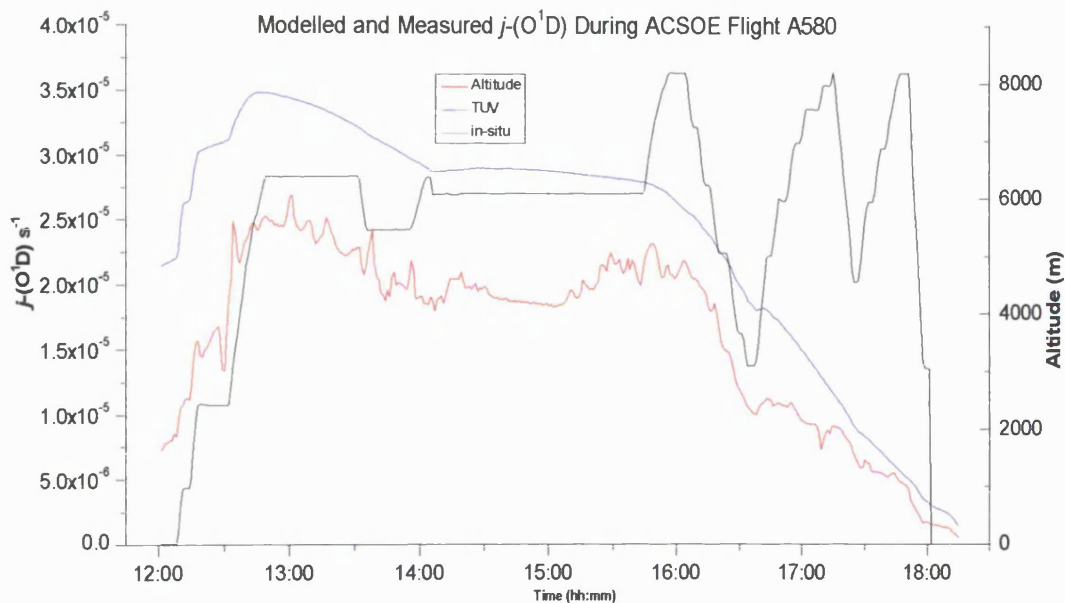
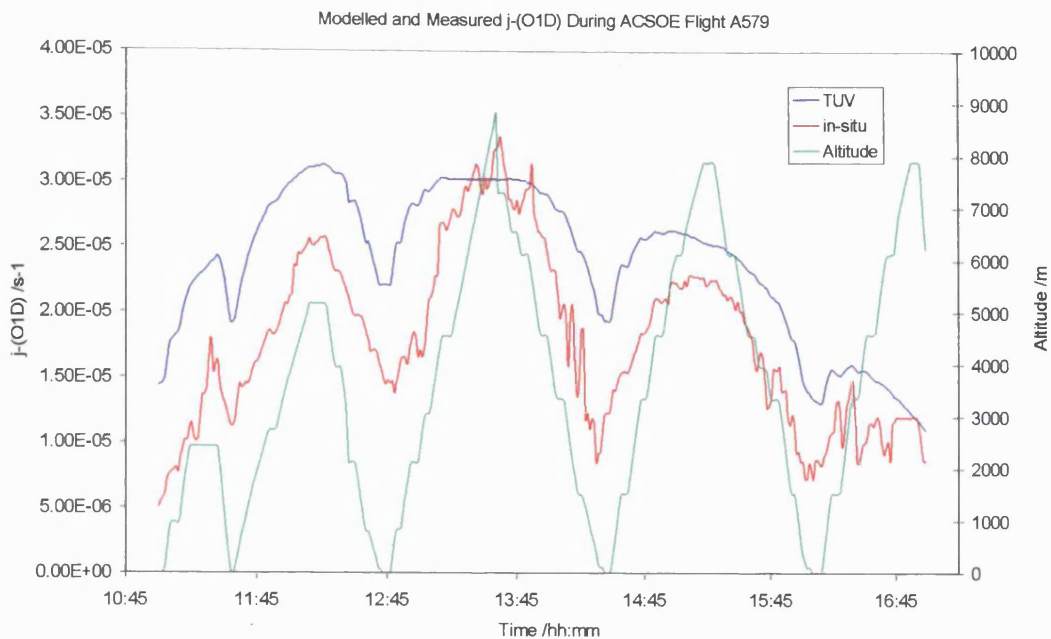
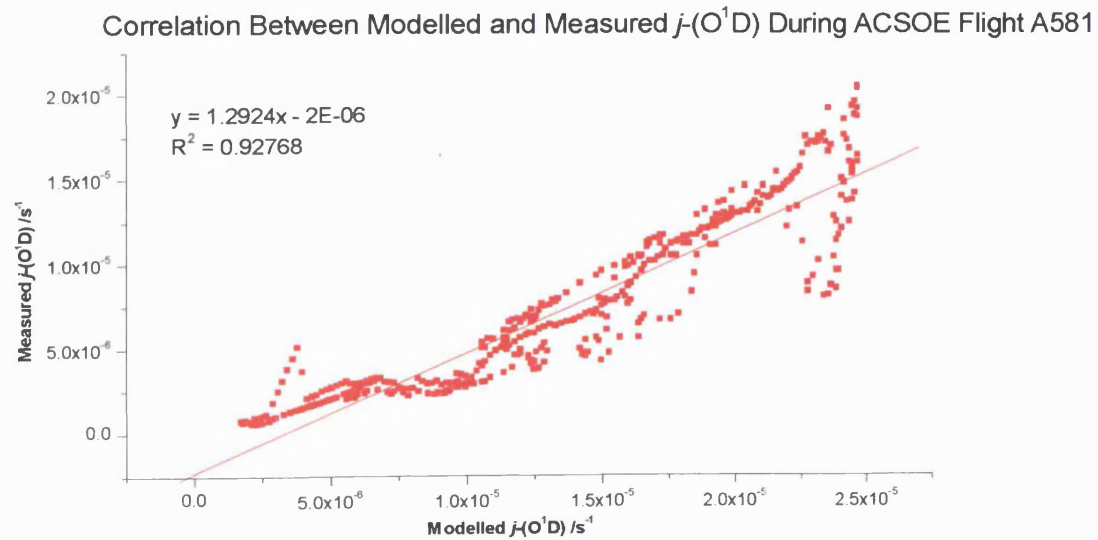
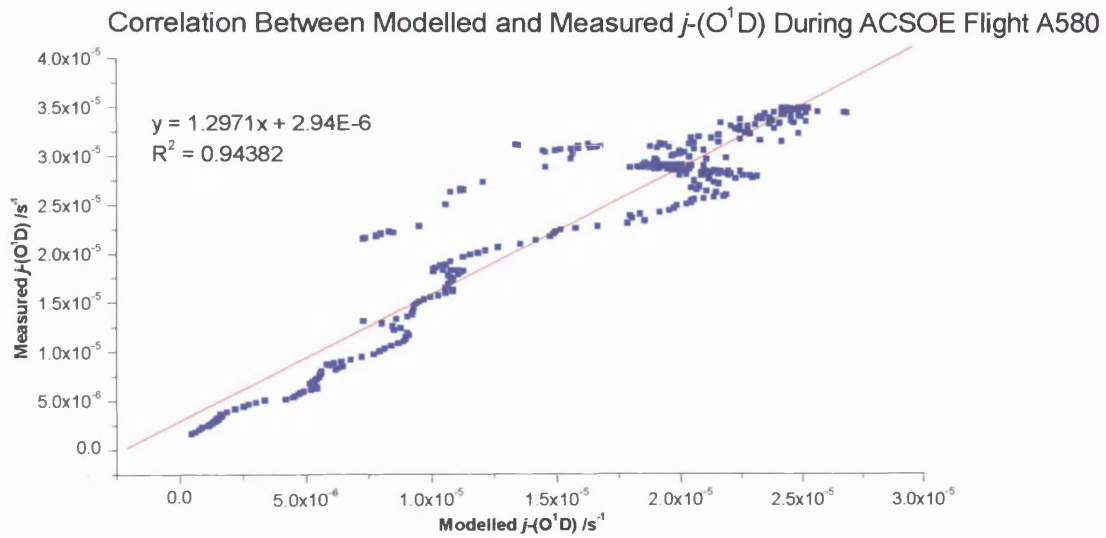
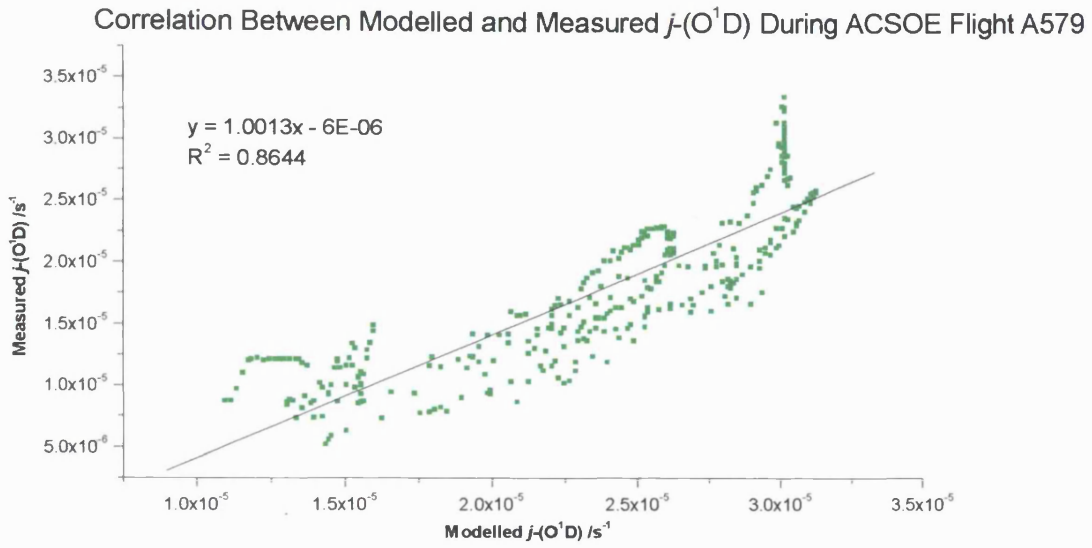


Figure 5.22 Correlation Between Measured and Modelled j -(O¹D) During ACSOE Azores Campaign



In order to test the model reproducibility of $j\text{-(O}^1\text{D)}$ along aircraft flight tracks, tests were made against an independent measurement of photolysis frequency. $j\text{-(O}^1\text{D)}$ data recorded *in-situ* the by the airborne spectroradiometer run by NCAR during the 1997 SONEX campaign was compared to predictions from the TUV model. This instrument has been shown to have good agreement to model data (Bais *et al.* [2000]), on the ground and *via* aircraft platforms (B. Lefer, *private communication*). The flight tracks for two separate SONEX flights were run through the model and again, the model appeared to show an overestimation of the *in-situ* measured photolysis frequency. The plot of the flight track TUV data together with *in-situ* $j\text{-(O}^1\text{D)}$ for the SONEX mission on 28/10/97 is shown in Figure 5.23. Although the general trend of the flight-track is reproduced quite well, there is a net overestimation of absolute $j\text{-(O}^1\text{D)}$ in SONEX of *ca.* 27%. The overestimation of this independent measurement would suggest that the overestimation found in the ACSOE campaign comparisons of modelled data vs. measured data is a general feature of the TUV model.

Figure 5.23: Flight Track TUV with *in-situ* $j\text{-(O}^1\text{D)}$ for SONEX mission 28/10/97

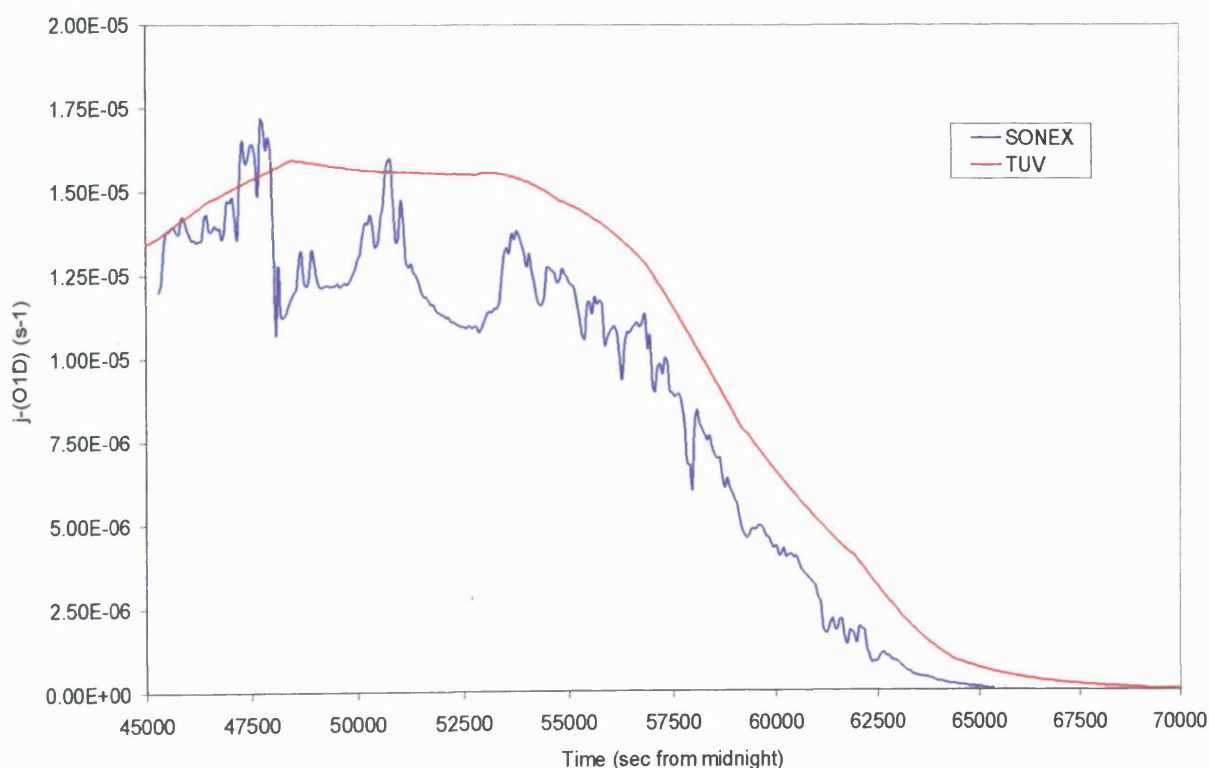


Figure 5.24: In-situ and TUV j -(O^1D) Profiles for ACSOE Flight A579.

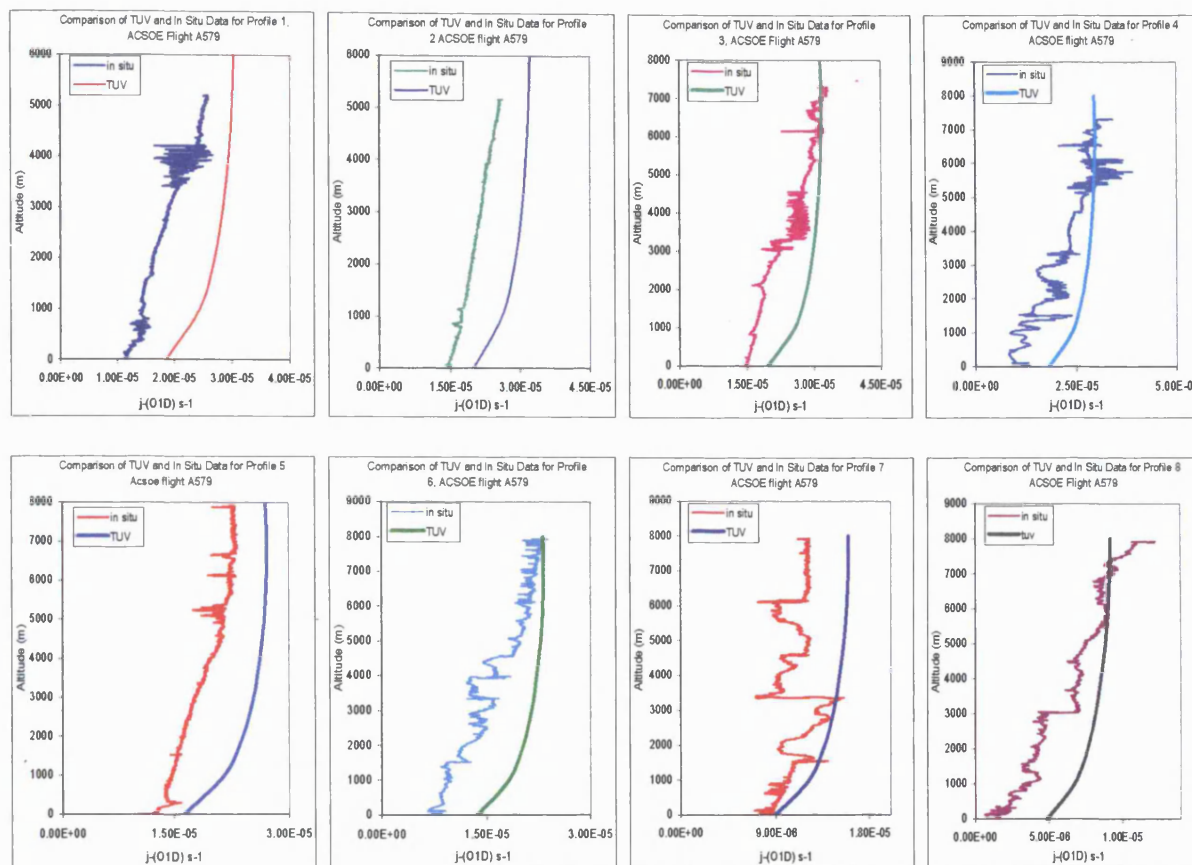
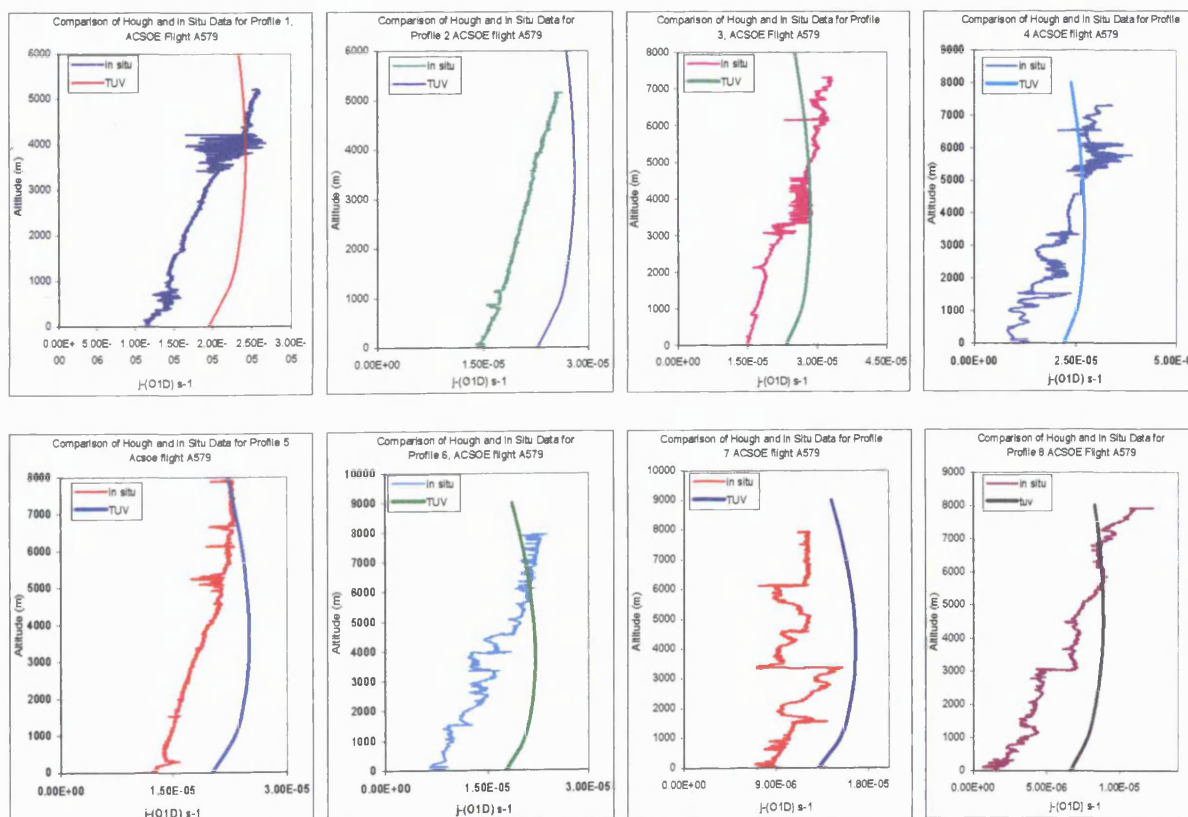


Figure 5.25: In-situ and Hough j -(O^1D) Profiles for ACSOE Flight A579.



5.6: Model and Measured j -(O¹D) Profiles

A second test of the performance of the aircraft radiometers was the comparison of measured j -(O¹D) profiles to that predicted from the TUV model and from the two-stream radiative transfer code developed by Hough (1988). The profiles taken during the saw tooth frontal crossing flight A579, as shown in Figure 5.17 were compared to the model prediction under clear sky, no aerosol conditions. Figure 5.24 shows profile plots of the TUV predictions for j -(O¹D) with those measured during profiles 1-8 of flight A579. In all cases, the model overestimates the absolute photolysis frequency with respect to those data measured *in-situ*. However, the overestimation is not a constant offset. In several of the profiles the agreement is quite good while for others, there is a larger overestimation in the model data. In general, the profiles taken in the middle of the flight seem to have better agreement than those taken at the beginning and end of the flight. The model data shows a characteristically curved plot where as the measured data shows a linear increase. The net result is that at around 1 km, the model overestimation is at a maximum. At higher altitudes, *ca.* 8 km, the model and measured agreement is often very good and crosses the *in-situ* data. Data for the comparison of the Hough model with those data measured *via* the C-130 platform during the September 1997 ACSOE Azores flight campaign is shown in Figure 5.25. From Figure 5.25 data from the two-stream model shows a similar pattern to those data derived from the TUV model. A statistical summary of the comparison between TUV data, the Hough two-stream model and measured j -(O¹D) is shown in Table 5.5.

Table 5.5: Statistical Comparison Between TUV, Two-stream code and *in-situ* j -(O¹D) for ACSOE Flight A579

Profile	Average <i>in-situ</i> j -(O ¹ D)	Average TUV	Overestimation (%)	Average 2-stream	Overestimation (%)
1	1.89×10^{-5}	2.69×10^{-5}	30	2.28×10^{-5}	17
2	2.03×10^{-5}	2.85×10^{-5}	29	2.63×10^{-5}	23
3	2.41×10^{-5}	2.88×10^{-5}	16	2.67×10^{-5}	10
4	2.22×10^{-5}	2.69×10^{-5}	17	2.54×10^{-5}	13
5	1.93×10^{-5}	2.46×10^{-5}	21	2.35×10^{-5}	17
6	1.57×10^{-5}	2.09×10^{-5}	25	2.06×10^{-5}	24
7	1.10×10^{-5}	1.42×10^{-5}	23	1.56×10^{-5}	30
8	4.3×10^{-6}	7.01×10^{-6}	39	7.30×10^{-6}	41

5.7: Remaining Issues

Despite the relatively good performance of the fixed bandwidth radiometers with respect to measurement of *in-situ* $j\text{-}(O^1D)$, there are several outstanding issues that need to be addressed with respect to the reliability of these data. The first, and most important, is the radiometer calibration. As described in section 5.3.5 the aircraft radiometer calibration relied on the cross calibration of these devices with a fixed bandwidth radiometer that is used for ground based evaluations of $j\text{-}(O^1D)$. Figures 5.12 and 5.13 suggested that this calibration gave a good estimate of $j\text{-}(O^1D)$ when the radiometers operated on the ground. The validity of this calibration when the two aircraft devices operate at altitude does need consideration.

There are two areas of potential concern, the first is the effect of column ozone. As described in more detail in Chapter 6, the effective ozone column changes with altitude and as solar zenith angle increases. The reference radiometer that was used in the cross calibration with respect to the aircraft radiometers was calibrated with a fixed ozone column of 290 DU. The effect of variations in this effective overhead ozone column owing to increased altitude and over a range of solar zenith angles results in a potential breakdown of the cross calibration for the aircraft radiometers. In addition, the radiometers were calibrated across a far narrower temperature range than can be expected for the altitude envelope of the C-130 (see Table 5.2). As outlined in section 5.2.2 and described in depth by Hofzumahaus *et al.* [2000], the large temperature dependence of molecular parameters that contribute to $j\text{-}(O^1D)$ are likely to cause potentially significant effects in the radiometer data, despite the fact that the cross calibration was against a radiometer which itself was calibrated against a chemical actinometer.

In order to eliminate these problems it is necessary to perform a new calibration of the radiometers. This is possible by using calibrated light sources such as tungsten halogen lamps. From detailed analysis of the spectra function of the instrument, it is possible to ascertain the relative transmittance in photons at each wavelength across the $j\text{-}(O^1D)$ bandwidth. From knowledge of the lamp output, the wavelength dependent relative response can be calculated in terms of the summation of actinic flux across this waveband. This provides an estimate of the actinic flux detected by the radiometer against the calibration light source and also in the real atmosphere. From the use of these data, together with suitable molecular parameters a summation of the total product of ϕ , σ F , *i.e.* $j\text{-}(O^1D)$, can be calculated.

5.8: Overall Summary

In this chapter, the measurement of the photolysis frequency $j\text{-}(O^1D)$ from an aircraft platform has been described. It has been shown that in order to evaluate changes in $j\text{-}(O^1D)$ typically encountered as aircraft move vertically and horizontally in the atmosphere, several factors need to be considered. The first is the general change in the actinic flux that is capable of producing ozone photolysis. This is reflected in the change in the relative contributions of upwelling, downwelling and direct contributions to actinic flux. In addition, the importance of the large-scale temperature dependence has been evaluated. It has been shown that the effect of decreasing temperature with respect to altitude has little effect on ozone molecular absorption cross-section, but large effects on the O^1D quantum yield.

In order to address these factors in the *in-situ* measurement of $j\text{-}(O^1D)$ via aircraft platforms, two fixed bandwidth radiometers have been designed and built. A full characterisation has been performed for these instruments, which were deployed on the MRF C-130 aircraft for the first time during the ACSOE Azores campaign of 1997. Although there are several unresolved issues, data from these radiometers have been shown to be able to measure $j\text{-}(O^1D)$ with a reasonable degree of accuracy when compared to model prediction. Data for the aircraft latitude, longitude and height have been used to produce $j\text{-}(O^1D)$ data along aircraft flight tracks via a modified version of the Troposphere Ultraviolet-Visible (TUV) model (Madronich [1997]). The modelled data seem to overestimate those data measured *in-situ* by up to *ca.* 30% for most cases. However, this is within the estimated accuracy of the *in-situ* measurement. Data from both TUV and a two-stream isotropic scatter model based on the radiative transfer code of Hough (1988), have been compared to *in-situ* aircraft profiles with similar modelled/measured agreements.

Chapter Six: The IPMMI Experiment

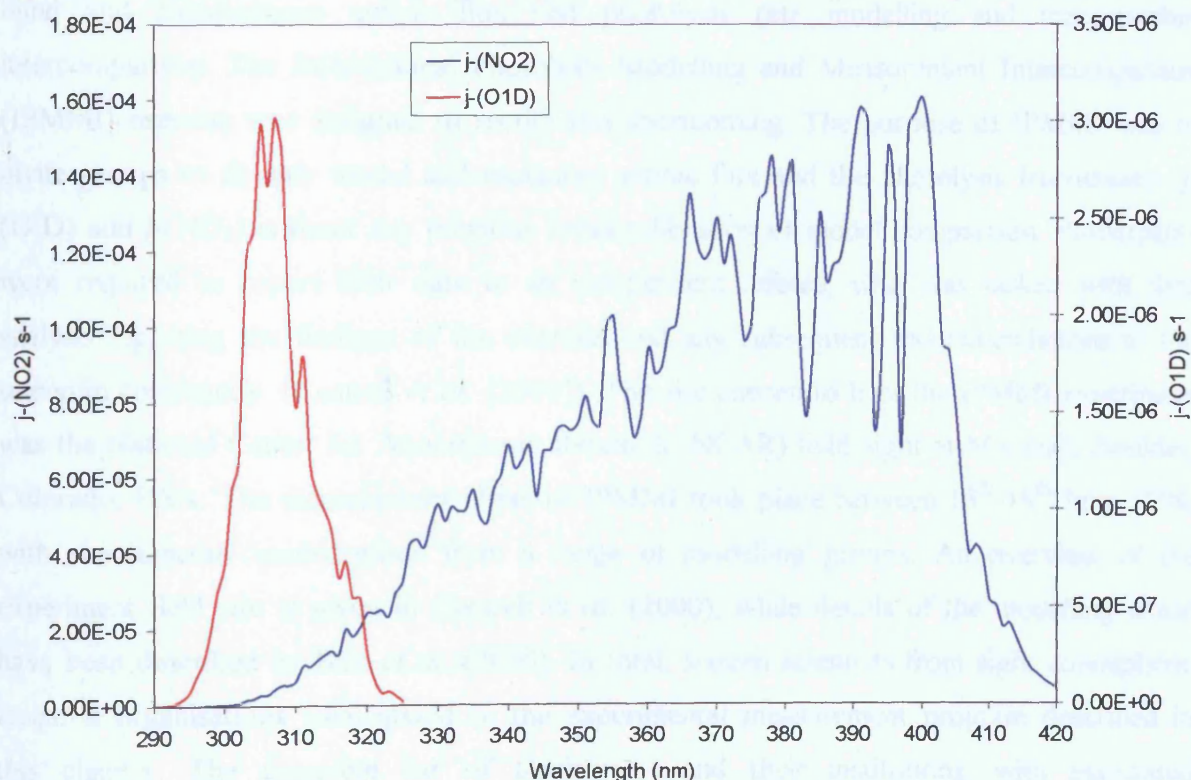
6.1)	Introduction	196
6.2)	<i>j</i>-O(¹D) Filter Radiometer	198
6.3)	Performance of <i>j</i>-(O¹D) filter radiometer at IPMMI	200
6.4)	<i>j</i>-(NO₂) Filter radiometer	202
6.5)	Performance of <i>j</i>-(NO₂) filter radiometer at IPMMI	206
6.6)	Diode Array Spectroradiometer	207
6.7)	Importance of Stray Light and Dark current	214
6.8)	Improved Stray Light Corrections	225
6.9)	Effect of Molecular Parameters	228
6.10)	Conclusions	233

Chapter 6: The International Photolysis Modelling and Measurement Intercomparison (IPMMI) Experiment

6.1 Introduction

Accurate measurement and modelling of atmospheric photolysis frequencies is necessary in order to fully account for the photochemical transformation of key atmospheric trace gases such as ozone, nitrogen dioxide, formaldehyde and acetone. Measurement and calculation of photochemical rate constants are however complicated by the natural variability of the background atmospheric radiation field. Local meteorology such as variable amounts of cloud and aerosol can dramatically alter the measured photolysis frequency over a range of a few kilometres. All of these so-called "*j*-values" are found to have strong wavelength dependencies and their measurement often calls for detailed molecular data with respect to absorption cross-section and quantum yield, which in themselves are observed to have both wavelength and temperature dependencies. The calculation of photolysis frequencies by modelling, like the experimental measurements, often has several uncertainties. A comparison of the significant wavelengths for two of these photolysis frequencies, $j(\text{O}^1\text{D})$ and $j(\text{NO}_2)$, are shown in Figure 6.1.

Figure 6.1: Relative Distributions of the Spectral Photolysis Frequencies of Ozone and NO_2



There have been several field campaigns published in the literature describing the comparison of various methods of measuring and modelling atmospheric photolysis frequencies. These include the photolysis of ozone into excited oxygen, $j\text{-}(O^1D)$, and the photolysis of NO_2 , $j\text{-}(NO_2)$ as described in section 1.4 of Chapter One. Data suggest that the photolysis rate coefficients $j\text{-}(O^1D)$ and $j\text{-}(NO_2)$ can be measured with accuracy of often $>90\%$. Data taken during MLOPEX 2 in the Hawaiian Islands in 1994 (Shetter *et al.* [1996]) suggested good agreement between the predicted and measured data in the experiment. The work of Müller *et al.* (1995) described agreement to within 14% from comparisons of $j\text{-}(O^1D)$ filter radiometers, spectroradiometers and chemical actinometer instruments participating in the 1994 POPCORN series of experiments. These correlation errors were shown to be within the error estimates of the individual instruments. Similar results have also been achieved in the JCOM97 field experiment where in addition to $j\text{-}(O^1D)$, $j\text{-}(NO_2)$ was also measured (Kraus *et al.* [2000]). In addition, there have been modelling studies that have attempted to ascertain radiation fields in cloud free atmospheres and with cloud and aerosol effects added. These have included simple two-stream radiative transfer codes that assume actinic flux comes from the sum of upwelling and downwelling flux (*e.g.* Hough [1988], Toon *et al.* [1989]) and more complex multi-stream models (*e.g.* Stamnes, [1988], Ruggaber *et al.* [1994], Madronich [1998]).

Despite the large volume of work in this area, so far there has not previously been a purely blind and simultaneous actinic flux and photolysis rate modelling and measurement intercomparison. The International Photolysis Modelling and Measurement Intercomparison (IPMMI) exercise was designed to rectify this shortcoming. The purpose of IPMMI was to invite groups to directly model and measured actinic flux and the photolysis frequencies $j\text{-}(O^1D)$ and $j\text{-}(NO_2)$ without any previous cross-calibration or model comparison. Participants were required to report their data to an independent referee, who was tasked with data analysis reporting the findings of the exercise and any subsequent recommendations to the scientific community. (Cantrell *et al.* [2000]). The site chosen to host the IPMMI experiment was the National Center for Atmospheric Research (NCAR) field site at Marshall, Boulder, Colorado, USA. The measurement phase of IPMMI took place between 15th-19th June 1998, with simultaneous contributions from a range of modelling groups. An overview of the experiment field site is given in Cantrell *et al.* (2000), while details of the modelling phase have been described by Bais *et al.* (2000). In total, sixteen scientists from eight atmospheric research organisations participated in the experimental measurement program described in this chapter. The complete list of participants and their institutions, with associated abbreviations are shown in Table 6.1.

Table 6.1: IPMMI Participants and Institute Abbreviations

NAME	INSTITUTION	Abbreviation
Alexander Kraus, Martin Müller, Andreas Hofzumahaus	FZ Jülich, Germany	FZJ
Wolfgang Junkermann	Fraunhofer Institute, Germany	IFU
Rick Shetter, Barry Lefer, Sam Hall	National Center for Atmospheric Research, USA	NCAR
Paul S. Monks, Gavin D. Edwards	University of Leicester, UK	ULi
William Swartz, Russ Dickerson	University of Maryland, USA	UMD
Richard McKenzie, Paul V. Johnson	National Institute for Water and Atmospheric Research, New Zealand	NIWA
John Barrick, Jim Crawford	NASA Langly, USA	NASA
Rainer Schmitt	Meteorologie Consult, Germany	METCON

This chapter describes the deployment of traditional filter radiometers and a new commercially available instrument that was run for the first time at IPMMI. The latter instrument is a single monochromator diode array spectroradiometer that was used to measure total actinic flux and also values of j -(O¹D) and j -(NO₂). The majority of this chapter focuses on the data gathered during IPMMI by the new spectroradiometer. The accuracy of spectroradiometer measurements is compared to photolysis frequencies derived using similar and differing experimental techniques. The instrument performed adequately, but there were several problems identified with the field performance of this spectroradiometer, and the instrument has the potential to propagate significant errors in the data. Hence, a full error analysis together with instrument characterisation has been performed and is reported here. The feasibility of using such an instrument in the field for the measurement of atmospheric photolysis frequencies is also discussed.

6.2: j -O(¹D) Filter Radiometer

The j -O(¹D) filter radiometer deployed by the University of Leicester during IPMMI was constructed based on the original concepts detailed by Junkermann *et al.* (1989) and includes technical modifications of the inlet optics and the optical filter combination described by Volz-Thomas *et al.* (1996) and Hofzumahaus *et al.* (1999). The entrance optic of the radiometer consists of a polished 2π quartz dome/diffuser that was supplied commercially by Meteorologie Consult GmbH, Glashütten, Germany. The diffusely transmitting quartz dome has a nearly uniform angular response to radiation incident from the upper hemisphere over a solid angle of 2π sr. The collected radiation is transmitted *via* a collimator assembly to an optical bandpass filter (centre wavelength *ca.* 300 nm, FWHM = 10 nm) and the resultant signal is detected by a solar-blind photomultiplier tube (*Hamamatsu*, R431S). The photocurrent is converted into a voltage signal *via* a current-to-voltage amplifier. During IPMMI, the PMT signal voltage was recorded by a data logging system (21X Micrologger supplied by *Campbell Scientific Limited*) with an integration time of 60 s. The optical train was temperature stabilised at $30(\pm 1)^\circ\text{C}$ at all times.

The filter radiometer was originally calibrated against a chemical actinometer in order to convert from raw data to j -O(¹D). Using the molecular parameter recommendations of Molina and Molina (1986) with respect to the absorption cross-section, with the quantum yield recommendations of JPL 1997 (DeMore *et al.* [1997]), the radiometer voltage can be converted to an integrated j -O(¹D) between $\lambda=290 - 320$ nm. Despite the fact that spectral response of the filter radiometer does not match exactly the spectral shape of the O₃ → O(¹D) photodissociation cross-section, the relationship between the radiometer signal and j -O(¹D) is approximately linear. The conversion function needed for the calculation of photolysis frequencies from the radiometer signal (U) depends only on the solar zenith angle, total vertical ozone column, temperature and dark current offset. For the conditions of IPMMI, the radiometer was calibrated assuming a constant ozone column of 290DU together with *in-situ* zenith angle determination. Dark current offset was determined daily from radiometer dark current measurements. The conversion function, is given by equation (6.1), where

$$j\text{-O}^1\text{D} = (7.09 \times 10^{-5}) + (3.79 \times 10^{-7} * \theta) - (1.61 \times 10^{-9} * \theta^2) * U \quad (6.1)$$

Where θ = Solar Zenith angle and U = radiometer signal, minus the PMT dark current (in volts)

This filter radiometer has been run in several previous field experiments (*e.g.* Monks *et al.* [1996], [2000] Zanis *et al.* [1999]). A full characterisation of the instrument suggests that instrumental errors are *ca.* 6%. The error associated with temperature factors, corrections for solar zenith angle and O₃ column corrections to filter radiometer signals are *ca.* 10%. The overall error in $j\text{-(O}^1\text{D)}$ as measured by this photoelectric radiometer is estimated to be *ca.* 12% at solar zenith angles < 60°.

6.3: Performance of $j\text{-(O}^1\text{D)}$ filter radiometer at IPMMI

The raw $j\text{-(O}^1\text{D)}$ data recorded by the filter radiometer during IPMMI was submitted to the IPMMI referees according to the IPMMI protocol (Cantrell *et al.* [2000]). Figures and statistical data involving the correlations of one instrument against another were circulated to the IPMMI community by the IPMMI referee. The IPMMI referee reported that the agreement between the University of Leicester (ULi) $j\text{-(O}^1\text{D)}$ filter radiometer and the eight $j\text{-(O}^1\text{D)}$ filter radiometers, spectroradiometers and chemical actinometers deployed at IPMMI were within the state errors of each instrument. In the majority of cases, these differences were < 10%. A summary of the correlation coefficients derived by the IPMMI referee for 19/6/98 is shown in Table 6.2. Similar agreements were observed throughout the campaign. Correlation plots of the agreements between ULi filter radiometer data and photolysis frequencies measured by the NCAR chemical actinometer for all of the IPMMI campaign is shown in Figure 6.2.

Although the overall performance of the ULi filter radiometer was good with respect to other independent instruments, there are areas of potential concern regarding the accurate measurement of $j\text{-(O}^1\text{D)}$. The first was the ozone slant column correction. As stated above, the ULi filter radiometer was originally calibrated against a chemical actinometer. In the calibration, it was assumed that the overhead ozone column was 290DU. The effective ozone column changes however, with the apparent passage of the sun across the sky. When the sun is at a very large solar zenith angle, the effective ozone column that the incoming solar radiation must pass through is much larger than for smaller solar zenith angles (Dickerson *et al.* [1982], Hofzumahaus *et al.* [1992]). Figure 6.3 shows the change in the effective ozone column over the course of one diurnal cycle. From this figure, for data taken at solar zenith angles > *ca.* 65° the effective ozone column is sufficiently large to cause problems in assuming that column O₃ = 350 DU in the absolute calibration of the photoelectric radiometer.

Table 6.2: Correlation Between ULi Filter Radiometer j -(O¹D) data to Other Instruments at IPMMI on 19/6/98 for 1 minute averaged data.

Instrument	Quantum Yield Recommendation (where relevant)	Correlation Coefficient
IFU Filter Radiometer (FR)	-	0.942
FZ Jülich Filter Radiometer (FR)	-	0.995
FZ Jülich Spectroradiometer (SR)	DeMore <i>et al.</i> (1997)	0.998
	Talukdar <i>et al.</i> (1998)	0.998
NCAR Spectroradiometer (SR)	DeMore <i>et al.</i> (1997)	0.977
	Talukdar <i>et al.</i> (1998)	0.977
NCAR Spectroradiometer (SR)		
NCAR CA	-	0.987
METCON Spectroradiometer (SR) 1	-	0.996
METCON Spectroradiometer (SR) 2	-	0.994
		0.993
METCON Filter Radiometer (FR)		
ULi Spectroradiometer (SR)	DeMore <i>et al.</i> (1997)	0.994
ULi Spectroradiometer (SR)	Talukdar <i>et al.</i> (1998)	0.993

Figure 6.2 Correlations Between ULi Filter Radiometer $j(O^1D)$ and NCAR Chemical Actinometer Data During the IPMMI Campaign.

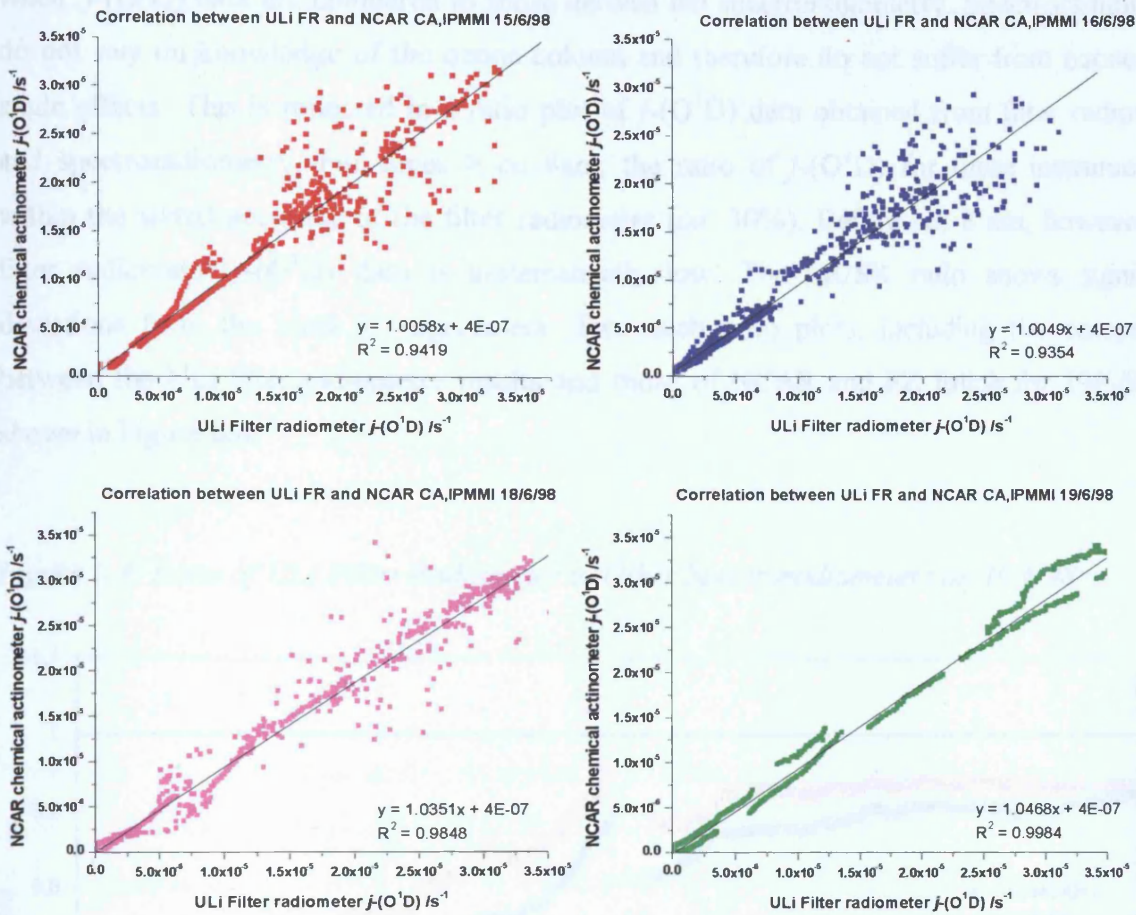
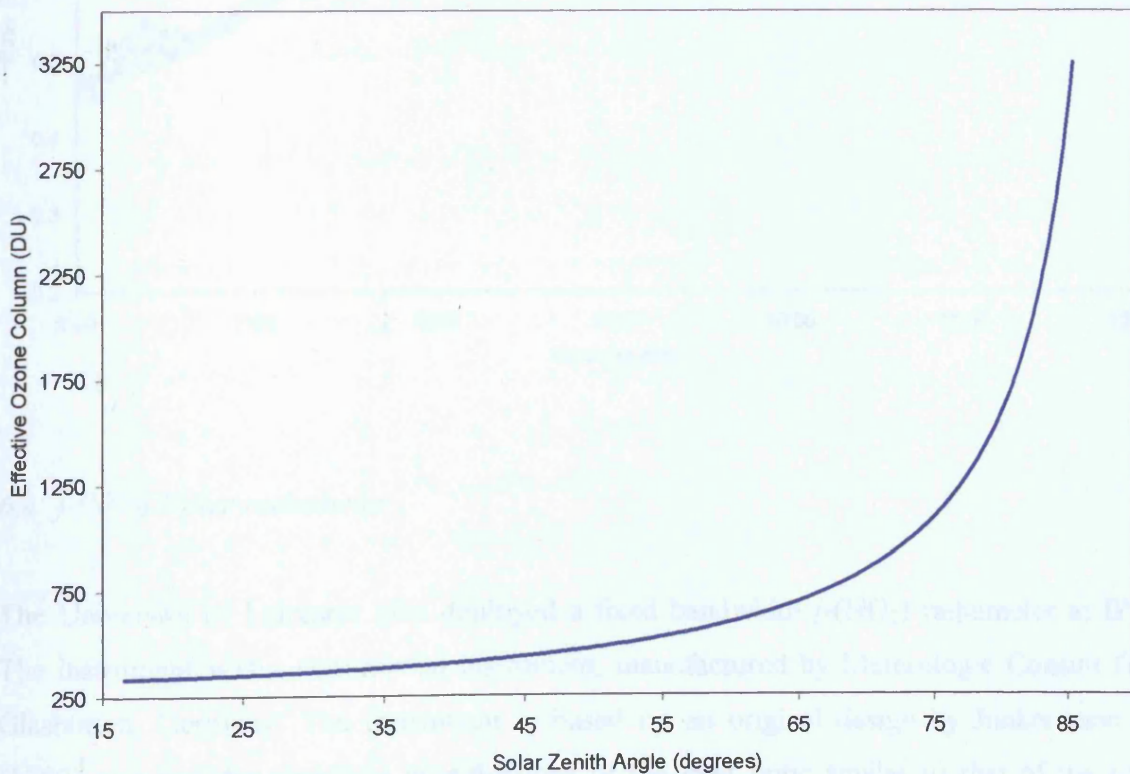
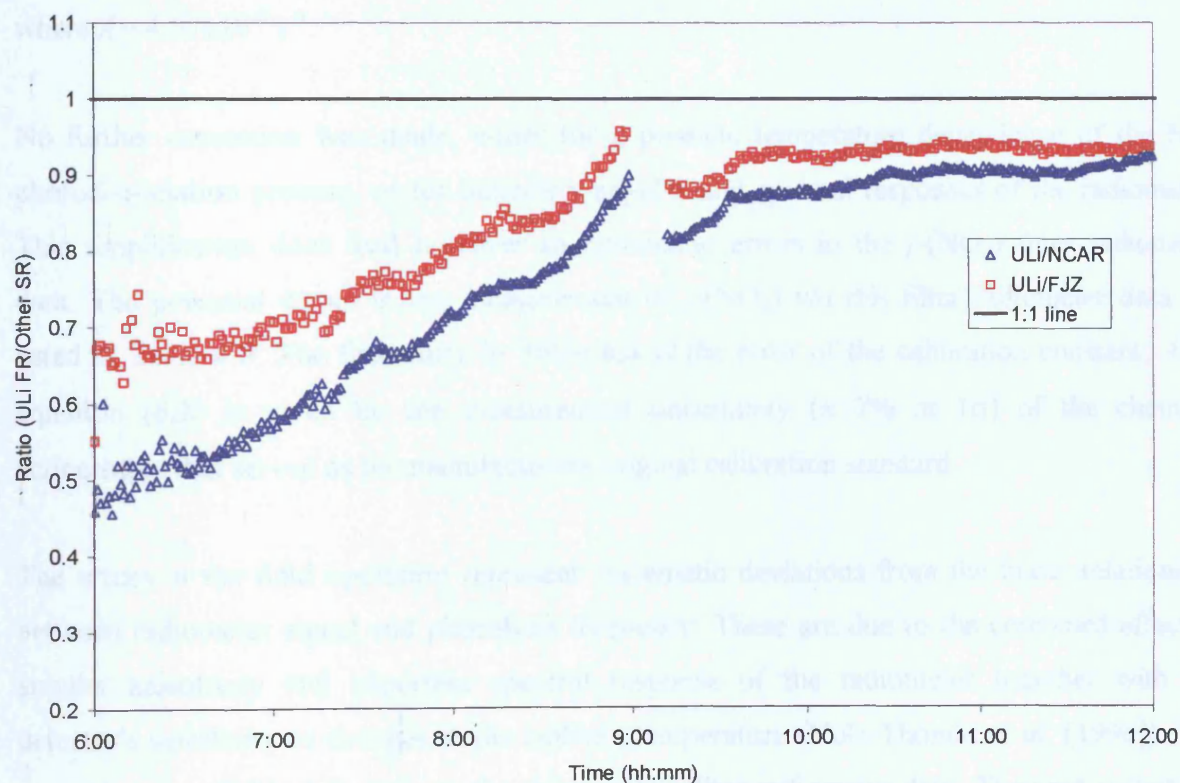


Figure 6.3: Change in Slant Ozone Column with Solar Zenith Angle, IPMMI 19/6/98



At these solar zenith angles, the effective ozone column is large enough to cause an underestimation of the photolysis frequency greater than the stated accuracy of the instrument, when $j\text{-(O}^1\text{D)}$ data are compared to those derived *via* spectroradiometry. Spectroradiometers do not rely on knowledge of the ozone column and therefore do not suffer from ozone slant angle effects. This is reflected in a ratio plot of $j\text{-(O}^1\text{D)}$ data obtained from filter radiometry and spectroradiometry. For times $> ca$ 8am, the ratio of $j\text{-(O}^1\text{D)}$ for these instruments is within the stated accuracy of the filter radiometer (*ca.* 30%). Before *ca.* 8 am, however, the filter radiometer $j\text{-(O}^1\text{D)}$ data is systematically low. The FR/SR ratio shows significant deviations from the ideal 1:1 agreement. Two such ratio plots, including the comparison between the ULi filter radiometer results and those of NCAR and FZ Jülich for 19/6/98 are shown in Figure 6.4.

Figure 6.4: Ratio of ULi Filter Radiometer to Other Spectroradiometers on 19/6/98



6.4: $j\text{-(NO}_2\text{)}$ Filter radiometer

The University of Leicester also deployed a fixed bandwidth $j\text{-(NO}_2\text{)}$ radiometer at IPMMI. The instrument was a commercial instrument, manufactured by Meteorologie Consult GmbH, Glashütten, Germany. The instrument is based on an original design by Junkermann *et al.* (1989) and includes technical modifications of the inlet optic similar to that of the $j\text{-(O}^1\text{D)}$

filter radiometer (Volz-Thomas *et al.* [1996]). The entrance optic of the radiometer consists of diffusely transmitting 2π sr quartz domes and has a nearly uniform angular response to radiation incident from the upper hemisphere. The collected radiation is optically filtered by a glass filter combination (2 mm UG3, 1 mm UG5, Schott, GmbH) and is detected by a vacuum photodiode having a Cs-Sb photocathode. A single-stage current-to-voltage amplifier converts the photocurrent into a voltage signal. During IPMMI, data were recorded by a data logging system (21X Micrologger, Campbell Scientific Ltd.) with a sample time of 1 seconds and a total integration time of 60 seconds. The signal of the filter radiometer depends on the broadband integrated actinic flux ($\lambda=290\text{nm} \rightarrow 420\text{nm}$), which is effectively proportional to the NO_2 photolysis frequency. Accordingly, $j\text{-(NO}_2\text{)}$ values were determined from the radiometer signal (U) by applying a constant conversion factor A , so that

$$j\text{-(NO}_2\text{)} = A * U. \quad (6.2)$$

where $A = 4.57 \times 10^{-6} \text{ s}^{-1}$.

No further correction was made, either for a possible temperature dependence of the NO_2 photodissociation process, or for imperfect angular and spectral responses of the radiometer. This simplification does lead however to systematic errors in the $j\text{-(NO}_2\text{)}$ filter radiometer data. The potential errors in the measurement of $j\text{-(NO}_2\text{)}$ via this filter radiometer data are listed in Table 6.3. The first entry in Table 6.3 is the error of the calibration constant, A , in equation (6.2) is given by the measurement uncertainty ($\pm 7\%$ at 1σ) of the chemical actinometer that served as the manufacturers original calibration standard.

The errors in the field operation represent systematic deviations from the linear relationship between radiometer signal and photolysis frequency. These are due to the combined effect of angular anisotropy and imperfect spectral response of the radiometer together with the detector's sensitivity to changes in the ambient temperature (Volz-Thomas *et al.* [1996]). The errors listed in Table 6.3 apply to the uncorrected filter radiometer data. They are systematic and are correlated with each other, *e.g.* the temperature influence on the instrument is positively correlated with the solar-zenith angle dependent error caused by imperfect spectral response of the instrument. It is therefore more appropriate to sum the errors of the field operation linearly rather than quadratically. Thus, systematic deviations of up to $\pm 6.5\%$ (at 2σ) can be expected under clear sky conditions and up to $\pm 8.5\%$ (at 2σ) under cloudy conditions. This variability adds to the constant calibration error. The neglect of a possible temperature dependence of the NO_2 photolysis process has also been considered in Table 6.3.

For j -(NO₂), this is known to be small (DeMore *et al.* [1997], [2000], Harder *et al.* [1997]) and for the temperature range encountered over the course of the IPMMI experiment was assumed <3%.

Table 6.3: Estimated Errors in j -(NO₂) Filter Radiometer Measurements at IPMMI

Error Type	Magnitude (%)
Calibration	± 7 (1σ)
Temperature effect	± 3 (1σ)
Imperfect spectral response	± 5 (1σ)
Imperfect angular response	± 3 (1σ)

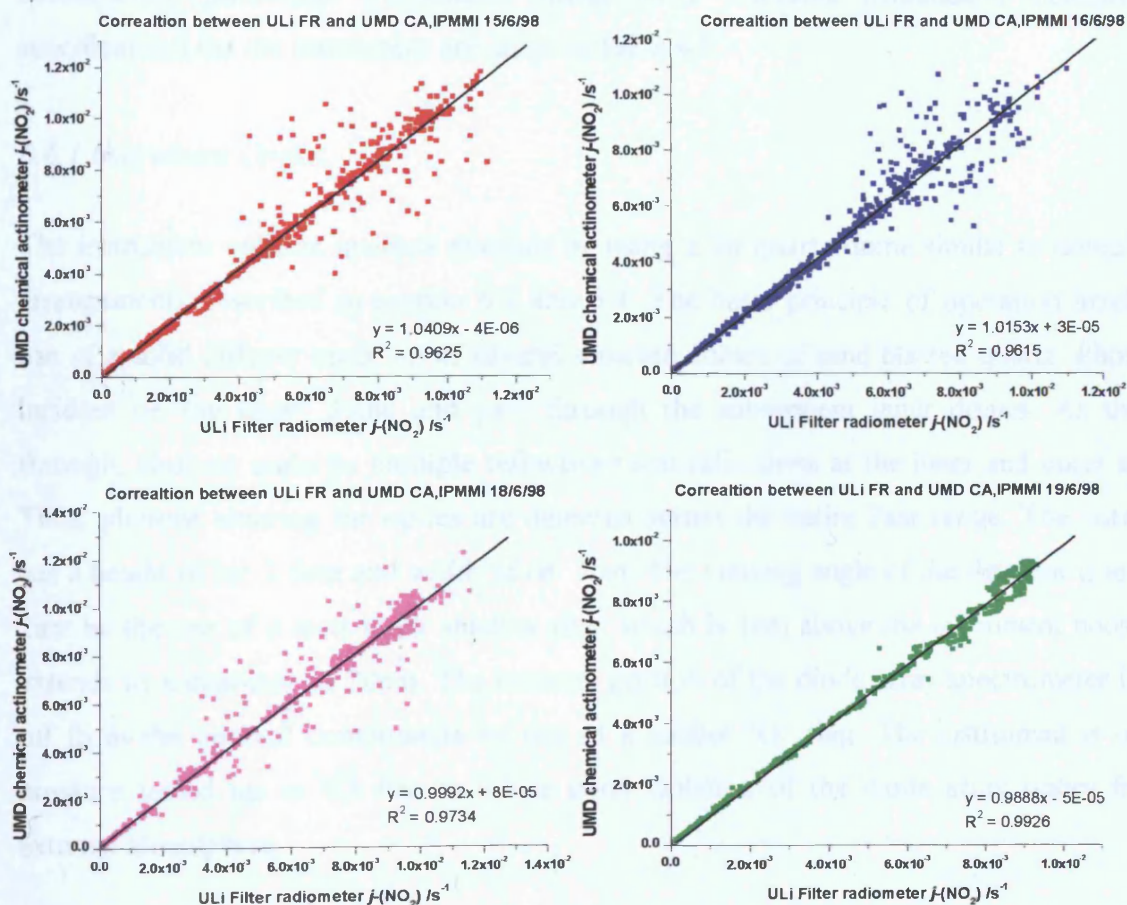
Table 6.4: Correlation of ULi Filter Radiometer j -(NO₂) Data to Other Instruments at IPMMI on 19/6/98 for 1 minute averaged data.

Instrument	Cross-Section Recommendation (where relevant)	Correlation Coefficient
IFU FR	-	0.996
FZ Jülich FR	-	0.996
FZ Jülich SR	DeMore <i>et al.</i> (1997)	0.997
FZ Jülich SR	Harder (1997)	0.997
NCAR SR	DeMore <i>et al.</i> (1997)	0.994
NCAR SR	Harder (1997)	0.994
UMD CA	-	0.993
ULi SR	DeMore <i>et al.</i> (1997)	0.992
ULi SR	Harder (1997)	0.992

6.5: Performance of ULi j -(NO₂) Filter Radiometer at IPMMI

Six instruments measured the photolysis frequency j -(NO₂) at IPMMI. The data taken from the ULi j -(NO₂) filter radiometer were compared to these other instruments by the IPMMI referee in a similar way to the measurements of j -(O¹D). The referee reported a high degree of correlation between University of Leicester j -(NO₂) measurements and other filter radiometers, spectroradiometers and chemical actinometer data. Correlation coefficients for j -(NO₂) between the ULi filter radiometer and other groups for the IPMMI clear sky day (19/6/98) are shown in Table 6.4. Correlation of the data measured by the ULi filter radiometer and UMD chemical actinometer for each day of the IPMMI intensive is shown in Figure 6.5. From this figure, in all cases the correlation coefficients are *ca.* 0.9, suggesting that with respect to this photolysis frequency, the ULi instrument measured j -(NO₂) with accuracy within the stated uncertainty of this measurement technique (*ca.* 12%)

Figure 6.5: ULi Filter Radiometer j -(O¹D) with UMD Chemical Actinometer data



6.6: Diode Array Spectroradiometer

The diode array spectroradiometer deployed by the University of Leicester during IPMMI, is a commercially available instrument (*Meteorologie Consult*, Glashütten, Germany). In brief, the diode array spectrometer collects photons *via* a polished quartz dome/diffuser arrangement assumed to have an isotropic detection across a solid angle of 2π sr. Photons are passed through a round-to-slit converter ($70\mu\text{m} \times 2500\mu\text{m}$) giving a spectral bandpass of the order of *ca.* 2nm at FWHM. Photons entering the entrance slit are dispersed using a flat field diffraction grating ($248 \text{ lines mm}^{-1}$) and are detected using a 512-pixel diode array (*Carl Zeiss*). The manufacturer-quoted wavelength drift for this arrangement is $5 \times 10^{-4} \text{ nm K}^{-1}$. For experimental deployment, wavelengths were calibrated using a low-pressure mercury discharge lamp (*Oriel*) and a Na (D emission line) lamp. Spectra were collected over the wavelength region $\lambda=280\text{-}450\text{nm}$ at four integration times (0.5, 1, 3 and 5 s). Data is processed using an Interactive Data Language (IDL) program, written at the University of Leicester. The IDL program was used to convert the raw data into actinic flux and subsequently photolysis frequencies, using NIST traceable (irradiance) standards. The specifications for the instrument are given in Table 6.5.

6.6.1 Instrument Optics.

The instrument collects incident photons by using a 2π quartz dome similar to dome/diffuser arrangements described in section 6.2 and 6.4. The basic principle of operation involves the use of a solid diffuser made up of several separate domes of sand blasted quartz. Photons are incident on the outer dome and pass through the subsequent inner domes. As they pass through, photons undergo multiple refractions and reflections at the inner and outer surfaces. Thus, photons entering the optics are detected across the entire 2π sr range. The outer dome has a height of *ca.* 3.5cm and width of *ca.* 3cm. The viewing angle of the detector is limited to 2π sr by the use of a matt black shadow ring, which is 1cm above the instrument housing and extends to a diameter of 20cm. The external portion of the diode array spectrometer is sealed off from the internal components by use of a rubber "O" ring. The instrument is regularly pressure tested up to 0.5 bar to insure good isolation of the diode array optics from the external atmosphere.

Table 6.5: Characteristics of the Diode Array Spectroradiometer Used at IPMMI

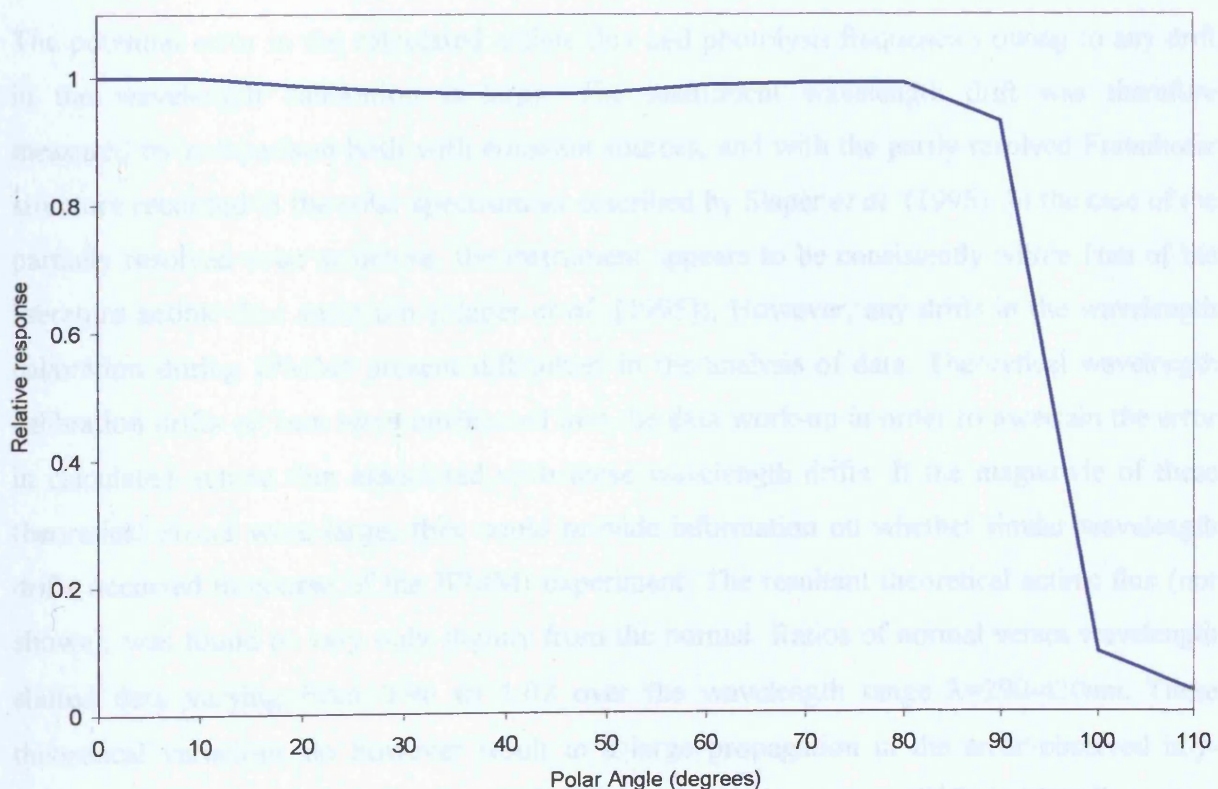
Entrance Optics	Quartz Actinic Diffuser
Quantity Measured	Actinic Flux
Entrance optics	Round-to-slit converter (70 μ m x 2500 μ m)
Grating Flat-field	248 lines mm ⁻¹ diffraction grating
Wavelength drift	5 x 10 ⁻⁴ nm K ⁻¹
Wavelength Range	285-450nm
Diode Wavelength Separation	0.83nm
Resolution	ca. 2nm at FWHM
Detector	512-pixel diode array (Carl Zeiss), pixel distance ca. 0.83 μ m.
Calibration	NIST traceable 1000 W Tungsten Halogen Lamp.
Minimal Detected Actinic Flux	ca. 1 x 10 ¹⁰ photons cm ⁻² nm ⁻¹ (\pm 5%)
Minimal Detected j -(O ¹ D)	ca. 3 x 10 ⁻⁷ s ⁻¹ (\pm 13%)
Estimated Signal:Noise Ratio	4:1
Scan Time	Variable, four integration times (0.5, 1, 3 and 5 s) over λ =280-450nm region during IPMMI.

As described in Chapter 5, for an instrument of ideal sensitivity, all photons that incident the $2\pi sr$ solid angle would have the same probability of detection by the diode array. In addition, the instrument would have a perfect rejection characteristics and detect no photons at polar angles $>90^\circ$. The dome used for the detection for photons by the instrument was optimised by the manufacturer to be as close to these ideal criteria as possible. However, perfect isotropic detection and perfect angular rejection are not achievable in a working instrument. Estimates of the potential anisotropy in the $2\pi sr$ optics, together with angular rejection the instrument were obtained. The spectroradiometer was mounted on a platform that was capable of rotation through 180° in one plane in a "light-box". This is a homemade aluminium construction consisting of a rectangular box of length 2m, width 1m and height 1m. The box is separated into two sections of equal size, separated from each other by a 2mm thick aluminium divider of equal height and width dimensions to the surrounding box. In one chamber sits a mounting point for the spectrometer. The second half of the tank contains a lamp mounting connected to a suitable power supply. NIST traceable tungsten halogen lamps (200 W and 1000W, *Oriel*) were used as the light source for this analysis. Light from these lamps was allowed to enter

the chamber containing the spectroradiometer through an iris that effectively limited the illumination of the diode array to the $2\pi sr$ dome only. Photon counts recorded in the usual way. (see Chapter 5). Light scattering from surfaces was minimised by painting all internal surfaces matt black. External light was also minimised by performing all experiments in a blacked-out laboratory.

Rotation of the quartz dome through 180° in a simple plane while monitoring the change in signal with the angle of incidence, gives a useful estimate of the angular response error. Plotting the relative response of the instrument against the angle of rotation showed a deviation in the angular response that was shown to be $\pm 2\%$ or less for angles $\leq 80^\circ$. Between 80° and 90° , the sensitivity of the instrument was observed to decrease by *ca.* 6%, before rapidly falling to zero at angles between 100° and 110° . The experiment was repeated for several wavelengths in the UV and visible and at several incident geometry's. All experiments showed a similar profile, indicating that there is negligible wavelength and geometric dependence in the angular response of the instrument. A typical plot of the incident angle vs. relative response is shown in Figure 6.6.

Figure 6.6: Averaged Angular Response for Diode Array $2\pi sr$ Optics



6.6.2: Spectroradiometer Wavelength Calibration Drift and Resolving Power

The entrance optics for the single monochromator is a 70 μm round-to-slit converter (70 μm x 2500 μm). Photons passing through the slit are dispersed by a 248 lines mm^{-1} flat field diffraction grating. The detection of the photons is *via* a 512-pixel diode array (*Carl Zeiss*), capable of detecting photons from $\lambda=285\text{-}710\text{nm}$. The output of both a sodium lamp and low-pressure Hg discharge lamp were measured using the spectroradiometer in order estimate wavelength calibration drift and resolving power of the instrument. The latter was determined to be *ca.* 2nm at full width, half maximum (FWHM). This is in agreement with the manufacturer quoted value of 2.1nm.

For the sodium lamp, the instrument measured the sodium "D" emission lines centred on $\lambda=589\text{nm}$ with no significant wavelength drift ($\ll 1\%$). The manufacturer originally checked the wavelength calibration before the IPMMI experiment with no significant drifts from the literature values were observed. Similar checks were made against the UV output of the Hg pen-ray lamp following the conclusion of IPMMI. Using the recommendations of Madronich and Weller (1990), it is possible to estimate the error in the actinic flux detection for a spectral resolution of this magnitude. For the spectroradiometer describe here, the resolving power of the spectroradiometer suggests an error in the actinic flux of $<5\%$.

The potential error in the calculated actinic flux and photolysis frequencies owing to any drift in the wavelength calibration is large. The instrument wavelength drift was therefore measured by comparison both with emission sources, and with the partly resolved Fraunhofer structure recorded in the solar spectrum as described by Slaper *et al.* (1995). In the case of the partially resolved solar structure, the instrument appears to be consistently within 1nm of the literature actinic flux spectrum (Slaper *et al.* [1995]). However, any drifts in the wavelength calibration during IPMMI present difficulties in the analysis of data. Theoretical wavelength calibration drifts of 1nm were introduced into the data work-up in order to ascertain the error in calculated actinic flux associated with these wavelength drifts. If the magnitude of these theoretical errors were large, they could provide information on whether similar wavelength drifts occurred in course of the IPMMI experiment. The resultant theoretical actinic flux (not shown), was found to vary only slightly from the normal. Ratios of normal verses wavelength shifted data varying from 0.96 to 1.02 over the wavelength range $\lambda=290\text{-}420\text{nm}$. These theoretical variations do however result in a large propagation in the error observed in $j\text{-(O}^1\text{D)}$. For a wavelength calibration drift of 1nm, the total error in $j\text{-(O}^1\text{D)}$ is 15%. For a 2nm theoretical wavelength calibration drift, the error in $j\text{-(O}^1\text{D)}$ is 40%. Since the photolysis

frequencies calculated by the spectroradiometer show agreement within these errors, it was concluded that the wavelength calibration for the instrument made by the manufacture was accurate during the course of IPMMI and any possible drifts in wavelength calibration were considerably less than 1nm.

6.6.3: Instrument Calibration

Raw data recorded by the spectroradiometer were in a series of data counts proportional to the number of incident photons upon the diode array, with the raw counts converted to actinic flux by absolute calibration against NIST traceable irradiance standards. Two separate calibrations of the diode array have been performed over the course of this work. The first was performed at the National Center for Atmospheric Research, (NCAR, *Table Mesa Drive, Boulder, CO, USA.*) using their custom made "light-box". The instrument was placed at a fixed distance of 50cm from a 1000W NIST calibrated quartz tungsten-halogen lamp (*Oriel*). For these standards, an inverse square law relationship exists between the intensity of emission and distance from the source. Using the inverse square approximation, spectra of these lamps were recorded as a function of the lamp output, (in raw diode array counts) and converted into photon flux ($\text{photons cm}^{-2} \text{ nm}^{-1} \text{ s}^{-1}$). The instrument was also re-calibrated in the "light-box" at the University of Leicester against a second tungsten halogen lamp (200 W, NIST traceable lamp, *Oriel Ltd.*) following the conclusion of the IPMMI experiment.

In this form of calibration, the precision can be equated to the variation in the detected counts between each individual spectrum. This "shot-to-shot" standard deviation is combined with the errors associated with the inverse square-law approximation. The lamp itself was assumed to be unchanging in brightness, since power was supplied by an ultra-low voltage ripple power supply (model 68831, *Oriel Ltd*). The "shot-to-shot" variation for the diode array has a standard deviation of *ca.* 13 counts in 500 (2.6% at 2σ) over the signal. Using an uncertainty estimate for calibration precision of *ca.* 2.5% in actinic flux data work-up gives a total error in the overall actinic flux determination of *ca.* 2.8%. This was propagated through to the determination of photolysis frequencies, resulting in an error of 4% in $j(\text{O}^1\text{D})$, while for $j(\text{NO}_2)$, the error was 2.5%.

These uncertainties are coupled with other possible sources of error in the determination of photon flux, the magnitudes of which are shown in Table 6.6. These include errors arising from the inverse square approximation that was used in the calibration procedure (*ca.* 1%), and the so-called "equivalence plane receiver" or EPR error. The EPR error arises owing to

the assumption that the diode array optics behaves as a plane receiver that is irradiated at normal incidence. The consequences of this assumption are described in detail by Hofzumahaus *et al.* (1999). Using the assumptions described by Hofzumahaus and co-workers, error propagation owing to the equivalence plane receiver assumption is *ca* 1% for this spectroradiometer.

Table 6.6: Estimated Errors in Diode Array Spectroradiometer Measurements at IPMMI

Source of Error	Uncertainty in Actinic Flux data
Shot to shot lamp variation	<i>ca.</i> 2.5 % over 290-450nm range
Inverse square law approximation	1%
EPR assumptions	1% (from Hofzumahaus <i>et al.</i> 1999)
Accuracy of lamp calibration factors	1-3% (from lamp manufacturer)
Stability of instrument (dark current)	3% for times < 6am, 1% all other times
Angular response error	2%
Stray light	Variable for $\lambda < 325$ (see text), negligible for $\lambda=325-450$
Slit function	< 5% (Madronich and Weller, 1990)

6.6.4 Effect of Uncertainties in Molecular Parameters

Errors in the published molecular data are a major source of error in a spectroradiometer derived photolysis frequencies (Hofzumahaus *et al.* [1999]). The effect of these errors with respect to IPMMI has recently been considered by Hofzumahaus *et al.* (2000). The error in the calculated ozone absorption cross-section is usually quoted as 3% (Molina and Molina, [1986]), while errors in the quantum yield can be up to 10% (Shetter *et al.* [1996], Hofzumahaus *et al.* [1999]). Using an maximum assumed error of 10% in the work-up of JPL quantum yield data (DeMore *et al.* [1997]), together with a 3% error in the absorption cross-section data, the root mean square error propagated in j -(O¹D) is found to be 10%. For j -(NO₂), the assumed molecular parameter errors were 4% for absorption cross-section and 10% for quantum yield. Using this data, the root mean square error in photolysis for j -(NO₂) is 11%.

6.6.5 Absolute Sensitivity

The absolute sensitivity of the single monochromator diode was investigated as part of the instrument characterisation. The absolute sensitivity of the instrument is defined as the minimum measurable photon flux per count. Using the calibration against lamp standards and assuming a signal to noise ratio of 1:1, the raw data showed that the sensitivity of the diode array in the 290-300nm region was of the order of 1×10^{10} photons $\text{cm}^{-2} \text{nm}^{-1} \text{s}^{-1}$ as shown in Table 6.7. Data taken in the field showed that the signal-to-noise ratio is closer to 4:1 for 10 minute averaged actinic flux spectra. The net result is that the diode array has a sensitivity that is considerably lower than the equivalent double monochromator spectroradiometers. Therefore, the instrument suffers from a relatively poor sensitivity even when the diode array signal-to-noise ratio is maximised at 1:1. These results suggest that even with perfect stray light rejection, close to the atmospheric cut-off (*ca.* 290nm) a single monochromator diode array spectroradiometer of this type overestimates the actinic flux, when compared to an equivalent double monochromator spectroradiometer.

Table 6.7: Relative Sensitivity of Single Monochromator Diode Array Spectroradiometer

Wavelength(nm)	Standard Lamp Output (photons $\text{cm}^2 \text{nm}^{-1} \text{s}^{-1}$)	Raw diode array counts	Absolute Sensitivity (1:1 S/N ratio)
290	9.41×10^{12}	825	1.14×10^{10}
291	9.44×10^{12}	835	1.13×10^{10}
292	9.45×10^{12}	843	1.12×10^{10}
293	9.48×10^{12}	846	1.12×10^{10}
294	9.49×10^{12}	854	1.11×10^{10}
295	9.51×10^{12}	856	1.11×10^{10}
296	9.53×10^{12}	858	1.11×10^{10}
297	9.54×10^{12}	859	1.11×10^{10}
298	9.56×10^{12}	863	1.11×10^{10}
299	9.58×10^{12}	865	1.12×10^{10}
300	9.60×10^{12}	866	1.11×10^{10}

6.7 Importance of Stray Light and Dark current

As with most photoelectric devices, there is a systematic "dark current" offset in the diode array spectroradiometer. Using data collected overnight when there are no atmospheric light sources, levels are generally around 200 ($\pm 2\%$ at 1σ) diode counts. This dark current precision is significantly smaller than the error owing to stray light and therefore it might be assumed that dark current is not as significant a factor in the error propagation as stray light. This hypothesis was tested by constantly subtracting a spectrally white 200 count dark current offset from each spectrum without any stray light corrections. A dark current uncertainty of 2% was found to produce a maximum error in actinic flux of 3% up to 6am. This was the only time of data where the error is significant owing to the intrinsically low light levels, such that any variation in dark current has a relatively large effect. In comparison, at 7am, the dark current precision error dropped to $<1\%$. Working this uncertainty through to photolysis frequencies, the net $j\text{-(NO}_2\text{)}$ is essentially unaffected by dark current uncertainties, while $j\text{-(O}^1\text{D)}$ shows an influence owing to dark current uncertainty only for times that are before 6am or after 8pm. At these times, the uncertainty propagation is 5% at 1σ .

6.7.1: Stray Light Rejection Estimation and Incorporation

The importance of stray light (SL) rejection in monochromator systems and therefore photolysis coefficients, has been described by several authors (*e.g.* Hofzumahaus *et al.* [1999]). The spectroradiometer used in this work has photodiodes sensitive to radiation with wavelength less than the atmospheric cut-off (*ca.* $\lambda=290\text{nm}$). During a typical experiment, wavelength range between $\lambda = 285$ and 450nm were scanned. In order to make the necessary corrections, the assumption that counts between 285 and 290nm were entirely due to stray light and dark current was applied, with the spectral variation of SL across the whole spectrum assumed to be minimal.

From application of this *in-situ* measurement of stray light, it is possible to correct each spectrum by subtraction of the average counts at 285-290nm. The need for a method of accurate SL subtraction is highlighted upon examination of Figure 6.7. Here, actinic fluxes measured by the diode array spectroradiometer are compared to flux measurements made from a double monochromator spectroradiometer from FZ Jülich on 19/8/98. The flux comparison shows that the actinic flux data measured by the single monochromator are significantly greater than data measured by the double monochromator system in the region less than *ca.* 330nm. From comparison of measured fluxes and the ratio of one instrument to

another it is clear that the ULi diode array data shows the most significant deviation from the data of other instruments at times that are very early in the morning and/or near the atmospheric cut-off between $\lambda=290-310\text{nm}$. The calculated flux data was rechecked to evaluate the effect of this stray light correction when employed during data work up. Figure 6.8 shows a comparison of the percentage contribution of stray light to the detected diode array counts at 7am and 12 noon for diode array data taken on 16/6/98. It is clear that although the detected counts at 7am are much smaller than those at 12pm, the percentage of these counts that may be attributed to stray light is considerably greater than at noon. This analysis confirms the importance of a full and accurate correction for SL when dealing with actinic flux data collected by single monochromator diode arrays.

Figure 6.7: Flux Ratios for FZJ/ULi with no Stray Light Correction

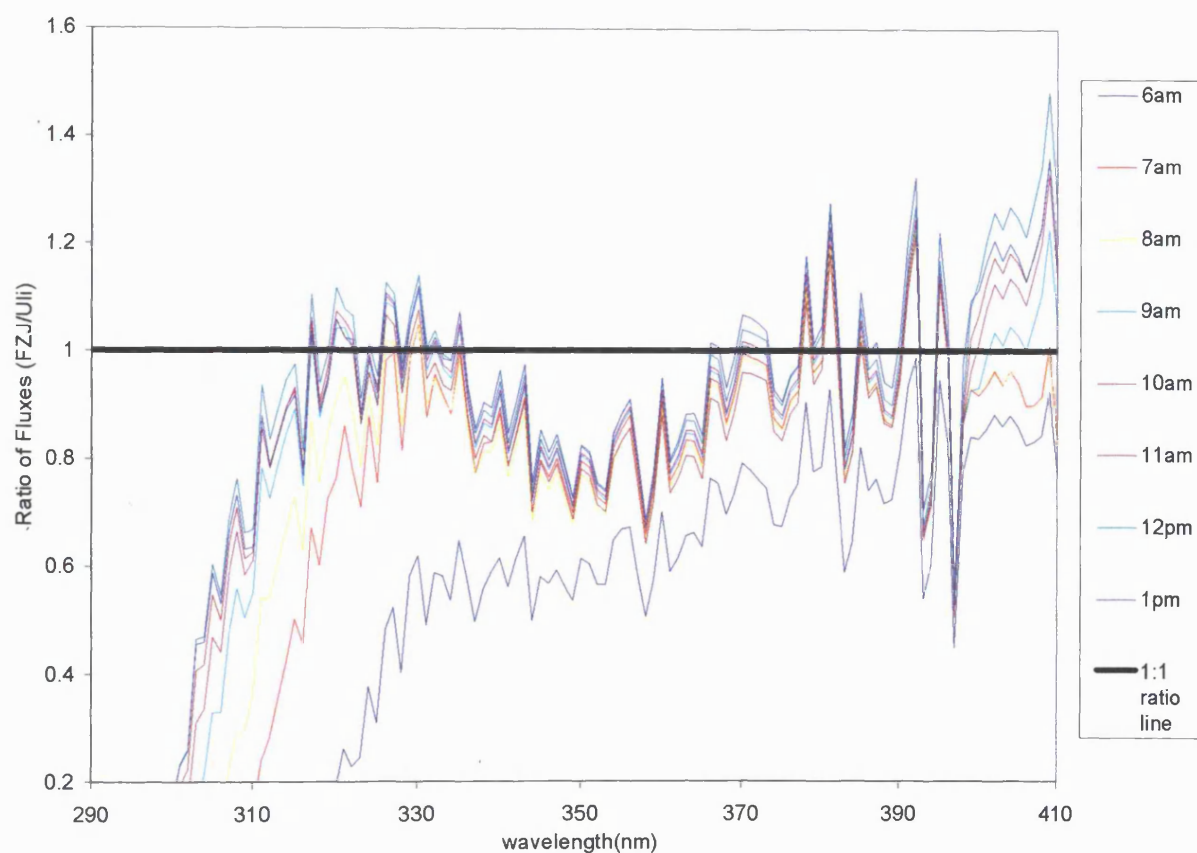


Figure 6.8: Percentage contribution of Stray Light in Diode Array Data

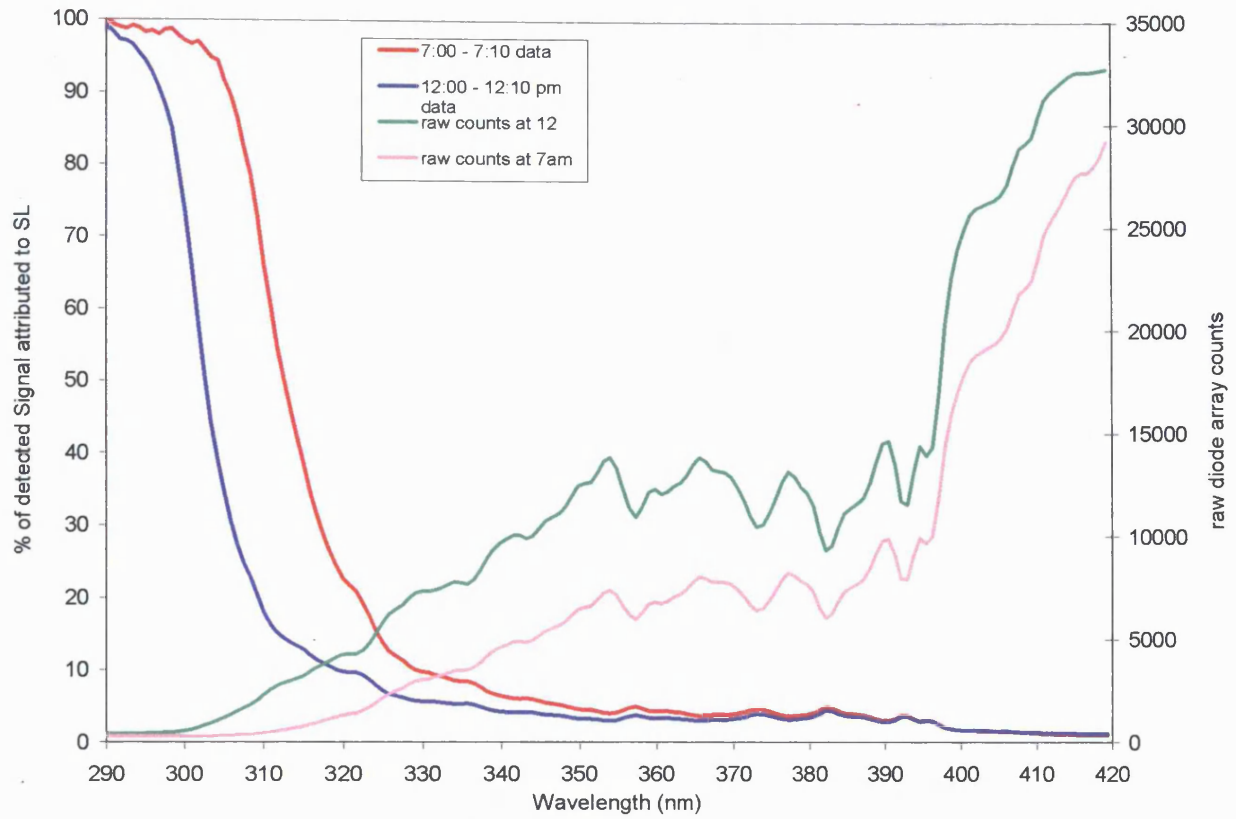
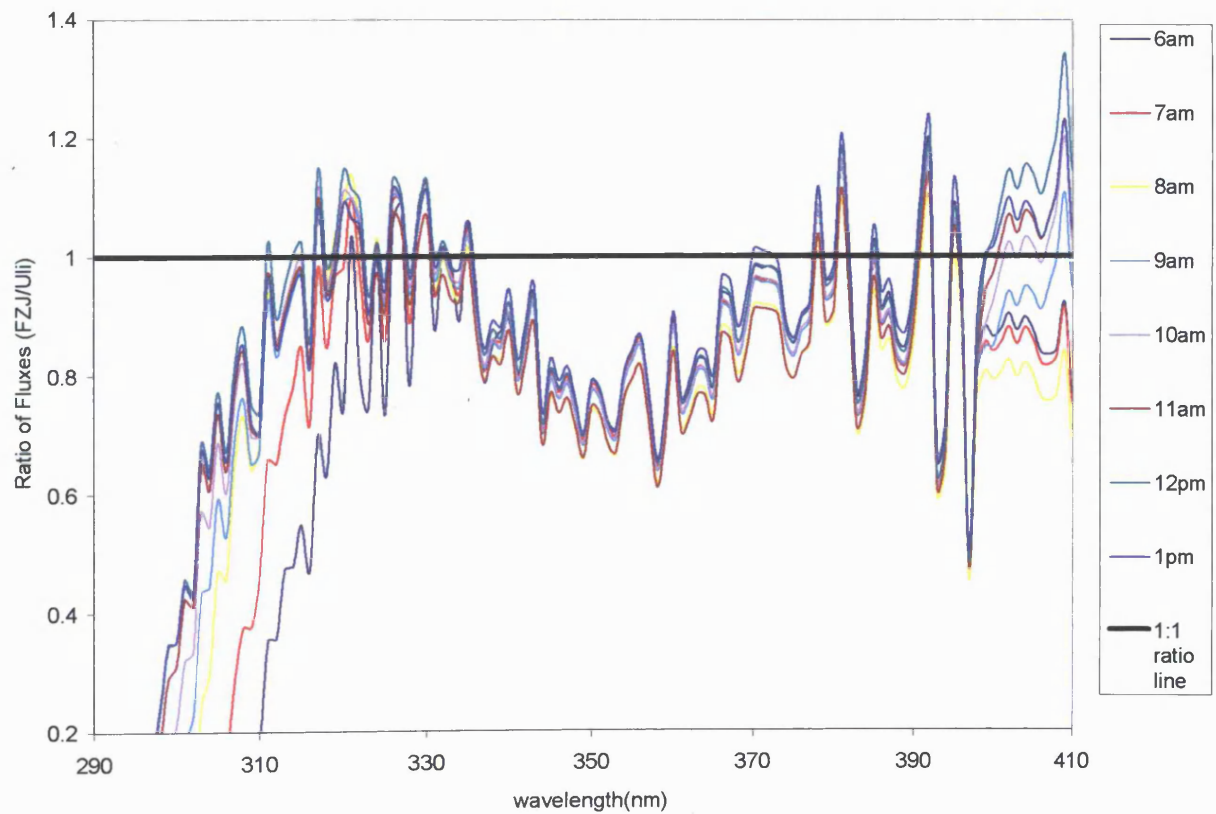


Figure 6.9: Flux Ratios for FZJ/ULi with Stray Light Correction



Actinic flux data worked up from the raw counts with the *in-situ* corrections described above were compared to both the data obtained from the FZ-Jülich double monochromator spectroradiometer. Figure 6.9 shows the effect of applying the *in-situ* SL correction. It is clear from Figure 6.9 that the stray light corrected data show improvement in this stray light affected region (<300nm), but there are still considerable differences between these corrected fluxes and the data from the FZ-Jülich spectroradiometer.

6.7.2: Comparisons to Model Data

The IPMMI experiment was an international comparison of both measured and modelled photolysis frequencies. Data obtained by these models was similarly compared to the diode array spectroradiometer data to further quantify SL errors associated with this instrument. Around 20 groups participate in the modelling phase of the IPMMI experiment. Essentially, the model groups were asked to provide data on actinic flux at solar noon in addition to photolysis frequency $j(\text{NO}_2)$ and $j(\text{O}^1\text{D})$ via individual radiative transfer codes. Full details of the modelling part of the intercomparison may be found elsewhere (e.g. Bais *et al.* [2000], Cantrell *et al.* [2000]).

Three models were used for the initial comparison, ACD, BAS and KNM. The Atmospheric Chemistry Division at NCAR submitted the ACD data. The model used by this group was the pseudo-spherical eight-stream discrete ordinate TUV model described by Madronich *et al.* (1998). The British Antarctic Survey submitted the BAS model data to IPMMI. The model used is an in-house model developed by BAS and based on the DISTORT code of Stamnes *et al.* (1988), and the pseudo-spherical adaptations of Dahlback and Stamnes (1991). The KNM model was a radiative transfer model developed by Van de Hulst, (1980). The current version used as part of the IPMMI experiment is described by De Haan *et al.* (1987). All of the above models show similar trends when compared to the diode array data as was found in data comparisons with FZ-Jülich and NCAR (see Figure 6.9). Specifically, a large overestimation of the actinic flux in the 290-310nm waveband is observed with much better agreement in the >310-420nm region. Plots of the ratios of the modelled and measured fluxes are shown in Figure 6.10-6.12.

Figure 6.10: Flux Ratios for ACD/ULi with Stray Light Correction

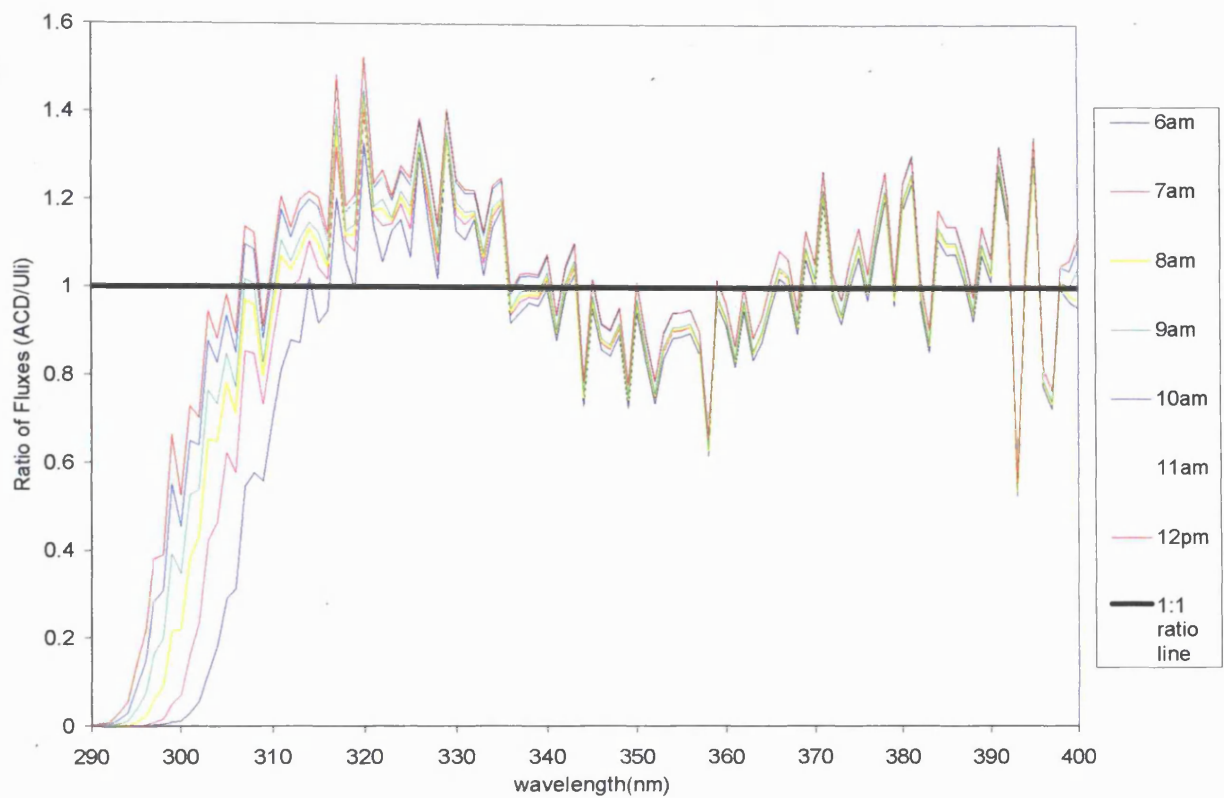


Figure 6.11: Flux Ratios for BAS/ULi with Stray Light Correction

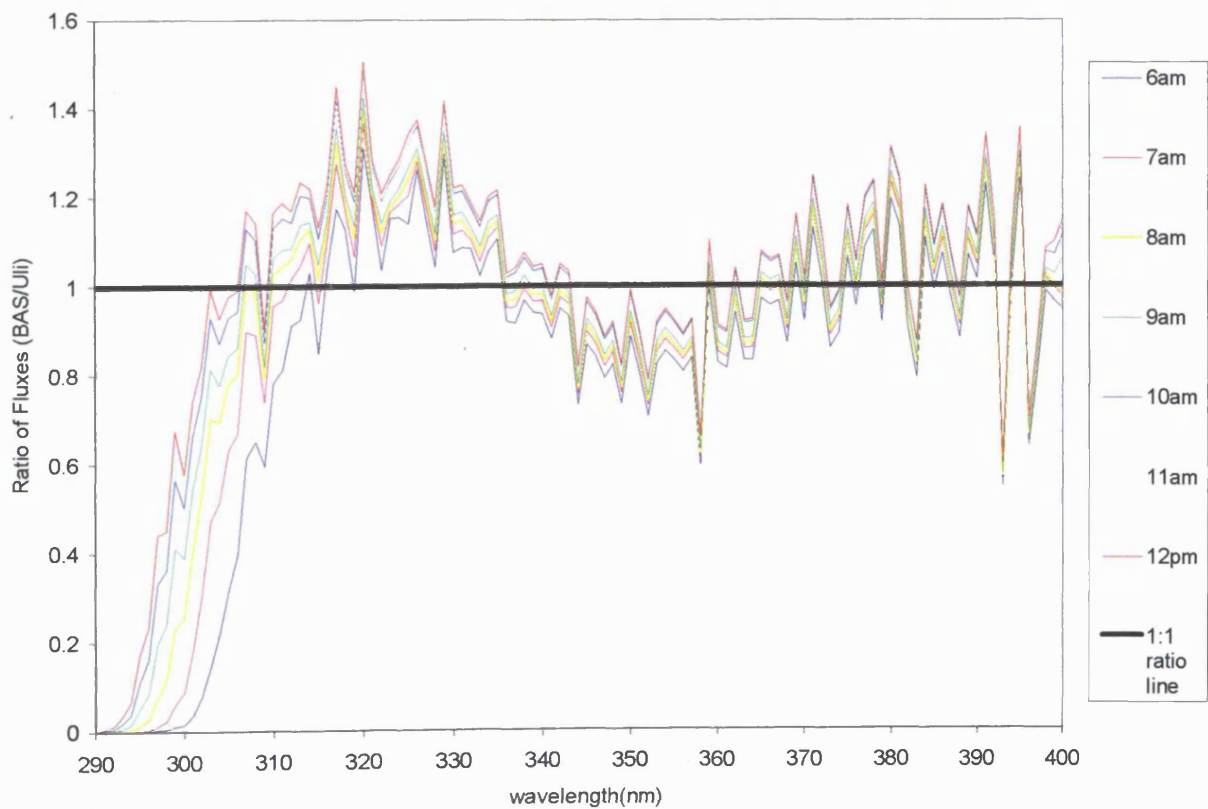
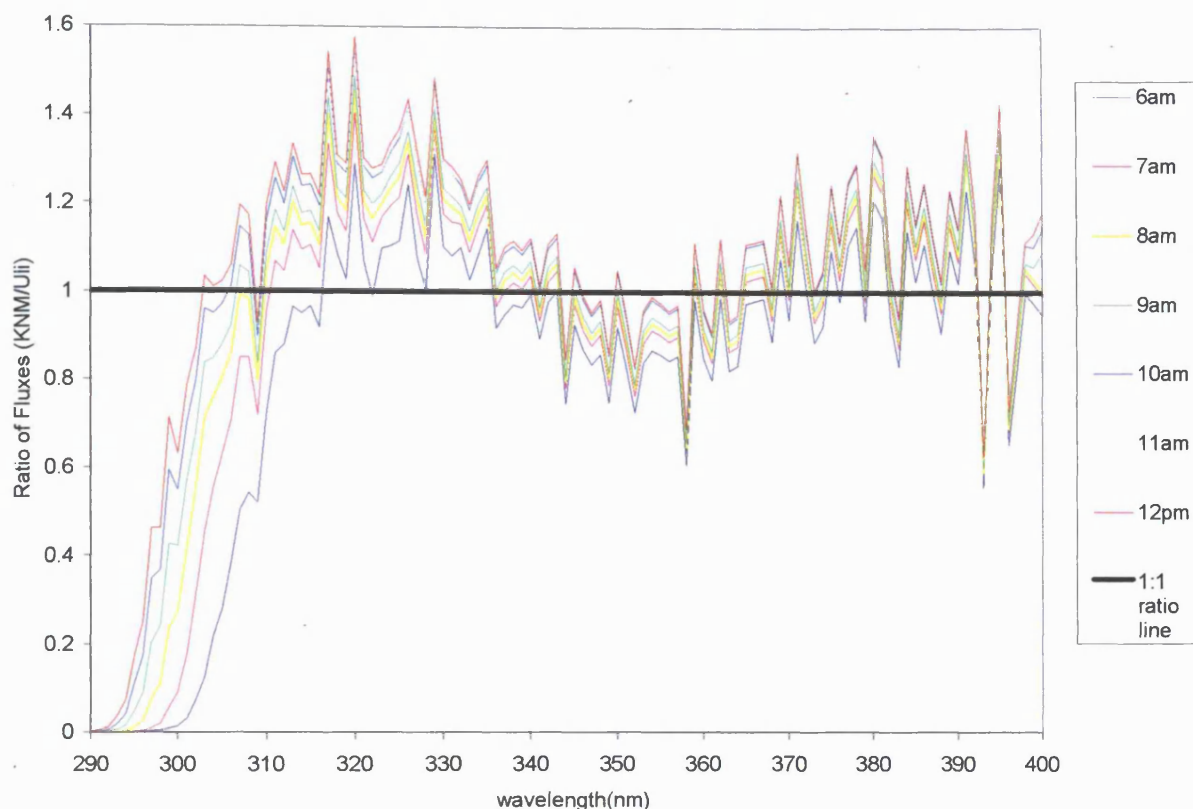


Figure 6.12: Flux Ratios for KNM/ULi with Stray Light Correction



The problems identified in both the model and measured comparison of spectra is an area of potential concern as these fluxes were used to calculate the photolysis frequencies $j\text{-(NO}_2\text{)}$ and $j\text{-(O}^1\text{D)}$ from the spectroradiometer. The standard deviation in SL from one spectrum to another has also been estimated. Using the spectral region $\lambda=285\text{-}290$ data as a measure of SL, additive with a dark current, at solar noon. The noon data were used, as it was assumed there should be minimal changes in absolute light intensity at this time and hence, one additional variable of a rapidly changing incident flux could be removed. Using this assumption, the SL standard deviation at 1σ was of the order of 1-1.5%. This held true for several different days and overhead cloud conditions during IPMMI.

6.7.3: Implications of Stray Light Rejection for Measured Photolysis Frequencies

Considering the effect on $j\text{-(NO}_2\text{)}$, it might be assumed that the influence of stray light and subsequent overestimation of actinic flux in the 290-310nm region would be relatively small owing to the $j\text{-(NO}_2\text{)}$ spectral "window", *i.e.* $\lambda=290\text{-}420\text{nm}$. Overestimation of flux in the 290-310nm portion of the "window", owing to poor stray light correction, should be a small error when compared to the overall actinic flux in the NO_2 photolysis range. This assumption was

Figure 6.13: Comparison of ULi Filter Radiometer and Diode Array Spectroradiometer $j(\text{NO}_2)$ During IPMMI, 18/6/98.

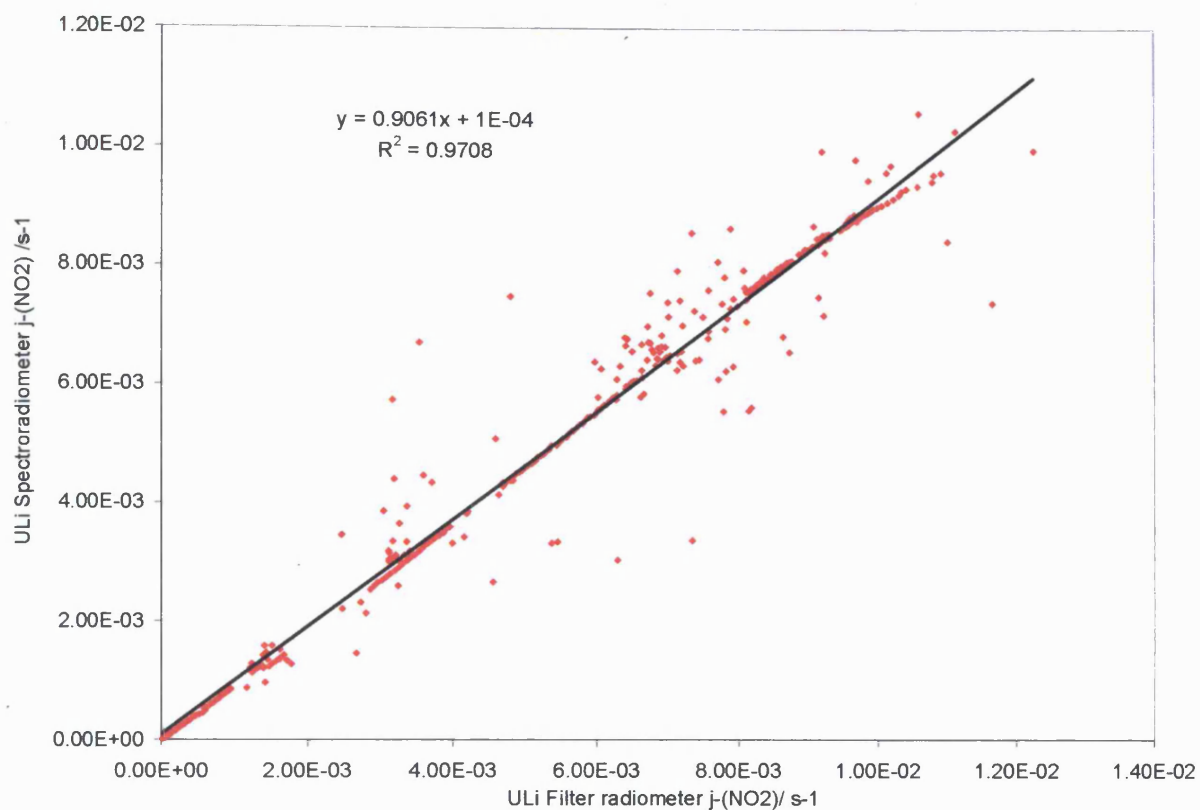
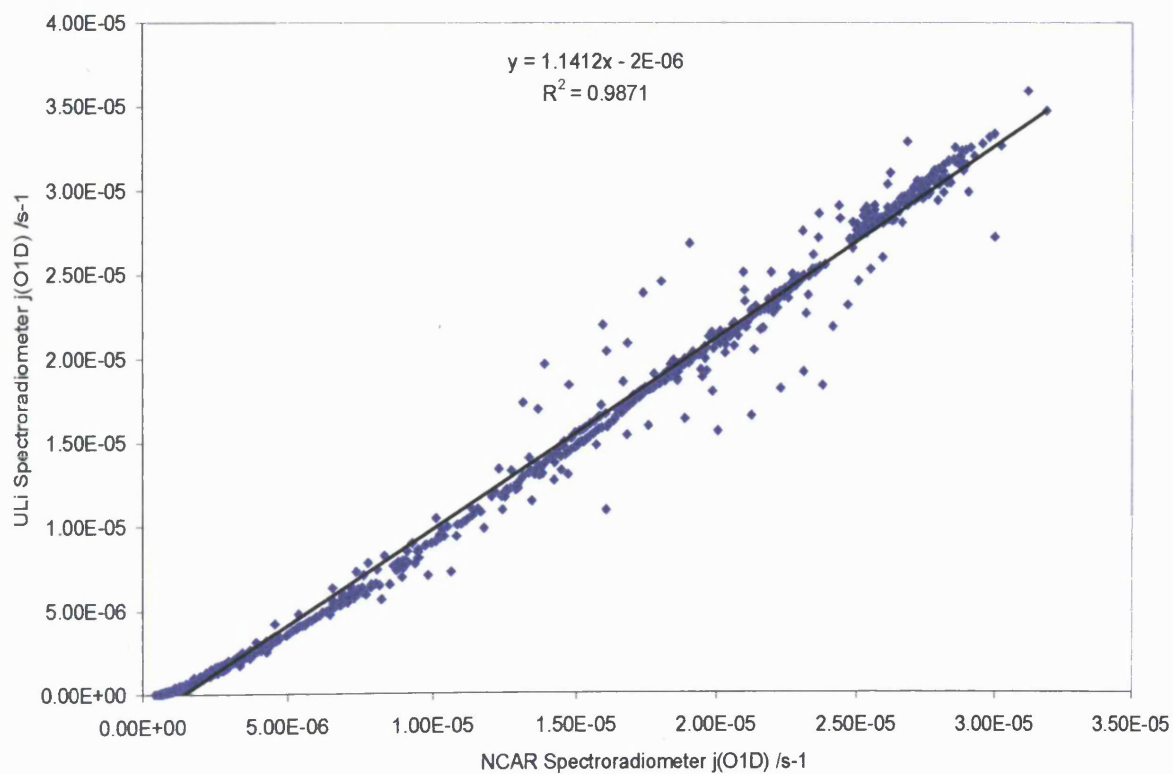


Figure 6.14: Comparison of NCAR Spectroradiometer and ULi Spectroradiometer $j(\text{O}^1\text{D})$ Data During IPMMI, 18/6/98.



checked by comparison of the $j\text{-(NO}_2\text{)}$ data obtained by the single monochromator diode array with the photolysis frequencies obtained from the ULi filter radiometer, as well as those values reported by other IPMMI participants. Comparing data from filter radiometer measurements to the diode array $j\text{-(NO}_2\text{)}$, correlation coefficients ranging from 0.985 at best to 0.940 at worst were observed over the four intensive days at IPMMI. The correlation plot of data for 18/6/98 is shown in Figure 6.13.

Similarly, the comparisons between diode array data and the UMD chemical actinometer made by the referee also indicated good agreement with correlation coefficients ranging from 0.996 at best to 0.939 at worst. From these results, it would seem that the influence of stray light on $j\text{-(NO}_2\text{)}$ data is negligible.

It would be expected that the calculation of $j\text{-(O}^1\text{D)}$ would be most sensitive to the levels of stray light. Since $j\text{-(O}^1\text{D)}$ is evaluated across such a narrow wavelength range, $\lambda = 290\text{-}325\text{nm}$, any overestimation of the actinic flux in the 290-310nm window is likely to have a major effect on the overall $j\text{-(O}^1\text{D)}$ data obtained from the integral of these fluxes with respect to wavelength. Figure 6.14 shows the correlation between diode array $j\text{-(O}^1\text{D)}$ data and photolysis frequencies from the NCAR double monochromator spectroradiometer on 18/6/98. The IPMMI referees reported this high degree of correlation was repeated for all days of the intensive, with correlation coefficients range from 0.961 to 0.993 over the course of the campaign. (J. Calvert, *private communication*) Similarly, the referees showed an average correlation coefficient of 0.992 between the ULi spectroradiometer and NCAR chemical actinometer when averaged over the whole campaign. By plotting the diurnal cycles, residual deviations between the diode array spectroradiometer and other instruments may be observed. Figure 6.15 shows good agreement between the instruments overall, especially at solar noon. However, there were deviations between the instruments, most clearly observed at times in where the intensity of light was low, *i.e.* early morning and late afternoon. Since, from Figure 6.7, stray light influence is largest at such times, it follows that the overestimation of $j\text{-(O}^1\text{D)}$ at these times is a direct result of the influence of poor stray light rejection in the single monochromator diode array.

The next step of the analysis was to consider the contribution to overall photolysis frequency by wavelength. Photon flux was therefore separated into several wavelength bands in order to identify the most significant parts of the spectrum. There may be the potential for the overestimation of flux at the lower end of the photolysis waveband for $j\text{-(O}^1\text{D)}$ to be counterbalanced with an underestimation of the flux at longer wavelengths.

Figure 6.15: Comparison of NCAR Actinometer and ULi Diode Array $j-(O^1D)$ Data During IPMMI, 15/6/98.

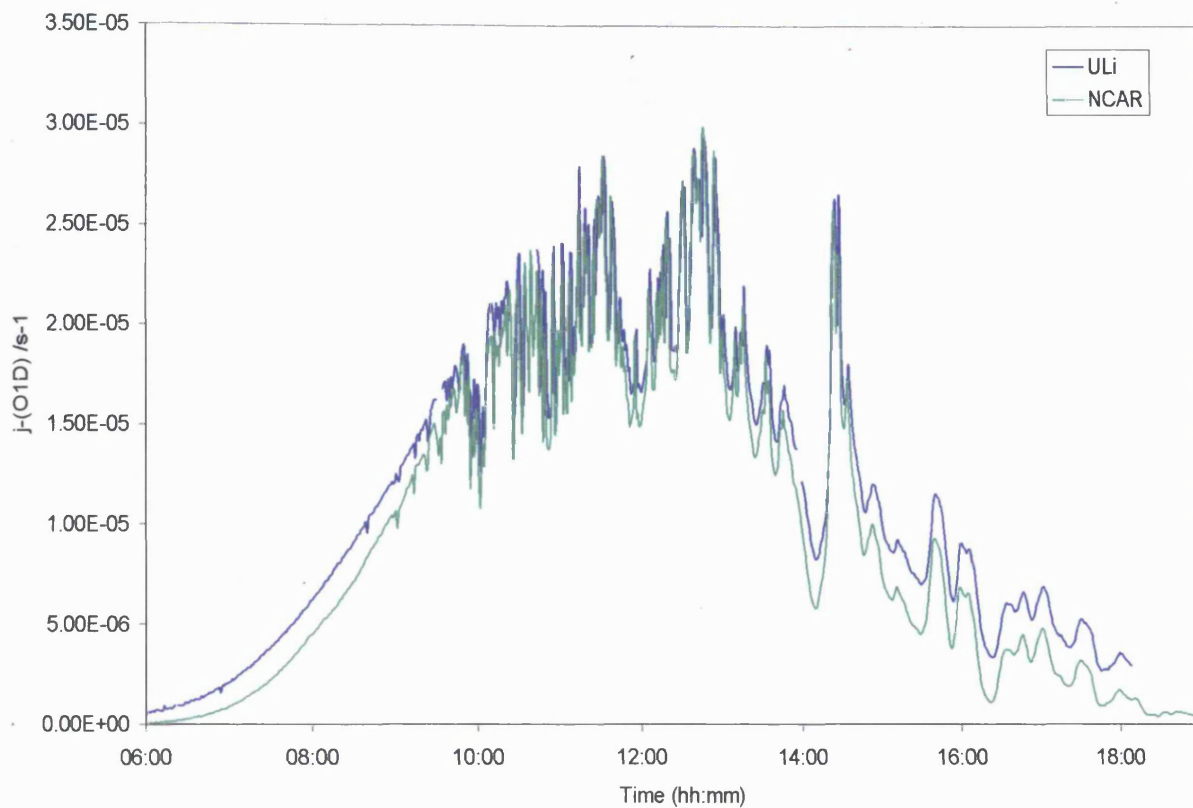


Figure 6.16: Percentage Contribution to $j-(O^1D)$ for Four Wavelength Bands

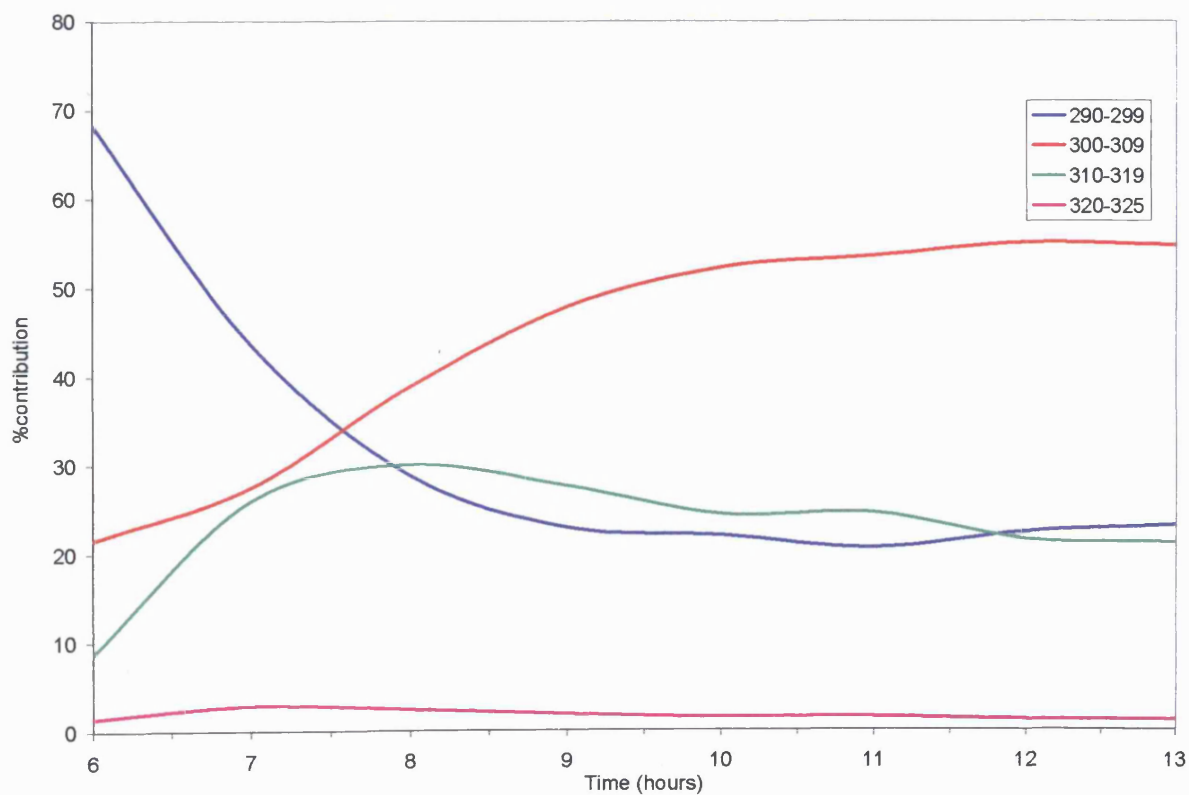


Figure 6.17: Contribution to $j-(O^1D)$ with Wavelength for ULi Data During IPMMI, 16/6/98

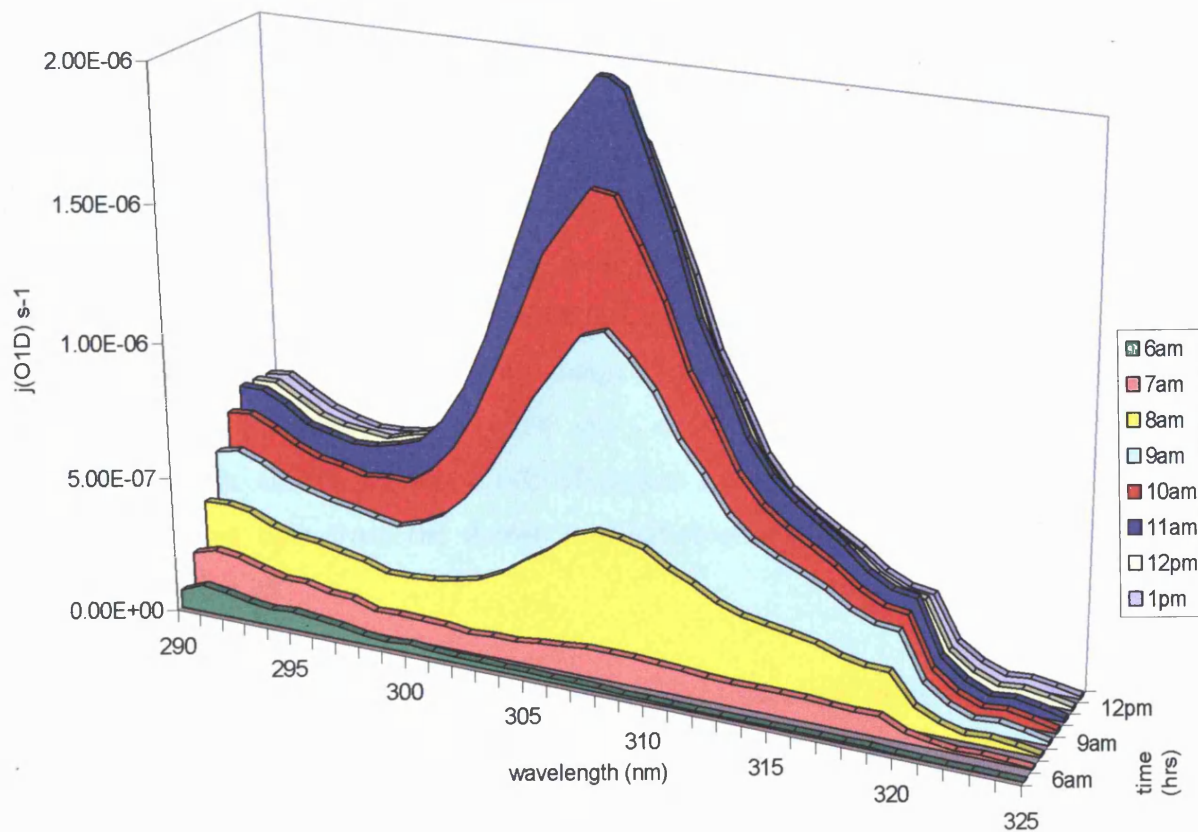
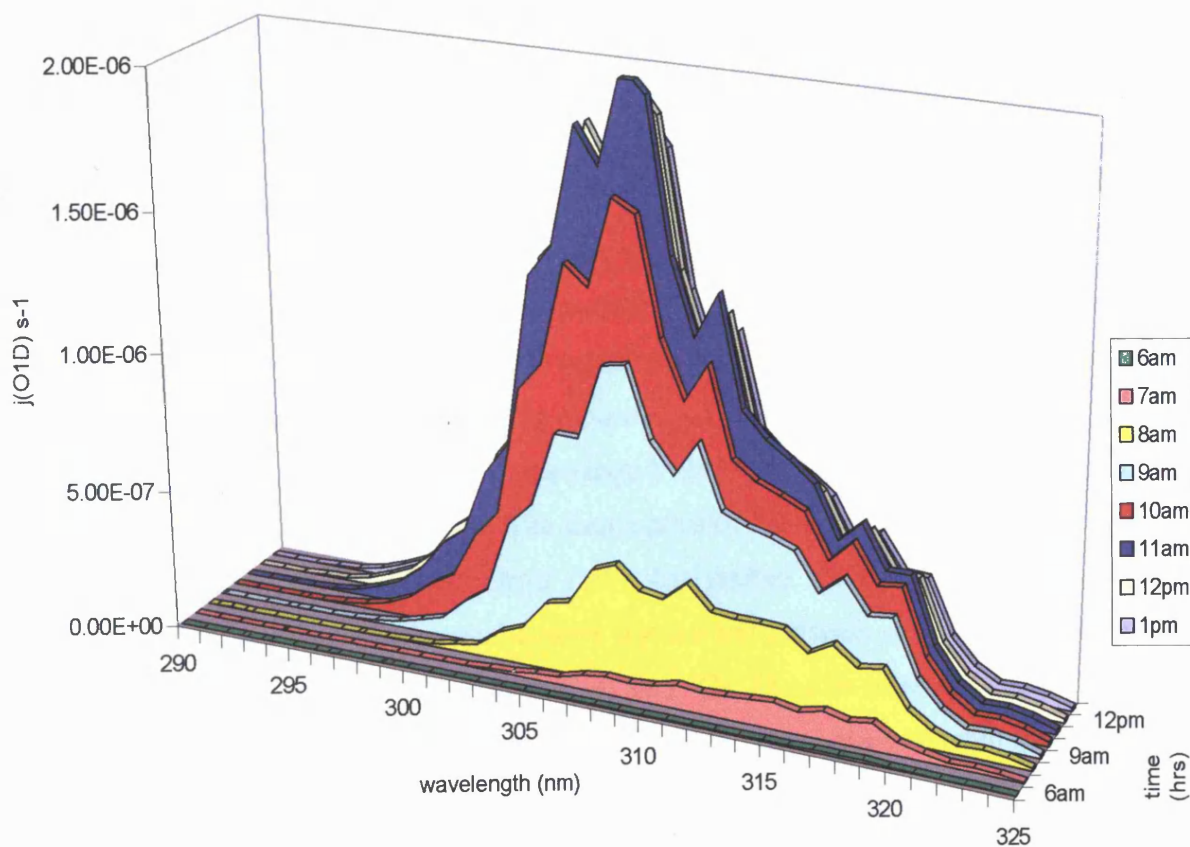


Figure 6.18: Contribution to $j-(O^1D)$ with Wavelength for FZJ Data During IPMMI, 16/6/98



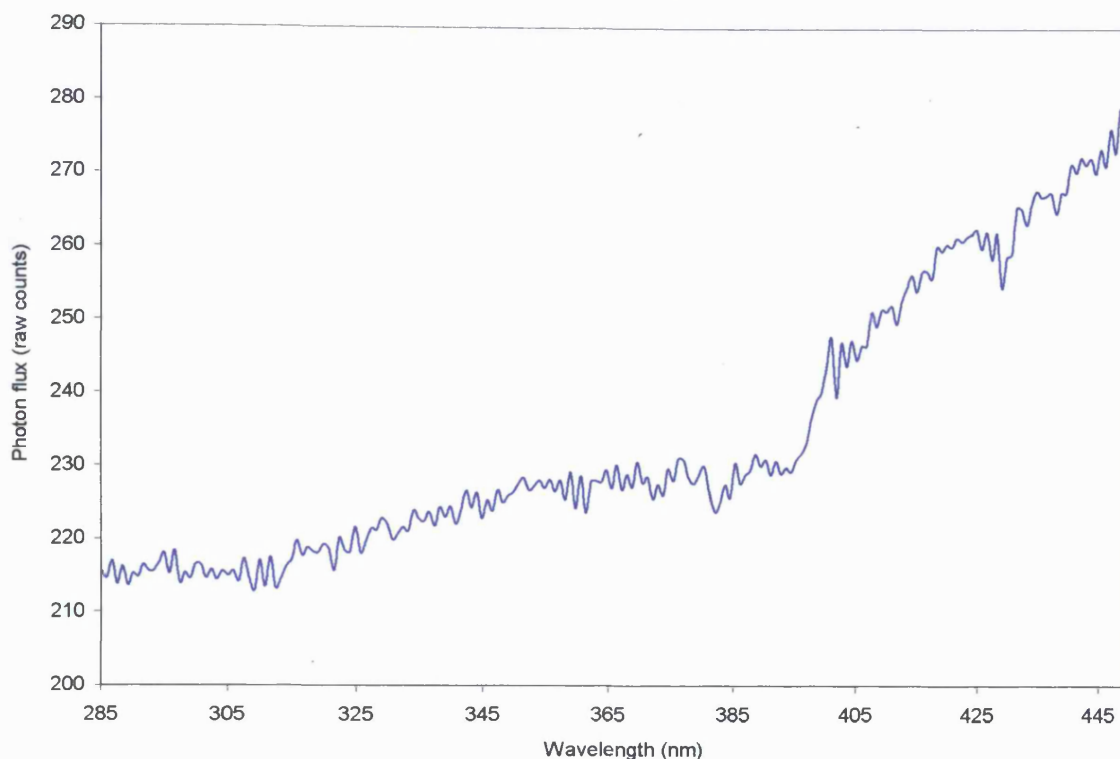
From a breakdown of the individual contributions to $j\text{-(O}^1\text{D)}$, it was found that wavelength regions not affected by stray light or sensitivity problems had good agreement to the data for other instruments. Figure 6.16 shows the waveband contribution to $j\text{-(O}^1\text{D)}$ for the diode array spectroradiometer. The strongest influence in $j\text{-(O}^1\text{D)}$ shifts between 290-299nm at times early in the day, to between 300 and 309nm at time around solar noon. The detection limit for $j\text{-(O}^1\text{D)}$ for the diode array was *ca.* $1.18 \times 10^{-7} \text{ s}^{-1}$, assuming a signal-to-noise ratio of 1:1. This sensitivity increases to $3.26 \times 10^{-7} \text{ s}^{-1}$ if a more realistic signal-to-noise ratio of 4:1 was used. These results contrast the FZ Jülich and NCAR data sets where the 300-309nm dominated at all times of the day, with the 290-299nm range contributing little, even in early morning. The uncorrected contributions to $j\text{-(O}^1\text{D)}$ for each wavelength for the diode array spectroradiometer across the entire $j\text{-(O}^1\text{D)}$ action spectrum is shown Figure 6.17, while a similar plot using data from the double monochromator spectroradiometer of FZ-Jülich is shown in Figure 6.18.

The problem of poor instrument stray light rejection in the single monochromator diode array spectroradiometer deployed by the University of Leicester at IPMMI has implications for the accuracy of the derived photolysis frequencies. The *in-situ* stray light correction procedures when applied to the data produced actinic fluxes and photolysis frequencies in better agreement with those from the double monochromator based instruments. From the above discussion, it is also evident that there are still further correction procedures required before the stray light errors are fully accounted for.

6.8: Improved Stray Light Corrections

In order to characterise the instrument further, an *in-situ* stray light spectrum with respect to wavelength was measured following the conclusion of the IPMMI experiment. (Figure 6.19). The method of stray light rejection (SLR) calculation was similar to that employed by Shetter and Müller (1999), where the array was mounted so that the atmosphere served as a light source. The instrument was set to scan the range $\lambda=285\text{-}450\text{nm}$ and the counts recorded were integrated over the wavelength range. The $2\pi\text{sr}$ optics of the instrument were then covered by an interference filter (Filter 59492 *Oriel Ltd.*) that limited the transmission of photons to wavelengths of $\lambda>500\text{nm}$. The manufacturers quoted transmission of photons of this cut-off filter in the scanning range $\lambda=285\text{-}450$ was less than 1%. In order to estimate the SLR for the single monochromator, the integral of the counts recorded with the unfiltered optics was then divided by the difference in the recorded counts with and without the interference filter at a wavelength of 285nm. Only stray light photons were expected to be recorded at these

Figure 6.19: Stray light Spectra for Diode Array Spectroradiometer



wavelengths. From these experiments, the SL rejection of the single monochromator was found to be 5×10^4 . This value is in good agreement with simulations for both single and double monochromators made by Hofzumahaus *et al.* (1999).

By recording the *in-situ* stray light spectrum in the manner described above, these data could be subtracted from the real data when the array was collecting spectra as normal. It was assumed that the percentage reduction in the data due to the filter in this experiment was the same as if the experiment was repeated under IPMMI conditions. Hence, the percentage contribution of stray light and dark current at each individual wavelength was evaluated and the necessary stray light subtraction applied to the IPMMI data.

The IPMMI referees gave the opportunity for groups with unforeseen problems in their data such as this to resubmit corrected actinic flux and photolysis frequencies. The corrected ULi diode array spectroradiometer data were therefore resubmitted to the IPMMI referees but was not included in the initial "blind" phase of the intercomparison (Cantrell *et al.* [2000], Hofzumahaus *et al.* [2000]).

The application of this method to data recorded during IPMMI was found to improve the overall quality of diode array $j\text{-(O}^1\text{D)}$ data when compared to that of other participants. Figure 6.20 shows the correlation between the ULi re-submitted $j\text{-(O}^1\text{D)}$ data and data from the

spectroradiometer of FZ-Jülich. The overall agreement between these two instruments was now of the order of 0.98-0.99 for the four days of the IPMMI campaign. In an analogous plot to Figure 6.15, Figure 6.21 shows a comparison of the $j(O^1D)$ diurnal cycle as measured by the NCAR chemical actinometer and the revised ULi spectroradiometer data. Figure 6.21, shows much better agreement at times that were identified in Figure 6.14 as being periods where stray light influences were large.

Figure 6.20: Correlation between Re-submitted ULi SR data and FZ-Jülich SR $j(O^1D)$ data

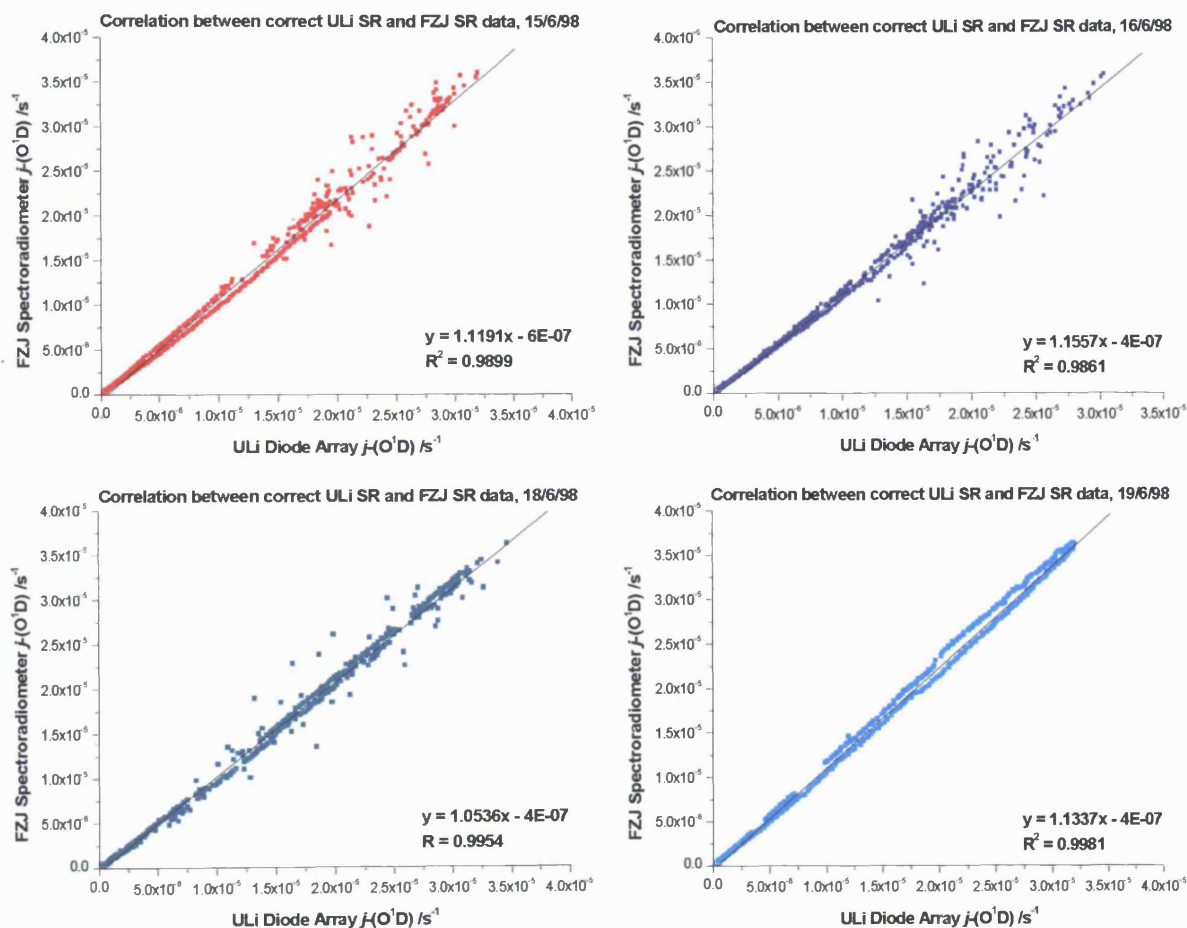
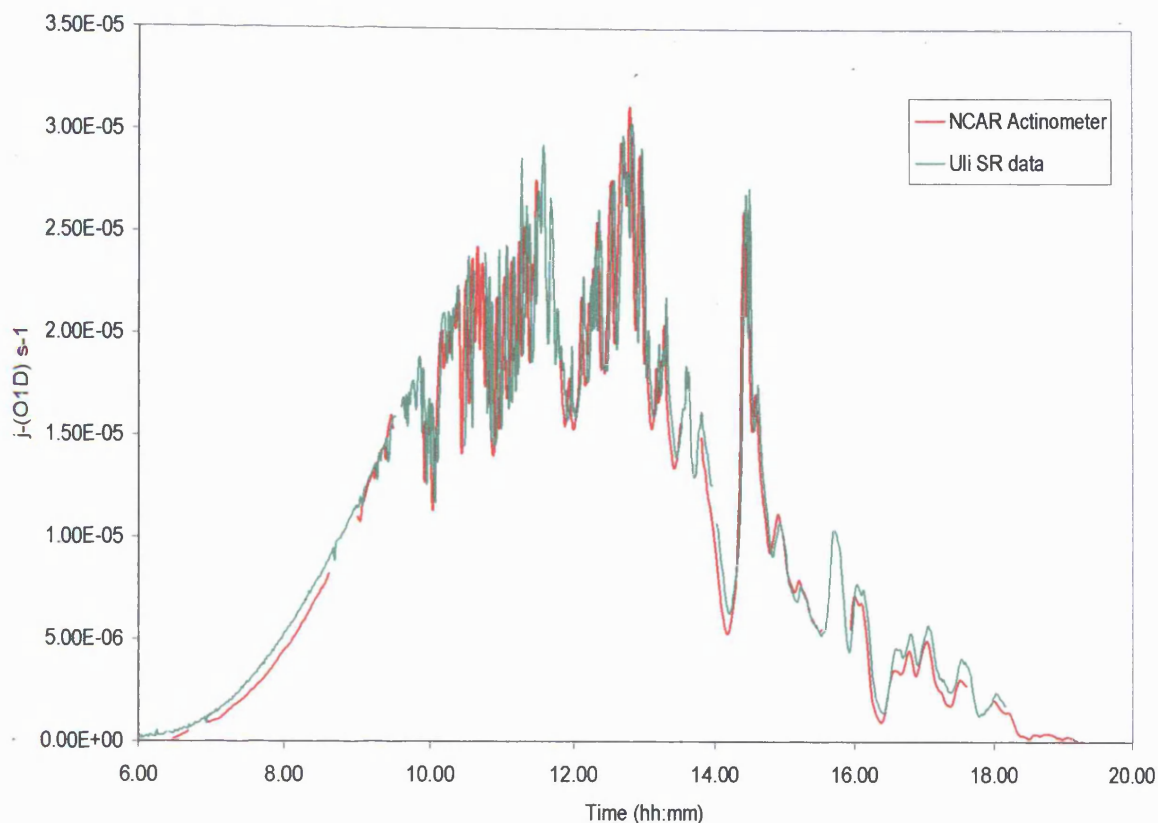


Figure 6.21: Comparison Between NCAR Actinometer and Corrected ULi Diode Array j -(O^1D) Data During IPMMI, 15/6/98



6.9: Effect of Molecular Parameters

As outlined by Cantrell *et al.* (2000), there has been an ongoing debate in the literature over the last few years regarding the exact nature of ozone molecular parameters. Although many authors (*e.g.* Molina and Molina [1986], Malicet *et al.* [1995]) have revised the absorption cross-sections for ozone, most authors have found good agreement in the absolute values of σ over a wide range of wavelengths and temperatures. This has been in direct contrast to the many suggested revisions of $O(^1D)$ quantum yields in recent years. Several authors (*e.g.* Michelson *et al.* [1994], Talukdar *et al.* [1998], Bauer *et al.* [2000]) have reported significant formation of $O(^1D)$ at wavelengths where it was previously assumed that production was not possible (DeMore *et al.* [1994]). These more recent recommendations suggest that at wavelengths greater than the "threshold" of $\lambda=310\text{nm}$, there is significant formation of $O(^1D)$ owing to excited ozone molecules (up to a cut-off of *ca.* $\lambda=325\text{nm}$) and spin forbidden routes (beyond 325nm). Current recommendations therefore suggest that the threshold for production of $O(^1D)$ may even extend to 375nm or beyond (Bauer *et al.* [2000]). In consequence, j -(O^1D) could be significantly higher than previously thought. Although absorption cross-section decreases rapidly at $\lambda>320\text{nm}$, a small quantum yield beyond 325nm

will contribute significantly to the overall photolysis frequency, particularly at high zenith angle. (Talukdar *et al.* [1999]). It was a major aim of IPMMI to ascertain the effect of these recently revised molecular data on $j\text{-}(\text{O}^1\text{D})$ photolysis frequencies measured in the field under different conditions.

For the IPMMI intensive, the quantum yields of Talukdar *et al.* (1998) were compared to those of DeMore *et al.* (1997) and with the cross-section recommendations of Molina and Molina (1986) only. For the purposes of this thesis, additional comparisons with other data have been used. These included the quantum yield recommendations of JPL (DeMore *et al.* [1994]) and the subsequent revisions made by DeMore and co-worker (2000). The absorption cross-section data of Bass and Paur (1985) and the cross-section recommendations of Malicet *et al.* (1995) were also considered. Photolysis frequencies were calculated using actinic flux measurements from the both the NCAR scanning double monochromator as described by Shetter and Müller (1999) and from the NCAR chemical actinometer described by Shetter *et al.* (1996).

6.9.1: Effect of Quantum Yield on $j\text{-}(\text{O}^1\text{D})$

In the case of quantum yield data, significant variations in $j\text{-}(\text{O}^1\text{D})$ were observed. Figure 6.22 shows that the choice of quantum yield recommendation has a major influence on the overall measured photolysis frequency. From Figure 6.22, there appear to be three distinct groups of $j\text{-}(\text{O}^1\text{D})$ diurnal cycles. The lowest of these are those calculated with the quantum yield recommendations of DeMore *et al.* (1994). The peak $j\text{-}(\text{O}^1\text{D})$ at solar noon for the 1994 recommendation is $2.94 \times 10^{-5} \text{ s}^{-1}$. These data are over 30% lower than the highest photolysis frequencies calculated at solar noon. This is owing to the relatively low wavelength "cut-off" in these recommendations where ϕ tends to zero at $\lambda > 310\text{nm}$ (DeMore *et al.* [1994]). As described above, the role of vibrationally excited and spin forbidden channels in the production of O^1D at wavelengths $> 310\text{nm}$ is critical in the correct evaluation of ϕ . This problem was identified in the recommendations from DeMore *et al.* [2000], where significant production of O^1D was considered important out to wavelengths $> 330\text{nm}$. The $j\text{-}(\text{O}^1\text{D})$ calculated from the revised JPL recommendations (DeMore *et al.* [2000]) are highest shown in Figure 6.22, where $j\text{-}(\text{O}^1\text{D})$ at solar noon is $3.75 \times 10^{-5} \text{ s}^{-1}$.

The third "cluster" of $j\text{-}(\text{O}^1\text{D})$ values observed midway between the recommendations of JPL (1994) and the revised data of DeMore *et al.* [2000], are the recommendations of DeMore *et al.* (1997) and Talukdar *et al.* (1998). $j\text{-}(\text{O}^1\text{D})$ data for both the recommendations of Talukdar

et al. (1998) and DeMore *et al.* (1997) lead to $j\text{-}(O^1D)$ values at solar noon of $ca. 3.5 \times 10^{-5} \text{ s}^{-1}$. For these data, the wavelength "cut-off" in O^1D production was also lower than that recommended by DeMore *et al.* (2000). The revised data of DeMore and co-workers extends the active "window" much further into the blue-region of the spectrum and has the net effect of producing higher photolysis frequencies than the previous recommendations of Talukdar (1998) or the data of JPL (1997), which assumes O^1D production tends to zero at $ca. 335\text{-}330\text{nm}$. Peak $j\text{-}(O^1D)$ values using each set of recommendations are shown in Table 6.8.

Figure 6.22: The Effect of Different Assumed Quantum Yields on overall $j\text{-}(O^1D)$, IPMMI 19/6/98

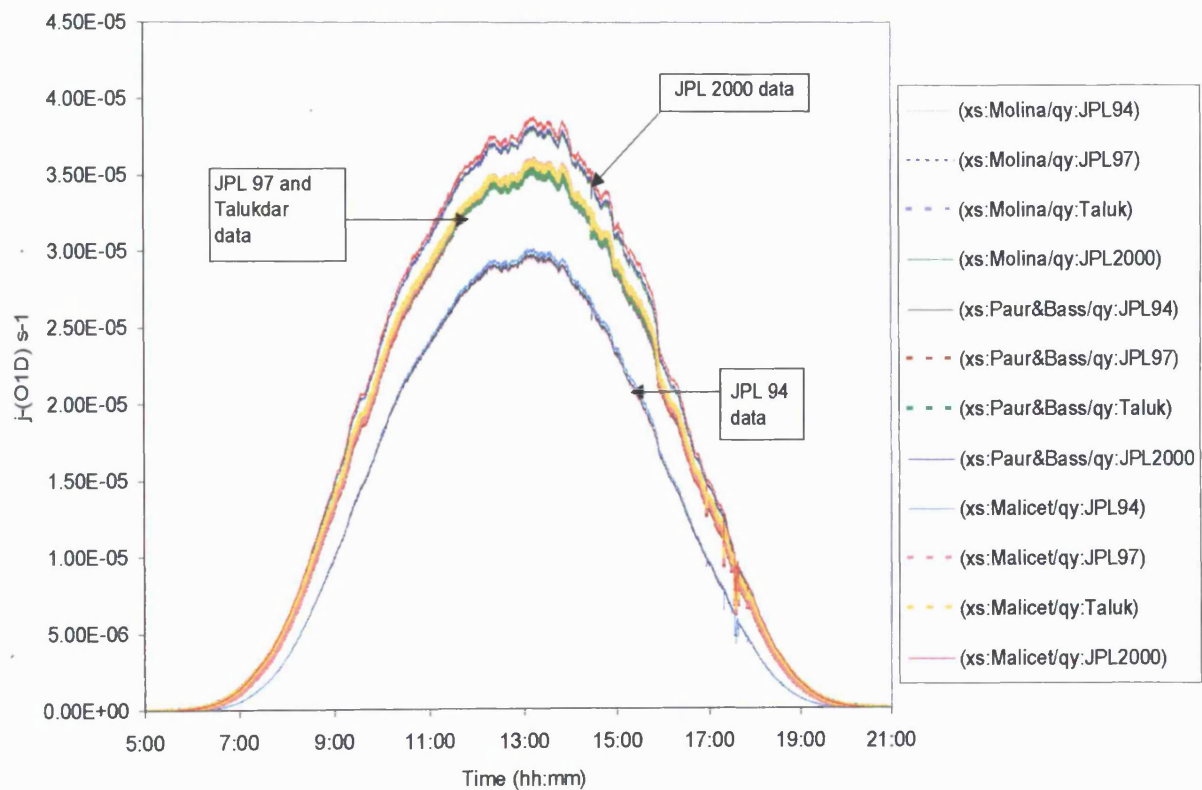


Table 6.8: Relative intensity of spectroradiometer j -(O¹D) data recorded at IPMMI using different quantum yield recommendations

Quantum Yield Recommendation	Solar Noon j -(O ¹ D) /s ⁻¹	FWHM /s ⁻¹
DeMore <i>et al.</i> (1994)	2.94 x 10 ⁻⁵	4.41 x 10 ⁻⁵
DeMore <i>et al.</i> (1997)	3.50 x 10 ⁻⁵	1.83 x 10 ⁻⁵
Talukdar <i>et al.</i> (1998)	3.49 x 10 ⁻⁵	1.83 x 10 ⁻⁵
DeMore <i>et al.</i> (2000)	3.75 x 10 ⁻⁵	7.13 x 10 ⁻⁵

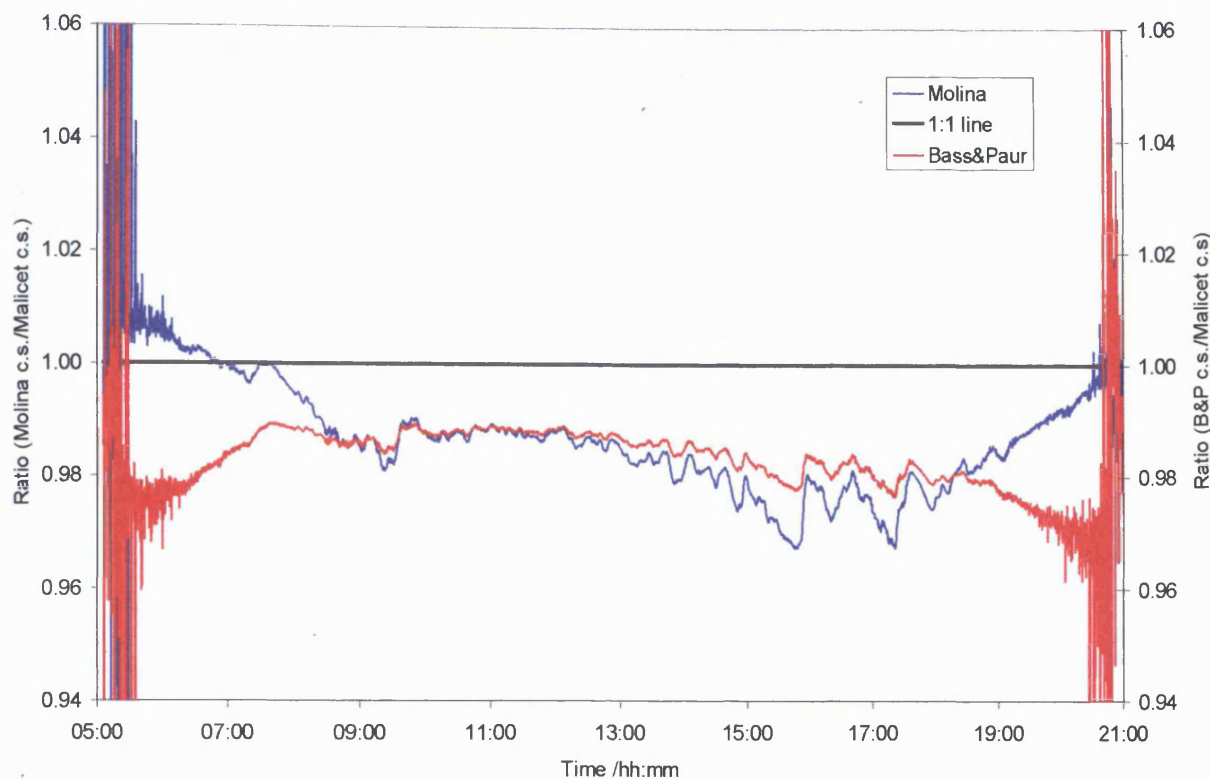
6.9.2: Effect of Cross-section on j -(O¹D)

When comparing the recommendations with respect to absorption cross-sections, most data seem to agree over a wide range of temperatures and wavelengths. j -(O¹D) data derived using the recommendations of Bass and Paur (1985) were compared to the j -(O¹D) data derived using the recommendations of Malicet *et al.* (1995). Similarly, those data derived using the recommendations of Molina and Molina (1986) were also compared j -(O¹D) data derived using the recommendations of Malicet *et al.* (1995). j -(O¹D) values were calculated using the same quantum yield data in each case, in order to remove any variations associated with the ϕ recommendations. The data chosen for this work were those recommended by DeMore *et al.* [2000], together with the actinic flux measurements made by the NCAR spectroradiometer. Figure 6.23 shows that the overall level of agreement between these data was very good. The two sets of j -(O¹D) photolysis frequencies were within 3% of each other, with no significant difference observed across the diurnal cycle except at times approaching sunrise/sunset.

6.9.3: "Best" Molecular Data Recommendations During IPMMI

It is worth considering which is the "best" recommendation with respect to molecular parameters for the conditions of IPMMI. For absorption cross-section, Figure 6.23 suggests that both the data of Molina and Molina (1986), Bass and Paur (1985) and Malicet *et al.* (1995) are equally applicable. In order to find the "best" recommendation with respect to quantum yield, further analysis was required. Ratio plots of spectroradiometer and chemical actinometer data were calculated for all the data taken during IPMMI. Chemical actinometry is a "primary" technique that is a direct measure of a photolysis rate (*e.g.* Shetter *et al.* [1996]), as the molecule of interest is exposed to the incident solar radiation.

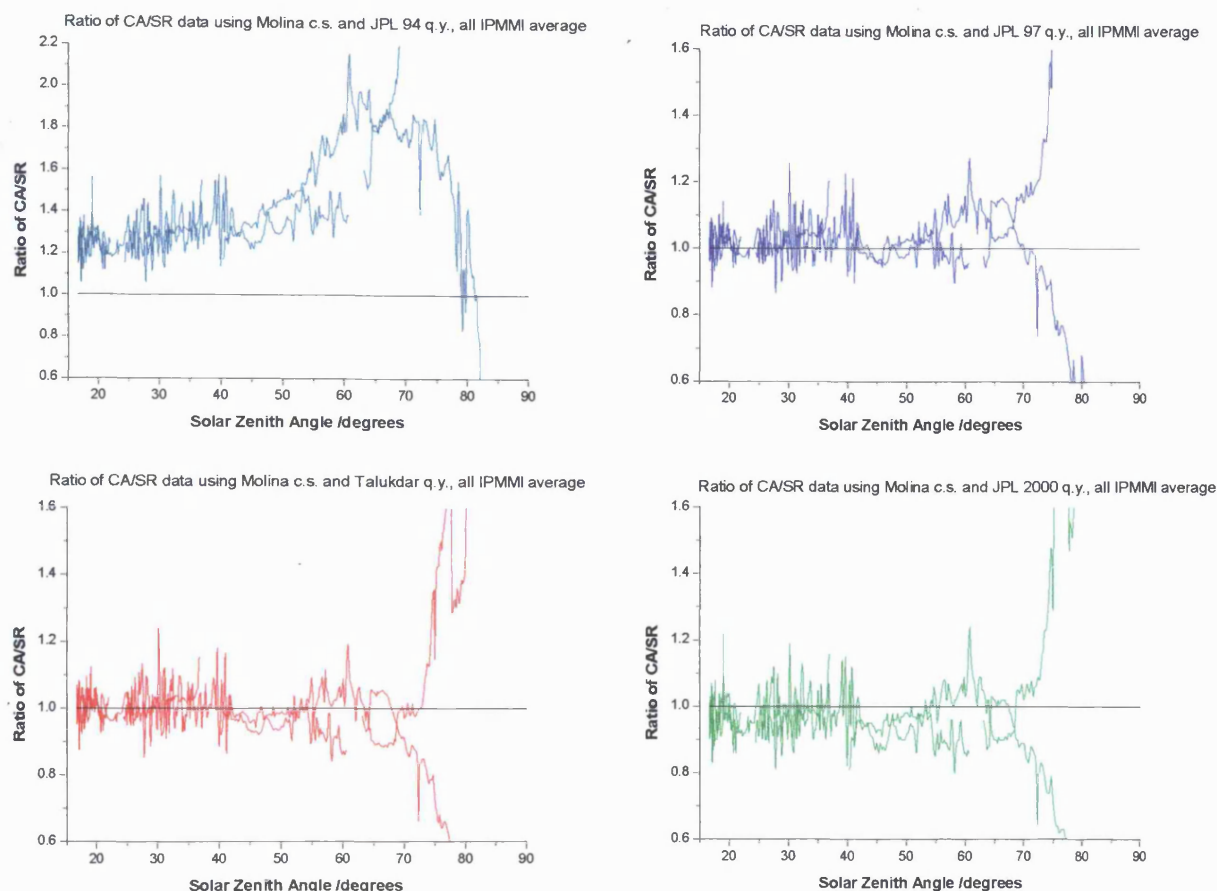
Figure 6.23: Ratio of $j\text{-}(O^1D)$ data using Molina C.S.: Bass and Paur C.S. IPMMI, 19/6/98



The advantage of actinometry is that it does not depend on the accuracy of molecular parameters and hence variations in quantum yield recommendations can be tested against this primary technique. Assuming the chemical actinometer deployed at IPMMI by NCAR gave an accurate evaluation of $j\text{-}(O^1D)$, average ratios of the $j\text{-}(O^1D)$ measured by the chemical actinometer to the NCAR spectroradiometer were made for all four days of the IPMMI campaign. The spectroradiometer values were calculated using actinic flux data measured by NCAR at IPMMI, together with the quantum yield recommendations of DeMore *et al.* (1994), DeMore *et al.* (1997), Talukdar *et al.* (1998) and DeMore *et al.* (2000). In all cases, the cross-section recommendations of Molina and Molina (1986) were used.

Figure 6.24 shows the change in the ratio of chemical actinometer/spectroradiometer with solar zenith angle for these four quantum yield recommendations. From Figure 6.24, the greatest deviation from the 1:1 line of ideal agreement comes from the recommendations of DeMore *et al.* (1994), which seems to consistently underestimate the total $j\text{-}(O^1D)$ measured by the chemical actinometer. This is in agreement with the results presented in the diurnal cycle shown in Figure 6.22. With respect to the other quantum yield data used in this analysis, the calculated $j\text{-}(O^1D)$ values are very similar to the data from the chemical actinometer. As the solar zenith angle changes the ratio is observed to be very close to the 1:1 line for all three data sets where solar zenith angle $>70^\circ$. Upon closer examination data shows that each of the four recommendations, the deviation from perfect 1:1 agreement varies with solar zenith

Figure 6.24: Ratio of Chemical actinometer/Spectroradiometer IPMMI j -(O^1D) data using differing ϕ recommendations



angle. Subtraction of the average ratio on all four IPMMI days from ideal 1:1 agreement suggests that the recommendations of Talukdar (1998) provides spectroradiometer data that is closest to the j -(O^1D) data of the NCAR chemical actinometer, followed by the ϕ data of DeMore *et al.* (2000) and finally data from DeMore *et al.* (1997).

In order to verify these findings the data were binned by solar zenith angle. 15 data bins, ranging from 15° to 90° , in 5° intervals were created and data sorted accordingly. The change in the chemical actinometer/spectroradiometer ratio with respect to solar zenith angle for these binned data is shown in Figure 6.25. These data show that, in general, the ratio of spectroradiometer to chemical actinometer j -(O^1D) is consistent for all four days of the IPMMI campaign for each quantum yield recommendation. From Figure 6.25, j -(O^1D) data using the recommendations of DeMore *et al.* (1994) show a net underestimation relative to the chemical actinometer by *ca.* 38% (± 0.37 at 1σ) for data taken at solar zenith angle $>85^\circ$. The updated JPL data of 1997 and 2000 have better agreement, with a deviation from the chemical actinometer j -(O^1D) of 3.6% (± 0.13 at 1σ) and 2.5% (± 0.17 at 1σ) respectively. However,

for the conditions of the IPMMI experiment, the quantum yield recommendations of Talukdar *et al.* (1998) seem to provide the most accurate spectroradiometer j -(O¹D) data in comparison to data derived *via* chemical actinometry, with a net deviation of 0.6% (± 0.11 at 1σ). The deviations from idealality for each quantum yield recommendation are shown in Table 6.9.

This data analysis was repeated using the four quantum yield recommendations described previously, this time the ozone absorption cross-section data from the recommendations of Bass and Paur (1989). Similar trends to those observed in Table 6.9 were also observed using the recommendations of Bass and Paur (1989). These results suggest that, when averaged over the entire dataset for IPMMI, under these conditions, the quantum yield recommendations of Talukdar *et al.* (1998) provide the "best" quantum yield for the work up of spectroradiometer data.

Figure 6.25: Binned data with Respect to Solar Zenith Angle for the Ratio of Chemical Actinometer/Spectroradiometer j -(O¹D) IPMMI data (using Molina and Molina [1986] σ values and differing ϕ recommendations)

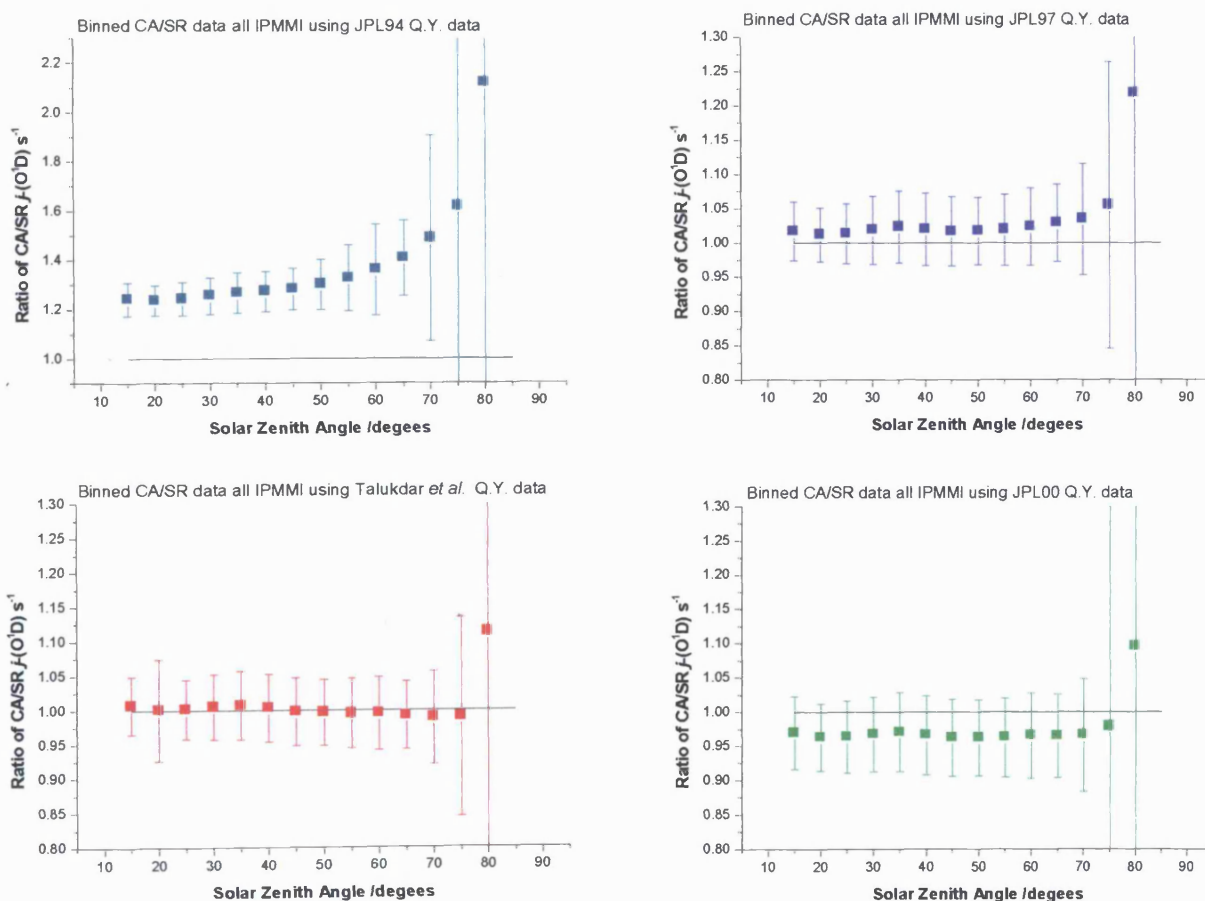


Table 6.9: Deviations from 1:1 Agreements in Spectroradiometer/Chemical Actinometer j -(O^1D) Data Recorded at IPMMI (using Molina and Molina [1986] σ values and differing ϕ recommendations)

SZA			Talukdar					
Bin (deg)	JPL(94)	Stdev*	JPL(97)	Stdev*	(98)	Stdev*	JPL(00)	Stdev*
90-85	21.57	6.01	15.99	8.87	8.94	6.53	8.54	1.84
85-80	2.12	2.93	1.22	1.02	1.11	0.82	1.10	0.72
80-75	1.62	0.78	1.05	0.21	0.99	0.14	0.98	0.98
75-70	1.49	0.42	1.03	0.08	0.99	0.07	0.97	0.08
70-65	1.41	0.15	1.03	0.06	0.99	0.05	0.96	0.06
65-60	1.36	0.18	1.02	0.06	0.99	0.05	0.97	0.06
60-55	1.33	0.13	1.02	0.05	0.99	0.05	0.96	0.06
55-50	1.30	0.10	1.02	0.05	1.00	0.05	0.96	0.06
50-45	1.28	0.08	1.02	0.05	1.00	0.05	0.96	0.06
45-40	1.27	0.08	1.02	0.05	1.00	0.05	0.97	0.06
40-35	1.27	0.08	1.02	0.05	1.01	0.05	0.97	0.06
35-30	1.26	0.07	1.02	0.05	1.00	0.05	0.97	0.05
30-25	1.24	0.07	1.01	0.04	1.00	0.04	0.96	0.05
25-20	1.24	0.06	1.01	0.04	1.00	0.07	0.96	0.05
20-15	1.24	0.07	1.02	0.04	1.01	0.04	0.97	0.05
Average	+38.75	0.37	+3.66	0.13	+0.64	0.11	-2.46	0.17

*where Stdev is the 1 σ standard deviation

6.10: Conclusions

In this chapter, the data collected by University of Leicester instruments that participated during the International Photolysis Measurement and Modelling Intercomparison (IPMMI) have been investigated. Overall, the data obtained by filter radiometry has been shown to be in excellent agreement to photolysis frequencies measured by other groups from a variety of instruments. It was a major aim of the IPMMI to examine the effect of factors such as temperature dependence of j -(O^1D) and the effect of revised molecular parameters on " j " values. It has been shown in this chapter that the choice of molecular data in the calculation of j -(O^1D) has major implications for this photolysis frequency. The use of data where $\phi > 310$ tends to zero (e.g. the data for DeMore *et al.* [1994]) can lead to large underestimation of the calculated photolysis frequency. Further analysis of these data has shown that for the conditions of this intercomparison exercise, the recommendations of Talukdar *et al.* (1998) provided the most accurate assessment of the (O^1D) quantum yield.

It has also been shown that choice of absorption cross-sections data for ozone was less critical. For the conditions of IPMMI, σ recommendations of Bass and Paur (1985), Molina and Molina (1986) and Malicet *et al.* (1995) were found to within 3% of each other and showed no significant deviations across the diurnal cycle.

In this chapter, an extensive evaluation of a new spectroradiometer has also been carried out. The use of this instrument for the first time at the IPMMI experiment has shown that single monochromator instruments have both benefits and potential problems as working field spectroradiometers. Using the data taken at the intercomparison, it is clear that the ULi instrument performed adequately with respect to the measurement of atmospheric photolysis frequencies and actinic flux. The ULi spectroradiometer agreed quite well when compared to chemical actinometers, filter radiometers and double monochromator spectroradiometers. Nevertheless, poor stray light rejection, combined with poor sensitivity and potential variable offsets make the accurate assessment of diode array data very difficult. With the increasing drive for measurement devices capable of rapid time responses in atmospheric chemistry, the use of single monochromator diode array spectroradiometers is likely to become much more widespread. The time resolution that these instruments offer is not found in other scanning double monochromators or chemical actinometers, thus making such instruments an obvious choice for the measurement of actinic flux and/or photolysis frequencies in the field. Therefore, in order for the data to be useful and accurate with respect to measurement of flux and photolysis frequencies, a full and extensive error correction regime must be employed to overcome the shortcomings of such instruments.

Chapter Seven: Overall Summary

Chapter 7: Overall Summary

The work presented in this thesis has shown that aircraft platforms can provide a wealth of data on the atmospheric chemistry in environments such as the North Atlantic. The data described in Chapter 2 has shown that the instruments mounted on MRF C-130 aircraft provided excellent *in situ* measurements of the concentrations of trace gases in the free troposphere in this region during the recent ACSOE campaign. These data have been analysed *via* a trace gas climatologies approach over the latitude range 20° N to 60° N. Data bins ranging from 0-8 km were created providing an insight into the distribution of trace gas in this region. The analysis has been able to compare seasonal distributions and results suggest a number of photochemical tracers show pronounced variation over altitudes less than 8km during spring and summer. The exact nature of this seasonal variation, with respect to factors such as photochemical environment has shown there is possible evidence of a wide spread photochemical source for a pronounced springtime ozone maximum in these environments.

Ozone concentrations over the unpolluted North Atlantic ocean suggest a maximum concentration in late April up to an altitude of *ca.* 3 km. Concentrations of ozone in the spring were found to be *ca.* 10-15 ppb higher than for similar altitudes encountered during summer. This seems to agree with reports in the literature from surface sites of Northern Hemisphere spring ozone maximum (*e.g.* Monks [2000]). This spring excess has been shown to be closely linked to [NO_y]. Spring data shows that [NO_y] ranges from 150-500 pptv, as compared to 100-400 pptv in summer. NO_x/NO_y ratios suggest that there are major influences of other reactive nitrogen reservoirs, possibly PAN during the spring flights which are not present during summer owing to recycling of NO_y back to NO_x *via* thermal decomposition, or other NO_y destruction routes.

The validation of aircraft measurements has been investigated *via* model analysis described in Chapter 3. Bin modelling of the ACSOE spring and summer climatologies has shown production of HO_x in both seasons was controlled by the reaction of O(¹D) atoms with water over essentially all altitudes. Loss of HO_x in both seasons was predominantly controlled by HO₂ self-reaction. P(O₃) and L(O₃) are in close balance during both legs of ACSOE campaign. Maximum loss rates of *ca.* 4 ppbv per day were calculated for spring *c.f.* 1 ppbv per day for summer. Levels of critical NO, (NO_{critical}), were found to be *ca.* 15 pptv for spring flights, and 24 pptv during summer.

Climatology data has been compared to the outputs of a chemistry transport model (Flatøy *et al.* [2000]) for the 1999 MAXOX aircraft campaign (Hov *et al.* [2000]). Data suggests the Bergen CTM model was able to reproduce the seasonal and latitudinal variations for some trace gases (*e.g.* ozone) quite well. In contrast, other tracers such as $[\text{NO}_x]$ and $[\text{NO}_y]$ have been shown to be underestimated by the model. A combination of model and measured data has been used to calculate net ozone tendencies for the August series of MAXOX aircraft missions. Net ozone production was observed in all flights. This suggests that ozone production in the free troposphere sampled during MAXOX was under NO_x limitation with overall average levels of NO only just greater than $\text{NO}_{\text{critical}}$. The development of a 0-D Flight Track Box Model (FTBM) and its application to aircraft data was described in Chapter 4. The model has been used to investigate the oxidising capacity of the free troposphere *via* comparisons of modelled $[\text{HO}_2]$ and $[\text{OH}]$ to concentrations measured *in situ* during the 1997 SONEX aircraft campaign (Thompson *et al.* [2000]) and to data derived from the application of simple "steady state" algorithms. Results suggest that the FTBM is able to reproduce $[\text{HO}_x]$ with reasonable accuracy, where simple "steady-state" models seem to underestimate $[\text{HO}_x]$ owing to the complex chemistry of the mid and upper-troposphere.

The measurement of the photolysis frequency $j\text{-(O}^1\text{D)}$ from the C-130 aircraft platform during the ACSOE and MAXOX campaigns was described in Chapter 5. The results show that a full characterisation of these radiometers suggests the two fixed-bandwidth photoelectric radiometers developed by the University of Leicester were able to measure $j\text{-(O}^1\text{D)}$ to an accuracy of 30% when compared to modelled photolysis frequencies. A similar performance was observed in ground-based instruments for the measurement of photolysis frequencies described in Chapter 6 during field deployment at the 1998 International Photolysis Modelling and Measurement Intercomparison (Cantrell *et al.* [2000]). The results of this experiment have also emphasised potential problems in the performance of a new diode array spectroradiometer instrument. The relative accuracy of the spectroradiometer measurements when compared to photolysis frequencies derived using similar and differing experimental techniques suggests the instrument suffered poor stray light rejection in the single monochromator used in the instrument. The net result was the overestimation of actinic flux and the photolysis frequency $j\text{-(O}^1\text{D)}$. Therefore, in order for the data to be useful and accurate with respect to measurement of flux and photolysis frequencies the need for a full error correction regime was highlighted.

Reference

- Akimoto, H., H. Mukai, M. Nishikawa, K. Murano, S. Hatakeyama, C.M Liu, M. Buhr, K.J Hsu, D.A. Jaffe, L. Zhang, R. Honrath, J.T. Merrill and R.E. Newell, Long Range Transport of Ozone into the Pacific Rim Region, *J. Geophys. Res.*, **101**, pp.1999-2010, 1996.
- Ames, J., T.C. Myers, L.E. Reid, D.C. Whitney, S.H. Golding, S.R. Hayes and S.D. Reynolds, User Manual for the SAI Airshed Model, *Report to the EPA*, Contract N^o. 68-02-2429, 1978.
- Anderson, B.E., G.L. Gregory, J.D.W. Barrick, J.E. Collins, G.W. Sachse, D. Bagwell, M.C. Shipman, J.D. Bradshaw and S.T. Sandholm, The Impact of U.S. Continental Outflow on Ozone and Aerosol Distribution over the North Atlantic, *J. Geophys. Res.*, **98**, pp. 23 477-23 489, 1993.
- Ayres, G.P., S.A. Penkett, R.W. Gillett, B.J. Bandy, I.E. Galbally, C.P. Meyers, C.M. Elsworth, S.T. Bentley and B.W. Forgan, Evidence for Photochemical Control of Ozone Concentration in Unpolluted Air, *Nature*, **360**, pp. 446-448, 1992.
- Ayres, G.P., R.W. Gillett, H. Granek, C. de Serves and R.A. Cox, Formaldehyde Production in Clean Air, *Geophysical Research Letters*, **24**, pp. 401-404, 1997.
- Bahe, F.C., W.N. Marx, U. Schurath and E.P. Roth, Determination of the Absolute Photolysis Rate of Ozone by Sunlight at Ground Level, *Atmospheric Environment*, **13**, pp.1515 - 1522, 1979.
- Bais, A.F. S. Madronich, J. Calvert, C. Cantrell, R. Shetter, J. Crawford, A. Hofzumahaus, P.S. Monks, G. D. Edwards, M. Muller, A. Kraus, B. Lefer, *et al.* International Photolysis Frequency Measurement and Model Intercomparison: Spectral Solar Flux Measurements and Modelling, *Submitted to J. Geophys. Res.*, 2000.
- Ball, S.M., G. Hancock, S.E. Martin, and J.C. Pinot et Moira, A Direct Measurement of the O(¹D) Quantum Yields from the Photodissociation of Ozone between 300 and 328 nm, *Chem. Phys. Lett.*, **264**, pp. 531-538, 1997.

- Bass, A.M., and R.J. Paur, The Ultraviolet Cross-Sections of Ozone: I, II, in: *Atmospheric Ozone, Proceedings of the Quadrennial Ozone Symposium*, Greece, edited by C.S. Zerefos and A. Ghazi, publisher D. Reidel. Norwell, Massachusetts, pp. 606-616, 1985.
- Bauer, D., L.D'Ottone and A.J. Hynes, O(¹D) Quantum Yield from Ozone Photolysis in the Near UV region between 305 and 375nm, *J. Phys Chem*, **2**, pp.1421-1424, 2000.
- Beine, H.J., D.A Jaffe, J.A. Herring, J.A. Kelley, T. Krognes, and F. Stordal, High-latitude Springtime Photochemistry, NO_x, PAN and ozone relationships, *J. Atms Chem.* **27**, pp.127-153 1997
- Beine, H.J., A. Dahlback and J.B. Øræk, Measurement of *j*-(NO₂) at Ny-Ålesund, Svalbard, *J. Geophys. Res.*, **104**, pp. 16 009-16 0019, 1999.
- Bethan, S., G. Vaughan, C. Gerbig, A. Voltz-Thomas, H. Richer and D.A. Tidderman, Chemical Air Mass Differences near Fronts, *J. Geophys. Res.*, **103**, pp. 13,413-13,434, 1998.
- Blackburn, T.E., S.T. Bairai and D.H. Steadman, Solar Photolysis of Ozone into Singlet D Oxygen Atoms. *J. Geophys. Res.*, **97**, pp. 10,109 - 10,117, 1992.
- Blake, D.R., T.Y. Chen, T.Y. Smith, C.J.L. Wang, O.W. Wingenter, N.J. Blake, F.S. Rowland and E.W. Mayer, Three Dimensional Distribution of NMHC's and Halocarbons over the Pacific during PEM-West (A), *J. Geophys. Res.*, **101**, pp.1763-1778, 1996.
- Blindauer, C., V. Rozonov and J.P Burrows, Actinic Flux Frequency Comparisons using the PHOTOGT Model. *J. Atms. Chem.*, **24**, pp. 1-21, 1996.
- Brasseur, G.P., J.F. Muller, C. Granier, Atmospheric impact of NO_x emissions by subsonic aircraft: A three-dimensional model study. *J. Geophys. Res.*, **101**, pp. 1423-1428, 1996.
- Brasseur, G.P., J.T. Kiehl, J.F. Muller, T. Schneider, C. Granier, X.X. Tie and D. Hauglustaine, Past and Future Changes in Global Tropospheric Ozone: Impact on radiative forcing. *Geophysical Research Letters*, **20**, pp. 3807-3810, 1998.
- Brassuer, G.P., J.J. Orlando and G. S. Tyndall, Atmospheric Chemistry and Global Change, *Oxford University Press*, 1998.

Bregman, A., P.F.J. van Velthoven, F.G. Wienhold, H. Fischer, T. Zenker, A. Waibel, A. Frenzel, F. Arnold, G.W. Harris, M.J.A. Bolder and J. Leiienveld, Aircraft Measurements of O₃, HNO₃ and NO₂ during STREAM 1. *J. Geophys. Res.*, **100**, pp. 11,245 – 11,260, 1995.

Brock, J.C., and R.T. Watson, Laser Flash Photolysis of Ozone: O(¹D) Quantum Yields in the fall-off region 297-325 nm, *Chem. Phys.*, **46**, 477-484, 1980.

Brune, W.H., I.F. Faloona D. Tan, A.J. Weinheimer, T. Campos. B.A. Ridley, S.A. Vay, J.E. Collins, J.W. Jaeglé and D.J. Jacob, Airborne *in-situ* HO₂ and OH Observations in the Cloud-Free Troposphere and Lower Stratosphere during SUCCESS. *Geophysical Research Letters*, **25**, pp. 1701-1704, 1998.

Brune, W.H., D. Tan, I.F. Faloona, L. Jaeglé, D.J. Jacob, B.G. Heikes, J. Snow, Y. Kondo, R. Shetter, G.W. Sachse, B. Anderson, G.L. Gregory, S. Vay, H.B. Singh, D. Davis, J. H. Crawford and D.R. Blake, OH and HO₂ Chemistry in the North Atlantic Free Troposphere., *Geophysical Research Letters*, **26**, pp. 3077-3080, 1999.

Cantrell, C.A. and D. H. Steadman, A Possible Technique for the Measurement of Atmospheric Peroxy Radicals, *J. Geophys. Res.*, **9**, pp. 846-849, 1982.

Cantrell, C.A., R. E. Shetter, J. Calvert, F. Eisele, E. Williams, K. Baumaunn, W.H. Brune, P.S. Stevens and J.H. Mather, Peroxy Radicals from Photostationary State Derivations and Steady State Calculations during the Tropospheric OH Photochemistry Experiment at Idaho Hill, Colorado, 1993, *J. Geophys. Res.*, **102**, pp. 6369 – 6378. 1996.

Cantrell, C.A., J.G. Calvert and A. Bais, The International Photolysis Modelling and Measurement (IPMMI) Experiment: An Overview, *Submitted to J. Geophys. Res.*, 2000.

Carpenter, L.C., P.S. Monks B. J. Bandy. S.A. Penkett, I.E. Galbally and C.P. Meyer, A Study of Peroxy Radicals at Coastal Sites in the Northern and Southern Hemispheres. *J. Geophys. Res.*, **102**, pp. 25 417- 25 427, 1997.

Carpenter, L.J., K.C. Clemitshaw, R.A. Burgess, S.A. Penkett, J.N. Cape and G.C. McFadyen, Investigation and Evaluation of the NO_x/O₃ Photochemical Steady State, *Atmospheric Environment*, **32**, pp. 3 353-3 365, 1998.

Carpenter, L.J., T.J. Green, G.P. Mills, S. Bauguitte, S.A. Penkett, P. Zanis, E. Schuepbach, N. Schmidbauer, P.S. Monks, C. Zellweger, Oxidized Nitrogen and Ozone Production Efficiencies in the Springtime Free Troposphere over the Alps, *J. Geophys. Res.*, **105**, pp. 14 547-14 559, 2000.

Carslaw, N., D.J. Creasey, D.E. Heard, A.C. Lewis, P.S. Monks, B.J. Bandy and S.A. Penkett, Modelling OH, HO₂ and RO₂ Radicals in the Marine Boundary Layer: Model construction and comparison with field measurements, *J. Geophys. Res.*, **104**, pp. 30 241-30 255, 1999-A.

Carslaw, N., D.J. Creasey, D.E. Heard, A.C. Lewis, P.S. Monks, B.J. Bandy and S.A. Penkett, Modelling OH, HO₂ and RO₂ Radicals in the Marine Boundary Layer: Mechanism reduction and uncertainty analysis *J. Geophys. Res.*, **104**, pp. 30 241-30 255, 1999-B.

Cess, R.D., M. Zhang, P.J. Valero, S.K. Pope, A. Bucholtz, B. Bush, C.S. Zender and J. Vitko Absorption of Solar Radiation by the Cloudy Atmosphere: Interpretation of Collected Aircraft Measurements. *J. Geophys. Res.*, **104**, pp. 2059-2066, 1999.

Chamedies, W.L. and J.C.G. Walker, A Photochemical Theory for Tropospheric Ozone, *J. Geophys. Res.*, **78**, pp. 8751-8760, 1973.

Cohan, D.S., M.G. Schultz, D.L. Jacob, B.G. Heikes and D.R. Blake, Convective Injection and Photochemical Decay of Peroxides in the Upper Troposphere: Methyl Iodide as a Tracer of Marine Convection, *J. Geophys. Res.*, **104**, pp. 5717-5724, 1999.

Collins, W.J., D.S. Stevenson, C.E. Johnson, and R.G. Derwent, Role of Convection in Determination of the Budget of Odd Hydrogen in the Upper Troposphere, *J. Geophys. Res.*, **104**, pp. 26 927-26 941, 1999.

Cox, R.A. and R.G. Derwent, Gas Kinetics and Energy Transfer, *Specialist Periodical Reports of the Chemical Society*, **4**, pp. 189, 1981.

Crawford, J.D., D.D. Davis, G. Chen, J. Bradshaw, S. Sandholm, Y. Kondo, S. Liu, E. Browell, G. Gregory, B. Anderson, G. Sachse, J. Collins, J. Barrick, D. Blake, R. Talbot and H. Singh, An Assessment of Ozone Photochemistry in the Extratropical Western North Pacific: Impact of Continental Outflow during Late Winter/Early Spring, *J. Geophys. Res.*, **102**, pp. 28 469- 28 487, 1997.

Crawford, J. D., Davis, G. Chen, R. Shetter, M. Müller, J. Barrick and J. Olson, An Assessment of Cloud Effects on Photolysis Rate Coefficients: Comparison of Experimental Value, *J. Geophys. Res.*, **104**, pp. 5725 – 5734, 1999.

Crutzen, P., A Discussion of Minor Constituents of the Stratosphere and Troposphere, *Pure and Applied Geophysics*, **106-108**, pp. 1385-1399, 1973.

Crutzen, P.J., M.G. Lawrence, and U. Pöschl, On the Background Photochemistry of Tropospheric Ozone., *Tellus*, **51**, pp. 123-146, 1999.

Curtis, A.R., and W.P. Sweetenham, FACSIMILE Users Manual, AERER 12805, HMSO, London, 1987.

Dahlback, A. and K. Stamnes, A Spherical Model for the Computation of the Radiation Available for Heating and Photolysis at Twilight. *Planetray Space Science*, **39**, pp. 671-683, 1991.

DeHann, J.F., P.B. Bosma and J.W. Hovenier, An Adding Method for Multiple Scattering Calculations of Polarized Light, *Astron. Astrophys.*, **183**, pp. 371-391, 1987.

Davis, D.D., G. Chen, W. Chamedies, J. Bradshaw, S. Sandholm, M. Rodgers, J. Schendal, S. Madronich, G. Sachse, G. Gregory, B. Anderson, J. Barrick, M.M. Shipham, J. Collins, L. Wade, and D. Blake, A Photostationary State Analysis of the NO₂-NO System Based on Airbourne Observations from the Subtropical Tropical North and South Atlantic, *J. Geophys. Res.*, **98**, pp. 23501-23523, 1993.

Davis, D.D., J. Crawford, C.Chen, W. Chameides, S. Liu, J. Bradshaw, S. Sandholm, G. Sachse, G. Gregory, B. Anderson, J. Barrick, J. Collins, E. Browell, D. Blake, S. Rowland, Y. Kondo, H. Singh, R. Talbot, B. Heikes, J. Merrill, J. Rodriguez and R.E. Newell, Assesment of Ozone Photochemistry in the Western North Pacific from PEM-West A Observations During Fall 1991, *J. Geophys. Res.*, **101**, pp. 2111-2134, 1996.

DeMore, W.B., S.P. Sander, C.J. Howard, A.R. Ravishankara, D.M. Golden, C.E. Kolbe, R.F. Hampson, M.J. Kurylo and M.J. Molina. *Chemical Kinetics and Photochemical Data for use in Stratospheric Modelling*, **11**, NASA JPL Publications, Pasadena California, 94 - 26, 1994.

DeMore, W.B., S.P. Sander, C.J. Howard, A.R. Ravishankara, D.M. Golden, C.E. Kolb, R.F. Hampson, M.J. Kurylo and M.J. Molina. *Chemical Kinetics and Photochemical Data for use in Stratospheric Modeling*, **12**, NASA JPL Publications, Pasadena California, 1997.

DeMore, W. B., S. P. Sander, R. R. Friedl, A. R. Ravishankara, D. M. Golden, C. E. Kolb, M. J. Kurylo, R. F. Hampson, R. E. Huie, M. J. Molina and G. K. Moortgat. *Chemical Kinetics and Photochemical Data for Use in Stratospheric Modeling: Supplement to Evaluation 12: Update of Key Reactions*, Evaluation Number **13**, NASA JPL Publications, Pasadena California, 2000.

Dearellano, J.V., P.G. Duynkerke and M. van Weele, Balloon Measurements of Actinic Flux in a Cloud Capped Boundary Layer, *J. Geophys. Res.*, **99**, pp. 3699–3705, 1994.

Derwent, R.G., P.G. Simmonds, and W.J. Collins, Ozone and Carbon Monoxide Measurements at a Remote Maritime Location, Mace Head, Ireland, from 1990 to 1992, *Atmos. Environ.*, **28**, pp. 2623-2637, 1994.

Derwent, R.G., Influences of Human Activity on the Atmospheric OH Radical, *Philosophical Discussions of the Royal Society*, **354**, Part 1707, pp. 501-531, 1996.

Derwent, R.G. and T.J. Davis, Modelling the Impact of NO_x and Hydrocarbon Control on Photochemical Ozone in Europe. *Atmospheric Environment*, **28**, pp. 2039-2052, 1999.

Dickerson, R.R., D.H. Steadman, and A.C. Delany, Direct Measurement of Ozone and Nitrogen Dioxide Photolysis Rates in the Troposphere *J. Geophys. Res.*, **87**, pp. 4933 - 4946, 1982.

Edwards, G.D. and P.S. Monks, "The Performance of a Single Monochromator Diode Array Spectroradiometer at IPMMI: An Evaluation", *Submitted to J. Geophys. Res.*, 2000.

Edwards, G.D., P.S. Monks, B. Bandy, G. Mills, T. Green, S. Baugeitte, H. Richer S. A Penkett *et al.*, Spring and Summer Trace Gas Climatologies over the North Atlantic, *manuscript in preperation*, 2000.

Ehhalt, D.H., Free Radicals in the Atmosphere, *Free Radical Research Commission*, **3**, pp. 153 – 164, 1987.

Ehhalt, D.H., H.P. Dorn, and D. Popp.e, The Chemistry of the OH Radical in the Troposphere, *Proceedings of the Royal Society of Edinburgh*, **97B**, 17- 34, 1991.

Ehhalt, D.H., and F. Rohrer, The Dependence of OH concentration on Solar UV radiation, *J. of Geophys. Res.*, **105**, pp. 3565-3571, 2000.

Eisele, F.L. and D.J. Tanner, Ion assisted Troposphere OH Measurements, *J. Geophys. Res.*, **96**, pp.9295, 1994.

Eisele, F.L., D.J. Tanner, C.A. Cantrell and J.G. Calvert, Measurements and steady-state calculations of OH concentrations at Mauna Loa Observatory, *J. Geophys. Res.*, **101**, pp.14665-14679, 1996.

Eisele, F.L., G.H. Mount, D. Tanner, A. Jefferson, R. Shetter, J.W. Harder, and E.J. Williams, Understanding the Production and Interconversion of the Hydroxyl Radical during the Tropospheric OH Photochemistry Experiment, *J. Geophys. Res.*, **102**, pp. 6457 – 6465, 1997.

Fabien, P. and P.G. Pruchniewz, Meridional Distribution of Ozone in the Troposphere and it's Seasonal Variation, *J. Geophys. Res.*, **82**, pp. 2063-2073, 1977.

Fahey, D.W., K.K. Kelly, G.V. Ferry, L.R. Poole and J.C. Wilson, *In-situ* Measurement of Total Reactive Nitrogen, Total Water and Aerosol in a Polar Stratospheric Cloud in the Antarctic, *J. Geophys. Res.*, **94**, pp. 11 299-11 315, 1989.

Faloona, I., D. Tan, W.H. Brune, L. Jaegle, D.J. Jacob, Y. Kondo, M. Koike R. Chaterfield, R. Pueschel, G. Ferry, G.W. Sachse, S.A. Vay, B. Anderson, J. Hannon and H. Fuelberg Observations of HO_x and it's Relation to NO_x in the Upp.er Troposphere during SONEX, *J. of Geophys. Res.*, **105**, pp. 3771-3783, 2000.

Farman, J.C., B.G. Gardiner and J.D. Large Losses of total Ozone in Antartica Reveal easonal NO_x and ClO_x, *Nature*, **315**, pp. 217-219, 1985.

Finlayson-Pitts, B.J., and J.N. Pitts, Atmospheric Chemistry, Fundamentals and Experimental Technique, *J. Wiley and sons, New York*, 1986.

Finlayson-Pitts, B.J., and J.N. Pitts, Chemistry of the Upper and Lower Atmosphere, *Academic Press Inc.* 2000.

Flatøy, F., Ø. Hov, C. Gerbig and S.J. Oltmans, Model Studies of the Troposphere over the North Atlantic. *J. Geophys. Res.*, **101**, pp. 29 317 –29 334, 1996.

Flatøy, F., H. Smith and Ø. Hov, 3 Dimensional Studies of the Exchange Processes of Ozone in the European Troposphere. *J. Geophys. Res.*, **100**, pp. 11 465 – 11 481, 1995.

Flatøy, F., Ø. Hov and H. Schlarger, Chemical Forecasts used in Measurement Flight planning during POLINAT-2. *Geophysical Research Letters*, **27**, pp. 951-954, 2000.

Folkens, I., R. Chatfield, H. Singh, Y. Chen and B. Heikes, Ozone Production Efficiencies of Acetone and Peroxide in the Upper Troposphere, *Geophysical Research Letters*, **25**, No 9, pp.1305-1308, 1998.

Foot, J.S, P. Hignett, and C.G. Kilsby, Investigations into errors associated with upwards facing pyrometers fitted to the MRF Hercules. *MRF Internal Note* **31**, 1986.

Gidel, L.T. Cumulus Cloud and Transport of Tracers, *J. Geophys. Res.*, **88**, pp. 6587-6599, 1983.

Gerbig, C., D. Kley, A.VolzThomas, J. Kent, K. Dewey and D.S. McKenna, Fast Response Resonance Fluorescence CO Measurements aboard the C-130: Instrument Characterization and Measurements made during North Atlantic Regional Experiment (NARE) 1993, *J. Geophys. Res.*, **101**, pp.29 229-29 238, 1996.

Grant, W.B., E.V. Browell, C.F. Butler, M.A. Fenn, M.B. Clayton, J.R. Hannan, H.E. Fuelberg, D.R. Blake, N.J. Blake, G.L Gregory, B.G. Heikes, G.W. Sachse, H.B. Singh, J. Snow and R.W. Talbot, A Case Study of Transport of Tropical Marine Boundary Layer Air Masses to Northern Mid Latitudes, *J. of Geophys. Res.*, **105**, pp. 3757-3769, 2000.

Gregory, G.L., H.E. Fuelberg, S.P Longmore, B.E. Anderson, J.E. Collins and D.R. Blake Chemical characteristics of tropospheric air over the tropical South Atlantic ocean, *J. Geophys. Res.*, **101**, pp. 23 957-23 972, 1996.

Gronas, S. and N.G. Kvamsto, Numerical Simulations of Arctic Polar Lows, *Tellus*, **47**, pp. 797 – 814. 1995.

Hallock-Waters, K.A., B.G. Doddridge, R.R. Dickerson, S. Spitzer, J.D. Ray, Carbon monoxide in the US Mid-Atlantic troposphere: Evidence for a decreasing trend. *Geophysical Research Letters*, **26**, pp.2861-2864, 1999.

Hard, T.M., R.J. O'Brien, C.Y. Chan and A.A. Mehrabzadeh, Tropospheric free-radical determination by FAGE, *Environ. Sci. Technol.*, **18**, pp. 768-777, 1984.

Hard, T.M., C.Y. Chan, A.A. Mehrabzadeh and R.J. O'Brien, Diurnal HO₂ cycles at clean-air and urban sites in the troposphere, *J. Geophys. Res.*, **97**, pp. 9785-9794, 1992.

Harder, J.W., J.W. Brault, P.V. Johnston, and G.H. Mount, Temperature Dependent NO₂ Cross Sections at High Spectral Resolution, *J. Geophys. Res.*, **102**, pp. 3861-3879, 1997.

Harris, J.M., S.J. Oltmans, E.J. Dlugokencky, P.C. Novelli, B.J. Johnson and T. Mefford, An Investigation into the Source of the Upper Troposphere Ozone Maximum at the Mauna Loa Observatory, *Geophysical Research Letters*, **25**, pp. 1895-1898, 1998.

Hartley, W.N., On the Absorption of Solar Rays by Atmospheric Ozone. *Journal of the Chemical Society*, **39**, p111, 1881.

Hoell, J.M., D.D. Davis, S.C. Liu, R. Newell, M. Shipham, H Akimoto, R.J. McNeal, R.J. Bendura RJ, and J.W. Drewry, Pacific exploratory Mission-West A (PEM-West A): September October 1991, *J. Geophys. Res.*, **101**, pp.1641-1653, 1996.

Hofzumahaus, A., T. Brauers, U. Platt and J. Callies, Latitudinal Variation of the Measured O₃ Photolysis Frequencies j -(O¹D) and Primary OH Production Rates over the Atlantic Ocean between 50°N and 30°S. *J. Atms. Chem.*, **8**, pp. 203-227, 1992-A.

Hofzumahaus, A., T. Brauers, U. Platt and J. Callies, Latitudinal Variation of Measured j -(NO₂) Rates over the Atlantic Ocean between 50°N and 30°S. *J. Atms. Chem.*, **15**, pp. 269-282, 1992-B.

Hofzumahaus, A., A. Kraus and M. Müller, Solar Actinic Flux Spectroradiometry: A Technique for the measurement of Photolysis Frequencies in the Atmosphere, *Applied Optics*, **38**, N° 21. pp. 4443- 4461, 1999.

Hofzumahaus, A., B. Bohn, B. Mayer, P. S. Monks, G.D. Edwards, S. Hall, B. Lefer, R.E. Shetter *et al.* Measurement of Photolysis Frequency $j\text{-}(O^1D)$ at the The International Photolysis Modelling and Measurement Intercomparison, *Submitted to J. Geophys. Res.*, 2000.

Houzeau, A., Preuve de la presence dans l'atmosphere d'un nouveau principe gazeux, l'oxygene naissant. *Academic Society of Paris*, **46**, p 89, 1858.

Hough, A.M., The Development of a Two Dimensional Global Tropospheric Model, *Atmospheric Environment*, **23**, 6, pp. 1235 – 1262, 1988.

Hov, Ø., F. Flatøy, J.S. Foot, K. Dewey, P.S. Monks, H. Richer, B. Bandy, A. Kaye, G.P. Mills, S. Bauguitte, S.A. Penkett *et al.*, Testing Atmospheric Chemistry in Anticyclones (TACIA), *Final Report*, Contract No. ENV4-CT95-0038, CEC Brussels (1998).

Hov, Ø., F. Flatøy, J.S. Foot, K. Dewey, H. Richer, P.S. Monks, G.D. Edwards, T.J. Green, N. Brough, G.P. Mills, B. Bandy, S.A. Penkett *et al.*, Maximum Oxidation Rates in the FT (MAXOX), *Final Report*, Contract No. ENV4-CT97-0525, CEC Brussels (2000).

Hübner, G., D. Perner, U. Platt, A. Thoennissen and D.H. Ehhalt, Ground Level OH Radical Concentrations: New Measurements by Optical Absorption. *J. Geophys. Res.*, **89**, pp. 1309-1319, 1984.

Jaeglé, L., D.J. Jacob, P.O. Weenber, C.M. Spivakovsky, T.F. Hanisco, E.J. Lanzendorf, E.J. Hinst, D.W. Fahey, Observed OH and HO₂ in the Upper Troposphere Suggesting a Major Source from Convective Injection of Peroxides. *Geophysical Research Letters*, **24**, pp. 3181-3184, 1997.

Jaeglé, L., D.J. Jacob, W.H. Brune, D. Tan, I.C. Faloona, A.J. Weinheimer, B.A. Ridley, T.L. Campos and G.W. Sachse, E.R. Keim, M.H. Proffitt, E.L. Atlas, F. Flocke, S. Schauffler, C.T. McElroy, C. Midwinter, L. Pfister, J.C. Wilson Sources of HO_x and Production of Ozone in the Upper Troposphere Over the United States. *Geophysical Research Letters*, **25**, pp. 1709-1712, 1998.

Jaeglé, L., D.J. Jacob, Brune W.H., I.F. Faloona, D. Tan, Y. Kondo, G.W. Sachse, , B. Anderson, G.L. Gregory S. Vay, H.B. Singh, D.R. Blake and R. Shetter, Ozone Production in the Upper Troposphere During SONEX: Approach of NO_x Saturated Conditions, *Geophysical Research Letters*, **26**, pp. 3081-3084, 1999.

Jaeglé, L. D.J. Jacob, W.H. Brune. I. Faloona, D. Tan, B.G. Heikes, Y. Kondo, G.W. Sachse, B. Anderson G.L. Gregory, H.B. Singh, R. Pueschel, G. Ferry, D.R. Blake and R.E. Shetter, Photochemistry of HO_x in the Upper Troposphere at Northern Midlatitudes, *J. of Geophys. Res.*, **105**, pp. 3877-3892, 2000.

Jacob, D.J., J.A. Logan, G.M. Gardener, R.M. Yevich, C.M. Spivakovsky, S.C. Wofsy, S. Sillman and M.J. Prather, Factors Regulating Ozone Over the USA and its Export to the Global Troposphere, **98**, pp. 14 817-14 826 1993.

Jacob, D.J., B.G. Heikes, S.M Fan, J.A. Logan, D.L. Mauzerall, J.D. Bradshaw, H.B. Singh, G.L. Gregory, R.W. Talbot, D.R. Blake and G.W. Sachse, Origins of Ozone and NO_x in the Tropical Troposphere, Aircraft Observations over the Southern Atlantic. *J. Geophys. Res.*, **101**, pp. 24,235 – 24,250, 1996.

Junge, G.E. The Global Ozone Budget and Exchange Between the Stratosphere and Troposphere, *Tellus*, **14**, pp. 363-377, 1962.

Junkerman, W., U. Platt and A. Voltz-Thomas, A Photoelectric Detector for the Measurement of Photolysis Frequencies of Ozone and other Atmospheric Molecules., *J. Atms. Chem.*, **8**, pp. 203-227, 1989.

Kleinman, L.I., Seasonal Dependence of Boundary Layer Peroxide Concentration, Low and High NO_x regimes. *J. Geophys. Res.*, **96**, pp. 20721-20733, 1991.

Klemm, O., W.R. Stockwell, H.Schlager, and M. Krautstrunk, NO_x or VOC limitation in East German ozone plumes? *J. Atms Chem.*, **35**, pp.1-18, 2000.

Knapp., K.G, M.L. Jensen, B.B. Bognar, S.J. Oltmans, T.W. Smith and J.W. Birks, Observation of Dry O₃ rich Plumes in the Free Troposphere, *J. Geophys. Res.*, **103**, pp. 13,389 – 13,397, 1998.

Koike, M., Y. Kondo, H. Ikeda, G.L. Gregory, B.E. Anderson, G.W. Sachse, D.R. Blake, S.C. Liu, H.B. Singh, A.M. Thompson, K. Kita, Y. Zhao, T. Sugita, R.E. Shetter and N.Toriyama, Impact of aircraft emissions on reactive nitrogen over the North Atlantic Flight Corridor region, *J. Geophys. Res.*, **105**, pp. 3665-3677 2000.

Kondo, Y., S. Kawakami, M. Koike, D.W. Fahey, H. Nakajima, Y. Zhao, N. Toriyama, M. Kanada, G.W. Sachse, and G.L. Gregory, Performance of an aircraft instrument for the measurement of NO_y, *J. Geophys. Res.*, **102**, pp. 28 663-28 671, 1997.

Kraus, A. and A. Hofzumahaus, Field Measurements of Atmospheric Photolysis Rates by UV Spectroradiometry. *J. Atms. Chem.*, **31**, pp. 161-180, 1998.

Kraus, A., F. Rohrer and A. Hofzumahaus, Intercomparison of NO₂ Photolysis Frequency Measurement by Actinic Flux Spectroradiometry and Chemical Actinometry during JCOM97, *Geophysical Research Letters*, **27**, pp. 1115-1118, 2000.

Law, K.S., P.H. Plantevin, V. Thouret, A. Marenco, W.A.H. Asman, M. Lawrence, P.J. Crutzen, J.F. Muller, D.A. Hauglustaine and M. Kanakiodu, Comparisons Between Global Chemistry Transport Model results and Measurement of Ozone and Water Vapour by Airbus In-Service Aircraft (MOZAIC) data, *J. Geophys. Res.*, **105**, pp. 1503-1525, 2000.

Levy, H. Photochemistry of the Lower Troposphere, *Planetary Space Science*, **20**, pp. 919-935, 1972.

Levy, H. Photochemistry of Minor Constituents in the Troposphere, *Planetary Space Science*, **21**, pp. 575- 591, 1973.

Levy, H., J.D. Mahlman, W.J..Moxim and S.C. Lui, Troposphere Ozone: The Role of Transport, *J. Geophys. Res.*, **90**, pp. 3753-3772, 1985.

- Leighton, P.A., Photochemistry of Air Pollution, *New York Academic Press*, 1961.
- Logan, J.A. Tropospheric Chemistry, A Global Perspective, Abstracts of Papers to the American Chemical Society, **182**, pp.78-PHYS, 1981.
- Liang, J.Y., L.W Horowitz, D.J. Jacob, W.H. Wang, A.M. Fiore, J.A. Logan, G.M. Gardner, J.W. Munger, Seasonal budgets of reactive nitrogen species and ozone over the United States, and export fluxes to the global atmosphere, *J. Geophys. Res.*, **103**, pp. 13435-13450, 1998.
- Liao, H., Y.L. Yung, and J.H Seinfeld, Effects of aerosols on tropospheric photolysis rates in clear and cloudy atmospheres, *J. Geophys. Res.*, **104**, pp.23697-23707, 1999.
- Logan, J.A., Tropospheric Ozone, Seasonal Behavior, Trends and Anthropogenic Influence, *J. Geophys. Res.*, **90**, pp.463-482, 1985.
- Lowe, D.C. and U. Schmidt, Formaldehyde Measurements in the Non-Urban Atmosphere, *J. Geophys. Res.*, **88**, pp.844-858, 1983.
- Lui, S.C., M. Trainer, F. Fehsenfeld, D. Parrish, E.J. Williams, D.W. Fahey, G Hübler and P.C. Murphy, Ozone Production in the Free Troposphere and Implications for Regional and Global Distributions, *J. Geophys. Res.*, **92**, pp. 4191-4207, 1987.
- Madronich, S., Photodissociation in atmosphere, Actinic flux and the effect of Ground Reflections and Clouds., *J. Geophys. Res.*, **92**, pp. 9740-9752, 1987.
- Madronich, S. and G. Weller, Numerical intergration Errors in Calculated Tropospheric Photolysis Coefficients, *J Atms. Chem.* **10**, pp. 289-300, 1990.
- Madronich, S., and S.J. Flocke, The Role of Solar Radiation in Atmospheric Chemistry *Handbook of Environmental Chemistry*, Vol. II, Part L, Reactions and Processes, ed. P. Boule, pp. 1-26, Springer-Verlag, Heidelberg, 1997.
- Madronich, S., *Tropospheric Ultra Violet Visible Radiation Model*, available at <http://acd.ucar.edu/models/UV/TUV/index.html>, 1999

Malicet, J., D. Daumont, J. Charbonnier, C. Parisse, A. Chakir, and J. Brion, Ozone U.V. Spectroscopy II.: Absorption cross-sections and temperature dependence. *J. Atmos. Chem.*, **21**, pp. 263-273, 1995.

Marenco, A., V. Thouret, P. Nédélec, H. Smit, M. Helten, D. Kley, F. Karcher, P. Simon, K. Law, J. Pyle, G. Poschmann, R. Von Wrede, C. Hume and T. Cook, Measurement of Ozone and Water Vapour by Airbus In-Service Aircraft: The MOZAIC Airbourne Program, An Overview, *J. Geophys. Res.*, **103**, pp. 25,631-25,643, 1998.

Mather, J.H., P.S. Stevens and W.H. Brune, OH and HO₂ Measurements using Laser-Induced Fluorescence, *J. Geophys. Res.*, **102**, pp. 6427-6436, 1997.

Matthijsen, K., K. Suhre, R. Rosset, F.L. Eisele, R.L. Mauldin, and D.J. Tanner, Photodissociation and Radiative Transfer in a cloudy Atmosphere: Modeling and Measurements, *J. Geophys. Res.*, **103**, pp. 16 665- 16 676, 1998.

Mauldin, R.L., S. Madrinoch, S.J.Flocke and F.L. Eisele, New insights on OH: Measurements in and around Clouds. *Geophysical Research Letters*, **24**, pp. 3033-3036, 1997.

McKeen, S.A., G.H. Mount, F. Eisele, E. Williams, J. Harder, P. Goldan, W. Kuster, S.C. Liu, K. Brumaunn, D. Tanner, A. Fried, S. Sewell, C. Cantrell and R. Shetter, Photochemical Modelling of the Hydroxyl Radical and it's Reltionships to other Species during the Tropospheric OH Photochemistry Experiment. *J. Geophys. Res.*, **102**, pp. 6467 – 6493, 1997.

McElroy, C.T., C. Midwinter, D.V. Barton and R.B. Hall, A Comparison of J values from the composition and Photodissociative Flux Measurements with Model Calculations, *Geophysical Research Letters*, **22**, pp. 1365-1368, 1995.

Merrill, J.T., J.L. Moody JL, S.J Oltmans and H. Levy(III), Meteorological Analysis of Tropospheric Ozone Profiles at Bermuda, *J. Geophys. Res.*, **101** pp. 29 201-29 211, 1996.

Michelson, R.A., R.J. Salawitch, P.O. Wennberg, and J.G. Anderson, Production of O(¹D) from the Photolysis of O₃. *Geophysical Research Letters*, **21**, pp. 2227-2230, 1994.

Molina, M.J. and F.S. Rowland, Stratospheric Sink for Chlorofluoromethane: Chlorine Catalysed Destruction of Ozone. *Nature*, **249**, pp. 810-812, 1974.

- Molina, M.J. and L.T. Molina, Absorption Cross Sections of Ozone in the 185 to 350nm Wavelength Range, *J. Geophys. Res.*, **91**, pp. 14 501-14 508, 1986.
- Monks, P.S., L.J. Carpenter and S.A. Penkett, Night-time Peroxy Radical Chemistry in the Remote Marine Boundary Layer. *Geophysical Research Letters*, **23**, pp. 535-538, 1996.
- Monks, P.S., L.J. Carpenter and S.A. Penkett, Fundamental Ozone Chemistry in the Remote Marine Boundary Layer: The SOAPEX experiment, Measurement and Theory, *Atms Environment*, **32**, pp.3647-3664, 1998.
- Monks, P.S., G. Salisbury, G. Holland, S.A. Penkett, G.P.Ayers, A seasonal comparison of ozone photochemistry in the remote marine boundary layer, *Atmosphere Environment*, **34**, pp.2547-2561, 2000.
- Monks, P.S. A Review of the Observations and Origins of the Spring Ozone Maximum, *Atmospheric Environment*, **34**, pp. 3545-3561, 2000.
- Mount, G.H. and E.J. Williams, An Overview of the Tropospheric OH Photochemistry Experiment, Fritz Peak/Idaho Hill, Colorado during Fall 1993. *J. Geophys. Res.*, **105**, pp. 6171- 6186. 1997.
- Müller, M., A Kraus and A. Hofzumahaus, $O_3 \rightarrow O(^1D)$ Photolysis Frequencies Determined from Spectroradiometric Measurements of Solar Actinic UV Radiation. *Geophysical Research Letters*, **22**, pp. 679-682, 1995.
- Nicholls, S. Measurements of Turbulence by Aircraft in a Convective Boundary Layer Over the Sea. *Quarterly Journal of the Royal Met. Society*, **104**, pp. 653-676, 1978.
- Nordeng, T.E., A Hierarchy of Non Linier Filter Models, *Monthly Weather Review*, **112**, 10, pp. 2048-2059, 1984.
- Northalt, J., G.C. Toon, C.P. Rinsland, N.S. Pougatchev, N.B. Jones, B.J. Connor, R. Weller, M. Gautrois and O. Schrems, Latitudinal Variations of Trace Gas Concentrations in the Free Troposphere Measured by Solar Absorption Spectroscopy During a Ship Cruise, *J. Geophys. Res.*, **105**, pp. 1337-1349, 2000

Oltmans, S.J. Surface Ozone Measurements in Clean Air, *J. Geophys. Res.*, **86**, pp. 1174-1180 1981.

Oltmans, S.J. and H. Levy(III), Surface Ozone Measurements from a Global Network, *Atmospheric Environment*, **28**, pp. 9-24, 1994.

Oltmans, S.J., H. Levy II, J.M. Harris, J.T. Merrill, J.L. Moody, J.A. Lanthrop, E. Cuevas, M.Trainer, M.S. O'Neill, J.M. Prospero, H. Vömel and B.J. Johnson, Summer and Spring Ozone Profiles over the North Atlantic from Ozonesonde Measurements, *J. Geophys. Res.*, **101**, pp. 29,179-29,200, 1996.

Oltmans, S.J., A.S Lefohn, H.E. Scheel, J.M. Harris, H. Levy II, I.E. Galbally, E.G. Brunke, C.P. Mayer, J.A. Lanthrop, B.J. Johnson, D.S. Shadwick, E. Cuevas, F.J. Schmidlin, D.W. Tarasick, H. Claude, J.B. Kerr, O. Uchino and V. Mohnen, Trends in Ozone in the Troposphere, *Geophysical Research Letters*, **25**, pp. 143-146, 1998.

O'Sullivan, D.W., B.G. Heikes. M. Lee, W. Chang, G.L. Gregory, D.R. Blake and G.W. Sachse, Distribution of Hydrogen Peroxide and Methylhydrogenperoxide over the Pacific and Southern Atlantic Oceans, *J. Geophys. Res.*, **104**, pp. 5635-5646, 1999.

Parrish, D.D., J.S. Holloway, M. Trainer, P.C. Murphy, G.L. Forbes and F.C. Fehsenfeld, Export of North American Pollution the the North Altantic Ocean, *Science*, **259**, pp. 1436-1439, 1993.

Parrish, D.D., M. Trainer, J.S. Holloway, J.E. Yee, M.S. Warshawsky and F.C. Fehsenfeld, Relationships between Ozone and Carbon Monoxide at Surface sites in the North Atlantic Region. *J. Geophys. Res.*, **103**, pp. 13,357-13,376, 1998.

Penkett, S.A., and K.A. Brice, The Spring Maximum of Photo-oxidants in the Northern Hemisphere Troposphere, *Nature*, **319**, pp. 655-657, 1986.

Penkett, S.A., P.S. Monks, L.C. Carpenter, K.C. Clemitshaw, G.P. Ayers. R.W. Gillett, I.E. Galbally and C.P. Mayer, Relationships between Ozone Photolysis and Peroxy Radical Concentration in Clean Marine Air over the Southern Ocean. *J. Geophys. Res.*, **102**, pp.12 805-12 817, 1997.

Penkett, S.A., C.E. Reeves, B.J Bandy, J.M. Kent and H. Richer, Comparison of Calculated and Measured Peroxide Data Collected in Marine Air to Investigate Prominat Features of the Annual Cycle of Ozone, *J. Geophys. Res.*, **103**, pp. 13 377- 13 388, 1998.

Perner, D., U. Platt, M. Trainer, G. Huebler, J. Drummond, W. Junkermann, W. Rudolf, B. Schubert, A. Voltz, D.H. Ehhlat, K.J. Rumble and G Helas, Measurements of Troposphere OH Concentration: A Comparison of Field Data and Model Predictions, *J. Atmos Chem*, **5**, pp. 185-216, 1987.

Perros, P.E., Large Scale Distribution of Hydrogen Peroxide from Aircraft Measurments During TROPOZ II. *Atmospheric Environment*, **27A**, pp. 1695-1708, 1993.

Peterson, M.C., R.E. Honrath, D.D. Parrish and S.J. Oltmans, Measurements of Nitrogen Oxides and Modelling of NO_y in the Remote Northern Atlantic, *J. Geophys. Res.*, **103**, pp.13 489-13 504, 1998.

Platt, U., M. Rateike, W. Junkermann, J. Rudolf and D.H. Ehhalt, New Tropospheric OH Measurements, *J. Geophys. Res.*, **93**, pp. 5159-5166, 1988.

Plas-Dülmer C., T. Brauers and J. Rudolph., POPCORN: A Field Study pf Photochemisty in North Eastern Germany, *J. Atms. Chem.*, **31**, pp. 5-31, 1998.

Rickard, A.R., G. Salisbury, P.S. Monks, *et al.* Comparison of Measured Ozone Production Efficiencies in the Marine Boundary Layer under Polluted Regimes, *manuscript in preparation*, 2000.

Ruggaber, A., R. Dlugi and T. Nakajima, Modelling Radiation Quantities and Photolysis Frequencies in the Troposphere. *J. Atms. Chem.*, **18**, pp. 171-210, 1994.

Schonbien, C.F., Recherches sur la nature de l'odeur qui se manifeste dans certaines actions chimiques, *Academic Society of Paris*, **10**, p706, 1840.

Schultz, M., R. Schmitt, K. Thomas and A. Volz-Thomas, Photochemical Box Modelling of long Range Transport from North America to Tenerife During the Northern Atlantic Regional Experiment (NARE) 1993, *J. Geophys. Res.*, **103**, pp. 13 477- 13 488, 1998.

Saunders, R.W., G. Brogniez, J.C. Buriez, R. Meerkotter and P. Wendling, A Comparison of Measured and Modelled Aircraft data during ICE '89. *Journal of Atmospheric and Oceanic Technology*, **9**, pp. 391 – 406, 1992.

Schere, K.L. and K. Demerjian, A Photochemical Box Model for Urban Air Quality, *Proceedings of the 4th Joint Conference on Sensing of Environmental Pollutants*, pp. 427-433, Washington D.C., 1978.

Schonbien, C.F., Recherches sur la nature de l'odeur qui se manifeste dans certaines actions chimiques, *Academic Society of Paris*, **10**, p706, 1840.

Schuepbach, E., T.D. Davies and A.C. Massacand, An Unusual Springtime Ozone Episode at High Elevation in the Swiss Alps: Contributions from Cross Tropopause Exchange and from the Boundary Layer. *Atmospheric Environment*, **33**, pp. 1735-1744, 1999.

Seinfeld, J.H. and S.N. Pandis, *Atmospheric Chemistry and Physics*, John Wiley & Sons, 1997.

Shetter, R.E., C. A. Cantrell, K.O. Lantz, S.J. Flocke, J.J. Orlando, G.S. Tyndall, T.M. Gilpin, C.A. Fischer, S. Madronich, J.G. Calvert and W. Junkermann, Actinometric and Radiometric and Modelling of Photolysis Coefficient of Ozone to O(¹D) during MLOPEX 2. *J. Geophys. Res.*, **101**, pp. 14 631-14 641, 1996.

Shetter, R.E. and M. Müller, Photolysis Frequency Measurements using Actinic Flux Spectroradiometry during PEM-Tropics. *J. Geophys. Res.*, **104**, pp. 5647-5661, 1999.

Singh, H.B., D. O'Hara, D. Herlth, W. Sachse, D.R. Blake, J.D. Bradshaw, M. Kanakidou and P.J. Crutzen, Acetone in the Atmosphere: Distribution, Sources and Sinks. *J. Geophys. Res.*, **99**, pp. 1805-1819, 1995.

Singh, H.B., M. Kandaidou, P.J. Crutzen and D.J. Jacob, High Concentrations and Photochemical Fate of Oxygenated Hydrocarbons in the Global Troposphere. *Nature*, **378**, pp. 50-53, 1997.

Singh, H.B., A.M. Thompson and H. Schlager, SONEX Airbourne Missions and Coordinated POLINAT-2 Activities: Overview and Accomplishments, *Geophysical Research Letters*, 26, pp. 3053-3056 1999.

Simpson, I.J., B.C Sive, D.R. Blake, N.J. Blake, T.Y Chen, J.P. Lopez, B.E. Anderson, G.W. Sachse, S.A. Vay, H.E Fuelberg, Y. Kondo Y, A.M Thompson, and F.S. Rowland, Nonmethane hydrocarbon measurements in the North Atlantic Flight Corridor during SONEX, *J. Geophys. Res.* **105**, pp. 3785-3793, 2000.

Slaper, H., H.A.J.M. Reinen, M. Blumthaler, M. Huber and F. Kuik, Comparing ground-level Spectrally Resolved Solar UV Measurements Using Various Instruments, *Geophysical Research Letters*, **22**, pp. 2721-2724, 1995.

Stamnes, K., S.-C. Tsay, W. Wiscombe, and K. Jayaweera, Numerically stable algorithm for discrete-ordinate method radiative transfer in multiple scattering an emitting layered media, *App. lied Optics*, **27**, pp. 2502-2509, 1988.

Stull, R.B. *An Introduction to Boundary Layer Meterology*, Kluwer Academic Press, 2-5, 1988.

Swartz, W.H., S.A. Lloyd, T.L. Kusterer, D.E. Anderson, C.T. McElroy and C. Midwinter, A Sensitivity Study of Photolysis Rate Coefficients During POLARIS, *J. Geophys. Res.*, **104**, 26 pp. 725-26 735, 1999.

Tan, D., I. Faloona, W.H. Brune, A. Weinheimer, T. Campos, B. Ridley , S Vay, J Collins and G.Sachse, *In-situ* measurements of HO_x in aircraft exhaust plumes and contrails during SUCCESS. *Geophysical Research Letters*, 25, pp. 1721-1724 , 1998.

Talukdar, R.K., C. Longfellow, M. Gilles and A.R. Ravishankara, Quantum Yields of O(¹D) in the Photolysis of Ozone Between 289 and 329nm as a Function of Temperature, *Geophysical Research Letters*, **25**, pp. 143 – 146, 1998.

Talbot, R.W., J.E. Dibb, B.L. Lefer, J.D. Bradshaw, S.T. Sandholm, D.R. Blake, N.J. Blake, G.W. Sachse, J.E. Collins, B.G. Heikes, J.T. Merrill, G.L. Gregory, B.E. Anderson, H.B. Singh, D.C. Thornton, A.R. Bandy and R.F. Pueschel, Chemical characteristics of continental outflow from Asia to the troposphere over the western Pacific Ocean during February-March 1994: Results from PEM-West B, *J. Geophys. Res.*, **102**, pp.28255-28274, 1997.

Talbot, R.W., J.E. Dibb, E.M. Scheuer, Y. Kondo, M. Koike, H.B. Singh, L.B. Salas, Y. Fukui, J.O. Ballenthin, R.F. Meads, T.M. Miller, D.E. Hunton, A.A. Viggian, D.R. Blake, N.J. Blake, E. Atlas, F. Flocke, D.J. Jacob and L. Jaeglé, *Geophysical Research Letters*, **26**, pp.3 057-3 060, 1999.

Talbot, R.W., J.E. Dibb, E.M. Scheuer, J.D. Bradshaw, S.T. Sandholm, H.B. Singh, D.R. Blake, N.J. Blake, E. Atlas and F. Flocke, Troposphere Reactive Nitrogen Over the South Pacific in Austral Springtime, *J. Geophys. Res.*, **105**, pp. 6 6681-6 694, 2000.

Thompson, A.M., K.E. Pickering, R.R. Dickerson, W.G. Ellis, D.J. Jacob, J.R. Scala, W.K. Tao, D. P. McNamara and J. Simpson, Convective Transport over the USA and its role in Regional CO and Ozone Budgets, *J. Geophys. Res.*, **99**, pp. 18 703-18 711, 1994.

Thompson, A.M., H.B. Singh and H. Schlager, Subsonic Assessment of Ozone and Nitrogen Oxide Experiment (SONEX) and Pollution from Aircraft Emissions in the North Atlantic Flight Corridor (POLINAT 2), *J. of Geophys. Res.*, **105**, pp. 3595-3603, 2000.

Toon, O.B., R.P. Turco, D. Westphal, R. Malone and M.S. Liu, a Multidimensional Model for Aerosols, *Journal of the Atmospheric Sciences*, **45**, pp. 2123-2143, 1988.

Tsay, S.C., and K. Stammes, UV radiation and the Impact and Implications for O₃ Depletion and Cloud Effects. *J. Geophys. Res.*, **97**, pp. 7829-7840, 1992.

Van de Hulst, H.C., Multiple Light Scattering, Vol. I and II, *Academic Press*, New York, 1980.

Van Weele, M., and P.G. Duynkerke, Effect of Clouds on the Photodissociation of NO₂, Observations and Modelling, *J. Atms. Chem.*, **16**, pp. 231-255, 1995.

Vay, S.A., B.E. Anderson, G.W. Sachse, J.E. Collins, J.R. Podolske, C.H. Twohy, B. Gandrud, K.R. Chan, S.L. Baughcum, H.A. Wallio, DC-8-based Observations of Aircraft CO, CH₄, N₂O, and H₂O Emission Indices during SUCCESS, *Geophysical Research Letters*, **25**, pp. 1717-1720, 1998.

Vay, S.A., B.E. Anderson, E.J. Jensen, G.W. Sachse, J. Ovarlez, G.L. Gregory, S.R. Nolf, J.R. Podolske, T. A. Slate and C.E. Sorenson Tropospheric water vapor measurements over the North Atlantic during SONEX, *J. Geophys. Res.*, **105**, pp. 3 745-3 755, 2000.

Volz, A and D. Kley, Evaluation of the Montsouris Series of Ozone Measurements made in the 19th Century, *Nature*, **332**, pp.240-242, 1988.

Volz-Thomas, A., A. Lerner, H.S. Patz, M. Schultz, D. McKenna, R. Schmitt, S. Madronich and E. Roth, Airborne Measurements of the Photolysis of NO₂. *J. Geophys. Res.*, **101**, pp. 18 613-18 627, 1996.

Volz-Thomas, A. H. Geiss and N. Kalthoff, Schauinsland Ozone Precursor Experiment (SLOPE96): Scientific background and main results, *J. Geophys. Res.*, **105**, pp. 1553-1561, 2000.

Wang, Y.H., S.C. Liu, H.B. Yu, S.T. Sandholm, T.Y. Chen and D.R. Blake, Influence of Convection and Biomass Burning Outflow on Tropospheric Chemistry over the Tropical Pacific, *J. Geophys. Res.*, **105**, pp. 9321-9333, 2000.

Wayne, L.G., A. Kokin and M. Wiesburd, Controlled Evaluation of the Reactive Environmental Simulation Model, *NTIS Publication PB220456/8*, 1973.

Wayne, R.P., *Chemistry of Atmospheres*, Second edition, Oxford University Press, 1995.

Weinstein-Lloyd, J.B., P.H. Daum, L.J. Nunnermacker, J.H. Lee and L.I. Kleinmann Measurement of Peroxides and Related Species in the 1993 North Atlantic Regional Experiment. *J. Geophys. Res.*, **101**, pp. 29 081- 29090, 1996.

Wennberg, P.O., T.F. Hanisco, L. Jaeglé, D.J. Jacob, E.J. Hinst, E.J. Lanzendorf, J.G. Anderson, R.S. Gao, E.R. Keim, S.G. Donnelly, L.A. Del Negro, D.W. Fahey, S.A. McKeen, R.J. Salawitch, C.R. Webster, R.D. May, R.L. Herman, M.H. Proffitt, J.J. Margitan, E.L.

Atlas, S.M. Schauffler, F. Flocke, C.T. McElroy and T.P. Bui Hydrogen Radicals, Nitrogen Radicals and the Production of O₃ in the Upper Troposphere, *Science*, **279**, pp. 49-51, 1998.

Winkler, P., Surface Ozone over the Atlantic Ocean, *J. Atmos. Chem.*, **7**, pp. 73-91, 1988.

Yienger, J.J., A.A. Klonecki, H. Levy II, W.J. Moxim and G.R. Carmichael, An Evolution of Chemistry's Role in the Winter-Spring Ozone Maximum found in the Northern Midlatitude Free Troposphere, *J. Geophys. Res.*, **104**, pp. 3655-3667, 1999.

Zanis, P. *In-situ* Photochemical Control of Ozone at the Jungfraujoch in the Swiss Alps, *Ph.D. Thesis*, University of Berne Switzerland, 1999.

Zanis P, P.S Monks, E. Schuepbach, S.A Penkett On the relationship of HO₂+RO₂ with *j*-(O¹D) during the Free Tropospheric Experiment (FREETEX '96) at the Jungfraujoch Observatory in the Swiss Alps, *J. Geophys. Res.*, **104**, pp.26 913-26 925, 1999.

Zeng, J., S. Madronich and K. Stamnes, A Note on the use of Two-Stream Delta-Scalling Approximation for the Calculation of Atmospheric Photolysis Rate Coefficients, *Geophysical Research Letters*, **101**, pp. 14 525-14 527, 1996.

Postgraduate Record 1997-2000

Talks and Lectures Attended

5/11/97 "*Dye Sensitised Solar Cells*" by Prof. P. Laurie, University of Bath, UK.

14/11/97 "*Spectroscopy- a Tool for Reaction Analysis*" by Prof. J. Brown, Oxford University, UK.

18/2/98 "*Structure of Molecular Dications*" by Dr. I MacNab, University of Newcastle, UK

26/5/98, The Bourke Lecture, "*High Resolution Spectroscopy and Bond Breaking*", Prof T. Miller, University of Ohio, USA

5/10/98: "*The Role of Chemistry in the Development of Neutron Capture Therapy*" by Prof. M.F. Hawthorne, UCLA, USA.

7/10/98: "*Cavity Ring Down Spectroscopy and it's Applications in Dynamics and Atmospheric Chemistry*", by Dr. A. Orr-Ewing, University of Bristol, UK

26/10/98: "*The Shape of Things to Come*" by Prof. B. Johnson, University of Cambridge, UK.

11/11/98: "*Recent Advances in the Study of Chemical Surfaces and Interfaces by Specular Neutron Reflection*" by Dr. J. Penfold, ISIS, UK.

18/11/98: "*Studies into Atmospheric Photochemistry and the Composition of Clean Air*" by Prof. S. A. Penkett, University of East Anglia, UK.

17/2/99: "*Hydrogen Bonding, from Solubility in Water to the Blood-Brain Barrier*" by Dr. Michael Abraham, University Collage London, UK.

18/2/99: "*Experimentally Determined Properties of Transition Metal Molecules in the Gaseous State*" by Prof. Timothy C. Steimle, Arizona State University, Arizona, USA.

1/3/99: "*The Book, The Disc and The Future*" by Prof. Peter W. Atkins Lincon College, Oxford University, UK.

17/3/99: Third Year Physical Chemistry Research Project student presentations

5/5/99: "*Laser Spectroscopy of Ba-OH and Sr-OH*" by Mr. M. Beardah, Final Year Ph.D. research presentation, University of Leicester, UK

19/5/99: "*Electrochemistry in Supercritical Media*" by Mr. C. Eardly, Final Year PhD research presentation, University of Leicester, UK.

26/5/99: "*Modelling Protein Structure, Function and Dynamics*" by Prof. Rod Hubbard, University of York, UK.

25/5/99: "*LIF spectroscopy of Alkali Metal Oxides*" by Miss A. Little, Final Year Ph.D. research presentation, University of Leicester, UK.

26/5/99: "*Investigations of Transient Molecules and Radicals in the Gas Phase*" by Prof. Frantisek Turecek, University of Washington, USA.

16/6/99: "*Electrochemistry and the EQCM*" by Mr. L. Bailey, Final Year Ph.D. research presentation, University of Leicester, UK.

20/10/99: "*Water Clusters: Little molecules make a big splash!*" by Prof. David Clary, University College London, UK.

17/11/99: "*Timescales in Atmospheric Chemistry*" by Prof. M. Pilling, University of Leeds, UK.

12/1/00: "*Atmospheric Chemistry and the Transport of Ozone Experiment*", first Year Ph.D. Talk by Mr. G.J. Phillips, University of Leicester, UK

16/2/00: "*NMR of liquid crystalline Samples*" by Prof. Jim Emsley, University of Southampton, UK.

3/5/00: Second Year PhD research presentations, University of Leicester, UK.

10/5/00: "*EQCM studies of ridged and non ridged films*", by Miss A. Jackson, Final Year PhD research presentation, University of Leicester, UK.

17/5/00: "*Laser Spectroscopy of Metal Containing Molecules*", by Mr. G. Greetham, Final Year PhD research presentation, University of Leicester, UK.

22/9/00: Research Seminars from potential physical chemistry staff applicants

11/10/00: "*Chaos, Lyapunov and Transport Coefficients*", by Prof D.J. Evans, Australian National University.

18/10/00: "*Peroxy Radical Measurements in the Marine Boundary Layer*", Third Year Research Seminar, Mr. G. Salisbury, University of Leicester, UK.

15/11/00: "*Using Templates to Change the Shape of Macromolecules*", Prof. T.C. Cosgrove, University of Bristol, UK.

22/11/00: "*Exploiting Protein Structure in the Post-Genome Era*", Dr. M.J.E. Sternberg, Imperial Cancer Research Fund, UK.

Lecture Courses Attended

24/9/97 "**Introduction and Safety**" by D. Sutherland (internal postgraduate skills lecture)

26/11/97 "**Use of the Library**" by L. Wilson (internal postgraduate skills lecture)

3/12/97 "**1D NMR**" by Dr. G. Griffith (internal postgraduate skills lecture)

10/12/97 "**2D NMR**" by Dr. G. Griffith (internal postgraduate skills lecture)

11/2/98 "**Lecture Presentation**" by Prof. J.H. Holloway (internal postgraduate skills lecture)

25/2/98 "**The NoE**" by Dr. G. Griffith (internal postgraduate skills lecture)

11/3/98 "**ChemDraw and Powerpoint**" by Prof. P.Cullis (internal postgraduate skills lecture)

18/3/98 "**Intergration of NMR Spectra**" by Dr. G. Griffith (internal postgraduate skills lecture)

Oct-Nov 98: "**C: Programming Introduction**" A lecture course by W. Rathman, Dept. of Earth Observation Science, University of Leicester

2/6/99: "**Endnote**" by Dr. D. Davies, University of Leicester (internal postgraduate skills lecture)

9/6/99 "**Scientific Writing**" by Dr. J. Malpass, University of Leicester (internal postgraduate skills lecture)

16/6/99: "**WIN:NMR**" by Dr. G. Griffith, University of Leicester (internal postgraduate skills lecture)

Meetings and Conferences Attended

26/1/98 - 27/1/98: *Testing Atmospheric Chemistry in Anticyclones (TACIA) Project Final Meeting*, held at the Meteorological Research Flight, Farnborough, UK.

2/3/98 - 3/3/98: *C-130 Users Meeting*, held at The University of Cambridge, UK

17/4/98: *Royal Metrological Society Specialist Group Meeting*, at Imperial College, London, UK

26/5/98: *The Free Radicals in the Oceanic Environment, "FRACAS" meeting*, at University of Leicester, UK.

8/6/98 - 11/6/98: "*Challenges in Tropospheric Photochemistry Workshop*", held at The National Centre for Atmospheric Research (NCAR), Boulder, Colorado, USA, sponsored by the German-American Academic Council.

23/10/98: "*The Southern Ocean Atmospheric Photochemistry Experiment (SOAPEX)-2: final pre-campaign meeting*", held at University of Leicester, UK.

17/12/98: "*First Upper Troposphere/Lower Stratosphere (UTLS) Project meeting*", held at The University of Cambridge, UK

12/7/99 – 17/7/99, "*Atmospheric Chemistry Studies in the Oceanic Environment (ACSOE) Scientific Symposium*" held at The University of East Anglia, Norwich, UK

12/11/99: "*Atmosphere Chemistry and Transport of Ozone (ACTO) Start-up Meeting*", held at The University of Leicester, UK.

15/12/99-17/12/99: "*Third Upper Troposphere/Lower Stratosphere (ULTS) Meeting*", held at the University of Leeds, UK.

1/2/00-2/2/00: "*Final Maximum Oxidation Rates of the Free Troposphere (MAXOX) Meeting*", held at The University of East Anglia, Norwich, UK

17/4/00: *The Royal Meteorological Society: Polluted Troposphere Meeting*, held at University of Leicester, UK.

30/5/00- 3/6/00: *American Geophysical Union Spring Meeting*, held at Washington DC, U.S.A.

13/9/00: *26th Annual Conference of the Remote Sensing Society*, held at University of Leicester.

18/12/00-20/12/00: "*Fourth Upper Troposphere/Lower Stratosphere (ULTS) Meeting*", held at the University of Leicester, UK.

Talks and Presentations Given

14/1/98: First Year Ph.D. Seminar: - "**Aircraft Measurement of Tropospheric Ozone Photolysis**", given to Dept of Chemistry, *University of Leicester*, UK.

27/1/98: - " **j -(O¹D) Radiometers**" at TACIA/MAXOX aircraft meeting, *Farnborough*, UK

17/7/98: "**The IPMMI Experiment**" (at PSM Group Meeting)

20/11/98: "**Characterisation of j -(NO₂) and j -(O¹D) Filter radiometers**" (at PSM group meeting)

28/4/99: "**Aircraft Measurement over the North Atlantic**", Second Year PhD. Progress Seminar, given to Chemistry Dept., *University of Leicester*, UK

25/6/99: "**The Physics and Chemistry of Scattering**" (at PSM group meeting)

10/9/99: "**Aircraft Data Analysis**" (at PSM group meeting)

1/11/99: "**Spring Summer Trace Gas Climatologies**" (at PSM group meeting)

12/11/99: "**Error evaluation for aircraft j -(O¹D) radiometers**" given at ACTO Start-up Meeting, *University of Leicester*, UK

1/2/00-2/2/00: "**Vertical and Horizontal Distribution of Atmospheric Trace Gases Measured during the ACSOE, TACIA and MAXOX Aircraft Campaigns**" given at Final MAXOX Meeting, *University of East Anglia*, Norwich, UK.

14/4/00: "**Planetary Atmospheres**" invited lecture at *Bridgend Astronomical Society*, Bridgend, South Wales, UK.

10/5/2000: Third Year Ph.D. Research Seminar- "**Aircraft Trace Gas Measurements in Clean and Polluted Environments**" given to Chemistry Dept., *University of Leicester*, UK.

1/6/00: "**The Performance of a Single Monochromator Diode Array Spectroradiometer at IPMMI**" given at the American Geophysical Union Spring Conference, Washington D.C., U.S.A.

16/11/00: "**Aircraft Measurements of Atmosphere Chemistry over the Northern Atlantic Ocean**, Summary of Ph.D. Research, Dept of Earth Observation Science, *University of Leicester*, UK.

Field Work

15/6/98 – 19/6/98: The International Photolysis Modelling and Measurement Intercomparison (IPMMI) Experiment, *Marshall Field Site of NCAR*, Boulder, Colorado, U.S.A.

6/4/99 to 11/6/99: The Maximum Oxidation of the troposphere (MAXOX) Aircraft Campaign flying from *RAF Boscombe Down/RAF Lyham*, UK, Mission Scientist in two C-130 Hercules flights.

7/00-7/00 Roof Observations of Ozone and PHotochemistry EXperiment (ROOPHEX) campaign at the *University of Leicester*, UK.

Poster Presentations

"**Aircraft studies of j -(O¹D)**", presented during attendance of *GAAC Workshop*, Boulder, Colorado, USA, June 6-11, 1998.

"**Steady State Analysis of HO_x from Aircraft**", presented at the *ACSOE Scientific Symposium*, UEA, Norwich, July 12-19, 1999

"**Trace Gas Climatologies over the North Atlantic**", presented at the *Third ULTS meeting*, University of Leeds, Dec 15-17, 1999

"**The Role of Temperature Dependence of the Quantum Yield for O₃→O(¹D) in the determination of the photolysis frequency for Ozone from Measurements made during IPMMI**", presented at the *American Geophysical Union Spring Meeting*, Washington D.C., USA, May 30-June 3, 2000.

Publications

"Seasonal Trace Gas Climatologies over the North Atlantic", A contribution to the sub-project TOR-2, 1999.

A.F. Bais, S. Madronich, J. Crawford, J. Calvert, C. Cantrell, R. Shetter, A. Hofzumahaus, P.S. Monks, G.D. Edwards, B. Lefer, *et al.* **"The International Photolysis Modelling and Measurement Intercomparison: Spectral Solar Flux Measurement and Modelling"**, *Submitted to J. Geophys. Res.*, 2000.

G.D. Edwards and P.S. Monks, **"The Performance of a Single Monochromator Diode Array Spectroradiometer at IPMMI: An Evaluation"**, *manuscript in preparation*, 2000.

G.D. Edwards P.S. Monks, B. Bandy, G. Mills, T. Green, S. Bauguitte, H. Richer, K. J. Dewey and S. A Penkett **"Spring and Summer Trace Gas Climatologies over the North Atlantic"**, *manuscript in preparation*, 2000.

A. Hofzumahaus, B. Bohn, B. Mayer, P. S. Monks, G.D. Edwards, S. Hall, B. Lefer, R. Shetter *et al.* **Measurement of Photolysis Frequency j -(O¹D) at the The International Photolysis Modelling and Measurement Intercomparison**, *Submitted to J. Geophys. Res.*, 2000.

Ø. Hov, F. Flatoy, S. Solberg, J.S. Foot, K. Dewey, D. Kley, S.A. Penkett, P.S. Monks, G.D. Edwards, *et al.* **Maximum Oxidation of the Troposphere (MAXOX) Final Report**, Contract No. ENV4-CT97-05025, CEC Brussels (2000).